



On Simulating Ultra-fast Chemical Processes and their Spectroscopic Signatures

Schnack-Petersen, Anna Kristina

Publication date:
2022

Document Version
Publisher's PDF, also known as Version of record

[Link back to DTU Orbit](#)

Citation (APA):
Schnack-Petersen, A. K. (2022). *On Simulating Ultra-fast Chemical Processes and their Spectroscopic Signatures*. DTU Chemistry.

General rights

Copyright and moral rights for the publications made accessible in the public portal are retained by the authors and/or other copyright owners and it is a condition of accessing publications that users recognise and abide by the legal requirements associated with these rights.

- Users may download and print one copy of any publication from the public portal for the purpose of private study or research.
- You may not further distribute the material or use it for any profit-making activity or commercial gain
- You may freely distribute the URL identifying the publication in the public portal

If you believe that this document breaches copyright please contact us providing details, and we will remove access to the work immediately and investigate your claim.

Doctor of Philosophy
PhD thesis in Theoretical Chemistry

DTU Chemistry
Department of Chemistry

On Simulating Ultra-fast Chemical Processes and their Spectroscopic Signatures

Anna Kristina Schnack-Petersen



Supervisor: Prof. Klaus Braagaard Møller

Co-supervisors: Prof. Sonia Coriani & Prof. Henrik Koch

DTU Kemi
Department of Chemistry
Technical University of Denmark
Kemitorvet
Building 207
2800 Kongens Lyngby, Denmark

Resumé

I denne Ph.D. afhandling undersøges forskellige teoretiske metoder til at beskrive kemiske processer vha. røntgenspektroskopi og særligt røntgenabsorption (XAS). Dette inkluderer både metodeudvikling, sammenligning af metoder og analyse af eksperimentel data. I afhandlingen introduceres de vigtigste teoretiske koncepter indenfor elektronstruktur og molekyledynamik samt relevante egenskaber. Sidstnævnte bygger på én molekylestruktur, der bestemmes vha. en molekylegradient. En sådan gradient er som en del af denne afhandling blevet implementeret på coupled cluster singles and doubles (CCSD) niveau for både grundtilstanden og exciterede tilstande. Dermed kan ligevægtsstrukturer bestemmes i begge tilfælde. Derudover er implementeringen grundlaget for at beskrive molekyledynamik på CCSD-niveau. Molekyledynamik er her simuleret vha. tidsafhængig density functional theory (TDDFT) med bl.a. trajectory surface hopping (TSH), der beskriver atomkernerne vha. klassisk mekanik. Det ses, at TSH kan beskrive molekyledynamikken kvalitativt, selv når relativt få bevægelsesbaner simuleres. TSH er ydermere en glimrende basis for at foretage en kvantedynamik-simulering. Til at beskrive forskellige typer af statiske røntgen-spektre er CCSD metoden benyttet. For bl.a. XAS, røntgenfotoelektronspektroskopi og resonant inelastisk røntgenspredning er der generelt stor lighed mellem CCSD baserede resultater og eksperiment. Dette indikerer, at CCSD giver en god beskrivelse af de undersøgte processer. Eksperimentelle spektre af heterocyklen oxazoles grundtilstand blev eksemplevis analyseret vha. CCSD beregninger. Dette er fundamentet for senere at undersøge fotoexcitationen af molekylet med tidsopløst XAS (tr-XAS). I dette studie blev også TDDFT benyttet til at beregne XAS spektre. Denne mindre beregningstunge metode viste sig at beskrive XAS på lige fod med CCSD. Dette blev også senere bemærket i forbindelse med analysen af eksperimentel tr-XAS data for et større molekyle. Simuleringer af tr-XAS baseret på de ovennævnte metoder viste desuden, at det er muligt udelukkende at basere beregningerne på optimerede strukturer, hvis molekylet er relativt stift. Hvis molekylet opholder sig længe i samme elektroniske tilstand, er det endda muligt helt at undgå en dynamikberegning. Detter er dog ikke tilfældet, hvis flere elektroniske tilstande er i spil, idet populationerne af disse tilstande i så fald må bestemmes. For mere bevægelige molekyler må disse konklusioner undersøges yderligere.

Summary

This Ph.D. thesis explores different theoretical methods to describe chemical processes via X-ray spectroscopy with an emphasis on X-ray absorption spectroscopy (XAS). This includes method development, comparisons of methods, and analysis of experimental data. The thesis reviews the theory for describing electronic structure and nuclear dynamics, and the properties of interest are presented. These rely on a single molecular geometry, which is determined by using a molecular gradient. An efficient implementation of such a gradient has been carried out as part of the presented work at the coupled cluster singles and doubles (CCSD) level of theory for both ground and excited states. Thus, the corresponding equilibrium structures can be determined. Also, the implementation lays the ground work for describing nuclear dynamics at the CCSD level of theory. Nuclear dynamics is here simulated with time-dependent density functional theory (TDDFT) using, e.g., trajectory surface hopping (TSH), where nuclei are treated with classical mechanics. This gives a qualitatively good description of the nuclear dynamics, even for a limited number of trajectories. A TSH calculation is also found to be a good basis for a quantum dynamics simulation. The CCSD method was employed to calculate different static X-ray spectra. It showed an overall good agreement with experiment for, e.g., XAS, X-ray photoelectron spectroscopy and resonant inelastic X-ray scattering. This indicates that the method yields a good description of the studied processes. The CCSD method was, for instance, used to analyse experimental ground state spectra of the heterocycle oxazole. This is a first step towards analyzing future time-resolved XAS (tr-XAS) experiments of the system. In the present study, TDDFT was also employed to calculate XAS spectra. Here, this less computationally expensive method turned out to yield results of similar accuracy to CCSD. This was also noticed in the analysis of experimental tr-XAS data for a larger molecule. Moreover, simulations of tr-XAS based on the above mentioned methods, showed that for rigid molecules, tr-XAS can be simulated based on optimized geometries alone. Indeed, when the molecule remains in the same electronic state for a long time, one might even avoid a nuclear dynamics simulation. Several states of interest will, however, require such a simulation to predict the evolution of state populations. These conclusions must be further investigated for less rigid molecules.

Preface

This Ph.D. thesis is the result of the work carried out at the Technical University of Denmark (DTU) from November 1st 2019 until December 2nd 2022 under the joint supervision of professors Klaus B. Møller and Sonia Coriani. At DTU, collaborations with other colleagues, in particular Dr. Mátyás Papái and Dr. Torsha Moitra, were also commenced. Moreover, part of the work for this thesis was carried out during an external stay at the Norwegian University of Science and Technology (NTNU) under the supervision of professor Henrik Koch from August 30th 2021 to November 30th 2021. In addition, collaboration with the group at NTNU, in particular Dr. Eirik Kjørstad, was conducted through online discussions.

Furthermore, a collaboration with researchers at various other institutions, in particular Dr. Anja Röder, was initiated at a virtual summer school and led to a joint experimental and theoretical study.

This thesis has been submitted to the Department of Chemistry at DTU as part of the fulfillment of the requirements for a Ph.D. degree in the field of theoretical chemistry.

Kongens Lyngby, 2nd December 2022



Anna Kristina Schnack-Petersen

Acknowledgements

During the three years I have spent working on this project, I have been lucky enough to be surrounded by many talented people. You have all, in your own way, contributed to this final product by inspiring and teaching me as well as by encouraging and in other ways supporting me.

Firstly, I would like to thank my supervisors at DTU, profs. Klaus B. Møller and Sonia Coriani, for always finding time for engaging science discussions despite their busy schedules. You have both taught me a lot, and I appreciate the collaboration we have had. I would also like to thank my co-supervisor, prof. Henrik Koch, at NTNU for interesting collaboration, an excellent course on coupled cluster theory, and the opportunity to visit his amazing group at NTNU.

Furthermore, I wish to thank Torsha, Mátyás, Eirik, and Anja for good and fruitful collaborations. Particularly, I would like to thank Mátyás for patiently introducing me to the SHARC and MCTDH programs, which have been an essential part of this thesis. Also, I would like to thank Eirik for receiving me at NTNU for my external stay and for introducing me to the code of the e^T program in which all of the implementation work presented here has been carried out.

Next, I would like to thank the entire theoretical chemistry group at DTU for creating a good work environment - especially Josefine and Torsha. The Ph.D. study would not have been the same without you. Moreover, I would like to extend a special thank you to Josefine for not only providing moral support, but for also taking the time to give me feedback on sections of this thesis. In addition, I would like to thank the theoretical chemistry group at NTNU, and in particular Regina, for making me feel so very welcome during my external stay. I hope we will all meet again in the future. Furthermore, I wish to thank the Ultrafast Materials Physics group at DTU Physics for interesting group meetings and a good beamtime experience at SwissFEL.

Finally, I must also thank my parents and Mathias for always supporting me and believing in me through all my ups and downs.

List of Publications

Publications included in this thesis

1. "Efficient implementation of molecular CCSD gradients with Cholesky-decomposed electron repulsion integrals"
Anna Kristina Schnack-Petersen, Henrik Koch, Sonia Coriani and Eirik F. Kjønstad
J. Chem. Phys., 2022, **156**, 24411
2. "Core spectroscopy of oxazole"
Anna Kristina Schnack-Petersen, Bruno N. Cabral Tenorio, Sonia Coriani, Piero Decleva, Jan Troß, Krupa Ramasesha, Marcello Coreno, Roberta Totani and Anja Röder
J. Chem. Phys., 2022, **157**, 214305
3. "Azobenzene photoisomerization dynamics: Revealing the key degrees of freedom and the long timescale of the trans-to-cis process"
Anna Kristina Schnack-Petersen, Mátyás Pápai and Klaus Braagaard Møller
J. Photoch. Photobio. A, 2022, **428**, 113869

Manuscripts included in this thesis

1. "New Implementation of an Equation-of-Motion Coupled Cluster Damped-Response Framework with Illustrative Applications to Resonant Inelastic X-ray Scattering"
Anna Kristina Schnack-Petersen, Torsha Moitra, Sarai D. Folkestad and Sonia Coriani
Submitted to J. Phys. Chem. A, November 2022
2. "A theoretical study of the time-resolved X-ray absorption spectra of the photoionized BT-1T cation"
Anna Kristina Schnack-Petersen, Mátyás Pápai, Sonia Coriani and Klaus Braagaard Møller
To be submitted to Struct. Dynam.

Work in progress discussed in this thesis

1. "An experimental and theoretical investigation of BT-1T based on time-resolved X-ray absorption spectroscopy"
Suraj Manikandan, Camila Bacellar Cases da Silveira, Emma V. Beale, Claudio Cirelli, Sonia Coriani, Asmus O. Dohn, Kristoffer Haldrup, Bianca L. Hansen, Morten L. Haubro, Phillip Johnson, Victoria Kabanova, Abdullah Kahraman, Theresa I. M. Kapunan, Kerstin Mitterer, Klaus B. Møller, Martin M. Nielsen, Anna Kristina Schnack-Petersen and Jens Wenzel Andreassen
2. "Molecular CCSD gradients with Cholesky-decomposed electron repulsion integrals for core excited states"
Anna Kristina Schnack-Petersen, Henrik Koch, Sonia Coriani and Eirik F. Kjørstad

Publications not included in this thesis

1. "The Second-Order-Polarization-Propagator-Approximation (SOPPA) in a four-component spinor basis"
Anna Kristina Schnack-Petersen, Mats Simmermacher, Elke Fasshauer, Hans Jørgen Aa. Jensen and Stephan P. A. Sauer
J. Chem. Phys., 2020, **152**, 134113
2. "RPA(D) and HRPA(D): calculation of carbon-carbon spin-spin coupling constants for saturated cycloalkanes"
Christoffer H. S. Møller, Anna Kristina Schnack-Petersen and Stephan P. A. Sauer
Mol. Phys., 2020, **118**, 19-20

Abbreviations

AES	Auger-Meitner electron spectroscopy
AIMS	Ab initio multiple spawning
BOA	Born-Oppenheimer approximation
BT-1T	4-(2-thienyl)-2,1,3-benzothiadiazole
CC	Coupled cluster
CC2	Second-order approximate coupled cluster singles and doubles
CCSD	Coupled cluster singles and doubles
CCSD(T)	Coupled cluster singles and doubles with approximate triples
CHELPG	Charges from electrostatic potentials using a grid-based method
CI	Conical intersection
CVS	Core-valence-separation
CVS-uS	Core-valence-separation with valence uncoupled singles
DFT	Density functional theory
DOF	Degree of freedom
EOM	Equation-of-motion
EXAFS	Extended X-ray absorption fine structure
fc	Frozen core
IMOM	initial maximum overlap method
HF	Hartree-Fock
HOMO	Highest occupied molecular orbital

HWHM	Half width at half maximum
KS	Kohn-Sham
LR	Linear response
LUMO	Lowest unoccupied molecular orbital
MCH	Molecular Coulomb Hamiltonian
MCTDH	Multi-configurational time-dependent Hartree
MOM	Maximum overlap method
NEXAFS	Near-edge X-ray absorption fine structure
PES	Potential energy surface
QY	Quantum yield
RASPT2	Restricted-active-space perturbation theory of second order
RIXS	Resonant inelastic X-ray scattering
RPA	Random phase approximation
SCF	Self consistent field
SH	Surface hopping
SOMO	Singly occupied molecular orbital
TDA	Tamm-Dancoff approximation
TDDFT	Time-dependent density functional theory
TDH	Time-dependent Hartree
TDHF	Time-dependent Hartree-Fock
UV-Vis	Ultraviolet and visible
XAS	X-ray absorption spectroscopy
XANES	X-ray absorption near edge spectroscopy
XES	X-ray emission spectroscopy
XPS	X-ray photoelectron spectroscopy

Contents

Resumé	i
Summary	iii
Preface	v
Acknowledgements	vii
List of Publications	ix
Abbreviations	xi
Contents	xiii
Introduction	1
I Theoretical Concepts	5
1 Describing the Molecular System	7
1.1 The Ground State	9
1.1.1 Hartree-Fock	10
1.1.2 Coupled Cluster Theory	11
1.1.3 Density Functional Theory	13
1.2 Properties and Excited States	14
1.2.1 Response Theory	15
1.2.2 TDDFT	18
1.2.3 Equation-of-Motion CCSD	19
1.2.4 Maximum Overlap Method	22
2 Molecular Properties of Interest	25

2.1	Molecular Gradients	25
2.2	X-ray Absorption, Emission and Photoelectron Spectroscopy. . . .	27
2.2.1	XAS	27
2.2.1.1	Core-Valence-Separation	28
2.2.1.2	Frozen Core	29
2.2.1.3	Transition Moments and Oscillator Strengths	29
2.2.2	XPS	29
2.2.3	XES	30
2.3	RIXS	31
2.3.1	Complex Damped Response Solver	32
2.4	Auger-Meitner Electron Spectroscopy	32
2.5	Line Broadening	33
3	Nuclear Dynamics	35
3.1	Surface Hopping	37
3.2	Multi-Configurational Time-Dependent Hartree	42
II	Results	45
4	Static Spectra	47
4.1	Oxazole	47
4.2	RIXS	48
4.3	BT-1T	49
4.3.1	Neutral Molecule	50
4.3.2	Cation	58
5	Nuclear Dynamics Simulations	61
5.1	Azobenzene	61
5.2	BT-1T	62
6	Time-resolved Spectra	65
6.1	Neutral BT-1T	65
6.2	BT-1T ⁺	73
	Outlook and Conclusions	75
	Appendices	79
	Appendix A Publication 1	81
A.1	Article	82

A.2	Corrections	94
Appendix B	Publication 2	95
B.1	Article	96
Appendix C	Publication 3	111
C.1	Article	112
Appendix D	Manuscript 1	123
D.1	Manuscript	124
D.2	Supplementary Information	170
Appendix E	Manuscript 2	223
E.1	Manuscript	224
E.2	Supplementary Information	261
Appendix F	BT-1T: Molecular Orbitals and XAS Data	343
F.1	Molecular Orbitals	343
F.2	Natural Transition Orbitals for Valence Excitation at the BHHLYP Level of Theory	344
F.3	XAS Data	345
F.3.1	BHHLYP/aug-cc-pVTZ (S)/cc-pVDZ (remaining atoms) . .	345
F.3.1.1	Natural Transition Orbitals for S_0 XAS	346
F.3.1.2	Natural Transition Orbitals for S_1 XAS	349
F.3.2	fc-CVS-EOM-CCSD/aug-cc-pVTZ (S)/cc-pVDZ (remaining atoms)	351
F.3.3	CVS-EOM-CCSD and CVS-EOM-CCSDR(3)/cc-pVDZ . .	352
F.3.3.1	Natural Transition Orbitals for S_0 XAS	353
Bibliography		355

Introduction

When developing and improving new tools and technologies, understanding what drives the relevant processes involved are of key importance. To systematically guide the optimization of certain processes, a thorough fundamental understanding of the systems involved is required at a molecular level. Information of this kind can be obtained by shining light on the molecule(s) involved and investigate the resulting interactions. Depending on the chosen wavelength, different transitions in the molecule are probed. Thus, different information about the molecule, its properties, and its reactions can be revealed. Whereas light in the infrared region reveals information of the vibrational levels of the system, ultraviolet (UV) and visible (Vis) light probes electronic energy transitions in the valence region. X-rays, like UV-Vis light, probes electronic transitions. However, rather than the valence region, it is here the core region that is explored. Moreover, X-ray spectroscopies are element specific, which allows the local environment around specific atoms to be probed selectively. Understanding the electronic energy levels, whether they are probed by core or valence transitions, are of great importance, for instance, when designing solar cells [1]. When employing pump-probe X-ray spectroscopy, a time-resolution on the *fs* timescale is becoming achievable with the emergence of increasingly sophisticated X-ray facilities [2, 3]. Thus, X-rays offer the possibility of investigating processes on the *ps* and to some extent even the sub-*ps* timescale, typical for molecular reactions.

The extraction of information from experimental spectra is far from trivial [4, 5]. While the experimental spectrum holds all the information, and an experienced eye might perceive much of this, the finer details are often difficult to discern. In order to capture these details, theory is a valuable interpretation tool. For a sufficiently accurate and efficient theory, it might even be possible to determine which experiments are most likely to be of interest. Thus, it might be possible to avoid performing expensive tests with little output.

Unfortunately, the computational resources for performing state-of-the-art calculations in a short (or even reasonable) amount of time only exist for smaller systems [6]. Therefore, one must choose a level of theory that offers a good compromise between accuracy and computational costs. A very popular and successful method for describing the electronic structure of a system is density

functional theory (DFT), introduced by Hohenberg and Kohn in 1964 [7]. It is a method that relies on choosing the description of what is known as the exchange-correlation energy in the shape of a functional [8]. Such functionals are based on a fit of certain parameters [8]. Hence, the quality of a DFT calculation depends on how well the functional describes whichever property is investigated. This, however, is generally impossible to predict, although schemes, such as Jacob's ladder [9, 10], exist for guiding the choice of functional. Nevertheless, results obtained with DFT-based methods are generally rather good, while the computational costs are low [11]. It is therefore no surprise that the method is popular, despite the rather unpredictable quality of its results. An alternative method, which has received increasing attention over the last decades, is coupled cluster (CC) [12, 13]. It was introduced by Coester and Kümmel [14, 15] in the late 1950's and extended by Čížek [16] in the 1960's. Unlike DFT, it is a wavefunction-based method, which does not rely on fitting parameters. It consists of a series of systematically improvable methods, describing the wavefunction in an increasingly accurate way. It is also in this family of methods that the current state-of-the-art methods for predicting properties (determined for a set of static nuclei) can be found for systems that are well described by a single electronic configuration. When a single electronic configuration is no longer a sufficient description of the system, such as in the vicinity of conical intersections (CIs), multiconfigurational methods are required [17]. These will not, however, be discussed in this work. Unfortunately, the high accuracy CC methods are computationally expensive and thus the size of the systems that can be investigated at the higher levels of theory are limited [6, 13]. In this work, both CC methods as well as DFT-based methods have been employed.

In addition to the theoretical method, it must be determined on which molecular geometry the (property) calculation should be based. If experimental geometries are available, these can be utilized, but this is often not the case. Thus, the molecular structure must be determined theoretically. When properties are considered for a static system, an obvious choice of structure is the one corresponding to the lowest energy on the potential energy surface (PES), which governs the forces that make the nuclei of the molecule move. As the minimum-energy point is approached, the forces working on the molecule will diminish. Hence, at the minimum-energy point, the (optimized) structure is considered to be relaxed. This structure is the most energetically favourable, and therefore it is the most probable geometry of a system in equilibrium. Such an equilibrium structure can be determined by optimization at any given level of theory, if the molecular gradient is available. In case of a dynamic system, e.g., if a chemical reaction is investigated, one must determine not just one but several structures. Since the molecule is now moving, a structure must be determined for each investigated timestep. In principle, this can be done by solving the time-dependent

Schrödinger equation, however, such calculations quickly become too demanding for practical purposes. Hence, approximations must be made. The molecule can, e.g., be approximated as moving along only a few degrees of freedom, limiting the computational costs but also the flexibility of the system. Alternatively, the time-dependent equation for the movement of the nuclei can be approximated by Newton's second law, i.e., classical mechanics. This again requires the molecular gradient to be computed. Both of these approaches have been considered in this work. Once the necessary molecular structure has been determined for a given time-delay, the properties of interest can be computed as for a static molecule. In this thesis, it has been explored how to simulate ultra-fast chemical reactions. This includes describing molecular movement as well as spectroscopic properties, necessary to determine spectroscopic signatures observable in experiments. The work presented cover both method development, evaluation of the performance of theoretical methods in describing X-ray spectra and theoretical analysis of experimental data. The simulation of X-ray spectra has been focused on the CC singles and doubles (CCSD) method. It is also based on this wavefunction that the implementations presented have been carried out. In addition, the second-order approximate coupled cluster singles and doubles method has been considered for evaluating resonant inelastic X-ray scattering (RIXS) spectra. Furthermore, DFT-based methods have been employed to evaluate spectra based on X-ray absorption spectroscopy (XAS). Moreover, all nuclear dynamics simulations presented were based on DFT. The thesis is organized as follows:

The first part of the thesis introduces the necessary theoretical concepts. This part is split into three chapters. In the first chapter, the electronic structure theory for the methods, which are the basis of this work, is reviewed. The second chapter introduces the reader to the molecular properties considered. It is also in this section the molecular gradient, which was implemented at the CCSD level of theory for this work (see Publication 1), is presented. The third chapter is focused on nuclear dynamics and introduces different approaches to such simulations. In the second part of the thesis, the calculations carried out for this work are presented. First, the analysis of ground state experimental data of oxazole is presented (Publication 2). Then, the implementation of RIXS cross sections is evaluated by comparing theoretical results at two levels of theory and experimental data (Manuscript 1). Third, XAS spectra are presented for a larger molecule (BT-1T), interesting for its applications in solar cells (Manuscript 2). Next, the simulation of nuclear dynamics is considered. A study of azobenzene, carried out using trajectory surface hopping, is presented (Publication 3), followed by a study employing both trajectory surface hopping and multi-configurational time-dependent Hartree (Manuscript 2). The latter also considers the BT-1T molecule for which time-resolved XAS are then presented (Manuscript 2). At the end of the thesis, the results are summarized.

Part I

Theoretical Concepts

CHAPTER 1

Describing the Molecular System

When we aim to describe a molecule theoretically, the quantum mechanical starting point is usually the time-dependent Schrödinger equation, here given in atomic units (see, e.g., Ref. 18):

$$i \frac{\partial}{\partial t} \Psi(r, R, t) = \hat{H}(r, R) \Psi(r, R, t), \quad (1.1)$$

where $\Psi(r, R, t)$ is the wavefunction describing the system, i is the imaginary unit, r and R are the position vectors of all electrons and nuclei, respectively, and t is the time. The Hamiltonian, \hat{H} , is given as a sum of the kinetic energy operators of the electrons, $\hat{T}_e(r)$, and the nuclei, $\hat{T}_N(R)$, and the potential energy operators for the electron-electron, $\hat{V}_{ee}(r)$, electron-nuclei, $\hat{V}_{eN}(r, R)$, and nuclei-nuclei, $\hat{V}_{NN}(R)$, interactions. In atomic units, which will be used throughout, for a system of M electrons and K nuclei, \hat{H} is given as [18]

$$\begin{aligned} \hat{H}(r, R) &= \hat{T}_e(r) + \hat{T}_N(R) + \hat{V}_{ee}(r) + \hat{V}_{eN}(r, R) + \hat{V}_{NN}(R) \\ &= -\frac{1}{2} \sum_i^M \nabla_i^2 - \frac{1}{2} \sum_A^K \frac{1}{m_A} \nabla_A^2 \\ &\quad + \sum_{i < j}^M \frac{1}{|r_i - r_j|} - \sum_{iA}^{M,K} \frac{Z_A}{|R_A - r_i|} + \sum_{A < B}^K \frac{Z_A Z_B}{|R_B - R_A|}, \end{aligned} \quad (1.2)$$

where m_A is the mass of nucleus A and Z_A denotes its charge.

It should be noted that Eq. (1.1) gives a non-relativistic description of the system although relativistic effects can be included in a perturbative manner when describing properties [19, 20]. For a fully relativistic description of the system, one should instead start from the Dirac equation [21]. This work is not focused on describing molecules containing heavy elements nor indeed relativistic effects. Nonetheless, relativistic effects can play a role when simulating core spectroscopy,

even for lighter elements [22]. These effects at the K -edge, which is the focus of this study, can often be accounted for by a simple overall shift of the excitation energies [22]. Hence, relativistic effects will not be discussed further in this thesis, and we content ourselves with the Schrödinger equation as our starting point.

As a standard manner of simplification, Eq. (1.1) can be split into a time-dependent and a time-independent part by utilizing a special case of the adiabatic approximation known as the Born-Oppenheimer approximation (BOA). The adiabatic approximation consists in assuming that the system evolves on a single electronic state [18]. Mathematically, this corresponds to truncating the exact expansion of the wavefunction in a complete basis to one term only. To obtain the BOA, the movement of the electrons is furthermore considered instantaneous with respect to the nuclei [23]. The BOA thus gives the well known electronic time-independent Schrödinger Equation in Eq. (1.3) and the equation of motion for the nuclei in Eq. (1.4) (see, e.g., Ref. 18):

$$\hat{H}_e(r; R)\Psi^{\text{elec}}(r; R) = E(R)\Psi^{\text{elec}}(r; R) \quad (1.3)$$

$$i\frac{\partial}{\partial t}\chi(R, t) = [E(R) + \hat{T}_N(R)]\chi(R, t), \quad (1.4)$$

where $\hat{H}_e(r; R)$ is the electronic Hamiltonian, which consists of the kinetic energy operator for the electrons and all the potential energy operator terms. This Hamiltonian depends only on the positions of the electrons and *parametrically* on the positions of the nuclei. This is also the case for the wavefunction, $\Psi^{\text{elec}}(r; R)$, describing the electronic part of the system. The electronic Schrödinger equation, Eq. (1.3), describes the electronic structure of the system, while the time-dependent equation, Eq. (1.4), allows us to describe nuclear dynamics.

Time-dependence of the electrons is required when computing many molecular properties, usually determined as response properties. Here, it is utilized that one can go from the time to the frequency domain by a Fourier transform. While geometrical parameters and other zeroth order properties are computed from Eq. (1.3), properties related to spectroscopy generally require us to solve a time-dependent electronic Schrödinger equation. Such an equation may be obtained by first assuming that the time-dependence can be written as a phase. This means that we can separate time-dependence from both the electronic and nuclear coordinates, allowing us to split Eq. (1.1) in two (see, e.g., Ref. 24):

$$\hat{H}(r, R)\Psi(r, R) = E\Psi(r, R) \quad (1.5)$$

$$i\frac{\partial}{\partial t}\vartheta(t) = E\vartheta(t). \quad (1.6)$$

Eq. (1.6) is a simple differential equation which has the well known solution (see, e.g., Ref. 24)

$$\vartheta(t) = e^{-iEt}. \quad (1.7)$$

By applying the BOA to (1.5) and assuming slowly moving nuclei, i.e., $\hat{T}_N(R)\chi(R) = 0$, the time-dependent electronic Schrödinger equation (see, e.g., Ref. 23),

$$i \frac{\partial}{\partial t} \Psi^{\text{elec}}(r, t; R) = \hat{H}_e(r, t) \Psi^{\text{elec}}(r, t; R), \quad (1.8)$$

can then be obtained. This equation allows us to simulate response properties and hence spectra.

The above approach should be noted to only provide a dynamic picture of the electrons. The nuclei, and hence the molecular structure, remain static. Such a static structure is often of great interest when characterizing molecules and can provide information about electronically excited states. It does not, however, allow us to describe the nuclear dynamics of molecular reactions, which instead requires us to solve Eq. (1.4). This will be discussed further in Chapter 3. Observe that the equation of motion for the nuclei depends on the electronic energy at any given position of the nuclei, since this is the potential in which they move. Consequently, solving Eq. (1.4) cannot be done without first solving the electronic time-independent Schrödinger equation.

Regardless of whether it is the static properties or the dynamics of the nuclei one wishes to describe, the electronic Schrödinger equation must therefore be solved to a satisfactory degree of accuracy. Unfortunately, this equation cannot be solved exactly for system with more than one electron due to the Coulomb repulsion term [25]. In order to describe molecules, approximations must then be made. Many excellent schemes are available, and a review can be found in, e.g., Ref. 26.

In this work, only three strategies shall be considered, namely Hartree-Fock (HF) theory, density functional theory (DFT), and coupled cluster (CC) theory. Of these, only the latter two have been utilized in the present work, but since HF theory is the foundation of the wavefunction-based methods, such as CC, this will also briefly be discussed. As this chapter is concerned with the *electronic* part of the system, i.e., solving Eqs. (1.3) and (1.8), the superscript as well as the explicit parametrical dependence on the position of nuclei shall be omitted for brevity of notation. Thus, in the remainder of this chapter $\Psi^{\text{elec}}(r, t; R) = \Psi(r, t)$ and $E(R) = E$. Furthermore, the bracket notation shall be employed with the ket-state corresponding to $\Psi(r, t)$ denoted as $|\Psi(t)\rangle$.

1.1 The Ground State

The first step when attempting to describe a system is to describe its ground state without any perturbations. Hence, we must consider how to solve Eq. (1.3)

and obtain the electronic energy. Here, we can either consider wavefunction-based methods, such as HF and CC, which focus on the choice of an approximate wavefunction, i.e. $\Psi(r) = \Psi^{\text{method}}(r)$, or we might turn to DFT. In the latter approach, the energy expression is rewritten in terms of the electron density rather than a wavefunction.

1.1.1 Hartree-Fock

HF theory is the simplest wavefunction-based method and is described in many textbooks, e.g., Refs. 24, 23, and 25. This brief introduction will follow that of Ref. 24 unless otherwise stated.

In HF theory the wavefunction of a system with N electrons in k spin-orbitals, $\psi_i(r_j)$, is described as a single Slater determinant:

$$\Psi^{\text{HF}}(r_1, r_2, \dots, r_N) = \frac{1}{\sqrt{N!}} \begin{vmatrix} \psi_1(r_1) & \psi_2(r_1) & \dots & \psi_k(r_1) \\ \psi_1(r_2) & \psi_2(r_2) & \dots & \psi_k(r_2) \\ \dots & \dots & \dots & \dots \\ \psi_1(r_N) & \psi_2(r_N) & \dots & \psi_k(r_N) \end{vmatrix}, \quad (1.9)$$

where $\frac{1}{\sqrt{N!}}$ is a normalization factor and each spin-orbital is a product of a spatial, $\phi_i(r_j)$, and a spin function, $\sigma_i(r_j)$. The Slater determinant ensures that the wavefunction is antisymmetric when exchanging two particles. This is a requirement for fermions as per the Pauli principle. In the Slater determinant, exchanging two particles corresponds to exchanging two rows of the determinant, which in turn results in a change of sign. Furthermore, the Slater determinant enforces the more specific Pauli exclusion principle. This principle states that two fermions cannot have the same set of quantum numbers, which corresponds to two identical columns of the Slater determinant.

The HF method relies on the variational principle that states that the energy of a given approximate wavefunction is always higher than or equal to the exact energy. Hence, one can optimize the wavefunction by determining the set of spin-orbitals that gives the lowest possible energy. This is done by performing a constrained optimization utilizing Lagrange's method of undetermined multipliers with the orthonormality condition as the constraint [24]. This leads to a set of equations from which the spin-orbitals leading to the lowest possible energy can be determined. These eigenvalue equations are known as the HF equations:

$$\hat{f}(r_i)\psi_k(r_i) = \epsilon_k\psi_k(r_i) \quad (1.10)$$

with

$$\hat{f}(r_i) = \hat{h}(r_i) + v^{\text{HF}}(r_i) \quad (1.11)$$

$$\hat{h}(r_i) = -\frac{1}{2}\nabla_i^2 - \sum_A^{N_{\text{nuclei}}} \frac{Z_A}{r_{iA}} \quad (1.12)$$

$$v^{\text{HF}}(r_i) = \sum_j^N (2\hat{J}_j(r_i) - \hat{K}_j(r_i)) \quad (1.13)$$

$$\hat{J}_j(r_i)\psi_k(r_i) = \int dr_l \frac{\psi_j^*(r_l)\psi_j(r_l)}{r_{il}} \psi_k(r_i) \quad (1.14)$$

$$\hat{K}_j(r_i)\psi_k(r_i) = \int dr_l \frac{\psi_j^*(r_l)\psi_k(r_l)}{r_{il}} \psi_j(r_i), \quad (1.15)$$

where $v^{\text{HF}}(r_i)$ is the *average* electronic repulsion felt by electron i , and \hat{J}_j and \hat{K}_j are the Coulomb and exchange operators, respectively. The Coulomb operator can be interpreted as the Coulomb repulsion between two electrons, while the exchange operator has no simple classical interpretation. The exchange term ensures that we take into account spin-correlation, i.e., that electrons with parallel spins lowers the overall energy more than electrons with antiparallel spins [23]. The notation r_{ij} is short for $|r_j - r_i|$, while r_{iA} is short for $|R_A - r_i|$. The eigenvalues ϵ_i are the HF orbital energies.

Since the average potential in Eq. (1.13) depends on the spin-orbitals (see Eqs. (1.14) and (1.15)), one cannot solve Eq. (1.10) without already having a guess for these spin-orbitals. Therefore, the problem must be solved in an iterative manner using a self-consistent field (SCF) approach.

1.1.2 Coupled Cluster Theory

In HF theory, the electron-electron interactions are approximated as an interaction between each electron and an *average* location of the remaining electrons (see Eqs. (1.13)-(1.15)), and we say that *electron correlation* is neglected [23]. In fact, the correlation energy is defined as the difference between the exact energy and the HF energy [23]. Unfortunately, electron correlation is recognized to be very important for many molecular applications [25, 27], and at higher levels of theory one attempts to include this effect.

There are two types of electron correlation; static and dynamical [28]. Static correlation is a result of (near) degeneracies and thus becomes important for systems that are not described well by a single electron configuration (i.e., a single Slater determinant) [28]. Dynamical correlation, on the other hand, is related to the lack of a satisfactory description of the instantaneous interaction

between the electrons [28, 29]. Both types of correlation can be remedied by including more electron configurations and thus describing the wavefunction as a linear combination of Slater determinants. When one primarily treats static correlation, a few determinants are included with similar weights to allow the electron density to be equally spread over the degenerate states. Dynamical correlation, however, is treated by considering many determinants in order to include flexibility, but only one (the reference) will have a large weight.

As was the case for HF theory, CC methods are described in several textbooks and the introduction here will follow that of reference 25.

The CC family of methods mainly treats dynamical correlation and are based on the exponential ansatz given in Eq. (1.16):

$$|\Psi^{CC}\rangle = e^{\hat{T}} |0\rangle. \quad (1.16)$$

In Eq. (1.16), \hat{T} is the cluster operator, which is the sum of all possible excitations of the system (see Eq. (1.17)), and $|0\rangle$ is a reference single Slater determinant, usually the simple ground state HF wavefunction. The cluster operator, \hat{T} , is defined as

$$\hat{T} = \sum_{\mu} t_{\mu} \hat{\tau}_{\mu}, \quad (1.17)$$

where μ denotes an excitation, t_{μ} is the CC amplitude for the given excitation and $\hat{\tau}_{\mu}$ is the excitation operator so that $\hat{\tau}_{\mu} |0\rangle = |\mu\rangle$. Thus, when the excitation operator, $\hat{\tau}_{\mu}$, works on the (HF) reference state, an excited determinant, $|\mu\rangle$, is created by promoting one or more electrons from orbitals that were occupied in the reference to those that were virtual.

Inserting this wavefunction in the time-independent Schrödinger equation in Eq. (1.3) yields

$$\hat{H}_e e^{\hat{T}} |0\rangle = E^{CC} e^{\hat{T}} |0\rangle. \quad (1.18)$$

We multiply Eq. (1.18) by $e^{-\hat{T}}$ from the left for later convenience. One could now apply the variational principle and optimize the CC wavefunction with respect to the amplitudes. This, however, results in a rather complicated set of non-linear equations, which becomes computationally expensive to solve [25]. To avoid this, the variational principle is abandoned for optimizing the wavefunction, and instead the projected Schrödinger equation is considered. The CC energy, E^{CC} , can then be obtained by projecting onto Eq. (1.18) the reference state. An equation for the CC amplitudes, which is required to determine the wavefunction, can be obtained by projection upon an excited state, $\langle\mu|$. Thus, the CC equations

become

$$\langle 0 | e^{-\hat{T}} \hat{H}_e e^{\hat{T}} | 0 \rangle = E^{CC} \quad (1.19)$$

$$\langle \mu | e^{-\hat{T}} \hat{H}_e e^{\hat{T}} | 0 \rangle = 0. \quad (1.20)$$

Observe that the exponential operator can be written in terms of its Taylor expansion. This allows the derivation of specific CC equations for different levels of theory within the hierarchy.

The obtained energy is no longer variational and hence, does not give an upper bound for the exact energy. Nevertheless, the quality of the results obtained by utilizing CC methods is often so high that this matters little in practical applications [25]. In fact, today, the golden standard of static calculations for single reference wavefunctions is considered to be obtained with CCSD(T) [30] and CC3 [31]. These are CC methods where all single and double excitations are included in the cluster operator, and where triple excitations are treated perturbatively. Unfortunately, these methods are computationally too expensive to be used routinely on molecules containing more than approximately 15 second row elements [6]. Thus, alternatives must be considered. One such is the successful CCSD method [32] based on a cluster operator containing all single and double excitations. This method has proven most successful over the past years [12, 25] and is the one that has been used for static calculations throughout this work.

1.1.3 Density Functional Theory

DFT is a very popular theory for describing the electronic structure of molecular systems. Despite its low computational costs, it often yields results of good quality, which makes it a very powerful and much used tool [11]. The major drawback of the DFT-based methods is the fact that no real hierarchy exists for systematically improving results, although Jacob's ladder can work as a guideline [9, 10]. DFT is based on the idea that the total electronic energy, as well as other observable properties, of any given system can be written as a *functional* of the electron density, $\rho(r)$ [7]. In addition, this functional is universal for all systems and the global minimum can be found by inserting the exact ground state electron density. This was proved by Hohenberg and Kohn in 1964 [7]. Considering the electron density rather than the wavefunction, simplifies our problem immensely. While the density is only a function of three coordinates (one given position), the wavefunction is a function of all positions of all electrons, i.e., $3N$ coordinates. Employing this so-called orbital free formulation, where the functional is expressed only in terms of the electron density without considering orbitals, is not without problems. While such an immense simplification is indeed tantalizing, the orbital free formulation shows a poor representation of the kinetic energy [27].

Hence, the foundation for the use of DFT in chemistry today is the reintroduction of orbitals by Kohn and Sham, giving rise to the Kohn-Sham (KS) formulation of DFT [33]. In KS theory, the kinetic energy is computed as a sum of the exact kinetic energy for a non-interacting reference system and a correction, which can again be split in two parts. Thus, the energy functional can now be written as a sum of four terms [27]:

$$E[\rho(r)] = E_T[\rho(r)] + E_V[\rho(r)] + E_J[\rho(r)] + E_{XC}[\rho(r)], \quad (1.21)$$

where $E_T[\rho(r)]$ is the exact kinetic energy of the reference system for non-interacting electrons, $E_V[\rho(r)]$ is the potential resulting from the Coulomb interaction between electrons and (fixed) nuclei, $E_J[\rho(r)]$ is the potential energy resulting from the *average* Coulomb interaction between electrons, and the last term, $E_{XC}[\rho(r)]$, is the correction to the exact energy of the reference system known as the exchange-correlation energy. Hence, we note that electron correlation is included at the DFT level of theory. The degree to which it is included depends on the choice of functional, though [34].

The reference system is, analogously to the one in HF theory, described as a single Slater determinant consisting of (molecular) spin-orbitals. These orbitals are determined from a set of self-consistent equations known as the Kohn-Sham (KS) equations (see, e.g., Ref. [24]):

$$\left[-\frac{1}{2}\nabla_k^2 + v_{\text{eff}}(r_k) \right] \psi_i(r_k) = \epsilon_i \psi_i(r_k), \quad (1.22)$$

where $v_{\text{eff}}(r)$ is an average potential energy that depends on the energy functional in Eq. (1.21), and ϵ_i is an orbital energy. Observe that the KS equations in form are identical to the HF equations, Eq. (1.10).

Unfortunately, while the first three terms of the energy expression in Eq. (1.21) can be readily evaluated, this is not the case for the last one, i.e., the exchange-correlation energy. Various methods for evaluating approximations exist, each optimized for different properties [27]. It is the choice of this part of the energy functional, which makes the prediction of the quality of DFT results so difficult [9, 10]. Still, DFT is a most powerful tool [11, 35]. Together with time-dependent DFT (TDDFT), used for excited state calculations, it has been used throughout this work for dynamics simulations as well as for some static X-ray absorption spectra calculations.

1.2 Properties and Excited States

When we wish to consider an excited state, or indeed many ground state properties, we consider the interaction of our system with light. For the excited state,

the frequency of the light should correspond to the excitation energy associated with this state. For other properties, different frequencies may be relevant. Upon interaction with light, the system can be considered as a perturbed state with respect to the ground state. For a small perturbation, which will be the only type discussed here, we can employ perturbation theory to derive expressions for the perturbed systems. These expressions can then be used to determine both excited states and properties. This is known as response theory and will be briefly recapped in the following section by following the derivations of Ref. 20. Alternatively, one can describe the excited states by way of the equation-of-motion (EOM) formulation, which will also be recapped below for CC.

1.2.1 Response Theory

In order to describe the perturbation of the system, it is necessary to add to the Hamiltonian a term accounting for this perturbation. The electronic Hamiltonian can in this case be written as a perturbation series of the form

$$\hat{H}(t) = \hat{H}^{(0)} + H^{(1)}(t) + H^{(2)}(t) + \dots, \quad (1.23)$$

where for brevity the subscript e as well as the explicit dependence on electron positions has been omitted. The notation $\hat{H}^{(n)}(t)$ indicates the n th order time-dependent perturbation correction to the unperturbed, or zeroth order, Hamiltonian, $\hat{H}^{(0)}$. In general, we can consider the interaction with light as an interaction with an external oscillating electromagnetic field, $\mathcal{F}(t)$, with three components, $\mathcal{F}_\alpha(t)$. The perturbation corrections to the Hamiltonian can then be written

$$\hat{H}^{(1)}(t) = \sum_{\alpha} \hat{X}_{\alpha} \mathcal{F}_{\alpha}(t) \quad (1.24)$$

$$\hat{H}^{(2)}(t) = \sum_{\alpha, \beta} \mathcal{F}_{\alpha}(t) \hat{X}_{\alpha\beta} \mathcal{F}_{\beta}(t), \quad (1.25)$$

$$(1.26)$$

where \hat{X}_{α} and $\hat{X}_{\alpha\beta}$ are perturbation operators. Such operators could, for instance, be electric dipole and quadrupole operators. As we consider oscillating and thus time-dependent fields, we need to consider our system as being time-dependent. We therefore need to solve the time-dependent electronic Schrödinger equation, Eq. (1.8), where we must consider the perturbed Hamiltonian, $\hat{H}(t)$. Likewise, we also define our wavefunction as a perturbation series,

$$|\Psi(t)\rangle = |\Psi^{(0)}(t)\rangle + |\Psi^{(1)}(t)\rangle + \dots, \quad (1.27)$$

where the zeroth order (unperturbed) wavefunction can be expressed as

$$\left| \Psi^{(0)}(t) \right\rangle = \vartheta(t) \left| \Psi_0 \right\rangle, \quad (1.28)$$

and $|\Psi_0\rangle$ is the lowest energy solution to the time-independent electronic Schrödinger equation, Eq. (1.3), as indicated by the subscript "0". For brevity of notation this solution shall hence forth be denoted as $|0\rangle$. Higher energy solutions (i.e., excited states) are likewise denoted $|\mu\rangle$. The first-order correction to the wavefunction is found to be

$$\left| \Psi^{(1)}(t) \right\rangle = -i \int_{-\infty}^t dt' e^{-i(t-t')\hat{H}^{(0)}} \hat{H}^{(1)}(t') \left| \Psi^{(0)}(t) \right\rangle. \quad (1.29)$$

By now utilizing that we can express a property, Y , as an expectation value of the property operator, \hat{Y} , we can, to first-order in our perturbation series, write

$$\begin{aligned} \langle Y \rangle &= \langle \Psi(t) | \hat{Y} | \Psi(t) \rangle \\ &= \left\langle \Psi^{(0)}(t) \right| \hat{Y} \left| \Psi^{(0)}(t) \right\rangle \\ &+ \left\langle \Psi^{(1)}(t) \right| \hat{Y} \left| \Psi^{(0)}(t) \right\rangle + \left\langle \Psi^{(0)}(t) \right| \hat{Y} \left| \Psi^{(1)}(t) \right\rangle \\ &= \langle 0 | \hat{Y} | 0 \rangle \\ &- i \int_{-\infty}^t dt' \left\langle \Psi^{(0)}(t) \right| [\hat{Y}^I(t), \hat{H}^{(1)}(t')] \left| \Psi^{(0)}(t) \right\rangle \end{aligned} \quad (1.30)$$

with

$$\hat{Y}^I(t) = e^{i\hat{H}^{(0)}t} \hat{Y} e^{-i\hat{H}^{(0)}t}. \quad (1.31)$$

By inserting now the first order perturbation of the Hamiltonian, i.e., terms linear in the field, and utilizing the (reverse) Heaveside step function, $\Theta(t - t')$, which allows us to integrate over the entire time-range (from $-\infty$ to ∞), we obtain

$$\begin{aligned} \langle Y \rangle &= \langle 0 | \hat{Y} | 0 \rangle \\ &- i \sum_{\alpha} \int_{-\infty}^{\infty} dt' \mathcal{F}_{\alpha}(t') \Theta(t - t') \left\langle \Psi^{(0)}(t) \right| [\hat{Y}^I(t), \hat{X}_{\alpha}^I(t')] \left| \Psi^{(0)}(t) \right\rangle, \end{aligned} \quad (1.32)$$

from where the linear response is defined as the term linear in the perturbing field. The linear response function in the time domain is therefore given as

$$\langle \langle \hat{Y}^I(t); \hat{X}_{\alpha}^I(t') \rangle \rangle = \Theta(t - t') \left\langle \Psi^{(0)}(t) \right| [\hat{Y}^I(t), \hat{X}_{\alpha}^I(t')] \left| \Psi^{(0)}(t) \right\rangle, \quad (1.33)$$

where the linear response function for the operators, \hat{X} and \hat{Y} , is denoted $\langle\langle\hat{X};\hat{Y}\rangle\rangle$. This expression can be rewritten to only depend on the time difference, $t - t'$, i.e.,

$$\langle\langle\hat{Y};\hat{X}_\alpha^I(t-t')\rangle\rangle = \Theta(t-t') \langle 0 | [\hat{Y}, \hat{X}_\alpha^I(t-t')] | 0 \rangle. \quad (1.34)$$

Since we would like to relate the response to the frequency of the radiation, rather than considering a certain time, a Fourier transformation is performed on Eq. (1.34).

$$\langle\langle\hat{Y};\hat{X}_\alpha\rangle\rangle_\omega = \int_{-\infty}^{\infty} \langle\langle\hat{Y};\hat{X}_\alpha^I(t)\rangle\rangle \exp(-i\omega t) dt, \quad (1.35)$$

By inserting Eq. (1.34) into Eq. (1.35) and evaluating the expression, the spectral representation [20] is obtained:

$$\langle\langle\hat{Y};\hat{X}_\alpha\rangle\rangle_\omega = \sum_{\mu \neq 0} \frac{\langle 0 | \hat{Y} | \mu \rangle \langle \mu | \hat{X}_\alpha | 0 \rangle}{\omega + E_0^{(0)} - E_\mu^{(0)}} + \sum_{\mu \neq 0} \frac{\langle 0 | \hat{X}_\alpha | \mu \rangle \langle \mu | \hat{Y} | 0 \rangle}{-\omega + E_0^{(0)} - E_\mu^{(0)}}. \quad (1.36)$$

Here, $E_0^{(0)}$ is the eigenvalue of the unperturbed time-independent wavefunction of the reference state, $|0\rangle$. Likewise, $E_\mu^{(0)}$ is the eigenvalue of the unperturbed time-independent wavefunction of the excited state, $|\mu\rangle$, while ω is the frequency of the perturbing field. For further details see, e.g., Ref. 20.

The spectral representation can be recast in a matrix form for approximate methods (see e.g. Refs. 36 and 37 for a detailed derivation). For a HF wavefunction as the unperturbed reference, time-dependent HF (TDHF) [38] also known as the Random Phase Approximation¹ (RPA) [41, 42] is then obtained:

$$\langle\langle\hat{Y}_\alpha; \hat{X}_\beta\rangle\rangle_\omega = \begin{pmatrix} {}^e\mathbf{Y}_\alpha & {}^d\mathbf{Y}_\alpha \end{pmatrix}^T \left[\omega \begin{pmatrix} \mathbf{1} & \mathbf{0} \\ \mathbf{0} & -\mathbf{1} \end{pmatrix} - \begin{pmatrix} \mathbf{A}^{(0,1)} & \mathbf{B}^{(1)*} \\ \mathbf{B}^{(1)} & \mathbf{A}^{(0,1)*} \end{pmatrix} \right]^{-1} \begin{pmatrix} {}^e\mathbf{X}_\beta \\ {}^d\mathbf{X}_\beta \end{pmatrix} \quad (1.37)$$

¹The random phase approximation consists in assuming that the response of the system has two contributions: the first depends on the positions of the particles and is out of phase with the perturbing field, while the second is independent of the particle positions and in phase with the perturbing field [39]. For many randomly distributed particles, the first contribution will even out to zero. Thus, only the second needs to be evaluated. This contribution consists of independent particles affected by an average potential [40], which is also the basis of HF theory. Hence, the same equations are obtained.

with

$${}^e\mathbf{Y}_{\alpha,ai} = ({}^d\mathbf{Y}_{\alpha,ai})^* = \langle \Psi_0^{HF} | [\hat{Y}_\alpha, \hat{\tau}_{ai}] | \Psi_0^{HF} \rangle = \langle \psi_i | \hat{y}_\alpha | \psi_a \rangle \quad (1.38)$$

$${}^e\mathbf{X}_{\alpha,ai} = ({}^d\mathbf{X}_{\alpha,ai})^* = \langle \Psi_0^{HF} | [\hat{\tau}_{ai}^\dagger, \hat{X}_\alpha] | \Psi_0^{HF} \rangle = \langle \psi_a | \hat{x}_\alpha | \psi_i \rangle \quad (1.39)$$

$$\begin{aligned} \mathbf{A}_{aibj}^{(0,1)} &= \langle \Psi_0^{HF} | [\hat{\tau}_{ai}^\dagger, [\hat{H}^{(0)}, \hat{\tau}_{bj}]] | \Psi_0^{HF} \rangle \\ &= (\epsilon_a - \epsilon_i) \delta_{ij} \delta_{ab} + (ai|jb) - (ab|ji) \end{aligned} \quad (1.40)$$

$$\begin{aligned} \mathbf{B}_{aibj}^{(1)} &= \langle \Psi_0^{HF} | [\hat{\tau}_{ai}^\dagger, [\hat{H}^{(0)}, \hat{\tau}_{bj}^\dagger]] | \Psi_0^{HF} \rangle, \\ &= (aj|bi) - (ai|bj) \end{aligned} \quad (1.41)$$

where $\hat{\tau}_{ai}^\dagger$ is the de-excitation operator corresponding to the excitation operator, $\hat{\tau}_{ai}$, that promotes an electron from orbital i to orbital a . The operators \hat{y}_α and \hat{x}_α are one electron operators, and the full many-electron operators, \hat{Y}_α and \hat{X}_α , can be written as a sum of these, i.e.,

$$\hat{Y}_\alpha = \sum_k^{N_{\text{elec}}} \hat{y}_\alpha(r_k). \quad (1.42)$$

Furthermore, $(pq|rs)$ are two-electron integrals given in Mulliken notation.

It is evident from the spectral representation in Eq. (1.36) that in the case where the frequency of the perturbing field corresponds to an excitation energy of the system, the linear response function will have a pole. Thus, the excitation energies and corresponding excited states can be determined by solving the eigenvalue problem

$$\omega \begin{pmatrix} \mathbf{1} & \mathbf{0} \\ \mathbf{0} & -\mathbf{1} \end{pmatrix} \begin{pmatrix} {}^e\mathbf{T} \\ {}^d\mathbf{T} \end{pmatrix} = \begin{pmatrix} \mathbf{A}^{(0,1)} & \mathbf{B}^{(1)*} \\ \mathbf{B}^{(1)} & \mathbf{A}^{(0,1)*} \end{pmatrix} \begin{pmatrix} {}^e\mathbf{T} \\ {}^d\mathbf{T} \end{pmatrix}, \quad (1.43)$$

where $\begin{pmatrix} {}^e\mathbf{T} \\ {}^d\mathbf{T} \end{pmatrix}$ is a solution vector.

1.2.2 TDDFT

TDDFT is in many ways equivalent to RPA in form [27], as might be expected from the equivalence of the HF and KS equations. At the TDDFT level of theory, however, the $\mathbf{A}^{(0,1)}$ and $\mathbf{B}^{(1)}$ elements are not identical to those given for RPA. Instead, the expressions each include a term originating from the exchange-correlation part of the energy [43]:

$$\mathbf{A}_{aibj}^{(0,1)} = (\epsilon_a - \epsilon_i) \delta_{ij} \delta_{ab} + (ai|jb) + \langle \psi_i \psi_j | \hat{f}_{xc} | \psi_a \psi_b \rangle \quad (1.44)$$

$$\mathbf{B}_{aibj}^{(1)} = -(ai|bj) + \langle \psi_i \psi_j | \hat{f}_{xc} | \psi_a \psi_b \rangle \quad (1.45)$$

with

$$\hat{f}_{xc} = \frac{\partial V_{XC}[\rho]}{\partial \rho}, \quad (1.46)$$

where $V_{XC}[\rho]$ is the exchange-correlation potential.

A common approximation when employing TDDFT is the Tamm-Dancoff approximation (TDA), where $\mathbf{B}^{(1)}$ is set to zero. The $\mathbf{B}^{(1)}$ -matrix, however, introduces, to some extent, electron correlation in the description of the ground state [27]. Thus, setting these matrix blocks to zero means neglecting some electron correlation. Neglecting electron correlation can lead to problems known as triplet instabilities, when considering triplet states or triplet properties. Since triplet states are degenerate, they require static correlation to be accounted for to some extent. In this work, triplet states and triplet properties have not been considered, and thus the TDA has been utilized for all of the calculations on which the presented dynamics are based.

1.2.3 Equation-of-Motion CCSD

In CC theory, it is possible to compute molecular properties by using the EOM-CC [42,44,45] method². It is more approximate compared to rigorously following linear response (LR) theory, however, EOM-CC often yields results of similar accuracy to LR-CC at a slightly reduced cost [47]. Since it is the EOM-CC approach that has been utilized throughout this work, this formalism will be considered here, while LR-CC will not be discussed. In EOM-CC, the excited state is defined as an excitation of the CC ground state, $|\Psi_0^{CC}\rangle$, i.e., (see, e.g., Ref. 48)

$$|\Psi_\mu^{CC}\rangle = \hat{R}_\mu |\Psi_0^{CC}\rangle \quad (1.47)$$

$$\langle \Psi_\mu^{CC} | = \langle \Psi_0^{CC} | \hat{L}_\mu, \quad (1.48)$$

where

$$\hat{R}_\mu = \sum_{\nu=0} R_\nu^\mu \hat{\tau}_\nu \quad (1.49)$$

$$\hat{L}_\mu = \sum_{\nu=0} L_\nu^\mu \hat{\tau}_\nu^\dagger, \quad (1.50)$$

²The equation-of-motion can be written as [42,45] $[\hat{H}, \hat{\Omega}_k] = \omega_k \hat{\Omega}_k$, where $\hat{\Omega}_k$ is the operator that creates the excited state wavefunction and ω_k is the corresponding excitation energy. Thus, the excited state is generated by allowing some operator to work on the ground state [45,46], which is also how we define it in Eqs. (1.47) and (1.48). Based on the given expression for the equation-of-motion, it is possible to obtain Eqs. (1.51) and (1.55) [45].

and R_ν^μ and L_ν^μ are excitation coefficients for the excitation, ν , needed to to generate the excited state wavefunction Ψ_μ^{CC} . The excitation operator $\hat{\tau}_0$ corresponds to an identity operation. By inserting this wavefunction, Eq. (1.47), in the time-independent electronic Schrödinger equation and considering all states, $|\Psi_\mu^{CC}\rangle$, we obtain the matrix eigenvalue equation (see, e.g., Ref. [25])

$$\begin{aligned} \mathbf{H}\mathbf{R} &= \mathbf{E}\mathbf{R} \\ \Downarrow \\ \begin{pmatrix} E_0^{CC} & \boldsymbol{\eta} \\ 0 & \mathbf{A} + E_0^{CC}\mathbf{1} \end{pmatrix} \begin{pmatrix} \mathbf{R}_0 \\ \mathbf{R}_\mu \end{pmatrix} &= \begin{pmatrix} E_0^{CC} & 0 \\ 0 & E_\mu^{CC} \end{pmatrix} \begin{pmatrix} \mathbf{R}_0 \\ \mathbf{R}_\mu \end{pmatrix} \end{aligned} \quad (1.51)$$

with

$$\eta_\mu = \langle 0 | \hat{H} e^{\hat{T}} | \mu \rangle \quad (1.52)$$

$$A_{\mu\nu} = \langle \mu | e^{-\hat{T}} [H, \hat{\tau}_\nu] e^{\hat{T}} | 0 \rangle \quad (1.53)$$

$$E_\mu^{CC} = E_0^{CC} + \omega_\mu, \quad (1.54)$$

where ω_μ is the excitation energy associated with the excited state, $|\Psi_\mu^{CC}\rangle$, and the matrix \mathbf{A} here denotes the CC Jacobian. We recall from Section 1.1.2 that $|0\rangle$ and $|\mu\rangle$ denote the ground and μ -excited state of the (HF) reference, respectively. The Hamiltonian matrix, \mathbf{H} , is non-symmetric. Therefore, the left and right hand side (LHS and RHS) wavefunctions (Eqs. (1.47) and (1.48)) are not adjoint [25], and we need to solve both Eq. (1.51) and

$$\mathbf{L}^T \mathbf{H} = \mathbf{L}^T \mathbf{E}. \quad (1.55)$$

Normally, the equations to consider are the level-shifted ones (i.e., $E_0^{CC}\mathbf{R}$ is subtracted from Eq. (1.51) and $\mathbf{L}^T E_0^{CC}$ is subtracted from Eq. (1.55)) [25],

$$\Delta \mathbf{H} \mathbf{R} = \boldsymbol{\omega} \mathbf{R} \quad (1.56)$$

$$\mathbf{L}^T \Delta \mathbf{H} = \boldsymbol{\omega} \mathbf{L}^T, \quad (1.57)$$

which gives the excitation energies ω_μ as the eigenvalues and has (from Eq. 1.51)

$$\Delta \mathbf{H} = \begin{pmatrix} 0 & \boldsymbol{\eta} \\ 0 & \mathbf{A} \end{pmatrix}. \quad (1.58)$$

Observe that the eigenvectors are not changed by considering the level-shifted eigenvalue problem.

Based on the level-shifted eigenvalue problem, the R_0 and L_0 coefficients can be determined both for the ground and excited states. The ket ground state was

already defined in Eq. (1.16), i.e., $R_0^0 = 1$ and $R_\mu^0 = 0$. The corresponding bra-state can then be determined based on the requirement that it must be biorthonormal to the ket-state. This yields the Λ -state (see, e.g., Ref. [25]),

$$\langle \Psi_0^{CC} | = \langle \Lambda | = \langle 0 | e^{-\hat{T}} + \sum_{\nu \neq 0} \bar{t}_\nu \langle \nu |, \quad (1.59)$$

where the CC multipliers, \bar{t}_ν , are determined as [25]

$$\bar{\mathbf{t}}^T \mathbf{A} = -\boldsymbol{\eta}. \quad (1.60)$$

For the excited states, biorthogonality to the ground state is required, which yields (see, e.g., Pawłowski *et al.* [49]):

$$|\Psi_\mu^{CC}\rangle = -\sum_{\nu \neq 0} \bar{t}_\nu R_\nu^\mu |\Psi_0^{CC}\rangle + \sum_{\nu \neq 0} R_\nu^\mu e^{\hat{T}} |\nu\rangle \quad (1.61)$$

$$\langle \Psi_\mu^{CC} | = \sum_{\nu \neq 0} L_\nu^\mu \langle \nu | e^{-\hat{T}}. \quad (1.62)$$

Based on the EOM parametrization of the excited state wavefunction, the matrix form of Eq. (1.36) becomes (see, e.g., Ref. 49):

$$\langle \langle \hat{X}; \hat{Y} \rangle \rangle_\omega = \frac{1}{2} C^{\pm\omega} (\boldsymbol{\eta}^X \mathbf{t}^Y(\omega) + \boldsymbol{\eta}^Y \mathbf{t}^X(\omega)) \quad (1.63)$$

with $C^{\pm\omega}$ being the complex conjugation and frequency inversion operator and

$$\eta_\mu^X = \langle \Lambda | \hat{X} e^{\hat{T}} |\mu\rangle - \langle X \rangle^{CC} \bar{t}_\mu, \quad (1.64)$$

where

$$\langle X \rangle = \langle \Lambda | \hat{X} | \Psi_0^{CC} \rangle. \quad (1.65)$$

Note that the definition of η^X is not the same in EOM-CC and LR-CC. In the above, η^X is given for EOM-CC, while the LR-CC expression is (see, e.g., Ref. 50):

$$^{\text{LR}}\eta_\mu^X = \langle \Lambda | [\hat{X}, \hat{\tau}_\mu] | \Psi_0^{CC} \rangle. \quad (1.66)$$

The response equations, from which to determine the RHS and LHS response amplitudes, $\mathbf{t}^X(\omega)$ and $\bar{\mathbf{t}}^X(\omega)$, are given as [49]

$$(\mathbf{A} - \omega \mathbf{1}) \mathbf{t}^X(\omega) = -\boldsymbol{\xi}^X \quad (1.67)$$

$$\bar{\mathbf{t}}^X(\omega) (\mathbf{A} + \omega \mathbf{1}) = -\boldsymbol{\eta}^X \quad (1.68)$$

with

$$\xi_{\mu}^X = \langle \mu | e^{-T} \hat{X} e^T | 0 \rangle. \quad (1.69)$$

Note that ξ^X is the same for both EOM-CC and LR-CC.

For simply computing excitation energies, EOM-CCSD yields results identical to those obtained by using LR-CC [51]. When evaluating other properties, however, the results differ, except in the full configuration interaction limit [51]. For practical purposes, the differences between the obtained results are small [47]. The computationally cheaper EOM method can therefore be used with advantage. In fact, only for systems of a size that challenges the computational feasibility of the CC methods anyway, do the discrepancy become too large for EOM results to be considered reasonable [47].

1.2.4 Maximum Overlap Method

Yet another way of generating an excited state is by utilizing the Maximum Overlap Method [52] (MOM). Usually, when the SCF equations (either HF or KS) are solved, the aufbau principle is used. This means that the electrons are placed in the orbitals with the lowest energies. In MOM, instead of demanding that the lowest energy orbitals be filled, we demand that the overlap with some guess state is maximized. The initial guess state is a set of orbitals, usually obtained from a converged calculation of a ground state (based on the aufbau principle). It is then specified which of these orbitals should be occupied, and which should be unoccupied, in the new calculation. In each iteration, the overlap between the old set of orbitals specified to be occupied and a new set of orbitals will then be evaluated as [52]

$$\mathbf{O} = \left(\mathbf{C}^{\text{old}} \right)^{\dagger} \mathbf{S} \mathbf{C}^{\text{new}}, \quad (1.70)$$

where O_{ij} is the overlap between the i th old and j th new orbital, and \mathbf{C} and \mathbf{S} are the MO coefficient matrices and overlap matrix, respectively. To determine the occupation of the new guess state, the projections of the j th new orbital onto the old space is evaluated [52],

$$p_j = \sum_i^n O_{ij} = \sum_q^{N_{\text{orbitals}}} \left[\sum_p^{N_{\text{orbitals}}} \left(\sum_i^{N_{\text{occ}}} C_{ip}^{\text{old}} \right) S_{pq} \right] C_{qj}^{\text{new}}. \quad (1.71)$$

The orbitals chosen as occupied in the new guess state are those showing the largest p_j . This procedure is repeated until convergence is reached when solving the SCF equations.

A modification of MOM is *initial* MOM [53] (IMOM). Here, rather than updating the old guess in each iteration, one always considers the overlap to the initial guess. This procedure shows improved convergence compared to MOM, and the generated states are less likely to fall back on the ground state, which is sometimes the case for MOM [53]. One disadvantage of MOM and IMOM that should be kept in mind is that the excited states generated by this approach are not orthogonal to the ground state [52].

CHAPTER 2

Molecular Properties of Interest

Once a method for solving Eq. (1.3) has been chosen, molecular properties can be determined by considering Eq. (1.36). The chosen methods for this work have been CCSD and TDDFT. As all method development has been for CCSD, presented in the previous chapter, all equations in this chapter will be given only for this method. First, the molecular gradient is introduced followed by different X-ray spectroscopies considered in this work. At the end of the chapter, line broadening is discussed, as this is an important part of simulating spectra.

2.1 Molecular Gradients

One very important property of the molecule is its molecular gradient, $\frac{\partial E}{\partial R} \equiv \nabla E$. Firstly, is it paramount for the optimization of molecular geometries to the minimum-energy structures. The most obvious choice of geometry for computing static spectra is the equilibrium geometry, found at the bottom of the potential energy well. The optimized structures are therefore the natural starting point of any calculation. Secondly, the molecular gradient is also of great importance when considering nuclear dynamics (see Section 3.1). During this project, the molecular gradient was implemented at the CCSD level of theory for both ground and excited states (see Publication 1, Appendix A). The implementation was carried out in the open source program *eT* [54], using a very efficient Cholesky-based scheme. Here, we utilize that the two-electron integrals can be written [55, 56]

$$\begin{aligned} g_{pqrs} &= (pq|rs) = \sum_{KL} (pq|K)(S^{-1})_{KL}(L|rs) \\ &= \sum_J L_{pq}^J L_{rs}^J \end{aligned} \tag{2.1}$$

with

$$S_{KL} = (K|L), \quad (2.2)$$

for the elements K and L in the Cholesky basis. The molecular gradient can be written as the derivative of the Lagrangian, \mathcal{L} , i.e., [57, 58]

$$\mathcal{L}^{(1)} = \sum_{pq} h_{pq}^{(1)} D_{pq} + \sum_{pqrs} g_{pqrs}^{(1)} d_{pqrs} + \sum_{p \leq q} \bar{\kappa}_{pq} F_{pq}^{(1)}, \quad (2.3)$$

where $\mathcal{L}^{(1)}$ is the derivative Lagrangian ($\frac{\partial \mathcal{L}}{\partial R} = \frac{\partial E}{\partial R}$). D_{pq} and d_{pqrs} are the one- and two-electron densities, $\bar{\kappa}_{pq}$ are the orbital rotation multipliers, $h_{pq}^{(1)}$ and $g_{pqrs}^{(1)}$ are the one- and two-electron derivative integrals, and $F_{pq}^{(1)}$ is the derivative Fock matrix. In Publication 1, these derivative integrals are evaluated in a basis that is strictly orthonormal at all geometries [59, 60]. The main focus of the implementation was on the two-electron part of the gradient. Here, it was utilized that one can avoid storing the OV^3 and V^4 blocks of the two-electron density matrix and instead directly construct two- and three-index intermediates [61]. Furthermore, as the derivative integrals involving the Cholesky basis are constructed on-the-fly, these need not be stored, thus avoiding an $N(O^4)$ storage requirement [61].

In this work, only geometry optimizations have been considered, however, with further work, it might also be possible to consider nuclear dynamics. The new implementation was shown to be efficient, taking up around 7% of the calculation time for geometry optimizations in the ground state and only 5% for the excited state [61]. Moreover, the implementation showed considerable time savings compared to other codes [61]. This, however, to a large extent can be attributed to the general efficiency of the ground and excited state codes of the respective programs [61]. For further details of the implementation of the molecular gradient at the CCSD level of theory, see Publication 1 in Appendix A.

Work towards extending the CCSD implementation to core excited states is in progress. When valence excited states are considered, one only needs to evaluate the virtual-occupied block of the orbital rotation multipliers [58, 62]. When one considers core excited states (and hence a CVS-based method), the remaining blocks of these multipliers must also be evaluated [62]. This means modifying the orbital relaxation and reorthonormalization contributions to the molecular gradient.

2.2 X-ray Absorption, Emission and Photoelectron Spectroscopy.

With the increasing availability and continuous development of X-ray facilities allowing for still more accurate experiments [63], the computation of X-ray spectra have become a field of great interest. A review of the developments of the related theory can be found in, e.g., Ref. 64. For some time now, the computation of X-ray absorption, emission and photoelectron spectroscopy (XAS, XES and XPS) has been well established, even at higher levels of theory, such as CCSD [54, 64–68]. These calculations can be carried out in several quantum chemistry codes [54, 65, 68]. This work has been concerned with all of the above mentioned types of spectroscopy, although mainly XAS. As such, a brief introduction will be presented.

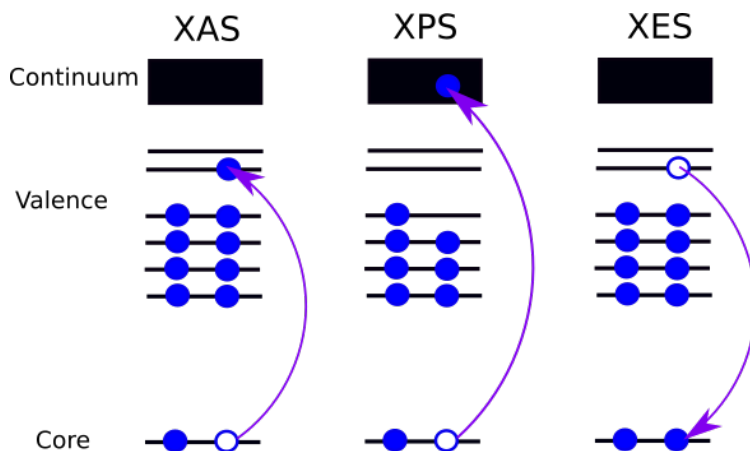


Figure 2.1. Schematic illustration of the XAS (left), XPS (middle) and XES (right) processes. Filled circles indicate an electron, while an empty circle indicates a hole, i.e., a removed electron.

2.2.1 XAS

The spectra resulting from absorption of a photon with sufficient energy to excite a core electron (see Fig. 2.1, left) are known as XAS. Technically, experiments in the region where only the bound-to-bound states are considered are known as X-ray absorption near edge spectroscopy (XANES), while experiments in the energy

regions above the core ionization threshold, in which scattering dominates, are denoted near edge X-ray absorption fine structure (NEXAFS) and extended X-ray absorption fine structure (EXAFS). Throughout this work, we consider only the bound-to-bound excitations and thus XAS will here refer only to XANES.

In principle, the idea for simulating core excitations is the same as for valence excitations. The latter are determined by solving a set of equations such as Eq. (1.43) for TDDFT or Eqs. (1.56) and (1.57) for CC. The computations are, however, more complicated for core excitations. Standard eigenvalue solvers, such as, e.g., the Davidson solver [69], determines the lowest eigenvalues first. Core excited states can therefore be reached only after first determining all valence excited states. Computing core excitations in this manner would therefore be tedious, if at all possible. By employing the core-valence-separation (CVS) [70, 71] scheme, the valence excitations can be filtered out, and the core excitations are then easily reached. For further details, see Section 2.2.1.1.

The excitation energies give only the expected positions of signals in an experimental spectrum, but it is of course also necessary to consider intensities. Such intensities of the transitions are theoretically computed as oscillator strengths, which are related to the transition probabilities. The oscillator strengths are discussed in Section 2.2.1.3.

Throughout this work, XAS spectra have been computed for many different molecules using existing implementations (see Publication 2 and Manuscripts 1-2 in Appendices B, D, and E). Note that the damped response solver, implemented for this work (See Manuscript 1, Appendix D), could in principle also have been employed.

2.2.1.1 Core-Valence-Separation

The general idea behind the CVS approximation [70] is that the core and valence space can be separated. In practice, where the linear equations are solved iteratively using a set of trial vectors, this means zeroing out all elements in the trial vectors that do not involve a core orbital.

For CCSD, the approximation can be considered in different flavours [72]. One could, for instance, retain all the elements of the single excitation part of the trial vector, while zeroing out elements not involving the core orbitals in the double excitation part [72]. This is known as the CVS with valence uncoupled singles (CVS-uS) approximation. Only the standard CVS approximation is so far available for computing XAS with the standard response solver in the e^T and Q-Chem codes. Both the standard CVS and the CVS-uS approximations have, however, been implemented for the damped response solver in this work (see Manuscript 1, Appendix D).

2.2.1.2 Frozen Core

A related approximation, which reduces computational costs, is the frozen core (fc) approximation [73]. As in CVS, the core and valence orbitals are considered to be non-interacting, but now both core-core and core-valence correlation are neglected [73]. For CC-based methods, the fc approximation means that the elements of the ground state amplitudes, t_μ , and multipliers, \bar{t}_μ , are set to zero if they refer to excitations involving a core electron [66]. Thus, fc corresponds to freezing the core orbitals [73]. This approximation is always invoked for generating the ground state in the existing implementation of core spectroscopy at the CC level of theory in Q-Chem [66]. Observe though that in Q-Chem, the implementation for core spectroscopy is more of a "frozen edge" approximation. Here, the frozen orbitals are only those associated with the same or lower energies compared to the probed K -edge. Only for calculations at the carbon K -edge is the approximation therefore a true fc. In this work, we will, however, not distinguish.

The fc approximation is not yet available for core excited states within the e^T program [54], where implementations have been carried out for this work.

2.2.1.3 Transition Moments and Oscillator Strengths

The intensities of transitions in absorption spectra are calculated as the oscillator strengths, f_{osc}^{if} , for each electronic transition from an initial state, $\langle i|$, to a final state, $\langle f|$:

$$f_{osc}^{if} = \frac{2}{3} \omega_{if} \sum_{\alpha} \langle i | \hat{\mu}_{\alpha} | f \rangle \langle f | \hat{\mu}_{\alpha} | i \rangle, \quad (2.4)$$

where $\hat{\mu}_{\alpha}$ is the α -component of the dipole operator and ω_{if} is the excitation energy. The integrals $\langle i | \hat{\mu}_{\alpha} | f \rangle$ and $\langle f | \hat{\mu}_{\alpha} | i \rangle$ are known as the transition moments, which are denoted $T_{\mu_{\alpha}}^{if}$ and $T_{\mu_{\alpha}}^{fi}$ respectively. In the EOM-CC formalism, they are given as

$$\text{EOM} T_{\mu_{\alpha}}^{if} = \sum_{\nu} L_{\nu}^f \xi_{\nu}^{\mu_{\alpha}} \quad (2.5)$$

$$\text{EOM} T_{\mu_{\alpha}}^{fi} = \sum_{\nu} \eta_{\nu}^{\mu_{\alpha}} R_{\nu}^f. \quad (2.6)$$

2.2.2 XPS

XPS has only been considered for a few calculations throughout this work. The existing XPS (development) code as well as the valence photoelectron spectroscopy

code of the e^T program was, however, used in the presented implementation of XES (see Manuscript 1, Appendix D). Therefore, a brief note on the underlying idea is in order.

Just as XAS, XPS is a one photon process, where the molecule, upon absorption of a photon, promotes an electron to the continuum. This creates a state with one electron less than the original state (see Fig. 2.1, middle). At the EOM-CC level of theory, the approach for computing ionized states is similar to that for computing excitations. A difference is that, instead of using excitation operators in Eqs. (1.49) and (1.50), one uses ionization operators [74], i.e.,

$$\hat{R}^{\text{ionize}} = \sum_i R_i a_i + \sum_{i < j, a} R_{ij}^a a_a^\dagger a_j a_i + \dots, \quad (2.7)$$

where a_a^\dagger is a creation operator, creating an electron in orbital a , while a_i is an annihilation operator, removing an electron from orbital i . Here, i, j, \dots refers to occupied orbitals, while a, b, \dots refers to virtual orbitals in the HF-reference. Thus, $\hat{\tau}_{ai} = a_a^\dagger a_i$.

The intensities of ionization spectra are determined as the squared norm of the Dyson orbitals [67],

$$\|\phi_{if}^d\|^2 = \sum_p \gamma_p^2 \quad (2.8)$$

with

$$\phi_{if}^d = \sqrt{N} \langle \Psi_i^N | \Psi_f^{N-1} \rangle = \sum_p \gamma_p \psi_p \quad (2.9)$$

$$\gamma_p = \langle \Psi^N | a_p^\dagger | \Psi^{N-1} \rangle, \quad (2.10)$$

$$(2.11)$$

where ϕ_{if}^d is a Dyson orbital, $\langle \Psi_i^N |$ denotes the initial state of the wavefunction with N electrons and $\langle \Psi_f^{N-1} |$ is the final state with $N - 1$ electrons. The Dyson orbital can be expanded in a set of reference molecular orbitals, ψ_p , where p denotes a general orbital with amplitude γ_p . In CC, the $\langle \Psi_0^{CC} |$ and $|\Psi_0^{CC}\rangle$ states are not adjoint (see Section 1.2.3). Therefore, both RHS and LHS amplitudes must be calculated separately to construct the squared norm of the Dyson orbitals [75].

2.2.3 XES

XES is also a one photon process, where one photon is emitted by a molecule in an excited state, resulting in de-excitation (see Fig. 2.1, right). The energy

emitted from de-exciting a valence electron to the core region can be considered as [50]

$$E_{em} = E_{ip}^c - E_{ip}^v, \quad (2.12)$$

where E_{ip}^c and E_{ip}^v are the core and valence ionization energies. The oscillator strength of this process, f_{osc}^{vc} , is determined from the expression [50]

$$f_{osc}^{vc} = \frac{2}{3}(E_{ip}^c - E_{ip}^v)(S_{XX}^{vc} + S_{YY}^{vc} + S_{ZZ}^{vc}) \quad (2.13)$$

with

$$S_{XX}^{vc} = T_X^{vc} T_X^{cv} \quad (2.14)$$

$${}^{\text{EOM}}T_X^{vc} = (L_v \mathbf{A}^X R_c) - (\bar{t} R_c)(L_v^{\text{EOM}} \eta^X) - (L_v \mathbf{I} R_c)(\bar{t}^{\text{EOM}} \eta^X), \quad (2.15)$$

where S_{ii}^{vc} denotes the diagonal elements of the transition strength matrix.

This efficient and simple implementation scheme was recently proposed by Faber and Coriani [50]. It is by following this approach that XES has been implemented in the open source e^T program as part of this work. For further details, see Faber and Coriani [50] and Manuscript 1 (Appendix D).

2.3 RIXS

Where XAS, XES, and XPS are all one photon processes, resonant inelastic X-ray scattering (RIXS) is a two-photon process. It can be thought of as the absorption of one photon in the X-ray area, resulting in the excitation of one core electron, followed by the emission of another photon, also in the X-ray energy region [76]. It is this emission that is recorded as RIXS. The two-photon process results in the molecule ending up in a valence excited state. Thus, the transition energies are determined as the difference between the (resonant) core excitation energy and valence excitation energies. The intensities of the emission can be calculated as [50, 77]

$$\sigma_{\theta}^{if} = \frac{\omega_{em}}{\omega} \frac{1}{15} \sum_{XY} \left[\left(2 - \frac{1}{2} \sin^2 \theta \right) \mathcal{F}_{XY}^{0f}(\omega) \mathcal{F}_{XY}^{f0}(\omega) \right. \quad (2.16)$$

$$\left. + \left(\frac{3}{4} \sin^2 \theta - \frac{1}{2} \right) (\mathcal{F}_{XX}^{if}(\omega) \mathcal{F}_{YY}^{fi}(\omega) + \mathcal{F}_{YY}^{if}(\omega) \mathcal{F}_{XX}^{f0}(\omega)) \right], \quad (2.17)$$

where $\mathcal{F}_{XY}^{if}(\omega)$ and $\mathcal{F}_{XY}^{fi}(\omega)$ are transition moments, calculated based on a damped response solver (see Section 2.3.1). The core resonance energy (i.e., the core excitation energy) is denoted ω , and ω_{em} is the emission energy (i.e., the energy

difference between the core and valence excitation). The angle, θ , is defined as the angle between the incident photon and the scattered photon [50].

The mathematical background for RIXS at the CCSD level of theory is described in detail in Ref. 50 and will not be discussed further here.

As is the case for Raman spectroscopy, RIXS is complementary of the corresponding absorption spectroscopy, i.e., XAS, as the two methods have different selection rules [72]. It should be observed that, while formally a one-photon process, XES corresponds to RIXS computed at a non-resonant frequency, i.e., core transitions above the ionization threshold. Whereas XAS probes the unoccupied valence states, and XES probes the occupied core states, RIXS probes both of these types of states as well as their correlation [78].

2.3.1 Complex Damped Response Solver

The basis for computing RIXS spectra is a damped response solver. Such a solver has been implemented at various levels of theory over the past decades [22, 50, 79–90]. In this work, only the CCSD level implementation has been considered, which is thoroughly described by, e.g., Kauczer *et al.* [85] and Faber and Coriani [50]. The equations shall therefore not be repeated. Suffice to say that a damping factor, γ , is introduced around the excitation energy when solving the linear response equations, Eqs. (1.67) and (1.68). This effectively sets $\omega_{\text{damped}} = \omega + i\gamma$, where i is the imaginary phase. Using the damped response solver allows the molecular properties to be evaluated at all energies, without encountering singularities [79]. Such a damped response solver was implemented in the e^T code for this work based on the equations given in Refs. 50 and 85 (see Manuscript 1, Appendix D).

2.4 Auger-Meitner Electron Spectroscopy

Another process that has been considered is Auger-Meitner electron spectroscopy (AES). While spectra have been simulated for the study of Oxazole (Publication 2, Appendix B), the theory behind has not been considered. Instead, the existing EOM-CCSD implementation of Skomorowski and Krylov [91, 92] in Q-Chem has been employed almost as a black box method. This is also the case for the new one-center-approximation implementation in OpenMolcas [93], as these calculations were run by a colleague. Thus, the equations behind these implementations will not be discussed. A few notes on the process will, however, be given.

The Auger process consists in the decay of a core excited state resulting in the simultaneous emission of light and a valence electron [94]. Two kinds of Auger spectroscopy exist: normal and resonant. In the normal Auger process, the initial

state is prepared by core ionization [92]. This state can then undergo spontaneous emission, releasing energy, which allows a valence electron to be ejected [92]. The final state can therefore either have singlet or triplet spin symmetry (assuming a closed-shell initial state), and these two decay channels are distinguished in calculations [92]. In the resonant Auger process, the initial state is created by a resonant excitation of a core electron to a valence unoccupied orbital [92]. As for the normal Auger process, this state then undergoes spontaneous emission, and the released energy allows an electron to be ejected [92]. The ejected electron can here either be the one initially excited from the core, which gives rise to a participator type decay, or it can be another valence electron, resulting in a spectator type decay [92]. As was the case with singlet and triplet decay channels for the normal Auger process, the participator and spectator decay channels can be distinguished theoretically [92]. At the CCSD level of theory, the spectator decay channel is not well described. Skomorowski and Krylov [91, 92] reported that the method is unable to satisfactorily describe $2h1p$ ionizations, which are required to describe this decay channel. The poor description of $2h1p$ ionizations was also observed by Moitra *et al.* [95].

2.5 Line Broadening

So far, it has been discussed how to obtain transition energies and intensities in order to simulate experimental spectra. These properties, however, leads only to a spectrum consisting of sticks, since the transition energies are determined as a set of discrete values. In principle, with a damped response solver, one can compute intensities for all energies within a given range, but this is not the approach typically adopted. An experimental spectrum does not consist of sticks. Each signal has some width, and we must therefore consider a line broadening of the theoretically determined transitions. There are several effects that contribute to this broadening, e.g., Doppler broadening and lifetime broadening [23]. Doppler broadening is caused by the molecules of the sample moving, since a small increase in frequency is observed when the molecule moves towards the detector. Likewise, a small decrease is seen, if the molecule is moving away from the detector [23]. Generally, such broadening can be described by a Gaussian function. As the movement of molecules can be limited by decreasing the temperature, this effect can to some extent be controlled, if the sample can be kept sufficiently cold [23]. Lifetime broadening, on the other hand, cannot be controlled [23]. It stems from the energy-time uncertainty principle, stating that one cannot know with arbitrary precision the energy of a state with a finite lifetime (τ_{life}) [23]:

$$\Delta E \approx \frac{1}{\tau_{\text{life}}}. \quad (2.18)$$

This type of broadening can be described by a Lorentzian function [96]. As lifetime broadening cannot be eliminated, this is the type of line broadening that has been taken into account when simulating the spectra in this work. Thus, the broadened intensity, $I_{\text{br}}(\omega)$, at a given energy, ω can be determined as [96,97]

$$I_{\text{br}}(\omega) = \frac{I_{ex}}{1 + \left(\frac{\omega - \omega_{ex}}{\Gamma}\right)^2}, \quad (2.19)$$

where Γ is the half width at half maximum (HWHM) of the signal centered around the transition with transition energy ω_{ex} and transition strength I_{ex} . The width is generally determined by fitting to experimental data.

Observe that the introduction of the damping factor, γ , in the damped response solver also in principle introduces some line broadening. The damped response solver can therefore, as mentioned, be used to evaluate the cross sections in a given energy range [79]. Nevertheless, in this work, the damped response solver has, however, only been used for calculating RIXS (stick) spectra. Thus, the broadening was added only when plotting by use of the Lorentzian function in Eq. (2.19).

CHAPTER 3

Nuclear Dynamics

In order to study the dynamics of a system experimentally, the system must be pumped by a short laser pulse (purple arrow in Fig. 3.1), resulting in a photoexcited or photoionized state. Following this perturbation, the system is

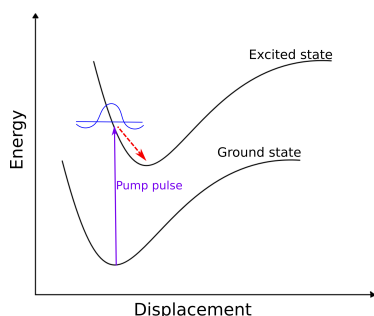


Figure 3.1. Illustration of the excitation process (purple arrow) and subsequent relaxation (red arrow) of a system, illustrated by a (blue) wavepacket, on the excited state.

no longer at its equilibrium structure (the bottom of the energy well in Fig. 3.1). The system must therefore relax on the potential energy surface (movement along the red arrow in Fig. 3.1). The resulting electronic and nuclear dynamics can then be studied, if the system is probed in a manner suited to reveal the desired information. Some of these possible methods, such as, e.g., XAS, were discussed in the previous chapter. Theoretically, the challenge then becomes to describe the nuclear motion of the system, in addition to the electronic structure, discussed in Chapters 1.1 and 1.2. When considering the equation of motion for the nuclei, it is instructive to take a step back from the BOA, which was employed to obtain Eq. (1.4). If we simply expand the total wavefunction in a complete basis consisting of solutions to the electronic Schrödinger equation, Eq. (1.3), and expansion coefficients, $\chi(R, t)$, so that [18]

$$|\Psi\rangle = \sum_p |\Psi_p^{\text{elec}}\rangle \chi_p(R, t), \quad (3.1)$$

we can write Eq. (1.1) as

$$i \frac{\partial}{\partial t} \sum_p |\Psi_p^{\text{elec}}\rangle \chi_p(R, t) = [\hat{H}_e + \hat{T}_N] \sum_p |\Psi_p^{\text{elec}}\rangle \chi_p(R, t). \quad (3.2)$$

To obtain the equation of motion of the nuclei, we now use that the solutions to the electronic wavefunction are orthonormal and independent of time. We thus project onto Eq. (3.2) the electronic wavefunction of state q , $\langle \Psi_q^{\text{elec}} |$ [98]:

$$\begin{aligned} i \sum_p \langle \Psi_q^{\text{elec}} | \Psi_p^{\text{elec}} \rangle \frac{\partial}{\partial t} \chi_p(R, t) &= \sum_p \langle \Psi_q^{\text{elec}} | [\hat{H}_e + \hat{T}_N] | \Psi_p^{\text{elec}} \rangle \chi_p(R, t) \\ &\Downarrow \\ \frac{\partial}{\partial t} \chi_q(R, t) &= [\hat{T}_N + E(R)] \chi_q(R, t) \\ &\quad - \frac{1}{2} \sum_p \sum_A^{N_{\text{nuclei}}} \frac{1}{m_A} \left[\langle \Psi_q^{\text{elec}} | \nabla_A^2 | \Psi_p^{\text{elec}} \rangle \chi_p(R, t) \right. \\ &\quad \left. + 2 \langle \Psi_q^{\text{elec}} | \nabla_A | \Psi_p^{\text{elec}} \rangle \nabla_A \chi_p(R, t) \right] \end{aligned} \quad (3.3)$$

The last two terms of Eq. (3.3) that were not present when employing the BOA (see Eq. (1.4)) are known as the non-adiabatic coupling terms. In the adiabatic approximation, the wavefunction evolves on a single electronic state. Therefore, p has only one possible value ($p = q$), and only the diagonal coupling terms are retained. Note that these terms do not couple different states. Instead, they provide a correction to the electronic energy and hence, the potential energy surface (PES) considered [98].

It is thus Eq. (3.3) that must be solved when we wish to describe nuclear dynamics. In practice this is done by following one of two possible approaches. Either it is attempted to solve the equation directly, by, e.g., considering wavepackets¹ [99], or the single surface movement of the nuclei is approximated as classical. In the latter case, Eq. (3.3) is replaced by Newton's second law:

$$-\nabla E = m \ddot{R}, \quad (3.4)$$

¹In quantum mechanics, a particle can be described as a wave (e.g., a sine function for a harmonic wave), defined by a momentum [23]. As per the Heisenberg uncertainty principle, the exact momentum and position of a particle cannot be known simultaneously [23]. If only a single wave is considered, the momentum is known, however, the position is not. If the wave is described not by a single function but by a superposition of functions with different momenta, the particle position will become more localized. The momentum, on the other hand, is no longer known exactly. Such a superposition of waves to describe a particle is known as a wavepacket [23].

where ∇E is the molecular gradient of the relevant PES (see Chapter 2.1), m is the vector containing the atomic masses, and $\ddot{\mathbf{R}}$ is the second time-derivative of the vector containing all nuclear positions.

The former approach of solving the time-dependent Schrödinger equation directly is of course formally the most precise. It is, however, very computationally expensive and generally one can only consider a few degrees of freedom (DOFs) [100]. The system must therefore be restricted to movement along a subset of DOFs. Thus, both methods involve approximations of Eq. (3.3) beyond that of the choice of wavefunction method (or, if DFT is considered, the choice of functional). The approach based on Newton's second law, while obviously an approximation, allows us to consider all DOFs [101]. In addition, approximating the single surface movement of the nuclei as classical is reasonable, since the nuclei are heavy from a quantum mechanical point of view [23]. Several computational schemes exist for simulating the full nuclear dynamics [99, 101–104]. When considering classical nuclei, for instance, surface hopping (SH) [101, 102] and ab initio multiple spawning (AIMS) [103] are available. Time-Dependent Hartree (TDH) [99] and multi-configurational TDH (MCTDH) [100, 104], on the other hand, both treat the nuclei quantum mechanically. Here, we shall consider only the two methods, which have been utilized for the present project. First, the simple surface hopping scheme [102], as implemented in the SHARC-2.1.1 program [101, 105, 106], based on solving Newton's second law. Second, the MCTDH [100, 104] approach, as implemented in the MCTDH-8.4.12 program [107], based on considering the time-dependent problem quantum mechanically with a limited number of DOFs.

3.1 Surface Hopping

In surface hopping, the adiabatic movement of the nuclei is treated classically, thus reducing the total Hamiltonian to the electronic Hamiltonian ($\hat{H} = \hat{H}_e$). Hence, Eq. (1.1) can in this case be rewritten as [106]

$$i \frac{\partial}{\partial t} \sum_p |\Psi_p^{\text{elec}}\rangle c_p(t) = \hat{H}_e \sum_p |\Psi_p^{\text{elec}}\rangle c_p(t), \quad (3.5)$$

where the electronic wavefunction has been expanded in a set of basis functions. These are the solutions to the time-independent Schrödinger equation, Eq. (1.3), $|\Psi_p^{\text{elec}}\rangle$, and are recalled to depend parametrically on the time-dependent nuclear coordinates. The corresponding expansion coefficients, $c_p(t)$, are also defined as time-dependent.

By projecting against the electronic state $\langle \Psi_q^{\text{elec}} |$, we obtain [106]

$$i \frac{\partial}{\partial t} c_q(t) = \sum_p H_{qp} c_p(t) - i \sum_p \langle \Psi_q^{\text{elec}} | \frac{\partial}{\partial t} | \Psi_p^{\text{elec}} \rangle c_p(t), \quad (3.6)$$

where the last term is usually computed as [106]

$$\langle \Psi_q^{\text{elec}} | \frac{\partial}{\partial t} | \Psi_p^{\text{elec}} \rangle c_p(t) = \sum_A^{N_{\text{nuclei}}} \langle \Psi_q^{\text{elec}} | \nabla_A | \Psi_p^{\text{elec}} \rangle \frac{dR_A}{dt} c_p(t), \quad (3.7)$$

which we recognize as the velocity of the nuclei A multiplied by a non-adiabatic coupling term. The explicit calculation of this term is often avoided by using the local diabatization scheme suggested by Granucci *et al.* [108]. Instead, the overlap, $S_{qp}(t, t + \delta t)$, between the electronic wavefunction in states q and p , respectively, at the nuclear geometries corresponding to two subsequent time steps (t and $t + \delta t$), is evaluated [106]:

$$S_{qp}(t, t + \delta t) = \langle \Psi_q^{\text{elec}, t} | \Psi_p^{\text{elec}, t+\delta t} \rangle. \quad (3.8)$$

This expression is used when defining a propagator, based on Eq. (3.5), to calculate the expansion coefficient for a new time step, $c_p(t + \delta t)$, from that of a previous one, $c_p(t)$. While Eq. (3.8) does not replace the non-adiabatic coupling term in Eq. (3.6) one to one, it does allow the computation of $c_p(t + \delta t)$ to be independent of this non-adiabatic coupling term [109]. For further details, see, e.g., Ref. 109. Note that in SH calculations, the sum over p is truncated to only include predefined states of interest [105]. Observe also that in Eq. (3.6), $H_{qp} = \delta_{pq} E_q$ when the basis functions are eigenfunctions of the electronic Hamiltonian. This is true, if \hat{H}_e is defined as the molecular Coulomb Hamiltonian (MCH), which is defined in Eq. (1.2). In this case, we say that we use the MCH representation [106]. One might, however, include additional coupling terms, accounting for interactions with an external field or indeed any interactions going beyond the Coulomb interaction [106]. This was, for instance, done in Eq. (1.23), where a perturbation of the system was included and the MCH was denoted $H^{(0)}$. For additional interaction terms, $|\Psi_p^{\text{elec}}\rangle$ is no longer an eigenstate of $\hat{H}_e^{\text{total}} = \hat{H}_e^{\text{MCH}} + \hat{H}^{\text{interaction}}$. The total Hamiltonian can be diagonalized by a unitary transformation of the MCH to yield the diagonal representation [106]:

$$\mathbf{H}^{\text{diag}} = \mathbf{U}^\dagger \mathbf{H}^{\text{MCH}} \mathbf{U} \quad (3.9)$$

$$|\Psi_q^{\text{elec,diag}}\rangle = \sum_p |\Psi_p^{\text{elec,MCH}}\rangle U_{pq}, \quad (3.10)$$

where

$$H_{pq}^{\text{diag}} = \langle \Psi_q^{\text{elec,diag}} | \hat{H}_e^{\text{total}} | \Psi_p^{\text{elec,diag}} \rangle \quad (3.11)$$

$$H_{pq}^{\text{MCH}} = \langle \Psi_q^{\text{elec,MCH}} | \hat{H}_e^{\text{total}} | \Psi_p^{\text{elec,MCH}} \rangle \quad (3.12)$$

$$\hat{H}_e^{\text{MCH}} | \Psi_p^{\text{elec,MCH}} \rangle = E_p | \Psi_p^{\text{elec,MCH}} \rangle. \quad (3.13)$$

In one of the studies presented here, spin-orbit coupling terms were included in the Hamiltonian and the diagonal representation was used (see Chapter 5.2). These couplings should, however, only be large, when heavy atoms are considered [105]. Furthermore, these couplings are mainly of interest when studying inter system crossings [101], which have not been considered here. The MCH and diagonal representations should therefore in our study be very similar. The similarity between calculations employing the two representations is indeed noted by investigating Manuscript 2 and its corresponding supplementary information (Appendix E).

When employing the surface hopping procedure, as implemented in SHARC, the system we wish to investigate is initially prepared by optimizing its geometry to the equilibrium structure of the initial PES at a chosen level of theory. Moreover, all DOFs of the system, expressed in terms of normal modes, are computed. This is based on the harmonic oscillator approximation. In this approximation, the potential is considered to be of the form $\frac{1}{2} \sum_i a_i Q_i^2$, where i is a normal mode, Q_i is the displacement along that mode, and a_i is a coefficient that depends on the masses of the atoms involved in the normal mode [24]. Note that this approximation is only valid for small displacements away from equilibrium [24].

Since the nuclei move according to the laws of classical mechanics, at each time step the system described by a given trajectory can have one geometry and reside in one electronic state only. In order to simulate the quantum behaviour of the system, i.e., that a particle can be in many places at once until measured, we must prepare a number of geometries from which our trajectories can start. These can be computed by use of a probability distribution function. Hence, a given number of geometries can be determined based on the initially optimized geometry and this probability distribution. The Wigner distribution function [110] was introduced as a reformulation of non-relativistic quantum mechanics [111] and is thus a popular choice, when performing surface hopping simulations [106, 112]. A script for generating initial conditions based on this distribution function is available in SH programs, such as, e.g., SHARC and NewtonX [113, 114]. Once the initial geometries are found, the electronic Schrödinger equation, Eq. (1.3), must be solved for all the geometries. Here, it is necessary to compute not only ground state energies but also excitation energies and their corresponding oscillator strengths for all states to be considered in the calculation. Initial conditions, from which to start trajectories, are then chosen based on which geometries show

a large probability of reaching the desired excited state, when a given distribution of excitation energies is employed. It is also possible to calculate initial conditions based on ionization energies rather than excitation energies. The probability of the ionizations are then determined from the Dyson orbital squared norms, whereas the excitation process considers the oscillator strengths (see also Chapters 2.2.1.3 and 2.2.2).

Once the initial geometries are found, the forces of the system must be computed, to solve Eq. (3.4). For each initial condition, one trajectory can be simulated. At each step, one must compute the molecular gradient using quantum mechanics in order to obtain the forces and hence the PES on-the-fly. This requires Eq. (1.3) to be solved using the MCH representation for the current geometry of the trajectory. Here, it is again necessary to compute both the ground state energies and excitation energies as well as the gradient of the current electronic state of the trajectory. If one desires to simulate the nuclear dynamics using the diagonal representation, which can be advantageous [106], the gradient is transformed to this basis. Based on the computed gradient, giving the forces working on the molecule, the trajectory can then be propagated classically using Eq. (3.4).

For a classical trajectory, it is only possible to move on one PES, i.e., adiabatic dynamics. In general, what is of interest, when we simulate nuclear dynamics, is the non-adiabatic dynamics, i.e., when the molecule moves *between* PESs. In order to allow this behaviour, at each timestep probabilities of a jump between the current electronic state and all other electronic states are computed. This is done based on Tully's fewest switches SH (FSSH) approach [102]. For a time step of length δt , the probability of a jump from state p to state q , $p^{p \rightarrow q}(t)$, (see, e.g., Refs. 98 and 115) is

$$p^{p \rightarrow q}(t) = \sum_A^{N_{\text{nuclei}}} \frac{\langle \Psi_p^{elec} | \nabla_A | \Psi_q^{elec} \rangle \frac{dR_A}{dt} \text{Re}[c_p^*(t)c_q(t)] \delta t}{|c_p(t)|^2} \quad (3.14)$$

based on the time dependent expansion coefficients of the wavefunction, $c_p(t)$, which are obtained by solving Eq. (3.6). In SHARC, the diagonal representation is generally preferred [106], which yields a modified equation for computing the probabilities compared to Eq. (3.14). For further details, see Ref. 106.

Quantum mechanics is non-deterministic in the sense that the outcome of an experiment can only be determined with a certain probability [23]. The probabilities (and corresponding outcomes) are, however, deterministic. In order to simulate this quantum behaviour of the system, a random number, X , is then generated and the trajectory will jump from the current electronic state, p , to a

new electronic state, q , if (see e.g. Ref. 115)

$$\sum_r^{q-1} \max\{0, p^{p \rightarrow r}(t)\} < X \leq \sum_r^q \max\{0, p^{p \rightarrow r}(t)\}. \quad (3.15)$$

It is this procedure of allowing trajectories to hop between PESs that has given the method its name.

In this work we have employed DFT methods to simulate the forces driving the nuclear dynamics, since this is a feasible method that generally yields results of a reasonable accuracy [35, 116–118]. When approaching the CI between S_0 and S_1 , DFT, however, inherently encounters problems [119, 120]. This is due to the single reference character of the (KS-)DFT ground state, which is not a good description of the system close to the CI. A way of circumventing this problem, which has also been utilized in this work (see Publication 3, Appendix C), is the procedure of using forced jumps to the ground state [116, 117]. This simply means that, if the energy gap between the current state and the ground state falls below a preset threshold, the jumping probability will be set to one. Thus, the trajectory will be forced to jump. This procedure can therefore be expected to give rise to too short life times as well as too small quantum yields (QY). The method has, however, been utilized with success also in other works [116, 117].

One shortcoming of SH that has so far not been discussed is its treatment of decoherence. Decoherence is a quantum effect, not included in the classical description of the nuclei [98, 106]. In quantum mechanics, a wavepacket will be spread over all the considered states. Therefore the gradient of each state must be evaluated so that the wavepacket can evolve on all electronic state based on their respective gradients [98, 106]. The geometries associated with the different states will thus diverge over time. When nuclear motion is considered to be classical, only the gradient associated with the current active state, which determines the next step, is evaluated [98, 106]. Hence, the same geometry will always be associated with all states. In quantum mechanics, the overlap of the wavepackets in the different states will therefore diminish over time. The superposition of the electronic states for classical trajectories will instead continue to evolve in a coherent manner [98, 106]. This difference affects the state populations, which for a single trajectory, k , can be evaluated based on the expansion coefficients, $c_s^k(t)$, for the state of interest, s (see e.g. Ref. 115):

$$pop_s^k(t) = |c_s^k(t)|^2. \quad (3.16)$$

Different schemes exist to correct for this deficiency [121, 122]. In this work, the energy-based correction scheme by Granucci *et al.* [121] was employed.

3.2 Multi-Configurational Time-Dependent Hartree

When attempting to solve the Schrödinger equation - be it the time-dependent or time-independent one, we generally expand our wavefunction in a set of basis functions. For a complete basis this would be exact [25], however, only for the smallest of systems is it possible to avoid truncation of the wavefunction. Thus, the wavefunction becomes, in practise, an approximation.

A popular and most successful approach, when solving the equation of motion for the nuclei, Eq. (3.3), is to use MCTDH. Here, the basis as well as the expansion coefficients are chosen to be time-dependent. For a system with f nuclear DOFs and n_k basis functions for the k th degree of freedom, the wavefunction can then be written as [104]

$$\chi(Q, t) = \sum_{j_1}^{n_1} \cdots \sum_{j_f}^{n_f} A_{j_1 \dots j_f}(t) \prod_k^f \phi_{j_k}^k(Q_k, t), \quad (3.17)$$

where $A_{j_1 \dots j_f}(t)$ are the expansion coefficients, $\phi_{j_k}^k(Q_k, t)$ are the basis functions, known as single particle functions, and Q are the nuclear (normal mode) coordinates. In addition, it should be noted that the product $\prod_k^f \phi_{j_k}^k(Q_k, t)$ is the Hartree product. Here, a basis of such Hartree products is used, instead of one consisting of the more complicated Slater determinants.

The Hartree product, unlike a Slater determinant, is not antisymmetric and therefore distinguishes between identical particles. Electrons are fermions. Thus, when one considers the electronic Schrödinger equation, it is essential to use an antisymmetric wavefunction to include exchange interactions between electrons [123]. For nuclei, on the other hand, these exchange interactions are small [123]. In practice, the use of a Hartree product rather than a Slater determinant does therefore not affect the results significantly [123].

As mentioned, our basis cannot be infinite, which naturally leads to an approximation of the wavefunction. Another important point to note is that the problem becomes too big to solve for all degrees of freedom with the current computational resources [100]. It is illustrative to consider that at the turn of the millennium, pyrazine, including all 24 DOFs, was the largest system considered using the MCTDH method and that required mode combination [124, 125]. Mode combination is a way of reducing the computational costs by limiting the number of single particle functions needed [100]. Rather than defining the wavepacket by Eq. (3.17), it is written as an expansion over p generalized particles

$$\chi(q, t) = \sum_{j_1}^{\tilde{n}_1} \cdots \sum_{j_f}^{\tilde{n}_p} A_{j_1 \dots j_p}(t) \prod_k^p \phi_{j_k}^k(q_k, t), \quad (3.18)$$

where q_k consists of a set of normal mode coordinates combined to a single particle, i.e. $q_k = (Q_l, Q_m, \dots)$. Thus, rather than considering n_i single particle functions, one now considers $\tilde{n}_i < n_i$ *multimode* single particle functions.

Despite the passing of two decades, the calculation of pyrazine remains one of the only examples of a full dimensional quantum dynamics calculation of a larger system [126]. In general, it becomes challenging, if at all possible, to consider more than six DOFs when using the MCTDH method without employing mode combination [100, 127]. Such combination, however, relies on knowing which modes to combine, which can be difficult. As a rule of thumb, the combined modes should have similar vibrational frequencies.

When actually performing an MCTDH calculation, the first step is to construct the Hamiltonian and PES. Unlike what is done in SH, the PES is not constructed on-the-fly, but must be determined prior to the propagation of the wavepacket. In this work, the PES of each normal mode has been approximated as a harmonic oscillator, since this is a good approximation for small displacements [24]. It is, however, possible to employ other models, such as, e.g., a Morse potential. The Hamiltonian is approximated as the vibronic coupling Hamiltonian [128–130]

$$\hat{\mathbf{H}}^{VC} = -\mathbf{1} \sum_k^f \frac{\omega_k}{2} \frac{\partial^2}{\partial Q_k^2} + \mathbf{1} \sum_k^f \frac{\omega_k}{2} Q_k^2 + \mathbf{W} \quad (3.19)$$

$$\mathbf{W}_{ss} = \epsilon_s + \sum_k^f \kappa_k^{(s)} Q_k + \sum_k^f \sum_l^f \gamma_{k,l}^{(s)} Q_k Q_l \quad (3.20)$$

$$\mathbf{W}_{sr} = \sum_k^f \lambda_k^{(s,r)} Q_k + \dots, \quad (3.21)$$

where the $\kappa_k^{(s)}$ -, $\gamma_{k,l}^{(s)}$ - and $\lambda_k^{(s,r)}$ -terms give the vibronic coupling and correspond to the non-adiabatic coupling terms in Eq. (3.3). Here, ω_k is the frequency of normal mode k in the ground state, and ϵ_s is the excitation energy for state s . The fitting parameter $\kappa_k^{(s)}$ is the linear intra-state coupling of normal mode k for state s , which modifies the energy gap between the states along mode k [128]. The parameter $\gamma_{k,l}^{(s)}$ accounts for the coupling between modes l and k in state s , while $\lambda_k^{(s,r)}$ is the linear inter-state coupling between electronic states s and r for normal mode k [128, 130]. Additional fitting parameters to account for the non-adiabatic couplings can be included [128], but will not be considered in this work. For further details, see, e.g., Refs. 128 and 129. Observe that all fitting parameters are based on adiabatic energies calculated by a chosen quantum chemistry method. In this work, the method of choice was TDDFT.

Once the PES has been constructed and the Hamiltonian defined (The Heidelberg MCTDH package includes the VCHAM program, which has excellent scripts

for assisting in defining the PES), the program propagates one wavepacket along the PES.

The modes to combine can be chosen by investigating the generated fitting parameters and, as mentioned, by generally considering modes of similar frequencies. Newer versions of MCTDH [131] also have scripts to assist in evaluating the choice of mode combination. This was not utilized in this work, where an older version of the program without this functionality was employed [107].

Part II

Results

CHAPTER 4

Static Spectra

4.1 Oxazole

Oxazole is a small aromatic heterocycle. It is an important building block in many molecules of pharmacological activity [132, 133] as well as in organic electronic devices [134].

The ground state characterization of this molecule, reported in Publication 2 (Appendix B), was carried out by investigating the valence photoelectron spectrum, XPS, XAS, and Auger-Meitner spectra at all second row atomic 1s core levels in the gas phase. This study was carried out as preparation for future time-resolved X-ray experiments on the molecule.

The experimental spectra were recorded at the Gas Phase Photoemission beamline at Elettra (Trieste, Italy) [135] by experimental collaborators. The supporting theoretical calculations were performed as part of the work for this thesis. Note that the restricted-active-space perturbation theory of second order (RASPT2) calculations presented in Publication 2 were performed by a theoretical collaborator.

Both occupied and unoccupied valence orbitals in oxazole were found to be typical for heterocycles [136]. In Publication 2, the highest occupied molecular orbitals (HOMOs) were found to consist of lone electron pair orbitals on the two hetero atoms as well as π orbitals [136]. The lowest unoccupied molecular orbitals (LUMOs) were instead seen to consist of π^* orbitals followed by σ^* orbitals [136]. As also observed in other small organic molecules [137, 138], the energetic ordering of the XAS peaks at the C K -edge was found to correspond well with the trends in electronegativity of the atoms bound to the respective carbons [136]. The agreement between experiment and theory, found in Publication 2, was generally good for both the valence photoelectron spectrum, XPS, and XAS. The theoretical understanding, and hence description of these processes, is thus noted to be good at the CC level of theory. Nevertheless, for XAS, relaxation effects from dynamical electron correlation were found to be of great importance [136]. In order to describe the spectra at the O and N K -edges properly, improvements on the CCSD method by including the effect of triple excitations in an iterative

manner via CCSDR(3) [71,139] were necessary. Such systematical improvements were not possible at the TDDFT level of theory. The TDDFT results were generally in excellent agreement with those obtained at the CCSD level of theory but were calculated at a lower computational cost [136]. It should be noted that absolute values of the excitation energies calculated at the CC level of theory were found to be in good agreement with experimental results (see Publication 2, Appendix B). This was not the case for TDDFT [136]. Here, the excitation energies displayed large shifts for XAS in agreement with previous studies [140].

The AES simulations proved more challenging [136]. The normal AES spectra were in reasonable agreement with experiment at the fc-CVS-EOM-CCSD level of theory, showing that the decay was dominated by the singlet decay channel [136]. The resonant spectra, on the other hand, could not be reproduced by the fc-CVS-EOM-CCSD calculations [136]. This was attributed to the fact that the CCSD method is only able to satisfactorily describe the participator decay channel, which dominates the high kinetic energy region of the spectra [136]. As already mentioned, this shortcoming in the CCSD-based calculations of resonant AES has previously been discussed by Skomorowski and Krylov [92]. They attribute it to the poor description of $2h1p$ states, due to the lack of $3h2p$ excitations in the CCSD model. The RASPT2 calculations [93] of the resonant spectra, though, were in good agreement with experiment, as it managed to describe both decay channels [136].

For further information, see Publication 2 in Appendix B.

4.2 RIXS

A damped response solver was implemented in a local development version of the e^T code [54] in order to simulate RIXS spectra (see Manuscript 1 in Appendix D). The code was tested by comparison to the existing implementation in the Q-Chem-5.4 code [65, 78], which employs the fc approximation for computing the ground state. This approximation was not invoked for calculations with our implementation. For further details, see Manuscript 1 (Appendix D).

The performance of the implementation was evaluated both at the CCSD level of theory and at the computationally cheaper second-order approximate coupled cluster singles and doubles (CC2) level of theory. Observe however that our implementation of the damped response solver was focused on CCSD. Hence, as mentioned in Manuscript 1, the CC2 problem can only be solved in full space at this point, which is inefficient. It was found that, while CC2 does not describe XAS spectra as well as CCSD, the description of RIXS was comparable between the methods (see Manuscript 1, Appendix D). It was therefore concluded in Manuscript 1 that computational effort might be saved without significant loss

of accuracy by employing CC2 when simulating these spectra. It was, however, noted to require the same valence transitions to be determined at the two levels of theory (see Manuscript 1, Appendix D).

Moreover, the implementation was evaluated for CCSD utilizing the full CVS as well as the alternative CVS-uS approximations in the damped response solver. In Manuscript 1, it was found that in some cases the results obtained using the CVS approximation differs from those obtained using the CVS-uS approximation. Here, the CVS-uS results were found to more closely resemble the spectra simulated without any CVS approximation. This has also previously been reported by Nanda and Krylov [72].

The performance of the implementation was, in addition, tested on imidazole in an aqueous solution. These calculations were performed by explicit inclusion of four water molecules. The resulting XAS was found to be well reproduced by this approach (see Manuscript 1, Appendix D) as also reported by Thomason [141]. The RIXS spectra, obtained in this manner, were likewise reported to be in excellent agreement with experiment. It was, however, noted to be difficult to obtain the spectra due to a large number of states required to converge in the damped response solver. If only nonresonant simulations were considered, the spectral shape of the RIXS could be reasonably well reproduced in a computationally cheaper way (see Manuscript 1, Appendix D). It is, however, reported in Manuscript 1 that some peak separations were overestimated. This was not the case in the full RIXS calculation. Moreover, as mentioned in Manuscript 1, the nature of the valence transitions probed could not be determined when only considering nonresonant spectra. More work is needed to evaluate the general performance of the implementation for solvated molecules. For further details, see Manuscript 1 in Appendix D.

4.3 BT-1T

4-(2-thienyl)-2,1,3-benzothiadiazole (BT-1T), shown in Fig. 4.1, is a molecule that belongs to the family of π -conjugated polymers that is of interest as building blocks for organic solar cells [142–144]. Recently, the BT-1T molecule has been studied theoretically, both for the case of photoexcitation [145] and for photoionization [146]. A time-resolved XAS experiment has also been carried out at SwissFEL by Wenzel Andreasen and co-workers, studying the former process [147]. This will be the subject of a future publication. Here, XAS calculations have been performed for both processes. Previously, the low level HF and configuration interaction singles methods with the small 6-31G basis have been employed to study the processes [145, 146]. Here, they are studied utilizing both TDDFT with the BHHLYP functional and *fc*-CVS-EOM-CCSD. In both cases,

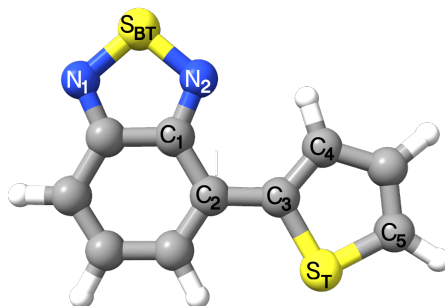


Figure 4.1. BT-1T. Molecular structure with labels to indicate the sulfur atom of the benzothiadiazole unit (left) labelled S_{BT} and of the thiophene unit (right) labelled S_T . Other C and N atoms relevant for structural parameters of interest are also labelled. The figure was adapted from Manuscript 2, Appendix E.

the aug-cc-pVTZ basis was employed on the sulfur atoms and the cc-pVDZ basis was used on the remaining atoms. In this section, only the static spectra are considered, while time-resolved spectra will be discussed in sections 6.1 and 6.2.

4.3.1 Neutral Molecule

The molecular structure was optimized to the ground state (S_0) PES at the BHHLYP/cc-pVDZ level of theory, as this was the method used in the dynamics simulations presented in section 5.2. Based on this structure the HOMO and LUMO (see Appendix F, Fig. F.1) were determined as well as the lowest lying valence excitation. Excitation energies of 3.41 eV and 3.96 eV were found at the BHHLYP and fc-EOM-CCSD levels of theory, respectively, with oscillator strengths of 0.2251 and 0.2568. To distinguish the HOMO and LUMO obtained in these calculations from those obtained for the photoionized cation, they shall henceforth be denoted HOMO_0 and LUMO_0 , respectively.

The first valence transition was, unsurprisingly, found to be the HOMO_0 - LUMO_0 transition with the fc-EOM-CCSD level NTOs shown in Fig. 4.2. The BHHLYP level predicts the same NTO pair, which is therefore shown only in Appendix F (Fig. F.3). The orbitals found in these calculations are noted to be in good agreement with those previously presented [145].

Ground state XAS calculations can be readily carried out in quantum chemistry codes such as Q-Chem [65] at both the TDDFT and fc-CVS-EOM-CCSD levels of theory. The results of these calculations can be seen in Fig. 4.3. Note that the two theoretical S_0 XAS calculations are from Manuscript 2 (Appendix E).

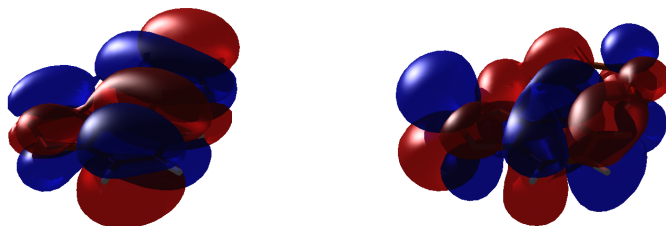


Figure 4.2. BT-1T. Main NTOs of the lowest lying valence transition at the S_0 minimum-energy structure calculated at the BHHLYP/cc-pVDZ level of theory. The hole NTO (left) resembles HOMO_0 , while the particle NTO (right) resembles LUMO_0 . The transitions are calculated at the fc-EOM-CCSD level of theory with the aug-cc-pVTZ basis on S and the cc-pVDZ basis on the remaining atoms. Contour value is ± 0.01 a.u. and the NTO weight, σ_K^2 , is 0.73.

The same qualitative shape of the spectra are obtained at the two levels of theory. As also reported in Manuscript 2, it is observed that the first three of the four main transitions, giving rise to the main band in our calculations, occur with a very small separation at the BHHLYP level of theory. At the fc-CVS-EOM-CCSD level of theory, the four transitions are spread out more evenly. Thus, two peaks arise in the BHHLYP spectrum with the given broadening, while only one is observed at the fc-CVS-EOM-CCSD level of theory (see also Manuscript 2, Appendix E). The ground state XAS calculated by Khalili *et al.* [145] does not cover as large an energy range as shown here. Nonetheless, the main band was also in the previous study predicted to be a double peak [145].

In Manuscript 2, the four main transitions computed in this band are noted to be the same regardless of whether the fc-CVS-EOM-CCSD or BHHLYP method is utilized. The NTOs calculated at the fc-CVS-EOM-CCSD level of theory are shown in Fig. 4.4, while the BHHLYP level NTOs are shown in Appendix F (Fig. F.4). The two most intense transitions are seen to originate on S_T and S_{BT} , respectively, and both have a σ^* -type final state (Fig. 4.4 and Appendix E). For additional NTOs of the S_0 spectrum, see the supplementary information of Manuscript 2 in Appendix E.

Note that the $\pi_{1,BT}^*$ and $\pi_{2,T}^*$ NTOs found for the second and third transitions of the ground state XAS both resemble LUMO_0 (see Fig. F.1). The electron density is, however, more localized on either the thiophene or the benzothiadiazole unit compared to LUMO_0 in Appendix F (Fig. F.1) and Fig. 4.2.

The overall qualitative agreement between experiment and theory is accept-

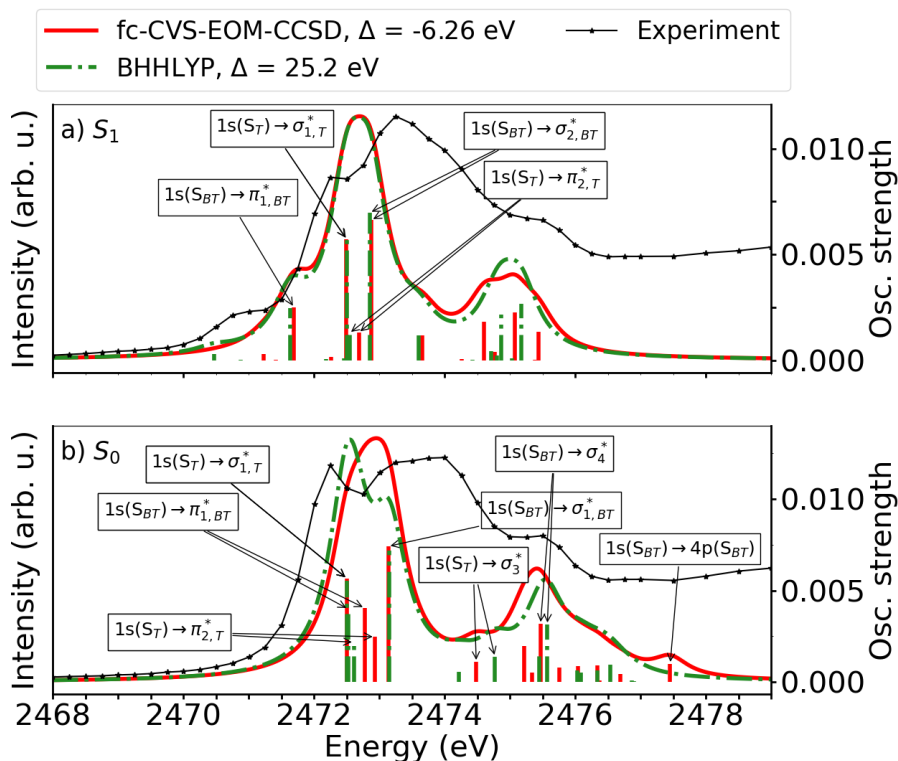
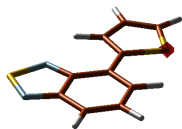
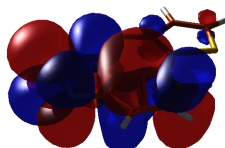
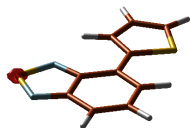


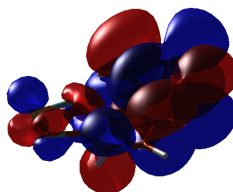
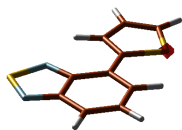
Figure 4.3. BT-1T. XAS spectra of the S_0 (bottom) and S_1 (top) states. In each state, the spectrum has been calculated at the fc-CVS-EOM-CCSD (red) and BHHLYP (green) level of theory for a geometry optimized to the S_0 state at the BHHLYP/cc-pVDZ level of theory. For the XAS calculations, the aug-cc-pVTZ basis was employed on S, while the cc-pVDZ basis was employed on the remaining atoms. The calculated XAS in a) are based on the IMOM procedure and assumes 100% photoexcitation yield. The spectra were simulated by employing a Lorentzian broadening with HWHM=0.33 eV to the stick spectra. The spectra have been shifted by Δ to align with the ground state experiment. The excited state spectrum was measured with a time-delay of 5 ps. Labels show the characters of the indicated transitions. Theoretical S_0 XAS results are from Manuscript 2, Appendix E.



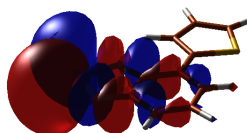
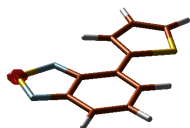
(a) Hole (left) and particle (right) NTOs of the 1st core excitation. The hole NTO is 1s of S_T . The NTO weight, σ_K^2 , is 0.85.



(b) Hole (left) and particle (right) NTOs of the 2nd core excitation. The hole NTO is 1s of S_{BT} . The NTO weight, σ_K^2 , is 0.79.



(c) Hole (left) and particle (right) NTOs of the 3rd core excitation. The hole NTO is 1s of S_T . The NTO weight, σ_K^2 , is 0.80.



(d) Hole (left) and particle (right) NTOs of the 4th core excitation. The hole NTO is 1s of S_{BT} . The NTO weight, σ_K^2 , is 0.85.

Figure 4.4. BT-1T. Main NTOs for the four main core transitions in S_0 calculated at the fc-CVS-EOM-CCSD level of theory at the S_0 optimized geometry. The aug-cc-pVTZ basis was used on S, and the cc-pVDZ basis was used on the remaining atoms. Contour value is ± 0.01 a.u. The transitions are labelled in Fig. 4.3 based on character. These NTOs are reproduced from the supplementary information of Manuscript 2, Appendix E.

able for S_0 . A discrepancy is, however, observed with respect to the main feature of the spectrum. Both theoretical methods predict this feature to be significantly more narrow than is the case. In the experiment, the main feature is a double peak, consisting of one relatively sharp feature and a very broad one (approximately 2 eV broad). To reproduce this, a larger separation is needed between the four transitions associated with the double peak. Changing the HWHM of the Lorentzian broadening cannot cause the band to spread out significantly beyond the energy range covered by the transitions of intensity. Therefore, the desired additional broadening cannot be obtained simply by utilizing a larger HWHM. Note that, while the theoretical spectra are gasphase spectra and do not take temperature effects into account, the experimental spectra were obtained in solution (approximately 10mM toluene solution). Thus, differences between the spectra could be a result of the calculations failing to take into account solvation and temperature effects. Nevertheless, for the CCSD calculations, it was investigated if further broadening could be acquired by including additional dynamical electron correlation in the description of core excitation energies. This was done by employing the CCSDR(3) method [139] as implemented in the Dalton program [148, 149], which includes the effect of triple excitations in an approximate manner. The correction provided by CCSDR(3) was seen to be necessary for a good description of the N and O K -edge XAS of oxazole (see Section 4.1 and Publication 2, Appendix B). The CCSDR(3) method is significantly more computationally demanding than CCSD. Therefore, only the first 8 transitions were computed for a smaller basis set: cc-pVDZ on all atoms. The calculation should therefore not be compared to results in Fig. 4.3. It is simply a way of investigating if the additional dynamical electron correlation corrects the spectrum by broadening the main feature. Note also that the correction was attempted only for the ground state. Moreover, the oscillator strengths were determined at the CCSD level of theory. In Fig. 4.5, we observe that the transitions do indeed spread out when CCSDR(3) is employed, resulting in a broader main band. The characters of the first four transitions can again be attributed to transitions from the two sulfur atoms to π^* - and σ^* -type orbitals. Moreover, the intensity ratios of the transition types appear to be roughly the same as in the calculation with a larger basis set on the sulfur atoms. The energetic ordering has, however, changed when the smaller basis set is used. Nevertheless, since it is the effect of the triples correction that is investigated, we shall not concern ourselves with such changes further. Thus, while the BHHLYP and CCSD results are of similar quality, the CCSD method has the advantage of being systematically improvable. This appears to be necessary to reproduce the experimental spectrum and will be further discussed in a future publication [147]. Note that both solvent and temperature effects might still be required to fully describe the experimental spectrum.

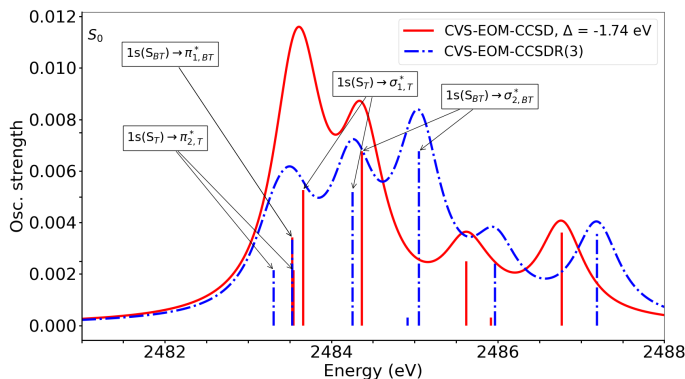


Figure 4.5. BT-1T. Ground state XAS calculated at the CVS-EOM-CCSD (red) and CVS-EOM-CCSDR(3) (blue) levels of theory. In both calculations, the cc-pVDZ basis was employed on all atoms. The oscillator strengths were in both cases calculated at the CVS-EOM-CCSD level of theory and the spectra simulated by employing a Lorentzian broadening with HWHM=0.33 eV. The CVS-EOM-CCSD spectrum has been shifted by Δ to align with the CVS-EOM-CCSDR(3) calculation. Labels show the characters of the indicated transitions.

Turning our attention to the excited state XAS, further considerations are required in order to calculate the transitions of interest. It is possible to compute intensities of some excited state transitions by considering the transition moment between the initial valence excited state and the core excited state as a kind of quadratic response (see, e.g., Ref. 150). The corresponding excitation energies can then be computed as the energy difference between the two states. Such an approach, though, only gives reliable results for transitions into the lowest singly-occupied molecular orbital (SOMO) [150]. This is because the final states for higher excitations cannot be described as a single photon process from the ground state. An alternative way of predicting the full excited state XAS is by utilizing IMOM (see Section 1.2.4). Here, one generates the wavefunction for an excited state configuration and calculates the XAS transitions as one-photon processes. A drawback of the method is that spin contaminated states might be obtained [150]. Also, as previously mentioned, the generated excited states are in this approach no longer orthogonal to the ground state. Furthermore, there must be one set of MOs that describe the desired excitation well, for the excited state to be constructed in this manner. Nonetheless, the method has previously been

reported to yield good results for both CCSD- and TDDFT-based excited state XAS calculations [150]. While both the quadratic response-like approach and the IMOM procedure are available in Q-Chem at the fc-CVS-EOM-CCSD level of theory, only the IMOM procedure is available at the TDDFT level of theory in Q-Chem. For this system, the core-to-SOMO transitions (where the SOMO is here HOMO₀) were predicted to be dark, regardless of the calculation method (see Tables F.1 and F.3). This is in good agreement with results by Khalili *et al.* [145], who predicted very low intensities of these transitions. Furthermore, the electron density on the two sulfur atoms is noted to be low in HOMO₀ (Fig. F.2), where the sulfur atoms both fall at the edge of the regions of density. In Fig. 4.3a, only the IMOM-based excited state XAS spectra are shown. Observe that the spin-contamination in these excited state calculations resulted in $\langle S^2 \rangle = 1.0282$ for BHHLYP and $\langle S^2 \rangle = 1.1888$ for fc-EOM-CCSD. For a pure singlet state $\langle S^2 \rangle = 1.0$. Note also that the calculated excited state spectrum only consists of the excited state signal. The experimental spectrum, on the other hand, is a weighted sum of both the excited state and ground state XAS depending on the photoexcitation yield. The calculated spectrum in 4.3a is thus only the total spectrum after photoexcitation in case of 100% yield of the photoexcitation.

As also observed for the S_0 spectra, the agreement between the two computed excited state spectra is good. The agreement between the excited state spectra is noted to be greater than between the ground state spectra. This has also previously been reported by Tsuru *et al.* [150] for other systems. In the excited state, a low intensity peak is observed to emerge on the low energy side of the main feature compared to the ground state spectra (See XAS in Fig. 4.3a). This is attributed to a core-to-LUMO₀ transition (see Figs. 4.6 and F.6). The electron density of the relevant particle NTO is, as previously mentioned, somewhat more localized on the benzothiodiazole unit compared to LUMO₀. Khalili *et al.* [145] predicted no distinguishable core-to-LUMO₀ transitions, and hence no easy way of distinguishing the ground and excited state XAS. The core-to-HOMO₀ transitions are of so low intensity that they are considered dark. These can be found at a lower energy still compared to the main band. The peak visible in the experimental excited state spectrum is thus attributed to the core-to-LUMO₀ transition originating on S_{BT} .

The three transitions, giving rise to the main peak of the excited state spectrum, is found to be the same as those observed in the S_0 spectrum with the same intensity ratios (see Figs. 4.6 and F.6).

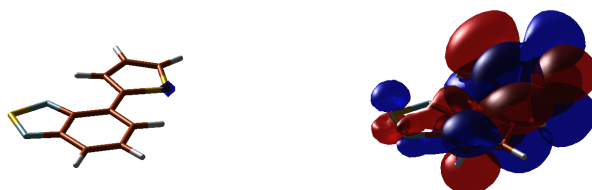
For the excited state, the experiment once again shows a broader main feature compared to the theoretical calculations. Otherwise, the qualitative agreement of the spectra is good. Further broadening in the theoretical spectra might be obtained by including additional dynamical correlation, as indicated by the ground state calculation in Fig. 4.5. Alternatively, this broadening could, as mentioned



(a) Hole (left) and particle (right) NTOs of the 3rd core excitation. The hole NTO is 1s of S_{BT} . The (α -spin) NTO weight, σ_K^2 , is 0.78.



(b) Hole (left) and particle (right) NTOs of the 5th core excitation. The hole NTO is 1s of S_T . The (β -spin) NTO weight, σ_K^2 , is 0.56.



(c) Hole (left) and particle (right) NTOs of the 7th core excitation. The hole NTO is 1s of S_T . The (α -spin) NTO weight, σ_K^2 , is 0.77.



(d) Hole (left) and particle (right) NTOs of the 8th core excitation. The hole NTO is 1s of S_{BT} . The (α -spin) NTO weight, σ_K^2 , is 0.67.

Figure 4.6. BT-1T. Main NTOs for the first four bright core transition of the neutral molecule in the S_1 excited state calculated at the IMOM-fc-CVS-EOM-CCSD level of theory at the S_0 optimized geometry. The aug-cc-pVTZ basis was used on S, and the cc-pVDZ basis was used on the remaining atoms. Contour value is ± 0.01 a.u. The transitions are labelled in Fig. 4.3 based on character.

above, be a result of solvation and temperature effects not accounted for in the calculations.

4.3.2 Cation

In Manuscript 2 (Appendix E), the XAS of the states of interest have also been determined for the photoionized molecule (BT-1T⁺) at both the BHHLYP and fc-CVS-EOM-CCSD level of theory. All calculations were based on the structure optimized on the ground state of the neutral molecule (S_0) at the BHHLYP/cc-pVDZ level of theory. In order to compute these spectra, IMOM was again utilized. The doublet states, D_0 - D_3 , were thus generated by choosing the orbital with the same character as HOMO₀, (HOMO-1)₀, (HOMO-2)₀ or (HOMO-3)₀, respectively, to be a SOMO (see Manuscript 2, Appendix E). Except for an overall shift, the CCSD and BHHLYP level spectra are once again reported to show excellent agreement with only few discrepancies. The main difference was found to be that BHHLYP finds a higher intensity of a high energy transition in the main band for D_2 and D_3 (see Manuscript 2, Appendix E). Observe, however, that the predicted core-to-SOMO transitions were found in the same region and with the same intensity ratios. Both D_1 and D_2 showed bright core-to-SOMO transitions, while this was not the case for D_0 and D_3 (see Manuscript 2, Appendix E).

One interesting discrepancy observed in Manuscript 2 was for the NTO pair of the core-to-SOMO transition in the D_1 state at the fc-CVS-EOM-CCSD level of theory. Here, the NTO pair indicated an excitation into (HOMO-2)₀, which should be occupied. The TDDFT calculation, on the other hand, gave rise to the expected transition into (HOMO-1)₀. This discrepancy was, as can be seen from Manuscript 2, attributed to uncertainties related to several transitions contributing to the considered excitation. Indeed, when using the orbitals of the cation in D_0 as the starting guess for IMOM, the expected NTO pairs were found also for CCSD (see Manuscript 2, Appendix E). Regardless of whether the orbitals of the neutral molecule or those of the cation were used as the starting guess in the IMOM procedure, the same spectral shape was found. Moreover, the CCSD level calculations showed good agreement with the one carried out at the BHHLYP level of theory (see Manuscript 2, Appendix E). It was thus concluded, that the spectral shape determined with the IMOM procedure was reliable. The assignment of the transition character based on NTOs should, however, be done with care. At the BHHLYP level of theory all core-to-SOMO NTO pairs showed the expected characters. For further details, see Manuscript 2 (Appendix E).

Manuscript 2 also reports a reordering of the orbitals at both levels of theory, when generating the excited states. This resulted in the SOMO being highest in energy for all states, regardless of the character of this orbital. This in turn

gave rise to the separation between the core-to-SOMO and main bands of the computed spectra decreasing from D_1 to D_3 (see Manuscript 2, Appendix E). The opposite trend would be expected if the orbitals had remained unchanged compared to the S_0 reference. For further details, see Manuscript 2 in Appendix E.

The main peaks of the spectrum can for all states be attributed to relatively close-lying transitions both originating on S_T and S_{BT} as also seen for the neutral molecule (see Manuscript 2, Appendix E, for details).

CHAPTER 5

Nuclear Dynamics Simulations

During this project, two separate molecular dynamics studies have been carried out utilizing two different methods. First, a study of the well known and extensively investigated photoisomerization of azobenzene was carried out. Secondly, the charge transfer reaction of the recently studied BT-1T molecule [145,146] was also investigated.

5.1 Azobenzene

The photoisomerization process of azobenzene was studied using surface hopping with forced jumps to the ground state as implemented in SHARC-2.1.1 [105] (see Publication 3, Appendix C). Here, the MCH representation was utilized. For this simulation, the energies and gradients required were calculated at the BHHLYP/cc-pVDZ level of theory. The study focused on investigating, which DOFs must be considered to give the best possible description of the reaction in both directions. As mentioned in Publication 3, the generally established

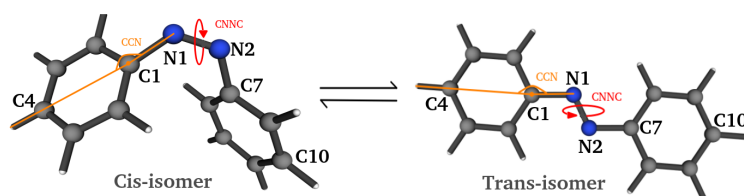


Figure 5.1. Azobenzene. Structures of the cis- and trans-isomers involved in the photoisomerization with the CNNC dihedral angle and the CCN angle marked in red and orange, respectively. The figure is from Ref. 118 (Publication 3, Appendix C).

procedure is to consider the CNNC dihedral angle, which changes from approximately 0° for the cis-isomer to 180° for the trans-isomer. In addition, a few other DOFs to consider might possibly be chosen *a priori* based on a suggested mechanism [151–157].

We found that considering the reaction along only a single DOF (the CNNC angle) gave a good description of the trans-to-cis isomerization [118], as also noted by Tavadze *et al.* [155]. The cis-to-trans isomerization, on the other hand, required two DOFs to obtain a satisfactory description of the reaction [118]. These two normal modes were found to be related to the CNNC dihedral angle and the CCN angles as shown in Fig. 5.1. See Publication 3 in Appendix C for details. The trans-to-cis isomerization was concluded to follow the oscillations of the dihedral angle, while the cis-to-trans isomerization was found to happen stepwise [118]. Here, an initial rapid decrease of the dihedral angle and jump to the ground state was observed, followed by a structural rearrangement, allowing the CCN angles to relax. Lastly, the final relaxation of the structure to its equilibrium on the trans-isomer ground state was found to take place [118]. These observations of the cis-to-trans isomerization were noted to be in good agreement with a previously proposed twist mechanism [152, 153]. For further details, see Publication 3 in Appendix C.

Another part of the study was to investigate the reason for the long timescale of the trans-to-cis isomerization. It was discovered that, rather than an energy barrier on the excited state halting the reaction, the oscillations of the CNNC dihedral angle simply happen on a long timescale [118]. As the reaction follows these oscillations, its timescale must depend on this oscillation frequency. For further details, see Publication 3 (Appendix C).

The utilization of the SH approach proved very useful in this study. Since the reaction could be considered along all degrees of freedom, it was possible to investigate, which DOFs were more active. Despite the limited number of trajectories considered, good agreement of quantum yield and time of jump was found between the present results and those obtained by experiment [158] and previous theoretical calculations [120, 159, 160] (see Publication 3, Appendix C). Thus, it was concluded that little accuracy was lost by using the computationally cheap approach with forced jumps and a relatively small number of trajectories [118]. Note that the number of trajectories might not have been sufficient to describe the process, had it concerned rare events.

5.2 BT-1T

The charge transfer reaction of BT-1T was recently studied at a relatively low level of theory [145, 146]. It has therefore been investigated what could be gained

by utilizing a more sophisticated simulation method. The previous simulations were carried out for the photoexcited neutral molecule [145] and for the cation obtained by photoionization of the neutral molecule [146]. Both studies employed SH, albeit without forced jumps to the ground state.

SH simulations for both the neutral and ionized molecule were carried out at the BHHLYP/cc-pVDZ level of theory, as also employed for azobenzene. The diagonal representation was used for the calculations here, as spin-orbit couplings were included. Only a small number of trajectories (25) was investigated, as the simulation was simply used to identify relevant normal modes to include in the subsequent MCTDH simulation. Moreover, the simulations by Khalili *et al.* [145,146] indicated that the decay of the excited state was not a rare event for either species. The neutral molecule was simulated for 800 fs, as it was predicted by Khalili *et al.* [145] that approximately 20% of the trajectories would jump within 400 fs. The current simulation, indicates a much longer lifetime of the S_1 -state, since during the simulation, no trajectories jumped to S_0 , despite the use of forced jumps. A longer lifetime was found to be in good agreement with the experiment carried out by Wenzel Andreasen and co-workers (approximately 20 picoseconds) [147]. This might indicate that the inclusion of some electron correlation or simply a larger basis set is needed to simulate the dynamics of the system in a satisfactory way. The above-mentioned experiment will be the subject of a future publication [147]. Due to the long lifetime of S_1 , we have in the present study chosen to focus on the reaction of the photoionized species for the two types of dynamics simulation (see Manuscript 2, Appendix E). The neutral species will thus only be studied based on a few optimized geometries (see Section 6.1).

In the previous study of the cation by Khalili *et al.* [146], the molecular geometry was optimized for the ground state of the neutral molecule at the restricted-HF/6-31G level of theory. As also done in our study, the desired amount of trajectories were obtained by sampling initial conditions using a Wigner distribution. The excited states and PES were then modeled by using Koopmans' theorem,

$$E_i^{IP} = -\epsilon_i. \quad (5.1)$$

Here, the ionization energies are approximated as the orbital energy of the occupied orbital i from which the electron is to be removed. Thus, the first ionization energy would be equal to minus the orbital energy of the HOMO.

We carried out the SH simulation for 400 fs by considering a photoexcitation of a cation (see Manuscript 2, Appendix E). The excited state PESs were likewise based on excitation energies of the cation. The final doublet states obtained in this way are noted to correspond to a photoionization (see Manuscript 2, Appendix E).

The simulation showed a significantly lower QY of the D_0 state compared to the simulation by Khalili *et al.* [146] (15% compared to 90%). The trends observed with a fast decay from D_3 to D_2 and D_1 are, however, in good agreement with previous results [146] (see Manuscript 2, Appendix E). Therefore, the number of simulated trajectories was deemed sufficient for determining the relevant normal modes. Based on the normal modes determined to be of importance, an MCTDH calculation was carried out. This simulation reproduced the SH results well, suggesting a low QY of the D_0 state (see Manuscript 2, Appendix E). One discrepancy to note, however, was a significantly longer predicted lifetime of the D_3 state in the MCTDH simulation compared to all SH simulations (see Manuscript 2, Appendix E). It was investigated, if this was due to the initial condition sampling, where SH allows all modes to be varied, while the MCTDH simulation freezes most normal modes. An SH simulation based on initial conditions generated only from the normal modes selected for the MCTDH simulation was, however, found to show the same trends as the other SH simulations (see Manuscript 2, Appendix E). Again, an extremely fast decay of the D_3 state (50% decay within the first 5 fs) was observed. Moreover, since the molecule is relatively rigid, it was concluded in Manuscript 2 that the reduced number of DOFs was not the main cause of the difference. Instead it was suggested to be related to the lack of, e.g., decoherence in the SH simulations. For further details, see Manuscript 2 in Appendix E.

CHAPTER 6

Time-resolved Spectra

6.1 Neutral BT-1T

BT-1T is a relatively rigid molecule, as can be observed by comparing structures optimized to the S_0 and S_1 states. The changes in some key geometrical parameters (see Fig. 4.1) can be found in the supplementary information of Manuscript 2 (Appendix E). Here, it is evident that only small changes occur. It must nonetheless be investigated how these small changes affect the XAS. The spectra for the S_0 optimized structure in both the S_0 and S_1 states were already shown in section 4.3.1. In Fig. 6.1, these spectra are compared to those obtained at the S_1 optimized geometry. As also done before, the simulations at the fc-CVS-EOM-CCSD and BHHLYP levels of theory are compared.

Evidently, changing the level of theory affects the XAS only little, as also observed for the S_0 optimized structure. The same applies when changing the geometry. Note particularly that, despite changing the geometry, the core-to-LUMO₀ transition ($1s(S_{BT}) \rightarrow \pi_{1,BT}^*$) does not become distinguishable from the main band in the S_0 XAS. In the S_1 XAS, on the other hand, this feature is clearly distinguishable at both levels of theory for both investigated geometries. It is thus a signature of the excited state. Note however, that this feature can only be captured by employing the IMOM procedure.

Despite the overall excellent agreement between the computed spectra, small differences upon a change in geometry are observable in the intensity of the main band. This band increases and narrows for the S_1 optimized structure compared to the S_0 optimized structure. Moreover, at the S_1 optimized geometry, the separation between the main peak and the lower energy shoulder in the S_1 excited state spectrum also increases slightly. Hence, it is concluded that small changes in the geometry do not significantly affect the qualitative description of XAS. However, since small changes in the intensities are observed, we expect the

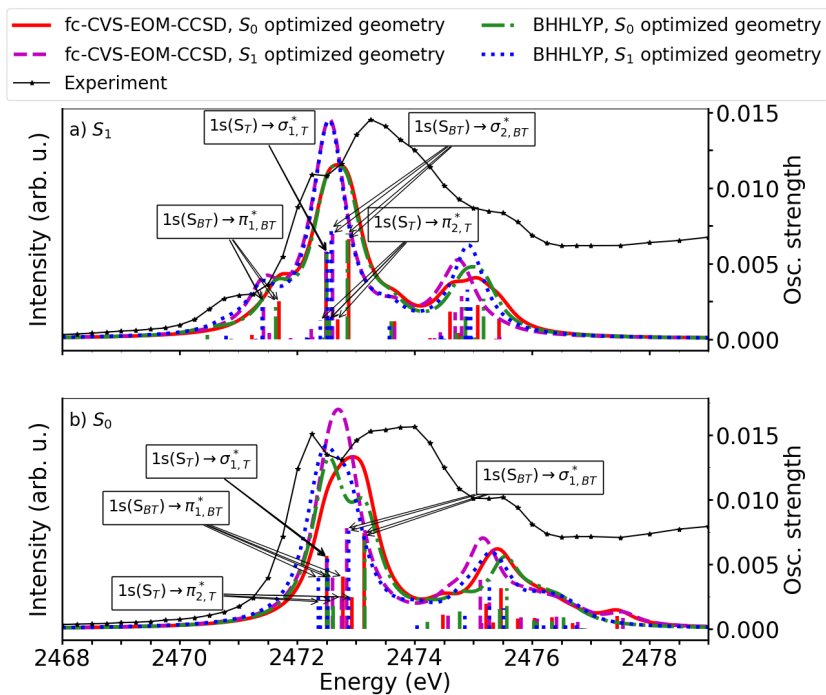


Figure 6.1. BT-1T. XAS spectra. The spectra are shown for the S_0 (bottom) and S_1 (top) states. In each state, the spectrum has been calculated at the fc-CVS-EOM-CCSD level of theory for a geometry optimized to S_0 (red) and S_1 (magenta), as well as the BHHLYP level of theory also for a geometry optimized to S_0 (green) and S_1 (blue). The calculated XAS in a) are based on the IMOM procedure and assumes 100% photoexcitation yield. The aug-cc-pVTZ basis was employed on S, while the cc-pVDZ basis was employed on the remaining atoms. The spectra were simulated using a Lorentzian broadening with $\text{HWHM}=0.33$ eV. In order to align with experiment, BHHLYP results are shifted by 25.20 eV, while fc-CVS-EOM-CCSD results are shifted by -6.26 eV. The experimental excited state spectrum was obtained at a time delay of 5 ps. Transition characters are indicated by arrows. The S_0 XAS results computed at the S_0 optimized structure are from Manuscript 2, Appendix E.

difference spectrum to be affected. In other words, as the molecule relaxes on the S_1 excited state, the intensity of the main peak is expected to increase. This should be observable as an increasing positive signal in the difference spectrum. The latter is calculated in Fig. 6.2 and is found to be in good agreement with the experimental time-evolution of the difference spectrum shown in Fig. 6.3. Note that the spectral shape will be unchanged regardless of the S_1 photoexcitation yield, as this only gives rise to an overall scaling.

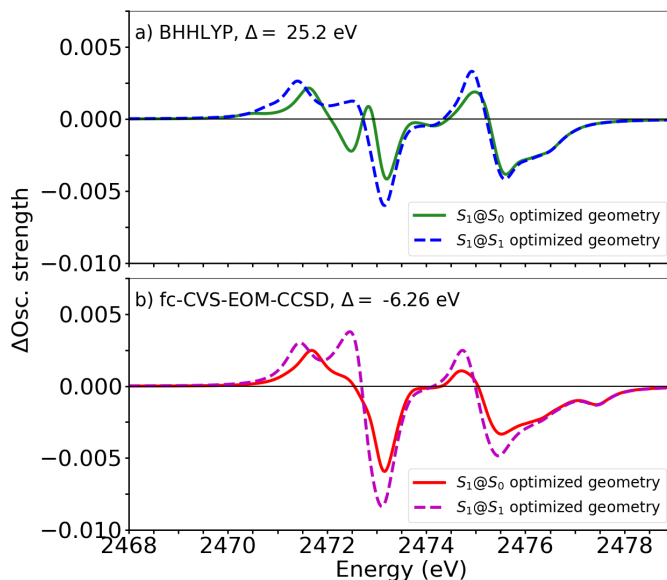


Figure 6.2. BT-1T. Difference XAS spectrum for 100% of the sample excited to S_1 at (a) the BHHLYP level of theory and (b) the fc-CVS-EOM-CCSD level of theory. The spectrum is shown for both $S_1@S_0$ optimized geometry (solid) and $S_1@S_1$ optimized geometry (dashed) calculated using the IMOM procedure. The subtracted XAS is in all cases $S_0@S_0$ optimized geometry.

The overall shape of the experimental difference spectrum is well reproduced by theory, at least up until 2475 eV. It is observed that the intensity (both positive and negative) of the difference spectrum increases over time compared to the initial difference spectrum obtained directly following the photoexcitation (at approximately 0.17 ps). This trend is also observed when comparing the computed difference spectra. Note the slight decrease in the experimental intensity of the low energy peak of the difference spectrum after approximately 5 ps. This could be an indication of a beginning decay of the excited state or oscillations around the excited state equilibrium structure. By using singular-value-decomposition

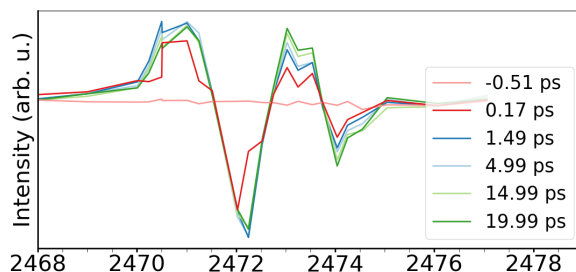


Figure 6.3. BT-1T. Experimental difference XAS spectrum at different time delays after photoexcitation to S_1 . Unpublished results from a recent experimental campaign led by Wenzel Andreasen [147].

(SVD), the difference spectrum was found to consist of multiple components, which can be seen in Fig. 6.4. Here, it is evident that the main feature (shown in blue) has a long lifetime of more than 20 ps. This feature shows a strong resemblance to the computed difference spectrum and is thus associated with the excited state. In contrast, the other two components have significantly faster decay rates (of the order of a few picoseconds). The decaying signal might thus be the result of the decay of these other components rather than the decay of the excited state. This will be considered further in a dedicated publication on the experimental campaign [147] and will not be discussed more here.

To investigate the overall change in the computed difference spectra further, the nature of the most intense transitions underlying the main band of both the S_0 and S_1 XAS as well as the low energy feature in the S_1 XAS was investigated in terms of NTOs. These were already shown for the S_0 optimized structure in Figs. 4.4 and 4.6 (fc-CVS-EOM-CCSD) and in Appendix F (BHHLYP). At the fc-CVS-EOM-CCSD level of theory, the NTOs obtained at the S_1 optimized structure are shown in Fig. 6.5 for the S_0 XAS and Fig. 6.6 for the S_1 XAS. They are seen to remain unchanged for the small geometrical change considered. At the BHHLYP level (see Appendix F), the NTOs obtained are the same, however, the order of the extremely close-lying transitions is noted to change when the geometry changes. As these transitions occur at almost the same energies, this does not affect the spectral shape.

Note that, according to our calculations, the highest intensity transitions in each peak of all calculated spectra originates on S_{BT} (see also the supplementary information of Manuscript 2 in Appendix E). Particularly, it is noted to be the case for the excited state bright core-to-LUMO₀ transition, which, as mentioned, is a signature of the S_1 XAS. The main band of the excited state spectrum consists of several transitions, which do not all originate on S_{BT} . In contrast, the

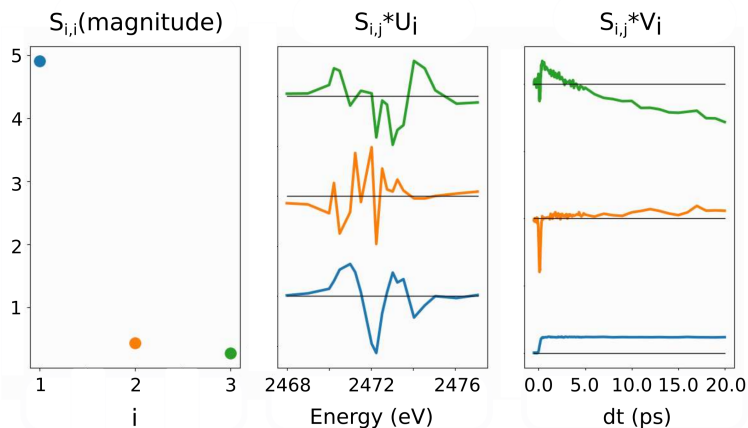


Figure 6.4. BT-1T. SVD of the experimental difference spectrum. Left: weight of the three components, middle: shape of the three components, right: decay of the three components over time. Unpublished results from a recent experimental campaign led by Wenzel Andreasen [147].

low energy peak is solely a result of the core-to-LUMO₀ transition originating on S_{BT} . An increased electron density on S_{BT} will therefore be observable as an increase in the intensity of this low energy feature.

To theoretically determine if such a redistribution of charge might occur, the charge distribution on the two sulfur atoms was considered (see Table 6.1). The charges are determined as charges from electrostatic potentials using a grid-based method [161] (CHELPG) in the Gaussian program [162], as also done for the cation (see Manuscript 2, Appendix E). The partial charge on S_{BT} , according to the CHELPG calculation scheme, becomes less positive upon excitation. Also, when the molecular structure relaxes on the S_1 PES, this positive charge decreases further. The opposite occurs for the S_T atom. This indicates that some (negative) charge transfer from S_T to S_{BT} takes place, when the molecule is excited and thereafter relaxes on the excited state PES. This was also concluded in the previous study [146]. The transfer of electron density from S_T to S_{BT} is thus expected to allow the core-to-LUMO₀ band to increase. Hence, the difference spectrum should display a peak of increasingly positive intensity around 2471 eV. This is indeed observed in the experiment (Fig. 6.3), which thus allows us to not only detect the excited state but also follow the charge transfer reaction.

The main band does, as mentioned, consist of several strong transitions. Likewise, more than one strong transition is observed for the high energy feature. Therefore, the effect of a charge transfer on these bands might be difficult to

predict. It should, however, be observed that the transition of highest intensity underlying the main band moves towards lower energies at the S_1 optimized structure. Therefore a region of increased intensity followed by a region of decreased intensity is found theoretically in the energy region associated with this peak. The high energy peak, on the other hand, appears to remain in the same place for the two geometries. Thus, a positive difference signal is found here. These features are also observable in the experiment.

Despite the lack of trajectories describing the molecular dynamics of the pho-

Table 6.1. BT-1T. CHELPG charges of the sulfur atoms of the neutral BT-1T molecule in S_0 and S_1 calculated at the BHHLYP/cc-pVDZ level of theory.

	S_{BT}	S_T
$S_1@S_1$ optimized geometry	0.193004	-0.022770
$S_1@S_0$ optimized geometry	0.196535	-0.031069
$S_0@S_0$ optimized geometry	0.310480	-0.052415

toexcited BT-1T molecule, the time-resolved experiment can be analysed using the calculations shown. Hence, it would appear that for rigid systems primarily moving on one PES, molecular dynamics simulations can thus be avoided. In this case, single point calculations at a few optimized structures provide sufficient information to interpret experimental data.



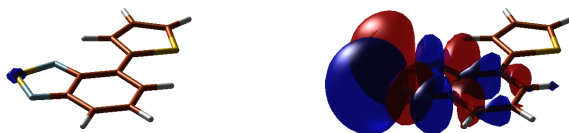
(a) Hole (left) and particle (right) NTOs of the 1st core excitation. The hole NTO is 1s of S_T . The NTO weight, σ_K^2 , is 0.85.



(b) Hole (left) and particle (right) NTOs of the 2nd core excitation. The hole NTO is 1s of S_{BT} . The NTO weight, σ_K^2 , is 0.78.

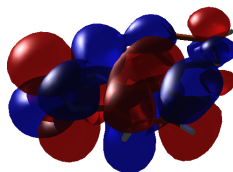
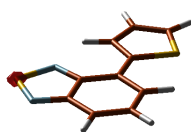


(c) Hole (left) and particle (right) NTOs of the 3rd core excitation. The hole NTO is 1s of S_T . The NTO weight, σ_K^2 , is 0.79.

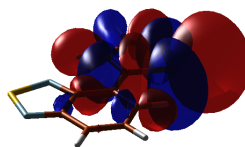
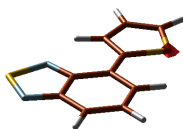


(d) Hole (left) and particle (right) NTOs of the 4th core excitation. The hole NTO is 1s of S_{BT} . The NTO weight, σ_K^2 , is 0.85.

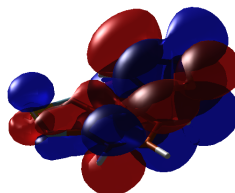
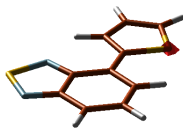
Figure 6.5. BT-1T. Main NTOs of the four bright core transitions constituting the main peak in the S_0 XAS calculated at the fc-CVS-EOM-CCSD level of theory at the S_1 optimized geometry. The aug-cc-pVTZ basis was used on S, and the cc-pVDZ basis was used on the remaining atoms. Contour value is ± 0.01 a.u. NTOs calculated at the BHHLYP level of theory are the same (but reordered, as also seen when inspecting intensities of the transitions) and can be seen in Appendix F. The transitions are labelled in Fig. 6.1 based on character.



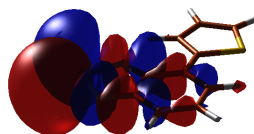
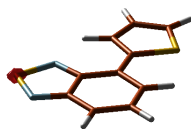
(a) Hole (left) and particle (right) NTOs of the 1st core excitation. The hole NTO is 1s of S_{BT} . The (α -spin) NTO weight, σ_K^2 , is 0.78.



(b) Hole (left) and particle (right) NTOs of the 6th core excitation. The hole NTO is 1s of S_T . The (β -spin) NTO weight, σ_K^2 , is 0.52.



(c) Hole (left) and particle (right) NTOs of the 7th core excitation. The hole NTO is 1s of S_T . The (α -spin) NTO weight, σ_K^2 , is 0.77.



(d) Hole (left) and particle (right) NTOs of the 8th core excitation. The hole NTO is 1s of S_{BT} . The (α -spin) NTO weight, σ_K^2 , is 0.67.

Figure 6.6. BT-1T. Main NTOs of the first four bright core transitions in S_1 calculated at the IMOM-fc-CVS-EOM-CCSD level of theory at the S_1 optimized geometry. The aug-cc-pVTZ basis was used on S, and the cc-pVDZ basis was used on the remaining atoms. Contour value is ± 0.01 a.u. NTOs calculated at the IMOM-BHHLYP level of theory are the same (but reordered, as also seen when inspecting intensities of the transitions) and can be seen in Appendix F. The transitions are labelled in Fig. 6.1 based on character.

6.2 BT-1T⁺

The tr-XAS were also computed for the BT-1T cation at the BHHLYP level of theory in Manuscript 2 (Appendix E). Again, the aug-cc-pVTZ basis was used on the sulfur atoms, while the cc-pVDZ basis was employed on the remaining atoms. No CC-based calculations were performed here due to convergence problems in the IMOM procedure (See Manuscript 2, Appendix E). Since the TDDFT results yielded results of a similar quality (see Section 4.3.2), this was not thought to affect the results significantly. The spectrum was computed at three time-delays based on centroid geometries from an MCTDH simulation employing BHHLYP/cc-pVDZ level calculations (see Section 5.2 and Appendix E). As the actual yield of photoionization is unknown, the spectra were computed under the optimistic assumption of 100% yield. As previously mentioned, this affects the total spectra, but only results in a scaling of the difference spectra. The latter are of main interest when considering the changes of the system, which is the focus here. In Manuscript 2 it was found that the intensity of the spectrum decreases in regions generally associated with transitions originating on S_T . An increased intensity on the other hand is reported in the region associated with transitions originating on S_{BT} . According to our calculations, the charge-transfer reaction of interest is thus observable (see Manuscript 2, Appendix E). This was also concluded by Khalili *et al* [146]. For further details, see Manuscript 2 in Appendix E.

Another conclusion reached was that the total XAS and, in particular, the difference spectra of BT-1T⁺ were mainly affected by changes in the electronic states (see Manuscript 2, Appendix E). The changes to the molecular structure were found to result in only minor changes. In fact, it was concluded in Manuscript 2 that the difference spectra might be simulated simply by utilizing the spectra calculated at the S_0 optimized geometry. In order to obtain the tr-XAS difference spectrum, these spectra would then need to be scaled by the populations determined in the dynamics simulation. Thus, significant computational savings might be obtained when simulating the 2D tr-XAS difference spectra. This conclusion of Manuscript 2, however, requires further investigations for less rigid molecules as well as for more structurally dependent spectroscopies. See Manuscript 2 in Appendix E for details.

Outlook and Conclusions

In this thesis, different tools for simulating ultra-fast chemical processes have been investigated. The work presented here has included both method development and computational studies using existing code. In addition to stand alone theoretical studies, combined theoretical and experimental studies have been presented.

An implementation of both the ground and excited state molecular gradient at the coupled cluster singles and doubles (CCSD) level of theory was presented (Publication 1). The implementation relied on Cholesky decomposition of the two-electron integrals, which allows for a very efficient code. Indeed, the new implementation in the open source program e^T was shown to be faster than other existing implementations. Currently it is possible to perform geometry optimizations, which can be used as the foundation for subsequent calculations of spectroscopic properties of interest. In time, this implementation might also lay the foundation for studying molecular dynamics at the CCSD level of theory, although this will require further work. Moreover, work is in progress to allow the gradient to be determined for core excited states in addition to valence excited states.

Throughout this thesis, the performance of coupled cluster based methods, and in particular CCSD, has been evaluated for describing different X-ray properties. An implementation of one such property, namely the resonant inelastic X-ray scattering (RIXS) cross section, was also presented (Manuscript 1). The implementation was once again carried out in the open source program e^T . To the best of our knowledge, this makes it the first equation-of-motion (EOM-)CCSD level implementation in an open source production level code. Although the implementation was focused on EOM-CCSD, the code also allows EOM second-order approximate coupled cluster singles and doubles (EOM-CC2) calculations to be carried out. The latter type of calculations are, however, inefficient as the current implementation works in full doubles space. In future, however, this should be optimized, as the EOM-CC2 results were observed to be of similar quality to

the EOM-CCSD ones, when considering the same valence transitions. Moreover, the new implementation showed promising results for calculating RIXS spectra of solvated molecules. The new implementation might furthermore be extended to the coupled cluster singles and doubles with perturbative triples method and thereby allow for state-of-the-art calculations. While only ground state RIXS has been considered here, the implementation might in time be extended to allow also time-resolved experiments to be analysed.

In addition to the good performance of CCSD in simulating RIXS spectra, the method also showed good results compared to experiment for valence photoelectron spectroscopy, X-ray photoelectron spectroscopy, X-ray absorption spectroscopy (XAS) and normal Auger-Meitner spectroscopy (Publication 2). Resonant Auger-Meitner spectra could, though, not be satisfactorily reproduced at the CCSD level of theory due to the inability of the method to describe the spectator decay channel. The XAS simulations were carried out both at the CCSD and TDDFT levels of theory and the two methods showed good agreement. This was also the case when simulating the XAS spectra for 4-(2-thienyl)-2,1,3-benzothiadiazole (BT-1T). In both cases, the agreement with experiment was improved by adding a correction to the CCSD calculations. Thus, the computationally cheaper TDDFT method was shown to be a good alternative to CCSD for the systems investigated here (oxazole, BT-1T and BT-1T⁺). Nonetheless, the CCSD method is noted to be systematically improvable, which was necessary to reproduce the experimental XAS of oxazole and BT-1T to a satisfactory degree.

An essential part of describing ultra-fast chemical processes is to simulate the nuclear dynamics. Such simulations yield information on molecular structures as well as populations of states, which are required when simulating time-resolved (tr) spectroscopy. It was found that molecular dynamics can be qualitatively well described classically by utilizing surface hopping and a limited number of trajectories, as long as one does not study rare events (Publication 3). Such a study can reveal the most important degrees of freedom. This makes it ideal as a basis for a quantum dynamics calculation, since the latter is only computationally possible, when the number of degrees of freedom is limited (Manuscript 2).

Finally, it was found that for the relatively rigid BT-1T cation (Manuscript 2), the electronic state affected the resulting tr-XAS significantly more than the minor structural changes. In fact, it appeared that for the cation, one could simulate the difference spectrum equally well by considering only the ground state optimized structure. Avoiding the many calculations of static XAS at different geometries allows for significant savings in computational resources. For the neutral molecule, considering only ground- and excited state optimized geometries gave rise to difference spectra in good agreement with experimental results. The single point calculations were even able to provide an interpretation of these experimen-

tal results. Hence, for a rigid molecule mainly evolving on a single electronic state, a few single point calculations can yield sufficient information to give insights into experiments. For long lifetimes of several picoseconds, dynamics simulations are very time-consuming, if at all possible. Avoiding such simulations and instead considering single point calculations for the relevant electronic states therefore provides a feasible means of interpretation. Further investigations are needed to determine if the above conclusions can be extended to less rigid molecules or other X-ray spectroscopies that may be more sensitive to small structural changes.

Appendices

APPENDIX A

Publication 1

Reproduced from "Efficient implementation of molecular CCSD gradients with Cholesky-decomposed electron repulsion integrals", Anna Kristina Schnack-Petersen, Henrik Koch, Sonia Coriani and Eirik F. Kjørstad, *J. Chem. Phys.*, 2022, **156**, 24411 with the permission of AIP Publishing.

Only the article itself is reproduced here, while the supporting information can be accessed via <https://doi.org/10.1063/5.0087261>.

Efficient implementation of molecular CCSD gradients with Cholesky-decomposed electron repulsion integrals

Cite as: J. Chem. Phys. **156**, 244111 (2022); <https://doi.org/10.1063/5.0087261>

Submitted: 03 February 2022 • Accepted: 15 May 2022 • Accepted Manuscript Online: 16 May 2022 • Published Online: 27 June 2022

 Anna Kristina Schnack-Petersen,  Henrik Koch,  Sonia Coriani, et al.



View Online



Export Citation



CrossMark

ARTICLES YOU MAY BE INTERESTED IN

[Density-functional theory vs density-functional fits](#)

The Journal of Chemical Physics **156**, 214101 (2022); <https://doi.org/10.1063/5.0091198>

[A combined first- and second-order optimization method for improving convergence of Hartree-Fock and Kohn-Sham calculations](#)

The Journal of Chemical Physics **156**, 214111 (2022); <https://doi.org/10.1063/5.0094292>

[Cluster perturbation theory. VI. Ground-state energy series using the Lagrangian](#)

The Journal of Chemical Physics **157**, 024106 (2022); <https://doi.org/10.1063/5.0082583>



Efficient implementation of molecular CCSD gradients with Cholesky-decomposed electron repulsion integrals

Cite as: J. Chem. Phys. 156, 244111 (2022); doi: 10.1063/5.0087261

Submitted: 3 February 2022 • Accepted: 15 May 2022 •

Published Online: 27 June 2022



View Online



Export Citation



CrossMark

Anna Kristina Schnack-Petersen,¹ Henrik Koch,^{2,3} Sonia Coriani,^{1,3} and Eirik F. Kjønsdal^{3,a)}

AFFILIATIONS

¹Department of Chemistry, Technical University of Denmark, 2800 Kongens Lyngby, Denmark

²Scuola Normale Superiore, Piazza dei Cavalieri 7, 56126 Pisa, Italy

³Department of Chemistry, Norwegian University of Science and Technology, 7491 Trondheim, Norway

^{a)}Author to whom correspondence should be addressed: eirik.kjonstad@ntnu.no

ABSTRACT

We present an efficient implementation of ground and excited state coupled cluster singles and doubles (CCSD) gradients based on Cholesky-decomposed electron repulsion integrals. Cholesky decomposition and density fitting are both inner projection methods, and, thus, similar implementation schemes can be applied for both methods. One well-known advantage of inner projection methods, which we exploit in our implementation, is that one can avoid storing large V^3O and V^4 arrays by instead considering three-index intermediates. Furthermore, our implementation does not require the formation and storage of Cholesky vector derivatives. The new implementation is shown to perform well, with less than 10% of the time spent calculating the gradients in geometry optimizations. Furthermore, the computational time per optimization cycle is significantly lower compared to other implementations based on an inner projection method. We showcase the capabilities of the implementation by optimizing the geometry of the retinal molecule ($C_{20}H_{28}O$) at the CCSD/aug-cc-pVDZ level of theory.

Published under an exclusive license by AIP Publishing. <https://doi.org/10.1063/5.0087261>

I. INTRODUCTION

The gradient of the electronic energy with respect to the nuclear coordinates, known as the molecular gradient, is a particularly useful quantity in computational chemistry. It is essential for determining both local energy minima and equilibrium geometries¹ and, thus, for predicting the stability and structure of molecular systems, as well as their properties at equilibrium. In addition, the molecular gradient is essential for locating transition state geometries, which can aid in elucidating chemical reaction paths and in estimating reaction rates.² Moreover, molecular gradients are required for predicting the time evolution of molecular systems since the gradient provides the forces that act on the atomic nuclei in the absence of sizable non-adiabatic effects.^{3,4}

Over the past three decades, coupled cluster (CC) methods have gained popularity^{5–9} due to their high and systematically improvable accuracy. Today, they are widely considered the most efficient for describing dynamical correlation whenever the

ground state is dominated by a single determinant.^{9,10} Coupled cluster methods that include approximate triple excitations (such as CC3¹¹) are generally regarded as the state-of-the-art in computational chemistry, but they are still too costly for molecular systems with more than about fifteen second-row elements.¹² Nonetheless, coupled cluster calculations are becoming increasingly feasible, particularly for methods that include double excitations either approximately, such as CC2,¹³ or in full, that is, coupled cluster singles and doubles (CCSD).¹⁴

It is, therefore, of considerable interest to develop efficient implementations of molecular gradients at the CCSD level of theory, both for the ground state and the excited states. Implementations of such gradients already exist in a number of programs. Ground state gradients are available in commercial codes, such as Q-Chem^{15,16} and Gaussian,¹⁷ and in open-source programs, such as Psi4^{18,19} and Dalton,^{20,21} as well as in free programs, such as CFOUR^{22,23} and MRCC.^{24,25} However, out of the above-mentioned programs, only

Q-Chem, CFOUR, and MRCC include excited state gradients at the CCSD level.

Cholesky decomposition (CD) of the electron repulsion integrals^{26–34} has become a valuable tool for efficient implementations in quantum chemistry. Due to the rank-deficiency of the integral matrix, CD implies significantly reduced computational requirements, both in terms of storage and number of floating-point operations. The CD method dates back to the 1970s,²⁶ but it has seen a resurgence of interest over the past decades due to improvements in algorithms^{39,35,36} and computer hardware. These developments have made CD competitive with the prevailing inner projection method, the resolution-of-identity (RI) or density-fitting method.^{32,34,37–46} As a result, there is currently a demand for efficient CD-based coupled cluster implementations (e.g., for molecular gradients). To date, however, such implementations are still rather scarce. Indeed, out of the programs mentioned above, only Q-Chem offers an implementation of CCSD gradients based on Cholesky-decomposed integrals.¹⁶

The factorized form of the electron repulsion integrals, obtained by inner projection, has an interesting implication for molecular gradient algorithms. Two- and three-index density intermediates naturally arise, allowing one to avoid storing the V^3O and V^4 blocks of the density matrix. This has been exploited both in CD for complete active space self-consistent field (CASSCF)³⁵ and in RI for CCSD.¹⁹ The equivalence between CD and RI means that RI implementations can be adapted to the framework of CD, which is the focus of this work. This strategy was first employed by Aquilante *et al.*³¹ for molecular gradients in density functional theory. An alternative algorithm for CD-CCSD gradients was recently suggested by Feng *et al.*¹⁶ and implemented in Q-Chem.¹⁵ This algorithm similarly employs a strategy where V^3O and V^4 terms are avoided,^{16,33} but it relies on the calculation and temporary storage of Cholesky vector derivatives. This implies a relatively large $O(N^4)$ storage requirement, thereby imposing a limitation on the system size. Feng *et al.* report that, for a system with 418 basis functions, 0.9 and 91 GB RAM were required to compute the Cholesky vectors and their derivatives, respectively.¹⁶ While these vectors are processed and released directly after decomposition, the procedure still requires a large amount of memory. This storage requirement can, in principle, be reduced to $O(N^3)$ by utilizing the sparsity of the Cholesky vectors in the atomic orbital (AO) basis. Another approach, which we employ here, is to calculate the required terms on the fly, eliminating any need to store the derivatives.

This paper describes a new and efficient implementation of the ground and excited state CCSD gradients, which we have incorporated into a development version of the open-source program e^T (version 1.6).⁴⁷ This implementation is partly based on the one reported by Bozkaya and Sherrill for RI-CCSD,¹⁹ where the gradient is constructed from two- and three-index density intermediates; for these intermediates, see also the CD-CASSCF implementation by Delcey *et al.*³⁵ Our implementation makes use of the recent two-step CD algorithm by Folkestad *et al.*³⁶ and is well-suited for large-scale applications. In particular, as already noted, derivative integrals involving the auxiliary basis are calculated on the fly, ensuring that no $O(N^4)$ storage requirements are associated with the Cholesky vectors.

II. THEORY

A. Analytical expression for the molecular gradient

Using a closed-shell, spin-restricted formulation, the molecular CCSD gradient is conveniently derived from the Lagrangian

$$\begin{aligned}\mathcal{L} &= E + \sum_{\mu \neq 0} \bar{\zeta}_{\mu} \Omega_{\mu} + \sum_{p \leq q} \bar{\kappa}_{pq} (F_{pq} - \delta_{pq} \epsilon_p) + \bar{\lambda} \mathcal{O} \\ &= \sum_{pq} h_{pq} D_{pq} + \sum_{pqrs} g_{pqrs} d_{pqrs} + \sum_{p \leq q} \bar{\kappa}_{pq} (F_{pq} - \delta_{pq} \epsilon_p) + \bar{\lambda} \mathcal{O},\end{aligned}\quad (1)$$

where E is the energy, h_{pq} and g_{pqrs} are the one- and two-electron integrals associated with the Hamiltonian H , respectively, and D_{pq} and d_{pqrs} are one- and two-electron densities, respectively. Lagrangian multipliers are denoted with a bar ($\bar{\zeta}_{\mu}$, $\bar{\kappa}_{pq}$, $\bar{\lambda}$). Furthermore,

$$\Omega_{\mu} = \langle \mu | \hat{H} | \text{HF} \rangle, \quad (2)$$

where $|\text{HF}\rangle$ is the Hartree-Fock state and

$$\hat{H} = \exp(-T) \exp(\kappa) H \exp(-\kappa) \exp(T). \quad (3)$$

Here, κ denotes the orbital rotation operator, and it is implied that $\kappa = 0$ at the nuclear geometry where the derivative is to be evaluated.^{21,48} The cluster operator is $T = \sum_{\mu} t_{\mu} \tau_{\mu}$, where τ_{μ} is an excitation operator and excited configurations are denoted as $|\mu\rangle = \tau_{\mu} |\text{HF}\rangle$; in addition, $\tau_0 = \mathbb{I}$ and hence $|0\rangle = |\text{HF}\rangle$. Moreover, the Fock matrix is given as

$$F_{pq} = h_{pq} + \sum_k (2g_{pqkk} - g_{pkkq}), \quad (4)$$

and ϵ_p denotes the energy of the p th molecular orbital (MO). Finally, \mathcal{O} is defined such that $\mathcal{O} = 0$ ensures normalization, i.e., that the left and right coupled cluster states are binormal. This term is described in more detail below.

The integrals in the Fock matrix (F_{pq}) are always expressed in the MO basis, whereas the integrals in the coupled cluster energy are either expressed in the MO basis or in the T_1 -transformed basis. Above and throughout, p, q, r , and s are used to denote generic MOs; i, j, k , and l denote occupied MOs; and a, b, c , and d denote virtual MOs.

The expressions for the energy E and the normalization condition \mathcal{O} depend on whether we are considering the ground state or an excited state. In particular,

$$E^{\text{GS}} = \langle \text{HF} | \hat{H} | \text{HF} \rangle, \quad (5)$$

$$E^{\text{ES}} = \sum_{\mu\nu} L_{\mu} \langle \mu | \hat{H} | \nu \rangle R_{\nu}, \quad (6)$$

and

$$\mathcal{O}^{\text{GS}} = 0, \quad (7)$$

$$\mathcal{O}^{\text{ES}} = 1 - \sum_{\mu} L_{\mu} R_{\mu}, \quad (8)$$

where L_μ and R_μ denote the left and right excited state amplitudes, respectively. For the ground state, normalization is automatically fulfilled¹⁰ and can be ignored ($\mathcal{O}^{\text{GS}} = 0$).

The stationarity conditions with respect to $\tilde{\zeta}_\mu$ and $\tilde{\kappa}_{pq}$ are, respectively, the well-known amplitude and canonical Hartree–Fock equations, $\Omega_\mu = 0$ and $F_{pq} = \delta_{pq}\epsilon_p$. Furthermore, the stationarity condition with respect to $\tilde{\lambda}$ enforces the biorthonormality constraint. The orbital rotation multipliers $\tilde{\kappa}_{pq}$ are determined from the stationarity condition with respect to the orbital rotation parameters κ_{pq} ,^{21,48,49}

$$\frac{\partial \mathcal{L}}{\partial \kappa_{pq}} = 0 \iff \bar{\kappa} \bar{\kappa} \mathbf{A} = -\bar{\kappa} \boldsymbol{\eta}. \quad (9)$$

Here,

$$\begin{aligned} \bar{\kappa} A_{pqrs} &= \delta_{pr} \delta_{qs} (\epsilon_p - \epsilon_q) \\ &+ (v_s - v_r) (4g_{pqrs} - g_{prqs} - g_{psrq}), \end{aligned} \quad (10)$$

with v_r equal to 1 if orbital r is occupied and 0 otherwise.⁵⁰ In the case of CCSD, $\bar{\kappa} \boldsymbol{\eta}$ is given as^{21,50}

$$\begin{aligned} \bar{\kappa} \eta_{pq} &= \sum_t h_{pt} (D_{tq} + D_{qt}) - \sum_t h_{qt} (D_{tp} + D_{pt}) \\ &+ \sum_{rst} g_{ptrs} (d_{tqrs} + d_{qtrs}) - \sum_{rst} g_{qtrs} (d_{tprs} + d_{ptrs}). \end{aligned} \quad (11)$$

Similarly, the amplitude multipliers $\tilde{\zeta}_\mu$ are determined from the stationarity condition with respect to the coupled cluster amplitudes t_μ ,

$$\frac{\partial \mathcal{L}}{\partial t_\mu} = 0, \quad (12)$$

which yields different equations for the ground and the excited states. In particular,

$$\tilde{\zeta}^{\text{GS}} \mathbf{A} = -\boldsymbol{\eta}, \quad (13)$$

$$\tilde{\zeta}^{\text{ES}} \mathbf{A} = -\boldsymbol{\eta} - \mathbf{J}\mathbf{A} - \mathbf{F}(\mathbf{L})\mathbf{R}, \quad (14)$$

with

$$A_{\mu\nu} = \langle \mu | [\hat{H}, \tau_\nu] | \text{HF} \rangle, \quad (15)$$

$$\eta_\mu = \langle \text{HF} | [\hat{H}, \tau_\mu] | \text{HF} \rangle, \quad (16)$$

$$J_{ai} = \sum_{bj} L_{ij}^{ab} R_j^b, \quad (17)$$

$$F(\mathbf{L})_{\mu\nu} = \sum_\lambda L_\lambda \langle \lambda | [[\hat{H}, \tau_\mu], \tau_\nu] | \text{HF} \rangle. \quad (18)$$

For the ground state, we obtain the ground state multiplier equations, Eq. (13), and we will let $\tilde{\zeta}^{\text{GS}} = \mathbf{t}$, following the conventional notation for these multipliers.¹⁰ For the excited states, Eq. (14) is obtained. The excited state multipliers, referred to below as the amplitude response, will similarly be denoted as $\tilde{\zeta}^{\text{ES}} = \mathbf{t}^{\text{ES}}$.

With all orbital and wave function parameters variationally determined, the gradient can now be evaluated as the first partial

derivative of the Lagrangian with respect to the nuclear coordinates. With appropriately defined densities (see Appendix A), this derivative can be written as^{21,48}

$$\mathcal{L}^{(1)} = \sum_{pq} h_{pq}^{(1)} D_{pq} + \sum_{pqrs} g_{pqrs}^{(1)} d_{pqrs} + \sum_{p \leq q} \tilde{\kappa}_{pq} F_{pq}^{(1)}, \quad (19)$$

where $h_{pq}^{(1)}$ and $g_{pqrs}^{(1)}$ denote one- and two-electron derivative integrals, respectively, and $F_{pq}^{(1)}$ denotes the derivative Fock matrix. The one- and two-electron derivative integrals are here evaluated in an orthonormal MO (OMO) basis, i.e., a basis strictly orthonormal at all geometries.^{51,52} These OMOs are obtained from the nonorthogonal unmodified MOs (UMOs), which are defined from the AOs at the displaced geometry and the MO coefficients of the unperturbed geometry. The orthonormalization matrix that transforms UMOs to OMOs defines an orbital connection and is known as the connection matrix.⁵²

Here, we will use the symmetric connection for which the connection matrix is given as the inverse square root of the UMO overlap matrix.⁵¹ For this connection, the derivative of the OMO Hamiltonian can be written as

$$H^{(1)} = H^{[1]} - \frac{1}{2} \{S^{[1]}, H\}, \quad (20)$$

where $H^{[1]}$ and $S^{[1]}$ denote derivatives of the Hamiltonian and of the overlap in the UMO basis, respectively. The second term of Eq. (20) is known as the reorthonormalization term. The UMO derivatives are evaluated by differentiating the AO integrals and then transforming them to the UMO basis. The notation $\{A, B\}$ means the one-index transformation of operator B by the transformation matrix A ,⁵¹

$$\{A, B\}_{pq} = \sum_t (A_{pt} B_{tq} + A_{qt} B_{pt}), \quad (21)$$

$$\begin{aligned} \{A, B\}_{pqrs} &= \sum_t (A_{pt} B_{tqrs} + A_{qt} B_{ptrs} \\ &+ A_{rt} B_{pqts} + A_{st} B_{pqrt}). \end{aligned} \quad (22)$$

The expression for $F^{(1)}$ is similar to that for $H^{(1)}$ in Eq. (20) and is omitted. See Refs. 51 and 52 for further details on orbital connections.

We will begin by deriving expressions for the UMO contributions to the gradient, that is, the contributions originating from the first term in Eq. (20). The reorthonormalization contributions are presented separately (see Sec. II D).

The first term in Eq. (19) has been thoroughly described in other works for the CCSD case, e.g., by Scheiner *et al.*⁵³ The second and third terms are not trivial and will be described in more detail. For the second term, the CCSD two-electron densities are required. Expressions for both ground and excited state densities have been rederived and are given in Appendix A. Evaluating this term also requires that we consider the electron repulsion integrals. Below, unless otherwise specified, these integrals are expressed in the T_1 -transformed basis, and hence, the densities have been made

independent of T_1 , see Eq. (A1). In the T_1 -transformed basis, the Hamiltonian integrals can be written

$$h_{pq} = \sum_{rs} x_{pr} y_{qs} h_{rs}^{\text{MO}}, \quad (23)$$

$$g_{pqrs} = \sum_{tumn} x_{pt} y_{qu} x_{rm} y_{sn} g_{tumn}^{\text{MO}}, \quad (24)$$

where $\mathbf{x} = \mathbf{I} - \mathbf{t}_1$ and $\mathbf{y} = \mathbf{I} + \mathbf{t}_1^T$ and \mathbf{h}^{MO} and \mathbf{g}^{MO} denote integrals expressed in the MO basis.¹⁰

To find expressions for the derivatives of g_{pqrs} , we expand the integral matrix in terms of its Cholesky decomposition. That is, we write

$$\begin{aligned} g_{pqrs} &= (pq|rs) = \sum_{KL} (pq|K) (\mathcal{S}^{-1})_{KL} (L|rs) \\ &= \sum_J L_{pq}^J L_{rs}^J, \end{aligned} \quad (25)$$

where

$$\mathcal{S}_{KL} = (K|L), \quad (26)$$

and where K and L are elements in the Cholesky basis.^{26,30} The Cholesky decomposition of \mathcal{S} defines the \mathbf{Q} matrix, from which we can evaluate the inverse of \mathcal{S} ,

$$\mathcal{S} = \mathbf{Q}\mathbf{Q}^T \implies \mathcal{S}^{-1} = \mathbf{Q}^{-T}\mathbf{Q}^{-1}, \quad \mathbf{Q}^{-T} = (\mathbf{Q}^{-1})^T. \quad (27)$$

This yields the definition of the Cholesky vectors,

$$L_{pq}^J = \sum_K (pq|K) Q_{KJ}^{-T}. \quad (28)$$

The Cholesky vectors are also expressed in the T_1 -transformed basis, where

$$L_{pq}^J = \sum_{rs} x_{pr} y_{qs} (L_{rs}^J)^{\text{MO}}. \quad (29)$$

Here, $(L_{rs}^J)^{\text{MO}}$ denotes the Cholesky vectors in the MO basis. From the above definitions, we can write the derivative two-electron integrals as

$$\begin{aligned} (pq|rs)^{[1]} &= \sum_K (pq|K)^{[1]} Z_{rs}^K + \sum_L (rs|L)^{[1]} Z_{pq}^L \\ &\quad - \sum_{MN} Z_{pq}^M \mathcal{S}_{MN}^{[1]} Z_{rs}^N, \end{aligned} \quad (30)$$

where we have defined

$$Z_{rs}^K = \sum_L (\mathcal{S}^{-1})_{KL} (L|rs), \quad (31)$$

and used the identity

$$(\mathcal{S}^{-1})^{[1]} = -\mathcal{S}^{-1} \mathcal{S}^{[1]} \mathcal{S}^{-1}. \quad (32)$$

Upon contraction with the two-electron density, the UMO contribution to the second term of Eq. (19) becomes

$$\sum_{pqrs} d_{pqrs} (pq|rs)^{[1]} = 2 \sum_{pqK} (pq|K)^{[1]} W_{pq}^K - \sum_{MN} V_{MN} \mathcal{S}_{MN}^{[1]}, \quad (33)$$

with

$$W_{pq}^K = \sum_{rs} d_{pqrs} Z_{rs}^K, \quad (34)$$

$$V_{MN} = \sum_{pq} Z_{pq}^M W_{pq}^N. \quad (35)$$

The first term in Eq. (33) is more conveniently calculated in the non-transformed basis by transferring the T_1 -terms back to W_{pq}^K ,

$$(W_{pq}^K)^{\text{MO}} = \sum_{rs} x_{pr} y_{sq} W_{rs}^K, \quad (36)$$

before contracting with the differentiated MO integrals, $(pq|K)^{[1],\text{MO}}$.

B. Two-electron density intermediates

Expressions for various blocks of the two-electron density are reported in Appendix A. In this section, we describe in detail the two- and three-index density intermediates. All contributions to W_{pq}^J from the O^4 , O^3V , and O^2V^2 density blocks are constructed straightforwardly by contracting the density block with Z_{pq}^J ; hence, we will not discuss them further. To avoid storing the V^4 and OV^3 blocks of the density in memory, and, in addition, to avoid batching when constructing the OV^3 terms, we directly build their contributions to W_{pq}^J and store these instead. For improved readability, Einstein's implicit summation over repeated indices will be used in the remainder of this section. The contributions from the OV^3 -density blocks to the gradient are

$$\begin{aligned} d_{abci} (ab|ci)^{[1]} &= (ab|K)^{[1]} W_{ab}^K \\ &\quad + (ci|L)^{[1]} W_{ci}^L - V_{MN} \mathcal{S}_{MN}^{[1]}, \end{aligned} \quad (37)$$

$$\begin{aligned} d_{abci} (ab|ic)^{[1]} &= (ab|K)^{[1]} W_{ab}^K \\ &\quad + (ic|L)^{[1]} W_{ic}^L - V_{MN} \mathcal{S}_{MN}^{[1]}. \end{aligned} \quad (38)$$

For these terms, we directly construct the contributions to W_{ci}^K and W_{ic}^K , as well as to W_{ab}^K and V_{MN} , from the two OV^3 blocks of the two-electron density. From d_{abci} , we obtain, for the excited state, the contributions

$$W_{ab}^K = R_j^b X_{aj}^K, \quad (39)$$

$$W_{ci}^K = L_{ji}^{ac} R_{aj}^K, \quad (40)$$

$$V_{MN} = Z_{ab}^M W_{ab}^N + Z_{ci}^M W_{ci}^N, \quad (41)$$

where L_{ji}^{ac} and R_j^b denote excited state amplitudes (see Appendix A). For the ground state, all contributions from d_{abci} are zero. From d_{abic} , we similarly obtain

$$W_{ab}^K = L_m^a \tilde{Y}_{bm}^K (T_2) R_0, \quad (42)$$

$$W_{ic}^K = \tilde{\epsilon}_{im}^{cb} R_0 O_{bm}^K, \quad (43)$$

$$V_{MN} = Z_{ab}^M W_{ab}^N + Z_{ic}^M W_{ic}^N, \quad (44)$$

for the ground state, and

$$\begin{aligned}
 W_{ab}^K &= L_m^a \hat{\gamma}_{bm}^K(R_2) \\
 &+ 2X_{ab}(L_2, T_2)P^K - O_{ai}^J R_i^b \\
 &- (V_{akbi}(L_2, T_2) + Y_{akbi}(L_2, T_2))P_{ik}^K + 2Q_{ak}^K R_i^b \\
 &+ W_{am} \hat{\gamma}_{bm}^K(T_2) - K_{icab}Z_{ab}^K,
 \end{aligned} \quad (45)$$

$$\begin{aligned}
 W_{ic}^K &= (2\bar{R}_{mi}^{bc} - \bar{R}_{mi}^{cb})O_{bm}^K \\
 &+ 2C^K R_i^c - X_{ac}(L_2, T_2)P_{ai}^K \\
 &- K_{ik}^K R_i^c + 2Y_{akci}(L_2, T_2)P_{ak}^K \\
 &+ U_{bm}^K \bar{t}_{mi}^{bc} - S_{iacb}Z_{ab}^K,
 \end{aligned} \quad (46)$$

$$V_{MN} = Z_{ab}^M W_{ab}^N + Z_{ic}^M W_{ic}^N, \quad (47)$$

for the excited state. The introduced intermediates are given in Table I.

The V^4 density contribution to W_{ab}^I is also evaluated directly as a contraction between the density and Z_{cd}^K , albeit with batching. This contribution is the steepest-scaling term in the gradient and implies the calculation of the density contribution,

$$O_{abcd}^{(2)} = L_{ij}^{ac} C_{ij}^{bd}. \quad (48)$$

To evaluate this term as written would have a cost of $O^2 V^4$. However, it is possible to reduce the cost by a factor of four by adapting

TABLE I. Intermediates used to construct the W_{ab}^K , W_{ci}^K , and W_{ic}^K density intermediates. Here, C_2 denotes a set of double amplitudes, and $\bar{C}_{ij}^{ab} = 2C_{ij}^{ab} - C_{ji}^{ab}$. Also, \bar{R}_2 is a redefinition of the R_2 amplitudes (see Appendix A). In the expressions given in this table, $C_2 = T_2$. The definition of C_2 may be different as C_2 is merely a placeholder; see also Appendix A. Summation over repeated indices is assumed.

$$\begin{aligned}
 \bar{t}_{ij}^{ab} &= 2t_{ij}^{ab} - t_{ji}^{ab} \\
 W_{ai} &= L_{il}^{ad} R_{dl} \\
 X_{ab}(L_2, C_2) &= L_{kl}^{ad} C_{kl}^{bd} \\
 Y_{ajbi}(L_2, C_2) &= L_{jl}^{ad} C_{il}^{bd} \\
 V_{ajbi}(L_2, C_2) &= L_{ij}^{ac} C_{bk}^{bc} \\
 S_{iacb} &= B_{iamn} t_{mn}^{bc} \\
 B_{iamn} &= L_{mn}^{ad} R_i^d \\
 K_{ik}^K &= (V_{akbi}(L_2, T_2) + Y_{akbi}(L_2, T_2))Z_{ab}^K \\
 X_{aj}^K &= L_{ji}^{ac} Z_{ci}^K \\
 P_{aj}^K &= R_{ij}^b Z_{ab}^K \\
 \bar{Y}_{bm}^K(C_2) &= \bar{C}_{im}^{cb} Z_{ic}^K \\
 P_{ik}^K &= R_{ij}^b Z_{ab}^K \\
 O_{ai}^J &= X_{ac}(L_2, T_2)Z_{ic}^K \\
 P_{ik}^K &= R_{ij}^b Z_{ab}^K \\
 Q_{ak}^K &= Y_{akci}(L_2, T_2)Z_{ic}^K \\
 K_{icab} &= (L_{mn}^{ad} R_i^d) t_{mn}^{bc} \\
 Q^K &= X_{ab}(L_2, T_2)Z_{ab}^K \\
 P_{ai}^K &= R_{ij}^b Z_{ab}^K \\
 U_{bm}^K &= W_{am} Z_{ab}^K
 \end{aligned}$$

the well-known strategy for constructing the A2 term of Ω .³⁴ In the case of Eq. (48), we form the symmetric and anti-symmetric combinations of L_2 and C_2 ,

$$X_{ij}^{ab\pm} = X_{ij}^{ab} \pm X_{ji}^{ab}, \quad X = L_2, C_2. \quad (49)$$

Then, by contracting the symmetric and anti-symmetric terms separately and adding them together, we need not loop over all indices, but merely $i \geq j$, $a \geq c$, and $b \geq d$, leading to an eight-fold reduction in cost. However, since this must be done twice (for symmetric and anti-symmetric terms), the net reduction in cost is a factor of four.

C. Orbital relaxation contributions

In order to obtain the gradient, all three terms of Eq. (19) must be evaluated. So far, we have not yet discussed the third term. First, the $\bar{\kappa}$ parameters are determined from the Z-vector equation given in Eq. (9). Since CCSD is orbital invariant, we only consider the VO block of the $\bar{\kappa}$ vector.²¹ The UMO contribution to the orbital relaxation then reads

$$\sum_{ai} \bar{\kappa}_{ai} F_{ai}^{[1]} = \sum_{ai} \bar{\kappa}_{ai} \left(h_{ai}^{[1]} + \sum_j (2g_{aijj}^{[1]} - g_{ajji}^{[1]}) \right). \quad (50)$$

The integrals are here expressed in the MO basis. For efficiency, the second and third terms are rewritten by using the Cholesky decomposition,

$$\begin{aligned}
 \sum_{aij} \bar{\kappa}_{ai} (2g_{aijj}^{[1]} - g_{ajji}^{[1]}) &= \sum_{aiK} K_{ai}^K (a|K)^{[1]} \\
 &+ \sum_{jK} L^K (K|jj)^{[1]} + \sum_{ijK} N_{ji}^K (K|ji)^{[1]} \\
 &- \sum_{KL} M_{KL} S_{KL}^{[1]} + \frac{1}{2} \sum_{KL} O_{KL} S_{KL}^{[1]}.
 \end{aligned} \quad (51)$$

The introduced intermediates are given in Table II. The first three terms are added to the $W_{pq}^I g_{pqrs}^{[1]}$ term, while the remaining terms are added to the $V_{MN} S_{MN}^{[1]}$ term [see Eq. (33)].

To determine $\bar{\kappa}_{ai}$, we also need the right-hand-side of the Z-vector equation. This vector is conveniently constructed from a three-index intermediate $\bar{W}_{pq}^I = W_{pq}^I(L)$, defined as W_{pq}^I , but constructed using L_{pq}^I rather than Z_{pq}^I . In terms of this intermediate, and using integrals expressed in the MO basis, we have²¹

$$\bar{\kappa}_{ai} = (1 - P_{ai}) \left(\sum_t D_{ti} h_{at} + \sum_{ij} \bar{W}_{ti}^I L_{at}^I \right), \quad (52)$$

TABLE II. Intermediates used to construct $\sum_{aij} \bar{\kappa}_{ai} (2g_{aijj}^{[1]} - g_{ajji}^{[1]})$. Here, Z_{pq}^K is expressed in the MO basis.

$$\begin{aligned}
 K_{ai}^K &= \sum_j \bar{\kappa}_{ai} (2Z_{jj}^K - Z_{ji}^K) \\
 L^K &= 2 \sum_{ai} \bar{\kappa}_{ai} Z_{ai}^K \\
 N_{ji}^K &= - \sum_a \bar{\kappa}_{ai} Z_{aj}^K \\
 M_{KL} &= \sum_j L_{jj}^K Z_{jj}^L \\
 O_{KL} &= \sum_{ij} N_{ji}^K Z_{ji}^L
 \end{aligned}$$

where $P_{ai}X_{ai} = X_{ia}$ and

$$\mathcal{D}_{pq} = D_{pq} + D_{qp}, \quad (53)$$

$$\tilde{W}_{pq}^J = \tilde{W}_{pq}^J + \tilde{W}_{qp}^J. \quad (54)$$

D. Reorthonormalization contributions

The second term in Eq. (20) gives rise to reorthonormalization contributions to the gradient. These contributions can be expressed as $-\sum_{pq} \mathcal{F}_{pq} \mathcal{S}_{pq}^{[1]}$, where

$$\mathcal{F}_{pq} = \sum_i \left(\mathcal{D}_{pi} h_{qi} + \sum_j \tilde{W}_{pi}^J L_{qi}^J \right) + \mathcal{F}_{pq}^{\tilde{\kappa}}. \quad (55)$$

The orbital relaxation contribution $\mathcal{F}_{pq}^{\tilde{\kappa}}$ is described in detail in Appendix B. All terms in Eq. (55) are in the MO basis.

III. COMPUTATIONAL DETAILS

The CD-CCSD gradient for ground and excited states has been implemented in a development version of e^T 1.6. We apply the gradient implementation to determine equilibrium geometries for thymine, azobenzene, and retinal (see Fig. 1), where we consider the ground state in all three systems and the lowest singlet excited state in thymine and azobenzene. To perform these calculations, we have also implemented an optimizer that uses the Broyden–Fletcher–Goldfarb–Shanno (BFGS) algorithm with the rational function (RF)⁵⁵ level shift. This implementation makes use of the redundant internal coordinates introduced by Bakken and Helgaker,³⁶ along with the initial “simple model Hessian guess” proposed by the same authors.

For comparison, we carried out CD-CCSD calculations with Q-Chem 5.4¹⁵ and RI-CCSD calculations with Psi4 1.3.¹⁸ The aug-cc-pVDZ basis was used in all calculations. For consistency with our implementation, we disabled the frozen core approximation in Q-Chem and Psi4. Default thresholds were used in all calculations, except in the case of the CD convergence threshold. The reason for this is that a CD threshold of, e.g., 10^{-3} can result in slow convergence because the Cholesky basis varies on the potential energy surface, causing discontinuities of the same order of magnitude as

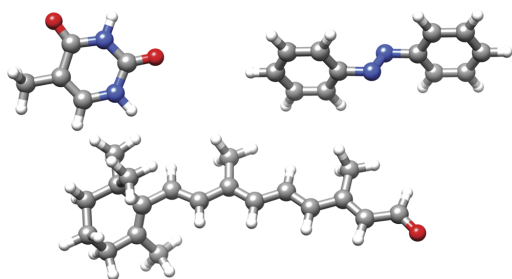


FIG. 1. Ground state geometries, optimized at the CCSD/aug-cc-pVDZ level, for thymine (top left), azobenzene (top right), and retinal (bottom).

the CD threshold. This was also observed by both Aquilante *et al.*³¹ and Feng *et al.*¹⁶ Thus, in order to converge the gradient to 3×10^{-4} (the Baker convergence criterion), we employed a tighter CD threshold of 10^{-4} throughout. The one exception to this was for the large retinal molecule, where we instead applied a CD threshold of 10^{-3} .

The e^T program does not utilize point group symmetry, whereas this was enabled in Q-Chem and Psi4. However, the initial geometries do not possess point group symmetry, and this should, therefore, not affect the comparison of timings significantly. Initial and optimized molecular geometries can be found in Ref. 57. At the initial geometries, the excitation energies in thymine and azobenzene are 5.20 and 3.46 eV, respectively; at the optimized excited state geometries, the excitation energies are 3.98 and 2.35 eV. All calculations were performed on one node with two Intel Xeon E5-2699 v4 processors with 44 cores and given 1 TB of shared memory.

IV. RESULTS AND DISCUSSION

A. Timing comparisons of different implementations

To demonstrate the efficiency of our implementation, we compare calculation times for geometry optimizations of a small system (thymine) and a medium-large system (azobenzene) with the Psi4 and Q-Chem programs. Excited state gradients are not available in Psi4, and thus, excited state geometry optimizations have not been performed with this program. We report the percentage of the time spent determining the gradients for the e^T calculations. This is not reported for Q-Chem or Psi4, as this time is not directly available from their respective outputs.

Timings for e^T and Psi4 are given in Table III. From the results, we see that the calculation of the gradient amounts to only 7% of the total calculation time, illustrating the efficiency of the gradient implementation. Here, the time required to determine the multipliers is not included in the gradient time. This task may represent a significant part of the total time, but it is determined by the efficiency of the existing implementation of Jacobian transformations, rather than the construction of the gradient, which is the focus of this work. We observe that the calculation time required by e^T , per optimization cycle, is roughly half of that required by Psi4. This primarily reflects the difference in the efficiency of the ground state implementation in the two programs.

When applying an inner projection method, the integral costs are proportional to the size of the auxiliary basis.³⁶ In the density-fitting scheme used in Psi4, the thymine calculation required 786 auxiliary basis functions, while 967 functions were used in our CD-based implementation. These two numbers are of the same order of magnitude; thus, the computational resources required should be comparable. This is also the case for the azobenzene calculations, in which Psi4 and e^T required 1238 and 1444 auxiliary basis functions, respectively. Hence, the two approaches are similar in terms of computational costs. However, note that the time spent on the Cholesky decomposition itself is negligible and that the resulting integral errors are strictly lower than the CD threshold (here 10^{-4}). Such strict error control is not possible with the density-fitting method.

Timings for e^T and Q-Chem are given in Table IV. We now also consider excited state geometry optimizations and observe once

TABLE III. Ground state calculation times for thymine and azobenzene using Psi4 and our new implementation in e^T . The number of optimization cycles required, n_{cycles} , is reported, as well as the total calculation time, t_{total} , and the time per cycle, t_{cycle} . The average fraction of time spent calculating the gradient per optimization cycle, t_{gradient} , is reported for e^T .

	e^T				Psi4		
	n_{cycles}	t_{total}	t_{cycle}	t_{gradient} (%)	n_{cycles}	t_{total}	t_{cycle}
Thymine	6	42 min	7 min	6.8	7	2 h 4 min	18 min
Azobenzene	10	7 h 42 min	46 min	7.1	7 ^a	14 h 27 min	2 h 4 min

^aThe optimization failed after seven cycles in Psi4.

TABLE IV. Ground and excited state calculation times for thymine and azobenzene using Q-Chem and our new implementation in e^T . The excited states are the lowest singlet states in all cases. The number of optimization cycles required, n_{cycles} , are reported, as well as the total calculation time, t_{total} , and the time per cycle, t_{cycle} . The average fraction of time spent calculating the gradient per optimization cycle, t_{gradient} , is reported for e^T .

	e^T				Q-Chem		
	n_{cycles}	t_{total}	t_{cycle}	t_{gradient} (%)	n_{cycles}	t_{total}	t_{cycle}
Thymine (GS)	6	42 min	7 min	6.8	7	3 h 42 min	32 min
Thymine (ES)	7	2 h 3 min	18 min	4.7	7	5 h 42 min	49 min
Azobenzene (GS)	10	7 h 42 min	46 min	7.1	7	22 h 53 min	3 h 16 min
Azobenzene (ES)	9	23 h 0 min	2 h 33 min	4.2	6	33 h 43 min	5 h 37 min

again that the calculation time is not dominated by the gradient. In fact, the calculation of the gradient amounts to 5% of the full calculation time for the excited state (compared to 7% for the ground state). Note that when reporting the time spent on determining the excited state gradients, we have again excluded the time needed to determine the amplitude response.

From Table IV, it is furthermore observed that we can carry out ground state optimizations in roughly 50% of the time required by Q-Chem, or even less. The savings are significantly larger for ground state optimizations. This can be attributed to differences, between the two programs, in the efficiency of the ground and excited state implementations. The calculation time in Q-Chem

can be significantly reduced with the utilization of the frozen core approximation (for timings, see the [supplementary material](#)), resulting in computation times for the excited state, which are comparable to those observed in e^T without this approximation. For the ground state, however, our new implementation still offers significant time savings, despite frozen core calculations being inherently less computationally demanding.

The reported comparisons were carried out without enforcing point-group symmetry. As also noted above, further improvements to the Q-Chem and Psi4 timings could have been obtained by starting from geometries with point-group symmetry. Further gains are also possible with a single-precision execution.⁵⁸

TABLE V. Optimized and experimental ground state bond lengths, r (pm), and angles, α (deg), for ten small molecules. The experimental and calculated CCSD/cc-pCVQZ results are taken from Ref. 10.

Molecule	Bond (r_{AB})	Angle (α)	CD-CCSD/cc-pCVQZ		CCSD/cc-pCVQZ		Experiment	
			r (pm)	α (deg)	r (pm)	α (deg)	r (pm)	α (deg)
H ₂ O	OH	\angle HOH	95.4	104.5	95.4	104.5	96.6	104.5
HOF	OH	\angle HOF	96.2	98.6	96.2	98.6	96.6	97.5
H ₂ O ₂	OH	\angle HOO	95.8	100.7	95.8	100.7	96.7	102.3
NH ₃	NH	\angle HNH	100.9	106.6	100.9	106.6	101.1	106.7
N ₂ H ₂	NH	\angle HNN	102.5	106.6	102.5	106.6	102.9	106.3
HNO	NH	\angle HNO	104.8	108.3	104.8	108.3	106.2	108.5
C ₂ H ₄	CH	\angle HCH	107.9	117.0	107.9	117.0	108.1	117.4
CH ₂ O	CH	\angle HCH	109.9	116.4	109.9	116.4	110.1	116.3
CH ₂	CH	\angle HCH	110.5	102.0	110.5	102.0	110.7	102.4
O ₃	OO	\angle OOO	124.1	117.8	124.1	117.8	127.2	116.8

B. Comparisons of obtained geometries for small molecules

In order to investigate the accuracy of our CD-CCSD implementation compared to standard CCSD, optimized bond lengths and bond angles have been determined for 10 small molecules. It is observed from Table V that our CD-CCSD/cc-pCVQZ results (CD-threshold 10^{-4}) exactly reproduce previously reported results¹⁰ using standard CCSD. Our results are thus well converged within the accuracy of the CCSD model, and hence, we conclude that no accuracy is lost by employing CD.

C. Convergence threshold effects

We have also studied the effect of changing the CD and gradient convergence thresholds on the final geometry of thymine—as measured by changes in redundant internal coordinates.⁵⁶ From Table VI, we observe that a very small error is obtained in the final geometry, even at a CD threshold of 10^{-3} . This small error was also pointed out by Feng *et al.*¹⁶ At our chosen CD threshold of 10^{-4} , the largest change in bond length is 0.01 pm; the changes in angles and dihedral angles are smaller than 0.002 radians, corresponding to about 0.01° . Thus, at the CCSD level of theory, the optimized geometry of thymine can be considered fully converged with our chosen CD threshold.

It must be noted, however, that even at this threshold, small differences in the CD basis can occur. This may cause changes in the number of required optimization cycles from run to run, but the final geometries remain unchanged within the specified convergence thresholds.

D. Illustration of large-scale application

To showcase the applicability of our implementation, we have also performed geometry optimization on retinal, which contains 49 atoms and 150 electrons, corresponding to 735 basis functions with our chosen basis set (aug-cc-pVDZ). This optimization was only carried out using e^T . Timings are summarized in Table VII. While the calculation does indeed put a strain on the computational resources, requiring 17 hours per optimization cycle, it can in fact be performed. As in the previous examples, the time spent calculating the gradient amounts to only a small fraction of the total calculation time. Note that this calculation was performed using a development version of e^T 1.4. The version used in the other calculations (e^T 1.6)

TABLE VII. Calculation time for optimizing the geometry of retinal in e^T . The number of optimization cycles required, n_{cycles} , are reported, as well as the total calculation time, t_{total} , the time spent per cycle, t_{cycles} , and the average time spent calculating the gradient per optimization cycle, t_{gradient} . The CD convergence threshold was here 10^{-3} .

	n_{cycles}	t_{total}	t_{cycle}	t_{gradient}
Retinal (GS)	24	17 d 10 h 23 min	17 h 26 min	6.6%

includes some optimizations of the left Jacobian transformation, potentially allowing for further reductions in computational cost.

V. CONCLUSIONS

We have presented an efficient implementation of CCSD gradients for ground and excited states based on Cholesky-decomposed electron repulsion integrals. Since CD is an inner projection scheme, we have chosen an implementation approach that follows earlier schemes^{19,35} for CD and RI where one avoids the storage of OV^3 and V^4 arrays by constructing three-index intermediates. We have, furthermore, chosen not to store the derivative Cholesky vectors; instead, the associated contributions are constructed on-the-fly. This allows us to significantly reduce the storage requirements.

Relative to Psi4 and Q-Chem, our implementation was shown to reduce the calculation time of geometry optimizations by roughly a factor of two. To a large extent, this reduction in time reflects the efficiency of the coupled cluster code in the e^T program. However, the calculation of gradients was found to require only a small fraction of the total calculation time, showcasing the efficiency of the gradient implementation.

The capabilities of our implementation were highlighted by showing that a geometry optimization of retinal could be carried out.

Further reduction in computational demands would be achieved by means of the frozen-core approximation. Work on this is currently in progress.

SUPPLEMENTARY MATERIAL

See the [supplementary material](#) for the comparison of frozen-core and non-frozen-core calculations in Q-Chem as well as a breakdown of timings for ground and excited state geometry optimization calculations of azobenzene and thymine.

ACKNOWLEDGMENTS

We thank Xintian Feng for taking the time to answer our questions about the Q-Chem gradient implementation. We acknowledge support from the DTU Alliance Ph.D. program (Ph.D. grant to A.K.S.-P.). A.K.S.-P. acknowledges funding from the European Cooperation in Science and Technology, COST Action Grant No. CA18222 Attochem. S.C. acknowledges support from the Independent Research Fund Denmark (DFF-RP2 Grant No. 7014-00258B). E.F.K., S.C., and H.K. acknowledge the Research Council of Norway through FRINATEK Project Nos. 263110 and 275506. Computing resources through UNINETT Sigma2—the National Infrastructure

TABLE VI. Deviations in the optimized geometry of thymine. The deviations are given relative to an optimized geometry obtained with a CD convergence threshold of 10^{-8} and a gradient convergence threshold of 3×10^{-8} . Changes in internal coordinates are measured by the largest change in a bond length (Δr), an angle ($\Delta \alpha$), and a dihedral angle ($\Delta \theta$).

CD threshold	Gradient threshold	Max Δr (pm)	Max $\Delta \alpha$ (rad)	Max $\Delta \theta$ (rad)
10^{-3}	3×10^{-3}	0.058	0.000 68	0.0012
10^{-4}	3×10^{-4}	0.012	0.000 40	0.0012
10^{-5}	3×10^{-5}	0.002	0.000 07	0.0010

for High Performance Computing and Data Storage in Norway (Project No. NN2962k) are also acknowledged.

AUTHOR DECLARATIONS

Conflict of Interest

The authors have no conflicts to disclose.

DATA AVAILABILITY

Geometries can be found in Ref. 54. The code will be released in an upcoming version of the e^T program, which is open-source.

APPENDIX A: TWO-ELECTRON DENSITIES

The two-electron density is here taken as

$$d_{pqrs} = L_v \langle v | e^{-T_2} e_{pqrs} e^{T_2} | \rho \rangle R_\rho, \quad (\text{A1})$$

where

$$e_{pqrs} = E_{pq} E_{rs} - \delta_{qr} E_{ps}. \quad (\text{A2})$$

Note that we are using a T_1 -transformed basis, where the T_1 -dependence has been moved into the derivative integrals, as they will be contracted with the density later on. Throughout, we assume a spin-adapted singlet basis, where the kets are expressed in the so-called elementary basis and bras are expressed in the basis biorthonormal to the kets.¹⁰

In the expression for the density, we can write, for the ground state,

$$L_0 = 1, \quad L_\mu = \tilde{t}_\mu, \quad (\text{A3})$$

$$R_0 = 1, \quad R_\mu = 0, \quad (\text{A4})$$

and, for excited states,

$$L_0 = 0, \quad L_\mu = L_\mu, \quad (\text{A5})$$

$$R_0 = 0, \quad R_\mu = R_\mu, \quad (\text{A6})$$

where \mathbf{R} and \mathbf{L} are defined for $\mu > 0$, and

$$\mathbf{A}\mathbf{R} = \omega\mathbf{R}, \quad (\text{A7})$$

$$\mathbf{A}^T\mathbf{L} = \omega\mathbf{L}. \quad (\text{A8})$$

In addition, for the excited state, we must add terms with

$$L_0 = 0, \quad L_\mu = \tilde{t}_\mu^{\text{ES}}, \quad (\text{A9})$$

$$R_0 = 1, \quad R_\mu = 0, \quad (\text{A10})$$

to the density in order to account for the amplitude response \tilde{z}_μ . These terms are formally identical to the terms of the ground state density that do not include L_0 , and they are, therefore, not written out explicitly. This also applies to the one-electron density.

In the following, we shall utilize that R_2 can be written as \tilde{R}_2 ,

$$\begin{aligned} R_2 &= \frac{1}{2} \sum_{aij} R_{aij} (1 + \delta_{ai,bj}) E_{ai} E_{bj} \\ &\equiv \frac{1}{2} \sum_{aij} \tilde{R}_{aij} E_{ai} E_{bj} = \tilde{R}_2. \end{aligned} \quad (\text{A11})$$

There are eight unique combinations of occupied and virtual indices because of the symmetry,

$$e_{pqrs} = e_{rspq} \Rightarrow d_{pqrs} = d_{rspq}. \quad (\text{A12})$$

For each of these combinations, we derive below the corresponding CCSD two-electron density block. For improved readability, Einstein's implicit summation over repeated indices will be used.

For the ground state, we obtain and implement

$$d_{ijkl}^{\text{gs}} = (L_0 R_0) \Lambda_{ijkl} + O_{ijkl}^{(2)}(L_2, T_2) R_0, \quad (\text{A13})$$

$$d_{aijk}^{\text{gs}} = (2L_i^a \delta_{jk} - L_k^a \delta_{ji}) R_0, \quad (\text{A14})$$

$$d_{ijka}^{\text{gs}} = O_{ijka}^{(M)}(L_1, T_2) R_0, \quad (\text{A15})$$

$$d_{abij}^{\text{gs}} = O_{abij}^{(2)}(L_2, T_2) R_0, \quad (\text{A16})$$

$$d_{aijb}^{\text{gs}} = L_{ij}^{ab} R_0, \quad (\text{A17})$$

$$d_{iajb}^{\text{gs}} = 2R_0 L_0 \tilde{t}_{ij}^{ab} + R_0 \frac{1}{2} O_{iajb}^{(2)}(L_2, T_2), \quad (\text{A18})$$

$$d_{aijb}^{\text{gs}} = O_{aijb}^{(M)}(L_2, T_2) R_0, \quad (\text{A19})$$

$$d_{abci}^{\text{gs}} = 0, \quad (\text{A20})$$

$$d_{abci}^{\text{gs}} = L_m^a \tilde{t}_{im}^{cb} R_0, \quad (\text{A21})$$

$$d_{abcd}^{\text{gs}} = O_{abcd}^{(2)}(L_2, T_2) R_0, \quad (\text{A22})$$

and, for the excited state, we similarly obtain and implement

$$d_{ijkl}^{\text{es}} = O_{ijkl}^{(2)}(L_2, \tilde{R}_2) + (\mathbf{L}^T \mathbf{R}) \Lambda_{ijkl} + O_{ijkl}^{[1]}(L_1, R_1), \quad (\text{A23})$$

$$d_{aijk}^{\text{es}} = -L_{ik}^{ad} R_{dj} + 2W_{ai} \delta_{jk} - W_{ak} \delta_{ji}, \quad (\text{A24})$$

$$\begin{aligned} d_{ijka}^{\text{es}} &= O_{ijka}^{(M)}(L_1, \tilde{R}_2) - 2X_{ij}(L_2, T_2) R_k^a + X_{kj}(L_2, T_2) R_i^a + X_{da} R_i^d \delta_{jk} \\ &\quad + (V_{dai}(L_2, T_2) + Y_{dai}(L_2, T_2) - 2\delta_{ij} X_{da}(L_2, T_2)) R_k^d \\ &\quad + (Z_{ijkl}(L_2, T_2) + X_{ij}(L_2, T_2) \delta_{jk} - 2\delta_{ij} X_{kl}(L_2, T_2)) R_i^a \\ &\quad - \tilde{t}_{ik}^{ea} W_{ej} - (\tilde{t}_{mi}^{ea} \delta_{jk} - 2\delta_{ij} \tilde{t}_{mk}^{ea}) W_{em} - \tilde{Y}_{djak}(L_2, T_2) R_i^d, \end{aligned} \quad (\text{A25})$$

$$d_{abij}^{\text{es}} = O_{abij}^{(2)}(L_2, \tilde{R}_2) + O_{abij}^{(1)}(L_1, R_1), \quad (\text{A26})$$

$$d_{aijb}^{\text{es}} = 0, \quad (\text{A27})$$

$$\begin{aligned} d_{iajb}^{\text{es}} &= O_{iajb}^{(2)}(L_2, \tilde{R}_2) + 2L_{ck} \tilde{t}_{ij}^{ac} R_{bj} - L_{ck} \tilde{t}_{jk}^{ac} R_{bi} + 2L_{ck} \tilde{t}_{jk}^{bc} R_{ai} \\ &\quad - L_{ck} \tilde{t}_{ik}^{bc} R_{aj} - Y_{cb} \tilde{t}_{ij}^{ac} - Y_{ca} \tilde{t}_{ji}^{bc} - Y_{jk} \tilde{t}_{ik}^{ab} \\ &\quad - Y_{ik} \tilde{t}_{kj}^{ab} + 2L_{ck} \tilde{t}_{ij}^{ab} R_{ck} + L_{kl}^{cd} \tilde{t}_{kl}^{cd} \tilde{t}_{ij}^{ab}, \end{aligned} \quad (\text{A28})$$

$$d_{aijb}^{\text{es}} = O_{aijb}^{(M)}(L_2, \tilde{R}_2) + 2L_{ai} R_{bj} - Y_{ab} \delta_{ij}, \quad (\text{A29})$$

$$d_{abci}^{\text{es}} = L_{ji}^{ac} R_j^b, \quad (\text{A30})$$

$$d_{abc}^{es} = L_m^a (2\tilde{R}_{mi}^{bc} - \tilde{R}_{mi}^{cb}) + 2X_{ab}(L_2, T_2)R_k^c \\ - (V_{akbi}(L_2, T_2) + Y_{akbi}(L_2, T_2))R_k^c + L_{mk}^{ad}\tilde{t}_{mi}^{bc}R_k^d \\ - L_{mi}^{ad}\tilde{t}_{mn}^{bc}R_k^d + \tilde{Y}_{akci}(L_2, T_2)R_k^b - X_{ac}(L_2, T_2)R_i^b, \quad (\text{A31})$$

$$d_{abcd}^{es} = O_{abcd}^{(2)}(L_2, \tilde{R}_2). \quad (\text{A32})$$

Here, we have defined the following quantities:

$$\Lambda_{ijkl} = 4\delta_{ij}\delta_{kl} - 2\delta_{il}\delta_{kj}, \quad (\text{A33})$$

$$O_{ijkl}^{(1)}(L_1, R_1) = -2Y_{ij}\delta_{kl} + Y_{il}\delta_{kj} - 2\delta_{ij}Y_{kl} + \delta_{il}Y_{kj}, \quad (\text{A34})$$

$$Y_{kj} = R_{ek}L_{ej} = R_k^e L_j^e, \quad (\text{A35})$$

$$O_{ijkl}^{(2)}(L_2, C_2) = -2\delta_{kl}X_{ij}(L_2, C_2) - 2\delta_{ij}X_{kl}(L_2, C_2) + \delta_{kj}X_{il}(L_2, C_2) \\ + \delta_{il}X_{kj}(L_2, C_2) + Z_{ijkl}(L_2, C_2), \quad (\text{A36})$$

$$X_{ij}(L_2, C_2) = C_{mi}^{ef}L_{mj}^{ef}, \quad (\text{A37})$$

$$Z_{ijkl}(L_2, C_2) = C_{ik}^{ef}L_{jl}^{ef}, \quad (\text{A38})$$

$$O_{ijka}^{(M)}(L_1, T_2) = L_{em}(2\delta_{ij}\tilde{t}_{km}^{ae} - \delta_{jk}\tilde{t}_{mi}^{ea})R_0 - L_{ej}\tilde{t}_{ik}^{ea}R_0, \quad (\text{A39})$$

$$\tilde{Y}_{djak}(L_2, T_2) = L_{mj}^{ed}\tilde{t}_{mk}^{ea}, \quad (\text{A40})$$

$$Y_{ab} = L_k^a R_k^b, \quad (\text{A41})$$

$$O_{abij}^{(1)}(L_1, R_1) = 2\delta_{ij}Y_{ab}(L_1, R_1) - L_j^a R_i^b, \quad (\text{A42})$$

$$O_{abij}^{(2)}(L_2, C_2) = 2\delta_{ij}X_{ab}(L_2, C_2) - Y_{ajbi}(L_2, C_2) - V_{ajbi}(L_2, C_2), \quad (\text{A43})$$

$$O_{iajb}^{(2)}(L_2, C_2) = \tilde{Y}_{ckai}(L_2, T_2)\tilde{C}_{kj}^{cb} + \tilde{Y}_{ckbj}(L_2, T_2)\tilde{C}_{ki}^{ca} \\ + Z_{ikjl}(L_2, T_2)C_{kl}^{ab} + Z_{imjm}(L_2, C_2)t_{mn}^{ab} \\ - X_{ca}(L_2, T_2)\tilde{C}_{ij}^{cb} - X_{ca}(L_2, C_2)\tilde{t}_{ij}^{cb} \\ - X_{ik}(L_2, T_2)\tilde{C}_{kj}^{ab} - X_{im}(L_2, C_2)\tilde{t}_{mj}^{ab} \\ - X_{jk}(L_2, T_2)\tilde{C}_{ik}^{ab} - X_{jm}(L_2, C_2)\tilde{t}_{im}^{ab} \\ - X_{cb}(L_2, T_2)\tilde{C}_{ji}^{ca} - X_{eb}(L_2, C_2)\tilde{t}_{ji}^{ea} \\ - \tilde{Y}_{embi}(L_2, C_2)t_{mj}^{ea} - Y_{emaj}(L_2, C_2)\tilde{t}_{mi}^{eb} \\ + Y_{ckbi}(L_2, C_2)t_{kj}^{ac} + Y_{ckbi}C_{kj}^{ac} \\ + V_{ckaj}(L_2, T_2)C_{ik}^{cb} + V_{ckbi}(L_2, T_2)C_{kj}^{ac}, \quad (\text{A44})$$

$$O_{aibj}^{(M)}(L_2, C_2) = -L_{im}^{ac}C_{jm}^{eb}R_0 + 2Y_{aibj}(L_2, C_2) - \delta_{ij}X_{ab}(L_2, C_2), \quad (\text{A45})$$

$$O_{abcd}^{(2)}(L_2, C_2) = L_{ij}^{ac}C_{ij}^{bd}, \quad (\text{A46})$$

where C_2 denotes a set of double amplitudes and \tilde{C}_2 is defined in an identical fashion to \tilde{t} .

All O^4 , O^3V , and O^2V^2 densities are directly constructed and stored in memory, while the OV^3 and V^4 densities are not explicitly constructed. As discussed in Sec. II B, we instead construct their contributions to the three-index density intermediates W_{pq}^I and store these in memory.

APPENDIX B: ORBITAL RELAXATION IN REORTHONORMALIZATION

The relaxation contributions—which we derive by expanding $h_{pq}^{(1)}$ and $g_{pqrs}^{(1)}$ using Eq. (21) and inserting into the differentiated Fock matrix, see Eqs. (4) and (20)—are

$$\mathcal{F}_{aq}^{\tilde{K}} = \frac{1}{2}\tilde{K}_{ai}h_{qi} + \left(g_{qiji} - \frac{1}{2}g_{ajji}\right)\tilde{K}_{ai}, \quad (\text{B1})$$

$$\mathcal{F}_{iq}^{\tilde{K}} = \frac{1}{2}\tilde{K}_{ai}h_{aq} + \left(g_{aqij} - \frac{1}{2}g_{ajij}\right)\tilde{K}_{ai} + 2g_{ajqi}\tilde{K}_{aj} - \frac{1}{2}g_{aqij}\tilde{K}_{aj} - \frac{1}{2}g_{ajij}\tilde{K}_{aj}. \quad (\text{B2})$$

These terms scale as $O(N^4)$ once expressed in terms of Cholesky vectors,

$$\mathcal{F}_{aq}^{\tilde{K}} = \frac{1}{2}\tilde{K}_{ai}h_{qi} + \gamma^j D_{qa}^j - \frac{1}{2}L_{qj}^j D_{ja}^j, \quad (\text{B3})$$

$$\mathcal{F}_{iq}^{\tilde{K}} = \frac{1}{2}\tilde{K}_{ai}h_{aq} + E_{qi}^j \gamma^j - \frac{1}{2}M_{aq}\tilde{K}_{ai} + 2\delta^j L_{qi}^j - \frac{1}{2}E_{qj}^j L_{ij}^j - \frac{1}{2}E_{ij}^j L_{qj}^j, \quad (\text{B4})$$

where

$$D_{qa}^j = L_{qi}^j \tilde{K}_{ai}, \quad (\text{B5})$$

$$\gamma^j = L_{jj}^j, \quad (\text{B6})$$

$$E_{qi}^j = L_{ai}^j \tilde{K}_{ai}, \quad (\text{B7})$$

$$M_{aq} = L_{aj}^j L_{jq}^j, \quad (\text{B8})$$

$$\delta^j = L_{ai}^j \tilde{K}_{ai}. \quad (\text{B9})$$

We have used Einstein's implicit summation in all these expressions.

REFERENCES

- H. B. Schlegel, *Wiley Interdiscip. Rev.: Comput. Mol. Sci.* **1**, 790 (2011).
- S. J. Klippenstein, V. S. Pande, and D. G. Truhlar, *J. Am. Chem. Soc.* **136**, 528 (2014).
- D. Marx and J. Hutter, *Ab Initio Molecular Dynamics: Basic Theory and Advanced Methods* (Cambridge University Press, 2009).
- B. F. E. Curchod and T. J. Martínez, *Chem. Rev.* **118**, 3305 (2018).
- J. Čížek, *J. Chem. Phys.* **45**, 4256 (1966).
- R. J. Bartlett, *Annu. Rev. Phys. Chem.* **32**, 359 (1981).
- R. J. Bartlett, *J. Phys. Chem.* **93**, 1697 (1989).
- T. D. Crawford and H. F. Schaefer III, "An introduction to coupled cluster theory for computational chemists," in *Reviews in Computational Chemistry* (John Wiley & Sons, Ltd., 2000), pp. 33–136.
- R. J. Bartlett and M. Musiał, *Rev. Mod. Phys.* **79**, 291 (2007).
- T. Helgaker, P. Jørgensen, and J. Olsen, *Molecular Electronic-Structure Theory* (John Wiley & Sons, 2014).
- H. Koch, O. Christiansen, P. Jørgensen, A. M. Sanchez de Merás, and T. Helgaker, *J. Chem. Phys.* **106**, 1808 (1997).
- R. Izsák, *Wiley Interdiscip. Rev.: Comput. Mol. Sci.* **10**, e1445 (2020).
- O. Christiansen, H. Koch, and P. Jørgensen, *Chem. Phys. Lett.* **243**, 409 (1995).
- G. D. Purvis and R. J. Bartlett, *J. Chem. Phys.* **76**, 1910 (1982).
- E. Epifanovsky, A. T. B. Gilbert, X. Feng, J. Lee, Y. Mao, N. Mardirossian, P. Pokhilko, A. F. White, M. P. Coons, A. L. Dempwolff, Z. Gan, D. Hait, P. R. Horn, L. D. Jacobson, I. Kaliman, J. Kussmann, A. W. Lange, K. U. Lao, D. S. Levine, J.

- Liu, S. C. McKenzie, A. F. Morrison, K. D. Nanda, F. Plasser, D. R. Rehn, M. L. Vidal, Z.-Q. You, Y. Zhu, B. Alam, B. J. Albrecht, A. Aldossary, E. Alguire, J. H. Andersen, V. Athavale, D. Barton, K. Begam, A. Behn, N. Bellonzi, Y. A. Bernard, E. J. Berquist, H. G. A. Burton, A. Carreras, K. Carter-Fenk, R. Chakraborty, A. D. Chien, K. D. Closser, V. Cofer-Shabica, S. Dasgupta, M. de Wergifosse, J. Deng, M. Diedenhofen, H. Do, S. Ehlert, P.-T. Fang, S. Fatehi, Q. Feng, T. Friedhoff, J. Gayvert, Q. Ge, G. Gidofalvi, M. Goldey, J. Gomes, C. E. González-Espinoza, S. Gulania, A. O. Gunina, M. W. D. Hanson-Heine, P. H. P. Harbach, A. Hauser, M. F. Herbst, M. Hernández Vera, M. Hodecker, Z. C. Holden, S. Houck, X. Huang, K. Hui, B. C. Huynh, M. Ivanov, Á. Jász, H. Ji, H. Jiang, B. Kaduk, S. Kähler, K. Khistyayev, J. Kim, G. Kis, P. Klunzinger, Z. Koczor-Benda, J. H. Koh, D. Kosenkov, L. Koulias, T. Kowalczyk, C. M. Krauter, K. Kue, A. Kunitsa, T. Kus, I. Ladžanski, A. Landau, K. V. Lawler, D. Lefrançois, S. Lehtola, R. R. Li, Y.-P. Li, J. Liang, M. Liebenthal, H.-H. Lin, Y.-S. Lin, F. Liu, K.-Y. Liu, M. Loipersberger, A. Luenser, A. Manjanath, P. Manohar, E. Mansoor, S. F. Manzer, S.-P. Mao, A. V. Marenich, T. Markovich, S. Mason, S. A. Maurer, P. F. McLaughlin, M. F. S. J. Menger, J.-M. Mewes, S. A. Mewes, P. Morgante, J. W. Mullinax, K. J. Oosterbaan, G. Paran, A. C. Paul, S. K. Paul, F. Pavosević, Z. Pei, S. Prager, E. I. Proynov, Á. Rák, E. Ramos-Cordoba, B. Rana, A. E. Rask, A. Rettig, R. M. Richard, F. Rob, E. Rossomme, T. Scheele, M. Scheurer, M. Schneider, N. Sergueev, S. M. Sharada, W. Skomorowski, D. W. Small, C. J. Stein, Y.-C. Su, E. J. Sundstrom, Z. Tao, J. Thirman, G. J. Tornai, T. Tsuchimoto, N. M. Tubman, S. P. Veccham, O. Vydrov, J. Wenzel, J. Witte, A. Yamada, K. Yao, S. Yeganeh, S. R. Yost, A. Zech, I. Y. Zhang, X. Zhang, Y. Zhang, D. Zuev, A. Aspuru-Guzik, A. T. Bell, N. A. Besley, K. B. Bravaya, B. R. Brooks, D. Casanova, J.-D. Chai, S. Coriani, C. J. Cramer, G. Cserey, A. E. DePrince, R. A. DiStasio, A. Dreuw, B. D. Dunietz, T. R. Furlani, W. A. Goddard, S. Hammes-Schiffer, T. Head-Gordon, W. J. Hehre, C.-P. Hsu, T.-C. Jagau, Y. Jung, A. Klamt, J. Kong, D. S. Lambrecht, W. Liang, N. J. Mayhall, C. W. McCurdy, J. B. Neaton, C. Ochsenfeld, J. A. Parkhill, R. Peverati, V. A. Rassolov, Y. Shao, L. V. Slipchenko, T. Stauch, R. P. Steele, J. E. Subotnik, A. J. W. Thom, A. Tkatchenko, D. G. Truhlar, T. Van Voorhis, T. A. Wesolowski, K. B. Whaley, H. L. Woodcock, P. M. Zimmerman, S. Faraji, P. M. W. Gill, M. Head-Gordon, J. M. Herbert, and A. I. Krylov, *J. Chem. Phys.* **155**, 084801 (2021).
- ¹⁶X. Feng, E. Epifanovsky, J. Gauss, and A. I. Krylov, *J. Chem. Phys.* **151**, 014110 (2019).
- ¹⁷M. J. Frisch, G. W. Trucks, H. B. Schlegel, G. E. Scuseria, M. A. Robb, J. R. Cheeseman, G. Scalmani, V. Barone, G. A. Petersson, H. Nakatsuji, X. Li, M. Caricato, A. V. Marenich, J. Bloino, B. G. Janesko, R. Gomperts, B. Mennucci, H. P. Hratchian, J. V. Ortiz, A. F. Izmaylov, J. L. Sonnenberg, D. Williams-Young, F. Ding, F. Lipparini, F. Egidi, J. Goings, B. Peng, A. Petrone, T. Henderson, D. Ranasinghe, V. G. Zakrzewski, J. Gao, N. Rega, G. Zheng, W. Liang, M. Hada, M. Ehara, K. Toyota, R. Fukuda, J. Hasegawa, M. Ishida, T. Nakajima, Y. Honda, O. Kitao, H. Nakai, T. Vreven, K. Throssell, J. A. Montgomery, Jr., J. E. Peralta, F. Ogliaro, M. J. Bearpark, J. J. Heyd, E. N. Brothers, K. N. Kudin, V. N. Staroverov, T. A. Keith, R. Kobayashi, J. Normand, K. Raghavachari, A. P. Rendell, J. C. Burant, S. S. Iyengar, J. Tomasi, M. Cossi, J. M. Millam, M. Klene, C. Adamo, R. Cammi, J. W. Ochterski, R. L. Martin, K. Morokuma, O. Farkas, J. B. Foresman, and D. J. Fox, *Gaussian 16*, Revision C.01, Gaussian, Inc., Wallingford, CT, 2016.
- ¹⁸D. G. A. Smith, L. A. Burns, A. C. Simmonett, R. M. Parrish, M. C. Schieber, R. Galvelis, P. Kraus, H. Kruse, R. Di Remigio, A. Alenaizan, A. M. James, S. Lehtola, J. P. Misiewicz, M. Scheurer, R. A. Shaw, J. B. Schriber, Y. Xie, Z. L. Glick, D. A. Sirianni, J. S. O'Brien, J. M. Waldrop, A. Kumar, E. G. Hohenstein, B. P. Pritchard, B. R. Brooks, H. F. Schaefer, A. Y. Sokolov, K. Patkowski, A. E. DePrince, U. Bozkaya, R. A. King, F. A. Evangelista, J. M. Turney, T. D. Crawford, and C. D. Sherrill, *J. Chem. Phys.* **152**, 184108 (2020).
- ¹⁹U. Bozkaya and C. D. Sherrill, *J. Chem. Phys.* **144**, 174103 (2016).
- ²⁰K. Aidas, C. Angeli, K. L. Bak, V. Bakken, R. Bast, L. Boman, O. Christiansen, R. Cimraglia, S. Coriani, P. Dahle, E. K. Dalskov, U. Ekström, T. Enevoldsen, J. J. Eriksen, P. Ettenhuber, B. Fernández, L. Ferrighi, H. Fliegl, L. Frediani, K. Hald, A. Halkier, C. Hättig, H. Heiberg, T. Helgaker, A. C. Hennum, H. Hettema, E. Hjertenes, S. Høst, I.-M. Høyvik, M. F. Iozzi, B. Jansik, H. J. A. Jensen, D. Jonsson, P. Jørgensen, J. Kauczor, S. Kirpekar, T. Kjaergaard, W. Klopper, S. Knecht, R. Kobayashi, H. Koch, J. Kongsted, A. Krapp, K. Kristensen, A. Ligabue, O. B. Lutnaes, J. I. Melo, K. V. Mikkelsen, R. H. Myhre, C. Neiss, C. B. Nielsen, P. Norman, J. Olsen, J. M. H. Olsen, A. Osted, M. J. Packer, F. Pawłowski, T. B. Pedersen, P. F. Provasi, S. Reine, Z. Rinkevicius, T. A. Ruden, K. Ruud, V. V. Rybkin, P. Salek, C. C. M. Samson, A. S. de Merás, T. Saue, S. P. A. Sauer, B. Schimmelpfennig, K. Sneskov, A. H. Steindal, K. O. Sylvester-Hvid, P. R. Taylor, A. M. Teale, E. I. Tellgren, D. P. Tew, A. J. Thorvaldsen, L. Thøgersen, O. Vahtras, M. A. Watson, D. J. D. Wilson, M. Ziolkowski, and H. Ågren, *Wiley Interdiscip. Rev.: Comput. Mol. Sci.* **4**, 269 (2014).
- ²¹K. Hald, A. Halkier, P. Jørgensen, S. Coriani, C. Hättig, and T. Helgaker, *J. Chem. Phys.* **118**, 2985 (2003).
- ²²D. A. Matthews, L. Cheng, M. E. Harding, F. Lipparini, S. Stopkowicz, T.-C. Jagau, P. G. Szalay, J. Gauss, and J. F. Stanton, *J. Chem. Phys.* **152**, 214108 (2020).
- ²³J. Gauss, J. F. Stanton, and R. J. Bartlett, *J. Chem. Phys.* **95**, 2623 (1991).
- ²⁴M. Kállay, P. R. Nagy, D. Mester, Z. Rolik, G. Samu, J. Csontos, J. Csóka, P. B. Szabó, L. Gyevi-Nagy, B. Hegely, I. Ladžanski, L. Szegedy, B. Ládóczi, K. Petrov, M. Farkas, P. D. Mezei, and Á. Ganyecz, *J. Chem. Phys.* **152**, 074107 (2020).
- ²⁵M. Kállay, J. Gauss, and P. G. Szalay, *J. Chem. Phys.* **119**, 2991 (2003).
- ²⁶N. H. F. Beebe and J. Linderberg, *Int. J. Quantum Chem.* **12**, 683 (1977).
- ²⁷I. Roeggen and E. Wisløff-Nilssen, *Chem. Phys. Lett.* **132**, 154 (1986).
- ²⁸D. W. O'neal and J. Simons, *Int. J. Quantum Chem.* **36**, 673 (1989).
- ²⁹H. Koch, A. Sánchez de Merás, and T. B. Pedersen, *J. Chem. Phys.* **118**, 9481 (2003).
- ³⁰F. Aquilante, T. B. Pedersen, and R. Lindh, *J. Chem. Phys.* **126**, 194106 (2007).
- ³¹F. Aquilante, R. Lindh, and T. B. Pedersen, *J. Chem. Phys.* **129**, 034106 (2008).
- ³²A. E. DePrince and C. D. Sherrill, *J. Chem. Theory Comput.* **9**, 293 (2013).
- ³³E. Epifanovsky, D. Zuev, X. Feng, K. Khistyayev, Y. Shao, and A. I. Krylov, *J. Chem. Phys.* **139**, 134105 (2013).
- ³⁴U. Bozkaya, *J. Chem. Theory Comput.* **10**, 2371 (2014).
- ³⁵M. G. Delcey, L. Freitag, T. B. Pedersen, F. Aquilante, R. Lindh, and L. González, *J. Chem. Phys.* **140**, 174103 (2014).
- ³⁶S. D. Folkestad, E. F. Kjønestad, and H. Koch, *J. Chem. Phys.* **150**, 194112 (2019).
- ³⁷J. L. Whitten, *J. Chem. Phys.* **58**, 4496 (1973).
- ³⁸B. I. Dunlap, J. W. D. Connolly, and J. R. Sabin, *J. Chem. Phys.* **71**, 3396 (1979).
- ³⁹M. Feyereisen, G. Fitzgerald, and A. Komornicki, *Chem. Phys. Lett.* **208**, 359 (1993).
- ⁴⁰O. Vahtras, J. Almlöf, and M. W. Feyereisen, *Chem. Phys. Lett.* **213**, 514 (1993).
- ⁴¹A. P. Rendell and T. J. Lee, *J. Chem. Phys.* **101**, 400 (1994).
- ⁴²F. Weigend, *Phys. Chem. Chem. Phys.* **4**, 4285 (2002).
- ⁴³A. Sodt, J. E. Subotnik, and M. Head-Gordon, *J. Chem. Phys.* **125**, 194109 (2006).
- ⁴⁴H.-J. Werner, F. R. Manby, and P. J. Knowles, *J. Chem. Phys.* **118**, 8149 (2003).
- ⁴⁵M. Schütz and F. R. Manby, *Phys. Chem. Chem. Phys.* **5**, 3349 (2003).
- ⁴⁶H.-J. Werner and M. Schütz, *J. Chem. Phys.* **135**, 144116 (2011).
- ⁴⁷S. D. Folkestad, E. F. Kjønestad, R. H. Myhre, J. H. Andersen, A. Balbi, S. Coriani, T. Giovannini, L. Goletto, T. S. Haugland, A. Hutcheson, I.-M. Høyvik, T. Moitra, A. C. Paul, M. Scavino, A. S. Skeidsvoll, Å. H. Tveten, and H. Koch, *J. Chem. Phys.* **152**, 184103 (2020).
- ⁴⁸T. Helgaker and P. Jørgensen, "Calculation of geometrical derivatives in molecular electronic structure theory," in *Methods in Computational Molecular Physics*, edited by S. Wilson and G. H. F. Dierksen (Springer, Boston, MA, 1992), pp. 353–421.
- ⁴⁹T. Helgaker and P. Jørgensen, *Theor. Chim. Acta* **75**, 111 (1989).
- ⁵⁰P. Jørgensen and T. Helgaker, *J. Chem. Phys.* **89**, 1560 (1988).
- ⁵¹T. Helgaker and P. Jørgensen, *Adv. Quantum Chem.* **19**, 183 (1988).
- ⁵²T. Helgaker, S. Coriani, P. Jørgensen, K. Kristensen, J. Olsen, and K. Ruud, *Chem. Rev.* **112**, 543 (2012).
- ⁵³A. C. Scheiner, G. E. Scuseria, J. E. Rice, T. J. Lee, and H. F. Schaefer, *J. Chem. Phys.* **87**, 5361 (1987).
- ⁵⁴G. E. Scuseria, C. L. Janssen, and H. F. Schaefer, *J. Chem. Phys.* **89**, 7382 (1988).
- ⁵⁵A. Banerjee, N. Adams, J. Simons, and R. Shepard, *J. Phys. Chem.* **89**, 52 (1985).
- ⁵⁶V. Bakken and T. Helgaker, *J. Chem. Phys.* **117**, 9160 (2002).
- ⁵⁷A. K. Schnack-Petersen, H. Koch, S. Coriani, and E. F. Kjønestad (2022). "Efficient implementation of molecular CCSD gradients with Cholesky-decomposed electron repulsion integrals," Zenodo. <https://doi.org/10.5281/zenodo.5957852>
- ⁵⁸P. Pokhilko, E. Epifanovsky, and A. I. Krylov, *J. Chem. Theory Comput.* **14**, 4088 (2018).

A.2 Corrections

Two equations were found to be written incorrectly in the publication.

- Eq. (51) displays a wrong sign and scaling factor of the last term. It should read:

$$\begin{aligned}
 \sum_{aij} \bar{\kappa}_{ai} (2g_{aijj}^{[1]} - g_{ajji}^{[1]}) &= \sum_{aiK} K_{ai}^K (ai | K)^{[1]} \\
 &+ \sum_{jK} L^K (K | jj)^{[1]} + \sum_{ijK} N_{ji}^K (K | ji)^{[1]} \\
 &- \sum_{KL} M_{KL} S_{KL}^{[1]} - \sum_{KL} O_{KL} S_{KL}^{[1]}.
 \end{aligned} \tag{A.1}$$

- The first equation in Table II should read:

$$K_{ai}^K = \sum_j (2\bar{\kappa}_{ai} Z_{jj}^K - \bar{\kappa}_{aj} Z_{ij}^K) \tag{A.2}$$

APPENDIX B

Publication 2

Reproduced from "Core spectroscopy of oxazole", Anna Kristina Schnack-Petersen, Bruno N. Cabral Tenorio, Sonia Coriani, Piero Decleva, Jan Troß, Krupa Ramasesha, Marcello Coreno, Roberta Totani and Anja Röder, *J. Chem. Phys.*, 2022, **156**, 24411 with the permission of AIP Publishing.

Only the article itself is reproduced here, while the supporting information can be accessed via <https://doi.org/10.1063/5.0122088>.

Core spectroscopy of oxazole

Cite as: J. Chem. Phys. **157**, 214305 (2022); <https://doi.org/10.1063/5.0122088>

Submitted: 22 August 2022 • Accepted: 08 November 2022 • Accepted Manuscript Online: 08 November 2022 • Published Online: 01 December 2022

 Anna Kristina Schnack-Petersen,  Bruno Nunes Cabral Tenorio,  Sonia Coriani, et al.



View Online



Export Citation



CrossMark

ARTICLES YOU MAY BE INTERESTED IN

[Communication: X-ray absorption spectra and core-ionization potentials within a core-valence separated coupled cluster framework](#)

The Journal of Chemical Physics **143**, 181103 (2015); <https://doi.org/10.1063/1.4935712>

[Natural transition orbitals](#)

The Journal of Chemical Physics **118**, 4775 (2003); <https://doi.org/10.1063/1.1558471>

[Software for the frontiers of quantum chemistry: An overview of developments in the Q-Chem 5 package](#)

The Journal of Chemical Physics **155**, 084801 (2021); <https://doi.org/10.1063/5.0055522>



[Learn More](#)

Special Topics Open for Submissions

Core spectroscopy of oxazole

Cite as: J. Chem. Phys. 157, 214305 (2022); doi: 10.1063/5.0122088

Submitted: 22 August 2022 • Accepted: 8 November 2022 •

Published Online: 1 December 2022



View Online



Export Citation



CrossMark

Anna Kristina Schnack-Petersen,¹ Bruno Nunes Cabral Tenorio,¹ Sonia Coriani,^{1,a)} Piero Decleva,² Jan Troß,³ Krupa Ramasesha,³ Marcello Coreno,⁴ Roberta Totani,^{4,a)} and Anja Röder⁵

AFFILIATIONS

¹Department of Chemistry, Technical University of Denmark, Kemitorvet Bldg. 207, DK-2800 Kgs. Lyngby, Denmark

²Istituto Officina dei Materiali IOM-CNR and Dipartimento di Scienze Chimiche e Farmaceutiche, Università degli Studi di Trieste, I-34121 Trieste, Italy

³Combustion Research Facility, Sandia National Laboratories, Livermore, California 94550, USA

⁴Istituto di Struttura della Materia-CNR (ISM-CNR), LD2 Unit, Basovizza Area Science Park, 34149 Trieste, Italy

⁵Max-Born-Institut für Nichtlineare Optik und Kurzzeitspektroskopie, Max-Born-Strasse 2A, D-12489 Berlin, Germany

^{a)}Authors to whom correspondence should be addressed: soco@kemi.dtu.dk and roberta.totani@trieste.ism.cnr.it

ABSTRACT

We have measured, analyzed, and simulated the ground state valence photoelectron spectrum, x-ray absorption (XA) spectrum, x-ray photoelectron (XP) spectrum as well as normal and resonant Auger–Meitner electron (AE) spectrum of oxazole at the carbon, oxygen, and nitrogen *K*-edge in order to understand its electronic structure. Experimental data are compared to theoretical calculations performed at the coupled cluster, restricted active space perturbation theory to second-order and time-dependent density functional levels of theory. We demonstrate (1) that both N and O *K*-edge XA spectra are sensitive to the amount of dynamical electron correlation included in the theoretical description and (2) that for a complete description of XP spectra, additional orbital correlation and orbital relaxation effects need to be considered. The normal AE spectra are dominated by a singlet excitation channel and well described by theory. The resonant AE spectra, however, are more complicated. While the participator decay channels, dominating at higher kinetic energies, are well described by coupled cluster theory, spectator channels can only be described satisfactorily using a method that combines restricted active space perturbation theory to second order for the bound part and a one-center approximation for the continuum.

Published under an exclusive license by AIP Publishing. <https://doi.org/10.1063/5.0122088>

I. INTRODUCTION

Heterocycles, specifically aromatic rings containing N or O atom(s), are ubiquitous in chemistry as building blocks in DNA, proteins, and substances of pharmacological and biological activity^{1,2} and even as building blocks of organic electronic devices.³ Understanding their electronic structure as well as their photoinduced reactions is therefore of fundamental interest,^{4–6} and studies of heterocycles such as isoxazole⁷ therefore continue to appear. The highest occupied molecular orbital (MO) in these systems typically exhibits π -character, while unoccupied MOs show π^* and σ^* character. The photochemistry of heterocycles is usually initiated by a bright $\pi\pi^*$ transition, and $n\sigma^*$, $\pi\sigma^*$ and triplet states mediate the formation of different products. Examples include return to the electronic ground state with a high degree of vibrational excitation

via a ring-puckering-type conical intersection (CI) observed, for instance, in the prototypical molecules furan⁸ and pyridine⁹ and passage through a CI connecting to a state with σ^* character, leading to breaking of a σ -bond and ring-opening. In the gas phase, such photoinduced reactions are studied using time-resolved spectroscopy, which is far from trivial: in a multichannel landscape, different mechanisms can lead to similar signals only distinguishable with strong theoretical support.^{10–12}

With the advent of ultrafast sources in the x-ray regime in recent years, new detection schemes have emerged to follow ultrafast photoinduced reactions: time-resolved (pump–probe) x-ray photoelectron spectroscopy (XPS),^{13,14} x-ray absorption spectroscopy (XAS),^{15,16} and Auger–Meitner electron spectroscopy (AES).^{17,18} These techniques utilize the element-specificity of x-rays, allowing them to follow a photoinduced reaction from different perspectives.

However, before such experiments can be conducted, a detailed understanding of the ground state spectra of the molecule in question is paramount. For instance, ground state XAS and XPS studies on small organic molecules such as thymine and adenine¹⁹ at all possible (second row) atomic 1s core levels helped in the interpretation of time-resolved XAS and AES spectra at the oxygen K-edge on thymine.^{20,21} There, XAS ground state spectra provided important information that allowed the excited state spectra to be predicted theoretically and later verified experimentally, shedding light on the $\pi\pi^*/n\pi^*$ internal conversion investigated in the time-resolved experiment.^{20,21} While the XAS experiment yielded information on the electronic characters of the involved states, it was shown to be insensitive with respect to small changes in the molecular structures.²⁰ AES, on the other hand, was found to be sensitive to such changes and thus provided insight into nuclear dynamics.²⁰

In this paper, we investigate the XAS, XPS, and normal and resonant AES of oxazole in the gas phase and compare them with state-of-the-art theoretical simulations in preparation for future time-resolved experiments. We employ the frozen-core core-valence separated equation-of-motion coupled cluster singles and doubles (fc-CVS-EOM-CCSD) method^{22–24} for the calculation of all types of spectra as well as the ever-popular time-dependent density functional theory (TDDFT)²⁵ for XAS spectra. Both methods, as well as the (extended) second-order algebraic-diagrammatic construction approach [ADC(2)-x],²⁶ have been employed in previous studies of core spectra for small organic molecules (see, e.g., Refs. 19, 22, 23, and 27–29). Generally, these methods reproduce well the spectral shape of the XAS spectra, even though TDDFT is typically plagued by much larger systematic errors than the other two methods. We refer the interested reader to recent benchmark studies for an in-depth analysis.^{29,30} For AES, we will moreover employ a newly implemented approach³¹ utilizing multi-state restricted active space perturbation theory of second order (MS-RASPT2)^{32,33} coupled to the one-center approximation (OCA)^{31,34} for the calculation of Auger intensities.

This is to the best of our knowledge the first full characterization of this organic molecule in gas phase including XAS, XPS, and AES results for all its second row elements, i.e., carbon, nitrogen, and oxygen.

II. EXPERIMENTAL AND THEORETICAL METHODS

A. Experimental methods

98% pure oxazole (Sigma-Aldrich) was introduced into the system via an effusive needle source under low heating ($\sim 30^\circ\text{C}$). The sample was subjected to three freeze–pump–thaw cycles in order to eliminate water and air.

All spectra were recorded at the Gas Phase Photoemission beamline at Elettra (Trieste, Italy).³⁵ Valence photoelectron spectroscopy (PES), XPS, and AES spectra were recorded using a Scienta SES-200 photoelectron analyzer.³⁶ The analyzer was mounted at the magic angle of 54.7° , allowing it to record angle-integrated spectra insensitive to the photoelectron asymmetry parameter β . The photon energies, resolution, and calibrants of valence and core spectra are given in Table S1 of the [supplementary material](#). In order to measure XAS at the C, O, and N K-edges, a channel electron

multiplier measured the total ion yield close to the gas jet region. Simultaneously in a separate chamber before the gas jet, the total ion yield of a calibrant gas (CO_2 for C 1s and O 1s, and N_2 for the N 1s edge) was recorded with another channel electron multiplier. The XAS spectra were normalized to the photon flux measured with a photodiode placed after the gas jet region.

B. Theoretical methods

The ground state geometry of oxazole given at the CASSCF(10,8)/6-31*G level of theory by Cao *et al.*³⁷ was planarized and optimized at the MP2/cc-pCVTZ level of theory (see Sec. S2). No imaginary frequencies were found. All simulated spectra were determined based on this structure.

Different methods and codes were used for the spectral simulations. Unless otherwise stated, the Q-chem program package³⁸ was used. The PES spectrum was computed within the sudden approximation limit using frozen-core equation-of-motion coupled cluster singles and doubles (fc-EOM-CCSD). XPS and XAS spectra were simulated at the fc-CVS-EOM-CCSD level of theory.^{22,23} The XAS spectra were additionally computed at the TDDFT level of theory using the CAMB3LYP functional, as well as by employing coupled cluster calculations that include a perturbative correction for the effect of triple excitations [CVS-EOM-CCSDR(3)],^{39,40} thus improving on the description of double excitation contributions to the excited state vectors. At the CVS-EOM-CCSDR(3) level of theory, only the excitation energies were corrected, while the oscillator strengths are those of CVS-EOM-CCSD level of theory.⁴⁰ The order of transitions remained unchanged. The CVS-EOM-CCSDR(3) calculations were performed using Dalton.^{41,42} Both normal and resonant AES spectra were simulated at the fc-CVS-EOM-CCSD level of theory as implemented in Q-Chem,^{24,43} adopting a plane wave description of the continuum orbital required to describe the Auger–Meitner decay process.

All CCSD calculations of XAS, XPS, and PES spectra employed the aug-cc-pVTZ basis set^{44,45} including additional Rydberg functions (3s3p3d).⁴⁶ For the computationally more expensive CVS-EOM-CCSDR(3) calculations, the aug-cc-pCVTZ basis set⁴⁷ without additional Rydberg functions was applied to the atom(s) of the considered core transitions (i.e., on nitrogen for N K-edge spectra), while aug-cc-pVDZ^{44,45} was used for the remaining atoms. In the case of AES spectra at the fc-CVS-EOM-CCSD level of theory, the aug-cc-pVTZ basis set without additional Rydberg functions was applied to all atoms. The XAS spectra were simulated by Lorentzian broadening of the calculated fc-CVS-EOM-CCSD oscillator strengths with the full width at half maximum (FWHM) reported in the relevant figure captions. The PES and XPS spectra were likewise generated by Lorentzian broadening of the squared norms of the fc-EOM-CCSD (PES) and fc-CVS-EOM-CCSD (XPS) Dyson orbitals, with FWHM values reported in the relevant figure captions.^{23,48,49}

As stated in the Introduction, additional calculations of PES, resonant AES, and AES spectra were performed at the multi-state restricted active space perturbation theory of second order (MS-RASPT2) level.³³ Auger–Meitner transition rates were calculated using the one-center approximation (OCA) for the electron in the continuum.^{34,50} The spin-adapted Auger matrix elements were obtained within the state-interaction approximation⁵¹ with a

developer version of OPENMOLCAS.⁵² For further details about the OCA-RASPT2 implementation, please consult Ref. 31.

In order to reduce the computational effort of the RASPT2 calculations, we adopted the cc-pVTZ basis set⁴⁴ on the atoms bearing the core hole—that is, nitrogen and oxygen—and cc-pVDZ⁴⁴ on the carbon and hydrogen atoms. Core-excited and core-ionized states relevant for normal and resonant Auger–Meitner spectra were computed by placing the pertinent core orbitals in the RAS1 space and enforcing single electron occupation in it by means of the HEXS projection technique⁵³ available in OPENMOLCAS,⁵² which corresponds to applying the core–valence separation.⁵⁴ An imaginary level shift of 0.25 hartree was applied to avoid intruder-state singularities in the MS-RASPT2 calculations. The active space was formed by distributing 26 electrons (for the neutral species) as follows: the 1s orbital of interest in the RAS1 subspace and the occupied 7–15a' and 1–3a'' orbitals in the RAS2 subspace. The virtual orbitals 4a'' and 5a'', both of π^* character, were included in the RAS3 subspace, restricted to a maximum occupation of two electrons. Final cationic states were obtained by state-averaging over 200 states for each irreducible representation of the C_s point group symmetry. The PES intensities are given as the squared norm of the RASPT2 Dyson orbitals representing the ionization channels (see, e.g., Ref. 55 for details).

Since all theoretical methods employ approximations, they inherently include systematic errors that can often be remedied by an overall shift to align with experiment.^{56,57} Furthermore, our calculations neglect relativistic effects, which can affect the spectra.⁵⁸ At the K-edge of lighter elements, which is the focus of this study, relativistic effects typically correspond to a constant energy shift for each type of nucleus, so an overall shift is often sufficient to correct for their neglect.^{56,58} Therefore, all core spectra have here been shifted to align with experiment.

All calculations were carried out on the DTU High-Performance Computing Cluster.⁵⁹

III. RESULTS AND DISCUSSION

A. Electronic structure and valence photoelectron spectroscopy (PES)

Oxazole is a planar molecule of C_s symmetry (see Fig. 1). The seven highest occupied valence molecular orbitals of ground state oxazole can be characterized as follows:

$$1a''(\pi_1) 12a'(\sigma_1) 13a'(\sigma_2) 14a'(n(O)) 2a''(\pi_2) 15a''(n(N)) 3a'(\pi_3),$$

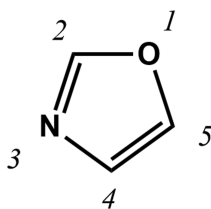


FIG. 1. Molecular structure of oxazole, with numbering of its second row atoms.

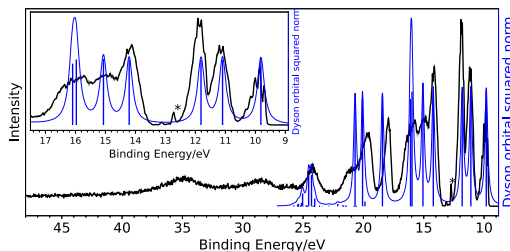


FIG. 2. Experimental (black) and calculated (fc-EOM-CCSD/aug-cc-pVTZ, blue) valence photoelectron spectrum. A Lorentzian broadening of the Dyson orbital square norms with a FWHM of 0.27 eV has been utilized to simulate the PES spectrum. No shift has been applied to the theoretical data. The inset shows the energy region from 9 to 17 eV.

which represents a typical aromatic heterocycle (six conjugated electrons in a cycle), where the highest valence MOs have π - and lone-pair character.

The lowest unoccupied molecular orbitals depend on the basis set used. We employed an augmented basis set with additional Rydberg functions, and these molecular orbitals therefore have Rydberg and π^* character.

The experimental full valence photoelectron spectrum measured in the binding energy range between 9 and 45 eV at a photon energy of 98 eV is displayed in black in Fig. 2. It is consistent with previously reported valence spectra,⁶⁰ confirming the identity and purity of the sample. The only visible impurity is from traces of water at 12.6 eV (marked with an asterisk in Fig. 2),⁶¹ which conveniently allows calibration of the experimental PES spectrum.

The calculated valence photoelectron spectrum (blue trace in Fig. 2), obtained from the computed ionization energies and squared norms of the Dyson orbitals at the fc-EOM-CCSD level of theory,⁴⁸ agrees well with the experimental spectrum. It reflects the order of the highest occupied MOs as discussed above: The first two ionization transitions at 9.7 and 11.07 eV correspond to the ejection of an electron from the π_3 and $n(N)$ orbitals, respectively. The higher-lying transitions are mainly due to electron removal from σ -type molecular orbitals. We refer to Table I for the assignment of the PES peaks. RASPT2 ionization energies and intensities are also given in Table I, while the corresponding spectrum can be found in the upper panel of Fig. 8 in Sec. III D 2. Observe that the transitions with energies above 20.1 eV are mainly of two-hole/one-particle ($2h1p$) character and thus ionization satellites. Since this type of transition is generally poorly described at the CCSD level of theory (see, e.g., Moitra *et al.*⁶²), these transitions are not reported in Table I.

B. Core level photoelectron spectroscopy (XPS)

The experimental and simulated CCSD XPS spectra (see Fig. 3) at the probed core levels (1s) of carbon (top), nitrogen (middle), and oxygen (bottom) are very simple, showing, respectively, three, one, and one peak(s) (see Table II). Each transition in the spectrum can be assigned to the ionization of one core electron on each of the N, O, and C atoms. Our calculations are in good agreement with those presented at the DFT level of theory by Chong

TABLE I. Ionization energies (eV), corresponding MO of origin and its character for the ten lowest-lying valence ionizations. Experimental and calculated (fc-EOM-CCSD/aug-cc-pVTZ and RASPT2/cc-pVTZ) results. Dyson orbital square norms are given within square brackets. Note that only ionizations with pole strengths larger than 0.4 are reported.

Experiment	Ionization energy (eV)		Corresponding MO	MO character
	CCSD	RASPT2	CCSD	
9.7	9.8 [0.91]	9.72 [0.93]	3a''	π_3
11.07	11.1 [0.89]	11.3 [0.93]	15a'	$n(\text{N})$
11.8	11.8 [0.89]	12.2 [0.92]	2a''	π_2
12.6	Water
14.1	14.2 [0.89]	14.4 [0.94]	14a'	$n(\text{O})$
14.9	15.1 [0.90]	15.2 [0.95]	13a'	σ_2
15.8–16.4	16.0 [0.89]	16.0 [0.78]	12a'	σ_1
	16.1 [0.84]	16.6 [0.62]	1a''	π_1
17.9	18.4 [0.86]	18.4 [0.84]	11a'	σ
19.6	...	20.0 [0.60]
	20.1 [0.83]	20.6 [0.46]	10a'	σ

and Hu⁶³ and by Du *et al.*⁶⁴ In the C 1s spectrum, the lowest ionization energy corresponds to ionization from 1s(C4), while the second and third correspond to ionizations from 1s(C5) and 1s(C2), respectively. As also seen in the XAS spectrum (*vide infra*), the energetic order of the transitions follows the electronegativities of the atoms bound to the carbon in question. Thus, the binding energy increases with increasing electronegativity of the species surrounding the carbon atom. This was also observed for isoxazole⁷ and in calculations of both oxazole and isoxazole as well as a range of other small organic molecules including hetero atoms.⁶³ Despite an overall good agreement between theory and experiment, the computed separations between the peaks in the C 1s spectrum are slightly too large, in particular between the second and third peaks (0.7 eV in experiment vs 0.9 eV in the calculation). This could not be sufficiently corrected even when utilizing a higher level of theory (see Fig. S8 in the [supplementary material](#)). The CCSD results were slightly, but not to a sufficient degree, corrected when including additional dynamical correlation via CCSDR(3). We tentatively assign this effect to residual orbital relaxation effects, as well as additional dynamical correlation, which are not captured by the methods used for the calculations presented here. Such discrepancy could also be found between experiment and calculations at the DFT level of theory (using the M06-2X functional) for the C 1s spectrum of isoxazole,⁷ where the splitting between the carbon atoms with the lowest binding energies was slightly underestimated by the theoretical calculations.

C. X-ray absorption spectroscopy (XAS)

The experimental (black) and theoretical (green, red and blue) XAS spectra at the C, N, and O *K*-edge are displayed in Fig. 4, with the (unshifted) energetic positions and attributions of the main transitions summarized in Table III. The complete list of calculated excitation energies and oscillator strengths of the vertical core level transitions, together with the corresponding natural transition orbitals (NTOs), are available in Secs. S5–S7 of the [supplementary material](#).

As expected, the experimental XAS spectrum at the C *K*-edge (Fig. 4, top) displays three intense close-lying resonances at

286.0, 286.5, and 287.3 eV respectively, corresponding to 1s(C) π^* -transitions. The π^* orbitals reached in the three transitions are different, as can be seen from the NTOs in Secs. S6 and S7 of the [supplementary material](#). Both TDDFT and fc-CVS-EOM-CCSD agree that the energetic order of these transitions follows the electronegativity of the atoms bound to the carbon atom in question: The lowest energy transition corresponds to C4 (neighboring N), followed by C5 (neighboring O) and then C2 (neighboring both N and O). The spacing of these three peaks and the position of higher energy bands up to 291 eV are reasonably well reproduced by both theoretical methods. Observe that fc-CVS-EOM-CCSD predicts similar intensities for the two lowest energy transitions, while both experiment and TDDFT yield increasing intensities. Since these should basically reflect the on-site populations of atomic 2p(C) in π^* , this suggests that the CCSD calculation (or the underlying Hartree-Fock one) underestimates the contribution of C5 to π^* . The higher energy resonances in the C *K*-edge XAS spectrum mostly correspond to 1s(C) σ^* -transitions.

The shift for TDDFT is 10.48 eV and thus more than one order of magnitude higher than for fc-CVS-EOM-CCSD. Such high energy shifts are common when utilizing TDDFT based methods.⁵⁷

The experimental XAS spectrum at the N *K*-edge (Fig. 4, middle) exhibits two resonances, both from 1s(N) π^* transitions. The most intense one at 399.7 eV is attributed to the 1s(N) π_1^* transition and the second one at 401.5 eV to the 1s(N) π_2^* transition by both methods. Interestingly, fc-CVS-EOM-CCSD overestimates the relative energetic position of the second 1s(N) π^* resonance by roughly 1 eV compared to the TDDFT calculation. The excitation energies of fc-CVS-EOM-CCSD can be corrected by including the effect of triple excitations on the excitation energies in a non-iterative manner using CCSDR(3),⁶⁵ which can be important when describing relaxation effects.³⁹ The corrected spectrum can be seen in blue in Fig. 4. The additional relaxation introduced by the CVS-EOM-CCSDR(3) method to compute excitation energies is indeed needed when describing the XAS spectrum at the N *K*-edge, yielding better agreement with experiment. Unlike TDDFT, the coupled cluster method also captures the third peak of the

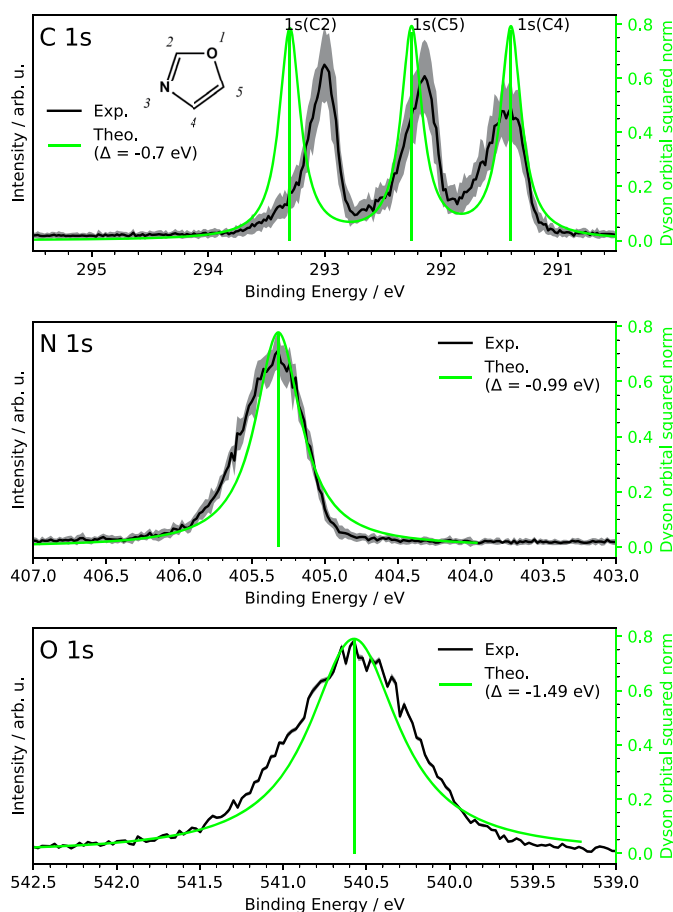


FIG. 3. Experimental, calibrated XPS spectra (black) at the C 1s, N 1s, and O 1s core levels as well as theoretically simulated spectra (green) at the fc-CVS-EOM-CCSD level of theory. A Lorentzian broadening has been applied to the latter with a FWHM of 0.22 eV for carbon, 0.38 eV for nitrogen, and 0.65 eV for oxygen to fit the experimental spectra. The theoretical spectra have been shifted by Δ to align with the experimental spectra.

spectrum, which is attributed to a transition from N 1s to diffuse Rydberg states.

The XAS spectrum at the oxygen *K*-edge (Fig. 4, bottom) is the simplest of the three XAS spectra, dominated by one main resonance

TABLE II. Assignment of the main transitions in the XPS spectra at the O 1s, N 1s and C 1s core levels without applying any shift as otherwise done in Fig. 3. Dyson orbital square norms are given within square brackets.

K-edge	Ionization energy (eV)		Ionized orbital
	Experiment	CCSD	
C	293.1	294.0 [0.78]	1s(C2)
C	292.1	293.0 [0.78]	1s(C5)
C	291.4	292.1 [0.78]	1s(C4)
N	405.3	406.3 [0.78]	1s(N)
O	540.2	542.1 [0.79]	1s(O)

at 535.0 eV, followed by a second broad band centered at 539 eV. These bands correspond to the $1s(O)\pi^*$ -transition and to a multitude of transitions from $1s(O)$ to diffuse orbitals with σ^* symmetry, respectively.

At the fc-CVS-EOM-CCSD level of theory, this second band shows increased intensity compared to experiment and has roughly twice the intensity compared to the TDDFT calculation. As was also seen for the N *K*-edge spectrum, the theoretical spectrum can be improved by correcting the excitation energies using the CVS-EOM-CCSDR(3) method, which yields an increased spread of the excitation energies, thus redistributing the intensities in the region of the second experimental peak.

D. Auger-Meitner spectroscopy (AES)

AES studies the relaxation of molecules following the creation of a core hole and therefore allows insight into their excited electronic structure. In normal AES, a photon far above the

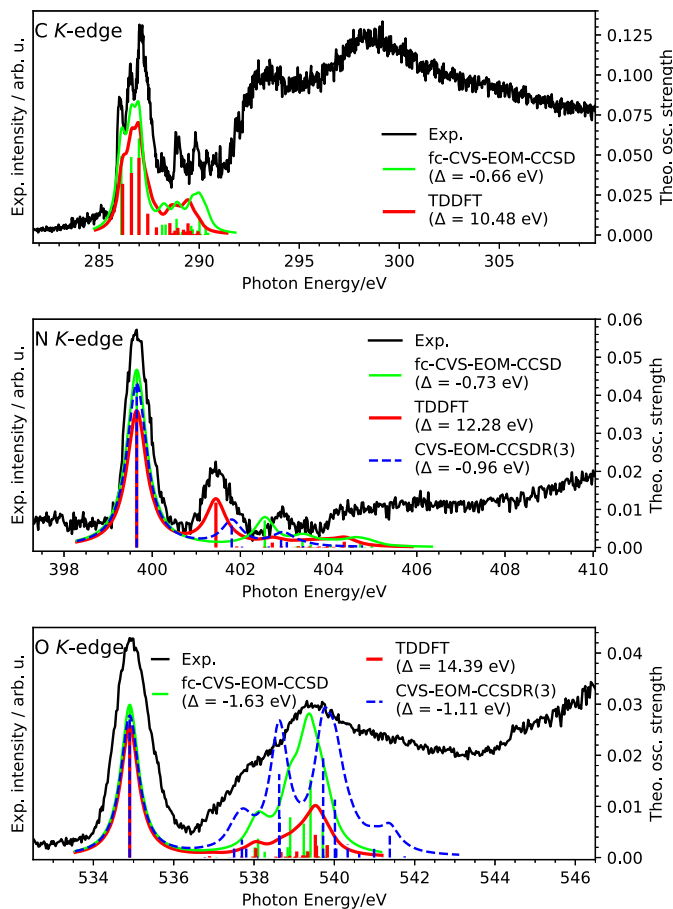


FIG. 4. Experimental, calibrated XAS spectra (black) at all three atomic K-edges as well as theoretically simulated spectra at the *fc*-CVS-EOM-CCSD (green), TDDFT (red), and CVS-EOM-CCSDR(3)[energies]/CVS-EOM-CCSD [strengths] (blue) level of theory. A Lorentzian broadening has been applied to the theoretical spectra with a FWHM of 1.08 eV for all atomic K-edges. The computed spectra have been shifted by Δ to align with experiment.

corresponding edge removes a core electron and the resulting cation rearranges its electronic structure, ejecting one or more electrons with different kinetic energies. Starting from a closed shell system, the doubly ionized cation thus formed will be either in a singlet or in a triplet final state.

On the other hand, in resonant AES, a core electron is first excited to an unoccupied orbital. The non-radiative decay of this state resulting in the ejection of an electron can then take place along two channels. If the initially core-excited electron is the one ejected as a result of the de-excitation of a core-excited state, the process is said to follow a participator channel, while a spectator channel is followed otherwise. Hence, the participator channel can be described by $1h$ configurations, while $2h1p$ configurations are required for the spectator channel.

In the following, we will first discuss normal AES, before discussing resonant AES (RAES).

1. Normal AES

The normal Auger–Meitner spectra, recorded at a photon energy at least 50 eV above the absorption edge, are displayed in Fig. 5. The AES calculations at the *fc*-CVS-EOM-CCSD/aug-cc-pVTZ level of theory gave reasonably good results in the high kinetic energy region of the spectra; however, not enough transitions converged to describe the full spectrum. For each carbon atom, 25 roots were converged per irreducible representation for both singlet and triplet final dicationic states, while for nitrogen and oxygen 50 and 45 roots per irreducible representation were converged for both singlet and triplet final states.

TABLE III. Assignment of main transitions in the XAS spectra at the O, N, and C K-edge without applying any shift, as otherwise done in Fig. 4. The corresponding natural transition orbitals (NTOs) can be found in Secs. S6 and S7 in the [supplementary material](#). Oscillator strengths are given within square brackets.

K-edge	Excitation energy (eV)			Transition character	
	Experiment	CCSD	CAMB3LYP	CCSD	CAMB3LYP
C	286.0	286.8 [0.049]	275.7 [0.032]	1s(C4) π^*	1s(C4) π^*
C	286.5	287.3 [0.049]	276.1 [0.039]	1s(C5) π^*	1s(C5) π^*
C	287.3	287.6 [0.060]	276.5 [0.048]	1s(C2) π^*	1s(C2) π^*
N	399.7	400.4 [0.047]	387.4 [0.036]	1s(N) π^*	1s(N) π^*
N	401.5	403.3 [0.007]	389.2 [0.012]	1s(N) π^*	1s(N) π^*
O	535.0	536.5 [0.030]	520.5 [0.026]	1s(O) π^*	1s(O) π^*
O	538.3	539.7 [0.004]	523.7 [0.002]	1s(O) σ^*	1s(O) σ^*
O	539.5	541.0 [0.015]	525.1 [0.004]	1s(O) σ^*	1s(O) σ^*

The parts of the normal AES spectra reached by calculations are in good agreement with experiment (see Fig. 5 and Sec. S9 in the [supplementary material](#)). At all three edges, the spectra are heavily dominated by the singlet decay channels, i.e., the final doubly charged states of the molecule are singlet states.

While all bands appear to consist of several transitions of similar intensities, a few of them can be clearly singled out. In carbon AES, for instance, the most intense transition underlying the experimental band centered at ≈ 264.5 eV is computed at 265.1 eV (264.6 eV in the shifted theoretical spectrum) and

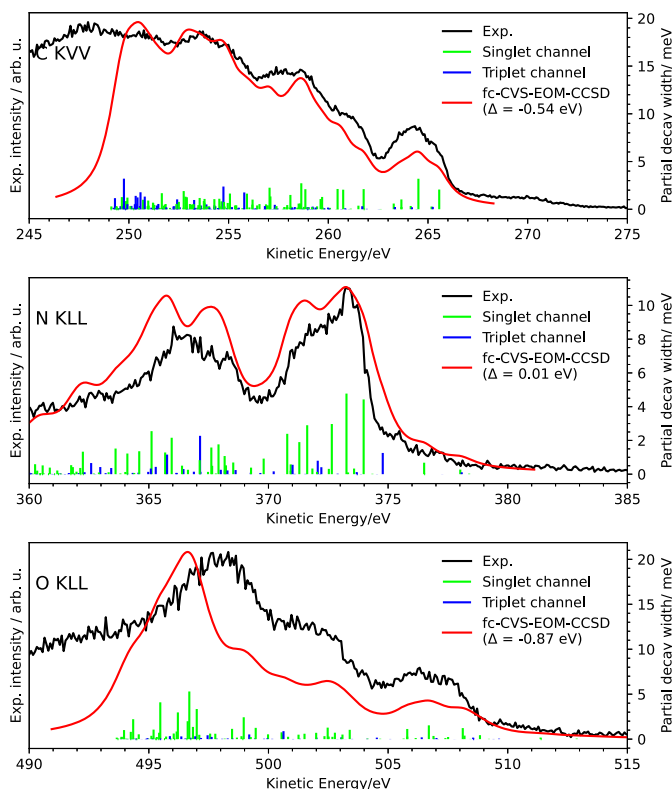


FIG. 5. Experimental normal C, N, and O AES spectra (black) and the corresponding simulated spectra at the fc-CVS-EOM-CCSD (red) level of theory. A Lorentzian broadening has been applied to the theoretical spectra with a FWHM of 1.36 eV for carbon, 0.54 eV for nitrogen, and 1.64 eV for oxygen. The theoretical spectra have been shifted by Δ to align with experiment.

originates on C5, with main contribution to the final singlet state $(3a'')^{-2}$.

The nitrogen AES spectrum shows two broad bands. In correspondence to the high energy one peaking at ≈ 373 eV, we find three transitions of larger intensity at 372.6, 373.2, and 374.0 eV (no shift applied) with the main orbital configurations of the final (singlet) cationic states $(15a')^{-2}$, $(2a'')^{-2}$, and $(15a')^{-1}(2a'')^{-1}$. The low energy band from 365 to 370 eV also consists of many transitions of similar intensity, of which the two most intense ones are found at 365.1 and 367.1 eV (unshifted), the latter corresponding to a triplet channel. The main contributions to these transitions are characterized as $(9a')^{-1}(15a')^{-1}$ and $(10a')^{-1}(15a')^{-1}$, respectively. At the oxygen *K*-edge, three broad features of increasing intensity are observed in the experimental spectrum, roughly centered at 507, 502, and 497.5 eV. The highest intensity transition in the low kinetic energy region is found at 497.6 eV (unshifted) and has the main orbital configuration $(1a'')^{-2}$. In correspondence to the band in the high kinetic energy region, we single out the transition at 507.6 eV (unshifted) with $(14a')^{-1}(2a'')^{-1}$ as the main orbital configuration.

Normal O and N AES were also simulated using the OCA-RASPT2 approach,³¹ see Fig. 6. As also seen for the normal fc-CVS-EOM-CCSD AES spectra, the singlet decay channels dominate. However, according to the results of the OCA-RASPT2 approach, the triplet channel is completely negligible, which was not the case in the fc-CVS-EOM-CCSD calculations, especially for nitrogen. As seen, the spectra obtained with OCA-RASPT2 reproduce rather well the main features of the experimental N and O AES spectra. Additionally, whereas many close-lying transitions with comparable intensities are observed at the fc-CVS-EOM-CCSD level of theory, a few transitions can be more easily singled out as dominant at the RASPT2 level of theory. Specifically, the three most relevant cationic states for the main peak of the nitrogen AES spectrum are found at 373.9, 373.4, and 372.6 eV (unshifted), with main orbital configurations $(15a')^{-1}(2a'')^{-1}$, $(15a')^{-2}$, and $(2a'')^{-2}$, respectively. From the second feature in the spectrum, the contributions of the two most intense decay channels are considered, and they show main orbital configuration $(10a')^{-1}(15a')^{-1}$ and $(1a'')^{-1}(2a'')^{-1}$ of the final state, calculated at 366.4 and 368.1 eV, respectively. The total intensity distribution around 366 eV obtained with the convoluted OCA-RASPT2 spectrum is lower compared to the experimental

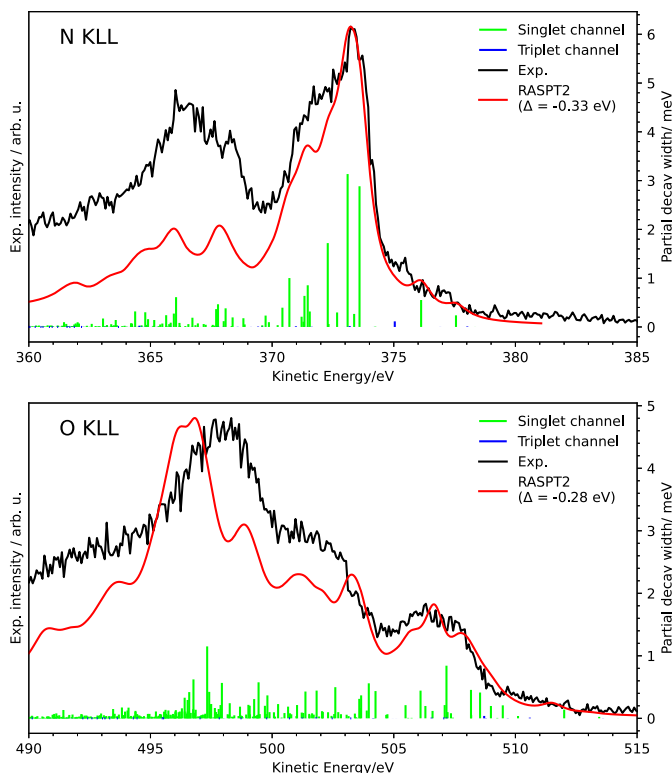


FIG. 6. Experimental normal N and O AES spectra (black) and simulated spectra using the OCA-RASPT2 (red) level of theory. A Lorentzian broadening has been applied to obtain the theoretical spectra, with a FWHM of 1.09 eV. The calculated spectra have been shifted by Δ to align with experiment.

spectrum and indeed also to the fc-CVS-EOM-CCSD simulation although both simulations yield good agreement with experiment.

The O AES spectra computed with the OCA-RASPT2 approach also exhibit nice agreement with the experiment. Two of the most prominent peaks were calculated at 497.5 and 507.4 eV, and they are attributed, respectively, to the following orbital configurations: $(12a')^{-1}(2a'')^{-1}$ and $(1a'')^{-2}$. Thus, at this level of theory, the state $(12a')^{-1}(2a'')^{-1}$ is the main cationic state associated with the broad peak observed in the experiment around 507 eV, while at the fc-CVS-EOM-CCSD level of theory it was predicted to be the $(14a')^{-1}(2a'')^{-1}$ state. At the fc-CVS-EOM-CCSD level of theory, however, this feature did not have one transition dominating as clearly as at the RASPT2 level of theory. The state $(1a'')^{-2}$ is found to be the main contributor to the broad and intense peak centered around 498 eV in both methods.

2. Resonant AES

In oxazole, only one nitrogen and one oxygen atom are present, leading to the simple XPS (one peak only) and XAS (dominated by one main resonance) spectra discussed earlier. The resonant Auger

spectra at the N and O *K*-edges, after excitation of the first core resonance at, respectively, 399.61 and 534.99 eV are shown in the middle and bottom panels of Fig. 7. The PES is also reproduced in the top panel to allow a visual comparison of the main ionizations involved in the valence photoionization and in the Auger–Meitner process. Dashed gray lines highlight some of the related ionizations in the PES and RAES spectra.

Figure 7 shows the simulated spectra calculated at the fc-CVS-EOM-CCSD level of theory. As earlier discussed, we were not able to converge a sufficient number of transitions to cover the full energy range of the experimental spectra. For nitrogen, 25 roots were converged in each symmetry, while only 20 roots could be converged in each irreducible representation for oxygen. Given the poor convergence of the fc-CVS-EOM-CCSD method for the O and N *K*-edge, the C *K*-edge was not computed, as similar convergence problems were expected, further complicated by the need of considering multiple scattering centers.

According to the CCSD results, at higher kinetic energies (lower binding energy) the participator channel dominates the RAES spectra, as also expected based on the PES results. The lower

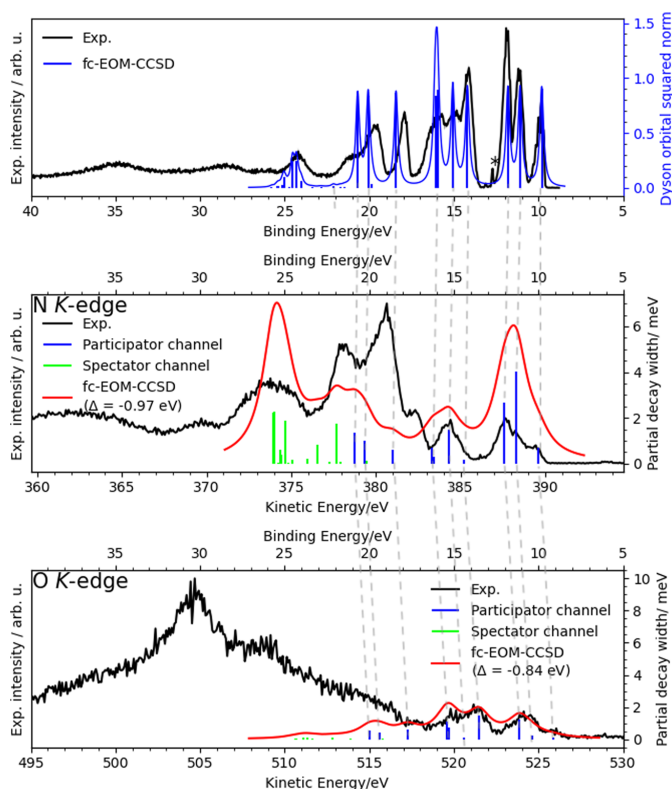


FIG. 7. Top: Experimental (black) and simulated (blue) PES spectrum at the fc-EOM-CCSD level of theory. A Lorentzian broadening of the pole strengths was applied with a FWHM of 0.27 eV. Middle and bottom: Experimental RAES spectra (black) at resonance with the first core excitation at the N and O *K*-edges and the corresponding simulated spectra (red) at the fc-CVS-EOM-CCSD level of theory with a plane wave description of the electron in the continuum. To simulate the spectra, a Lorentzian broadening was applied to the theoretical partial decay widths with a FWHM of 1.63 eV. The spectra were shifted by Δ to align with experiment. The theoretical resonance energies at the N and O *K*-edges are 400.38 and 536.53 eV, respectively, while the experimental ones are 399.61 and 534.99 eV.

kinetic energy region (i.e., higher binding energy region) is, however, dominated by the spectator channel, consistent with the higher binding energies of the $2h1p$ ionizations in the PES spectrum. Some “anomalies” are nonetheless noticed: The participator channel transitions are shown to give rise to more intense transitions in the middle region of the RAES spectra.

According to Fermi's golden rule, the intensity of a transition in AES depends on the matrix element of the Coulomb interaction between the initial (resonance) state and the final (here cationic) state, see, e.g., Eqs. (8) and (11) in Ref. 31. The greater the matrix element is, the more intense that decay channel will be. In the participator case, the electrons moving are the valence electron filling the core hole of the initial state and the particle electron being ejected, whereas in the spectator case a valence electron fills the hole and another is ejected. Participator intensity is generally smaller (much smaller if the “particle” electron is in a Rydberg orbital) because it interacts less with the localized core. In other words, spectator decay channel is generally expected to be more intense, unlike what is predicted here.

Notice the difference with PES, where the initial state is the neutral ground state, generally resulting in more intense transitions for $1h$ cationic final states compared to $2h1p$ ones.^{55,62}

At the N K -edge, fc-CVS-EOM-CCSD reproduces reasonably well the first two peaks centered around 388 and 384 eV, attributed to participator channels. The next two peaks at 378 and 380 eV are less well reproduced. We note, however, that transitions related to the spectator channel have been shown to be significantly shifted in energy using the CCSD method.^{24,43} Such a shift might be the reason for the poor agreement with experiment for the lower kinetic energy bands as these peaks are attributed to a mix of participator and spectator channels. The last peak at 374 eV for which transitions could be converged is tentatively attributed to the spectator channel. For the oxygen RAES spectrum, only a small portion of the spectrum could be reproduced using fc-CVS-EOM-CCSD. The agreement for this small part is excellent and is attributed nearly exclusively to the participator channel.

The limitations of the fc-CVS-EOM-CCSD approach for resonant Auger–Meitner decay were discussed by Skomorowski and Krylov.⁴³ Accordingly, states with $2h1p$ character, related to the spectator channel, are described less accurately at the fc-EOM-CCSD level of theory compared to those of $1h$ character related to the participator channel. This is due to the lack of $3h2p$ excitations in the EOM-CCSD model. This inability of EOM-CCSD to properly describe the $2h1p$ ionization energies for valence ionization

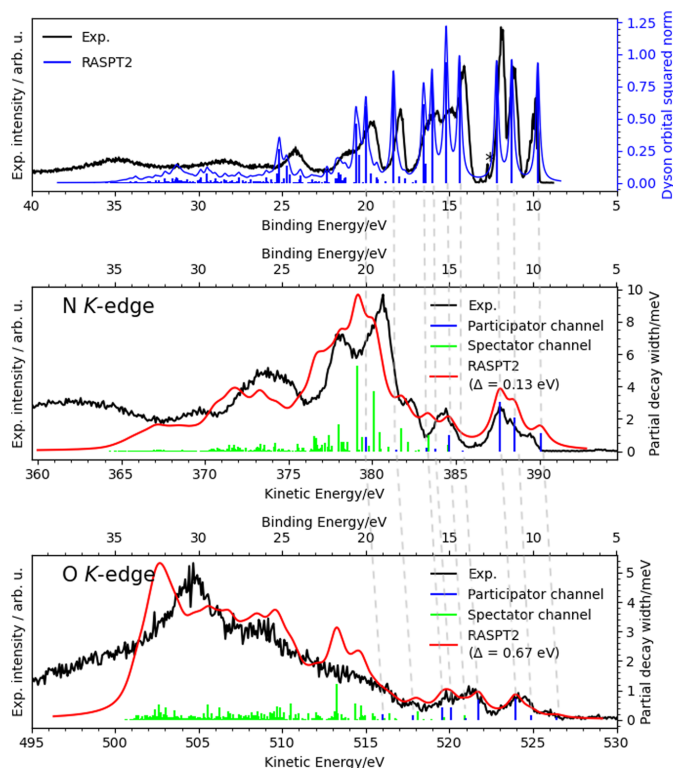


FIG. 8. Top: Experimental (black) and simulated (blue) PES spectrum at the RASPT2 level of theory (blue). A Lorentzian broadening of the pole strengths was applied with a FWHM of 0.27 eV. Middle and bottom: Experimental RAES spectra (black) at resonance with the first core excitation at the N and O K -edges and corresponding simulated spectra using the OCA-RASPT2 (red) level of theory. To simulate the spectra, a Lorentzian broadening was applied to the theoretical partial decay widths with a FWHM of 1.09 eV. The spectra have been shifted by Δ to align with experiment. The theoretical resonance energies are 399.66 eV (N K -edge) and 535.46 eV (O K -edge).

was further investigated by Moitra *et al.*⁶² There, it was found that while EOM-CCSD predicts $1h$ valence ionizations well, $2h1p$ ionization energies are significantly overestimated, which is also what is observed here with extremely low predicted kinetic energies for the spectator channel transitions. This behavior could possibly be improved by including additional dynamical electron correlation, e.g., by employing EOM-CC3, which, like CCSDR(3), includes triple excitations in a perturbative manner. At the EOM-CC3 level of theory, the valence ionization satellite states in PES appear to be well described.⁶²

To try and improve the description of the RAES spectra, we then utilized OCA-RASPT2 for simulations of the oxygen and nitrogen K -edges, see Fig. 8. The OCA-RASPT2 spectra show much better agreement with experiment than the fc -CVS-EOM-CCSD ones and are furthermore able to capture the $2h1p$ states characteristic of spectator decay channels (see Fig. 8). More states could be computed, and spectator channel states are now found in the mid-region of the RAES spectra. We also notice a sizable redistribution of intensity of both spectator and participator channels, also resulting in improved agreement with the experiment. For the participator channel, where both CCSD and RASPT2 performed well in terms of energy positions, the better agreement with experiment of RASPT2 as far as the spectral shape is concerned is probably related to a better description of the contributions of the electronic continuum by the OCA compared to the plane wave here used in the CCSD case.

IV. CONCLUSION

This study presents the first complete characterization (by XAS, XPS, and AES at all possible atomic $1s$ core levels, plus valence PES) of the organic molecule oxazole in the gas phase. We have characterized the ground state of oxazole by comparing experimental valence photoelectron and core spectra with simulations at the fc -EOM-CCSD/ fc -CVS-EOM-CCSD level of theory. TDDFT (with the CAMB3LYP functional) calculations were also employed for XAS along with MS-RASPT2 calculations of the normal and resonant AES spectra based on the one-center approximation. Both occupied and unoccupied valence orbitals in oxazole are typical for heterocycles: Lone electron pair orbitals on the two hetero atoms and π orbitals characterize the highest occupied valence MOs, while π^* and σ^* orbitals characterize the lowest unoccupied MOs. In addition, the XAS spectrum at the $C K$ -edge shows an energetic ordering of transitions that follows the trends in electronegativities of the atoms directly bonded to the carbon atoms.

In general, the agreement between experiment and theory at the coupled cluster level of theory is quite good: The energy shifts between XAS, XPS, and AES experiments and theory are below 1.5 eV. At the CAMB3LYP level of theory, the shifts of the XAS spectra are above 10 eV, which is common for TDDFT calculations. At the CAMB3LYP level of theory, the overall agreement with the XAS experiment in terms of spectral shapes is however still good, except for the failure of the method to capture the high energy peak at the $N K$ -edge. At this edge, the fc -CVS-EOM-CCSD spectrum, on the other hand, shows a slightly too large separation between the first two features. This was remedied by applying a perturbative correction for triple excitations [CVS-EOM-CCSDR(3)] in the calculation of excitation energies, which allows for a better

description of dynamical electron correlation used to capture relaxation effects. Such additional relaxation effects are also needed to properly describe the XAS spectrum at the $O K$ -edge, albeit to a lesser degree.

For the $C 1s$ XPS spectrum, even a better description of the dynamical electron correlation with CCSDR(3) was not sufficient to obtain a satisfactory match with experiment, indicating that other relaxation effects such as orbital relaxation and additional electron correlation might need to be considered, which goes beyond the scope of this work.

AES spectra are more challenging to describe theoretically: While fc -CVS-EOM-CCSD well described the normal AES spectra, showing the dominance of the singlet excitation channel, the same method failed to describe the resonant spectra. This is due to an inability to properly describe the spectator decay channel, which dominates at low kinetic energies of the ejected electron. The normal as well as resonant AES spectra could, however, be described satisfactorily using the one-center approximation at the RASPT2 level of theory, which is capable of describing both the participator and the spectator channels.

SUPPLEMENTARY MATERIAL

The computed core excitation energies as well as oscillator strengths are available for all shown spectra. Likewise, calculated ionization energies and the respective Dyson orbital squared norms are reported in the [supplementary material](#) along with data for the computed Auger–Meitner spectra. NTOs for the main core excitations are also available in the [supplementary material](#).

ACKNOWLEDGMENTS

C. Puglia (Uppsala University, Sweden) and the Carl Tyster Foundation are thanked for making available the VGScienta SES-200 photoelectron analyzer at the Gas Phase beamline, Elettra Synchrotron, Italy. A.R. is grateful to the Alexander von Humboldt foundation for financial support. A.K.S.-P. acknowledges the financial support provided by the DTU Alliance Ph.D. program and the travel grant provided by the Otto Mønsted Foundation to attend the WATOC2020 conference where part of this work was presented as a poster. B.N.C.T. acknowledges financial support from the European Union's Horizon 2020 Research and Innovation Program under the Marie Skłodowska-Curie Individual Fellowship (Grant Agreement No. 101027796). S.C. thanks the Independent Research Fund Denmark–Natural Sciences, DFF-RP2 Grant No. 7014-00258B. J.T. and K.R. were supported by the Division of Chemical Sciences, Geosciences and Biosciences, Office of Basic Energy Sciences (BES), U.S. Department of Energy (USDOE). This article has been authored by employees of National Technology and Engineering Solutions of Sandia, LLC under Contract No. DE-NA0003525 with the U.S. Department of Energy (DOE). The employees co-own right, title, and interest in and to the article and are responsible for its contents. The United States Government retains and the publisher, by accepting the article for publication, acknowledges that the United States Government retains a non-exclusive, paid-up, irrevocable, world-wide license to publish or reproduce the published form of this article or allow others to do so, for United States Government

- ²²M. L. Vidal, X. Feng, E. Epifanovsky, A. I. Krylov, and S. Coriani, "New and efficient equation-of-motion coupled-cluster framework for core-excited and core-ionized states," *J. Chem. Theory Comput.* **15**, 3117–3133 (2019).
- ²³M. L. Vidal, A. I. Krylov, and S. Coriani, "Dyson orbitals within the fc-CVSEOM-CCSD framework: Theory and application to X-ray photoelectron spectroscopy of ground and excited states," *Phys. Chem. Chem. Phys.* **22**, 2693–2703 (2020).
- ²⁴W. Skomorowski and A. I. Krylov, "Feshbach–Fano approach for calculation of Auger decay rates using equation-of-motion coupled-cluster wave functions. I. Theory and implementation," *J. Chem. Phys.* **154**, 084124 (2021).
- ²⁵N. A. Besley, "Modeling of the spectroscopy of core electrons with density functional theory," *Wiley Interdiscip. Rev.: Comput. Mol. Sci.* **11**, e1527 (2021).
- ²⁶J. Wenzel, M. Wormit, and A. Dreuw, "Calculating core-level excitations and x-ray absorption spectra of medium-sized closed-shell molecules with the algebraic-diagrammatic construction scheme for the polarization propagator," *J. Comput. Chem.* **35**, 1900–1915 (2014).
- ²⁷P. Bolognesi, P. O’Keeffe, V. Feyer, O. Plekan, K. Prince, M. Coreno, G. Mattioli, A. A. Bonapasta, W. Zhang, V. Carravetta, Y. Ovcharenko, and L. Avaldi, "Inner shell excitation, ionization and fragmentation of pyrimidine," *J. Phys.: Conf. Ser.* **212**, 012002 (2010).
- ²⁸G. Bilalbegović, A. Maksimović, L. A. Valencic, and S. Lehtola, "Sulfur molecules in space by X-rays: A computational study," *ACS Earth Space Chem.* **5**, 436–448 (2021).
- ²⁹S. Tsuru, M. L. Vidal, M. Pápai, A. I. Krylov, K. B. Møller, and S. Coriani, "An assessment of different electronic structure approaches for modeling time-resolved x-ray absorption spectroscopy," *Struct. Dyn.* **8**, 024101 (2021).
- ³⁰T. Fransson, I. E. Brumboiu, M. L. Vidal, P. Norman, S. Coriani, and A. Dreuw, "XABOOM: An X-ray absorption benchmark of organic molecules based on carbon, nitrogen, and oxygen $1s \rightarrow \pi^*$ transitions," *J. Chem. Theory Comput.* **17**, 1618–1637 (2021).
- ³¹B. N. C. Tenorio, T. A. Voß, S. I. Bokarev, P. Decleva, and S. Coriani, "Multireference approach to normal and resonant Auger spectra based on the one-center approximation," *J. Chem. Theory Comput.* **18**, 4387–4407 (2022).
- ³²P. Å. Malmqvist, K. Pierloot, A. R. M. Shahi, C. J. Cramer, and L. Gagliardi, "The restricted active space followed by second-order perturbation theory method: Theory and application to the study of CuO_2 and Cu_2O_2 systems," *J. Chem. Phys.* **128**, 204109 (2008).
- ³³V. Sauri, L. Serrano-Andrés, A. R. M. Shahi, L. Gagliardi, S. Vancouille, and K. Pierloot, "Multiconfigurational second-order perturbation theory restricted active space (RASPT2) method for electronic excited states: A benchmark study," *J. Chem. Theory Comput.* **7**, 153–168 (2011).
- ³⁴R. Fink, "Theoretical autoionization spectra of $1s \rightarrow \pi^*$ excited N_2 and N_2O ," *J. Electron Spectrosc. Relat. Phenom.* **76**, 295–300 (1995).
- ³⁵R. R. Blyth, R. Delaunay, M. Zitnik, J. Krempasky, R. Krempaska, J. Slezak, K. C. Prince, R. Richter, M. Vondracek, R. Camilloni, L. Avaldi, M. Coreno, G. Stefani, G. Furlani, M. de Simone, S. Stranges, and M.-Y. Adam, "The high resolution Gas Phase Photoemission beamline, Elettra," *J. Electron Spectrosc. Relat. Phenom.* **101–103**, 959–964 (1999).
- ³⁶N. Mårtensson, P. Baltzer, P. A. Brühwiler, J.-O. Forsell, A. Nilsson, A. Stenborg, and B. Wannberg, "A very high resolution electron spectrometer," *J. Electron Spectrosc. Relat. Phenom.* **70**, 117–128 (1994).
- ³⁷J. Cao, Z.-Z. Xie, and X. Yu, "Excited-state dynamics of oxazole: A combined electronic structure calculations and dynamic simulations study," *Chem. Phys.* **474**, 25–35 (2016).
- ³⁸E. Epifanovsky, A. T. B. Gilbert, X. Feng, J. Lee, Y. Mao, N. Mardirossian, P. Pokhilko, A. F. White, M. P. Coons, A. L. Dempwolff, Z. Gan, D. Hait, P. R. Horn, L. D. Jacobson, I. Kaliman, J. Kussmann, A. W. Lange, K. U. Lao, D. S. Levine, J. Liu, S. C. McKenzie, A. F. Morrison, K. D. Nanda, F. Plasser, D. R. Rehn, M. L. Vidal, Z.-Q. You, Y. Zhu, B. Alam, B. J. Albrecht, A. Aldossary, E. Alguire, J. H. Andersen, V. Athavale, D. Barton, K. Begam, A. Behn, N. Bellonzi, Y. A. Bernard, E. J. Berquist, H. G. A. Burton, A. Carreras, K. Carter-Fenk, R. Chakraborty, A. D. Chien, K. D. Closser, V. Cofer-Shabica, S. Dasgupta, M. de Wergifosse, J. Deng, M. Diedenhofen, H. Do, S. Ehlert, P.-T. Fang, S. Fatehi, Q. Feng, T. Friedhoff, J. Gayvert, Q. Ge, G. Gidofalvi, M. Goldey, J. Gomes, C. E. González-Espinoza, S. Gulania, A. O. Gunina, M. W. D. Hanson-Heine, P. H. P. Harbach, A. Hauser, M. F. Herbst, M. Hernández Vera, M. Hodecker, Z. C. Holden, S. Houck, X. Huang, K. Hui, B. C. Huynh, M. Ivanov, Á. Jász, H. Ji, H. Jiang, B. Kaduk, S. Kähler, K. Khistyayev, J. Kim, G. Kis, P. Klunzinger, Z. Koczor-Benda, J. H. Koh, D. Kosenkov, L. Koullas, T. Kowalczyk, C. M. Krauter, K. Kue, A. Kunitsa, T. Kus, I. Ladjanski, A. Landau, K. V. Lawler, D. LeFrancis, S. Lehtola, R. R. Li, Y.-P. Li, J. Liang, M. Liebenthal, H.-H. Lin, Y.-S. Lin, F. Liu, K.-Y. Liu, M. Loipersberger, A. Luenser, A. Manjanath, P. Manohar, E. Mansoor, S. F. Manzer, S.-P. Mao, A. V. Marenich, T. Markovich, S. Mason, S. A. Maurer, P. F. McLaughlin, M. F. S. J. Menger, J.-M. Mewes, S. A. Mewes, P. Morgante, J. W. Mullinax, K. J. Oosterbaan, G. Paran, A. C. Paul, S. K. Paul, F. Pavosević, Z. Pei, S. Prager, E. I. Proynov, Á. Rák, E. Ramos-Cordoba, B. Rana, A. E. Rask, A. Rettig, R. M. Richard, F. Rob, E. Rossomme, T. Scheele, S. Schreuer, M. Schneider, N. Sergueev, S. M. Sharada, W. Skomorowski, D. W. Small, C. J. Stein, Y.-C. Su, E. J. Sundstrom, Z. Tao, J. Thirman, G. J. Tornai, T. Tsuchimochi, N. M. Tubman, S. P. Veccham, O. Vydrov, J. Wenzel, J. Witte, A. Yamada, K. Yao, S. Yeganeh, S. R. Yost, A. Zech, I. Y. Zhang, X. Zhang, Y. Zhang, D. Zuev, A. Aspuru-Guzik, A. T. Bell, N. A. Besley, K. B. Bravaya, B. R. Brooks, D. Casanova, J.-D. Chai, S. Coriani, C. J. Cramer, G. Cserey, A. E. DePrince, R. A. DiStasio, A. Dreuw, B. D. Dunietz, T. R. Furlani, W. A. Goddard, S. Hammes-Schiffer, T. Head-Gordon, W. J. Hehre, C.-P. Hsu, T.-C. Jagau, Y. Jung, A. Klamt, J. Kong, D. S. Lambrecht, W. Liang, N. J. Mayhall, C. W. McCurdy, J. B. Neaton, C. Ochsenfeld, J. A. Parkhill, R. Peverati, V. A. Rassolov, Y. Shao, L. V. Slipchenko, T. Stauch, R. P. Steele, J. E. Subotnik, A. J. W. Thom, A. Tkatchenko, D. G. Truhlar, T. Van Voorhis, T. A. Wesolowski, K. B. Whaley, H. L. Woodcock, P. M. Zimmerman, S. Faraji, P. M. W. Gill, M. Head-Gordon, J. M. Herbert, and A. I. Krylov, "Software for the frontiers of quantum chemistry: An overview of developments in the Q-Chem 5 package," *J. Chem. Phys.* **155**, 084801 (2021).
- ³⁹S. Coriani, O. Christiansen, T. Fransson, and P. Norman, "Coupled-cluster response theory for near-edge x-ray-absorption fine structure of atoms and molecules," *Phys. Rev. A* **85**, 022507 (2012).
- ⁴⁰S. Coriani and H. Koch, "Communication: X-ray absorption spectra and core-ionization potentials within a core-valence separated coupled cluster framework," *J. Chem. Phys.* **143**, 181103 (2015).
- ⁴¹K. Aidas, C. Angeli, K. L. Bak, V. Bakken, R. Bast, L. Boman, O. Christiansen, R. Cimraglia, S. Coriani, P. Dahle, E. K. Dalskov, U. Ekström, T. Enevoldsen, J. J. Eriksen, P. Ettenhuber, B. Fernández, L. Ferrighi, H. Fliegl, L. Frediani, K. Hald, A. Halkier, C. Hättig, H. Heiberg, T. Helgaker, A. C. Hennum, H. Hettema, E. Hjertenaes, S. Host, I.-M. Høyvik, M. F. Iozzi, B. Jansik, H. J. Aa. Jensen, D. Jonsson, P. Jørgensen, J. Kauczor, S. Kirpekar, T. Kjaergaard, W. Klopper, S. Knecht, R. Kobayashi, H. Koch, J. Kongsted, A. Krapp, K. Kristensen, A. Ligabue, O. B. Lutnaes, J. I. Melo, K. V. Mikkelsen, R. H. Myhre, C. Neiss, C. B. Nielsen, P. Norman, J. Olsen, J. M. H. Olsen, A. Osted, M. J. Packer, F. Pawłowski, T. B. Pedersen, P. F. Provasi, S. Reine, Z. Rinkevicius, T. A. Ruden, K. Ruud, V. V. Rybkin, P. Salek, C. C. M. Samson, A. S. de Merás, T. Saue, S. P. A. Sauer, B. Schimelpennig, K. Snegov, A. H. Steindal, K. O. Sylvester-Hvid, P. R. Taylor, A. M. Teale, E. I. Tellgren, D. P. Tew, A. J. Thorvaldsen, L. Thøgersen, O. Vahtras, M. A. Watson, D. J. D. Wilson, M. Ziolkowski, and H. Ågren, "The Dalton quantum chemistry program system," *Wiley Interdiscip. Rev.: Comput. Mol. Sci.* **4**, 269–284 (2014).
- ⁴²J. M. H. Olsen, S. Reine, O. Vahtras, E. Kjellgren, P. Reinholdt, K. O. Hjorth Dunda, X. Li, J. Cukras, M. Ringholm, E. D. Hedegård, R. Di Remigio, N. H. List, R. Faber, B. N. Cabral Tenorio, R. Bast, T. B. Pedersen, Z. Rinkevicius, S. P. A. Sauer, K. V. Mikkelsen, J. Kongsted, S. Coriani, K. Ruud, T. Helgaker, H. J. A. Jensen, and P. Norman, "Dalton project: A Python platform for molecular- and electronic-structure simulations of complex systems," *J. Chem. Phys.* **152**, 214115 (2020).
- ⁴³W. Skomorowski and A. I. Krylov, "Feshbach–Fano approach for calculation of Auger decay rates using equation-of-motion coupled-cluster wave functions. II. Numerical examples and benchmarks," *J. Chem. Phys.* **154**, 084125 (2021).
- ⁴⁴T. H. Dunning, "Gaussian basis sets for use in correlated molecular calculations. I. The atoms boron through neon and hydrogen," *J. Chem. Phys.* **90**, 1007–1023 (1989).
- ⁴⁵R. A. Kendall, T. H. Dunning, and R. J. Harrison, "Electron affinities of the first-row atoms revisited. Systematic basis sets and wave functions," *J. Chem. Phys.* **96**, 6796–6806 (1992).

- ⁴⁶K. Kaufmann, W. Baumeister, and M. Jungen, "Universal Gaussian basis sets for an optimum representation of Rydberg and continuum wavefunctions," *J. Phys. B: At., Mol. Opt. Phys.* **22**, 2223–2240 (1989).
- ⁴⁷D. E. Woon and T. H. Dunning, "Gaussian basis sets for use in correlated molecular calculations. V. Core-valence basis sets for boron through neon," *J. Chem. Phys.* **103**, 4572–4585 (1995).
- ⁴⁸C. Melania Oana and A. I. Krylov, "Dyson orbitals for ionization from the ground and electronically excited states within equation-of-motion coupled-cluster formalism: Theory, implementation, and examples," *J. Chem. Phys.* **127**, 234106 (2007).
- ⁴⁹T. Moitra, S. Coriani, and P. Decleva, "Capturing correlation effects on photoionization dynamics," *J. Chem. Theory Comput.* **17**, 5064–5079 (2021).
- ⁵⁰H. Siegbahn, L. Asplund, and P. Kelfve, "The Auger electron spectrum of water vapour," *Chem. Phys. Lett.* **35**, 330–335 (1975).
- ⁵¹P.-Å. Malmqvist and B. O. Roos, "The CASSCF state interaction method," *Chem. Phys. Lett.* **155**, 189–194 (1989).
- ⁵²I. F. Galván, M. Vacher, A. Alavi, C. Angeli, F. Aquilante, J. Autschbach, J. J. Bao, S. I. Bokarev, N. A. Bogdanov, R. K. Carlson, L. F. Chibotaru, J. Creutzberg, N. Dattani, M. G. Delcey, S. S. Dong, A. Dreuw, L. Freitag, L. M. Frutos, L. Gagliardi, F. Gendron, A. Giussani, L. González, G. Grell, M. Guo, C. E. Hoyer, M. Johansson, S. Keller, S. Knecht, G. Kovačević, E. Källman, G. Li Manni, M. Lundberg, Y. Ma, S. Mai, J. P. Malhado, P. Å. Malmqvist, P. Marquetand, S. A. Mewes, J. Norell, M. Olivucci, M. Oppel, Q. M. Phung, K. Pierloot, F. Plasser, M. Reiher, A. M. Sand, I. Schapiro, P. Sharma, C. J. Stein, L. K. Sørensen, D. G. Truhlar, M. Ugandi, L. Ungur, A. Valentini, S. Vancollie, V. Veryazov, O. Weser, T. A. Wesolowski, P.-O. Widmark, S. Wouters, A. Zech, J. P. Zobel, and R. Lindh, "OpenMolcas: From source code to insight," *J. Chem. Theory Comput.* **15**, 5925–5964 (2019).
- ⁵³M. G. Delcey, L. K. Sørensen, M. Vacher, R. C. Couto, and M. Lundberg, "Efficient calculations of a large number of highly excited states for multiconfigurational wavefunctions," *J. Comput. Chem.* **40**, 1789–1799 (2019).
- ⁵⁴L. S. Cederbaum, W. Domcke, and J. Schirmer, "Many-body theory of core holes," *Phys. Rev. A* **22**, 206–222 (1980).
- ⁵⁵B. N. C. Tenorio, A. Ponzi, S. Coriani, and P. Decleva, "Photoionization observables from multi-reference Dyson orbitals coupled to B-spline DFT and TD-DFT continuum," *Molecules* **27**, 1203 (2022).
- ⁵⁶J. P. Carbone, L. Cheng, R. H. Myhre, D. Matthews, H. Koch, and S. Coriani, "Chapter eleven—An analysis of the performance of coupled cluster methods for K-edge core excitations and ionizations using standard basis sets," in *State of the Art of Molecular Electronic Structure Computations: Correlation Methods, Basis Sets and More*, Advances in Quantum Chemistry Vol. 79, edited by L. U. Ancarani and P. E. Hoggan (Academic Press, 2019), pp. 241–261.
- ⁵⁷P. J. Lestrage, P. D. Nguyen, and X. Li, "Calibration of energy-specific TDDFT for modeling K-edge XAS spectra of light elements," *J. Chem. Theory Comput.* **11**, 2994–2999 (2015).
- ⁵⁸T. Fransson, D. Burdakova, and P. Norman, "K- and L-edge X-ray absorption spectrum calculations of closed-shell carbon, silicon, germanium, and sulfur compounds using damped four-component density functional response theory," *Phys. Chem. Chem. Phys.* **18**, 13591–13603 (2016).
- ⁵⁹DTU Computing Center (2021). "DTU computing center resources," Technical University of Denmark. <https://doi.org/10.48714/DTU.HPC.0001>.
- ⁶⁰M. H. Palmer, G. Ganzenmüller, and I. C. Walker, "The electronic states of oxazole studied by VUV absorption and electron energy-loss (EEL) spectroscopies, and *ab initio* configuration interaction methods," *Chem. Phys.* **334**, 154–166 (2007).
- ⁶¹J. E. Reutt, L. S. Wang, Y. T. Lee, and D. A. Shirley, "Molecular beam photoelectron spectroscopy and femtosecond intramolecular dynamics of H_2O^+ and D_2O^+ ," *J. Chem. Phys.* **85**, 6928–6939 (1986).
- ⁶²T. Moitra, A. C. Paul, P. Decleva, H. Koch, and S. Coriani, "Multi-electron excitation contributions towards primary and satellite states in the photoelectron spectrum," *Phys. Chem. Chem. Phys.* **24**, 8329–8343 (2022).
- ⁶³D. P. Chong and C.-H. Hu, "Accurate density functional calculation of core-electron binding energies with a scaled polarized triple-zeta basis set. IV. Application to isomers of $\text{C}_3\text{H}_6\text{O}$, $\text{C}_3\text{H}_3\text{NO}$, and C_6H_6 ," *J. Chem. Phys.* **108**, 8950–8956 (1998).
- ⁶⁴X. Du, S.-Y. Wang, M. Wei, J.-R. Zhang, G. Ge, and W. Hua, "A theoretical library of N1s core binding energies of polynitrogen molecules and ions in the gas phase," *Phys. Chem. Chem. Phys.* **24**, 8196–8207 (2022).
- ⁶⁵O. Christiansen, H. Koch, and P. Jørgensen, "Perturbative triple excitation corrections to coupled cluster singles and doubles excitation energies," *J. Chem. Phys.* **105**, 1451–1459 (1996).

APPENDIX C

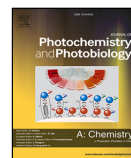
Publication 3

Reproduced from "Azobenzene photoisomerization dynamics: Revealing the key degrees of freedom and the long timescale of the trans-to-cis process",
Anna Kristina Schnack-Petersen, Mátyás Pápai and Klaus Braagaard Møller, *J. Photoch. Photobio. A*, 2022, **428**, 113869 with the permission of Elsevier.
Only the article itself is reproduced here, while the supporting information can be accessed via <https://doi.org/10.1016/j.jphotochem.2022.113869>.



Contents lists available at ScienceDirect

Journal of Photochemistry & Photobiology, A: Chemistry

journal homepage: www.elsevier.com/locate/jphotochem

Azobenzene photoisomerization dynamics: Revealing the key degrees of freedom and the long timescale of the trans-to-cis process

Anna Kristina Schnack-Petersen^{a,*}, Mátyás Pápai^{a,b}, Klaus Braagaard Møller^a^a Department of Chemistry, Technical University of Denmark, DK-2800 Kongens Lyngby, Denmark^b Wigner Research Centre for Physics, P.O. Box 49, H-1525 Budapest, Hungary

ARTICLE INFO

Keywords:

SHARC
Surface hopping
Azobenzene
Molecular dynamics
TDDFT

ABSTRACT

The photoisomerization reaction of azobenzene in both directions have been investigated with a density functional theory based approach using the surface hopping procedure with forced jumps. While the cis-to-trans isomerization was found to be a stepwise reaction along the CNNC dihedral angle, the trans-to-cis isomerization was observed to be one smooth step. The further unbiased full-dimensional analysis of the cis-to-trans isomerization revealed that, while the CNNC dihedral angle is an important degree of freedom for describing the reaction, it is insufficient for describing all of the dynamics. For a fuller picture two coupled modes must be considered. The trans-to-cis isomerization on the other hand was found to be well described along only the CNNC dihedral angle, and its longer timescale could be ascribed to the slow oscillations of this degree of freedom rather than a potential energy barrier in the excited state. The timescales observed in this study was found to be in good agreement with experiment, and thus this work provides insights into the interpretation of experimental observations. Finally, investigations of the structures of the CIs for both reactive and non-reactive trajectories showed a heavy functional dependency.

1. Introduction

Ever since the discovery of the photo-induced isomerization process of azobenzene in 1937 by Hartly [1], the molecule and its derivatives have been studied widely both experimentally [2] and theoretically [3–12]. The appeal of azobenzene derivatives stems from the many possible applications of the molecules [13]. This class of molecules is widely considered promising for applications in optical data storage and information transfer [14–20] and generally as good photoswitches [15, 21, 22], not to mention their applicational interest for photomodulable surfaces [23–25] and molecular machines and motors [26–29].

Despite the efforts to uncover the dynamics of azobenzene, the photoisomerization reaction is still not fully understood and both theoretical [3, 4, 10, 20, 22, 30–35] and experimental [25, 36] studies continue to be published. It remains unclear why the trans-to-cis isomerization happens on a significantly longer timescale than the cis-to-trans isomerization. A possible reason could be an energy barrier on the potential energy surface (PES) of the trans-to-cis isomerization, however not all theoretical studies have found such a barrier [2]. Also, the dynamics after the transition to the ground state is not clear, e.g. it is not known if the isomerization process happens stepwise or not. While the structure of the two isomers are characterized well by experiments [2] the reaction path is less well defined. Many theoretical and experimental

studies agree that the cis-to-trans isomerization follows a rotational path [2, 3, 6], however studies of the trans-to-cis isomerization do not agree whether a rotation or inversion pathway is dominant for the non-reactive pathway [2, 3, 5, 7, 30, 32, 37]. In addition, a twist mechanism has also been suggested for both isomerization reactions [9–12]. In fact, while studies suggest two distinguishable conical intersections (CIs) – a rotated and a planar – they seem to disagree about the importance of the planar CI [5, 8, 37]. Finally, the important degrees of freedom (DOFs) have not been studied thoroughly as it is generally acknowledged that the degree of freedom of main importance is the CNNC dihedral angle. While a few studies [8, 10, 12, 30, 31] suggested that one should consider other degrees of freedom, the main conclusion of a recent extensive study of the trans-to-cis isomerization by Tavazze et al. [30] was, that the trans-to-cis isomerization process was heavily dominated by the change in the CNNC dihedral angle, justifying that it is usually the only degree of freedom considered when investigating the PES of the reaction [3, 5, 6, 30]. Studies focused on the cis-to-trans isomerization also acknowledged the need to consider more degrees of freedom [9, 10, 38]. Here however, a few degrees of freedom were chosen a priori for the investigations, and were found to give a reasonable description of the reaction.

* Corresponding author.

E-mail addresses: akrsc@kemi.dtu.dk (A.K. Schnack-Petersen), kbm@kemi.dtu.dk (K.B. Møller).

<https://doi.org/10.1016/j.jphotochem.2022.113869>

Received 17 November 2021; Received in revised form 21 January 2022; Accepted 17 February 2022

Available online 26 February 2022

1010-6030/© 2022 The Authors. Published by Elsevier B.V. This is an open access article under the CC BY license (<http://creativecommons.org/licenses/by/4.0/>).

The dynamics of azobenzene have been studied with a range of theoretical methods. The dynamics have been simulated with e.g. surface hopping [7,10], while the electronic structure calculations have been performed with e.g. complete active space self consistent field (CASSCF) [6,37], complete active space 2nd order perturbation theory (CASPT2) [5] and (time-dependent) density functional theory (TD-DFT) [3,4,22]. DFT has proven a very powerful method with wide applications [39]. It is widely applicable even to large systems [39] and yields results in good agreement with experiment when calculating electronic excitation energies [39–41] in particular, but also when computing other properties [39,42]. Unfortunately, TD-DFT often gives questionable results close to CIs between the ground and first excited singlet state, as the ground state is described by a single Slater determinant. This leads to various problems, e.g. the rapid variation of the potential energy of response states in this area [43] and an artificial double cone structure of the CI [3]. It has previously been seen [44,45] that by utilizing surface hopping for the dynamics [46] and in addition invoking forced hops to the ground state, when the potential energy gap between states decrease below a certain threshold, this problem can be circumvented. In both previous studies a potential energy threshold of 0.15 eV has been used [44,45]. Thus, all trajectories have been forced to jump to a new state if the potential energy difference between the current state of the trajectory and the ground state (GS) drops to this threshold or below. Following these forced jumps, trajectories are no longer allowed to jump, but moves on the GS-PES for the remainder of the simulation. In the current study we employ the same strategy and value for the potential energy threshold as in the previous studies [44,45].

It should be observed that when employing the forced jump approach, one will underestimate relaxation lifetimes. In addition, the geometry at which a trajectory jumps from the excited state (ES) to the GS will influence whether or not isomerization occurs. Thus, the probability of isomerization, and hence the quantum yield (QY), is affected by fixing an energy gap to force jumps.

By computing the PESs along the CNNC dihedral angle several interesting observations can be made albeit a deeper understanding of the dynamics naturally requires further investigations. Considering the relaxed PESs (for the BHHLYP functional) shown in Fig. 1a, it is observed that while the path is downhill from the cis-isomer in the S_1 ES all the way to the CI, the path from the trans-isomer is much flatter. For the latter a slight slope downhill is observed from approximately 180° to approximately 105°, while the slope is slightly uphill on the last stretch up to the CI geometry, which might indicate a potential energy barrier that could slow down the reaction. These PESs are found to closely resemble those obtained by Pederzoli et al. [6] using SA3-CASSCF(10,8), those obtained by Hutcheson et al. [47] using coupled cluster (CC3), the ones by Yu et al. [32] using both CASPT2 and TDDFT, as well as the ones obtained by Ye et al. [4] using several different DFT/TDDFT methods.

Investigating Fig. 1a further, one can observe that when forcing the jump at 0.15 eV, the jump from trans-to-cis is expected to happen when the dihedral angle reaches a value of approximately 105°, which is nicely beyond the grey area in which the PESs plotted here cannot be expected to provide a good representation of the actual PESs and where problems in the calculations might arise from being too close to the CI. Indeed, no such convergence problems arise for the trans-to-cis isomerization. It should also be noted that the jump thus occurs before the slight upwards slope towards the CI is encountered, and thus this feature of the ES-PES is not expected to significantly influence the investigated dynamics in this study. Considering the cis-to-trans isomerization path, it is found that the jumps are expected to happen when the dihedral angle reaches approximately 85°, and thus rather close to the grey area and the CI compared to the trans-to-cis isomerization. Hence, these results might be expected to suffer somewhat from the close proximity to the CI, and indeed for some trajectories convergence becomes more cumbersome in this region (see Supporting

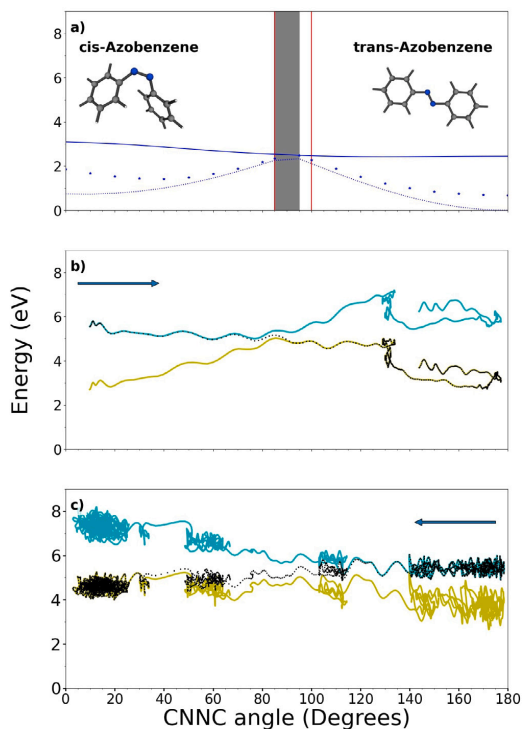


Fig. 1. (a) Calculated PESs along CNNC dihedral angle for S_0 using relaxed GS structures (dashed), S_1 using relaxed ES structures (solid) and S_0 calculated from relaxed ES structures (stars). Optimized structures could not be obtained in the grey area due to a too close proximity to the CI. Vertical red lines show the calculated points where the potential energy gap between S_1 and S_0 (calculated from ES structures) fall below 0.15 eV, and hence where our trajectories are not expected to go due to the chosen potential energy gap. The trans-isomer is shown in the inset on the right, while the cis-isomer is shown in the inset on the left. (b) Average electronic energy evolution of S_0 (green) and S_1 (cyan), and average potential energy evolution of the actual trajectory energy (black dots) from reactive cis-to-trans isomerization trajectories. (c) Average electronic energy evolution of S_0 (green) and S_1 (cyan), and average potential energy evolution of the actual trajectory energy (black dots) from reactive trans-to-cis isomerization trajectories. The arrows in (b) and (c) show the direction of reaction.

Information (SI), section 2.1). Another interesting point to note from Fig. 1a is that the slope of the ES-PES appears to be steeper on the cis-isomer side compared to the trans-isomer side of the CI. Thus, once a trajectory reaches the CI, we would expect that it has picked up more speed and is therefore more likely to continue in the forward direction after the jump coming from the cis-isomer side than coming from the trans-isomer side. Hence, the QY of the cis-to-trans isomerization is expected to be significantly larger than the QY from the trans-to-cis isomerization, and that is indeed what is observed both here, in other calculations [3] and in experiment [2].

At each timestep, the average CNNC dihedral angle as well as the average electronic energy for both GS and ES can be determined from the reactive trajectories. These average electronic energies, as well as the average potential energy of the reactive trajectories, are shown in Fig. 1b and c as a function of the corresponding average CNNC dihedral angle.

While the ES and GS electronic energies will of course be simple averages throughout the entire range, the average of the potential energy of the actual trajectory cannot be considered as such in the

region where the jumps to the ground state occur. Here, the average potential energy will in fact also be an average of the GS and ES energies as not all trajectories jump at the same time and dihedral angle. We observe that this region is significantly larger for the trans-to-cis isomerization in Fig. 1c, indicating a larger spread in the jump angles for this reaction, resulting in a larger spread of the jump times, as can be observed comparing Figs. 7 and 16.

Comparing the calculated PESs in Fig. 1a to the actual simulated evolution of the average potential energy (including zero point vibrational energy (ZPVE)) as a function of dihedral angle for reactive cis-to-trans trajectories (Fig. 1b), it is observed that the simulation seems to qualitatively follow the ES-PES towards the CI. After the jump, the potential energy is roughly constant until the CNNC angle reaches 130° , where it makes a significant drop and then qualitatively follows the GS-PES towards the trans-isomer. This very abrupt drop in energy at 130° is particularly interesting, as it indicates that other DOFs than the CNNC dihedral angle might be necessary to consider in order to fully describe the reaction.

Considering also the average of the simulated reactive trans-to-cis trajectories (Fig. 1c), one can recognize that this does indeed also qualitatively follow the calculated shape of the PESs albeit oscillations occur in the potential energy due to motion in other degrees of freedom, e.g. the CNN angles. The oscillations in the potential energy observed are noted to be larger on the cis-side in accordance with the molecule being in possession of excess kinetic energy after the jump. This behaviour is also observed for the cis-to-trans trajectory in Fig. 1b, where more oscillations are seen on the trans-side. Observe also that the ES electronic energy in Fig. 1b and c after the point of jump will never be reached as the trajectories here move on the GS, and thus these are not discussed.

In this study, we shed light on the origin of the slow trans-to-cis isomerization, showing that it is not a result of a large potential energy barrier in the ES, but rather of the reaction following slow oscillations in the CNNC dihedral angle. Furthermore, we show how the cis-to-trans isomerization happens as a result of motion along at least two degrees of freedom. Finally, we add to the discussion of the role of the planar CI, which appears inaccessible when applying one DFT functional, while it appears very important for the non-reactive trans-to-trans pathway, when another functional is applied.

2. Computational methods

The non-adiabatic dynamics simulations [48] were run with the SHARC-2.1.1 program package [49] and the required quantum chemistry TD-DFT calculations were performed by the ORCA-4.2.0 program package [50,51].

For the surface hopping [46], a timestep of 0.5 fs was employed and a potential energy gap of 0.15 eV was specified for forcing the trajectories to jump from one surface to another. In order to ascertain that the chosen potential energy gap gives a sufficiently good description of the molecular dynamics, another smaller potential energy gap was considered. Here, it was found that the behaviour of the trajectories were the same, except for a larger QY for the smaller potential energy gap. This however, is likely to be caused by the closer proximity to the CI, where the calculations become unreliable, and thus the chosen potential energy gap was deemed the most suitable. For more information see section 2.1 of the SI.

A recent study of the functional and basis set sensitivity was carried out for the cis-to-trans isomerization reaction of Azobenzene by Ye et al. [4] and their results as well as our subsequent study of the PESs, have guided our choice of basis set and functional. Thus we have utilized the BHandHLYP (BHHLYP) functional and cc-pVDZ basis set in the present study. For more details see section 1 of the SI.

For both the cis-to-trans and trans-to-cis isomerization 1000 initial conditions were prepared based on a Wigner distribution at zero kelvin determined by SHARC python scripts. The 3 lowest lying singlet states

(S_0 , S_1 and S_2) were considered in the calculations. Based on calculated excitation energies to the S_1 state from the two isomers excitation energies, an upper bound of the excitation energy of 3.0 eV was chosen for the cis-to-trans isomerization to ensure starting the trajectories in the S_1 state. This resulted in 37 trajectories to be simulated for 250 fs in accordance with the experimental lifetime. Likewise, an upper bound of the excitation energy of 4.0 eV was chosen for the trans-to-cis isomerization, giving 38 trajectories to be simulated for up to 2.0 ps corresponding to the longer lifetime of this reaction. Observe that the S_2 state was included in the simulation to allow for more flexibility, however in the simulations carried out for this study it was found to play no role in the reaction. Additional details can be found in section 1 of the SI.

The ORCA-4.2.0 program package has been used both for on-the-fly PES calculations needed by SHARC, as well as for the static PESs of the isomerization reaction along one or two DOFs. Observe that the CI structures were only possible to obtain when using the SHARC program interface [52], where gradients and energies (both potential and kinetic) were calculated by ORCA.

Visualization of the trajectories was done with the VMD-1.9.1-program [53] and OVITO [54], while visualization of the normal modes was done using molden [55].

As a way of verifying that the results obtained at the current level of theory are sound and that the simulated molecular dynamics are qualitatively accurate, we investigate the QY and timescale of the reaction. The timescale obtained using forced jumps might be expected to be too short, and also the QYs might be more uncertain. As long as a reasonable agreement with previous studies can be obtained however, the overall dynamics is expected to be unchanged. Due to the procedure of forcing the jump combined with previous studies indicating non-exponential dynamics [3,6], the lifetimes as such are not reported, but rather the lag times, i.e. the average time before a jump to the ground state is observed as also seen in Pápai et al. [45]. These are considered only for the reactive trajectories, since the point of interest in this study is the isomerization. The reactive trajectories are, thus, defined as trajectories that end up in the ground state of the isomer different from the one in which they began. Likewise, unreactive trajectories are those that end up in the ground state of the same isomer as the one in which they began. The QYs are reported as the percentage of reactive trajectories.

3. Conical intersections

In addition to investigating the one dimensional PESs along the CNNC dihedral angle it can also be useful to study some of the key structures of the reaction namely the cis- and trans-isomer GS structures as well as the CI structures. In this study, using the BHHLYP functional, no planar CI could be obtained, and all CI geometry optimizations of the jumping geometries of reactive as well as non-reactive trajectories for both the cis-to-trans and trans-to-cis isomerization resulted in the same rotated CI (see Fig. 2) in agreement with previous results [8,37] and as also indicated by the reported jumping geometries of Yue et al. [3], who found the dihedral angle at the time of the jump for the trans-to-cis isomerization to be around 120° . This contrasts however to the findings by Casellas et al. [5] and Yu et al. [32], who found also a planar CI, which was suggested to play a role for the non-reactive trans-to-cis trajectories. In addition this planar CI was also found to be of importance when employing the B3LYP functional rather than the BHHLYP functional (see SI, section 3.4). The CI determined in this study is in good agreement with the reported rotated CI found in other studies [3,5,6].

The average structure of the rotated CI is in addition presented in Table 1 along with the structures of the GS of the two isomers for some key geometrical parameters. From this table, we observe that while the CNNC dihedral angle and to some extent also the CNN angles and CN bond lengths change significantly upon going from the relaxed GS



Fig. 2. Structure of the rotated (left) and planar (right) CI. The former structure is from one of the reactive trans-to-cis trajectories, while the latter is from a non-reactive trans-to-cis trajectory run with B3LYP (see SI section 3.4), as the planar CI was not observable using BHHLYP. As can be seen from the SI all optimized CI structures from both reactive and non-reactive trajectories are very similar using the BHHLYP functional, and thus the shown rotated structure can be assumed representative.

Table 1

Geometry of GS cis and trans geometries as well as average optimized CI from jumping geometries of all trajectories for which the rotated CI is obtained.

Parameter	GS cis		Avg. rotated CI		GS trans	
	Theory	Exp. [56]	Theory		Theory	Exp. [57]
Dihedral angle ($C_1N_1N_2C_7$)	7.538°	8.0°	92.371°		179.998°	180.0° ^a
Angle ($C_4C_1N_1$)	173.943°	–	177.689°		175.449°	–
Angle ($C_{10}C_7N_2$)	173.943°	–	177.677°		175.450°	–
Angle ($C_1N_1N_2$)	123.712°	121.9°	119.613°		115.179°	114.1°
Angle ($C_7N_2N_1$)	123.712°	121.9°	137.142°		115.179°	114.1°
Bond length (N_1N_2)	1.229 Å	1.253 Å	1.247 Å		1.235 Å	1.259 Å
Bond length (C_1N_1)	1.429 Å	1.449 Å	1.393 Å		1.414 Å	1.428 Å
Bond length (C_7N_2)	1.429 Å	1.449 Å	1.347 Å		1.414 Å	1.428 Å

^aCoplanarity of $C_1N_1N_2C_7$ assumed.

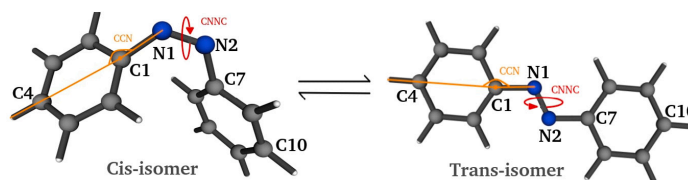


Fig. 3. The CNNC dihedral angle (red) and CCN angle (orange) marked on the structure of both the cis- (left) and trans-isomer (right). Relevant atom labels are depicted in black.

structure of either isomer to the CI structure, the remaining degrees of freedom change only very little, and we would not expect these to play a major role in the reaction. However, as we shall see, this is not the case for the CCN angle between N of the azo-bond and the nearest and para C 's of the benzene ring (See Fig. 3).

Considering now the jumping geometries we investigate Fig. 4. Firstly, it is noted that the predictions made about the CNNC dihedral angle at the time of jump based on Fig. 1a is in good agreement with the results observed in Fig. 4. Here, it is evident that only very few cis-to-trans trajectories and no trans-to-cis trajectories enter the grey area of Fig. 1a. It is observed that while most of the trajectories do jump at CNNC dihedral angles close to that of the rotated CI, a few of the non-reactive trans-to-cis trajectories appear to jump at a significantly larger dihedral angle. This might be indicative of these trajectories moving towards the predicted planar CI. In the study by Yu et al. [37] it was found that 45.4% of the non-reactive trajectories do go through a planar CI (see Fig. 2), with a dihedral angle of 180° [37]. This other planar CI has also been reported by other studies [3,5], however it was remarked by Casellas et al. [5] that the path towards the rotated CI would be preferred for systems without constrained rotation. By attempting to optimize a CI structure of a geometry very close to the reported planar CI, the rotated CI was once again obtained (see SI, Table 13).

Also note from Fig. 4 that the cis-to-trans trajectories jump at a significantly lower CCN angle than the trans-to-cis trajectories, indicating that this degree of freedom plays a role in the cis-to-trans isomerization.

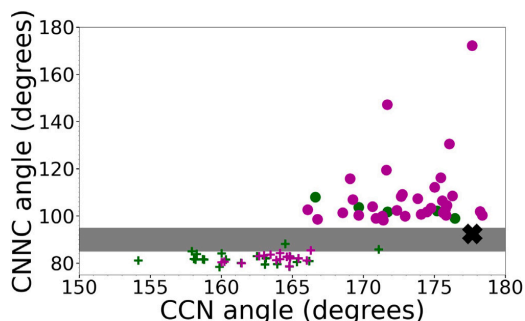


Fig. 4. Jumping geometries of the cis-to-trans (+) and trans-to-cis (dots) trajectories. Reactive trajectories are shown as green, while non-reactive are shown in magenta. The average optimized CI structure is shown as a black X. The grey area shows the region in which the CNNC angle is too close to the CI structure for optimized structures to be obtained. It is the same region as shown in Fig. 1a.

4. Cis-to-trans isomerization

4.1. QY and lag time

For the cis-to-trans isomerization, the calculation yielded 21 reactive (see Fig. 6) and 16 non-reactive (see Fig. 5) trajectories. Thus,

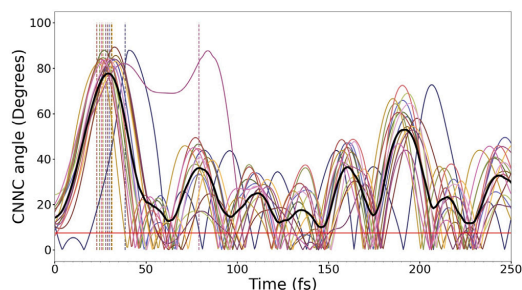


Fig. 5. All non-reactive trajectories from cis Azobenzene illustrated by the evolution of the dihedral angle over time. Time of jump is indicated by the vertical lines. Each colour represents one trajectory. The thick black line represents the average trajectory, while the horizontal red line shows the value of the CNNC dihedral angle of the minimum potential energy GS structure of the cis-isomer. Note that the values of the CNNC dihedral angle along the trajectories are reported only in the interval 0–180° (due to symmetry) and, therefore, that the average trajectory eventually oscillates around a larger positive value for the CNNC dihedral angle instead of the GS equilibrium value of the cis isomer.

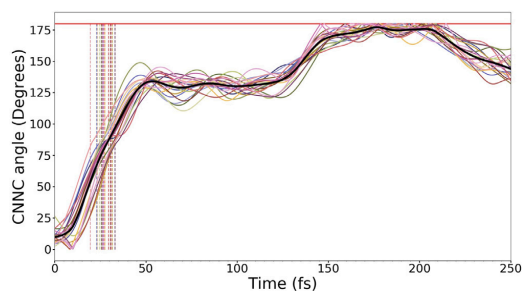


Fig. 6. All reactive trajectories from cis Azobenzene illustrated by the evolution of the absolute value of the dihedral angle over time. Time of jump is indicated by the vertical lines. Each colour represents one trajectory. The thick black line represents the average trajectory, while the horizontal red line shows the value of the CNNC dihedral angle at the minimum potential energy GS structure of the trans-isomer. Note that the values of the CNNC dihedral angle along the trajectories are reported only in the interval 0–180° (due to symmetry) and, therefore, that the average trajectory always stays at a value for the CNNC dihedral angle below 180°.

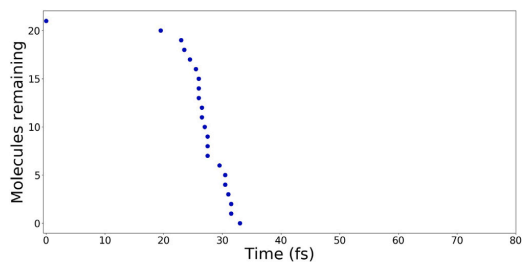


Fig. 7. Time of jump for all reactive trajectories. Each point signifies the jumping time of one reactive trajectory. Observe that the point at $t = 0.0$ has been added.

a QY of 57% was obtained in good agreement with previous calculations (10%–63% [4], 34%–65% [3] and 45%–68% [6]) and experiment (41%–56%) [2].

The time of jump for reactive trajectories was also considered (see Fig. 7) and found to be 19.5 fs–33 fs, yielding a lag time of 27.33 fs, in

reasonably good agreement with previously calculated lifetimes using the TDDFT method (52.7 fs–63.1 fs [3] and 33.9–63 fs [4]) and CAS-methods (53.1 fs–67 fs [3] and 60–67 [6]), but significantly smaller than the experimental value (100–170 fs) [2]. The lag time predicted from an S-curve and the lifetime of an exponential decay are assumed to be comparable as both should give an indication of the time it takes half the molecules to jump. The shorter lag of our calculation can partly be attributed to the method as can be seen from lifetimes of approximately 35 fs being obtained for similar calculations [4]. Also, the TDDFT ES-PES [4] seems to be a little more steep going from the cis-geometry to the CI compared to the ES-PES calculated using CASSCF [5,6]. Another factor, that will shorten the lag time compared to experimental and CASSCF lifetimes is the forcing of the jump. It should also be emphasized that our calculation shows ballistic dynamics rather than exponential, which might also be the cause of the discrepancy with the experimental lifetime. We do however note that such non-exponential decays are not only observed in TDDFT calculations but also in CASSCF simulations [6].

Hence, the simulation is deemed to describe the dynamics of the reaction to a satisfactory degree.

4.2. Normal mode analysis

It can be observed from Fig. 6 that while the jump to the trans GS happens after approximately 25 fs, it is only after 150 fs that the trajectories reach the equilibrium value of the dihedral angle for the trans-isomer. Indeed it seems the dihedral angle settles around a value of approximately 130° for about 100 fs. This feature is also observable in other TDDFT studies [3,9,10] and a recently published SA-CASSCF study [34], however it is not further investigated in either of these studies. Thus, it would appear that there might be other degrees of freedom at play than the CNNC dihedral angle traditionally investigated, as also mentioned by Böckmann et al. [9–11].

Rather than investigating certain DOFs related to important atoms or relevant for a certain mechanism, we now investigate which of all the DOFs are the most dominant. This is done by performing a normal mode analysis. As the molecule before the jump resembles the cis-isomer the most, the first 25 fs of the reaction were considered in relation to the normal modes of this isomer. Likewise, during the latter part of the reaction starting from 50 fs (were the CNNC dihedral angle is above 90° and the molecule thus can be considered to move on the trans-isomer GS) the molecule resembles the trans-isomer. Hence, this part of the reaction was considered in relation to the trans-isomer normal modes.

By visualizing the activity of the relevant normal modes (see SI for movies of trans-isomer normal modes 2 and 5), Fig. 8 was obtained. From here it can be seen that the most active modes during the first 25 fs of the reaction are modes 1–3. The remaining modes are however, also quite active, and thus while the first three normal modes might give a good indication of the important geometrical parameters, they are not expected to fully describe the dynamics on the ES. Considering instead the time following the jump and until the trans-isomer equilibrium structure is reached, it is clear that two trans-isomer normal modes 2 and 5 are significantly more active than the rest. Indeed, the remaining normal modes seem to show very little activity. Hence, these two normal modes are expected to be good DOFs along which to describe the reaction at least after the jump to the GS. Modes 2 and 5 can be related to the CNNC dihedral angle and the CCN angle as can be seen in Section 4.3. For further analysis of modes 2 and 5, see also the SI, section 2.2.2. That the reaction is well described by these two modes can also be seen in Fig. 9, where a smooth path towards the energy minimum is observed for the trajectory. The path does not appear to be the steepest possible downhill path, however this is hardly surprising considering the large kinetic energy available to the trajectories following the jump. The oscillations of the modes at longer timescales, caused by the kinetic energy available to the

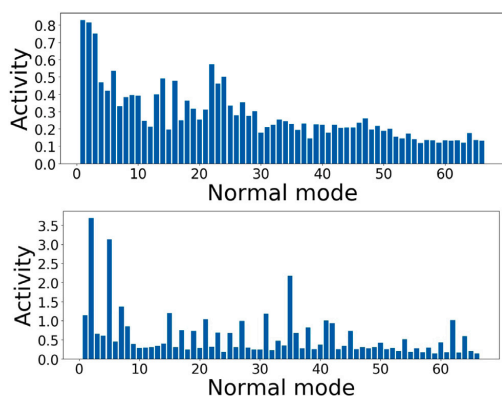


Fig. 8. The normal mode activity of reactive trajectories (top) between 0 fs and 25 fs for each of the cis-isomer normal modes and (bottom) between 50 fs and 150 fs for each of the trans-isomer normal modes.

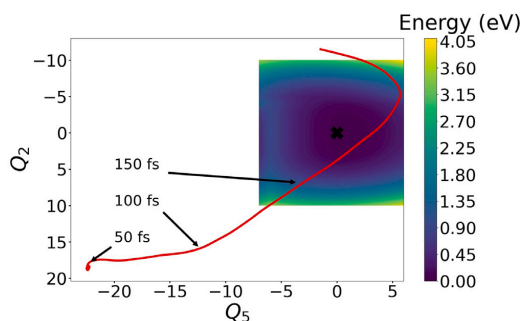


Fig. 9. Plot of a reactive trajectory along the trans-isomer normal modes 2 and 5. Normal mode 2 can be considered as oscillations in the CCN and to some extent also the CCN angles, while normal mode 5 only shows oscillations in the CCN angles. The large black X marks the equilibrium structure and around this point the unrelaxed 2D-GS-PES is shown in an area, in which this unrelaxed calculation can be expected to give a reasonable description of the PES. The three black arrows show the time at the indicated points.

molecule, are evident from the top right corner of the figure, where the trajectory appears to begin to move uphill in potential energy. Observe that the unrelaxed 2D GS-PES in Fig. 9 is only meaningful close to the minimum, and hence only a small part is shown to indicate the position of this minimum. At larger displacements along only these normal modes, the structure becomes highly distorted, which allows very large (unphysical) potential energies to be reached. This indicates that relaxation to some extent does of course occur in many degrees of freedom and not solely along the two considered here.

4.3. Relating the normal modes to angles

Based on visualizations of relevant normal modes, as well as reactive trajectories, structural parameters were determined for further investigation. The equilibrium structure of the appropriate isomer was then displaced along one of the normal modes of interest in 10 steps in either direction (+/−). For each resulting structure the structural parameters of interest were determined. It could thus be determined which parameters were affected by the given normal mode.

Visualizing the relevant cis-isomer modes shows that they all correspond to different twisting of the benzene rings. If their effect on

structural parameters as those presented in Table 1 are determined, it turns out, that only mode 3, which appears to be the least active of the three, changes the CCN angle, while all three modes to some extent affects the CCN angle. This might be an indication, that the CCN angle should be considered, when investigating the cis-to-trans isomerization. However, as the activity plot in Fig. 8 (top) shows that practically all cis-modes to some extent are active prior to the jump, this needs to be investigated further. By considering the trans-isomer modes in Fig. 8 (bottom), very few modes are observed to be active after the jump. It is found, that the trans-isomer mode 2 is simply an out of plane bend of the CCN angle, while the trans-isomer mode 5 is more of an in plane twist of the benzene rings. Both modes are observed to change the CCN angle, albeit the change is very small in mode 2. Only mode 2 changes the CCN angle. Firstly, it can be observed from Fig. 10 that the CCN angles rather surprisingly decrease during the first approximately 50 fs, despite the optimized geometries for both isomers as well as the CI indicating that no change should be observed in this angle. Considering the most active cis-isomer normal modes before the jump however, they all give rise to a change in this angle, explaining this initial behaviour. Thus, our findings show that simply considering optimized geometries along the reaction path is not sufficient, when attempting to describe the full dynamics.

After the first 50 fs, the CCN angles are observed to increase from approximately 140° to 180° during the time, where the dihedral angle seems settled around 130°.

Considering mode 5 in more detail, its frequency is found to correspond to an oscillation period of approximately 150 fs corresponding well with the timescale on which the CCN angle oscillates, underlining the importance of these angles. Hence, the settling of the CCN angle at a value below the equilibrium value as observed in Fig. 6 is ascribed to the distortion of the CCN angles, which must be relaxed sufficiently, before the CCN angle can reach its equilibrium. As both the trans-isomer mode 2 and cis-isomer mode 3 appear to change both the CCN and the CCN angles these DOFs must be considered coupled. Hence, once the reaction starts the cis-normal mode 3 is activated, which changes both the CCN dihedral angle and distorts the CCN angle. After the jump to the trans-isomer ground state, the distortion along normal modes related to these angles, i.e. trans-isomer modes 2 and 5, will be very large causing a significant gradient and thus movement along these modes. As the displacement along normal mode 5 is larger than along mode 2, the initial movement after the jump will primarily be along this mode, thus hindering the motion along the mode related to the CCN dihedral angle (normal mode 2), until the distortion along the two modes becomes comparable.

As what appears to be the most relevant normal modes, are strongly related to the CCN dihedral angle and the CCN angles, it would be natural to attempt to describe the reaction along those two DOFs instead. If we simply consider the trajectories along these two angles, we obtain Fig. 11. From this figure it is evident that all trajectories behave in the same way along these two degrees of freedom, and any trajectory can thus be considered representative for the reaction. We thus investigate how a reactive trajectory moves superimposed on a relaxed GS-PES computed along the CCN and CCN angles in Fig. 12. Firstly, it is noted from Fig. 12 that the differences in potential energies of the reactive trajectory at the points indicated by arrows are significantly larger than what would be expected from the underlying relaxed GS-PES. The GS-PES indicates a change of at most 0.5 eV, while a change of more than 1 eV is observed between the two arrows in the middle. This indicates that the relaxed GS-PES in these two degrees of freedom is not sufficient to explain the behaviour of the trajectories. In addition it is observed that, on this GS-PES, the initial movement of the trajectories are not along the steepest downhill slope towards the equilibrium structure. In fact, the trajectory appears to move with roughly constant potential energy. To investigate if this is caused by a potential energy barrier, a trajectory was simulated from the structure directly following the forced jump with zero initial

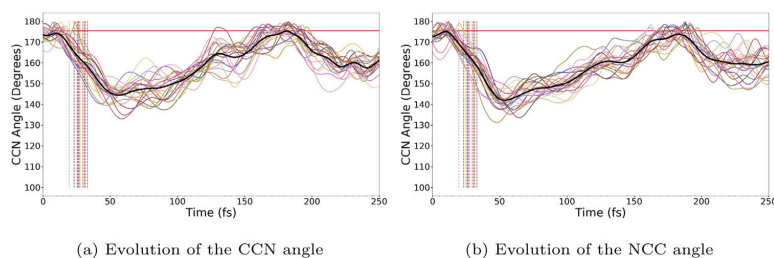


Fig. 10. All reactive trajectories from cis Azobenzene illustrated by CCN (10a) and NCC (10b) angles between the two carbons at the ends of the benzene ring and the closest nitrogen of the azo-group over time. Time of jump is indicated by the vertical lines. Each colour represents one trajectory, while the thick black line represents the average trajectory. The horizontal red line shows the value of the CCN angle at the minimum potential energy GS trans-isomer structure.

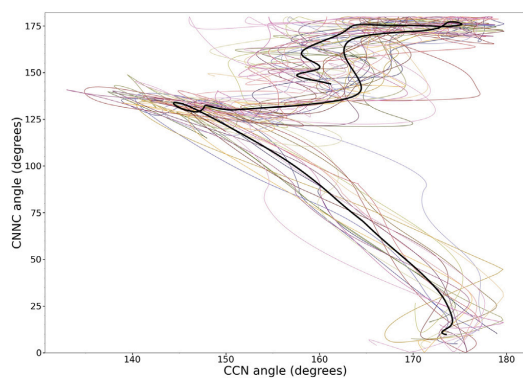


Fig. 11. Evolution of the CNNC angle vs the CCN angle of all reactive trajectories. Each colour represents one trajectory. The thick black line represents the average trajectory.

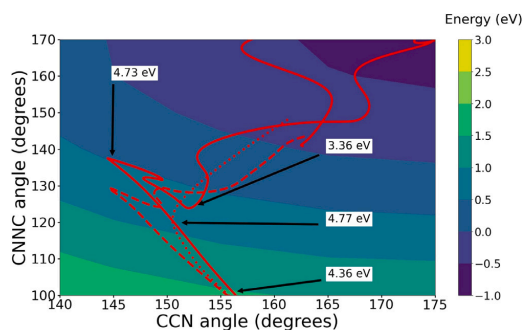


Fig. 12. 2D relaxed GS-PES along CNNC dihedral angle and the CCN angle (the corresponding NCC angle has been allowed to relax) overlaid with reactive cis-to-trans trajectories. The energies of the trajectory is observed to be much higher than those of the underlying PES, indicating a highly distorted molecular structure and hence, that the reaction cannot simply be considered along the CNNC and CCN angles, while all other DOFs relax. The black arrows show the potential energy of the reactive trajectory (solid red line) at the points indicated. The corresponding MEP (dotted red line) and trajectories starting with zero velocity (dashed red line) from the structure of the reactive trajectory directly following the forced jump to the GS is also shown.

velocity. This trajectory however is found to move in the same way as the original trajectory and thus it appears that it is not an energy barrier at this point that hinders the most direct movement towards the equilibrium structure. A minimum energy path (MEP) was also

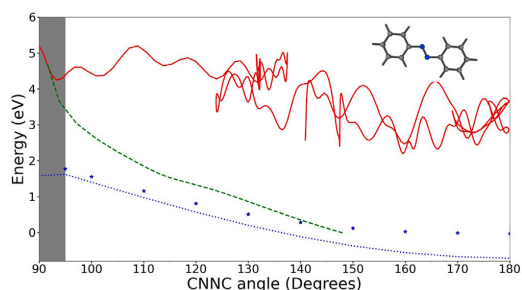


Fig. 13. Potential energy vs. CNNC angle on the trans-isomer side of the 1D-PES. The potential energy found by a relaxed energy scan is shown in blue for the GS (dotted) and for the GS potential energies computed from relaxed ES structures (stars). The green line represents the MEP of a (representative) reactive trajectory starting from the structure obtained shortly after the jump to the GS. The red line shows the actual potential energy of that same trajectory during simulation as also shown in Fig. 12. The potential energy equal to zero here corresponds to the energy of the equilibrium structure of the cis-isomer in the GS.

computed on the full-dimensional GS-PES from the structure directly following the forced jump and evidently shows the same movement trends in the CCN and CNNC angles as the other trajectories plotted. However, the MEP is observed to be significantly smoother than the trajectories that allow kinetic energy to be picked up along the path, which would allow for movement also towards areas of larger potential energy.

The observed behaviour indicates that the molecule needs to rearrange most likely due to a significant strain along these DOFs, before the equilibrium structure can be reached. This finding is in good agreement with the previously proposed twist mechanism [9,10], which does indeed consist in a change of the CNNC dihedral angle followed by rearrangement of the benzene rings. To investigate this further, the 1D relaxed GS-PES along the CNNC angle is considered. From Fig. 13 it is evident that the potential energy of the MEP and actual trajectory is initially much higher than for the relaxed structures. This however can be explained by the starting point of the calculation, which is a highly distorted structure compared to the 2D relaxed GS-PES. The main point of interest to note however, is that the slope of the MEP curve is much steeper than any of the relaxed curves indicating other degrees of freedom at play. This can also be seen from the actual trajectory, which shows an initial drop in potential energy, only to then use the gained kinetic energy to move towards an area of higher potential energy. This gain in kinetic energy also explains the many twists of the trajectory on the 2D relaxed GS-PES and indeed from Fig. 12 the MEP is observed to move rather smoothly towards the minimum potential energy point after the initial detour. This detour however cannot be

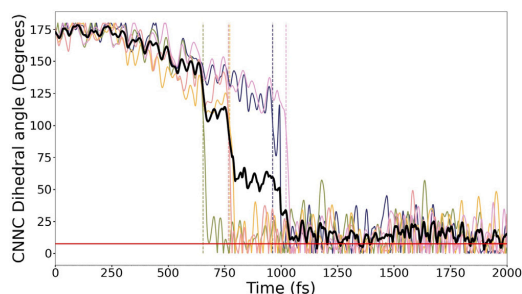


Fig. 14. Time evolution of the CNNC dihedral angle of all reactive trajectories starting from trans-azobenzene. Vertical lines indicate jump times. Each colour represents one trajectory. The horizontal red line shows the value of the CNNC dihedral angle at the minimum potential energy GS structure of the cis-isomer. The thick black curve shows the average reactive trajectory. Note that the values of the CNNC dihedral angle along the trajectories are reported only in the interval 0–180° (due to symmetry) and, therefore, that the average trajectory eventually oscillates around a larger positive value for the CNNC dihedral angle instead of the GS equilibrium value of the cis isomer.

explained by the 1D relaxed GS-PES. While the MEP does not move uphill in potential energy on the 2D relaxed GS-PES, it does not take the most direct route towards the minimum, indicating that while the two angles provide a good description of the reaction, they do not provide as full a picture of the reaction after the time of jump as the two trans-isomer normal modes. In addition, allowing the remaining DOFs to relax, while changing the CNNC and CCN angles was shown in Fig. 12 to produce a wrong description of the process, and thus we cannot study this reaction by a few static electronic structure calculations, but rather we need to simulate the actual dynamics in order to explain the isomerization, since the molecule during reaction appears to be very far from relaxed.

5. Trans-to-cis isomerization

5.1. QY and lag time

We now turn our attention to the slower trans-to-cis isomerization. From Fig. 1 a significantly lower QY of the trans-to-cis isomerization compared to that of the cis-to-trans isomerization was anticipated. Indeed, of the 38 simulated trajectories, 33 were non-reactive (See Fig. 15 and for further details section 3.2 in the SI), while 5 were reactive (See Fig. 14). This gives a QY of approximately 13.2%, which is in reasonable agreement with experiment (23%–35%) [2] and other simulations (11%–33%) [3] although on the low side.

Considering the jump times of the trans-to-cis reaction (0.655 ps–1.02 ps), a lag time of 0.84 ps is obtained (See Fig. 16), in good agreement with the experimental lifetime (0.9 ps–1.4 ps) [2]. This comparison has already been justified above. That the lag time is shorter than the experimentally determined lifetime is expected as the jump is forced.

In addition to the reasonable agreement with experiment, we observe that the reactive trajectories are very consistent in their behaviour. Hence, despite the small number of trajectories investigated, the simulation can be expected to offer a representative description of the reactive reaction path, thus allowing us to gain insights into the dynamics.

The non-reactive trajectories are observed to behave less consistently than the reactive ones with respect to the value of the CNNC angle at the time of jump. Here, a wide range of different values are observed, as can be seen from Fig. 15. As the non-reactive trajectories are not the main point of interest here, this will not be investigated or discussed further.

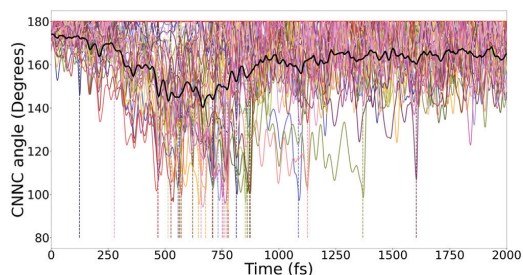


Fig. 15. Time evolution of the CNNC dihedral angle of all non-reactive trajectories starting from trans-azobenzene. Vertical lines indicate jump times. Each colour represents one trajectory. The horizontal red line shows the value of the CNNC dihedral angle at the minimum potential energy GS structure of the trans-isomer. The thick black curve shows the average non-reactive trajectory. Note that the values of the CNNC dihedral angle along the trajectories are reported only in the interval 0–180° (due to symmetry) and, therefore, that the average trajectory always stays at a value for the CNNC dihedral angle below 180°.

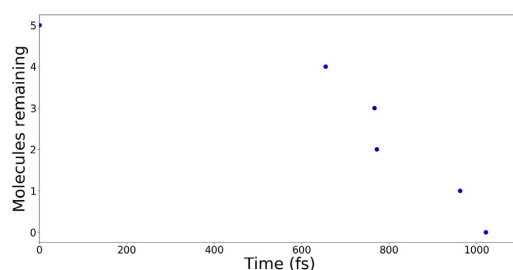


Fig. 16. Plot of jump times of the trans-to-cis isomerization. Each point represents the jump time of one reactive trajectory. Observe that the point at $t = 0.0$ has been added.

5.2. Explaining the longer timescale

In order to investigate the reason for the long lifetime of the trans-to-cis isomerization one might investigate the evolution of the often reported CNN angles over time, however as seen in Fig. 13 of the SI, no obvious indication of the relaxation of the CNN angles being a driving force can be seen.

Observing closely the evolution of the CNNC dihedral angle of the reactive trajectories in Fig. 14 prior to the jump to the ground state one can see a fairly smooth decrease in the CNNC dihedral angle over time. Indeed, if one considers an average reactive trajectory before the jump, one can fit a cosine function to this average, as seen in Fig. 17. The fit is reasonable good and would correspond to an ES oscillation half-period from the trans- (180°) to the cis-isomer (ca. 0°) of approximately 2.4 ps. A quarter period (1.2 ps) thus corresponds to the reaction time, i.e. the time it takes to reach the CI at a CNNC dihedral angle of approximately 90°. This reaction time is in good agreement with the experimentally determined lifetime of the reaction (0.9 ps–1.4 ps) [2]. The smoothness of the curve prior to the jump indicates that no potential energy barrier is present during the simulation as also expected from the 1D-ES-PES in Fig. 1a, when the forced jump is taken into account, and thus this cannot be the cause of the longer timescale. In addition, the good agreement between the oscillation period of the fitted cosine curve and the experimental lifetime indicates that the longer timescale of the trans-to-cis isomerization is simply a result of a slow (quarter of an) oscillation of the CNNC dihedral angle in the ES.

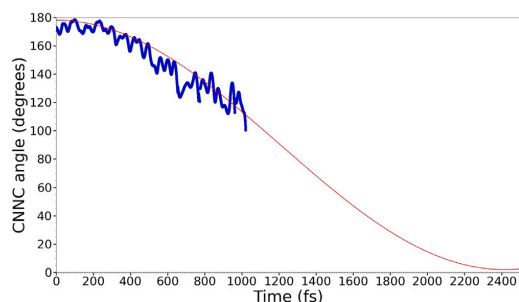


Fig. 17. Time evolution of the CNNC dihedral angle of an average of the reactive trans-to-cis trajectories (blue curve) fitted to a cosine function, $\theta_{CNNC} = 90^\circ + 88^\circ \cos\left(\frac{2\pi}{4833 \text{ fs}} t\right)$ (red curve). The evolution of the fit up to the point where a dihedral angle of approximately zero degrees (cis-isomer) is shown.

6. Conclusion

Simulations of the isomerization of Azobenzene have been carried out utilizing the procedure of forced jumps within the surface hopping framework in order to circumvent the problems often arising for TDDFT calculations around the area of the CI between the GS and first excited state.

The simulations for both the cis-to-trans and trans-to-cis isomerization showed results of QY and lag times in reasonable agreement with previous studies and experiment. In addition, the trajectories of the same type all seemed to behave in the same way with the exception of the non-reactive trans-to-cis trajectories, which showed a wider range of jumping values for the CNNC angle. It has therefore been concluded that the investigated reactive trajectories give a sufficiently representative description of the structural evolution of the molecule during the photoisomerization.

It was found that the cis-to-trans isomerization occurs as a result of movement along two normal modes, rather than simply along the CNNC dihedral angle, which is the most common description. While the first normal mode is largely responsible for the change in the dihedral angle both modes also influence the CCN angle between the benzene ring and the azobond, and the change in this angle appears to halt the change in the dihedral angle. It was found that while these two angles seem to be the most important in the reaction other degrees of freedom might also be needed in describing the reaction in such a coordinate system, as the description here did not appear as adequate as the one offered by considering the reaction along the two normal modes. Our observations for the cis-to-trans isomerization corroborate the previously proposed two-step twist mechanism. In contrast to the cis-to-trans isomerization, the trans-to-cis isomerization seems to happen in one smooth step albeit a slow one. The isomerization appears to simply be a result of slow excited-state oscillations in the CNNC dihedral angle, without the impeding of a significant potential energy barrier.

Finally, the importance of the previously reported planar CI was investigated and, while more studies will be required, it appears that the significance of this CI is not only geometry dependent as suggested in other studies, but is also strongly influenced by the choice of functional.

CRedit authorship contribution statement

Anna Kristina Schnack-Petersen: Writing – review & editing, Writing – original draft, Investigation, Formal analysis, Data curation, Visualization. **Mátyás Pápai:** Conceptualization, Formal analysis, Funding acquisition, Investigation, Supervision, Writing – review & editing. **Klaus Braagaard Møller:** Writing – review & editing, Supervision, Investigation, Funding acquisition, Formal analysis, Conceptualization.

Declaration of competing interest

The authors declare that they have no known competing financial interests or personal relationships that could have appeared to influence the work reported in this paper.

Acknowledgements

The research leading to the presented results has received funding from the Hungarian National Research, Development and Innovation Fund, Grant No. NKFIH PD 134976 (MP), the Government of Hungary and the European Regional Development Fund under grant VEKOP-2.3.2-16-2017-00015 (MP), and the Independent Research Fund Denmark, Grant No. 8021-00347B (KBM,MP).

MP acknowledges support from the János Bolyai Scholarship of the Hungarian Academy of Sciences.

AKSP thanks the DTU Partnership PhD programme for funding.

Appendix A. Supplementary data

Supplementary material related to this article can be found online at <https://doi.org/10.1016/j.jphotochem.2022.113869>.

- Further computational details
- Evaluation of a suitable potential energy gap for the forced jump
- Tables reporting jumping geometries
- Tables reporting optimized CI geometries
- Further investigations of the potential energy evolution of the cis-to-trans isomerization
- Additional normal mode analysis of trans-isomer normal modes
- Results for the cis-to-trans isomerization using the B3LYP functional
- Investigation of non-reactive trans-to-cis trajectories
- Investigation of the evolution of the CNN angles for reactive trans-to-cis trajectories
- Results for the trans-to-cis isomerization using the B3LYP functional
- Movies of BHHLYP cis-isomer normal modes 1–3
- Movies of BHHLYP trans-isomer normal modes 2 and 5
- Movies of 2 BHHLYP non-reactive and 2 reactive cis-to-trans trajectories
- Movies of 2 BHHLYP non-reactive and 2 reactive trans-to-cis trajectories

References

- [1] G. Hartley, The cis-form of azobenzene, *Nature* 140 (1937) 281, <http://dx.doi.org/10.1038/140281a0>.
- [2] H.M. Bandara, S.C. Burdette, Photoisomerization in different classes of azobenzene, *Chem. Soc. Rev.* 41 (5) (2012) 1809–1825, <http://dx.doi.org/10.1039/c1cs15179g>.
- [3] L. Yue, Y. Liu, C. Zhu, Performance of tddft with and without spin-flip in trajectory surface hopping dynamics: cis-trans azobenzene photoisomerization, *Phys. Chem. Chem. Phys.* 20 (2018) 24123–24139, <http://dx.doi.org/10.1039/C8CP03851A>.
- [4] L. Ye, C. Xu, F.L. Gu, C. Zhu, Functional and basis set dependence for time-dependent density functional theory trajectory surface hopping molecular dynamics: Cis-azobenzene photoisomerization, *J. Comput. Chem.* 41 (7) (2020) 635–645, <http://dx.doi.org/10.1002/jcc.26116>, <https://onlinelibrary.wiley.com/doi/pdf/10.1002/jcc.26116>. URL <https://onlinelibrary.wiley.com/doi/abs/10.1002/jcc.26116>.
- [5] J. Casellas, M.J. Bearpark, M. Reguero, Excited-state decay in the photoisomerisation of azobenzene: A new balance between mechanisms, *Chem. Phys. Chem.* 17 (19) (2016) 3068–3079, <http://dx.doi.org/10.1002/cphc.201600502>, <https://chemistry-europe.onlinelibrary.wiley.com/doi/pdf/10.1002/cphc.201600502>. URL <https://chemistry-europe.onlinelibrary.wiley.com/doi/abs/10.1002/cphc.201600502>.
- [6] M. Pederzoli, J. Pittner, M. Barbatti, H. Lischka, Nonadiabatic molecular dynamics study of the cis-trans photoisomerization of azobenzene excited to the s_1 state, *J. Phys. Chem. A* 115 (41) (2011) 11136–11143, <http://dx.doi.org/10.1021/jp2013094>, <https://doi.org/10.1021/jp2013094>.

- [7] G. Granucci, M. Persico, Excited state dynamics with the direct trajectory surface hopping method: azobenzene and its derivatives as a case study, *Theor. Chem. Acc.* 117 (2007) 1131–1143, <http://dx.doi.org/10.1007/s00214-006-0222-1>.
- [8] E. Wei-Guang Diao, A new trans-to-cis photoisomerization mechanism of azobenzene on the $s1(n, \pi^*)$ surface, *J. Phys. Chem. A* 108 (6) (2004) 950–956, <http://dx.doi.org/10.1021/jp031149a>, arXiv:https://doi.org/10.1021/jp031149a.
- [9] M. Böckmann, N.L. Doltsinis, D. Marx, Azobenzene photoswitches in bulk materials, *Phys. Rev. E* 78 (2008) 036101, <http://dx.doi.org/10.1103/PhysRevE.78.036101>, URL <https://link.aps.org/doi/10.1103/PhysRevE.78.036101>.
- [10] M. Böckmann, N.L. Doltsinis, D. Marx, Nonadiabatic hybrid quantum and molecular mechanic simulations of azobenzene photoswitching in bulk liquid environment, *J. Phys. Chem. A* 114 (2) (2010) 745–754, <http://dx.doi.org/10.1021/jp910103b>, arXiv:https://doi.org/10.1021/jp910103b.
- [11] M. Böckmann, S. Braun, N.L. Doltsinis, D. Marx, Mimicking photoisomerisation of azo-materials by a force field switch derived from nonadiabatic ab initio simulations: Application to photoswitchable helical foldamers in solution, *J. Chem. Phys.* 139 (8) (2013) 084108, <http://dx.doi.org/10.1063/1.4818489>, arXiv:https://doi.org/10.1063/1.4818489.
- [12] J.A. Gámez, O. Weingart, A. Koslowski, W. Thiel, Cooperating dinitrogen and phenyl rotations in trans-azobenzene photoisomerization, *J. Chem. Theory Comput.* 8 (7) (2012) 2352–2358, <http://dx.doi.org/10.1021/ct300303s>, pMID: 26588968, arXiv:https://doi.org/10.1021/ct300303s.
- [13] Z. Mahimwalla, J. Yager, K.G. Mamiya, A. Shishido, A. Primagi, C.J. Barret, Azobenzene photomechanics: prospects and potential applications, *Polym. Bull.* 69 (2012) 967–1006, <http://dx.doi.org/10.1007/s00289-012-0792-0>.
- [14] J. García-Amorós, D. Velasco, Recent advances towards azobenzene-based light-driven real-time information-transmitting materials, *Beilstein J. Org. Chem.* 8 (2012) 1003–1017, <http://dx.doi.org/10.3762/bjoc.8.113>.
- [15] N. Tamai, H. Miyasaka, Ultrafast dynamics of photochromic systems, *Chem. Rev.* 100 (5) (2000) 1875–1890, <http://dx.doi.org/10.1021/cr9800816>, arXiv:https://doi.org/10.1021/cr9800816.
- [16] H. Bach, K. Anderle, T. Fuhrmann, J.H. Wendorff, Biphoton-induced refractive index change in 4-amino-4'-nitroazobenzene/polycarbonate, *J. Phys. Chem.* 100 (10) (1996) 4135–4140, <http://dx.doi.org/10.1021/jp952094i>, arXiv:https://doi.org/10.1021/jp952094i.
- [17] Z. Liu, C. Zhao, M. Tang, S. Cai, Electrochemistry of cis-azobenzene chromophore in coulombically linked self-assembled monolayer-langmuir-blodgett composite monolayers, *J. Phys. Chem.* 100 (43) (1996) 17337–17344, <http://dx.doi.org/10.1021/jp9536615>, arXiv:https://doi.org/10.1021/jp9536615.
- [18] P.H. Rasmussen, P.S. Ramanujam, S. Hvilsted, R.H. Berg, A remarkably efficient azobenzene peptide for holographic information storage, *J. Am. Chem. Soc.* 121 (20) (1999) 4738–4743, <http://dx.doi.org/10.1021/ja981402y>, arXiv:https://doi.org/10.1021/ja981402y.
- [19] R. Hagen, T. Bieringer, Photoaddressable polymers for optical data storage, *Adv. Mater.* 13 (23) (2001) 1805–1810, [http://dx.doi.org/10.1002/1521-4095\(200112\)13:23<1805::AID-ADMA1805>3.0.CO;2-V](http://dx.doi.org/10.1002/1521-4095(200112)13:23<1805::AID-ADMA1805>3.0.CO;2-V), arXiv:https://onlinelibrary.wiley.com/doi/pdf/10.1002/1521-4095(28200112)2913%3A23%3C1805%3A%3AAID-ADMA1805%3E3.0.CO%3B2-V, URL [https://onlinelibrary.wiley.com/doi/abs/10.1002/1521-4095\(28200112\)2913%3A23%3C1805%3A%3AAID-ADMA1805%3E3.0.CO%3B2-V](https://onlinelibrary.wiley.com/doi/abs/10.1002/1521-4095(28200112)2913%3A23%3C1805%3A%3AAID-ADMA1805%3E3.0.CO%3B2-V).
- [20] M. Abedi, M. Pápai, N.E. Henriksen, K.B. Møller, M.B. Nielsen, K.V. Mikkelsen, Theoretical investigation on the control of macrocyclic dihydroazulene/azobenzene photoswitches, *J. Phys. Chem. C* 123 (42) (2019) 25579–25584, <http://dx.doi.org/10.1021/acs.jpcc.9b06975>, arXiv:https://doi.org/10.1021/acs.jpcc.9b06975.
- [21] T. Ikeda, O. Tsutsumi, Optical switching and image storage by means of azobenzene liquid-crystal films, *Science* 268 (5219) (1995) 1873–1875, <http://dx.doi.org/10.1126/science.268.5219.1873>, arXiv:https://science.sciencemag.org/content/268/5219/1873.full.pdf, URL <https://science.sciencemag.org/content/268/5219/1873>.
- [22] J. Pang, C. Gao, L. Shu, X. Hu, M. Li, Dft calculations: Bridged-azo working with visible light, *Comput. Theor. Chem.* 1191 (2020) 113041, <http://dx.doi.org/10.1016/j.comptc.2020.113041>, URL <https://www.sciencedirect.com/science/article/pii/S2210271X20303418>.
- [23] A. Natansohn, P. Rochon, Photoinduced motions in azo-containing polymers, *Chem. Rev.* 102 (11) (2002) 4139–4176, <http://dx.doi.org/10.1021/cr970155y>, arXiv:https://doi.org/10.1021/cr970155y.
- [24] V. Shibaev, A. Bobrovsky, N. Boiko, Photoactive liquid crystalline polymer systems with light-controllable structure and optical properties, *Prog. Polym. Sci.* 28 (5) (2003) 729–836, [http://dx.doi.org/10.1016/S0079-6700\(02\)00086-2](http://dx.doi.org/10.1016/S0079-6700(02)00086-2), URL <https://www.sciencedirect.com/science/article/pii/S0079670002000862>.
- [25] S. Krause, J.D. Evans, V. Bon, S. Crespi, W. Danowski, W.R. Browne, S. Ehrling, F. Walenszus, D. Wallacher, N. Grimm, et al., Cooperative light-induced breathing of soft porous crystals via azobenzene buckling, 2020, <http://dx.doi.org/10.26434/chemrxiv.13286009.v1>, URL https://chemrxiv.org/articles/preprint/Cooperative_Light-Induced_Breathing_of_Soft_Porous_Crystals_via_Azobenzene_Buckling/13286009/1.
- [26] A. Credi, Artificial molecular motors powered by light, *Aust. J. Chem.* 59 (2006) 157–169, <http://dx.doi.org/10.1071/CH06025>.
- [27] T. Hugel, N.B. Holland, A. Cattani, L. Moroder, M. Seitz, H.E. Gaub, Single-molecule optomechanical cycle, *Science* 296 (5570) (2002) 1103–1106, <http://dx.doi.org/10.1126/science.1069856>, arXiv:https://science.sciencemag.org/content/296/5570/1103.full.pdf, URL <https://science.sciencemag.org/content/296/5570/1103>.
- [28] A. Harada, Cyclodextrin-based molecular machines, *Acc. Chem. Res.* 34 (6) (2001) 456–464, <http://dx.doi.org/10.1021/ar000174l>, arXiv:https://doi.org/10.1021/ar000174l.
- [29] R. Ballardini, V. Balzani, A. Credi, M.T. Gandolfi, M. Venturi, Artificial molecular-level machines: Which energy to make them work? *Acc. Chem. Res.* 34 (6) (2001) 445–455, <http://dx.doi.org/10.1021/ar000170g>, arXiv:https://doi.org/10.1021/ar000170g.
- [30] P. Tavadze, G. Avendaño Franco, P. Ren, X. Wen, Y. Li, J.P. Lewis, A machine-driven hunt for global reaction coordinates of azobenzene photoisomerization, *J. Am. Chem. Soc.* 140 (1) (2018) 285–290, <http://dx.doi.org/10.1021/jacs.7b10030>, arXiv:https://doi.org/10.1021/jacs.7b10030.
- [31] F. Aleotti, L. Soprani, A. Nenov, R. Berardi, A. Arcioni, C. Zannoni, M. Garavelli, Multidimensional potential energy surfaces resolved at the rapt2 level for accurate photoinduced isomerization dynamics of azobenzene, *J. Chem. Theory Comput.* 15 (12) (2019) 6813–6823, <http://dx.doi.org/10.1021/acs.jctc.9b00561>, pMID: 31647648, arXiv:https://doi.org/10.1021/acs.jctc.9b00561.
- [32] J.K. Yu, C. Bannwarth, R. Liang, E.G. Hohenstein, T.J. Martínez, Nonadiabatic dynamics simulation of the wavelength-dependent photochemistry of azobenzene excited to the $\pi\pi^*$ and $\pi\pi^*$ excited states, *J. Am. Chem. Soc.* 142 (49) (2020) 20680–20690, <http://dx.doi.org/10.1021/jacs.0c09056>, pMID: 33228358, arXiv:https://doi.org/10.1021/jacs.0c09056.
- [33] F. Segatta, A. Nenov, S. Orlandi, A. Arcioni, S. Mukamel, M. Garavelli, Exploring the capabilities of optical pump x-ray probe nexafs spectroscopy to track photo-induced dynamics mediated by conical intersections, *Faraday Discuss.* 221 (2020) 245–264, <http://dx.doi.org/10.1039/C9FD00073A>.
- [34] I.C.D. Merritt, D. Jacquemin, M. Vacher, Cis \rightarrow trans photoisomerisation of azobenzene: a fresh theoretical look, *Phys. Chem. Chem. Phys.* 23 (2021) 19155–19165, <http://dx.doi.org/10.1039/D1CP01873F>.
- [35] F. He, X. Ren, J. Jiang, G. Zhang, L. He, Real-time, time-dependent density functional theory study on photoinduced isomerizations of azobenzene under a light field, *J. Phys. Chem. Lett.* 13 (2) (2022) 427–432, pMID: 34989580, arXiv:https://doi.org/10.1021/acs.jpclett.1c03442.
- [36] S. Saeed, P.A. Channar, A. Saeed, F.A. Larik, Fluorescence modulation of cdte nanowire by azobenzene photochromic switches, *J. Photochem. Photobiol. A* 369 (2019) 159–165, <http://dx.doi.org/10.1016/j.jphotochem.2018.09.035>, URL <https://www.sciencedirect.com/science/article/pii/S1010603018309158>.
- [37] L. Yu, C. Xu, Y. Lei, C. Zhu, Z. Wen, Trajectory-based nonadiabatic molecular dynamics without calculating nonadiabatic coupling in the avoided crossing case: trans \leftrightarrow cis photoisomerization in azobenzene, *Phys. Chem. Chem. Phys.* 16 (2014) 25883–25895, <http://dx.doi.org/10.1039/C4CP03498H>.
- [38] D. Keefer, F. Aleotti, J.R. Rouxel, F. Segatta, B. Gu, A. Nenov, M. Garavelli, S. Mukamel, Imaging conical intersection dynamics during azobenzene photoisomerization by ultrafast x-ray diffraction, *Proc. Natl. Acad. Sci. USA* 118 (3) (2021) <http://dx.doi.org/10.1073/pnas.2022037118>, arXiv:https://www.pnas.org/content/118/3/e2022037118.full.pdf, URL <https://www.pnas.org/content/118/3/e2022037118>.
- [39] K. Burke, J. Werschnik, E.K.U. Gross, Time-dependent density functional theory: Past, present, and future, *J. Chem. Phys.* 123 (6) (2005) 062206, <http://dx.doi.org/10.1063/1.1904586>, arXiv:https://doi.org/10.1063/1.1904586.
- [40] D.L. Wheeler, L.E. Rainwater, A.R. Green, A.L. Tomlinson, Modeling electrochromic poly(dioxythiophene)-containing materials through tddft, *Phys. Chem. Chem. Phys.* 19 (2017) 20251–20258, <http://dx.doi.org/10.1039/C7CP04130F>.
- [41] W. Li, X. Cai, Y. Hu, Y. Ye, M. Luo, J. Hu, A tddft study of the low-lying excitation energies of polycyclic cinnolines and their carbocyclic analogues, *J. Mol. Struct. - THEOCHEM* 732 (1) (2005) 21–32, <http://dx.doi.org/10.1016/j.theochem.2005.06.042>, URL <https://www.sciencedirect.com/science/article/pii/S0166128005005476>.
- [42] C.Y. Cheng, M.S. Ryley, M.J. Peach, D.J. Tozer, T. Helgaker, A.M. Teale, Molecular properties in the tamm-dancoff approximation: indirect nuclear spin-spin coupling constants, *Mol. Phys.* 113 (13–14) (2015) 1937–1951, <http://dx.doi.org/10.1080/00268976.2015.1024182>, arXiv:https://doi.org/10.1080/00268976.2015.1024182.
- [43] B.G. Levine, C. Ko, J. Quenneville, T.J. Martínez, Conical intersections and double excitations in time-dependent density functional theory, *Mol. Phys.* 104 (5–7) (2006) 1039–1051, <http://dx.doi.org/10.1080/00268970500417762>, arXiv:https://doi.org/10.1080/00268970500417762.
- [44] M. Abedi, M. Pápai, K.V. Mikkelsen, N.E. Henriksen, K.B. Møller, Mechanism of photoinduced dihydroazulene ring-opening reaction, *J. Phys. Chem. Lett.* 10 (14) (2019) 3944–3949, <http://dx.doi.org/10.1021/acs.jpclett.9b01522>, arXiv:https://doi.org/10.1021/acs.jpclett.9b01522.
- [45] M. Pápai, X. Li, M.M. Nielsen, K.B. Møller, Trajectory surface-hopping photoinduced dynamics from rydberg states of trimethylamine, *Phys. Chem. Chem. Phys.* (2021) <http://dx.doi.org/10.1039/D1CP00771H>.

- [46] M. Richter, P. Marquetand, J. González-Vázquez, I. Sola, L. González, SHARC: ab initio molecular dynamics with surface hopping in the adiabatic representation including arbitrary couplings, *J. Chem. Theory Comput.* 7 (5) (2011) 1253–1258, <http://dx.doi.org/10.1021/ct1007394>.
- [47] A. Hutcheson, A.C. Paul, R.H. Myhre, H. Koch, I.-M. Høyvik, Describing ground and excited state potential energy surfaces for molecular photoswitches using coupled cluster models, *J. Comput. Chem.* 42 (20) (2021) 1419–1429, <http://dx.doi.org/10.1002/jcc.26553>, arXiv:<https://onlinelibrary.wiley.com/doi/pdf/10.1002/jcc.26553>. URL <https://onlinelibrary.wiley.com/doi/abs/10.1002/jcc.26553>.
- [48] S. Mai, P. Marquetand, L. González, Nonadiabatic dynamics: The sharc approach, *WIREs Comput. Mol. Sci.* 8 (2018) e1370, <http://dx.doi.org/10.1002/wcms.1370>.
- [49] S. Mai, M. Richter, M. Heindl, M.F.S.J. Menger, A. Atkins, M. Ruckebauer, F. Plasser, L.M. Ibele, S. Kropf, M. Oppel, P. Marquetand, L. González, Sharc2.1: Surface hopping including arbitrary couplings — program package for non-adiabatic dynamics, 2019, sharc-md.org.
- [50] F. Neese, The orca program system, *WIREs Comput. Mol. Sci.* 2 (1) (2012) 73–78, <http://dx.doi.org/10.1002/wcms.81>, arXiv:<https://onlinelibrary.wiley.com/doi/pdf/10.1002/wcms.81>. URL <https://onlinelibrary.wiley.com/doi/abs/10.1002/wcms.81>.
- [51] F. Neese, Software update: the orca program system, version 4.0, *WIREs Comput. Mol. Sci.* 8 (1) (2018) e1327, <http://dx.doi.org/10.1002/wcms.1327>, arXiv:<https://onlinelibrary.wiley.com/doi/pdf/10.1002/wcms.1327>. URL <https://onlinelibrary.wiley.com/doi/abs/10.1002/wcms.1327>.
- [52] B.G. Levine, J.D. Coe, T.J. Martínez, Optimizing conical intersections without derivative coupling vectors: Application to multistate multireference second-order perturbation theory (ms-caspt2), *J. Phys. Chem. B* 112 (2) (2008) 405–413, <http://dx.doi.org/10.1021/jp0761618>, arXiv:<https://doi.org/10.1021/jp0761618>.
- [53] W. Humphrey, A. Dalke, K. Schulten, VMD – visual molecular dynamics, *J. Mol. Graph.* 14 (1996) 33–38.
- [54] A. Stukowski, Visualization and analysis of atomistic simulation data with OVITO-the Open Visualization Tool, *Modelling Simulation Mater. Sci. Eng.* 18 (1) (2010) <http://dx.doi.org/10.1088/0965-0393/18/1/015012>.
- [55] G. Schaftenaar, J. Noordik, Molden: a pre- and post-processing program for molecular and electronic structures, *J. Comput. Aided Mol. Des.* 14 (2000) 123–134, <http://dx.doi.org/10.1023/A:1008193805436>.
- [56] A. Mostad, C. Rømming, A refinement of the crystal structure of cis-azobenzene, *Acta Chem. Scand.* 25 (10) (1971) 3561–3568, <http://dx.doi.org/10.3891/acta.chem.sc{and}.25-3561>.
- [57] J.A. Bouwstra, A. Schouten, J. Kroon, Structural studies of the system *trans*-azobenzene/*trans*-stilbene. I. A reinvestigation of the disorder in the crystal structure of *trans*-azobenzene, C₁₂H₁₀N₂, *Acta Crystallogr. C* 39 (8) (1983) 1121–1123, <http://dx.doi.org/10.1107/S0108270183007611>.

APPENDIX D

Manuscript 1

The manuscript "New Implementation of an Equation-of-Motion Coupled Cluster Damped-Response Framework with Illustrative Applications to Resonant Inelastic X-ray Scattering" by Anna Kristina Schnack-Petersen, Torsha Moitra, Sarai D. Folkestad and Sonia Coriani has been submitted to *J. Phys. Chem. A* on November 22nd 2022 and awaits review.

New Implementation of an Equation-of-Motion Coupled-Cluster Damped-Response Framework with Illustrative Applications to Resonant Inelastic X-ray Scattering

Anna Kristina Schnack-Petersen,^{*,†} Torsha Moitra,^{†,‡} Sarai Dery Folkestad,[¶] and
Sonia Coriani^{*,†,¶}

[†]*DTU Chemistry, Technical University of Denmark, DK-2800 Kongens Lyngby, Denmark*

[‡]*Hylleraas Centre for Quantum Molecular Sciences, Department of Chemistry, UiT – The Arctic
University of Norway, 9037 Tromsø, Norway*

[¶]*Department of Chemistry, Norwegian University of Science and Technology, NO-7491
Trondheim, Norway*

E-mail: akrsc@kemi.dtu.dk; soco@kemi.dtu.dk

Abstract

We present an implementation of a damped response framework for calculating resonant inelastic X-ray scattering (RIXS) at the equation-of-motion coupled cluster singles and doubles (CCSD) and second-order approximate coupled cluster singles and doubles (CC2) levels of theory in the open-source program *e^T*. This framework lays the foundation for future extension to higher excitation methods (notably, the coupled cluster singles and doubles with perturbative triples, CC3) and to multilevel approaches.

Our implementation adopts a fully relaxed ground state, and different variants of the core-valence separation projection technique to address convergence issues. Illustrative results are compared with those obtained within the frozen-core core-valence separated approach, available in Q-Chem, as well as with experiment.

The performance of the CC2 method is evaluated in comparison with that of CCSD. It is found that, while the CC2 method is noticeably inferior to CCSD for X-ray absorption spectra, the quality of the CC2 RIXS spectra is often comparable to that of the CCSD level of theory, when the same valence excited states are probed. Finally, we present preliminary RIXS results for a solvated molecule in aqueous solution.

1 Introduction

X-ray spectroscopy has gained tremendous popularity over the past decades.¹⁻⁴ This is a result of massive investments in the development of improved light sources and the refinement of detection techniques, both at large scale experimental facilities and at table-top laboratory setups.^{1,3} Experiments such as X-ray absorption (XAS)²⁻⁴ and X-ray emission (XES)² are nowadays routinely carried out, in particular in the soft X-ray regime (0.1-5keV), where, e.g., the *K*-edge ($1s^{-1}$) of lighter elements like Carbon, Nitrogen and Oxygen, the *L*-edge ($2p^{-1}$) of third row elements like Sulfur, Chlorine and Silicon, and the *M*-edge ($3d^{-1}$) of transition metals are probed. Moreover, thanks to the X-ray pulse sources nowadays available from free-electron lasers and high-harmonic generation setups, it has become possible to use X-ray techniques to monitor ultrafast molecular

transformations with unprecedented temporal, spatial and energetic resolution.^{5,6}

An X-ray technique, which has significantly benefited from the recent advances in X-ray light sources and instrumentation, in particular synchrotrons, is resonant inelastic X-ray scattering (RIXS). This technique is also known as resonant (radiative) inelastic X-ray Raman scattering.⁷⁻¹¹ Broadly speaking, RIXS can be regarded as a two-photon process, equivalent to vibrational Raman scattering. The first step in both processes is the absorption of a photon, for RIXS in the X-ray region (i.e., XAS), and for conventional Raman in the near-IR to UV region.¹² Subsequently, another photon is emitted in the same energy region, i.e., XES for RIXS.^{7,13} Thus, where conventional Raman is used to probe vibrational energy states, RIXS probes (valence) electronic excited states. Like its (infrared-visible) analogue, this two-photon process in the X-ray region is complementary to simple absorption spectroscopy, since their selection rules differ. In terms of molecular orbitals, one can also say that, while XAS probes unoccupied valence orbitals, RIXS studies the correlation between occupied and unoccupied valence orbitals. Figure 1 schematically illustrates the RIXS process both in terms of orbital excitations/de-excitations and of transitions between electronic states. An important difference of RIXS compared to valence region Raman spectroscopy is its element specificity due to the localized nature of the core orbitals, which is seen for all X-ray spectroscopies.¹⁴

With RIXS experiments becoming more feasible and popular during the last decade, even in time-resolved regimes,¹¹ the interest in theoretical approaches capable of simulating the RIXS observables has also increased, as it is deemed essential for the interpretation of the experimental spectra.¹⁵⁻²⁴ A non-exhaustive list in this regard includes methods based on the adiabatic diagrammatic construction (ADC) approach,¹⁶ on time-dependent density functional theory (TDDFT),^{15,21,22} and on coupled cluster (CC) theory.¹⁷⁻²⁰

The key quantity when computing the spectra is the RIXS cross section,⁷ based on the Kramers-Heisenberg-Dirac (KHD) formula.²⁵⁻²⁷ In this formulation the amplitudes are given in terms of a sum-over-states (SOS) expression. It has been argued^{9,16,28} that the SOS formula may be slowly convergent and require a large number of terms in order to span the spectral range of valence and

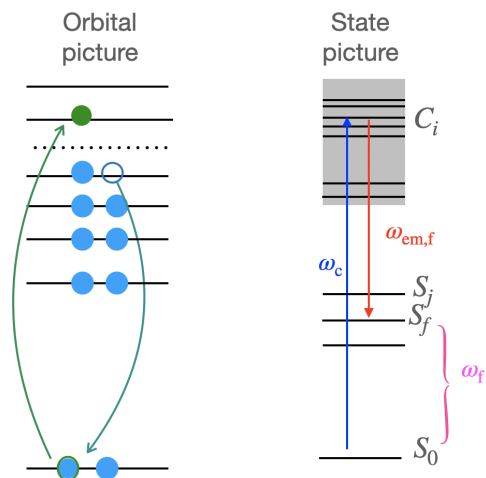


Figure 1: Orbital and state schematics of the RIXS process. *Left*: A core electron is excited to a virtual orbital, and a valence electron falls down to fill the core hole. *Right*: The system is excited into core state C_i (XAS), then decays into valence excited state S_f (XES), emitting photons of energy $\omega_{em,f}$, lower than that used in the XAS step.

core-excited states. A closed-form expression would then be preferable. One such expression was derived and implemented within the ADC framework by Rehn *et al.* in 2017.¹⁶ Two years later, Faber and Coriani¹⁷ proposed an analogous theoretical framework for computing RIXS spectra (along with XES) within coupled cluster singles and doubles (CCSD) response theory. Moreover, Faber and Coriani presented illustrative spectra for small molecular systems based on a prototyping python implementation. A similar framework was later developed for frozen-core equation-of-motion (fc-EOM-)CCSD by Nanda *et al.*,¹⁹ and implemented in the commercial code Q-Chem.²⁹ Although CCSD is not considered the gold standard within the framework of single reference wavefunctions, it provides a computationally feasible approach that yields high accuracy results.³⁰ The method is therefore of interest since approaches, like, e.g., coupled cluster singles and doubles with a perturbative treatment of triple excitations, CCSD(T) and CC3,^{31–33} often advocated as the gold standards, become computationally too demanding with the generally available resources, when considering molecules of a certain size.³⁰ In the future, though, it would be of interest to

extend the framework also to these methods.

When computing molecular properties within the CC framework, one can choose either the response (RSP) framework^{34–36} or the more approximate equation-of-motion (EOM) framework.^{37–40} The EOM framework is often the preferred choice, as it yields results of similar accuracy as RSP at a (slightly) lower cost.⁴¹ In the case of the full CC limit, i.e. all excitations included, the EOM method will in fact yield results identical to the response approach. On the down side, the error of the EOM methods scales with the size of the system. Fortunately, however, the error remains small until hundreds of correlated electron pairs are considered.⁴¹

Despite the results presented by Faber and Coriani,^{17,18} and by Nanda *et al.*^{19,20} appearing promising, available implementations of RIXS at the CC level are to date still scarce. To the best of our knowledge, none is available in an open-source code. In this study, we present such an implementation in the e^T code,⁴² which will be available in a future release. The e^T code features a very efficient implementation of the Cholesky decomposition^{43–46} of the two-electron integrals, which allows for cost-effective implementations in quantum chemistry. Unlike the approach of Refs. 19 and 20, we here work within the framework of a fully relaxed ground state and only invoke the frozen core approximation in the calculation of the valence excited states. Furthermore, the core-valence-separation⁴⁷ (CVS) projection within the damped response solver can be turned-off if desired, although it is generally recommended to use it for convergence.¹⁸ In addition, two possible flavours²⁰ of the CVS projector are available, namely CVS and CVS with uncoupled valence singles (CVS-uS).

We will begin by briefly reviewing the relevant theoretical background for the new implementation in Section 2. To validate it, the RIXS and XES spectra of H₂O will then be calculated at the EOM-CCSD and EOM-CC2 levels of theory and compared to results obtained using the fc-CVS-EOM-CCSD approach, as well as experiment (see Section 4.1). Furthermore, the performance of both levels of theory for RIXS calculations will be evaluated by simulating the RIXS spectra of methanol (CH₃OH) and comparing with experiment. The RIXS spectra of H₂S and para-nitro-aniline (PNA) were likewise evaluated, but here experimental data for comparisons are

not available (see Section 4.2). Finally, in Section 4.3, the CCSD implementation will be employed to simulate imidazole in an aqueous solution. Conclusive remarks are given at the end.

2 Quantities of interest and implementation details

The main quantity of RIXS is the RIXS cross section defined as^{7,9,16,17,48}

$$\sigma_{\theta}^{0f} = \frac{\omega_{\text{em},f}}{\omega_c} \frac{1}{15} \sum_{XY} \left\{ \left(2 - \frac{1}{2} \sin^2 \theta \right) \mathcal{F}_{XY}^{0f}(\omega_c) \mathcal{F}_{XY}^{f0}(\omega_c) + \left(\frac{3}{4} \sin^2 \theta - \frac{1}{2} \right) \left[\mathcal{F}_{XX}^{0f}(\omega_c) \mathcal{F}_{YY}^{f0}(\omega_c) + \mathcal{F}_{YY}^{0f}(\omega_c) \mathcal{F}_{XX}^{f0}(\omega_c) \right] \right\}, \quad (1)$$

where θ is the angle between the incident and emitted photon and X and Y indicate two components of the electric dipole moment operator, i.e., \hat{X} and \hat{Y} . Furthermore, as also shown in Fig. 1, ω_c is the (core) resonance energy and $\omega_{\text{em},f}$ is the emission energy associated with the final valence excited state, f , i.e. $\omega_{\text{em},f} = (\omega_c - \omega_f)$. The quantities $\mathcal{F}_{XY}^{0f}(\omega_c)$ and $\mathcal{F}_{XY}^{f0}(\omega_c)$ are the RIXS transition moments between the initial state, 0, and the final valence excited state, f . These transition moments can be calculated based on the SOS expression for the KHD amplitudes,^{7,16,28} which reads

$$\mathcal{F}_{XY}^{f0}(\omega_c) = \sum_n \left[\frac{\langle \Psi_f | \hat{X} | \Psi_n \rangle \langle \Psi_n | \hat{Y} | \Psi_0 \rangle}{\omega_n - (\omega_c + i\gamma_n)} + \frac{\langle \Psi_f | \hat{Y} | \Psi_n \rangle \langle \Psi_n | \hat{X} | \Psi_0 \rangle}{\omega_n + (\omega_{\text{em},f} + i\gamma_n)} \right], \quad (2)$$

where $|\Psi_n\rangle$ is the wavefunction for the excited state n . In addition, γ_n is the corresponding inverse lifetime, while i is the imaginary phase. In order to simplify this expression, one can assume that all excited states have the same inverse lifetime γ , resulting in

$$\mathcal{F}_{XY}^{f0}(\omega_c) = \sum_n \left[\frac{\langle \Psi_f | \hat{X} | \Psi_n \rangle \langle \Psi_n | \hat{Y} | \Psi_0 \rangle}{\omega_n - (\omega_c + i\gamma)} + \frac{\langle \Psi_f | \hat{Y} | \Psi_n \rangle \langle \Psi_n | \hat{X} | \Psi_0 \rangle}{\omega_n + (\omega_{\text{em},f} + i\gamma)} \right]. \quad (3)$$

As discussed elsewhere,^{16,17} this expression corresponds to a two-photon transition matrix element where a damping factor is added to the frequencies ω_c and $\omega_{\text{em},f}$ in order to maintain the resonant

condition $\omega_c - \omega_f = \omega_{\text{em},f}$.

Our implementation of the KHD amplitude in Eq. (3) is based on a CC ground-state wavefunction, i.e. on the exponential ansatz⁴⁹ $|\Psi_0^{\text{CC}}\rangle = \exp(T)|0\rangle$. Here, $|0\rangle$ is the reference (Hartree-Fock) wavefunction and $T = \sum_m t_m \hat{t}_m$ is the cluster operator, consisting of the excitation operators \hat{t}_m , acting as $\hat{t}_m|0\rangle = |m\rangle$, and of the coupled cluster amplitudes, t_m .

For the CCSD wavefunction considered here, only single and double excitations are included in the cluster operator. The equation of motion (EOM) CC formalism^{37,39} is moreover employed to formally parametrize the final state wavefunction Ψ_f and the intermediate state wavefunctions Ψ_n .

Following the derivation of Faber and Coriani,¹⁷ the EOM-CC right and left RIXS transition moments can be computed as

$$\begin{aligned} \mathcal{F}_{XY}^{0f}(\omega_c) = & \left[\bar{t}^X(\omega_{\text{em},f} - i\gamma) \mathbf{A}^Y + \bar{t}^Y(-\omega_c + i\gamma) \mathbf{A}^X \right. \\ & \left. - (\bar{t} \cdot \xi^X) \bar{t}^Y(-\omega_c + i\gamma) - (\bar{t} \cdot \xi^Y) \bar{t}^X(\omega_{\text{em},f} - i\gamma) \right] R_f \end{aligned} \quad (4)$$

$$\begin{aligned} \mathcal{F}_{XY}^{f0}(\omega_c) = & -L_f \left\{ \mathbf{A}^X t^Y(\omega_c + i\gamma) + \mathbf{A}^Y t^X(-\omega_{\text{em}} - i\gamma) \right. \\ & - (\bar{t} \cdot \xi^X) t^Y(\omega_c + i\gamma) - (\bar{t} \cdot \xi^Y) t^X(-\omega_{\text{em},f} - i\gamma) \\ & \left. - (\bar{t} \cdot t^Y(\omega_c + i\gamma)) \xi^X - (\bar{t} \cdot t^X(-\omega_{\text{em},f} - i\gamma)) \xi^Y \right\}. \end{aligned} \quad (5)$$

In the equations above, \bar{t} is the vector containing the CC ground-state multipliers, L_f and R_f are the left and right EOM-CC eigenvectors of state f , respectively. In addition, $t^X(\omega + i\gamma)$ and $\bar{t}^X(\omega - i\gamma)$ are the vectors containing the CC response amplitudes and multipliers, respectively, while \mathbf{A}^X is the EOM property Jacobian defined, for instance, in Eq. (20) of Ref. 17. The RHS vectors ξ^X and η^X can be found, for instance, in Eqs. (9) and (18) of Ref. 17, respectively.

Our implementation of the damped response solver, used to determine the response amplitudes and multipliers, is based on the algorithm presented in Refs. 17 and 50. We will therefore not repeat it here, but rather refer the reader to those publications for details. In essence, the com-

plex response amplitudes and multipliers are decomposed into real and imaginary components, e.g., $t^X(\omega + i\gamma) = t_{\Re}^X(\omega + i\gamma) + it_{\Im}^X(\omega + i\gamma)$. The response equations are then recast in a (real) pseudosymmetric form, like

$$\begin{pmatrix} (\mathbf{A} - \omega\mathbf{I}) & \gamma\mathbf{I} \\ \gamma\mathbf{I} & -(\mathbf{A} - \omega\mathbf{I}) \end{pmatrix} \begin{pmatrix} t_{\Re}^X \\ t_{\Im}^X \end{pmatrix} = \begin{pmatrix} -\xi_{\Re}^X \\ \xi_{\Im}^X \end{pmatrix} \quad (6)$$

and solved using an iterative subspace algorithm.^{17,50}

Note that within the EOM-CC framework, the solution of the left damped response equation, yielding the response multipliers, is strictly decoupled from the solution of the right damped equation (Eq. (6)). This is because the EOM right-hand-side (RHS) vector η^X does not contain contributions from the response amplitudes. This is not the case in CC linear response (LR-CC) theory, where the response amplitudes enter the RHS of the response multiplier equations.¹⁷ This implies that both RHS of the EOM response equations, ξ^X or η^X , are either strictly real or strictly imaginary, only depending on the nature of the operator \hat{X} . Since the damped response amplitudes and multipliers are decomposed into real and imaginary components, the real and imaginary parts of the transition moments in Eqs. (4)-(5) can be evaluated separately.

In RIXS, we consider only components of the real electric dipole moment operators, \hat{X} , and thus ξ_{\Im}^X and η_{\Im}^X are zero. Furthermore, it is the real part of the RIXS transition strengths that is of interest when computing intensities of the spectra. Thus, we only need to evaluate the real part of the transition moment products, e.g., $\mathcal{F}_{XY}^{0f}(\omega_c)\mathcal{F}_{ZU}^{f0}(\omega_c)$. Moreover, since the focus of our implementation has been on CCSD, the current damped response solver for CC2 is in full doubles space. This will be optimized in the future. Algorithm 1 summarizes the main steps in the calculation of the RIXS cross section.

Our current implementation of RIXS enables the user to either input a value for the core excitation energy, or to request a certain core excitation to be calculated as the initial step (see Algorithm 1). As an additional feature, one can switch on a projection in the damped response solver. It has previously been observed that larger systems, or even small systems described with larger basis

Algorithm 1 Schematic illustration of the RIXS implementation.

```
1: Calculate (or input) the resonant core excitation energy,  $\omega_c$ , using a Davidson solver and CVS.
2: Calculate valence excitation energies,  $\omega_f$ , and solution vectors,  $L_f$  and  $R_f$ , using a Davidson
   solver in a space orthogonal to the pure core space.
3: Determine emission energies  $\omega_{em,f} = \omega_c - \omega_f$ .
4: Collect  $\omega_c$  and  $\omega_{em}$  in array  $\omega$  and generate  $-\omega$ .
5: for  $\text{sign}(\omega)$  do
6:   for  $X = x, y, z$ -component of the dipole operator do
7:     Solve right damped response equations for the response amplitudes,  $t^X(\omega + i\gamma)$  and
        $t^X(-\omega - i\gamma)$ .
8:     Solve left damped response equations for the response multipliers,  $\bar{t}^X(-\omega + i\gamma)$  and
        $\bar{t}^X(\omega - i\gamma)$ .
9:   end for
10: end for
11: for  $f = 1, N_{\text{valence\_excitations}}$  do
12:   Calculate transition moments,  $\mathcal{F}_{XY}^{0f}(\omega_c)$  and  $\mathcal{F}_{XY}^{f0}(\omega_c)$  given in Eqs. (4) and (5).
13:   for  $\theta = \text{angle}_1, \text{angle}_M$  do
14:     Calculate RIXS cross section,  $\sigma_\theta^{0f}$ , for the angle,  $\theta$ , between the incident and scattered
       photon given in Eq. (1).
15:   end for
16: end for
```

sets, display a poor convergence in the damped response solver.^{18,20} This, however, can be remedied by applying a CVS projector in the solver.^{18,20} Faber and Coriani¹⁸ noted that when simply considering the convergence, this projection needs only be employed when solving the response amplitude equations with positive frequencies and the response multiplier equations with negative frequencies. Our implementation of the damped response solver includes the projection in this manner. Additionally, it was reported by Nanda and Krylov²⁰ that when considering systems with significant charge transfer character, the core and valence transitions cannot be completely decoupled. Indeed, the valence single excitations were shown to couple significantly to the core space, which then led the authors to formulate a different variant of CVS, named CVS-uS.²⁰ In CVS-uS, only the double valence excitations were excluded from the solution of the damped response equations. This procedure was found not to impede the convergence of the damped response equations, while it was shown to improve the description of the spectra. CVS-uS has also been implemented as a projector in e^T and can be invoked if desired. Note, however, that Nanda and Krylov²⁰ em-

ployed the CVS-uS scheme when solving for all damped response equations, and not only for the potentially divergent ones. This is also the case for their implementation of the “full” CVS (denoted CVS-0) in Q-Chem. In the following, we have chosen to apply the CVS and CVS-uS projectors primarily to improve convergence of the potentially divergent response equations. An in-depth investigation of the differences of the results following the two schemes is postponed to future studies. A schematic illustration of our implementation of the two projections can be found in Algorithm 2.

Algorithm 2 Schematic illustration of our implementation of the CVS and CVS-uS projectors on a vector. The projection is only invoked for the right (amplitude) response equations when the input frequency is positive, and for the left (multiplier) response equations when the frequency is negative.

```

1: if (CVS requested and (right equations and positive  $\omega$ ) or (left equations and negative  $\omega$ ))
   then
2:   for  $i=1, N_{\text{excitations}}$  do
3:     if  $i$  does not involve the core orbital of interest then
4:        $\text{vector}_i = 0.0$ 
5:     end if
6:   end for
7: elseif (CVS-uS requested and (right equations and positive  $\omega$ ) or (left equations and negative  $\omega$ ))
8:   for  $i=1, N_{\text{double\_excitations}}$  do
9:     if  $i$  does not involve the core orbital of interest then
10:       $\text{vector}_i = 0.0$ 
11:    end if
12:   end for
13: end if

```

Finally, the calculation of nonresonant X-ray emission spectra (XES) was also implemented, following the approach outlined by Faber and Coriani.¹⁷ Accordingly, we compute the emission energy as the difference between the ionization energy of the core ionized state, c , and the valence ionized state, v

$$E_{\text{em}} = \text{IE}^c - \text{IE}^v. \quad (7)$$

The intensities are based on the (EOM) dipole transition moments

$$T_X^{\text{vc}} = (L_v \mathbf{A}^X R_c) - (\bar{t} \cdot R_c)(L_v \cdot \eta^X) - (L_v \mathbf{I} R_c)(\bar{t} \cdot \eta^X). \quad (8)$$

A schematic illustration of the XES implementation can be found in Algorithm 3.

Algorithm 3 Schematic illustration of the XES implementation.

Note that XES calculations do not require the use of the damped response solver.

- 1: Calculate the desired core ionization energy, IE^c , and solution vectors, L_c and R_c , using a Davidson solver and CVS
- 2: Calculate valence ionization energies, IE^v , and solution vectors, L_v and R_v , using a Davidson solver in a space orthogonal to the pure core space
- 3: **for** $v = 1, N_{\text{valence_excitations}}$ **do**
- 4: **for** $X = x, y, z$ -component of the dipole operator **do**
- 5: Determine transition moments, T_X^{vc} and T_X^{cv} given in Eq. (8).
- 6: Determine diagonal element of the transition strength, $S_{XX}^{\text{vc}} = T_X^{\text{vc}} T_X^{\text{cv}}$
- 7: Add X component contribution to XES oscillator strength, $f_{\text{vc}}^{\text{osc}}$

$$f_{\text{vc}}^{\text{osc}} += \frac{2}{3}(\text{IE}^c - \text{IE}^v) S_{XX}^{\text{vc}}$$

- 8: **end for**
 - 9: **end for**
-

3 Computational Details

All calculations have been performed with a development version of the open source program e^T (Ref. 42). All core and valence excitation spectra have been determined with a regular Davidson solver. The core excitations were computed in a space orthogonal to the pure valence one, and vice versa for the valence excitations. The RIXS spectra have been determined by using our damped response solver with the CVS-uS and CVS projection. For H_2O and H_2S the damped response calculations have also been performed without any CVS projection. In addition, RIXS calculations for H_2O have been carried out at the fc-CVS-0-EOM-CCSD level of theory using Q-Chem. For H_2O , CH_3OH , H_2S and PNA calculations were performed both at the EOM-CCSD and EOM-CC2

levels of theory. For imidazole in aqueous solution, the calculations were only performed at the EOM-CCSD level of theory. The 6-311++G** basis^{51,52} with additional Rydberg functions (3s3p) was employed in the case of H₂O (see SI, Section S1.1.1), whereas for CH₃OH we adopted the aug-cc-pVTZ basis.^{53,54} For the remaining systems, the 6-311++G** basis set was used. Convergence thresholds for the response calculations were: 10^{-6} for CH₃OH, PNA and imidazole in H₂O, 10^{-8} for H₂O to compare with the study by Nanda et al.,¹⁹ and $2 \cdot 10^{-8}$ for H₂S as the RIXS cross sections are here very small. All RIXS calculations employed a damping factor of 0.0045563 a.u. and the RIXS cross sections are shown for a scattering angle of 45°.

The geometries of H₂O and H₂S were determined from experimental parameters,^{55,56} while the structure of PNA was taken from Nanda and Krylov.²⁰ The geometries of CH₃OH and of imidazole in H₂O were optimized at the MP2/cc-pCVTZ level of theory. The cartesian coordinates of all systems can be found in the SI, Section S1.

The Mulliken symmetry notation⁵⁷ has been employed throughout unless otherwise stated.

All calculations were carried out on DTU HPC resources.⁵⁸

4 Results and discussion

4.1 Validation

4.1.1 H₂O

H₂O was used to validate our approach by comparing different available CC implementations for the calculation of RIXS spectra.

As the RIXS calculations rely on the preliminary computation of the core transition, corresponding to the core resonance of interest, as well as of the valence transitions, the XAS and UV-Visible absorption spectra are also shown. Moreover, EOM-CC2 and EOM-CCSD results from e^T and fc-EOM-CCSD results from Q-Chem are compared. The XAS and valence spectra can be seen in Fig. 2. The underlying raw data (energies and oscillator strengths) used to build

the spectra can be found in Tables S1 and S2 in the SI. Table 1 collects the calculated ionization

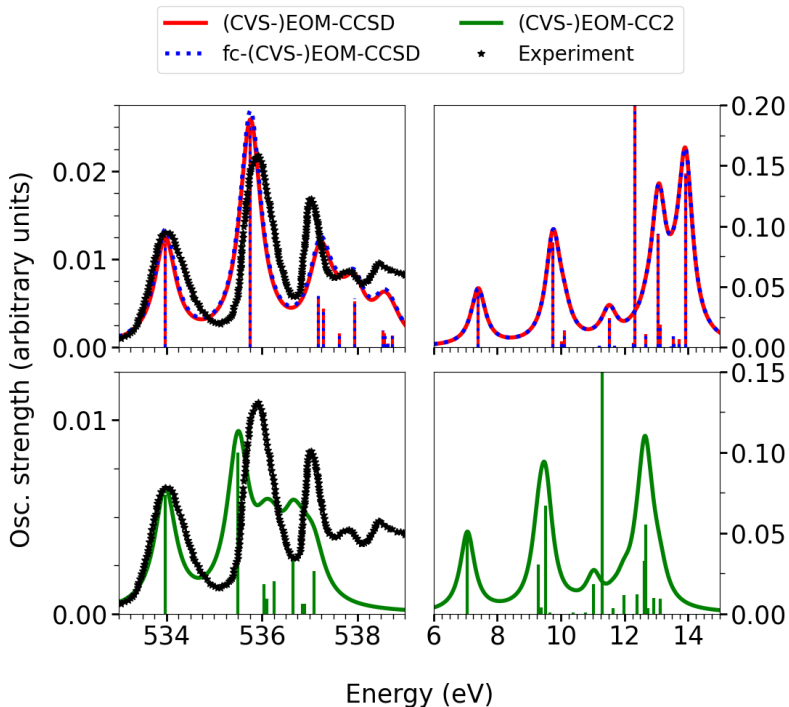


Figure 2: H_2O : XAS spectra at the O K -edge (left) and valence absorption spectra in a space orthogonal to the O core space (right) calculated using different methods. For all methods 10 core transitions and 20 valence transitions have been determined and plotted. The 6-311++G** basis with additional Rydberg functions was used for all calculations. Experimental data (black) digitized from Schirmer et al.⁵⁹ The spectrum was simulated by applying a Lorentzian broadening with a half width at half maximum (HWHM) of 0.27 eV. The calculated XAS spectra have been shifted to align with the first experimental band by -0.52 eV for CVS-EOM-CC2, -1.72 eV for CVS-EOM-CCSD and -1.24 eV for fc-CVS-EOM-CCSD. The first valence ionization energy is shown as a vertical line spanning the entire intensity range.

energy (IE) thresholds of all systems considered in this study.

As seen from Fig. 2 (and Table S1), the main differences between the CVS-EOM-CCSD and the fc-CVS-EOM-CCSD XAS results are a smaller shift in energy of the latter to align with experiment, and minimally larger oscillator strengths, as already reported in previous studies.⁷¹ The differences between the CCSD and CC2 spectra, on the other hand, are much larger. Apart

Table 1: First valence and core ionization energy thresholds calculated with e^T . Core ionization energies were obtained using the CVS projector to span a space orthogonal to the valence excitation space. Valence ionization energies were computed in a space orthogonal to the core space of interest. The core space considered is given in parenthesis next to the computed values.

Molecule	Method	IE/eV	Core IE/eV
H ₂ O	EOM-CC2	11.30(O)	538.09(O)
	EOM-CCSD	12.33(O)	541.46(O)
	fc-EOM-CCSD	12.31(O)	540.98(O)
	Experiment ^{60,61}	12.65	539.79(O)
CH ₃ OH	EOM-CC2	10.05(C);10.06(O)	293.07(C); 536.98(O)
	EOM-CCSD	11.02(C);11.03(O)	293.18(C); 540.43(O)
	Experiment ^{62–64}	10.85	292.42(C); 539.16(O)
H ₂ S	EOM-CC2	9.77(S)	2473.89(S)
	EOM-CCSD	10.00(S)	2475.72(S)
	Experiment ^{65,66}	10.46	2478.32(S)
PNA	EOM-CC2	7.8641(C)	291.58(C)
	EOM-CCSD	8.34(C)	292.31(C)
	Experiment ^{67,68}	8.43	291.1(C)
Imidazole in H ₂ O	EOM-CCSD	8.78(N)	406.41(N)
	Experiment ^{69,70}	8.51	403.9(N)

from the first two transitions, the CC2 core transitions are noticeably more closely spaced and their oscillator strengths are much smaller. As a result, where the CCSD spectra show reasonably good agreement with the experimental XAS spectrum in terms of both relative peak positions and intensities, the EOM-CC2 spectrum above 535.5 eV is compressed because of the too small separation between the peaks. This behaviour has already been reported in previous studies.^{72,73} It is a known fact that CC2 does not describe XAS to a fully satisfactory degree (see, e.g., Refs. 74 and 75).

Considering the valence excitation spectrum, see panel (b) of Fig. 2 and Table S2 in the SI, we observe that the only difference between the EOM-CCSD and fc-EOM-CCSD spectra is a small (0.02 eV) red shift of the latter with respect to the former. Aside from a slightly larger red shift, the CC2 UV spectrum corresponds well with the CCSD spectra with only small variations above the calculated ionization threshold. The CC2 ionization threshold is, however, obtained at a much lower energy (1 eV) than the CCSD one.

Despite the similar spectral shapes, closer inspection of the energies and intensities (tabulated in Table S2) reveals differences between CC2 and CCSD as far as the energetic ordering and symmetry of the states contributing to the peaks above 10 eV are concerned. This is expected to affect the appearance of RIXS spectral slices in the low emission energy region.

We now study the RIXS spectra (spectral slices) for the first two core resonances, $1s \rightarrow 4a_1$ (total symmetry A_1) and $1s \rightarrow 2b_2$ (total symmetry B_2), as well as the nonresonant XES spectra. The RIXS spectra are given in panels (b), (c), (e) and (f) of Fig. 3, and the nonresonant XES spectra in panels (a) and (d). As before, freezing the core orbitals in the ground state merely results in a shift compared to calculations based on a fully relaxed ground state. Also, for this molecule, using either the CVS or the CVS-uS projectors, when solving for the damped response vectors, does not affect the resulting spectra (see Fig. 3). This was also reported by Nanda and Krylov,²⁰ who noted that differences between the two schemes do not always arise, and in particular not for very small systems and/or small basis sets. On the other hand, we do observe noticeable differences between the CC2 and CCSD results. For the nonresonant case we observe an increased shift of the CC2 spectrum compared to that for RIXS, in accordance with the lower core ionization threshold found for CC2. Nevertheless, the two XES spectra show a similar spectral profile (shifted in energy). The CC2 and CCSD RIXS spectra at resonance with the first core excitation agree reasonably well for the two high energy features of the spectra, despite a decreased overall intensity of the CC2 spectrum. These features are also in good agreement with the experiment. Discrepancies arise for the third feature. This is, however, above the valence ionization threshold at both levels of theory, and where the valence spectra were observed to differ. One may even argue whether (some of) the peaks computed below 521.6 eV (523.4 eV in the unshifted case at CCSD level)—corresponding to emissions to excited states that lie above the first ionization limit—can be the results of artefacts due to the unphysical discretization of the continuum.

While all simulated spectra show the third feature at too low emission energy, CCSD predicts similar intensities of the second and third band, somewhat similar to what is seen in the experiment. CC2 on the other hand yields a much lower intensity of the third feature. In fact, the specific excited

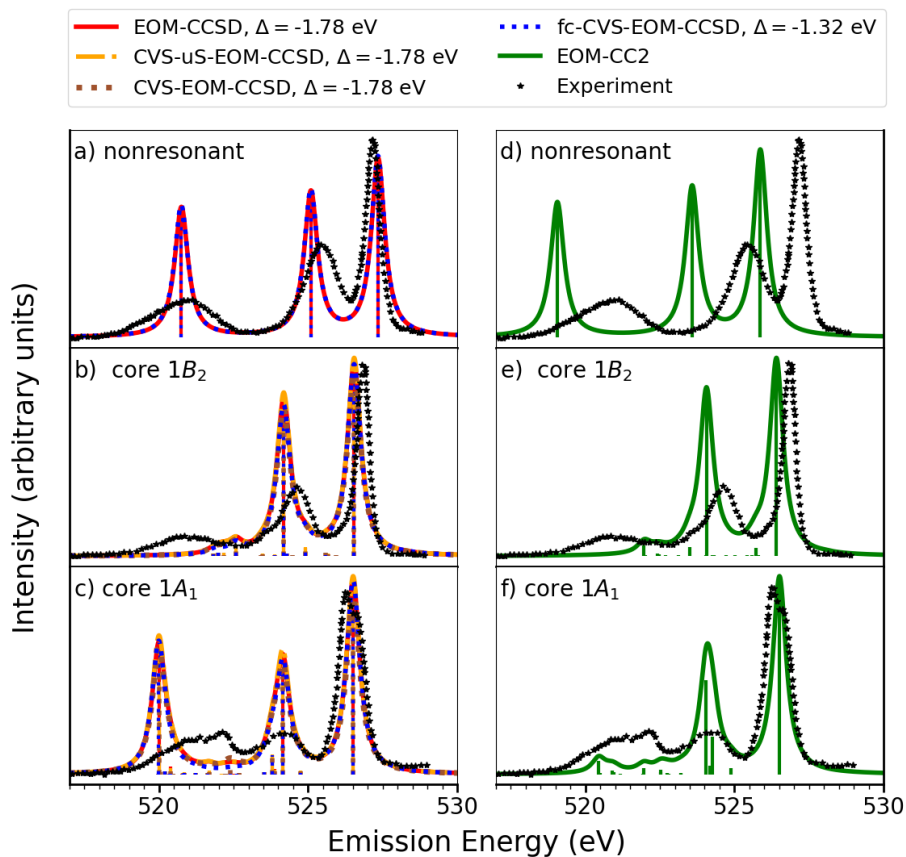


Figure 3: H_2O : Nonresonant XES (a and d) and RIXS spectra at resonance with the energy of the first (c and f) and second (b and e) core excitation at the O K -edge. The 6-311++G** basis with additional Rydberg functions was used for all calculations. The spectra were simulated with a Lorentzian broadening with $\text{HWHM}=0.27$ eV. Experimental data was digitized from Weinhardt et al.⁷⁶ No projector was employed in the damped response solver to obtain the EOM-CCSD and EOM-CC2 results, while the CVS and CVS-uS results were obtained by applying the CVS projectors to remove all valence excitations and all pure valence double excitations, respectively.

state probed at the CCSD level of theory, dominating the third RIXS peak ($4B_2$), is not amongst those reached at the CC2 level. Instead, it occurs at much higher valence excitation energy. As for the RIXS spectrum at resonance with the second core excitation, we observe a good correspondence between methods. Also, the theoretically predicted spectra are in reasonable agreement with experiment. We do observe a small additional shift though, which can be explained by the shift in energy of the theoretically predicted second core excitation compared to experiment. As the energy difference between the first and second core excitation is theoretically under estimated, the theoretical RIXS emission energies will likewise be underestimated. Thus, applying the same shift will result in the theoretically predicted spectra appearing at too low energies. In general, we find that the CC2-level calculation, while not nearly as adequate for simulating XAS as CCSD, yields results of a comparable quality for RIXS, when the same valence excited states are probed by the two methods.

In the RIXS spectrum at resonance with the first core excitation, it is the $1B_1$, $1A_1$, $4B_2$ states, and to some extent the $2A_1$ state, that are probed by EOM-CCSD, CVS-uS-EOM-CCSD, CVS-EOM-CCSD as well as fc-CVS-0-EOM-CCSD. The states probed by EOM-CC2 are $1B_1$, $1A_1$ and $2A_1$ (see Table 2 and Section S2, Tables S2-S4 in the SI). At resonance with the second core excitation, the states $1A_2$ and $1B_2$ are probed at all levels of theory.

Table 2: H_2O : Overview of valence states probed in RIXS by the different methods at the first and second core resonance (core $1A_1$ and core $1B_2$, respectively). As the results with EOM-CCSD, EOM-CVS-CCSD and EOM-CVS-uS-CCSD appear practically identical, the table only shows one set of results. The 6-311++G basis with additional Rydberg functions was used for all calculations. Reported energies are not shifted, as they are in Fig. 3.**

EOM-CCSD		fc-CVS-0-EOM-CCSD		EOM-CC2	
Energy/ eV	Probed state	Energy/ eV	Probed state	Energy/ eV	Probed state
core $1A_1$ resonance					
528.2906	$1B_1$	527.8331	$1B_1$	527.4307	$1B_1$
525.9389	$1A_1$	525.4821	$1A_1$	525.1898	$1A_1$
525.5838	$2A_1$	525.1229	$2A_1$	524.9754	$2A_1$
521.7740	$4B_2$	521.3106	$4B_2$	521.3625	$12B_1$
core $1B_2$ resonance					
528.3254	$1A_2$	527.8658	$1A_2$	527.3286	$1A_2$
525.9615	$1B_2$	525.5011	$1B_2$	524.9822	$1B_2$

4.2 Evaluation of performance of CC2 and CCSD for RIXS and XES

4.2.1 CH₃OH

The nonresonant emission and RIXS of methanol have been the subject of several studies in the past.^{77–79} In particular, a combined experimental and theoretical (based on density functional theory) study was carried out in 2016,⁷⁸ as well as a thorough computational investigation at the second-order ADC level of theory in 2019.⁷⁹ We use the molecule here to further evaluate the relative performance of CC2 and CCSD.

As for water, the computed valence spectra appear similar, while XAS spectra show large discrepancies between the EOM-CCSD and EOM-CC2 methods (see Section S3). The first two peaks in the oxygen *K*-edge XAS spectrum are of *A'* symmetry at both levels of theory, and they are in the following labelled “core 1*A'*” and “core 2*A'*” to distinguish them from the valence ones. Likewise, at the carbon *K*-edge, the first peak corresponds to a core excited state of *A'* symmetry.

The RIXS spectra have been computed at resonance with the first and second core excitation at the oxygen *K*-edge (unshifted values are 534.0 eV and 535.2 eV for EOM-CC2 and 535.5 eV and 537.5 eV for EOM-CCSD), and with the first core excitation at the carbon *K*-edge (unshifted values are 290.1 eV for EOM-CC2 and 289.0 eV for EOM-CCSD). Nonresonant X-ray emission spectra at both edges have also been computed. The spectra are shown in Figs. 4 and 5. Note that only the emission energy regions above 521 eV for O and 276 eV for C were reached in the RIXS spectra calculations with the number of valence excited states here considered.

At the oxygen *K*-edge (Fig. 4) the CVS-uS-EOM-CCSD and CVS-EOM-CCSD spectra are basically identical, and the EOM-CC2 results are in good qualitative agreement with the CCSD ones. It is, however, noted that the intensities predicted by EOM-CC2 are less than 50% of those predicted with the CCSD-based methods. As also seen previously, the EOM-CC2 spectra are shifted compared to the CCSD-based results. The transitions corresponding to the two most intense peaks are the same at the CC2 and CCSD levels (see Tables 3 and 4). At the carbon *K*-edge (Fig. 5) the CC2 and CCSD spectra show very similar spectral features. As also noted previously, for XES

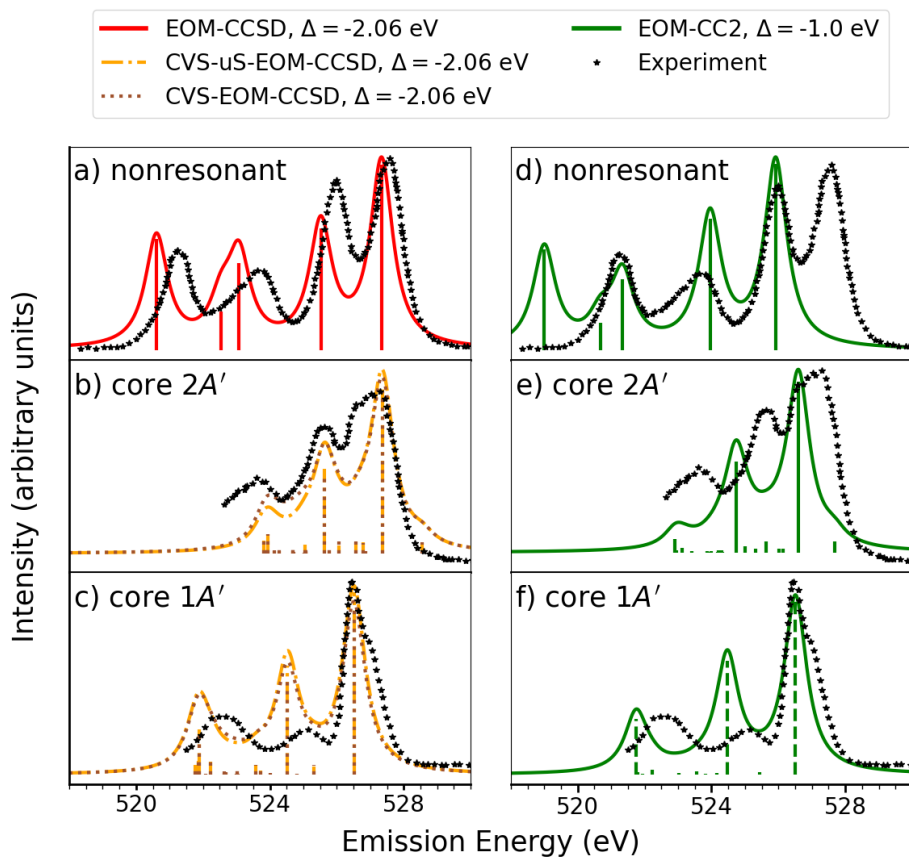


Figure 4: CH_3OH : Nonresonant XES (a and d) and RIXS spectra at resonance with the first (c and f) and second (b and e) core excitation at the O K -edge. All spectra were calculated using the aug-cc-pVTZ basis set. They were broadened by a Lorentzian broadening with $\text{HWHM}=0.41$ eV. Experimental data was digitized from Benkert et al.⁷⁸ No projections have been employed in the damped response solver to obtain EOM-CC2 results, while the CVS and CVS-uS results were obtained by applying a CVS projection removing all valence excitations and all pure valence double excitations, respectively.

Table 3: CH₃OH: Overview of valence states probed in RIXS with the different methods at the first and second core resonance at the O *K*-edge (1A' and 2A'). All calculations used the aug-cc-pVTZ basis set.

CVS-uS-EOM-CCSD		CVS-EOM-CCSD		EOM-CC2	
Energy/ eV	Probed state	Energy/ eV	Probed state	Energy/ eV	Probed state
core 1A' resonance					
528.5730	1A''	528.5730	1A''	527.5061	1A''
526.5896	2A'	526.5896	2A'	525.1898	2A'
525.6423	3A'	525.6423	3A'	-	-
523.9544	8A'	523.9544	8A'	522.7419	10A'
core 2A' resonance					
529.4225	2A''	529.4225	2A''	527.5958	2A''
527.6905	3A'	527.6905	3A'	525.7272	3A'
526.0026	8A'	526.0026	8A'	-	-

Table 4: CH₃OH: Overview of valence states probed in RIXS with the different methods at the first core resonance at the C *K*-edge (1A'). All calculations used the aug-cc-pVTZ basis set.

CVS-uS-EOM-CCSD		CVS-EOM-CCSD		EOM-CC2	
Energy/ eV	Probed state	Energy/ eV	Probed state	Energy/ eV	Probed state
core 1A' resonance					
282.1232	1A''	282.1232	1A''	283.5314	1A''
280.9191	2A''	280.9191	2A''	282.4503	2A''
280.1359	2A'	280.1359	2A'	281.4935	2A'
279.1827	3A'	279.1827	3A'	280.5784	3A'
277.4937	8A'	277.4937	8A'	278.7536	10A'
277.3721	11A''	277.3721	11A''	-	-

the EOM-CC2 spectrum is shifted compared to EOM-CCSD. The transitions that are probed at resonance with the core 1A'-state are found to be mainly the 10A', 2A' and 1A'' transitions for EOM-CC2, while according to the EOM-CCSD methods the probed transitions are 11A'', 8A', 2A' and 1A''. It is observed that while the most intense peak at the EOM-CC2 level of theory is described mainly by a single transition, it is described by two different transitions at the CVS-EOM-CCSD and CVS-uS-EOM-CCSD levels of theory. To ensure that this peak is described to a satisfactory degree, however, more valence excited states should be considered at both levels of theory.

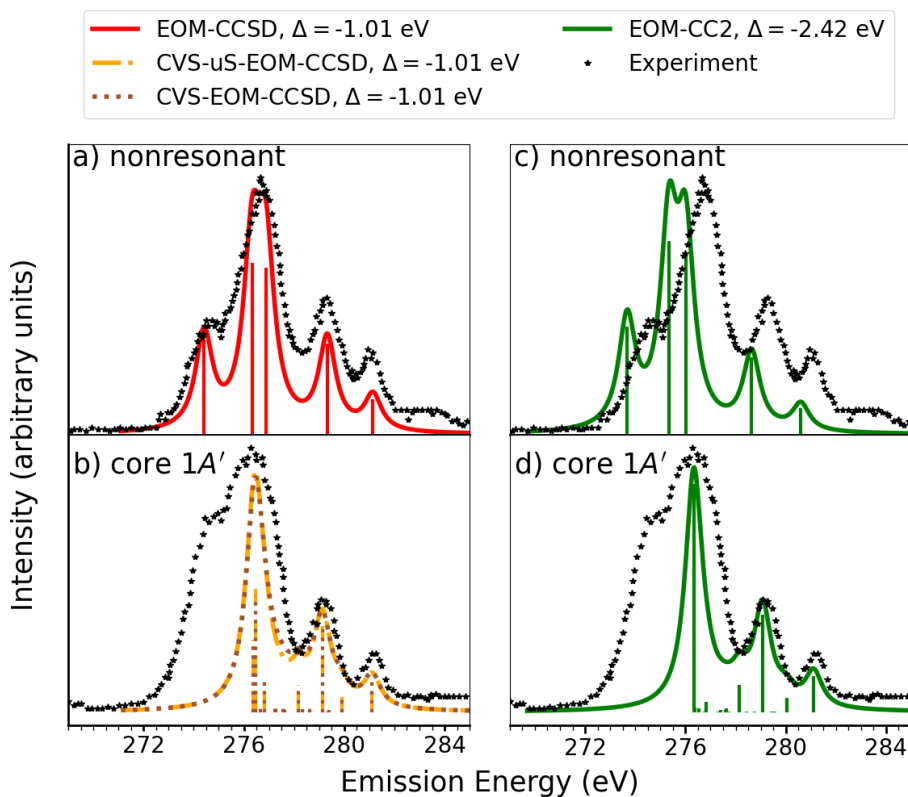


Figure 5: CH_3OH : Nonresonant (a and c) and RIXS spectra at resonance with the energy of the first core excitation (b and d) at the C K -edge. All spectra are computed with the aug-cc-pVTZ basis set. A Lorentzian broadening has been applied with $\text{HWHM}=0.41\text{eV}$. Experimental data was digitized from Benkert et al.⁷⁸ No projections have been employed in the damped response solver to obtain EOM-CCSD and EOM-CC2 results, while the CVS and CVS-uS projections have been used in the this solver to obtain the remaining results.

4.2.2 H₂S

As another showcase molecule, we consider H₂S. Experimental XAS spectra for this molecule have been reported by Bodeur and Esteve⁸⁰ and by Reynaud et al.,⁸¹ while an experimental *1s3p* RIXS map was reported as a conference communication by Kavčič et al.⁸² A computational benchmark study of XAS of sulfur containing molecules of interest in astrochemistry, here including H₂S, has been conducted by Bilalbegović et al.⁸³ Furthermore, Ertan et al.⁸⁴ computed both potential energy surfaces for core excited states and RIXS spectra for the first two core resonances. These spectra however focus on the energy region where the *S2p*⁻¹ excited states are probed, which is beyond the scope of our study. Additionally, the core excitations considered are very close in energy and might thus be excited simultaneously. In this study, we investigate the RIXS spectra for the core excitations of largest intensity for the three peaks visible in the experimental XAS spectrum. For both low energy peaks two close-lying transitions occur and therefore both are investigated.

Also in this case, the valence spectra are in good agreement between CC2 and CCSD methods, while the XAS spectra differ somewhat, albeit here the difference is small (see SI, Section S4). The core resonances to consider are the close-lying core *1B*₂ and core *1A*₁, as well as the close-lying core *1A*₂ and core *1B*₁. Finally, the resonance corresponding to the third peak in the XAS spectrum is core *3B*₂. This is the case at both levels of theory.

As mentioned, RIXS spectra have been computed at the resonance of the most intense transitions for the three peaks of the XAS (unshifted values are 2468.6 eV, 2468.8 eV, 2471.4 eV, 2471.6 eV and 2473.0 eV at the EOM-CC2 level of theory and 2469.8 eV, 2470.3 eV, 2473.3 eV, 2473.5 eV and 2475.2 eV at the EOM-CCSD level of theory). These are all below the calculated core ionization threshold at the CCSD level of theory, while the third experimental feature is above the threshold at the CC2 level (see Table 1). Nonresonant emission spectra were computed as well. As for H₂O, three different strategies were adopted to compute the CCSD RIXS spectra: no projection was applied during the solution of the (damped) response equations (label EOM-CCSD), a CVS projector was applied to remove all valence excitations (label CVS-EOM), and a CVS projector

was applied to remove all pure valence double excitations (label CVS-uS-EOM).

Table 5: H₂S: Overview of valence states probed in RIXS by the different methods at the considered core resonances corresponding to the low energy XAS peak. As CVS-uS-EOM-CCSD and EOM-CCSD results appear identical, these are only reported once under EOM-CCSD. Energies reported here are not shifted.

EOM-CCSD		CVS-EOM-CCSD		EOM-CC2	
Energy/ eV	Probed state	Energy/ eV	Probed state	Energy/ eV	Probed state
core 1B ₂ resonance					
2463.4265	1A ₂	2463.4265	1A ₂	2462.1849	1A ₂
2461.9345	2A ₂	2461.9345	-	2460.7734	2A ₂
2461.6200	2B ₁	2461.6200	-	2460.4409	2B ₁
2461.3149	-	2461.3149	1A ₁	2460.1634	-
2460.3345	3B ₁	2460.3345	-	2459.0692	3B ₁
2459.9138	4B ₁	2459.9138	-	2458.7552	3A ₂
2459.8942	3A ₂	2459.8942	-	2458.7546	4B ₁
2458.7911	-	2458.7911	2B ₂	2457.6041	-
core 1A ₁ resonance					
2463.9417	1A ₂	2463.9417	1A ₂	2462.4078	1A ₂
2462.4494	2A ₂	2462.4494	-	2460.9963	2A ₂
2462.1351	2B ₁	2462.1351	-	2460.6638	2B ₁
2461.8298	-	2461.8298	1A ₁	2460.3862	-
2460.8494	3B ₁	2460.8494	-	2459.292	3B ₁
2460.4289	4B ₁	2460.4289	-	2458.9780	3A ₂
2460.4093	3A ₂	2460.4093	-	2458.9775	4B ₁
2459.3059	-	2459.3059	2B ₂	2457.8273	-

Note that the RIXS cross sections are approximately one order of magnitude lower than those computed for H₂O and CH₃OH (see Sections S2-S4 of the SI). This is also the case for the XAS oscillator strengths.

Considering the RIXS spectra in Fig. 6, it is evident that employing the “full” CVS approximation when solving the damped response equations significantly affects the spectra. While we observe a good correspondence between the (unprojected) EOM-CCSD results and the CVS-uS-EOM-CCSD results, as well as the EOM-CC2 results (disregarding the energy shift), a different spectral shape is obtained when employing the full CVS approximation. This was also observed by Nanda and Krylov for the molecule para-nitro-aniline.²⁰

The shifts between the CC2 and CCSD results are found to changes at higher resonances.

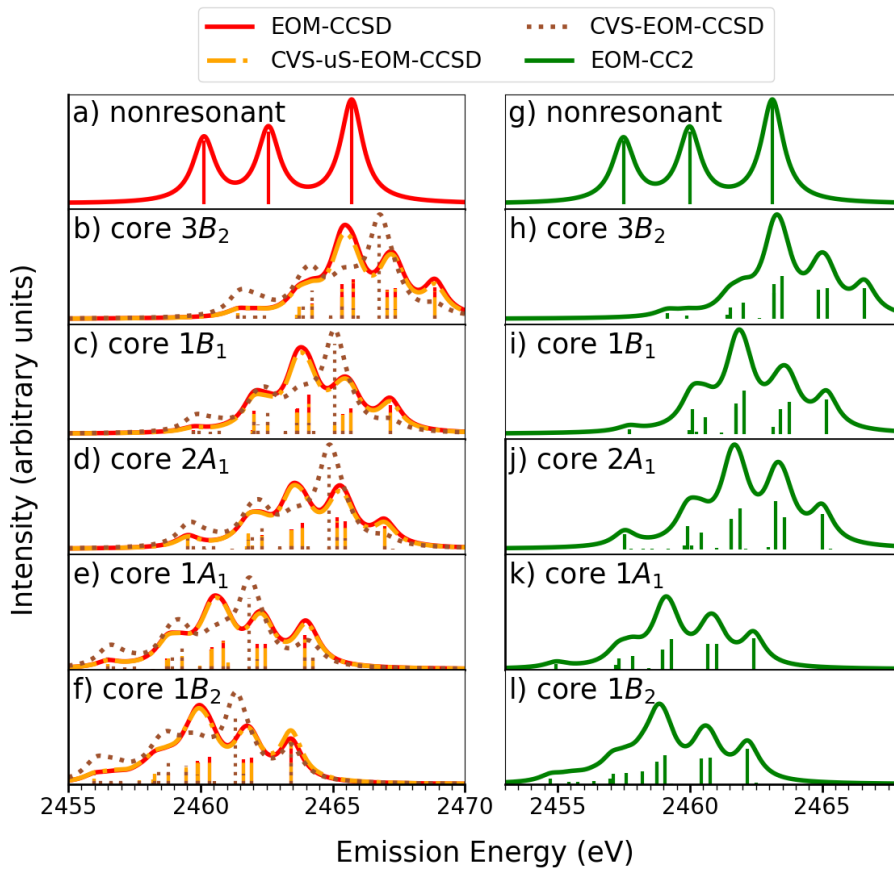


Figure 6: H₂S: Nonresonant (a and g) and RIXS spectra at resonance with the energy of the 1B₂ core excitation (f and l), 1A₁ core excitation (e and k), 2A₁ core excitation (d and j), 2B₂ core excitation (c and i) and 3B₂ core excitation (b and h) at the S *K*-edge. All spectra are computed with the 6-311++G**. No shift has been applied to the results. A Lorentzian broadening was applied with HWHM=0.51eV

Table 6: H₂S: Overview of valence states probed in RIXS by the different methods at the considered core resonances corresponding to the middle peak of the XAS. As CVS-uS-EOM-CCSD and EOM-CCSD results appear identical, these are only reported once under EOM-CCSD. Energies reported here are not shifted.

EOM-CCSD		CVS-EOM-CCSD		EOM-CC2	
Energy/ eV	Probed state	Energy/ eV	Probed state	Energy/ eV	Probed state
core 2A ₁ resonance					
2466.9583	1A ₂	2466.9583	-	2464.9966	1A ₂
2465.4663	2A ₂	2465.4663	-	2463.5852	2A ₂
2465.1517	2B ₁	2465.1517	-	2463.2529	2B ₁
2464.8464	-	2464.8464	1A ₁	2462.9754	-
2463.8660	3B ₁	2463.8660	-	2461.8812	3B ₁
2461.8064	5B ₁	2461.8064	-	2459.9136	5B ₁
core 1B ₁ resonance					
2467.1733	1A ₂	2467.1733	-	2465.1694	1A ₂
2465.6813	2A ₂	2465.6813	-	2463.7580	2A ₂
2465.0617	-	2465.0617	1A ₁	2463.1482	-
2464.0810	3B ₁	2464.0810	-	2462.0540	3B ₁
2462.0216	5B ₁	2462.0216	-	2460.0863	5B ₁

Thus, at the first two resonances the shift is approximately 1 eV (Figs. 6e, 6f, 6k and 6l), while it is approximately 2.5 eV at the third and fourth resonances (Figs. 6c, 6d, 6i and 6j) and approximately 2 eV at the last considered resonance (Figs. 6b and 6h). The shift between the nonresonant CCSD and CC2 spectra is approximately 3 eV (Figs. 6a and 6g). This is in line with our observations for CH₃OH, where the shift applied at the first resonance to align with experiment (Figs. 4c and 4f) was noted to no longer be sufficient at higher resonances, but to different degrees for CCSD and CC2 (Figs. 4a,b and 4d,e). As for CH₃OH, this observation is attributed to differences in the XAS, and for the nonresonant case, differences in the core and valence IEs.

At the first two resonances (Figs. 6e, 6f, 6k and 6l) the valence transitions probed are 1A₂ as well as 2A₂, 2B₁, 3B₁, 3A₂, 4B₁ and 1B₂ for both EOM-CCSD, EOM-CVS-uS-CCSD and EOM-CC2 methods. Likewise, these methods predict that at the next two resonances (Figs. 6c, 6d, 6i and 6j), associated with the second peak in the XAS, the valence transitions probed are the same except for 1B₂, which is replaced by 5B₁. Finally, EOM-CCSD and EOM-CVS-uS-CCSD predict once more the same valence transitions to be probed at the core 3B₂ resonance (Figs. 6b and 6h) as

Table 7: H₂S: Overview of valence states probed in RIXS by the different methods at the considered core resonance corresponding to the small XAS peak found just below the ionization threshold. As CVS-uS-EOM-CCSD and EOM-CCSD results appear identical, these are only reported once under EOM-CCSD. Energies reported here are not shifted.

EOM-CCSD		CVS-EOM-CCSD		EOM-CC2	
Energy/ eV	Probed state	Energy/ eV	Probed state	Energy/ eV	Probed state
core 3B ₂ resonance					
2468.8686	1A ₂	2468.8686	-	2466.6043	1A ₂
2467.3766	2A ₂	2467.3766	-	2465.1928	2A ₂
2467.0620	2B ₁	2467.0620	-	2464.8603	2B ₁
2466.7569	-	2466.7569	1A ₁	2464.5828	-
2465.7765	3B ₁	2465.7765	-	2463.4886	3B ₁
2465.3558	-	2465.3558	-	2463.1756	3A ₂
2465.3362	3A ₂	2465.3362	-	2463.1740	4B ₁
2464.2331	-	2464.2331	2B ₂	2462.0235	-

at the first two resonances, except the 1B₂, which is here replaced by 2B₂. The EOM-CVS-CCSD calculation indicates that it is mainly 1A₁ that is probed at all resonances. In addition, at this level of theory, the 1A₂, 1B₂, 2B₂, 3A₁ and 5B₂ states also appear to be probed at the first and second resonances. Likewise, the 2B₂ state is probed at the third and fourth resonances, while the 4B₁, 2B₂ and 3A₁ states are probed at the last considered resonance. In general, we observe that for this system it is the same transitions probed at all resonances unlike what was seen for H₂O.

The overall spectral shape showing three main features with varying relative intensities at all resonances is in agreement with experiment.⁸²

4.2.3 Para-nitro-aniline (PNA)

For the larger molecule PNA, both the XAS and valence absorption spectra show small discrepancies between CCSD and CC2 (see Figure S4). However, both methods predict the first bright core transition to be core 1B₁.

The nonresonant emission spectra, as well as the RIXS spectra resonant with the first bright core excitation at the C *K*-edge (computed at 288.0 eV at the EOM-CC2 level and at 286.7 eV at the EOM-CCSD level of theory without applying a shift), are shown in Fig. 7. In addition, the RIXS spectrum has been computed at the fc-CVS-0-EOM-CCSD level of theory (core 1B₁ resonance

Table 8: PNA: Overview of valence states probed in RIXS with the different methods at the first core resonance. The calculations all employed the 6-311++G basis set. Energies reported here are not shifted.**

CVS-uS-EOM-CCSD		CVS-EOM-CCSD		fc-CVS-0-EOM-CCSD		CVS-uS-EOM-CC2	
Energy / eV	Probed state	Energy / eV	Probed state	Energy / eV	Probed state	Energy / eV	Probed state
core $1B_1$ resonance							
282.0633	$1A_1$	282.0633	$1A_1$	281.5675	$1A_1$	283.5360	$1A_1$
280.3044	$2A_1$	280.3044	$2A_1$	279.8086	$2A_1$	281.7447	$2A_1$
279.5582	$3A_1$	279.5582	$3A_1$	279.0722	$3A_1$	280.9585	$3A_1$
278.9345	$5A_1$	278.9345	$5A_1$	278.4407	$5A_1$	-	-

at 288.9 eV). Here, we observe that the RIXS spectra at the CCSD level look similar, except for the intensity of the high energy feature. This feature is much more intense, when the full CVS approximation is employed only for solving the divergent damped response equations (labeled CVS-EOM-CCSD). In the fc-CVS-0-EOM-CCSD calculation (full CVS used when solving *all* damped response equations), this is not the case. It was found (see SI, Section S5) that it is indeed the difference between CVS and CVS-0 rather than the use of fc that gives rise to the large difference.

The same three valence transitions are probed in all CCSD based calculations, namely $1A_1$, $3A_1$ and $5A_1$. The CC2 spectrum looks similar to the CCSD ones, but it is observed that the low energy transitions are much more closely spaced, and thus we observe only two peaks rather than three. The transitions probed are again $1A_1$ and $3A_1$. As for the nonresonant spectra, the CC2 and CCSD spectra are somewhat similar in shape, with an additional shift of the CC2 spectrum compared to CCSD, as also observed for the other systems.

Our CVS-uS-EOM CCSD results are in good agreement with those presented by Nanda and Krylov.²⁰ It is, however, noted that our CVS-EOM-CCSD and CVS-uS-EOM-CCSD spectra are rather similar to each other compared to the results presented by Nanda and Krylov.²⁰ Nonetheless, our calculation utilizing the fc-CVS-0-EOM-CCSD level of theory, showed good agreement with our other results (see Fig 7 and Table S23 in Section S5). Discrepancies were, as mentioned, attributed to the fact that we employ the CVS approximation only when solving amplitude response

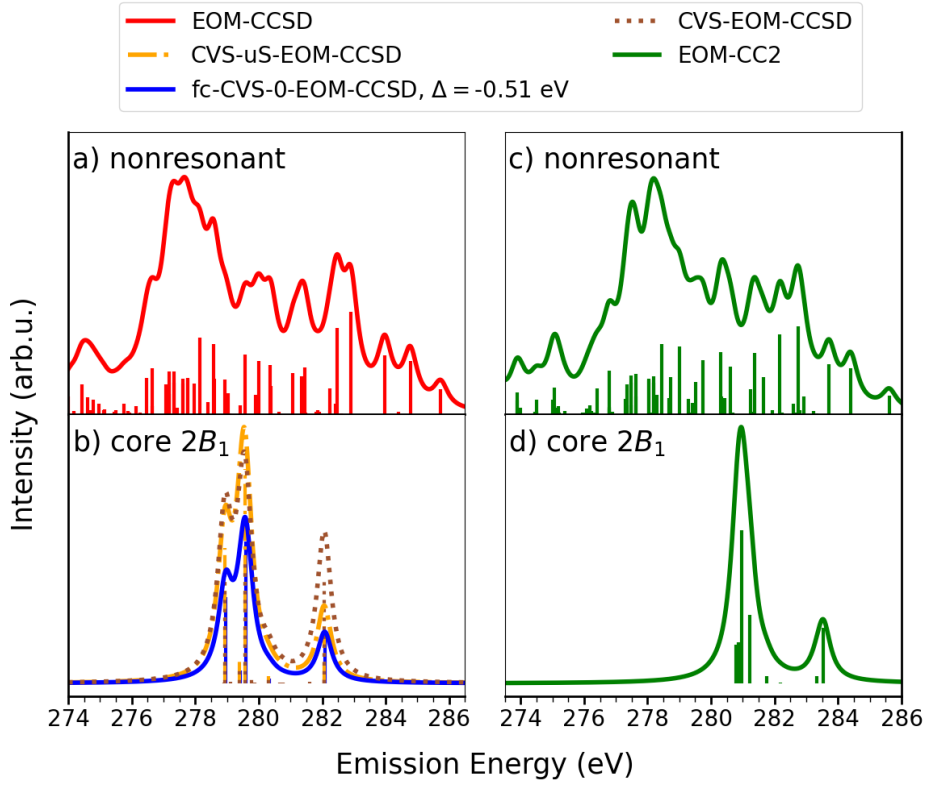


Figure 7: PNA: Nonresonant (a and c) and RIXS spectra at resonance with the energy of the first core excitation (b and d) at the C K -edge. The calculations all employed the 6-311++G** basis set. The fc-CVS-0-EOM-CCSD results are shifted to align with the EOM-CVS-uS-CCSD results. A Lorentzian broadening has been applied with HWHM=0.27 eV

equations for positive frequencies and multiplier response equations for negative frequencies. The implementation by Nanda et al.,^{19,20} on the other hand, employs CVS when solving all damped response equations.

4.3 Evaluation of performance of CCSD for a solvated molecule

X-ray experiments have been carried out in aqueous solution for imidazole.⁸⁵ Previous studies have shown that including explicit H₂O molecules can yield good results,^{86–88} although, one H₂O molecule is not enough for describing the XAS spectrum.⁸⁷ For the best results 15 or more H₂O molecules should be included.⁸⁷ We have chosen to include only 4 explicit H₂O molecules (see structure in Fig. 8), as this was shown by Thomason⁸⁷ to yield reasonable results and is computationally feasible even when treating the entire system at the CCSD level of theory.

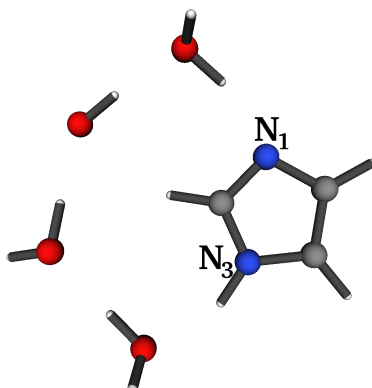


Figure 8: Structure of imidazole with 4 explicit H₂O molecules.

To reduce the computational cost in the RIXS calculations, we treated the solvent molecules at the Hartree-Fock (HF) level of theory and only employed coupled cluster methods for the imidazole molecule itself. In this “CCSD-in-HF” approach, HF orbitals localized on the region of interest (in our case, imidazole) are included in the CCSD calculation. The remaining orbitals enter the coupled cluster equations through their contribution to the Fock matrix.⁸⁹ In this work, we use Cholesky orbitals^{89,90} for the occupied space and orthonormalized projected atomic orbitals^{91,92}

for the virtual space. The CCSD-in-HF approach has been demonstrated to work well for localized transitions⁹³ such as those addressed in XAS. However, its accuracy relies on a sufficiently large active region to describe the transitions of interest, i.e., delocalized excitations that go outside of the active region cannot be described.

The simulated XAS was found to correspond well with experiment as well as with the calculation where the H₂O molecules are also treated at the CC level of theory (see Fig. S6, Section S6). Likewise, the simulated valence absorption spectrum (also in Fig. S6) was found to change only little when treating the solvent molecules at the HF level of theory compared to treating the entire system at the CC level of theory. We thus concluded that no significant accuracy is lost by treating the solvent molecules at a lower level of theory. Since the core transitions are very localized, this was expected for XAS.

We computed the RIXS spectra at resonance with the first two intense core transitions in the XAS spectrum, labeled “core 1A” and “core 2A”. Note that the “core 1A” resonance is primarily due to the excitation of a 1s(N1) electron, whereas the “core 2A” resonance is dominated by the excitation of an electron in the 1s orbital of N3. The nonresonant XES and resonant RIXS spectra can be found in Fig. 9; the valence states probed by RIXS are found in Table 9. Meyer et al.⁸⁵ analyzed the experimental RIXS spectra at these two resonances by considering only computed nonresonant emission spectra for each individual nitrogen. This has also been done here and can be seen in Fig. 10. In line with the localized nature (on specific N atoms) of the resonant core transitions considered, the nonresonant emission spectrum of N1 reproduces the spectral shape of the first resonance (see Fig. 10c). Likewise, the spectral shape of the RIXS at the second core resonance is reasonably well captured by the nonresonant emission spectrum of N3 (see Fig. 10b).

As discussed by Meyer et al.,⁸⁵ this XES-based analysis of the RIXS spectral slices highlights the fact that spectral changes are mainly due to the selective excitation of one particular nitrogen site. This approach is also computationally much cheaper than the computation of the full RIXS cross section.

To calculate the RIXS spectra as we do here using the damped response formalism, requires

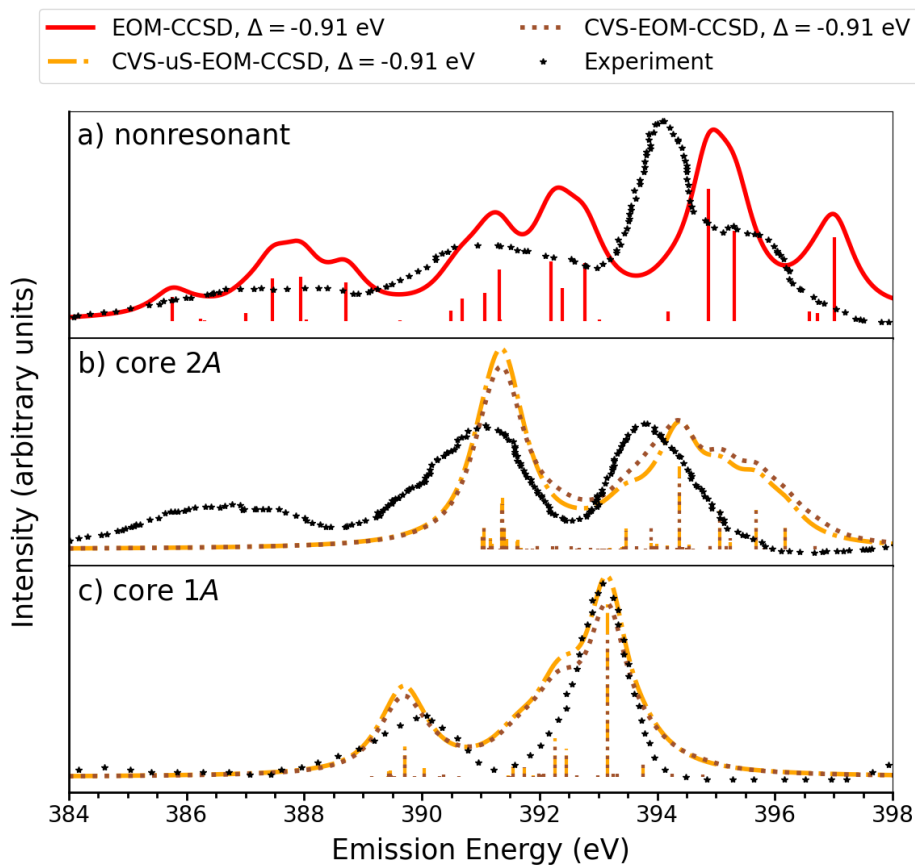


Figure 9: Imidazole with 4 explicit H₂O molecules, the latter treated at the HF level of theory: Nonresonant (a) and RIXS spectra at resonance with the energy of the first (c), and second (b) core excitation at the N *K*-edge. The results are shifted based on the RIXS experiment at resonance with the first core excitation. Experimental data in aqueous solution has been digitized from Meyer et al.⁸⁵ A Lorentzian broadening has been applied with HWHM=0.41 eV.

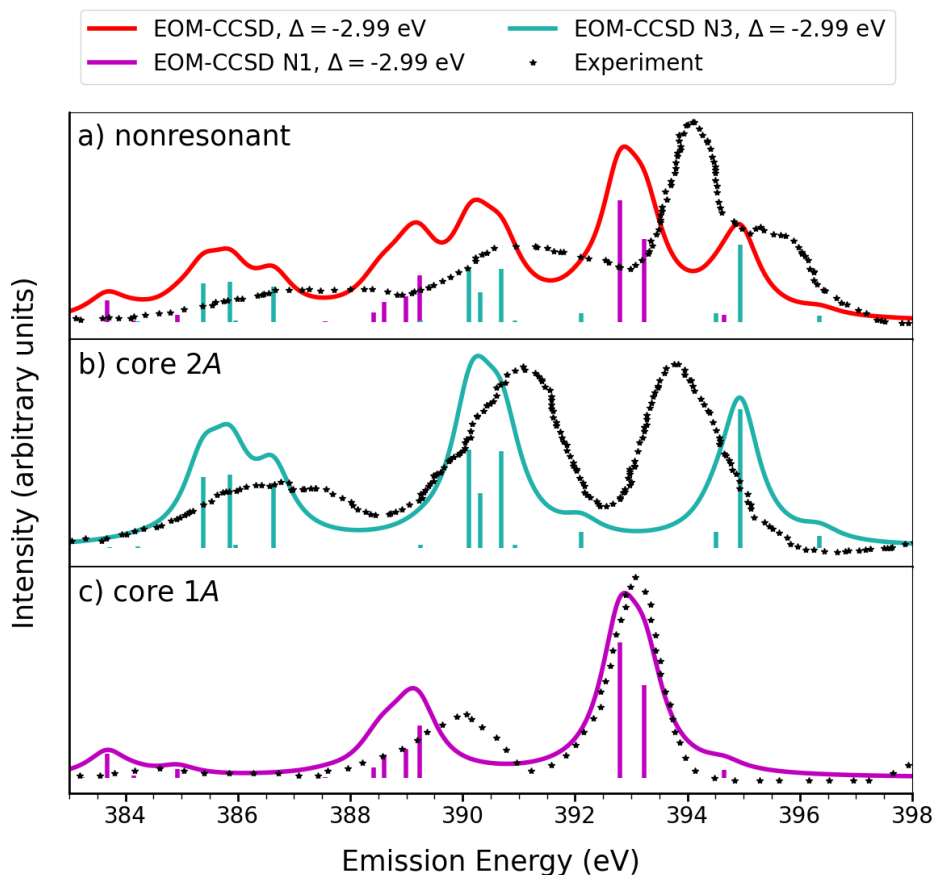


Figure 10: Imidazole with 4 explicit H₂O molecules, the latter treated at the HF level of theory: Nonresonant XES (a) and RIXS spectra at resonance with the energy of the first (c), and second (b) core excitation at the N *K*-edge. The results are shifted based on the RIXS experiment⁸⁵ at resonance with the first core excitation. The calculations all employed the 6-311++G** basis set and a Lorentzian broadening with HWHM=0.41 eV has been applied. For (b) and (c) the simulated spectra are the nonresonant ones of individual N as indicated in the legends. Experimental data in aqueous solution has been digitized from Meyer et al.⁸⁵

Table 9: Imidazole with 4 explicit H₂O molecules, the latter treated at the HF level of theory: Overview of valence states probed in RIXS at the first and second core resonance. All calculations employed the 6-311++G basis set. Tabulated energies have not been shifted.**

CVS-uS-EOM-CCSD		CVS-EOM-CCSD	
Energy/ eV	Probed state	Energy/ eV	Probed state
core 1A resonance			
394.0603	8A	394.0603	8A
393.3704	14A	393.3704	14A
393.1745	16A	393.1745	16A
390.6254	45A	390.6254	45A
390.6188	46A	390.6188	46A
core 2A resonance			
397.0810	2A	397.0810	2A
396.5893	5A	396.5893	5A
395.9735	8A	395.9735	8A
395.2837	14A	395.2837	14A
394.8075	-	394.8075	19A
394.3794	22A	394.3794	22A
392.3035	49A	392.3035	49A
392.2825	50A	392.2825	50A
392.2616	51A	392.2616	51A
391.9669	56A	391.9669	56A

solving the eigenvalue problem for a large number of roots. Moreover, a correspondingly large number of damped equations must be solved for the response amplitudes and multipliers, which is computationally expensive and may be difficult to converge. On the other hand, it allows for an assignment of the spectral bands in terms of probed valence excited states (as we probe the correlation between valence and core excitations). Furthermore, when considering the second resonance (Figs. 9b and 10b), the separation between the two peaks is noted to be better reproduced by the RIXS calculation. In general, our results show that, while the calculation is computationally challenging, the experimental results are well reproduced also for the solvated molecule. Other molecules in solution should also be considered, to verify whether this approach is capable of yielding good results for RIXS of solvated molecules in general. This, however, is beyond the aims of this study.

5 Conclusion

A new implementation of a damped response solver for the calculation, amongst others, of RIXS spectra at the EOM-CCSD and EOM-CC2 levels of theory in e^T was presented. It was found that while CVS-EOM-CC2 does not generally yield XAS spectra in sufficiently good agreement with experiment compared to CVS-EOM-CCSD, the RIXS spectra often appear similar at the two levels of theory, except for an overall energy shift. For the second core resonance of H₂O and CH₃OH, as well as the first core resonance of PNA, discrepancies were observed at the edge of the explored energy region. This, however, might be remedied by considering a larger number of roots. Thus, EOM-CC2 might be utilized for RIXS calculations with confidence on equal footing with EOM-CCSD. It was further found that the CVS-uS model proposed by Nanda and Krylov might improve RIXS results significantly compared to the regular CVS model even for smaller systems, as exemplified by H₂S. Finally, our EOM-CCSD implementation of RIXS was tested on imidazole in an aqueous solution. Further studies are, however, required to fully explore its capabilities in this respect, but the results are promising.

Acknowledgement

AKSP acknowledges support from the DTU Partnership PhD programme. SDF acknowledges funding from the Research Council of Norway through FRINATEK project 275506. SC acknowledges support from the Independent Research Fund Denmark (DFF-RP2 Grant 7014-00258B). The European Cooperation in Science and Technology, COST Action CA18222 *Attochem* is also acknowledged.

Supporting Information Available

The Supporting Information contains: Geometries of the investigated molecules; the 6-311++G** basis set including additional Rydberg functions used; all data tables for the plotted spectra;

XAS and valence absorption spectra for CH₃OH, H₂S, PNA, and imidazole with 4 explicit water molecules; comparisons of fc-CVS-0-EOM-CCSD, CVS-0-EOM-CCSD and CVS-EOM-CCSD results for PNA using a small basis; results of a calculation on pyridine.

References

- (1) Mobilio, S.; Boscherini, F.; Meneghini, C. *Synchrotron Radiation: Basics, Methods and Applications*; Springer, 2014.
- (2) Lamberti, C.; van Bokhoven, J. A. *X-Ray Absorption and X-Ray Emission Spectroscopy*; John Wiley & Sons, Ltd, 2016.
- (3) Bergmann, U.; Yachandra, V.; Yano, J. *X-Ray Free Electron Lasers: Applications in Materials, Chemistry and Biology*; The Royal Society of Chemistry, 2017.
- (4) Nisoli, M.; Decleva, P.; Calegari, F.; Palacios, A.; Martín, F. Attosecond Electron Dynamics in Molecules. *Chem. Rev.* **2017**, *117*, 10760–10825.
- (5) Kraus, P. M.; Zürich, M.; Cushing, S. K.; Neumark, D. M.; Leone, S. R. The ultrafast X-ray spectroscopic revolution in chemical dynamic. *Nat. Rev. Chem.* **2018**, *2*, 82.
- (6) Bhattacharjee, A.; Leone, S. R. Ultrafast X-ray Transient Absorption Spectroscopy of Gas-Phase Photochemical Reactions — A New Universal Probe of Photoinduced Molecular Dynamics. *Acc. Chem. Res.* **2018**, *51*, 3203–3211.
- (7) Gel'mukhanov, F.; Ågren, H. Resonant X-ray Raman Scattering. *Phys. Rep.* **1999**, *312*, 87.
- (8) Kotani, A.; Shin, S. Resonant inelastic x-ray scattering spectra for electrons in solids. *Rev. Mod. Phys.* **2001**, *73*, 203–246.
- (9) Ament, L. J. P.; van Veenendaal, M.; Devereaux, T. P.; Hill, J. P.; van den Brink, J. Resonant inelastic x-ray scattering studies of elementary excitations. *Rev. Mod. Phys.* **2011**, *83*, 705–767.

- (10) Eckert, S.; Norell, J.; Miedema, P. S.; Beye, M.; Fondell, M.; Quevedo, W.; Kennedy, B.; Hantschmann, M.; Pietzsch, A.; Van Kuiken, B. E.; Ross, M.; Minitti, M. P.; Moeller, S. P.; Schlotter, W. F.; Khalil, M.; Odelius, M.; Föhlisch, A. Ultrafast Independent N-H and N-C Bond Deformation Investigated with Resonant Inelastic X-ray Scattering. *Angew. Chemie Int. Ed.* **2017**, *56*, 6088–6092.
- (11) Dziarzhytski, S.; Biednov, M.; Dicke, B.; Wang, A.; Miedema, P. S.; Engel, R. Y.; Schunck, J. O.; Redlin, H.; Weigelt, H.; Siewert, F.; Behrens, C.; Sinha, M.; Schulte, A.; Grimm-Lebsanft, B.; Chiuzbăian, S. G.; Wurth, W.; Beye, M.; Rübhausen, M.; Brenner, G. The TRIXS end-station for femtosecond time-resolved resonant inelastic x-ray scattering experiments at the soft x-ray free-electron laser FLASH. *Struct. Dyn.* **2020**, *7*, 054301.
- (12) Miedema, P. S. Raman Spectroscopy with X-Rays. In *Raman Spectroscopy and Applications*; Maaz, K., Ed.; IntechOpen: Rijeka, 2017; Chapter 11.
- (13) Carra, P.; Fabrizio, M.; Thole, B. T. High Resolution X-Ray Resonant Raman Scattering. *Phys. Rev. Lett.* **1995**, *74*, 3700.
- (14) Schmitt, T.; de Groot, F. M. F.; Rubensson, J.-E. Prospects of high-resolution resonant X-ray inelastic scattering studies on solid materials, liquids and gases at diffraction-limited storage rings. *J. Synchr. Rad.* **2014**, *21*, 1065–1076.
- (15) Fouda, A. E. A.; Purnell, G. I.; Besley, N. A. Simulation of Ultra-Fast Dynamics Effects in Resonant Inelastic X-ray Scattering of Gas-Phase Water. *J. Chem. Theory Comput.* **2018**, *14*, 2586–2595.
- (16) Rehn, D. R.; Dreuw, A.; Norman, P. Resonant Inelastic X-ray Scattering Amplitudes and Cross Sections in the Algebraic Diagrammatic Construction/Intermediate State Representation (ADC/ISR) Approach. *J. Chem. Theory Comput.* **2017**, *13*, 5552–5559.
- (17) Faber, R.; Coriani, S. Resonant Inelastic X-ray Scattering and Nonesonant X-ray Emission

- Spectra from Coupled-Cluster (Damped) Response Theory. *J. Chem. Theory Comput.* **2019**, *15*, 520–528.
- (18) Faber, R.; Coriani, S. Core–valence-separated coupled-cluster-singles-and-doubles complex-polarization-propagator approach to X-ray spectroscopies. *Phys. Chem. Chem. Phys.* **2020**, *22*, 2642–2647.
- (19) Nanda, K. D.; Vidal, M. L.; Faber, R.; Coriani, S.; Krylov, A. I. How to stay out of trouble in RIXS calculations within equation-of-motion coupled-cluster damped response theory? Safe hitchhiking in the excitation manifold by means of core–valence separation. *Phys. Chem. Chem. Phys.* **2020**, *22*, 2629–2641.
- (20) Nanda, K. D.; Krylov, A. I. Cherry-picking resolvents: A general strategy for convergent coupled-cluster damped response calculations of core-level spectra. *J. Chem. Phys.* **2020**, *153*, 141104.
- (21) Vaz da Cruz, V.; Eckert, S.; Föhlisch, A. TD-DFT simulations of *K*-edge resonant inelastic X-ray scattering within the restricted subspace approximation. *Phys. Chem. Chem. Phys.* **2021**, *23*, 1835–1848.
- (22) Nascimento, D. R.; Biasin, E.; Poulter, B. I.; Khalil, M.; Sokaras, D.; Govind, N. Resonant Inelastic X-ray Scattering Calculations of Transition Metal Complexes Within a Simplified Time-Dependent Density Functional Theory Framework. *J. Chem. Theory Comput.* **2021**, *17*, 3031–3038.
- (23) Chen, Y.; Wang, Y.; Jia, C.; Moritz, B.; Shvaika, A. M.; Freericks, J. K.; Devereaux, T. P. Theory for time-resolved resonant inelastic x-ray scattering. *Phys. Rev. B* **2019**, *99*, 104306.
- (24) Eckstein, M.; Werner, P. Simulation of time-dependent resonant inelastic x-ray scattering using nonequilibrium dynamical mean-field theory. *Phys. Rev. B* **2021**, *103*, 115136.

- (25) Kramers, H.; Heisenberg, W. Über die Streuung von Strahlung durch Atome. *Z. Physik* **1925**, *31*, 681–708.
- (26) Dirac, P. A. M. The quantum theory of the emission and absorption of radiation. *Proceedings of the Royal Society of London. Series A, Containing Papers of a Mathematical and Physical Character* **1927**, *114*, 243–265, communicated by Niels Henrik David Bohr.
- (27) Dirac, P. A. M.; Fowler, R. H. The quantum theory of dispersion. *Proceedings of the Royal Society of London. Series A, Containing Papers of a Mathematical and Physical Character* **1927**, *114*, 710–728.
- (28) Long, D. A. *The Raman Effect: A Unified Treatment of the Theory of Raman Scattering by Molecules*; John Wiley & Sons Ltd., 2002.
- (29) Epifanovsky, E.; Gilbert, A. T. B.; Feng, X.; Lee, J.; Mao, Y.; Mardirossian, N.; Pokhilko, P.; White, A. F.; Coons, M. P.; Dempwolff, A. L.; Gan, Z.; Hait, D.; Horn, P. R.; Jacobson, L. D.; Kaliman, I.; Kussmann, J.; Lange, A. W.; Lao, K. U.; Levine, D. S.; Liu, J.; McKenzie, S. C.; Morrison, A. F.; Nanda, K. D.; Plasser, F.; Rehn, D. R.; Vidal, M. L.; You, Z.-Q.; Zhu, Y.; Alam, B.; Albrecht, B. J.; Aldossary, A.; Alguire, E.; Andersen, J. H.; Athavale, V.; Barton, D.; Begam, K.; Behn, A.; Bellonzi, N.; Bernard, Y. A.; Berquist, E. J.; Burton, H. G. A.; Carreras, A.; Carter-Fenk, K.; Chakraborty, R.; Chien, A. D.; Closser, K. D.; Cofer-Shabica, V.; Dasgupta, S.; de Wergifosse, M.; Deng, J.; Diedenhofen, M.; Do, H.; Ehlert, S.; Fang, P.-T.; Fatehi, S.; Feng, Q.; Friedhoff, T.; Gayvert, J.; Ge, Q.; Gidofalvi, G.; Goldey, M.; Gomes, J.; González-Espinoza, C. E.; Gulania, S.; Gunina, A. O.; Hanson-Heine, M. W. D.; Harbach, P. H. P.; Hauser, A.; Herbst, M. F.; Hernández Vera, M.; Hodecker, M.; Holden, Z. C.; Houck, S.; Huang, X.; Hui, K.; Huynh, B. C.; Ivanov, M.; Jász, A.; Ji, H.; Jiang, H.; Kaduk, B.; Kähler, S.; Khistyayev, K.; Kim, J.; Kis, G.; Klunzinger, P.; Koczor-Benda, Z.; Koh, J. H.; Kosenkov, D.; Koulias, L. et al. Software for the frontiers of quantum chemistry: An overview of developments in the Q-Chem 5 package. *J. Chem. Phys.* **2021**, *155*, 084801.

- (30) Izsák, R. Single-reference coupled cluster methods for computing excitation energies in large molecules: The efficiency and accuracy of approximations. *WIREs Comput. Mol. Sci.* **2020**, *10*, e1445.
- (31) Koch, H.; Christiansen, O.; Jørgensen, P.; de Merás, A. S.; Helgaker, T. The CC3 model: An iterative coupled cluster approach including connected triples. *J. Chem. Phys.* **1997**, *106*, 1808.
- (32) Christiansen, O.; Koch, H.; Jørgensen, P. Response functions in the CC3 iterative triple excitation model. *J. Chem. Phys.* **1995**, *103*, 7429–7441.
- (33) Paul, A. C.; Myhre, R. H.; Koch, H. New and Efficient Implementation of CC3. *J. Chem. Theory Comput.* **2021**, *17*, 126.
- (34) Koch, H.; Jørgensen, P. Coupled cluster response functions. *J. Chem. Phys.* **1990**, *93*, 3333–3344.
- (35) Christiansen, O.; Jørgensen, P.; Hättig, C. Response functions from Fourier component variational perturbation theory applied to a time-averaged quasienergy. *Int. J. Quantum Chem.* **1998**, *68*, 1–52.
- (36) Helgaker, T.; Coriani, S.; Jørgensen, P.; Kristensen, K.; Olsen, J.; Ruud, K. Recent Advances in Wave Function-Based Methods of Molecular Property Calculations. *Chem. Rev.* **2012**, *112*, 543–631.
- (37) Stanton, J.; Bartlett, R. The equation of motion coupled-cluster method. A systematic biorthogonal approach to molecular excitation energies, transition probabilities, and excited state properties. *J. Chem. Phys.* **1993**, *98*, 7029–7039.
- (38) Bartlett, R. J.; Musiał, M. Coupled-cluster theory in quantum chemistry. *Rev. Mod. Phys.* **2007**, *79*, 291–352.

- (39) Krylov, A. I. Equation-of-motion coupled-cluster methods for open-shell and electronically excited species: The hitchhiker's guide to Fock space. *Annu. Rev. Phys. Chem.* **2008**, *59*, 433–462.
- (40) Coriani, S.; Pawłowski, F.; Olsen, J.; Jørgensen, P. Molecular response properties in equation of motion coupled cluster theory: A time-dependent perspective. *J. Chem. Phys.* **2016**, *144*, 024102.
- (41) Caricato, M.; Trucks, G. W.; Frisch, M. J. On the difference between the transition properties calculated with linear response- and equation of motion-CCSD approaches. *J. Chem. Phys.* **2009**, *131*, 174104.
- (42) Folkestad, S. D.; Kjørstad, E. F.; Myhre, R. H.; Andersen, J. H.; Balbi, A.; Coriani, S.; Giovannini, T.; Goletto, L.; Haugland, T. S.; Hutcheson, A.; Høyvik, I.-M.; Moitra, T.; Paul, A. C.; Scavino, M.; Skeidsvoll, A. S.; Tveten, Å. H.; Koch, H. eT 1.0: An open source electronic structure program with emphasis on coupled cluster and multilevel methods. *J. Chem. Phys.* **2020**, *152*, 184103.
- (43) Beebe, N. H. F.; Linderberg, J. Simplifications in the generation and transformation of two-electron integrals in molecular calculations. *Int. J. Quantum Chem.* **1977**, *12*, 683–705.
- (44) Røeggen, I.; Wisløff-Nilssen, E. On the Beebe-Linderberg two-electron integral approximation. *Chem. Phys. Lett.* **1986**, *132*, 154–160.
- (45) Koch, H.; Sánchez de Merás, A.; Pedersen, T. B. Reduced scaling in electronic structure calculations using Cholesky decompositions. *J. Chem. Phys.* **2003**, *118*, 9481–9484.
- (46) Folkestad, S. D.; Kjørstad, E. F.; Koch, H. An efficient algorithm for Cholesky decomposition of electron repulsion integrals. *J. Chem. Phys.* **2019**, *150*, 194112.
- (47) Cederbaum, L. S.; Domcke, W.; Schirmer, J. Many-body theory of core holes. *Phys. Rev. A: At. Mol. Opt. Phys.* **1980**, *22*, 206–222.

- (48) Gel'mukhanov, F.; Ågren, H. Resonant inelastic x-ray scattering with symmetry-selective excitation. *Phys. Rev. A* **1994**, *49*, 4378–4389.
- (49) Helgaker, T.; Jørgensen, P.; Olsen, J. *Molecular electronic-structure theory*; John Wiley & Sons, 2014.
- (50) Kauczor, J.; Norman, P.; Christiansen, O.; Coriani, S. Communication: A reduced-space algorithm for the solution of the complex linear response equations used in coupled cluster damped response theory. *J. Chem. Phys.* **2013**, *139*, 211102.
- (51) Krishnan, R.; Binkley, J. S.; Seeger, R.; Pople, J. A. Self-consistent molecular orbital methods. XX. A basis set for correlated wave functions. *J. Chem. Phys.* **1980**, *72*, 650–654.
- (52) Clark, T.; Chandrasekhar, J.; Spitznagel, G. W.; Schleyer, P. V. R. Efficient diffuse function-augmented basis sets for anion calculations. III. The 3-21+G basis set for first-row elements, Li-F. *J. Comput. Chem.* **1983**, *4*, 294–301.
- (53) Dunning, T. H. Gaussian basis sets for use in correlated molecular calculations. I. The atoms boron through neon and hydrogen. *J. Chem. Phys.* **1989**, *90*, 1007–1023.
- (54) Kendall, R. A.; Dunning, T. H.; Harrison, R. J. Electron affinities of the first-row atoms revisited. Systematic basis sets and wave functions. *J. Chem. Phys.* **1992**, *96*, 6796–6806.
- (55) Hoy, A.; Bunker, P. A precise solution of the rotation bending Schrödinger equation for a triatomic molecule with application to the water molecule. *J. Mol. Spectrosc.* **1979**, *74*, 1–8.
- (56) Cook, R. L.; De Lucia, F. C.; Helminger, P. Molecular force field and structure of hydrogen sulfide: recent microwave results. *J. Mol. Struct.* **1975**, *28*, 237–246.
- (57) Mulliken, R. S. Report on Notation for the Spectra of Polyatomic Molecules. *J. Chem. Phys.* **1955**, *23*, 1997–2011.
- (58) DTU Computing Center, DTU Computing Center resources. 2021; <https://doi.org/10.48714/DTU.HPC.0001>.

- (59) Schirmer, J.; Trofimov, A. B.; Randall, K. J.; Feldhaus, J.; Bradshaw, A. M.; Ma, Y.; Chen, C. T.; Sette, F. *K*-shell excitation of the water, ammonia, and methane molecules using high-resolution photoabsorption spectroscopy. *Phys. Rev. A* **1993**, *47*, 1136–1147.
- (60) Snow, K. B.; Thomas, T. F. Mass spectrum, ionization potential, and appearance potentials for fragment ions of sulfuric acid vapor. *Int. J. Mass Spectrom.* **1990**, *96*, 49–68.
- (61) Sankari, R.; Ehara, M.; Nakatsuji, H.; Senba, Y.; Hosokawa, K.; Yoshida, H.; De Fanis, A.; Tamenori, Y.; Aksela, S.; Ueda, K. Vibrationally resolved O1s photoelectron spectrum of water. *Chem. Phys. Lett.* **2003**, *380*, 647–653.
- (62) Tao, W.; Klemm, R. B.; Nesbitt, F. L.; Stief, L. J. A discharge flow-photoionization mass spectrometric study of hydroxymethyl radicals (H_2COH and H_2COD): photoionization spectrum and ionization energy. *J. Phys. Chem.* **1992**, *96*, 104–107.
- (63) Drake, J. E.; Riddle, C.; Henderson, H. E.; Glavinčevski, B. ESCA investigations of Group IV derivatives. Part III. Binding energies for methyl substituted disilyl and digermyl chalcogenide series. *Can. J. Chem.* **1977**, *55*, 2957–2961.
- (64) Pellegrin, E.; Perez-Dieste, V.; Escudero, C.; Rejmak, P.; Gonzalez, N.; Fontseré, A.; Prat, J.; Fraxedas, J.; Ferrer, S. Water/methanol solutions characterized by liquid μ -jet XPS and DFT—The methanol hydration case. *J. Mol. Liq.* **2020**, *300*, 112258.
- (65) Prest, H.; Tzeng, W.-B.; Brom, J.; Ng, C. Molecular beam photoionization study of H_2S . *Int. J. Mass Spectrom. Ion Phys.* **1983**, *50*, 315–329.
- (66) Carroll, T. X.; Ji, D.; Maclaren, D. C.; Thomas, T.; Saethre, L. J. Relativistic corrections to reported sulfur 1s ionization energies. *J. Electron Spectros. Relat. Phenomena* **1987**, *42*, 281–284.
- (67) Johnstone, R. A. W.; Mellon, F. A. Effects of induction and resonance in the calculation

- of ionization potentials of substituted benzenes by perturbation molecular orbital theory. *J. Chem. Soc., Faraday Trans. 2* **1973**, 69, 36–42.
- (68) Turci, C. C.; Urquhart, S. G.; Hitchcock, A. P. Inner-shell excitation spectroscopy of aniline, nitrobenzene, and nitroanilines. *Canadian Journal of Chemistry* **1996**, 74, 851–869.
- (69) Tentscher, P. R.; Seidel, R.; Winter, B.; Guerard, J. J.; Arey, J. S. Exploring the Aqueous Vertical Ionization of Organic Molecules by Molecular Simulation and Liquid Microjet Photoelectron Spectroscopy. *J. Phys. Chem. B* **2015**, 119, 238–256.
- (70) Nolting, D.; Ottosson, N.; Faubel, M.; Hertel, I. V.; Winter, B. Pseudoequivalent Nitrogen Atoms in Aqueous Imidazole Distinguished by Chemical Shifts in Photoelectron Spectroscopy. *J. Am. Chem. Soc.* **2008**, 130, 8150–8151.
- (71) Vidal, M. L.; Feng, X.; Epifanovsky, E.; Krylov, A. I.; Coriani, S. New and Efficient Equation-of-Motion Coupled-Cluster Framework for Core-Excited and Core-Ionized States. *J. Chem. Theory Comput.* **2019**, 15, 3117–3133.
- (72) Coriani, S.; Christiansen, O.; Fransson, T.; Norman, P. Coupled-cluster response theory for near-edge x-ray-absorption fine structure of atoms and molecules. *Phys. Rev. A* **2012**, 85, 022507.
- (73) Carbone, J. P.; Cheng, L.; Myhre, R. H.; Matthews, D.; Koch, H.; Coriani, S. Chapter Eleven - An analysis of the performance of coupled cluster methods for *K*-edge core excitations and ionizations using standard basis sets. In *State of The Art of Molecular Electronic Structure Computations: Correlation Methods, Basis Sets and More*; Ancarani, L. U., Hoggan, P. E., Eds.; Advances in Quantum Chemistry; Academic Press, 2019; Vol. 79; pp 241–261.
- (74) Frati, F.; de Groot, F.; Cerezo, J.; Santoro, F.; Cheng, L.; Faber, R.; Coriani, S. Coupled cluster study of the x-ray absorption spectra of formaldehyde derivatives at the oxygen, carbon, and fluorine K-edges. *J. Chem. Phys.* **2019**, 151, 064107.

- (75) Reinholdt, P.; Vidal, M. L.; Kongsted, J.; Iannuzzi, M.; Coriani, S.; Odelius, M. Nitrogen K-Edge X-ray Absorption Spectra of Ammonium and Ammonia in Water Solution: Assessing the Performance of Polarizable Embedding Coupled Cluster Methods. *J. Phys. Chem. Lett.* **2021**, *12*, 8865–8871.
- (76) Weinhardt, L.; Benkert, A.; Meyer, F.; Blum, M.; Wilks, R. G.; Yang, W.; Bär, M.; Reinert, F.; Heske, C. Nuclear dynamics and spectator effects in resonant inelastic soft x-ray scattering of gas-phase water molecules. *J. Chem. Phys.* **2012**, *136*, 144311.
- (77) Larkins, F. P.; Seen, A. J. Ab initio studies of molecular X-ray emission processes: methanol. *Phys. Scripta* **1990**, *41*, 827–832.
- (78) Benkert, A.; Meyer, F.; Hauschild, D.; Blum, M.; Yang, W.; Wilks, R. G.; Bär, M.; Reinert, F.; Heske, C.; Weinhardt, L. Isotope Effects in the Resonant Inelastic Soft X-ray Scattering Maps of Gas-Phase Methanol. *J. Phys. Chem. A* **2016**, *120*, 2260–2267.
- (79) Vaz da Cruz, V.; Ignatova, N.; Couto, R. C.; Fedotov, D. A.; Rehn, D. R.; Savchenko, V.; Norman, P.; Ågren, H.; Polyutov, S.; Niskanen, J.; Eckert, S.; Jay, R. M.; Fondell, M.; Schmitt, T.; Pietzsch, A.; Föhlisch, A.; Gel'mukhanov, F.; Odelius, M.; Kimberg, V. Nuclear dynamics in resonant inelastic X-ray scattering and X-ray absorption of methanol. *J. Chem. Phys.* **2019**, *150*, 234301.
- (80) Bodeur, S.; Esteve, J. M. Photoabsorption spectra of H₂S, CH₃SH and SO₂ near the sulfur *K* edge. *J. Chem. Phys.* **1985**, *100*, 415–427.
- (81) Reynaud, C.; Gaveau, M.-A.; Bisson, K.; Millié, P.; Nenner, I.; Bodeur, S.; Archirel, P.; Lévy, B. Double-core ionization and excitation above the sulphur *K*-edge in H₂S, SO₂ and SF₆. *J. Phys. B: At. Mol. Opt. Phys.* **1996**, *29*, 5403–5419.
- (82) Kavčič, M.; Žitnik, M.; Bučar, K.; Mihelič, A. Resonant Inelastic X-ray Scattering study of H₂S molecules around the sulfur *K* absorption edge. *J. Phys. Conf. Ser.* **2009**, *194*, 022016.

- (83) Bilalbegović, G.; Maksimović, A.; Valencic, L. A.; Lehtola, S. Sulfur Molecules in Space by X-rays: A Computational Study. *ACS Earth and Space Chemistry* **2021**, *5*, 436 – 448.
- (84) Ertan, E.; Lundberg, M.; Sørensen, L. K.; Odelius, M. Setting the stage for theoretical x-ray spectra of the H₂S molecule with multi-configurational quantum chemical calculations of the energy landscape. *J. Chem. Phys.* **2020**, *152*, 094305.
- (85) Meyer, F.; Blum, M.; Benkert, A.; Hauschild, D.; Jeyachandran, Y. L.; Wilks, R. G.; Yang, W.; Bär, M.; Reinert, F.; Heske, C.; Zharnikov, M.; Weinhardt, L. Site-specific electronic structure of imidazole and imidazolium in aqueous solutions. *Phys. Chem. Chem. Phys.* **2018**, *20*, 8302–8310.
- (86) Jagoda-Cwiklik, B.; Slavíček, P.; Cwiklik, L.; Nolting, D.; Winter, B.; Jungwirth, P. Ionization of Imidazole in the Gas Phase, Microhydrated Environments, and in Aqueous Solution. *J. Phys. Chem. A* **2008**, *112*, 3499–3505.
- (87) Thomason, M. J. Soft X-ray Spectroscopy of Molecular Species in Solution: Studies of Imidazole and Imidazole/Water Systems. Ph.D. thesis, University of Manchester, 2012.
- (88) Gougoula, E.; Cole, D. J.; Walker, N. R. Bifunctional Hydrogen Bonding of Imidazole with Water Explored by Rotational Spectroscopy and DFT Calculations. *J. Phys. Chem. A* **2020**, *124*, 2649–2659.
- (89) Sánchez de Merás, A. M. J.; Koch, H.; Cuesta, I. G.; Boman, L. Cholesky decomposition-based definition of atomic subsystems in electronic structure calculations. *J. Chem. Phys.* **2010**, *132*, 204105.
- (90) Aquilante, F.; Bondo Pedersen, T.; Sánchez de Merás, A.; Koch, H. Fast noniterative orbital localization for large molecules. *J. Chem. Phys.* **2006**, *125*, 174101.
- (91) Pulay, P. Localizability of dynamic electron correlation. *Chem. Phys. Lett.* **1983**, *100*, 151–154.

- (92) Sæbø, S.; Pulay, P. Local treatment of electron correlation. *Annu. Rev. Phys. Chem.* **1993**, *44*, 213–236.
- (93) Folkestad, S. D.; Koch, H. Equation-of-motion MLCCSD and CCSD-in-HF oscillator strengths and their application to core excitations. *J. Chem. Theory Comput.* **2020**, *16*, 6869–6879.

D.2 Supplementary Information

New Implementation of an Equation-of-Motion Coupled-Cluster Damped-Response Framework with Illustrative Applications to Resonant Inelastic X-ray Scattering. Supplementary Information

Anna Kristina Schnack-Petersen,^{*,†} Torsha Moitra,^{†,‡} Sarai Dery Folkestad,[¶] and
Sonia Coriani^{*,†,¶}

[†]*DTU Chemistry, Technical University of Denmark, DK-2800 Kongens Lyngby, Denmark*

[‡]*Hylleraas Centre for Quantum Molecular Sciences, Department of Chemistry, UiT – The Arctic
University of Norway, 9037 Tromsø, Norway*

[¶]*Department of Chemistry, Norwegian University of Science and Technology, NO-7491
Trondheim, Norway*

E-mail: akrsc@kemi.dtu.dk; soco@kemi.dtu.dk

S1 Geometries

S1.1 H₂O determined from experimental parameters given in Angstrom

O	0.000000000000	0.000000000000	0.000000000000
H	0.756690223738	-0.585891838297	0.000000000000
H	-0.756690223738	-0.585891838297	0.000000000000

S1.1.1 6-311++G** basis with additional Rydberg functions on O in e^T format

H	0		
S	3	1.00	
	33.86500		0.0254938
	5.094790		0.190373
	1.158790		0.852161
S	1	1.00	
	0.325840		1.000000
S	1	1.00	
	0.102741		1.000000
S	1	1.00	
	0.0360000		1.0000000
P	1	1.00	
	0.750		1.000000

O	0		
S	6	1.00	
	8588.500		0.00189515
	1297.230		0.0143859
	299.2960		0.0707320
	87.37710		0.2400010

	25.67890	0.5947970	
	3.740040	0.2808020	
SP	3 1.00		
	42.11750	0.113889	0.0365114
	9.628370	0.920811	0.237153
	2.853320	-0.00327447	0.819702
SP	1 1.00		
	0.905661	1.000000	1.000000
SP	1 1.00		
	0.255611	1.000000	1.000000
SP	1 1.00		
	0.0845000	1.0000000	1.0000000
D	1 1.00		
	1.292	1.000000	
S	1 1.00		
	0.0058583805	1.000000	
S	1 1.00		
	0.0033459739	1.000000	
S	1 1.00		
	0.0020484225	1.000000	
P	1 1.00		
	0.0099882106	1.000000	
P	1 1.00		
	0.0056893607	1.000000	
P	1 1.00		
	0.0034756797	1.000000	

S1.2 CH₃OH optimized at the MP2/cc-pCVTZ level of theory given in Angstrom

C	-0.046496000000	0.660458000000	0.000000000000
O	-0.046496000000	-0.755349000000	0.000000000000
H	-1.084194000000	0.974061000000	0.000000000000
H	0.867053000000	-1.044140000000	0.000000000000
H	0.434040000000	1.075063000000	0.885955000000
H	0.434040000000	1.075063000000	-0.885955000000

S1.3 H₂S determined from experimental parameters given in Angstrom

S	0.000000000000	0.000000000000	0.000000000000
H	0.961928000000	0.927141000000	0.000000000000
H	-0.961928000000	0.927141000000	0.000000000000

S1.4 Para-nitro-aniline, taken from Ref. 1, given in Angstrom

C	0.000000000000	0.000000000000	0.7153356937
C	1.2195927633	0.000000000000	0.0255507248
C	1.2182354930	0.000000000000	-1.3699791187
C	0.000000000000	0.000000000000	-2.0937199737
C	-1.2182354930	0.000000000000	-1.3699791187
C	-1.2195927633	0.000000000000	0.0255507248
H	2.1553754221	0.000000000000	0.5869226624
H	2.1689860113	0.000000000000	-1.9130375835
H	-2.1689860113	0.000000000000	-1.9130375835
H	-2.1553754221	0.000000000000	0.5869226624
N	0.000000000000	0.000000000000	-3.4666053646
N	0.000000000000	0.000000000000	2.1848883212

O -1.0841264669 0.0000000000 2.7496493313
O 1.0841264669 0.0000000000 2.7496493313
H -0.8656098383 0.0000000000 -3.9833468735
H 0.8656098383 0.0000000000 -3.9833468735

S1.5 Imidazole optimized at the MP2/cc-pCVTZ level of theory given in Angstrom

N	-0.000000000000	1.099119000000	-0.000000000000
N	-0.737166000000	-0.988233000000	0.000000000000
C	-1.086139000000	0.283038000000	-0.000000000000
C	1.113483000000	0.304839000000	0.000000000000
C	0.632181000000	-0.980639000000	0.000000000000
H	-0.011890000000	2.102842000000	-0.000000000000
H	-2.091912000000	0.662041000000	-0.000000000000
H	2.107723000000	0.708934000000	0.000000000000
H	1.199092000000	-1.893448000000	0.000000000000

S1.6 Pyridine optimized at the MP2/cc-pCVTZ level of theory given in Angstrom

N	-1.199787000000	0.756514000000	-0.000000000000
C	1.168569000000	-0.737077000000	0.000000000000
C	-1.214844000000	-0.580128000000	-0.000000000000
C	-0.068612000000	-1.364965000000	-0.000000000000
C	1.202280000000	0.650257000000	0.000000000000
C	-0.000000000000	1.346133000000	0.000000000000
H	2.082445000000	-1.312980000000	0.000000000000
H	2.138511000000	1.188332000000	0.000000000000
H	-0.004177000000	2.427937000000	-0.000000000000
H	-0.149869000000	-2.441510000000	-0.000000000000

H -2.192759000000 -1.042694000000 -0.000000000000

S1.6.1 6-311++G** basis with additional Rydberg functions on N in e^T format

H	0		
S	3	1.00	
		33.86500	0.0254938
		5.094790	0.190373
		1.158790	0.852161
S	1	1.00	
		0.325840	1.000000
S	1	1.00	
		0.102741	1.000000
S	1	1.00	
		0.0360000	1.0000000
P	1	1.00	
		0.750	1.000000

C	0		
S	6	1.00	
		4563.240	0.00196665
		682.0240	0.0152306
		154.9730	0.0761269
		44.45530	0.2608010
		13.02900	0.6164620
		1.827730	0.2210060
SP	3	1.00	
		20.96420	0.114660 0.0402487
		4.803310	0.919999 0.237594

		1.459330	-0.00303068	0.815854
SP	1	1.00		
		0.4834560	1.000000	1.000000
SP	1	1.00		
		0.1455850	1.000000	1.000000
SP	1	1.00		
		0.0438000	1.0000000	1.0000000
D	1	1.00		
		0.626	1.000000	

N		0		
S	6	1.00		
		6293.480	0.00196979	
		949.0440	0.0149613	
		218.7760	0.0735006	
		63.69160	0.2489370	
		18.82820	0.6024600	
		2.720230	0.2562020	
SP	3	1.00		
		30.63310	0.111906	0.0383119
		7.026140	0.921666	0.237403
		2.112050	-0.00256919	0.817592
SP	1	1.00		
		0.684009	1.000000	1.000000
SP	1	1.00		
		0.200878	1.000000	1.000000
SP	1	1.00		
		0.0639000	1.0000000	1.0000000
D	1	1.00		

		0.913	1.000000
S	1	1.00	
		0.0112533427	1.0000000000
S	1	1.00	
		0.0058583805	1.0000000000
S	1	1.00	
		0.0033459739	1.0000000000
S	1	1.00	
		0.0020484225	1.0000000000
P	1	1.00	
		0.0192542060	1.0000000000
P	1	1.00	
		0.0099882106	1.0000000000
P	1	1.00	
		0.0056893607	1.0000000000
P	1	1.00	
		0.0034756797	1.0000000000
D	1	1.00	
		0.0274456919	1.0000000000
D	1	1.00	
		0.0142043987	1.0000000000
D	1	1.00	
		0.0080765930	1.0000000000
D	1	1.00	
		0.0049271863	1.0000000000

O	0		
S	6	1.00	
		8588.500	0.00189515

		1297.230	0.0143859		
		299.2960	0.0707320		
		87.37710	0.2400010		
		25.67890	0.5947970		
		3.740040	0.2808020		
SP	3	1.00			
		42.11750	0.113889	0.0365114	
		9.628370	0.920811	0.237153	
		2.853320	-0.00327447	0.819702	
SP	1	1.00			
		0.905661	1.000000	1.000000	
SP	1	1.00			
		0.255611	1.000000	1.000000	
SP	1	1.00			
		0.0845000	1.0000000	1.0000000	
D	1	1.00			
		1.292	1.000000		

S2 H₂O

Table S1: H₂O: Unshifted O *K*-edge XAS data using the 6-311++G** basis set with additional Rydberg functions on Oxygen.

EOM-CC2			EOM-CCSD			fc-EOM-CCSD		
Sym. ^a	$\omega_{obs,e}/\text{eV}$	f_{osc}	Sym. ^a	$\omega_{obs,e}/\text{eV}$	f_{osc}	Sym. ^b	$\omega_{obs,e}/\text{eV}$	f_{osc}
1A ₁	534.4946	0.00615	1A ₁	535.6955	0.01179	1A ₁	535.2154	0.01266
1B ₂	536.0207	0.00834	1B ₂	537.4812	0.02512	1B ₁	537.0019	0.02607
1B ₁	536.5695	0.00155	1B ₁	538.9083	0.00558	1B ₂	538.4294	0.00596
2A ₁	536.6292	0.00077	2A ₁	539.0138	0.00443	2A ₁	538.5350	0.00454
3A ₁	536.7800	0.00167	3A ₁	539.3419	0.00161	3A ₁	538.8632	0.00169
2B ₂	537.1659	0.00299	2B ₂	539.6601	0.00522	2B ₁	539.1814	0.00552
2B ₁	537.3722	0.00054	2B ₁	540.2582	0.00181	2B ₂	539.7796	0.00189
4A ₁	537.3945	0.00031	4A ₁	540.2979	0.00156	4A ₁	539.8193	0.00160
5A ₁	537.4230	0.00053	5A ₁	540.3714	0.00043	5A ₁	539.8929	0.00045
3B ₂	537.6143	0.00222	3B ₂	540.4529	0.00134	3B ₁	539.9744	0.00142

^a Dalton (Mulliken) symmetry notation.

^b Q-Chem (non-Mulliken) symmetry notation.

Table S2: H₂O: Unshifted valence absorption data using the 6-311++G** basis set with additional Rydberg functions on Oxygen. In addition, valence transitions were computed in a space orthogonal to the oxygen core space.

^a Dalton (Mulliken) symmetry notation. ^b Q-Chem (non-Mulliken) symmetry notation.

EOM-CC2			EOM-CCSD			fc-EOM-CCSD		
Sym. ^a	$\omega_{abs,v}/\text{eV}$	f_{osc}	Sym. ^a	$\omega_{abs,v}/\text{eV}$	f_{osc}	Sym. ^b	$\omega_{abs,v}/\text{eV}$	f_{osc}
1B ₁	7.0638	0.04923	1B ₁	7.4049	0.04683	1B ₂	7.3824	0.04678
1A ₂	8.6920	0.00000	1A ₂	9.1558	0.00000	1A ₂	9.1349	0.00000
1A ₁	9.3046	0.03077	1A ₁	9.7566	0.08667	1A ₁	9.7348	0.08688
2B ₁	9.3881	0.00424	2B ₁	10.0254	0.00499	2B ₂	10.0055	0.00500
2A ₁	9.5193	0.06698	2A ₁	10.1116	0.01412	2A ₁	10.0917	0.01395
3B ₁	9.6651	0.00101	3B ₁	10.3876	0.00032	3B ₂	10.3675	0.00031
2A ₂	10.0870	0.00000	2A ₂	10.7960	0.00000	2A ₂	10.7760	0.00000
3A ₁	10.3722	0.00007	4B ₁	11.2175	0.00127	4B ₂	11.1980	0.00127
4B ₁	10.3802	0.00106	3A ₁	11.2220	0.00004	3A ₁	11.2026	0.00004
5B ₁	10.4456	0.00001	5B ₁	11.3052	0.00017	5B ₂	11.2857	0.00017
3A ₂	10.6127	0.00000	3A ₂	11.4226	0.00000	3A ₂	11.4030	0.00000
6B ₁	10.7838	0.00078	1B ₂	11.5198	0.02398	1B ₁	11.5000	0.02407
4A ₁	10.8119	0.00000	6B ₁	11.6806	0.00123	6B ₂	11.6612	0.00123
7B ₁	10.8396	0.00018	4A ₁	11.6957	0.00000	4A ₁	11.6764	0.00000
1B ₂	11.0385	0.01837	7B ₁	11.7220	0.00008	7B ₂	11.7026	0.00008
4A ₂	11.0468	0.00000	4A ₂	11.8183	0.00000	4A ₂	11.7987	0.00000
8B ₁	11.6090	0.00001	8B ₁	12.2254	0.00014	8B ₂	12.2063	0.00014
5A ₁	11.6434	0.00362	5A ₁	12.2847	0.00365	5A ₁	12.2657	0.00364
6A ₁	11.9789	0.01160	6A ₁	12.6793	0.01097	6A ₁	12.6597	0.01095
2B ₂	12.4081	0.01235	9B ₁	13.0676	0.09370	9B ₂	13.0471	0.09350
9B ₁	12.6215	0.03281	2B ₂	13.1248	0.01858	5A ₂	13.1052	0.00000
7A ₁	12.6539	0.00116	5A ₂	13.1249	0.00000	2B ₁	13.1057	0.01861
10B ₁	12.6642	0.05516	10B ₁	13.4475	0.00034	10B ₂	13.4287	0.00033
5A ₂	12.6840	0.00000	7A ₁	13.4594	0.00093	7A ₁	13.4405	0.00092
8A ₁	12.7382	0.00361	11B ₁	13.5330	0.00896	11B ₂	13.5123	0.00902
3B ₂	12.9248	0.00991	8A ₁	13.5654	0.00350	8A ₁	13.5464	0.00349
9A ₁	13.0676	0.00008	3B ₂	13.7218	0.00666	3B ₁	13.7029	0.00669
11B ₁	13.0808	0.00016	9A ₁	13.8849	0.00012	9A ₁	13.8654	0.00012
10A ₁	13.1174	0.00390	4B ₂	13.9215	0.14358	4B ₁	13.9038	0.14340
12B ₁	13.1320	0.00927	12B ₁	13.9299	0.00002	12B ₂	13.9112	0.00002

Table S3: H₂O: Unshifted RIXS data for the pump frequency at resonance with the first core excitation (core 1A₁) calculated using different methods. RIXS cross sections for $\theta = 45^\circ$ at the EOM-CCSD, CVS-uS-EOM-CCSD and CVS-EOM-CCSD level of theory are all based on emission energies calculated at the EOM-CCSD level of theory. CVS and CVS-uS refer to a projection in the damped response solver. All calculations employed the 6-311++G** basis set with additional Rydberg functions on Oxygen.

ω_{em}			$\sigma_{45^\circ}^{RIXS}/\text{a.u.}$				
CCSD	fc-CCSD	CC2	EOM-CCSD	CVS-uS-EOM-CCSD	CVS-EOM-CCSD	fc-CVS-EOM-CCSD	EOM-CC2
528.2906	527.8331	527.4307	0.02113	0.02152	0.01928	0.02107	0.01259
526.5398	526.0807	525.8026	0.00040	0.00040	0.00034	0.00016	0.00038
525.9389	525.4821	525.1898	0.01162	0.01218	0.01067	0.01156	0.00244
525.6701	525.2100	525.1065	0.00063	0.00056	0.00032	0.00005	0.00055
525.5838	525.1229	524.9754	0.00210	0.00222	0.00231	0.00207	0.00606
525.3079	524.848	524.8295	0.00023	0.00024	0.00021	0.00023	0.00002
524.8995	524.4399	524.4075	0.00002	0.00001	0.00000	0.00003	0.00001
524.4780	524.0181	524.1223	0.00013	0.00012	0.00006	0.00001	0.00002
524.4736	524.0127	524.1144	0.00002	0.00002	0.00014	0.00002	0.00012
524.3903	523.931	524.0491	0.00005	0.00006	0.00005	0.00005	0.00000
524.2728	523.8113	523.8818	0.00003	0.00003	0.00000	0.00001	0.00001
524.1756	523.7160	523.7109	0.00035	0.00037	0.00086	0.00012	0.00005
524.0148	523.5555	523.6826	0.00007	0.00007	0.00004	0.00001	0.00001
523.9999	523.5392	523.6551	0.00000	0.00000	0.00010	0.00000	0.00009
523.9735	523.5120	523.4559	0.00006	0.00006	0.00003	0.00001	0.00031
523.8771	523.4167	523.4477	0.00011	0.00011	0.00003	0.00000	0.00014
523.4701	523.0086	522.8856	0.00046	0.00046	0.00023	0.00001	0.00043
523.4107	522.9487	522.8513	0.00011	0.00011	0.00021	0.00007	0.00007
523.0162	522.5568	522.5158	0.00018	0.00018	0.00017	0.00018	0.00001
522.6279	522.1677	522.0866	0.00020	0.00023	0.00018	0.00017	0.00003
522.5707	522.1106	521.8730	0.00005	0.00005	0.00012	0.00004	0.00017
522.5704	522.1106	521.8406	0.00020	0.00018	0.00005	0.00000	0.00001
522.2480	521.7868	521.8303	0.00010	0.00010	0.00005	0.00000	0.00000
522.2360	521.7759	521.8104	0.00001	0.00001	0.00007	0.00001	0.00026
522.1625	521.7024	521.7563	0.00083	0.00074	0.00032	0.00004	0.00000
522.1302	521.6697	521.5699	0.00003	0.00003	0.00004	0.00003	0.00002
521.9737	521.5119	521.4270	0.00031	0.00033	0.00032	0.00033	0.00000
521.8107	521.3514	521.4137	0.00001	0.00001	0.00025	0.00001	0.00009
521.774	521.3106	521.3772	0.01381	0.01449	0.01303	0.01429	0.00000
521.7655	521.3051	521.3625	0.00007	0.00007	0.00003	0.00000	0.00086

Table S4: H₂O: unshifted RIXS data for the pump frequency at resonance with the second core excitation (core $1B_2$ in Mulliken symmetry notation) calculated using different methods. RIXS cross sections for $\theta = 45^\circ$ at the EOM-CCSD, CVS-uS-EOM-CCSD and CVS-EOM-CCSD level of theory are all based on emission energies calculated at the EOM-CCSD level of theory. CVS and CVS-uS refers to a projection in the damped response solver. All calculations employed the 6-311++G** basis set with additional Rydberg functions on Oxygen.

ω_{em}			$\sigma_{45^\circ}^{RIXS}/a.u.$				
CCSD	fc-CCSD	CC2	EOM-CCSD	CVS-uS-EOM-CCSD	CVS-EOM-CCSD	fc-CVS-EOM-CCSD	EOM-CC2
530.0764	529.6182	528.9570	0.00007	0.00006	0.00004	0.00013	0.00005
528.3254	527.8658	527.3286	0.04099	0.04192	0.03876	0.04067	0.01648
527.7246	527.2671	526.7161	0.00010	0.00011	0.00020	0.00010	0.00012
527.4560	526.9950	526.6326	0.00063	0.00060	0.00037	0.00003	0.00074
527.3697	526.9107	526.5014	0.00017	0.00018	0.00072	0.00022	0.00009
527.0935	526.6331	526.3556	0.00000	0.00000	0.00001	0.00001	0.00010
526.6851	526.2249	525.9338	0.00188	0.00195	0.00179	0.00188	0.00010
526.2639	525.8032	525.6486	0.00012	0.00012	0.00007	0.00000	0.00001
526.2592	525.8004	525.6404	0.00005	0.00005	0.00020	0.00005	0.00012
526.1760	525.7161	525.5751	0.00000	0.00000	0.00000	0.00000	0.00000
526.0587	525.5991	525.4081	0.00052	0.00056	0.00050	0.00053	0.00001
525.9615	525.5011	525.2369	0.03230	0.03327	0.02982	0.03103	0.00006
525.8007	525.3406	525.2089	0.00005	0.00005	0.00004	0.00000	0.00001
525.7855	525.3242	525.1811	0.00003	0.00003	0.00014	0.00003	0.00008
525.7591	525.2998	524.9822	0.00005	0.00005	0.00002	0.00000	0.01365
525.6630	525.2018	524.9738	0.00031	0.00036	0.00027	0.00025	0.00012
525.2559	524.7963	524.4118	0.00064	0.00062	0.00036	0.00005	0.00077
525.1966	524.7365	524.3773	0.00011	0.00012	0.00029	0.00012	0.00004
524.8021	524.3419	524.0418	0.00005	0.00005	0.00005	0.00003	0.00010
524.4135	523.9555	523.6126	0.00007	0.00007	0.00001	0.00001	0.00008
524.3563	523.8956	523.3993	0.00217	0.00218	0.00191	0.00194	0.00017
524.3563	523.8956	523.3669	0.00027	0.00030	0.00017	0.00012	0.00000
524.0339	523.5718	523.3566	0.00012	0.00012	0.00006	0.00001	0.00000
524.0219	523.5609	523.3367	0.00001	0.00001	0.00008	0.00001	0.00025
523.9482	523.4902	523.2826	0.00075	0.00071	0.00031	0.00001	0.00001
523.9158	523.4548	523.0959	0.00000	0.00000	0.00002	0.00000	0.00003
523.7593	523.2997	522.9530	0.00083	0.00083	0.00070	0.00073	0.00000
523.5963	523.1364	522.9400	0.00034	0.00036	0.00059	0.00035	0.00010
523.5599	523.0983	522.9032	0.00008	0.00008	0.00004	0.00009	0.00000
523.5514	523.0902	522.8888	0.00008	0.00008	0.00004	0.00000	0.00089

Table S5: H₂O: Unshifted nonresonant (XES) data calculated using different methods. All calculations employed the 6-311++G** basis set with additional Rydberg functions on Oxygen.

ω_{em}			f_{osc}		
CCSD	fc-CCSD	CC2	EOM-CCSD	fc-CVS-EOM-CCSD	EOM-CC2
529.1262	528.6672	526.7877	0.05311	0.05361	0.05556
526.8753	526.4157	524.5019	0.04308	0.04359	0.04459
522.5313	522.0673	519.981	0.03881	0.03938	0.04028

S3 CH₃OH

The XAS spectrum is computed at both the CVS-EOM-CCSD and the CVS-EOM-CC2 level of theory. It is observed in Fig. S1 that the two methods give rather different results. For the O *K*-edge XAS spectra (Fig. S1 left) there is a large difference in the position of the second peak as well as its intensity. The differences are smaller for the C *K*-edge XAS spectra, where the CVS-EOM-CC2 results show a second peak with lower intensity and a third peak of higher intensity compared to both the CVS-EOM-CCSD result and experiment. Both methods show a red-shift of the second peak compared to experiment. The character of the first two transitions with respect to symmetry is A' at both computed levels of theory at the Oxygen *K*-edge. Likewise, both methods find the first core transition at the Carbon *K*-edge to have A' character. Observe that all the plotted core excitations are below the calculated ionization thresholds. Prince et al.² assigned the higher energy experimental features at the C *K*-edge mainly to vibrational states, but also to some extent to more diffuse orbitals as e.g. 5*p* and 6*p*. These features are not reproduced by our calculations. Improvements might be obtained by including more diffuse functions in the basis set, however, the features caused by vibrations would still be beyond such calculations. As our main concern is the first few strong features, we content ourselves with the chosen levels of theory as these show reasonable agreement for this region. We observe that the valence spectra in Fig. S2 are very similar for the two methods, except for a small difference in the shifts between the three peaks at lowest energy. The valence spectra also seem unaffected by changing which core space should be orthogonal to the space employed for the calculation.

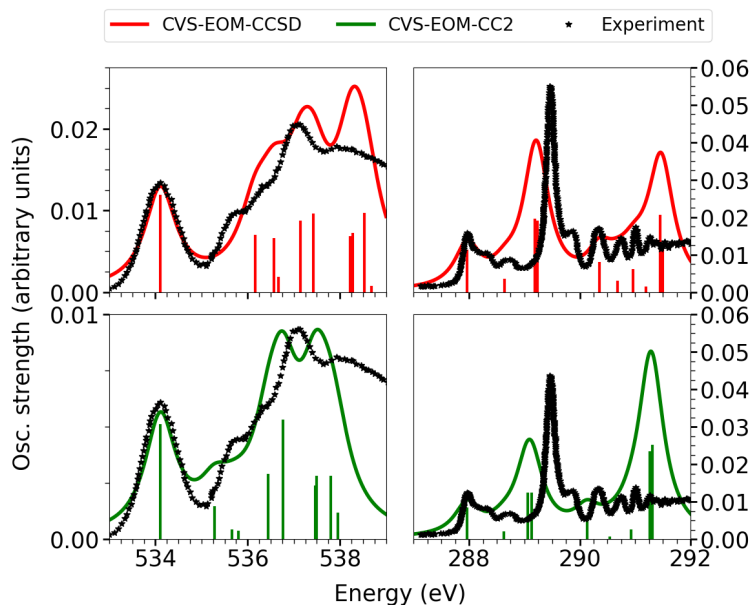


Figure S1: CH_3OH : XAS spectra at the Oxygen (left) and Carbon (right) K -edge calculated at the CVS-EOM-CC2/aug-cc-pVTZ (green) and CVS-EOM-CCSD/aug-cc-pVTZ (red) levels of theory. In all calculations 10 core transitions have been determined and plotted. The experimental data (black) was adapted from Prince et al.² A Lorentzian broadening has been applied with $\text{HWHM}=0.41$ eV for O K -edge and $\text{HWHM}=0.27$ eV for C K -edge. At the O K -edge the CVS-EOM-CCSD result was shifted by 0.07 eV to align with experiment, while the CVS-EOM-CC2 result was shifted by -1.39 eV. At the C K -edge the shifts were -2.09 eV and -1.07 eV, respectively

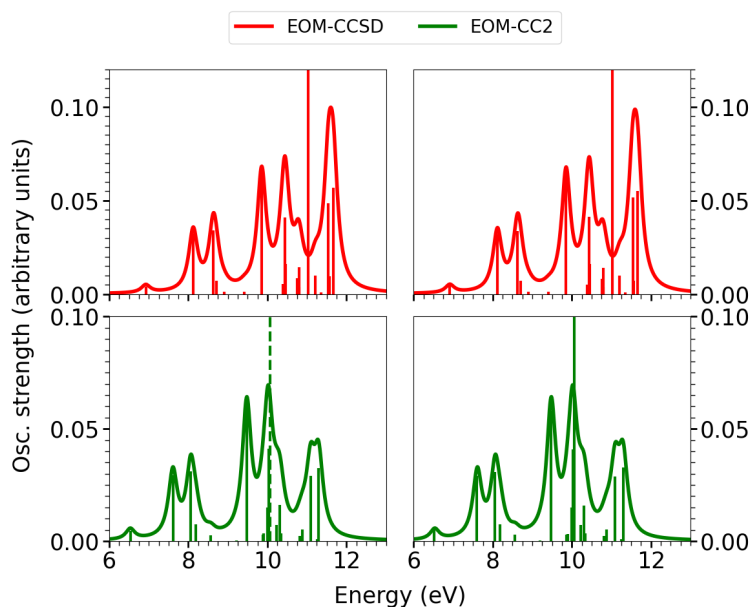


Figure S2: CH_3OH : Valence absorption spectra calculated in the space orthogonal to the O core space (left) or the C core space (right). The calculations employed the CVS-EOM-CC2/aug-cc-pVTZ level of theory (green) and the CVS-EOM-CCSD/aug-cc-pVTZ level of theory (red). For all methods 20 valence transitions have been determined and plotted. The first valence ionization potentials are shown as vertical lines spanning the entire intensity. Results have been shifted to match the EOM-CCSD results computed in a space orthogonal to the O core space. A Lorentzian broadening has been applied with $\text{HWHM}=0.41$ eV.

S3.0.1 Data tables

Table S6: CH₃OH: Unshifted XAS data calculated with the aug-cc-pVTZ basis.

^a Mulliken symmetry notation.

Oxygen <i>K</i> -edge						Carbon <i>K</i> -edge					
EOM-CC2			EOM-CCSD			EOM-CC2			EOM-CCSD		
Sym. ^a	$\omega_{abs,c}/\text{eV}$	f_{osc}	Sym. ^a	$\omega_{abs,c}/\text{eV}$	f_{osc}	Sym. ^a	$\omega_{abs,c}/\text{eV}$	f_{osc}	Sym. ^a	$\omega_{abs,c}/\text{eV}$	f_{osc}
1A'	534.0381	0.00512	1A'	535.4971	0.01195	1A'	290.0519	0.00838	1A'	289.0359	0.01128
2A'	535.2052	0.00146	2A'	537.5454	0.00699	2A'	290.7113	0.00213	2A'	289.7148	0.00348
1A''	535.5883	0.00043	3A'	537.9517	0.00663	1A''	291.1412	0.01245	1A''	290.2563	0.01956
3A'	535.7216	0.00038	1A''	538.0538	0.00186	3A'	291.2186	0.01251	3A'	290.3097	0.01906
4A'	536.3741	0.00290	4A'	538.5324	0.00877	4A'	292.2152	0.00567	4A'	291.4261	0.00799
5A'	536.6930	0.00533	5A'	538.8164	0.00959	5A'	292.6274	0.00070	5A'	291.7484	0.00299
2A''	537.3881	0.00238	2A''	539.6072	0.00687	6A'	293.0101	0.00259	4A''	292.0348	0.00617
6A'	537.4183	0.00283	6A'	539.6603	0.00723	2A''	293.0729	0.00001	6A'	292.2661	0.00151
7A'	537.7288	0.00281	7A'	539.9127	0.00971	A3''	293.3538	0.02341	7A'	292.5199	0.02069
8A'	537.8811	0.00118	8A'	540.0707	0.00078	7A'	293.3934	0.02527	3A''	292.5698	0.01331

Table S7: CH₃OH: Unshifted valence absorption data computed in a space orthogonal to the core space (with a "removed core") and aug-cc-pVTZ basis on all atoms.

^a Mulliken symmetry notation.

Oxygen as "removed core"						Carbon as "removed core"					
EOM-CC2			EOM-CCSD			EOM-CC2			EOM-CCSD		
Sym. ^a	ω_i/eV	f_{osc}	Sym. ^a	$\omega_{abs,v}/\text{eV}$	f_{osc}	Sym. ^a	$\omega_{abs,v}/\text{eV}$	f_{osc}	Sym. ^a	$\omega_{abs,v}/\text{eV}$	f_{osc}
1A''	6.5321	0.00473	1A''	6.9241	0.00415	1A''	6.5205	0.00486	1A''	6.9128	0.00427
2A''	7.6093	0.02929	2A''	8.1227	0.03225	2A''	7.6017	0.02902	2A''	8.1168	0.03193
1A'	8.0627	0.03106	1A'	8.6336	0.03401	1A'	8.0548	0.03088	1A'	8.6270	0.03384
3A''	8.1923	0.00737	3A''	8.7071	0.00699	3A''	8.1838	0.00737	3A''	8.6998	0.00700
2A'	8.5677	0.00252	2A'	8.9076	0.00122	2A'	8.5585	0.00273	2A'	8.8999	0.00137
4A''	8.8868	0.00011	4A''	9.4176	0.00130	4A''	8.8766	0.00010	4A''	9.4083	0.00126
5A''	9.2134	0.00024	5A''	9.7079	0.00000	5A''	9.2022	0.00025	5A''	9.6978	0.00000
3A'	9.4778	0.05852	3A'	9.8547	0.06272	3A'	9.4735	0.05814	3A'	9.8532	0.06236
4A'	9.8817	0.00282	4A'	10.4000	0.00548	4A'	9.8718	0.00275	4A'	10.3916	0.00491
6A''	9.9021	0.00350	6A''	10.4155	0.00304	6A''	9.8925	0.00327	6A''	10.4064	0.00277
7A''	10.0059	0.01499	5A'	10.4416	0.04089	7A''	10.0008	0.01497	5A'	10.4380	0.04128
5A'	10.0267	0.04102	7A''	10.4536	0.01617	5A'	10.0212	0.04093	7A''	10.4512	0.01624
8A''	10.2236	0.00728	8A''	10.7603	0.00835	8A''	10.2154	0.00719	8A''	10.7542	0.00799
6A'	10.3117	0.01606	6A'	10.8030	0.01431	6A'	10.3022	0.01586	6A'	10.7942	0.01412
9A''	10.3459	0.00338	9A''	10.8052	0.00351	9A''	10.3354	0.00345	9A''	10.796	0.00383
7A'	10.8107	0.00229	7A'	11.2132	0.01000	7A'	10.8039	0.00217	7A'	11.2091	0.00974
10A''	10.8845	0.00511	10A''	11.3563	0.00097	10A''	10.8805	0.00504	10A''	11.3536	0.00096
8A'	11.0923	0.02914	8A'	11.5426	0.04864	8A'	11.0865	0.02887	8A'	11.5422	0.05151
9A'	11.2540	0.00078	9A'	11.5664	0.00969	9A'	11.2462	0.00084	9A'	11.5620	0.00699
10A'	11.2963	0.03252	11A''	11.6661	0.05676	10A'	11.2985	0.03277	11A''	11.6638	0.05521

Table S8: CH₃OH: Unshifted RIXS data at the Oxygen *K*-edge for the pump frequency at resonance with the first core excitation (core 1A') calculated using different methods. RIXS cross sections for $\theta = 45^\circ$ at the CVS-uS-EOM-CCSD and CVS-EOM-CCSD level of theory are both based on emission energies calculated at the EOM-CCSD level of theory. CVS and CVS-uS refer to a projection in the damped response solver. All calculations employed the aug-cc-pVTZ basis.

ω_{em}		$\sigma_{45^\circ}^{RIXS}/\text{a.u.}$		
CCSD	CC2	CVS-uS-EOM-CCSD	CVS-EOM-CCSD	EOM-CC2
528.5730	527.5061	0.01759	0.01607	0.00671
527.3743	526.4288	0.00083	0.00095	0.00012
526.8636	525.9754	0.00010	0.00013	0.00001
526.7901	525.8459	0.00003	0.00003	0.00002
526.5896	525.4704	0.01048	0.00931	0.00437
526.0796	525.1512	0.00004	0.00017	0.00008
525.7893	524.8246	0.00038	0.00044	0.00003
525.6423	524.5601	0.00097	0.00098	0.00014
525.0970	524.1563	0.00004	0.00009	0.00002
525.0818	524.1359	0.00036	0.00043	0.00001
525.0554	524.0322	0.00007	0.00012	0.00000
525.0434	524.0113	0.00001	0.00004	0.00006
524.7367	523.8146	0.00022	0.00024	0.00002
524.6943	523.7264	0.00003	0.00032	0.00001
524.6918	523.6921	0.00010	0.00020	0.00002
524.2839	523.2273	0.00130	0.00141	0.00019
524.1408	523.1536	0.00001	0.00007	0.00000
523.9544	522.9457	0.00440	0.00398	0.00003
523.9307	522.7841	0.00135	0.00139	0.00010
523.8309	522.7419	0.00099	0.00089	0.00215

Table S9: CH₃OH: Unshifted RIXS data at the Oxygen *K*-edge for the pump frequency at resonance with the second core excitation (core 2A') calculated using different methods. RIXS cross sections for $\theta = 45^\circ$ at the CVS-uS-EOM-CCSD and CVS-EOM-CCSD level of theory are both based on emission energies calculated at the EOM-CCSD level of theory. CVS and CVS-uS refer to a projection in the damped response solver. All calculations employed the aug-cc-pVTZ basis.

ω_{em}		$\sigma_{45^\circ}^{RIXS}/\text{a.u.}$		
CCSD	CC2	CVS-uS-EOM-CCSD	CVS-EOM-CCSD	EOM-CC2
530.6212	528.6731	0.00053	0.00056	0.00013
529.4225	527.5958	0.00853	0.00813	0.00192
528.9118	527.1425	0.00012	0.00012	0.00005
528.8383	527.0130	0.00058	0.00056	0.00005
528.6378	526.6375	0.00059	0.00062	0.00012
528.1278	526.3183	0.00042	0.00060	0.00005
527.8375	525.9917	0.00019	0.00029	0.00007
527.6905	525.7272	0.00425	0.00387	0.00102
527.1452	525.3234	0.00005	0.00011	0.00001
527.1300	525.3030	0.00010	0.00027	0.00003
527.1039	525.1993	0.00045	0.00041	0.00003
527.0919	525.1784	0.00006	0.00005	0.00001
526.7849	524.9816	0.00004	0.00011	0.00002
526.7425	524.8935	0.00005	0.00040	0.00001
526.7403	524.8592	0.00011	0.00024	0.00002
526.3322	524.3944	0.00015	0.00038	0.00002
526.1890	524.3207	0.00012	0.00018	0.00000
526.0026	524.1128	0.00097	0.00097	0.00005
525.9789	523.9512	0.00005	0.00035	0.00002
525.8794	523.9087	0.00065	0.00062	0.00016

Table S10: CH₃OH: Unshifted nonresonant (XES) data at the Oxygen *K*-edge calculated using different methods. All calculations employed the aug-cc-pVTZ basis.

ω_{em}		f_{osc}	
CCSD	CC2	EOM-CCSD	EOM-CC2
529.4002	526.9142	0.04350	0.04827
527.5822	524.9542	0.02846	0.03404
525.1400	522.3356	0.02045	0.01837
524.5999	521.6776	0.00911	0.00697
522.6728	519.9984	0.02611	0.02611
517.2898	514.1692	0.00556	0.00495
513.7140	511.6056	0.00001	0.00000
512.9697	511.2113	0.00000	0.00000

Table S11: CH₃OH: Unshifted RIXS data at the Carbon *K*-edge for the pump frequency at resonance with the first core excitation (core 1A') calculated using different methods. RIXS cross sections for $\theta = 45^\circ$ at the CVS-uS-EOM-CCSD and CVS-EOM-CCSD level of theory are both based on emission energies calculated at the EOM-CCSD level of theory. CVS and CVS-uS refer to a projection in the damped response solver. All calculations employed the aug-cc-pVTZ basis.

ω_{em}		$\sigma_{45^\circ}^{RIXS}/\text{a.u.}$		
CCSD	CC2	CVS-uS-EOM-CCSD	CVS-EOM-CCSD	EOM-CC2
282.1232	283.5314	0.00495	0.00502	0.00345
280.9191	282.4503	0.00238	0.00255	0.00135
280.4089	281.9972	0.00011	0.00032	0.00008
280.3362	281.8682	0.00007	0.00007	0.00005
280.1359	281.4935	0.01342	0.01283	0.00942
279.6276	281.1754	0.00030	0.00055	0.00007
279.3381	280.8497	0.00003	0.00041	0.00002
279.1827	280.5784	0.00417	0.00395	0.00265
278.6442	280.1800	0.00002	0.00021	0.00001
278.6295	280.1596	0.00006	0.00035	0.00001
278.5979	280.0510	0.00021	0.00062	0.00034
278.5846	280.0306	0.00044	0.00071	0.0002
278.2817	279.8366	0.00054	0.00062	0.00021
278.2417	279.7498	0.00009	0.00095	0.00003
278.2398	279.7166	0.00006	0.00042	0.00006
277.8268	279.2480	0.00477	0.00478	0.00103
277.6823	279.1713	0.00047	0.00056	0.00005
277.4937	278.9653	0.01912	0.01798	0.00040
277.4738	278.8058	0.00383	0.00440	0.00042
277.3721	278.7536	0.01127	0.01032	0.02205

Table S12: CH₃OH: Unshifted nonresonant (XES) data at the Carbon *K*-edge calculated using different methods. All calculations employed the aug-cc-pVTZ basis.

ω_{em}		f_{osc}	
CCSD	CC2	EOM-CCSD	EOM-CC2
282.1594	283.0201	0.00551	0.00416
280.3381	281.0578	0.01414	0.01194
277.8888	278.4281	0.02593	0.02828
277.3448	277.7664	0.02667	0.03002
275.4262	276.0969	0.01472	0.01677
270.0133	270.2364	0.00075	0.00129
266.4646	267.7011	0.00000	0.00000

S4 H₂S

The XAS spectrum for H₂S at the sulfur *K*-edge can be seen in Fig. S3 along with the computed valence absorption spectrum. It can be seen from Fig. S3 that both methods give the same overall

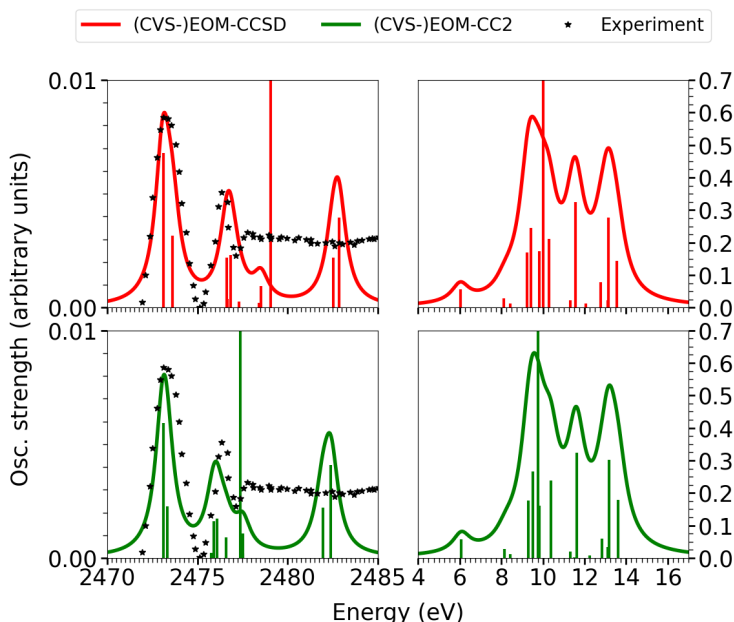


Figure S3: H₂S: XAS spectrum at the Sulphur *K*-edge (left) and valence absorption in a space orthogonal to the S core space (right) calculated at the (CVS-)EOM-CC2/6-311++G** (green) and (CVS-)EOM-CCSD/6-311++G** (red) level of theory. Experimental data adapted from Bodeur and Esteva.³ For all methods 10 core transitions and 20 valence transitions have been determined and plotted. The first core ionization potential is shown as a vertical line spanning the full intensity range. XAS results have been shifted to align with experiment: 3.35 eV for CVS-EOM-CCSD and 4.50 eV for CVS-EOM-CC2. A Lorentzian broadening with HWHM=0.506 eV has been applied.

shape of the spectrum. Both methods predict a shift between the two first peaks, which is slightly off compared to experiment, but in either direction: While CC2 predicts a too small separation, CCSD predicts one that is too large. The intensity ratio of the first two peaks is slightly better reproduced at the CCSD level of theory. Furthermore, the core ionization threshold appears closer to the two low energy peaks at the CC2 level compared to the CCSD level. Significantly lower CC2

core ionization thresholds compared to CCSD are not uncommon as also observed by Carbone et al.⁴ The main transitions of the two peaks below the ionization threshold can in both methods be characterized as core $1B_2$ and core $1B_1$, while the character of the main transition of the small peak (just below the ionization threshold at the CCSD level) is core $3B_2$. Observe that at the CC2 level of theory the third peak falls just above the core ionization threshold.

From the valence spectra in Fig. S3 it is observed that the two methods are in good agreement with each other both regarding the overall spectral profile, the relative intensities of peaks and the position of the ionization threshold relative to the spectral features.

S4.1 Data tables

Table S13: H₂S: Unshifted S *K*-edge XAS data using the 6-311++G** basis set.

^a Mulliken symmetry notation.

EOM-CC2			EOM-CCSD		
Sym. ^a	$\omega_{abs,e}/\text{eV}$	f_{osc}	Sym. ^a	$\omega_{abs,e}/\text{eV}$	f_{osc}
$1B_2$	2468.5932	0.00592	$1B_2$	2469.7535	0.00678
$1A_1$	2468.8162	0.00227	$1A_1$	2470.2684	0.00317
$2B_2$	2471.2486	0.00021	$2A_1$	2473.2851	0.00219
$2A_1$	2471.4052	0.00162	$2B_2$	2473.3233	0.00038
$1B_1$	2471.5780	0.00174	$1B_1$	2473.5002	0.00231
$3A_1$	2472.0885	0.00089	$3A_1$	2473.9623	0.00027
$3B_2$	2473.0127	0.00109	$4A_1$	2475.0892	0.00022
$4A_1$	2473.0275	0.00019	$3B_2$	2475.1955	0.00094
$4B_2$	2477.4436	0.00222	$4B_2$	2479.1842	0.00218
$5A_1$	2477.8977	0.00409	$5A_1$	2479.5026	0.00397

Table S14: H₂S: Unshifted valence absorption data computed using the 6-311++G** basis set in a spce orthogonal to the S core space.

^a Mulliken symmetry notation.

EOM-CC2			EOM-CCSD		
Sym. ^a	$\omega_{abs,v}/\text{eV}$	f_{osc}	Sym. ^a	$\omega_{abs,v}/\text{eV}$	f_{osc}
1B ₁	6.0808	0.05768	1B ₁	6.0274	0.05598
1A ₂	6.4085	0.00000	1A ₂	6.3268	0.00000
2A ₂	7.8199	0.00000	2A ₂	7.8189	0.00000
2B ₁	8.1523	0.0282	2B ₁	8.1334	0.02900
1A ₁	8.4299	0.01272	1A ₁	8.4386	0.01301
2A ₁	9.2958	0.17621	2A ₁	9.2271	0.16897
3B ₁	9.5241	0.26584	3B ₁	9.4191	0.24433
3A ₂	9.8380	0.00000	4B ₁	9.8396	0.17343
4B ₁	9.8386	0.16171	3A ₂	9.8591	0.00000
1B ₂	10.3798	0.23896	1B ₂	10.2891	0.21044
2B ₂	10.9891	0.00030	2B ₂	10.9625	0.00082
3A ₁	11.3289	0.01947	3A ₁	11.3255	0.02220
5B ₁	11.4916	0.00111	5B ₁	11.4787	0.00095
3B ₂	11.6126	0.32396	3B ₂	11.5525	0.32511
4A ₁	12.2359	0.00798	4A ₁	12.0743	0.01220
5A ₁	12.8240	0.05979	5A ₁	12.7794	0.07902
4B ₂	13.1295	0.03343	4B ₂	13.1249	0.02242
6A ₁	13.1775	0.30105	6A ₁	13.143	0.27669
7A ₁	13.6175	0.17971	7A ₁	13.5465	0.14309
5B ₂	13.8736	0.00060	5B ₂	13.7782	0.00018

Table S15: H₂S: Unshifted RIXS data for the pump frequency at resonance with the first core excitation (core 1B₂ in Mulliken symmetry notation) calculated using different methods. RIXS cross sections for $\theta = 45^\circ$ at the EOM-CCSD, CVS-uS-EOM-CCSD and CVS-EOM-CCSD level of theory are all based on emission energies calculated at the EOM-CCSD level of theory. CVS and CVS-uS refer to a projection in the damped response solver. To avoid reporting very small numbers all calculated cross sections have been multiplied with 10^3 . All calculations employed the 6-311++G** basis.

ω_{em}		$10^3 \sigma_{45^\circ}^{\text{RIXS}}/\text{a.u.}$			
CCSD	CC2	EOM-CCSD	CVS-uS-EOM-CCSD	CVS-EOM-CCSD	EOM-CC2
2463.7261	2462.5125	0.00084	0.00101	0.00114	0.00333
2463.4265	2462.1849	0.08424	0.10229	0.07107	0.07717
2461.9345	2460.7734	0.05791	0.05480	0.01905	0.05859
2461.6200	2460.4409	0.05539	0.05384	0.02322	0.05715
2461.3149	2460.1634	0.00031	0.00047	0.15542	0.00027
2460.5264	2459.2975	0.00096	0.00073	0.00824	0.00220
2460.3345	2459.0692	0.06058	0.05535	0.01417	0.06378
2459.9138	2458.7552	0.04814	0.04638	0.01607	0.05045
2459.8942	2458.7546	0.05204	0.04727	0.02233	0.04415
2459.4643	2458.2134	0.03201	0.03769	0.04086	0.02874
2458.7911	2457.6041	0.02460	0.02462	0.05278	0.02466
2458.4281	2457.2643	0.00086	0.00097	0.0306	0.000550
2458.2749	2457.1015	0.02357	0.02346	0.00959	0.02375
2458.2009	2456.9807	0.01069	0.01153	0.00461	0.01327
2457.6792	2456.3573	0.00837	0.00909	0.00936	0.00730
2456.9742	2455.7693	0.00582	0.00632	0.01429	0.00553
2456.6286	2455.4637	0.00337	0.00369	0.00422	0.00244
2456.6104	2455.4158	0.00490	0.00535	0.01194	0.00516
2456.2068	2454.9758	0.00204	0.00228	0.01636	0.00261
2455.9752	2454.7197	0.01208	0.01194	0.02731	0.01196

Table S16: H₂S: Unshifted RIXS data for the pump frequency at resonance with the second core excitation (core 1A₁ in Mulliken symmetry notation) calculated using different methods. RIXS cross sections for $\theta = 45^\circ$ at the EOM-CCSD, CVS-uS-EOM-CCSD and CVS-EOM-CCSD level of theory are all based on emission energies calculated at the EOM-CCSD level of theory. CVS and CVS-uS refer to a projection in the damped response solver. To avoid reporting very small numbers all calculated cross sections have been multiplied with 10^3 . All calculations employed the 6-311++G** basis.

ω_{em}		$10^3 \sigma_{45^\circ}^{RIXS}/\text{a.u.}$			
CCSD	CC2	EOM-CCSD	CVS-uS-EOM-CCSD	CVS-EOM-CCSD	EOM-CC2
2464.2410	2462.7354	0.02312	0.02574	0.02506	0.00002
2463.9417	2462.4078	0.07451	0.06620	0.02917	0.06808
2462.4494	2460.9963	0.05521	0.05340	0.01804	0.05588
2462.1351	2460.6638	0.05598	0.05329	0.02269	0.05585
2461.8298	2460.3862	0.00067	0.00083	0.15507	0.00000
2461.0412	2459.5203	0.01319	0.01452	0.01941	0.00002
2460.8494	2459.2920	0.06173	0.06113	0.01894	0.06683
2460.4289	2458.9780	0.04912	0.04546	0.01536	0.04397
2460.4093	2458.9775	0.04290	0.04166	0.01748	0.04285
2459.9794	2458.4365	0.00732	0.00753	0.00625	0.00314
2459.3059	2457.8273	0.02739	0.02926	0.05412	0.02889
2458.9429	2457.4871	0.00026	0.00027	0.03016	0.00000
2458.7897	2457.3247	0.02369	0.02367	0.00970	0.02323
2458.7160	2457.2036	0.02363	0.02123	0.01479	0.00934
2458.1941	2456.5802	0.00122	0.00125	0.00151	-0.00001
2457.4890	2455.9921	0.00042	0.00045	0.00562	0.00000
2457.1434	2455.6868	0.00022	0.00015	0.00038	0.00003
2457.1255	2455.6386	0.00093	0.00095	0.00500	0.00000
2456.7219	2455.1986	0.00034	0.00044	0.01692	0.00000
2456.4901	2454.9426	0.01247	0.01205	0.02713	0.01184

Table S17: H₂S: Unshifted RIXS data for the pump frequency at resonance with the 3rd (CCSD) or 4th (CC2) core excitation (core 2A₁ in Mulliken symmetry notation) calculated using different methods. RIXS cross sections for $\theta = 45^\circ$ at the EOM-CCSD, CVS-uS-EOM-CCSD and CVS-EOM-CCSD level of theory are all based on emission energies calculated at the EOM-CCSD level of theory. CVS and CVS-uS refer to a projection in the damped response solver. To avoid reporting very small numbers all calculated cross sections have been multiplied with 10^3 . All calculations employed the 6-311++G** basis.

ω_{em}		$10^3 \sigma_{45^\circ}^{RIXS}/\text{a.u.}$			
CCSD	CC2	EOM-CCSD	CVS-uS-EOM-CCSD	CVS-EOM-CCSD	EOM-CC2
2467.2576	2465.3243	0.00114	0.00097	0.00091	0.00035
2466.9583	2464.9966	0.05508	0.04866	0.01655	0.05445
2465.4663	2463.5852	0.06610	0.06196	0.02542	0.04952
2465.1517	2463.2529	0.07656	0.06614	0.03595	0.07570
2464.8464	2462.9754	0.00314	0.00485	0.19695	0.00318
2464.0581	2462.1095	0.00096	0.00116	0.00732	0.00042
2463.8660	2461.8812	0.06221	0.06141	0.01891	0.06400
2463.4456	2461.5672	0.04756	0.04549	0.01520	0.04740
2463.4260	2461.5666	0.04715	0.04562	0.02102	0.04442
2462.9961	2461.0254	0.00235	0.00230	0.00664	0.00210
2462.3226	2460.4161	0.03441	0.03220	0.05743	0.02589
2461.9596	2460.0763	0.00709	0.00794	0.03529	0.00616
2461.8064	2459.9136	0.03676	0.03790	0.02228	0.03652
2461.7326	2459.7925	0.00728	0.00742	0.00211	0.00569
2461.2110	2459.1693	0.00105	0.00110	0.00156	0.00045
2460.5057	2458.5813	0.00036	0.00042	0.00831	0.00017
2460.1604	2458.2757	0.00015	0.00019	0.00078	0.00006
2460.1421	2458.2278	0.00053	0.00059	0.00723	0.00046
2459.7386	2457.7878	0.00134	0.00169	0.01829	0.00039
2459.5070	2457.5315	0.02493	0.02167	0.03582	0.02284

Table S18: H₂S: Unshifted RIXS data for the pump frequency at resonance with the fifth core excitation (core $1B_1$ in Mulliken symmetry notation) calculated using different methods. RIXS cross sections for $\theta = 45^\circ$ at the EOM-CCSD, CVS-uS-EOM-CCSD and CVS-EOM-CCSD level of theory are all based on emission energies calculated at the EOM-CCSD level of theory. CVS and CVS-uS refer to a projection in the damped response solver. To avoid reporting very small numbers all calculated cross sections have been multiplied with 10^3 . All calculations employed the 6-311++G** basis.

ω_{em}		$10^3 \sigma_{45^\circ}^{RIXS}/\text{a.u.}$			
CCSD	CC2	EOM-CCSD	CVS-uS-EOM-CCSD	CVS-EOM-CCSD	EOM-CC2
2467.4729	2465.4971	0.00011	0.00006	0.00006	0.00007
2467.1733	2465.1694	0.05364	0.04752	0.01575	0.05442
2465.6813	2463.7580	0.04678	0.04513	0.01194	0.05098
2465.3667	2463.4257	0.03663	0.03532	0.00810	0.03935
2465.0617	2463.1482	0.01483	0.01623	0.16618	0.01131
2464.2731	2462.2823	0.00056	0.00055	0.00640	0.00040
2464.0810	2462.0540	0.07194	0.06489	0.02044	0.06844
2463.6606	2461.7400	0.04666	0.04462	0.01483	0.04772
2463.6410	2461.7394	0.04648	0.04511	0.02057	0.04332
2463.2110	2461.1982	0.00286	0.00275	0.00631	0.00191
2462.5378	2460.5889	0.02268	0.02177	0.04182	0.02654
2462.1748	2460.2491	0.00296	0.00225	0.01772	0.00365
2462.0216	2460.0863	0.04223	0.03702	0.02346	0.03894
2461.9476	2459.9653	0.00673	0.00659	0.00155	0.00594
2461.4260	2459.3421	0.00029	0.00043	0.00066	0.00016
2460.7206	2458.7541	0.00020	0.00019	0.00697	0.00011
2460.3753	2458.4485	0.00005	0.00004	0.00087	0.00003
2460.3571	2458.4006	0.00025	0.00023	0.00461	0.00015
2459.9536	2457.9606	0.00060	0.00035	0.01200	0.00008
2459.7220	2457.7043	0.00706	0.00647	0.01522	0.00790

Table S19: H₂S: Unshifted RIXS data for the pump frequency at resonance with the 8th (EOM-CCSD) and 7th (EOM-CC2) core excitation (core $3B_2$ in Mulliken symmetry notation). RIXS cross sections for $\theta = 45^\circ$ at the EOM-CCSD, CVS-uS-EOM-CCSD and CVS-EOM-CCSD level of theory are all based on emission energies calculated at the EOM-CCSD level of theory. CVS and CVS-uS refer to a projection in the damped response solver. To avoid reporting very small numbers all calculated cross sections have been multiplied with 10^3 . All calculations employed the 6-311++G** basis.

ω_{em}		$10^3 \sigma_{45^\circ}^{RIXS} / \text{a.u.}$			
CCSD	CC2	EOM-CCSD	CVS-uS-EOM-CCSD	CVS-EOM-CCSD	EOM-CC2
2469.1682	2466.9319	0.00005	0.00001	0.00002	0.00001
2468.8686	2466.6043	0.05485	0.04721	0.01562	0.05479
2467.3766	2465.1928	0.05352	0.05217	0.01716	0.05489
2467.0620	2464.8603	0.05065	0.04901	0.01909	0.05232
2466.7569	2464.5828	0.00011	0.00001	0.14283	0.00011
2465.9684	2463.7169	0.00003	0.00003	0.00560	0.00001
2465.7765	2463.4886	0.06749	0.06192	0.01844	0.07600
2465.3558	2463.1746	0.04067	0.03797	0.01016	0.06226
2465.3362	2463.1740	0.05946	0.05204	0.02731	0.04612
2464.9063	2462.6328	0.00350	0.00291	0.00743	0.00255
2464.2331	2462.0235	0.02612	0.02528	0.04890	0.02878
2463.8701	2461.6837	0.00002	0.00001	0.02669	0.00003
2463.7169	2461.5209	0.02062	0.02052	0.00715	0.02040
2463.6429	2461.4001	0.00795	0.00758	0.00207	0.00730
2463.1212	2460.7767	0.00015	0.00030	0.00057	0.00027
2462.4162	2460.1887	0.00084	0.00072	0.00900	0.00087
2462.0706	2459.8831	0.00487	0.00539	0.00582	0.00571
2462.0526	2459.8352	0.00069	0.00065	0.00582	0.00048
2461.6491	2459.3952	0.00005	0.00007	0.01446	0.00009
2461.4173	2459.1391	0.01065	0.01045	0.02455	0.01054

Table S20: H₂S: Unshifted nonresonant (XES) data at the sulfur K -edge calculated using different methods. All calculations employed the 6-311++G** basis.

ω_{em}		f_{osc}	
CCSD	CC2	EOM-CCSD	EOM-CC2
2465.7156	2463.1172	0.00606	0.00596
2462.5702	2459.9897	0.00431	0.00423
2460.1299	2457.4858	0.00378	0.00368
2454.1529	2450.8764	0.00001	0.00000
2453.3847	2449.2957	0.00013	0.00002
2452.6459	2449.0717	0.00000	0.00022
2451.5814	2449.0551	0.00012	0.00001

S5 Para-nitro-aniline

The XAS spectrum is computed at both the CVS-EOM-CCSD and the CVS-EOM-CC2 level of theory at the C K -edge (see Fig. S4). We observe that the core transitions are significantly more close-lying, according to the CVS-EOM-CC2 calculation compared to the CVS-EOM-CCSD one. The latter is in better agreement with experiment. The intensity ratios of the first three bright transitions predicted are however very similar in the two methods, and they both find the first bright transition to be core $1B_1$. We note that the EOM-CC2 and EOM-CCSD valence spectra in

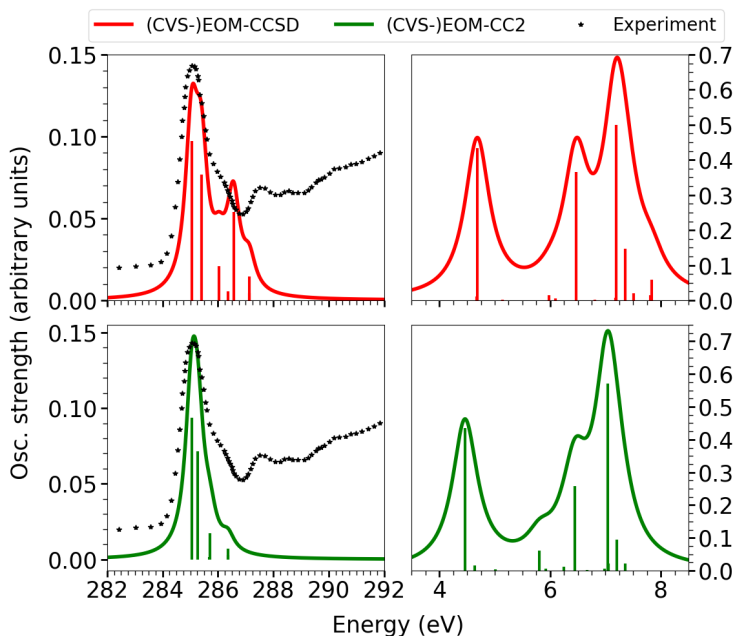


Figure S4: PNA: XAS spectra at the Carbon K -edge (left) and valence absorption (right) in the space orthogonal to the C core space, calculated using (CVS-)EOM-CC2/6-311++G** (green) and (CVS-)EOM-CCSD/6-311++G** (red) levels of theory. For all methods, 10 core transitions and 20 valence transitions were computed. A Lorentzian broadening with HWHM=0.27 eV has been applied. The theoretical spectra were shifted by -1.70 eV (CVS-EOM-CCSD) and -2.94 eV (CVS-EOM-CC2) to align with experiment, which was digitized from Turci et al.⁵

Fig. S4 are very similar. The general shape is the same, however the shift between the first and second feature is larger when using EOM-CC2. The low intensity feature between the two main

peaks at low energy is also more pronounced when employing EOM-CC2.

S5.1 Comparison of CVS-EOM-CCSD, CVS-0-EOM-CCSD and fc-CVS-0-EOM-CCSD

We investigate here whether the discrepancies between the calculated CVS-EOM-CCSD and fc-CVS-0-EOM-CCSD RIXS results are mainly due to the fc approximation or to the way our projectors are applied. Both CVS approximations consist in projecting out all excitations that do not involve a core orbital when solving the damped response equations. While this is done for all damped response equations for CVS-0, it is only done for the divergent damped response equations for CVS.

Therefore, we calculate, for a small basis set (6-31G), the RIXS spectra using the different projection schemes. The results are then compared to the fc-CVS-0-EOM-CCSD result calculated with Q-Chem (see Fig. S5). Here, it is noted that the CVS-0-EOM-CCSD and fc-CVS-0-EOM-CCSD are almost identical, with only a small overall decrease in intensity of the fc-CVS-0-EOM-CCSD result compared to CVS-0-EOM-CCSD. The CVS-EOM-CCSD result, on the other hand, shows larger discrepancies with these other spectra with respect to intensities, while it is still the same transitions that are probed. We thus conclude that the discrepancies are a result of the different ways the projection is applied, rather than an effect of the frozen core approximation.

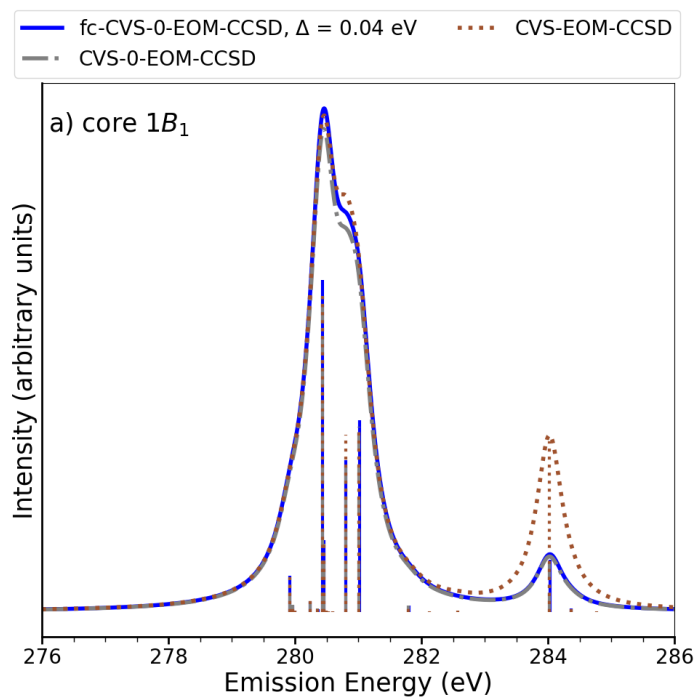


Figure S5: PNA: Comparison of the RIXS spectra at resonance with the energy of the first core excitation at the C K -edge (288.90 eV at the CVS-EOM-CCSD level of theory in e^T and 288.86 eV at the fc-CVS-0-EOM-CCSD level of theory in Q-Chem). The results are obtained using different CVS schemes during the solution of the damped response equations. The 6-31G basis set was employed in all calculations. The results are shifted based on the CVS-EOM-CCSD RIXS results. A Lorentzian broadening was applied with HWHM=0.27 eV.

S5.2 Data tables

Table S21: PNA: Unshifted C *K*-edge XAS data using the 6-311++G** basis set.

^a Mulliken symmetry notation.

EOM-CC2			EOM-CCSD		
Sym. ^a	$\omega_{abs,c}/\text{eV}$	f_{osc}	Sym. ^a	$\omega_{abs,c}/\text{eV}$	f_{osc}
1A ₂	287.9911	0.00000	1A ₂	286.7436	0.00000
1B ₁	287.9948	0.09372	1B ₁	286.7476	0.09708
2A ₂	288.2064	0.00000	2A ₂	287.0951	0.00000
2B ₁	288.2094	0.07154	2B ₁	287.0984	0.07664
3B ₁	288.6269	0.00145	3B ₁	287.7333	0.02084
3A ₂	288.6278	0.00000	4B ₁	288.0689	0.00555
4B ₁	288.6511	0.01726	3A ₂	288.0712	0.00000
1B ₂	289.3100	0.00716	5B ₁	288.2635	0.05398
1A ₁	289.3102	0.00273	1B ₁	288.8292	0.01455
4A ₂	289.3468	0.00000	1A ₁	288.8302	0.00443

Table S22: PNA: Unshifted valence absorption data computed using the 6-311++G** basis set in a space orthogonal to the C core space.

EOM-CC2			EOM-CCSD		
Sym. ^a	$\omega_{abs,v}/\text{eV}$	f_{osc}	Sym. ^a	$\omega_{abs,v}/\text{eV}$	f_{osc}
1A ₂	4.0521	0.00000	1A ₂	4.1467	0.00000
1A ₁	4.4589	0.43494	1B ₂	4.6753	0.01140
1B ₂	4.6369	0.01648	1B ₁	4.6841	0.00051
1B ₁	4.6579	0.00057	1A ₁	4.6844	0.43385
2B ₁	5.0109	0.00298	2B ₁	5.1392	0.00250
2A ₂	5.7592	0.00000	2A ₂	5.9266	0.00000
2B ₂	5.8044	0.06039	2B ₂	5.9810	0.01432
3B ₁	5.9175	0.00576	3B ₁	6.0947	0.00633
2A ₁	6.2502	0.01174	2A ₁	6.4433	-0.00002
3B ₂	6.4481	0.25818	3B ₂	6.4703	0.36542
4B ₁	6.6715	0.00262	4B ₁	6.8102	0.00231
3A ₂	6.6750	0.00000	3A ₂	6.8696	0.00000
5B ₁	6.7867	0.00014	4A ₂	6.9744	0.00000
4A ₂	6.8330	0.00000	5B ₁	7.1809	0.00778
6B ₁	6.9840	0.00588	3A ₁	7.1893	0.49992
3A ₁	7.0363	0.57029	4A ₁	7.3523	0.14729
4B ₂	7.0557	0.02146	6B ₁	7.5075	0.02095
5A ₂	7.1435	0.00000	5A ₂	7.6409	0.00000
4A ₁	7.2035	0.09528	5A ₁	7.8131	0.01506
7B ₁	7.3555	0.02174	4B ₂	7.8375	0.05817

^a Mulliken symmetry notation.

Table S23: PNA: Unshifted RIXS data for the pump frequency at resonance with the first bright core excitation (core $1B_1$ in Mulliken symmetry notation) calculated using different methods. RIXS cross sections for $\theta = 45^\circ$ at the CVS-uS-EOM-CCSD and CVS-EOM-CCSD level of theory are both based on emission energies calculated at the EOM-CCSD level of theory. CVS and CVS-uS refer to different types of projections in the damped response solver. All calculations employed the 6-311++G** basis.

ω_{em}			$\sigma_{45^\circ}^{RIXS}/\text{a.u.}$			
CCSD	fc-CCSD	CC2	CVS-uS-EOM-CCSD	CVS-EOM-CCSD	fc-CVS-0-EOM-CCSD	EOM-CC2
282.6010	282.0870	283.9428	0.00001	0.00001	0.00000	0.00001
282.0723	281.5863	283.5360	0.00006	0.00002	0.00000	0.01769
282.0636	281.5672	283.3580	0.00153	0.00114	0.02000	0.00010
282.0633	281.5509	283.3371	0.02315	0.04831	0.00000	0.00244
281.6083	281.1101	282.9839	0.00001	0.00047	0.00000	0.00002
280.8208	280.3210	282.2356	0.00004	0.00011	0.00000	0.00003
280.7667	280.2693	282.1904	0.00036	0.00033	0.00000	0.00023
280.6529	280.1577	282.0775	0.00003	0.00032	0.00000	0.00002
280.3044	279.8094	281.7447	0.00232	0.00536	0.00000	0.00234
280.2774	279.7740	281.5468	0.00004	-0.00001	0.00000	0.00000
279.9375	279.4420	281.3234	0.00012	0.00013	0.00000	0.00011
279.8780	279.3794	281.3199	0.00008	0.00028	0.00000	0.00008
279.7732	279.2815	281.2080	0.00005	0.00182	0.00000	0.02206
279.5667	279.0720	281.1618	0.00005	0.00016	0.07000	0.00008
279.5582	279.0692	281.0108	0.07177	0.06147	0.00000	0.00003
279.3952	278.9005	280.9585	0.00769	0.00653	0.01000	0.04890
279.2401	278.7454	280.9392	0.00001	0.00006	0.00000	0.00000
279.1068	278.6148	280.8513	0.00007	0.00050	0.00000	0.01321
278.9345	278.4407	280.7914	0.04520	0.05061	0.04000	0.01238
278.9100	278.4162	280.6393	0.00003	0.00031	0.00000	0.00000

Table S24: PNA: Unshifted nonresonant (XES) data at the Carbon K -edge for C1-C3 (the numbering is based on energies, so that first core excitation from $1s(\text{C1})$ has the lowest energy), calculated using different methods. All calculations employed the 6-311++G** basis.

C1		C2		C3	
EOM-CCSD	EOM-CC2	EOM-CCSD	EOM-CC2	EOM-CCSD	EOM-CC2
ω_{em}	f_{osc}	ω_{em}	f_{osc}	ω_{em}	f_{osc}
283.9697	0.01763	283.7159	0.01693	283.9703	0.00000
282.4720	0.00000	282.6554	0.00000	282.4726	0.02606
281.7985	0.00000	282.2347	0.00051	281.7991	0.00064
281.4744	0.00000	282.1681	0.00000	282.1686	0.02680
281.4255	0.00078	281.3572	0.00000	281.3577	0.00080
280.6467	0.00076	280.6829	0.00059	280.6472	0.00000
279.5800	0.01806	279.7433	0.01825	279.5805	0.00020
278.6028	0.01063	278.7171	0.01240	278.6034	0.00000
278.1438	0.02309	278.4390	0.02361	278.1443	0.00016
277.3277	0.00947	277.6213	0.00602	277.3282	0.01293
277.1742	0.00615	277.4768	0.01060	277.1748	0.01284
276.6376	0.00238	276.7848	0.00197	276.6382	0.01386
275.4488	0.00002	276.2199	0.00011	275.4493	0.00068
275.3328	0.00002	275.4983	0.00001	275.3334	0.00000
274.6996	0.00022	275.4011	0.00117	274.7002	0.00117
274.5037	-0.00002	274.5040	0.00089	274.5042	0.00000
274.1717	0.00082	274.4509	0.00086	274.1723	0.00094
274.0536	0.00000	273.3214	0.00039	274.0542	0.00000
273.9900	0.00059	273.2395	0.00000	273.9905	0.00526
273.5263	0.00000	272.8517	0.00000	273.5268	0.00004
				272.8522	0.00000
				273.9570	0.00000
				284.4005	0.00070
				282.9028	0.00000
				282.2293	0.00000
				281.9049	0.00000
				281.8560	0.00082
				281.0772	0.01227
				280.0105	0.01615
				279.0336	0.00620
				278.5745	0.02122
				277.7585	0.01103
				277.6047	0.01059
				277.0684	0.00000
				275.8792	0.00098
				275.7636	0.00035
				275.1301	0.00124
				274.9342	0.00004
				274.6025	0.00045
				274.4841	0.00000
				274.4207	0.00040
				273.8027	0.00006
				273.4147	0.00000

Table S25: PNA: Unshifted nonresonant (XES) data at the Carbon K -edge for C4-C6 (the numbering is based on energies, so that first core excitation from 1s(C1) has the lowest energy) calculated using different methods. All calculations employed the 6-311++G** basis.

C4				C5				C6			
EOM-CCSD		EOM-CC2		EOM-CCSD		EOM-CC2		EOM-CCSD		EOM-CC2	
ω_{em}	f_{osc}	ω_{em}	f_{osc}	ω_{em}	f_{osc}	ω_{em}	f_{osc}	ω_{em}	f_{osc}	ω_{em}	f_{osc}
284.4029	0.00000	284.2857	0.00000	284.7749	0.01592	284.3986	0.01552	285.7325	0.00758	285.6117	0.00634
282.9052	0.03094	283.2252	0.00103	283.2772	0.00000	283.3382	0.0003	284.2348	0.00000	284.5515	0.00004
282.2317	0.00113	282.8045	0.00113	282.6037	0.00030	282.9175	0.00610	283.5613	0.00006	284.1306	0.00001
281.9074	0.00075	282.7379	0.02961	282.2796	0.00000	282.8508	0.00000	283.2372	0.00000	284.0639	0.00000
281.8587	0.00128	281.9270	0.00125	282.2307	0.00773	282.0399	0.00000	283.1882	0.00001	283.2530	0.00000
281.0799	0.00000	281.2527	0.00000	281.4519	0.01417	281.3659	0.02053	282.4094	0.00315	282.579	0.00353
280.0129	0.00004	280.3131	0.00004	280.3852	0.00848	280.4260	0.00538	281.3425	0.01144	281.6391	0.01258
279.0360	0.00000	279.2869	0.00000	279.4080	0.00255	279.3999	0.00380	280.3656	0.01472	280.6129	0.01588
278.5770	0.00061	279.0088	0.00033	278.9490	0.00009	279.1218	0.00004	279.9065	0.00571	280.3351	0.00599
277.7609	0.01068	278.1911	0.01065	278.1329	0.00014	278.304	0.00646	279.0905	0.0003	279.5174	0.01077
277.6072	0.00925	278.0466	0.01140	277.9794	0.00917	278.1598	0.00001	278.9367	0.01035	279.3729	0.00050
277.0708	0.00887	277.3546	0.01002	277.4428	0.00201	277.4676	0.00294	278.4004	0.00370	278.6807	0.00541
275.8817	0.00003	276.7897	0.00031	276.2539	0.00047	276.9027	0.00088	277.2115	0.00034	278.1157	0.00056
275.7660	0.00000	276.0681	0.00000	276.1380	0.00232	276.181	0.00303	277.0956	0.00001	277.3941	0.00000
275.1326	0.00152	275.9709	0.00050	275.5048	0.00123	276.0839	0.00186	276.4624	0.01101	277.2970	0.00520
274.9369	0.00000	275.0738	0.00908	275.3089	0.00004	275.1867	0.00270	276.2665	0.00034	276.3998	0.00877
274.6049	0.00518	275.0207	0.00480	274.9769	0.00316	275.1336	0.00231	275.9345	0.00053	276.3467	0.00047
274.4868	0.00000	273.8912	0.00732	274.8588	0.00000	274.0041	0.00223	275.8164	0.00000	275.2172	0.00058
274.4232	0.00907	273.8095	0.00008	274.7951	0.00426	273.9225	0.00003	275.7527	0.00324	275.1356	0.00001
273.9595	-0.00003	273.4215	0.00000	274.3315	0.00000	273.5344	0.00000	275.2890	0.00000	274.7475	0.00000

Table S26: PNA (6-31G basis set): Unshifted RIXS data for the pump frequency at resonance with the first bright core excitation. RIXS cross sections for $\theta = 45^\circ$ at the CVS-EOM-CCSD and CVS-0-EOM-CCSD level of theory are both based on emission energies calculated at the EOM-CCSD level of theory. CVS and CVS-0 refer to a projection in the damped response solver. All calculations employed the 6-31G basis.

ω_{em}		$\sigma_{45^\circ}^{RIXS}/\text{a.u.}$		
CCSD	fc-CCSD	CVS-EOM-CCSD	CVS-0-EOM-CCSD	fc-CVS-0-EOM-CCSD
284.7741	284.7319	0.00012	0.00004	0.00003
284.3684	284.3265	0.00126	0.00094	0.00097
284.0590	284.0244	0.00003	0.00000	0.00000
284.0255	283.9891	0.05439	0.01593	0.01656
282.5713	282.5332	0.00048	0.00000	0.00000
282.1286	282.0897	0.00005	0.00000	0.00000
281.7953	281.7577	0.00195	0.00197	0.00203
281.7477	281.7060	0.00002	0.00002	0.00002
281.0143	280.9795	0.05859	0.05887	0.06103
280.8026	280.7645	0.05633	0.04625	0.04843
280.5980	280.5577	0.00012	0.00014	0.00015
280.5237	280.4869	0.00013	0.00000	0.00000
280.4908	280.4543	0.00041	0.00046	0.00046
280.4600	280.4216	0.02193	0.02179	0.02274
280.4336	280.3972	0.10116	0.10114	0.10567
280.3610	280.3237	0.00122	0.00117	0.00093
280.2410	280.2012	0.00384	0.00324	0.00335
280.0015	279.9618	0.00038	0.00034	0.00035
279.9615	279.9264	0.00231	0.00226	0.00199
279.9188	279.8829	0.01093	0.01072	0.0116

S6 Imidazole

S6.1 Treatment of solvent H₂O

The simulated XAS spectra in Fig. S6 (left panels) are found to correspond well with experiment. It is observed that the calculation treating the H₂O molecules at the HF level of theory (top) corresponds well with that treating both solvent and solute at the CCSD level of theory (bottom). In fact, the results of two calculations are difficult to distinguish. Both calculations show a too large splitting (ca. 1.9 eV vs. the experimental of ca. 1.6 eV) as well as a slightly different intensity ratio of the main peaks. The two main transitions are found to be core 1A and core 2A in both calculations.

Considering now the valence transitions also shown in Fig. S6(left), we observe that the two methods give similar results. It is, however, noted that the valence transitions fall in a wider energy range when treating the solvent molecules at the HF-level of theory. Furthermore, this treatment increases the intensities of the two main transitions of the high energy peak. Despite these differences at higher transition energies, we find that the significantly cheaper approach of treating the solvent molecules at the HF-level of theory is sufficient when it comes to describing also the more delocalized valence transitions.

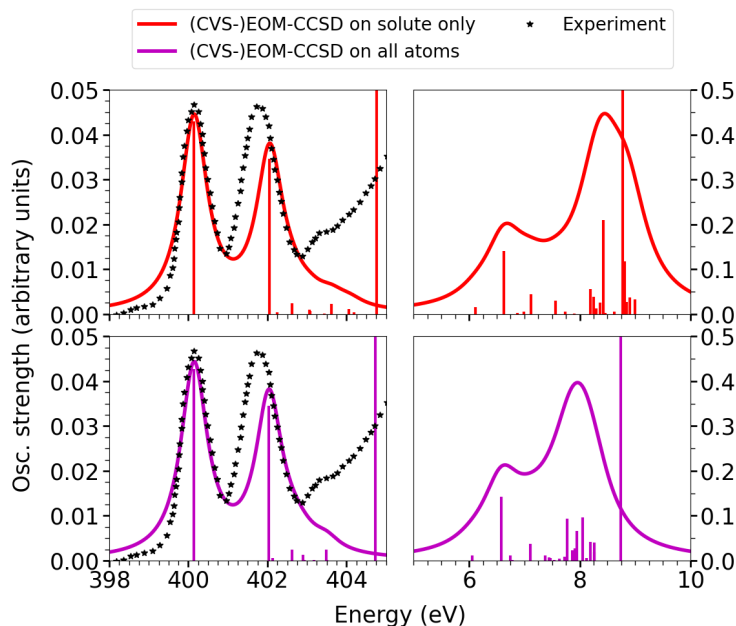


Figure S6: Imidazole with 4 explicit H₂O molecules: XAS spectra at the nitrogen *K*-edge (left) and Valence absorption spectra computed in the space orthogonal to the N core space (right). All spectra were calculated at the CVS-EOM-CCSD level of theory with the 6-311++G** basis. The solvent H₂O molecules are treated at the CVS-EOM-CCSD level of theory (bottom) and at the HF level of theory (top). Experimental XAS data was digitized from Meyer et al.⁶ The vertical lines spanning the entire height of the plot show the first ionization threshold. The computed XAS spectra were shifted by -1.67 eV to align with experiment when treating all atoms at the CCSD level of theory and -1.65 eV when treating the solvent molecules at the HF level of theory. 10 core transitions and 20 valence transitions are shown. A Lorentzian broadening with HWHM = 0.41 eV has been applied.

S6.2 Solvent H₂O treated at the CCSD level of theory

As also seen in the main text, as well as in Meyer et al.,⁶ the RIXS spectra at the two first resonances can be compared to the nonresonant spectra for each individual nitrogen. This can be seen in Fig. S7. It is observed that the RIXS spectrum for the first core resonance shows good agreement with the XES spectrum calculated for N1, while the signal at the second core resonance agrees well with the XES spectrum computed for N3.

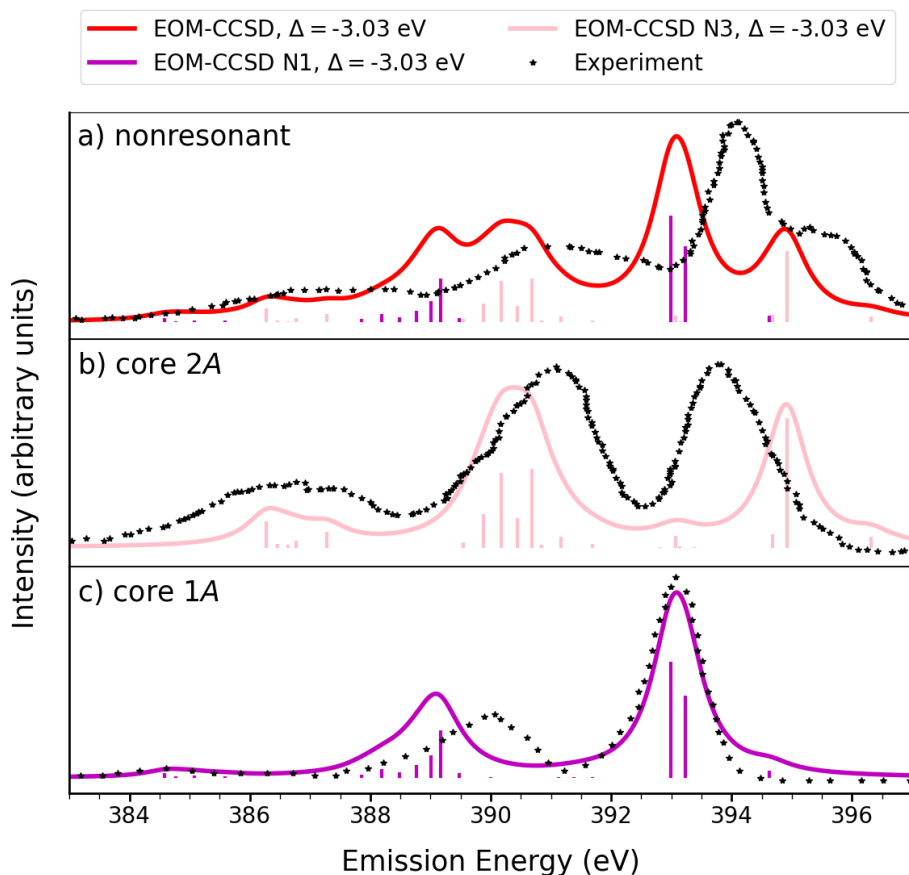


Figure S7: Imidazole with 4 explicit H₂O molecules: Nonresonant (a) and RIXS spectra at resonance with the energy of the first (c), and second (b) core excitation at the N *K*-edge. All spectra are computed with the 6-311++G** basis at the EOM-CCSD level of theory for both solute and solvent. The results are shifted based on the RIXS experiment at resonance with the first core excitation. A Lorentzian broadening of the spectra have been applied with HWHM=0.41 eV. For (b) and (c) the simulated spectra are the nonresonant ones of individual N-atoms as indicated in the legends. Experimental data was digitized from Meyer et al.⁶

S6.2.1 Data tables

Table S27: Imidazole with 4 explicit H₂O molecules: Unshifted N *K*-edge XAS data using the 6-311++G** basis set at the CVS-EOM-CCSD level of theory for all atoms.

Sym. ^a	$\omega_{abs,e}/\text{eV}$	f_{osc}
1A	401.8125	0.04270
2A	403.7078	0.03452
3A	403.799	0.00057
4A	404.282	0.00242
5A	404.5691	0.00133
6A	404.6025	0.00021
7A	404.8462	0.00007
8A	405.1582	0.00238
9A	405.1664	0.00014
10A	405.3222	0.00001

^a Mulliken symmetry notation.

Table S28: Imidazole with 4 explicit H₂O molecules: Unshifted valence excitation data computed using the 6-311++G** basis set in a space orthogonal to the N core space. For solute as well as solvent the EOM-CCSD level of theory was used.

Sym. ^a	$\omega_{abs,v}/\text{eV}$	f_{osc}
1A	6.0528	0.01210
2A	6.5819	0.14179
3A	6.7463	0.01116
4A	6.7841	0.00122
5A	7.1072	0.03736
6A	7.3754	0.01150
7A	7.4410	0.00719
8A	7.4629	0.00566
9A	7.5410	0.00147
10A	7.6324	0.00384
11A	7.7305	0.00817
12A	7.7752	0.09371
13A	7.8601	0.02239
14A	7.9173	0.02735
15A	7.9454	0.06602
16A	8.0535	0.09648
17A	8.1198	0.00562
18A	8.1901	0.04189
19A	8.2559	0.01930
20A	8.2657	0.04033

^a Mulliken symmetry notation.

Table S29: Imidazole with 4 explicit H₂O molecules: Unshifted nonresonant (XES) data at the Nitrogen *K*-edge for N1 and N3 calculated using EOM-CCSD on both solute and solvent. All calculations employed the 6-311++G** basis.

N1		N3	
ω_{em}	f_{osc}	ω_{em}	f_{osc}
397.6639	0.00230	399.3504	0.00195
396.2693	0.02449	397.9558	0.02294
396.0293	0.03446	397.7158	0.00236
394.7256	0.00019	396.4121	0.00016
394.4897	0.00014	396.1762	0.00030
394.4148	0.00017	396.1014	0.00214
394.1577	0.00017	395.8442	0.00006
393.0322	0.00023	394.7188	0.00075
392.5157	0.00137	394.2023	0.00197
392.1982	0.01407	393.8847	0.00061
392.0376	0.00679	393.7242	0.01400
391.7960	0.00376	393.4826	0.00528
391.5244	0.00174	393.2110	0.01329
391.2216	0.00279	392.9081	0.00595
390.8912	0.00109	392.5775	0.00103
388.6267	0.00054	390.3132	0.00278
388.1184	0.00072	389.8049	0.00128
387.9875	0.00012	389.6741	0.00050
387.8025	0.00044	389.4890	0.00070
387.6180	0.00142	389.3045	0.00463

S6.3 Solvent H₂O treated at HF level of theory

To save computational power we have treated the solvent molecules at the HF level of theory and only employ CCSD for the imidazole molecule itself. This approach was shown in section S6.1 to work excellently for the localized core transitions, and even for the more delocalized valence transitions did the method yield good results.

As the method is computationally cheaper compared to treating both solvent and solute at the CCSD level of theory, more valence transitions can be considered. The corresponding valence absorption spectrum is shown in Fig. S8

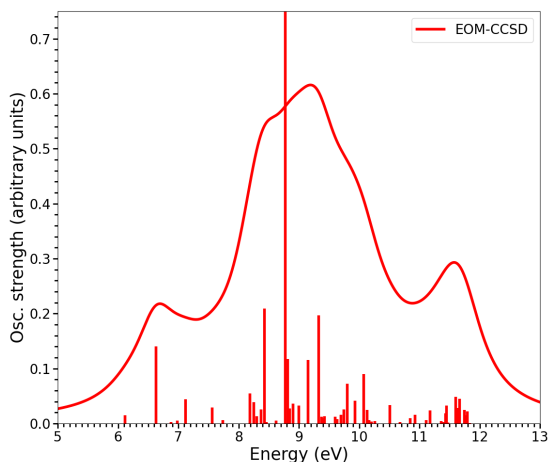


Figure S8: Imidazole with 4 explicit H₂O molecules, the latter treated at the HF level of theory: Valence absorption spectrum computed in the space orthogonal to the N core space and calculated at the EOM-CCSD (red) level of theory with the 6-311++G** basis. The vertical line spanning the entire height of the plot shows the first ionization threshold. A Lorentzian broadening was applied with HWHM=0.41 eV. 60 valence transitions are shown.

S6.3.1 Data tables

Table S30: Imidazole with 4 explicit H₂O molecules, the latter treated at the HF level of theory: Unshifted N *K*-edge XAS data using the 6-311++G** basis set and CVS-EOM-CCSD method.

^a Mulliken symmetry notation.

Sym. ^a	$\omega_{abs,e}/\text{eV}$	f_{osc}
1A	401.7992	0.04291
2A	403.7125	0.03463
3A	403.9067	0.00038
4A	404.2742	0.00242
5A	404.7165	0.00100
6A	404.7382	0.00063
7A	405.1006	0.00002
8A	405.2667	0.00224
9A	405.7138	0.00116
10A	405.8489	0.00032

Table S31: Imidazole with 4 explicit H₂O molecules, the latter treated at the HF level of theory: Unshifted valence absorption data computed using the 6-311++G** basis set in a space orthogonal to the N core space at the EOM-CCSD level of theory.

^a Mulliken symmetry notation.

Sym. ^a	$\omega_{abs,v}/\text{eV}$	f_{osc}
1A	6.1192	0.01508
2A	6.6315	0.13996
3A	6.8779	0.00300
4A	6.9847	0.00542
5A	7.1231	0.04414
6A	7.5644	0.02921
7A	7.6314	0.00011
8A	7.7390	0.00589
9A	7.9027	0.00024
10A	8.1887	0.05492
11A	8.2551	0.03864
12A	8.2980	0.01294
13A	8.3718	0.02535
14A	8.4288	0.20931
15A	8.4633	0.00245
16A	8.6246	0.00490
17A	8.8134	0.11727
18A	8.8470	0.02711
19A	8.9051	0.03635
20A	8.9965	0.03226
21A	9.1495	0.11523
22A	9.3329	0.19650
23A	9.3756	0.01266
24A	9.4043	0.00928
25A	9.4265	0.01289
26A	9.6032	0.01259
27A	9.6308	0.00754
28A	9.6997	0.01580
29A	9.7434	0.02551
30A	9.8054	0.07274
31A	9.9284	0.04141
32A	10.0725	0.09012
33A	10.1290	0.02495
34A	10.1644	0.00592

Table S31 – continued from previous page

Sym. ^a	$\omega_{abs,v}/\text{eV}$	f_{osc}
35A	10.2028	0.00328
36A	10.2592	0.00451
37A	10.5134	0.03315
38A	10.5817	0.00025
39A	10.6768	0.00235
40A	10.8473	0.00966
41A	10.9200	0.00131
42A	10.9296	0.01611
43A	11.0170	0.00001
44A	11.1113	0.00657
45A	11.1739	0.00038
46A	11.1805	0.02356
47A	11.3593	0.00398
48A	11.4035	0.00230
49A	11.4089	0.00264
50A	11.4300	0.01816
51A	11.4510	0.03238
52A	11.4711	0.00165
53A	11.6061	0.04848
54A	11.6326	0.02827
55A	11.6685	0.04525
56A	11.7457	0.02432
57A	11.7758	0.01495
58A	11.7916	0.02203
59A	11.8108	0.00115
60A	11.8383	0.00102

Table S32: Imidazole with 4 explicit H₂O molecules, the latter treated at the HF level of theory: Unshifted RIXS data for the pump frequency at resonance with the first bright core excitation (1A in Mulliken symmetry notation) calculated using different CCSD methods. All computed RIXS cross sections for $\theta = 45^\circ$ are based on emission energies calculated at the EOM-CCSD level of theory. CVS and CVS-uS refer to a projection in the damped response solver. All calculations employed the 6-311++G** basis.

ω_{em}	$\sigma_{45^\circ}^{\text{RIXS}}/\text{a.u.}$	
	CVS-uS-EOM-CCSD	CVS-EOM-CCSD
395.6799	0.00008	0.00134
395.1678	0.00116	0.00166
394.9212	0.00007	0.00031

Table S32 – continued from previous page

ω_{em}	$\sigma_{45^\circ}^{\text{RIS}}/\text{a.u.}$	
	CVS-uS-EOM-CCSD	CVS-EOM-CCSD
394.8146	0.00029	0.00032
394.6761	0.00576	0.00621
394.2347	0.00078	0.00158
394.1677	0.00116	0.00152
394.0603	0.08221	0.06826
393.8964	0.00047	0.00099
393.6105	0.00010	0.00009
393.5441	0.00107	0.00077
393.5013	0.00029	0.00033
393.4273	0.00017	0.00018
393.3704	0.01376	0.01199
393.3359	0.00020	0.00027
393.1745	0.01861	0.01545
392.9857	0.00156	0.00174
392.9522	0.00063	0.00126
392.8942	0.00151	0.00385
392.8028	0.00076	0.00070
392.6496	0.00473	0.00462
392.4662	0.00518	0.00458
392.4235	0.00070	0.00058
392.3949	0.00047	0.00025
392.3729	0.00083	0.00069
392.1960	0.00031	0.00011
392.1682	0.00025	0.00029
392.0994	0.00031	0.00030
392.0559	0.00003	0.00010
391.9938	0.00014	0.00021
391.8708	0.00007	0.00026
391.7269	0.00009	0.00009
391.6703	0.00007	0.00023
391.6349	0.00007	0.00006
391.5965	0.00007	0.00007
391.5399	0.00014	0.00039
391.2858	0.00002	0.00137
391.2175	0.00012	0.00060
391.1225	0.00008	0.00013
390.9519	0.00448	0.00395
390.8792	0.00013	0.00014

Table S32 – continued from previous page

ω_{em}	$\sigma_{45^\circ}^{\text{RIXS}}/\text{a.u.}$	
CCSD	CVS-uS-EOM-CCSD	CVS-EOM-CCSD
390.8697	0.00010	0.00012
390.7821	0.00056	0.00048
390.6879	0.00005	0.00003
390.6254	0.01555	0.01322
390.6188	0.01506	0.01283
390.4401	0.00061	0.00058
390.3957	0.00031	0.00053
390.3903	0.00098	0.00085
390.3693	0.00326	0.00293
390.3483	0.00298	0.00288
390.3282	0.00036	0.00033
390.1932	0.00018	0.00022
390.1666	0.00008	0.00007
390.1307	0.00001	0.00022
390.0534	0.00068	0.00055
390.0234	0.00011	0.00020

Table S33: Imidazole with 4 explicit H₂O molecules, the latter treated at the HF level of theory: Unshifted RIXS data for the pump frequency at resonance with the second bright core excitation (2A in Mulliken symmetry notation) calculated using different CCSD methods. All computed RIXS cross sections for $\theta = 45^\circ$ are based on emission energies calculated at the EOM-CCSD level of theory. CVS and CVS-uS refer to a projection in the damped response solver. All calculations employed the 6-311++G** basis.

ω_{em}	$\sigma_{45^\circ}^{\text{RIXS}}/\text{a.u.}$	
CCSD	CVS-uS-EOM-CCSD	CVS-EOM-CCSD
397.5931	0.00007	0.00137
397.0810	0.00366	0.00400
396.8345	0.00006	0.00027
396.7278	0.00025	0.00029
396.5893	0.00639	0.00668
396.1479	0.00117	0.00188
396.0810	0.00017	0.00091
395.9735	0.00621	0.00541
395.8097	0.00009	0.00069
395.5237	0.00019	0.00020
395.4573	0.00075	0.00048
395.4146	0.00019	0.00025

Table S33 – continued from previous page

ω_{em}	$\sigma_{45^\circ}^{\text{RIS}}/\text{a.u.}$	
	CVS-uS-EOM-CCSD	CVS-EOM-CCSD
395.3406	0.00041	0.00038
395.2837	0.01347	0.01160
395.2491	0.00017	0.00029
395.0878	0.00063	0.00058
394.8989	0.00091	0.00133
394.8654	0.00008	0.00097
394.8075	0.00110	0.00352
394.7161	0.00008	0.00019
394.5629	0.00005	0.00058
394.3794	0.00345	0.00305
394.3367	0.00047	0.00037
394.3082	0.00036	0.00017
394.2861	0.00008	0.00014
394.1092	0.00029	0.00010
394.0815	0.00016	0.00019
394.0126	0.00019	0.00018
393.9691	0.00003	0.00010
393.9071	0.00011	0.00020
393.7841	0.00009	0.00028
393.6401	0.00007	0.00007
393.5835	0.00008	0.00026
393.5481	0.00010	0.00008
393.5098	0.00006	0.00007
393.4532	0.00030	0.00055
393.1990	0.00001	0.00137
393.1307	0.00009	0.00056
393.0357	0.00000	0.00003
392.8651	0.00054	0.00077
392.7925	0.00003	0.00005
392.7830	0.00020	0.00019
392.6953	0.00006	0.00009
392.6012	0.00021	0.00016
392.5386	0.00160	0.00132
392.5321	0.00131	0.00110
392.3533	0.00169	0.00146
392.3089	0.00129	0.00140
392.3035	0.00394	0.00337
392.2825	0.00840	0.00727

Table S33 – continued from previous page

ω_{em}	$\sigma_{45^\circ}^{\text{RXS}}/\text{a.u.}$	
CCSD	CVS-uS-EOM-CCSD	CVS-EOM-CCSD
392.2616	0.00742	0.00667
392.2414	0.00016	0.00017
392.1065	0.00090	0.00083
392.0798	0.00182	0.00160
392.0439	0.00010	0.00029
391.9669	0.00434	0.00383
391.9367	0.00209	0.00193

Table S34: Imidazole with 4 explicit H₂O molecules, the latter treated at the HF level of theory: Unshifted nonresonant (XES) data at the Nitrogen *K*-edge calculated using EOM-CCSD for N1 and N3 using the 6-311++G** basis.

N1		N3	
ω_{em}	f_{osc}	ω_{em}	f_{osc}
397.6367	0.00221	399.3420	0.00197
396.2244	0.02475	397.9297	0.02302
395.7863	0.03618	397.4916	0.00267
393.3944	0.00010	395.1000	0.00266
392.2205	0.01403	393.9258	0.00054
391.9761	0.00771	393.6815	0.01598
391.5979	0.00620	393.3035	0.00902
391.3995	0.00287	393.1049	0.01633
390.5367	0.00033	392.2423	0.00053
387.9146	0.00237	389.6199	0.01064
387.2462	0.00000	388.9519	0.00047
387.1453	0.00070	388.8506	0.01216
386.6658	0.00659	388.3712	0.0117
386.2228	0.00018	387.9282	0.0000
385.5110	0.00010	387.2163	0.00028
385.3850	0.00000	387.0903	0.00001
385.1553	0.00000	386.8609	0.00000
384.9970	0.00000	386.7023	0.00010
384.8204	0.00000	386.5257	0.00001
384.5953	0.00001	386.3007	0.00001

S7 Pyridine

Another example molecule simulated with the new implementation is pyridine. The simulated XAS spectrum at the nitrogen K-edge is shown in Fig. S9. The CVS-EOM-CCSD result is observed to be in good agreement with the experimental spectrum, and is further more noted to be an improvement on the simulated DFT spectra shown in.⁷ The lack of the small shoulder on the main peak is expected, as this is reported to be the result of a dipole forbidden transition only allowed

through vibronic coupling,⁷ which is not included in this study. It can be seen from Fig. S9 that

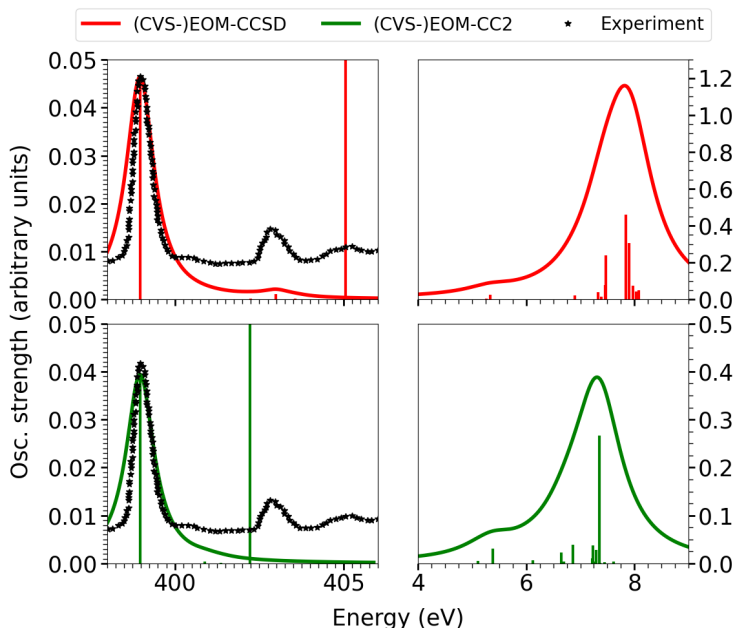


Figure S9: Pyridine: XAS spectrum at the nitrogen *K*-edge (left) and valence absorption in a space orthogonal to the N core space (right) calculated at the (CVS-)EOM-CC2 (green) and (CVS-)EOM-CCSD (red) level of theory with the 6-311++G** basis including additional Rydberg functions on N. Experimental data was digitized from Baiardi et al.⁷ The vertical lines spanning the entire height of the plot shows the first (core) ionization threshold. The Lorentzian broadening applied has HWHM=0.51 eV. The computed XAS were shifted to align with experiment: -1.69 eV for CVS-EOM-CCSD and -2.28 eV for CVS-EOM-CC2.

CVS-EOM-CC2 predicts the second (low intensity) peak far closer to the first peak compared to CVS-EOM-CCSD and experiment. Furthermore, this second feature at the CVS-EOM-CC2 level of theory shows even lower intensity compared to CVS-EOM-CCSD, which also shows a too low relative intensity of the second peak compared to experiment. The core ionization threshold with CC2 is predicted to be significantly lower than what is found with CCSD, which appears to be in better general agreement with experiment (if the shift applied in Fig. S9 is considered). The characters of the two main transition are for both methods core $1A''$ and core $3A'$, respectively. The ionization thresholds are shown in table S35. From the valence spectra in Fig. S9, it can be

Table S35: Pyridine: Valence and core ionization energies. All calculations employed the 6-311++G** basis on all atoms with additional Rydberg functions on N.

Method	IP/eV	Core IP/eV
EOM-CC2	9.35	404.50
EOM-CCSD	9.68	406.74
Experiment ^{8,9}	9.34	404.94

seen that, while the same overall shape is found for the two methods, a much larger intensity of the main peak is predicted by EOM-CCSD compared to EOM-CC2. This is caused by a much higher density of transitions around the main peak in the EOM-CCSD calculation. The main transition has $9A'$ character in the EOM-CC2 calculation, while it has $7A'$ character in the EOM-CCSD one.

The nonresonant as well as RIXS spectra have been computed at the resonance of the first two bright core transitions. Observe that it was not possible to converge the damped response equations for EOM-CC2, and hence the CC2 based RIXS spectrum is here CVS-uS-EOM-CC2. This might be related to the damped response solver being solved in full space in the current implementation.

The RIXS spectrum in Fig. S10, shows 3 features at the first resonance, when utilizing CCSD

Table S36: Pyridine: Overview of valence states probed in RIXS with the different methods at the first and second core resonance. The Mulliken symmetry notation has been used. All energies are unshifted.

CVS-us-EOM-CCSD		CVS-EOM-CCSD		CVS-us-EOM-CC2	
Energy/ eV	Probed state	Energy/ eV	Probed state	Energy/ eV	Probed state
core $1A''$ resonance					
395.40	$1A''$	395.40	$1A''$	396.15	$1A''$
393.75	$3A'$	393.75	$3A'$	394.39	$5A'$
392.82	$7A'$	392.82	$7A'$	-	-
core $3A'$ resonance					
-	-	-	-	398.06	$1A''$
-	-	397.90	$3A''$	-	-
397.23	$5A'$	397.23	$5A'$	-	-
-	-	396.60	$11A'$	-	-
-	-	-	-	396.47	$4A'$

based methods and only 2 when considering the CC2 based one. Both the CVS-EOM-CCSD and CVS-uS-EOM-CCSD results show the same features in the same positions and probe the valence $1A''$, $3A'$ and $7A'$ transitions, while the CVS-uS-EOM-CC2 simulation probes only the $1A''$ and

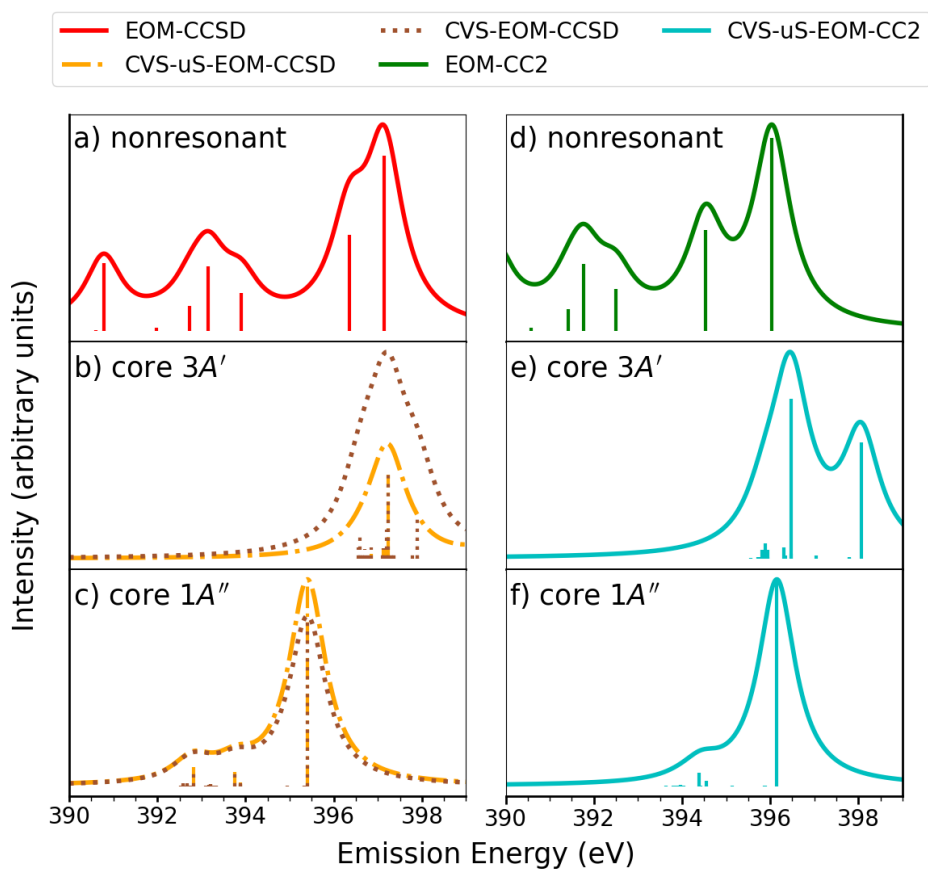


Figure S10: Pyridine: Nonresonant (a) and RIXS spectra at resonance with the energy of the first (c), and second (b) core excitation at the N K -edge. All spectra are computed with the 6-311++G** basis including additional Rydberg functions on N. The Lorentzian broadening applied has HWHM=0.51 eV.

5A' transitions. Comparing the CCSD and CC2 based results it is found that the first two features are described by all methods and with roughly the same separation despite the difference in the character of the second (low intensity) peak.

As also observed for the other molecules, the shift applied to align the spectra with the RIXS spectrum at the first core resonance does not overlay the CCSD and CC2 based results for the nonresonant spectra, but rather an additional shift is observed. It is furthermore noted, that while all calculations agree on the general shape of the spectra for the nonresonant spectrum as well as the RIXS spectrum at the first core resonance, there is a larger discrepancy at the second core resonance (core 3A'). While, the CVS-EOM-CCSD spectrum shows three main transitions resulting in one broad peak, probing the valence states 5A', 3A'' and 11A', the CVS-uS-EOM-CCSD spectrum shows only one main transition probing 5A'. The CVS-uS-EOM-CC2 result shows yet another spectral shape and appears to probe valence transitions 1A'' and 4A'.

S7.1 Data Tables

Table S37: Pyridine: Unshifted N *K*-edge XAS data using the 6-311++G** basis set with additional Rydberg functions on N.

^a Mulliken symmetry notation.

EOM-CC2			EOM-CCSD		
Sym. ^a	$\omega_{obs,e}/\text{eV}$	f_{osc}	Sym. ^a	$\omega_{obs,e}/\text{eV}$	f_{osc}
1A''	401.2539	0.03933	1A''	400.6602	0.04639
2A''	402.2851	0.00000	2A''	402.8414	0.00000
1A'	402.6349	0.00000	1A'	403.9262	0.00015
2A'	403.0715	0.00000	2A'	404.5937	0.00000
3A'	403.1699	0.00044	3A''	404.6680	0.00012
3A''	403.2020	0.00001	3A'	404.6858	0.00116
4A'	403.5812	0.00003	4A'	405.0469	0.00001
5A'	403.6243	0.00005	5A'	405.2475	0.00009
6A'	403.6554	0.00009	6A'	405.2568	0.00014
4A''	403.6918	0.00000	4A''	405.3636	0.00000

Table S38: Pyridine: Unshifted valence absorption data computed using the 6-311++G** basis set with additional Rydberg functions on N in a space orthogonal to the N core space.

^a Mulliken symmetry notation.

EOM-CC2			EOM-CCSD		
Sym. ^a	ω_{abs} /eV	f_{osc}	Sym. ^a	ω_{abs} /eV	f_{osc}
1A''	5.1037	0.00574	1A''	5.2561	0.00594
2A''	5.3701	0.00000	1A'	5.3357	0.02726
1A'	5.3816	0.03091	2A''	5.7078	0.00000
2A'	6.1211	0.00632	2A'	6.7854	0.00262
3A'	6.6432	0.0224	3A''	6.7864	0.00000
4A'	6.6966	0.00385	3A'	6.9009	0.02303
3A''	6.6971	0.00000	4A''	7.3326	0.04090
4A''	6.8249	0.00066	4A'	7.3874	0.01433
5A'	6.8637	0.03945	5A'	7.4557	0.07883
6A'	7.2215	0.01121	6A'	7.4717	0.24066
5A''	7.2286	0.0382	5A''	7.4870	0.00026
7A'	7.2515	0.0043	6A''	7.5540	0.00303
8A'	7.2899	0.02854	7A''	7.5711	0.00000
9A'	7.3525	0.26711	7A'	7.8417	0.46036
6A''	7.3600	0.00096	8A'	7.901	0.30515
7A''	7.4114	0.00000	8A''	7.9341	0.00000
10A'	7.4341	-0.00002	9A'	7.9778	0.07613
8A''	7.4459	0.00252	10A'	8.0367	0.04440
9A''	7.4478	0.00000	11A'	8.0854	0.05158
11A'	7.6111	0.00442	9A''	8.1321	0.00018

Table S39: Pyridine: Unshifted RIXS data for the pump frequency at resonance with the first core excitation (core 1A'' in Mulliken symmetry notation) calculated using different methods. RIXS cross sections for $\theta = 45^\circ$ at the CVS-uS-EOM-CCSD and CVS-EOM-CCSD level of theory are all based on emission energies calculated at the EOM-CCSD level of theory. CVS and CVS-uS refer to a projection in the damped response solver. All calculations employed the 6-311++G** basis with additional Rydberg functions on N.

ω_{em}		$\sigma_{45^\circ}^{RIXS}/\text{a.u.}$		
CCSD	CC2	CVS-uS-EOM-CCSD	CVS-EOM-CCSD	CVS-uS-EOM-CC2
395.4040	396.1501	0.10524	0.08637	0.09736
395.3245	395.8837	0.00000	0.00001	0.00003
394.9522	395.8723	0.00003	0.00001	0.00000
393.8747	395.1327	0.00176	0.00190	0.00001
393.8739	394.6107	0.00002	0.00092	0.00000
393.7593	394.5574	0.00734	0.00639	0.00252
393.3275	394.5569	0.00000	0.00016	0.00002
393.2728	394.4290	0.00000	0.00013	0.00001
393.2045	394.3903	0.00090	0.00103	0.00647
393.1884	394.0325	0.00000	0.00000	0.00032
393.1732	394.0252	0.00002	0.00049	0.00000
393.1062	394.0023	0.00003	0.00006	0.00000
393.0891	393.9639	0.00000	0.00017	0.00039
392.8183	393.9013	0.00967	0.00846	0.00000
392.7593	393.8940	0.00000	0.00010	0.00002
392.7261	393.8426	0.00002	0.00001	0.00000
392.6825	393.8197	0.00117	0.00131	0.00008
392.6235	393.8080	0.00000	0.00009	0.00006
392.5748	393.8061	0.00100	0.00132	0.00000
392.5280	393.6428	0.00000	0.00024	0.00000

Table S40: Pyridine: Unshifted RIXS data for the pump frequency at resonance with the second core excitation (core 3A' in Mulliken symmetry notation) calculated using different methods. RIXS cross sections for $\theta = 45^\circ$ at the CVS-uS-EOM-CCSD and CVS-EOM-CCSD level of theory are both based on emission energies calculated at the EOM-CCSD level of theory. CVS and CVS-uS refers to a projection in the damped response solver. All calculations employed the 6-311++G** basis with additional Rydberg functions on N.

ω_{em}		$\sigma_{45^\circ}^{RIXS}/\text{a.u.}$		
CCSD	CC2	CVS-uS-EOM-CCSD	CVS-EOM-CCSD	CVS-uS-EOM-CC2
399.4296	398.0663	0.00019	0.00011	0.00054
399.3502	397.7999	0.00000	0.00001	0.00001
398.9779	397.7882	0.00001	0.00001	0.00000
397.9003	397.0489	0.00002	0.00044	0.00001
397.8995	396.5267	0.00002	0.0009	0.00000
397.785	396.4734	0.00001	0.00016	0.00074
397.3531	396.4728	0.00006	0.0002	0.00002
397.2984	396.3449	0.00000	0.00015	0.00001
397.2301	396.3063	0.0019	0.00199	0.00005
397.2141	395.9485	0.00000	0.00000	0.00004
397.1988	395.9414	0.00026	0.00066	0.00001
397.1319	395.9185	0.00024	0.00023	0.00001
397.1147	395.8802	0.00000	0.00017	0.00007
396.844	395.8173	0.0001	0.00026	0.00000
396.7849	395.8099	0.00000	0.00012	0.00004
396.7517	395.7585	0.00001	0.00000	0.00000
396.7079	395.7357	0.00000	0.00022	0.00001
396.6491	395.724	0.00001	0.00014	0.00001
396.6004	395.7221	0.00007	0.00061	0.00000
396.5536	395.5588	0.00001	0.00026	0.00000

Table S41: Pyridine: Unshifted nonresonant (XES) data at the Nitrogen *K*-edge calculated using different methods. All calculations employed the 6-311++G** basis with additional Rydberg functions on N.

ω_{em}		f_{osc}	
CCSD	CC2	EOM-CCSD	EOM-CC2
397.1485	396.0404	0.03456	0.03739
397.0568	395.1555	0.00000	0.00000
396.3471	394.5316	0.01904	0.01956
393.9024	392.4991	0.00747	0.00822
393.1568	391.7691	0.01270	0.01297
392.7334	391.4161	0.00490	0.00426
391.9707	390.5742	0.00061	0.00061
390.7810	389.7628	0.01340	0.01475
390.6047	389.0661	0.00012	0.00009
389.0604	387.7067	0.00170	0.00150
387.9771	385.3961	0.00000	0.00000
387.2683	385.2941	0.00005	0.00000
387.0686	385.2881	0.00036	0.00000
386.8784	385.1847	-0.00004	0.00000
386.3167	385.1072	0.00005	0.00000
386.2636	385.1063	0.00776	0.00000
385.8811	385.0938	0.00000	0.00000
385.7657	385.0321	0.00009	0.00808

References

- (1) Nanda, K. D.; Krylov, A. I. Cherry-picking resolvents: A general strategy for convergent coupled-cluster damped response calculations of core-level spectra. *J. Chem. Phys.* **2020**, *153*, 141104.
- (2) Prince, K. C.; Richter, R.; de Simone, M.; Alagia, M.; Coreno, M. Near Edge X-ray Absorption Spectra of Some Small Polyatomic Molecules. *J. Phys. Chem. A* **2003**, *107*, 1955–1963.
- (3) Bodeur, S.; Esteva, J. M. Photoabsorption spectra of H₂S, CH₃SH and SO₂ near the sulfur *K* edge. *J. Chem. Phys.* **1985**, *100*, 415–427.
- (4) Carbone, J. P.; Cheng, L.; Myhre, R. H.; Matthews, D.; Koch, H.; Coriani, S. In *State of The Art of Molecular Electronic Structure Computations: Correlation Methods, Basis Sets and More*; Ancarani, L. U., Hoggan, P. E., Eds.; Advances in Quantum Chemistry; Academic Press, 2019; Vol. 79; pp 241–261.
- (5) Turci, C. C.; Urquhart, S. G.; Hitchcock, A. P. Inner-shell excitation spectroscopy of aniline, nitrobenzene, and nitroanilines. *Canadian Journal of Chemistry* **1996**, *74*, 851–869.
- (6) Meyer, F.; Blum, M.; Benkert, A.; Hauschild, D.; Jeyachandran, Y. L.; Wilks, R. G.; Yang, W.; Bär, M.; Reinert, F.; Heske, C.; Zharnikov, M.; Weinhardt, L. Site-specific electronic structure of imidazole and imidazolium in aqueous solutions. *Phys. Chem. Chem. Phys.* **2018**, *20*, 8302–8310.
- (7) Baiardi, A.; Mendolicchio, M.; Barone, V.; Fronzoni, G.; Cardenas Jimenez, G. A.; Stener, M.; Grazioli, C.; de Simone, M.; Coreno, M. Vibrationally resolved NEXAFS at C and N K-edges of pyridine, 2-fluoropyridine and 2,6-difluoropyridine: A combined experimental and theoretical assessment. *J. Chem. Phys.* **2015**, *143*, 204102.
- (8) Arimura, M.; Yoshikawa, Y. Ionization Efficiency and Ionization Energy of Cyclic Compounds by Electron Impact. *J. Mass Spectrom. Soc. Jpn.* **1984**, *32*, 375–380.

- (9) Brown, R. S.; Tse, A.; Vederas, J. C. Photoelectron-determined core binding energies and predicted gas-phase basicities for the 2-hydroxypyridine \rightleftharpoons 2-pyridone system. *J. Am. Chem. Soc.* **1980**, *102*, 1174–1176.

APPENDIX E

Manuscript 2

The manuscript "A theoretical study of the time-resolved X-ray absorption spectra of the photoionized BT-1T cation" by Anna Kristina Schnack-Petersen, Mátyás Pápai, Sonia Coriani and Klaus Braagaard Møller is still in preparation.

A theoretical study of the time-resolved X-ray absorption spectrum of the photoionized BT-1T cation

Anna Kristina Schnack-Petersen,¹ Mátyás Pápai,^{1,2} Sonia Coriani,¹ and Klaus Braagaard Møller¹

¹*Department of Chemistry, Technical University of Denmark, DK-2800 Kongens Lyngby, Denmark*

²*Wigner Research Centre for Physics, P.O. Box 49, H-1525 Budapest, Hungary*

(*Electronic mail: kbmo@kemi.dtu.dk)

(*Electronic mail: soco@kemi.dtu.dk)

The time-resolved X-ray absorption spectrum of the BT-1T cation (BT-1T⁺) is theoretically simulated in order to investigate the charge transfer reaction of the system. We employ both trajectory surface hopping and quantum dynamics to simulate the structural evolution over time and the changes in the state populations. To compute the static XAS of the ground and excited states, we apply both time-dependent density functional theory (TDDFT) and the coupled cluster singles and doubles (CCSD) method. The results obtained are in good agreement between the methods. It is furthermore found that the small structural changes that occur during the reaction have little effect on the static XAS. Hence, the tr-XAS can be computed based on the state populations determined from a nuclear dynamics simulation and *one set* of static XAS calculations, utilizing the ground state optimized geometry. This approach can save considerable computational resources, as the static spectra need not to be calculated for all geometries. As BT-1T is a relatively rigid molecule, further studies are required to determine whether this approach can also be employed for molecules more prone to nuclear motion.

Keywords: tr-XAS, BT-1T, MCTDH, trajectory surface hopping, TDDFT, CCSD

I. INTRODUCTION

The molecule 4-(2-thienyl)-2,1,3-benzothiadiazole (here denoted BT-1T) consists of an electron-accepting benzothiadiazole unit and an electron-donating thiophene unit (see Fig. 1). Several π -conjugated polymers, including either one or both of these units, have been scrutinized as potential organic solar cells¹⁻⁴ and generally for organic electronic devices.^{5,6} Particularly, applications in organic solar cells are of interest. Such solar cells are becoming a feasible alternative to the more established silicon- or metal-based ones due to their lower production costs^{7,8} and with organic solar cells now reaching efficiencies of around 18%.⁹⁻¹² An important property of an organic solar cell is its ability to form charge transfer states.^{13,14} Thus, this process must be investigated for any potential new solar cell in order to determine its suitability.¹³

Molecules including BT1T units have already been investigated both experimentally and theoretically.^{15,16} Only recently, though, has the small BT-1T molecule been studied theoretically on its own by Khalili *et al.*, who considered not only the photoexcitation,¹⁷ but also the photoionization of the system.¹⁸ So far, experimental studies of this system have not been published. Since experimental studies do typically rely on theoretical support for a full interpretation of the often complicated experimental spectra,¹⁹⁻²² further theoretical studies are nonetheless still required, especially at higher levels of theory.

Khalili *et al.*^{17,18} studied the BT-1T unit by simulating its time-resolved X-ray absorption

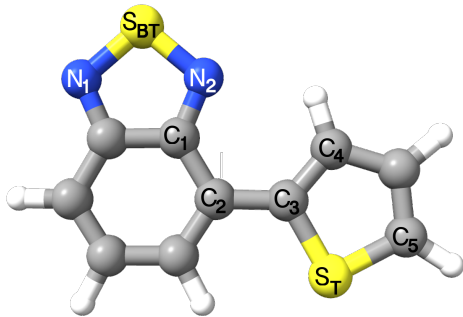


Figure 1: Structure of the BT-1T molecule optimized on S_0 at the BHHLYP/cc-pVDZ level of theory. The atoms important for the structural parameters considered are labeled. The benzothiadiazole unit is seen on the left, while the thiophene unit is the right part of the molecule.

spectra (tr-XAS). X-ray spectroscopy and scattering offer time-resolutions on the sub-picosecond timescale characteristic of molecular reactions.^{23–28} Furthermore, XAS, and especially excited state XAS, has proven sensitive to both electronic and structural changes in small organic molecules.^{22,29,30} In Ref. 18, the authors explored in particular the possibility to use tr-XAS to follow the charge dynamics of the BT-1T system after photoionization with a vacuum ultraviolet (VUV) pulse. They prepared the BT-1T⁺ cation in a state corresponding to the removal of one of the (HOMO-3) electrons in the neutral molecule (see Figs. 2 and 3).

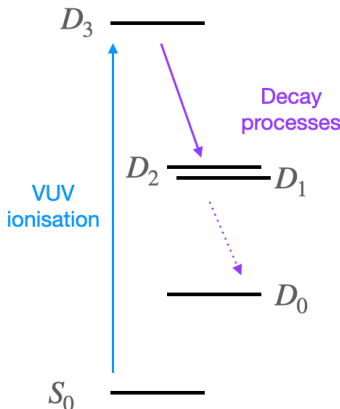


Figure 2: Schematic illustration of the studied process, where the molecule is photoexcited to the D_3 state. The system subsequently deexcites to the D_2 and D_1 states, while the D_0 state does not become significantly populated within the time studied here.

Khalili *et al.*¹⁸ employed Hartree-Fock (HF) level calculations using a small basis set, which is a rather low level of theory; calculations at a higher level of theory are therefore needed to determine the validity of the results. Moreover, the dynamics of the process was studied with trajectory surface hopping (TSH), which treats the nuclei classically. While this is often a good approximation, it is also of interest to investigate the effect of including quantum effects, i.e., treating the nuclei quantum mechanically allowing for, e.g., decoherence and tunneling. We will therefore study the BT-1T system quantum dynamically for the process of tr-XAS (probe step) following the VUV photoionization (pump step) of the neutral species. We will investigate, not only whether this type of experiment is suitable for studying the important charge transfer reaction, but also how much the conclusions are affected by resorting to a higher level of theory.

Khalili *et al.*¹⁸ employed ionic potential energy surfaces (PESs) based on Koopmans’ theorem (KT), as done by Khalili *et al.*¹⁸ Instead, we will investigate the nuclear dynamics by applying time-dependent density functional theory (TDDFT) directly to the cation. Unlike HF, TDDFT includes some electron correlation,³¹ without increasing the computational cost beyond feasibility. In general, TDDFT has proven a very successful method due to its low computational cost and overall good performance,^{32–34} even though the choice of functional can greatly affect the results and its effect is often difficult to predict.^{35,36} Fig. 3 pictorially illustrates the differences between the approach used by Khalili *et al.*¹⁸ and the one used in the present study when considering the molecular orbitals of the neutral molecule.

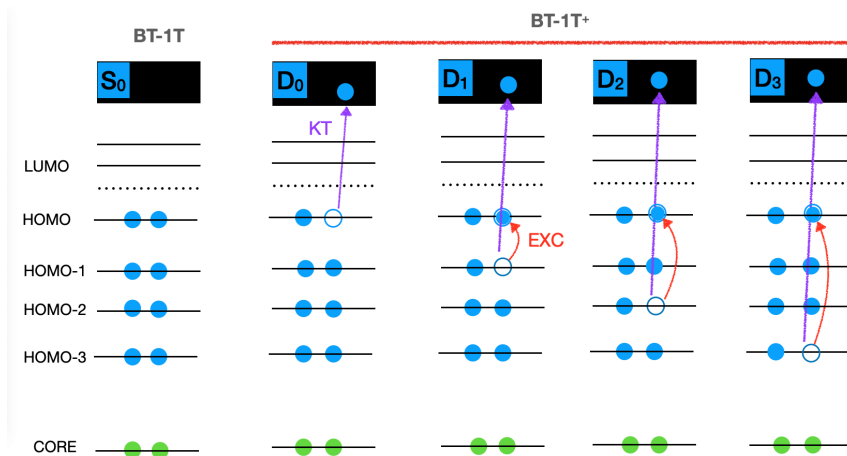


Figure 3: Molecular orbital schematic representation of how the relevant states of BT-1T⁺ are obtained in the present study (excitations from the ground state D_0 of the cation, red arrows) and by Khalili *et al.*¹⁸ (KT valence ionization from the S_0 ground state of the neutral molecule, blue arrows).

XAS calculations are subsequently carried out utilizing TDDFT as well as frozen core core-valence separated equations-of-motion coupled cluster singles and doubles (fc-CVS-EOM-CCSD).³⁷ This latter method is computationally more demanding, but the quality of the results obtained with CC methods is more predictable and can be systematically improved. Indeed, it is in the CC family of methods that the golden standard for calculations is to be found when the ground state is dominated by a single configuration.^{38–40} While not being the golden standard, CCSD still yields

results of relatively high quality and has become one of the methods of choice for accurately computing molecular properties at a reasonable cost.⁴⁰

The paper is organized as follows: Section II collects all information on the computational approaches utilized for this study. In Section III we present the relevant molecular orbitals (MOs) and valence transitions within the cation, while in Section IV we report the calculated charges on sulfur atoms in the electronic states of interest. Next, the dynamics simulation is presented in Section V. Here, we perform a TSH simulation⁴¹ for a limited number of trajectories in order to determine the normal modes to be included in a quantum dynamics simulation using the multi-configurational time-dependent Hartree (MCTDH) method.^{42,43} The results of these simulations are compared and evaluated, before the XAS are considered in section VI. To simulate the tr-XAS, the predicted average geometries and state populations from the MCTDH simulation are used in Section VIC. Here, both the importance of the geometrical changes, which are expected to be small due to the rigidity of the molecule, and the electronic state are evaluated.

II. COMPUTATIONAL METHODS

Geometries: The molecular geometry of the molecule before ionization was determined by optimizing the molecular structure of the neutral species on the ground state using the ORCA-5.0.0 program package.^{44,45} The optimization was carried out at the DFT level of theory employing the BHHLYP functional and the cc-pVDZ basis set.^{46,47}

Since the photoionization, starting the studied process, is fast, the initial geometry of interest (at a time delay of zero fs) is that of the neutral species. The geometries for non-zero time delays are determined as the average structures (i.e. centroid geometries) found in the quantum dynamics simulation.

Dynamics: For all calculations related to the dynamics simulations, the (TD)DFT/BHHLYP/cc-pVDZ level of theory was used. For excited-state calculations, the Tamm-Dancoff approximation (TDA) was employed. This approach has been used previously with good results.⁴⁸

First, the normal modes were determined analytically for the optimized structure. To determine the relevant normal modes to include in the MCTDH calculation, a TSH calculation was carried out in the SHARC-2.1.1 program package,^{41,49,50} interfaced with ORCA-4.2.0.^{44,51} The older version of ORCA was utilized here, since the auxiliary python-scripts necessary to perform the SHARC calculation were not adapted to the newer version. In the TSH simulation twenty five trajectories

were simulated for 400 fs. This number of trajectories is clearly too small to obtain good statistics for predicting quantum yields and lifetimes. It has, however, previously been shown that a limited number of trajectories can qualitatively determine the normal modes of interest,⁴⁸ as long as one is not concerned with rare events. The TSH simulation was carried out from a Wigner distribution of geometries and photoexcitation of the cation to simulate initial conditions. The final states considered are the same with respect to the occupation of neutral MOs, as those obtained by a photoionization of the neutral species (see Fig. 3). The gradient in all states, and hence the PES points, are, like the initial conditions, generated by considering photoexcitation of the ion. This way of generating the PES is the employed even if initial conditions are chosen based on photoionization of the neutral species (such a simulation can be found in the SI, Section S3.2). The (adiabatic) PES in the TSH simulation was determined on the fly. The simulation started in the third excited state (spin-state 7 in the diagonal representation). The calculation included spin-orbit couplings and was therefore performed with SHARC dynamics,⁵² i.e. based on the diagonal representation of the Hamiltonian. This is an alternative to the molecular Coulomb Hamiltonian (MCH) representation,⁵² which is known as regular surface hopping. Couplings between states were approximated based on wavefunction overlaps, and an energy based decoherence correction was employed.

The MCTDH simulation was carried out along selected normal modes of interest, determined based on the TSH simulation (see Section V B and Section S3.1 of the SI). The (diabatic) PESs for the MCTDH calculation were fitted to a vibronic-coupling Hamiltonian^{53,54} with an harmonic oscillator zero-order term and dimensionless mass-frequency scaled normal coordinates. Harmonic oscillator eigenfunctions were used as a basis for the PES fit. The fit for each normal mode was based on 31 points along the given mode for displacements $Q = -15$ to $Q = 15$ as some modes showed displacements of $|Q| > 10$. The fitting parameters are given in the SI (Section S3.4). All necessary points were calculated with ORCA-5.0.0 and the quantum dynamics simulation was then carried out with the MCTDH-8.4.12 program package.⁵⁵ Input for the latter program was based on a local development version of the VCHAM program,⁵⁶ modified to accommodate output files generated by ORCA-5.0.0.

The MCTDH calculation employed a primitive basis consisting of 45 basis functions for each normal mode chosen. The D_0 state for each mode was described by 5 single particle functions, while 10 functions were used to describe the remaining states for each mode. The grid populations were investigated and found to be below 10^{-5} , indicating a converged primitive basis. Likewise,

the natural weights were investigated to ensure convergence with respect to the single particle functions. Again, sufficiently small numbers were found (of the orders of magnitude: 10^{-7} - 10^{-3}). In addition, multimode single particle functions were used to combine modes in order to reduce computational costs.

Charges: Calculations of CHELPG (CHarges from ELectrostatic Potentials using a Grid based method⁵⁷) point charges were performed in Gaussian 16⁵⁸ at the BHHLYP/cc-pVDZ level of theory, in order to obtain the excited state charges. Such CHELPG charges have previously been successful in applications for classical nuclear dynamics.⁵⁹

X-ray absorption spectra: The XAS were calculated at both the TDDFT level of theory with the BHHLYP functional and at the fc-CVS-EOM-CCSD level of theory, adopting the aug-cc-pVTZ basis on sulfur and cc-pVDZ on the remaining atoms. Q-Chem-5.4.2⁶⁰ was used for these calculations.

The XAS spectrum of each electronic state of the cation was determined using TDDFT/fc-CVS-EOM-CCSD. These calculations were based on the Kohn-Sham/CCSD wavefunction of the given state optimized by employing the initial maximum overlap method^{61,62} (IMOM) procedure. Here, the excited state wavefunction is generated by solving the self-consistent field equations imposing as the constraint that the occupied orbitals have the largest possible overlap with an initial set of guess orbitals, rather than utilizing the Aufbau principle. This strategy has previously been employed with success in a number of cases.^{30,63–65} In our calculations, the choice of initial guess was based on the orbitals determined for the ground state of the neutral molecule. The occupied orbitals were then specified to be the same with one exception, since the cation has a singly occupied orbital. The choice of this singly occupied orbital for each investigated state is discussed in Section III and can also be anticipated based on Fig. 3. The IMOM approach has the disadvantage of generating excited states that are not orthogonal to the ground state. On the other hand, the XAS of the excited states can be straightforwardly computed as one-photon absorption of the IMOM-optimized state. Thus, one can obtain not only the core to singly occupied MO (SOMO) transitions, but also transitions from core orbitals to virtual MOs. An alternative approach for simulating excited state XAS is to compute the intensities as the transition strengths between two excited states, namely, the initial valence excited and the final core excited state. The corresponding transition energies are then computed as energy differences between the excitation energies of the two states from the ground state. At the CCSD level, this “quadratic response” approach can, however, only reliably describe core-to-SOMO transitions, as only these correspond

to a single photon process from the ground state. An equivalent approach for TDDFT is currently not available in Q-Chem-5.4.2.

A default convergence criterion of 10^{-6} was used for the excitation energy TDDFT calculations, while a convergence threshold of 10^{-5} was applied for the computationally more demanding EOM-CCSD calculations. All calculations on the cation employed an unrestricted formalism. TDA was not used for these calculations.

Orbitals: Ground state MOs are plotted based on Gaussian 16 calculations. Excited state MOs were, however, found by utilizing the Q-Chem-5.4.2 program package. All natural transition orbitals (NTOs) were determined based on calculations in Q-Chem-5.4.2. NTOs and MOs were plotted using Molden⁶⁶ and a contour value of 0.01.

III. ORBITALS OF INTEREST

The MOs of interest are the HOMO, HOMO-1, HOMO-2 and HOMO-3 displayed in Fig. 4 for both the neutral molecule and the cation. The obtained MOs for the neutral molecule are in good agreement with those presented by Khalili *et al.*^{17,18} The MOs of the cation will be discussed further below. Throughout the text we will refer to the orbitals for the neutral molecule with a subscript “0” and to those for the cation with a “ D_n ” subscript, indicating the considered state. Hence, the HOMO for the neutral molecule is denoted HOMO_0 .

To generate the wavefunction of the cation, a β -spin electron was removed from the neutral molecule. Removal of an electron from the HOMO results in a slightly spin contaminated D_0 state with $\langle S^2 \rangle = 0.8163$ at the BHHLYP/cc-pVDZ level of theory (a pure doublet spin state has $\langle S^2 \rangle = 0.75$).

Taking the D_0 state of the cation as reference, we also computed the NTOs for its first three valence transitions, which are shown in Fig. 5. These NTOs closely resemble the MOs shown in Fig. 4 (left). The particle NTO for all valence excitations corresponds to HOMO_0 , which must therefore be singly occupied in the cationic ground state denoted D_0 . D_0 corresponds to the hole in HOMO_0 , D_1 corresponds to the hole in $(\text{HOMO-1})_0$, D_2 corresponds to the hole in $(\text{HOMO-2})_0$ and, finally, D_3 corresponds to the hole in $(\text{HOMO-3})_0$. For consistency, we shall throughout denote the state associated with a hole in the $(\text{HOMO-n})_0$ MO as D_n .

The MOs and NTOs determined by using the methods and basis sets employed to calculate the

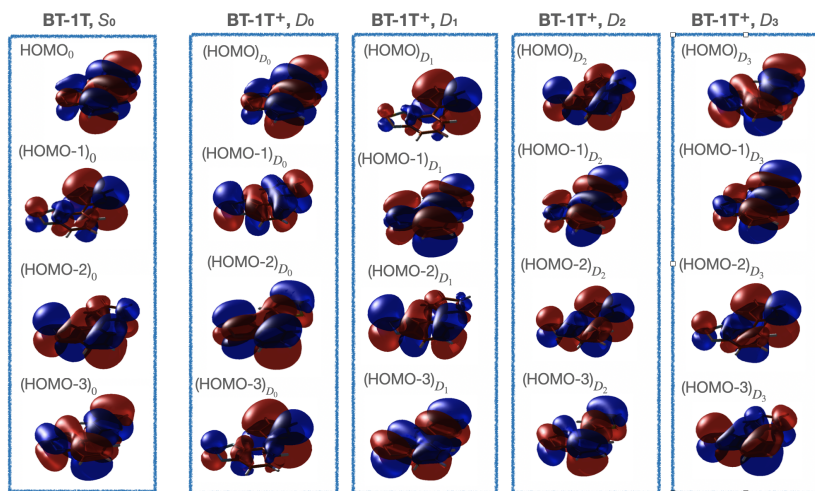
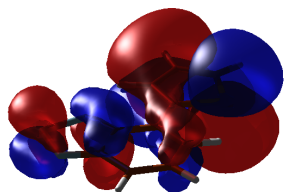
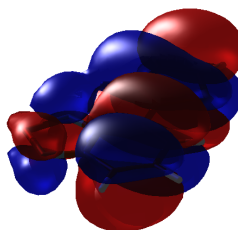


Figure 4: Highest-lying occupied MOs in BT-1T and in BT-1T⁺ in its ground state (D_0) and first three excited states (D_1 , D_2 and D_3). The MOs of S_0 were obtained at the BHHLYP/cc-pVDZ level of theory; those of the cation are BHHLYP results with the aug-cc-pVTZ basis on sulfur and the cc-pVDZ basis on the remaining atoms. Note the similarity between $(\text{HOMO})_{D_n}$ and $(\text{HOMO}-n)_0$.

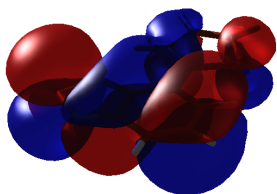
XAS are found to agree well with the MOs and NTOs shown here (see SI, Sections S2.2 and S2.3).



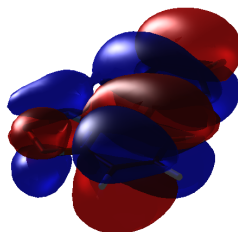
(a) Hole NTO of 1st excitation
(resembles $(\text{HOMO}-1)_0$, $\sigma_K^2 = 0.97$ (β))



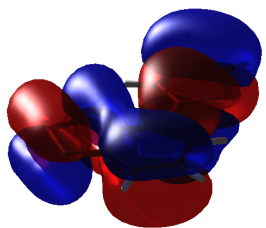
(b) Particle NTO of the 1st excitation
(resembles HOMO_0 , $\sigma_K^2 = 0.97$ (β))



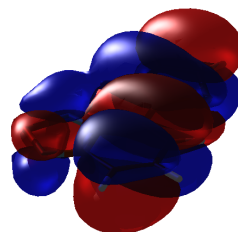
(c) Hole NTO of the 2nd excitation
(resembles $(\text{HOMO}-2)_0$, $\sigma_K^2 = 0.97$ (β))



(d) Particle NTO of the 2nd excitation
(resembles HOMO_0 , $\sigma_K^2 = 0.97$ (β))



(e) Hole NTO of the 3rd excitation
(resembles $(\text{HOMO}-3)_0$, $\sigma_K^2 = 0.90$ (β))



(f) Particle NTO of the 3rd excitation
(resembles HOMO_0 , $\sigma_K^2 = 0.90$ (β))

Figure 5: The dominating NTOs for the 3 lowest lying transitions in BT1T^+ at the minimum-energy structure of the neutral molecule calculated at the TDA/BHLYP/cc-pVDZ level of theory. The orbital of origin for the excited electron is denoted as hole, while the final orbital is denoted as particle. σ_K^2 indicates the weight of the NTO pair, while the spin of the NTO is given in parenthesis.

The four highest-energy occupied MOs of the cation, in each of the four different electronic states considered in the XAS calculations, are shown in columns 2 to 4 of Fig. 4. We only explicitly generate the states D_1 - D_3 when calculating the XAS. Therefore, the MOs of the cation are shown for the basis sets also employed in these calculations, i.e., the aug-cc-pVTZ basis on sulfur and cc-pVDZ on the rest. Note that the Unrestricted Hartree-Fock (UHF) MOs used in the CC calculations on the cation (Section S2.3) are in good agreement with the ones shown here. Furthermore, the MOs of D_0 clearly resemble those obtained at the BHHLYP/cc-pVDZ level of theory (see Section S2.1). We highlight the different energetic ordering of the MO orbitals of equivalent character in the neutral molecule and in each of the four states of the cation. For these cationic states, the orbital with the highest energy (the HOMO_{D_n}) is always the singly-occupied one, which corresponds to one of the four highest occupied MOs of the neutral molecule (the $(\text{HOMO-n})_0$). In short, the SOMO is in all cases HOMOD_n , which has the same character as $(\text{HOMO-n})_0$.

Based on the characters of the MOs obtained for D_0 (see Fig. 4), we note that generating, e.g., D_1 , corresponds to a hole in $(\text{HOMO-3})_{D_0}$. We inspected the weights of the different transitions contributing to the D_1 excitation and found that the main contribution to this excitation is indeed from the transition originating in $(\text{HOMO-3})_{D_0}$ and with final state in HOMO_{D_0} . We did, however, note from these weights that each state cannot be associated with only one transition (although one is found to dominate in each case). This might partly explain why the D_1 state is associated with a transition originating in the $(\text{HOMO-3})_{D_0}$. Despite the lower energy of the $(\text{HOMO-3})_{D_0}$ MO compared to $(\text{HOMO-1})_{D_0}$, the total energies of the D_n states increase as expected from D_0 to D_3 (see Table III). As previously mentioned, D_n is here generated by moving one electron from the MO with the character of $(\text{HOMO-n})_0$ to that with the character of HOMO_0 . Thus, our chosen naming convention of the states is also in line with the energetic ordering at the ground state optimized structure.

This reordering indicates that we cannot apply the simple picture of the MOs retaining a pre-determined ordering throughout the reaction, which is a requirement, e.g., when using Koopmans' theorem. Furthermore, it indicates that analyzing the process in terms of one electron moving stepwise down through the MOs might be too simple.

IV. CHARGE CALCULATIONS

In order to investigate the charge transfer reaction, we computed the CHELPG point charges of the cation in the ground state as well as in the three lowest lying excited states. We observe

Table I: CHELPG charges of the sulfur atoms of BT-1T⁺ in the ground state (D_0) and in the three lowest excited states (D_1 , D_2 and D_3), calculated at the BHHLYP/cc-pVDZ level of theory.

	S_{BT}	S_T
D_3	0.574118	0.040293
D_2	0.503436	0.015622
D_1	0.432363	0.412358
D_0	0.450336	0.023254

only small changes in the charge on the sulfur atom located in the benzothiadiazole unit (labelled S_{BT}) across the considered states. A large change is, however, observed on the sulfur atom in the thiophene unit (labelled S_T) in D_1 . We note that electron density is thus moved away from S_T in D_1 , as was also concluded by Khalili et al.¹⁸ One could, therefore, in principle observe the migration of electron density away from S_T by monitoring the deexcitation process from D_3 to D_1 . Another observable indication of the electron density migration might be the strength of the core transitions originating on the different sulfur atoms, since a high intensity is generally associated with high electron density on the atom on which the core transition originates. This will be further considered in Section VIC.

V. DYNAMICS SIMULATION

When performing the MCTDH calculation (as well as the TSH simulation), the PESs are calculated based on excited state energies of the cation. The starting point of the simulation is the D_3 excited state. The zero point energy of the calculation is set to the ground state energy of the neutral molecule at its equilibrium geometry, as this is the starting point of the corresponding experiment.

The normal modes that appear to be of interest in the TSH simulation are evaluated further in order to choose the modes to be included in the MCTDH calculation (see SI, Sections S3.1-S3.3).

A. Population analysis of TSH results

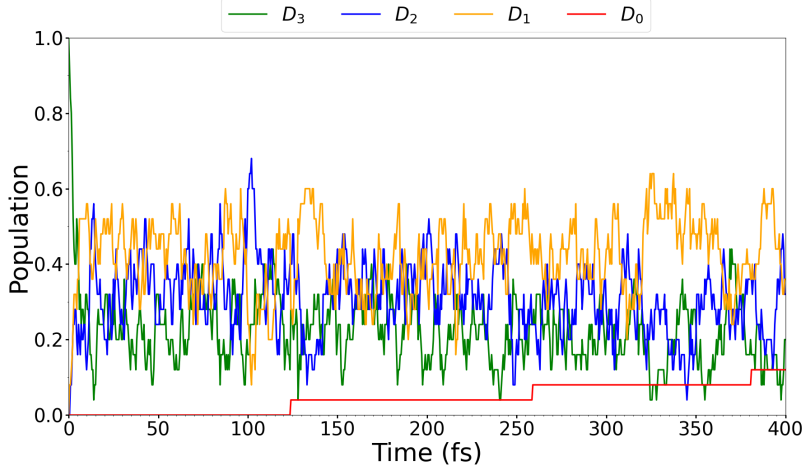
The evolution of populations in the TSH simulation is studied by considering the states based on energy ordering (i.e., adiabatic states), which is the natural choice for TSH simulations. It is also possible to consider the states based on oscillator strengths. The latter can be useful for excited states that are close in energy, but have oscillator strengths of different magnitudes. This is the case here (see Table II), however, the oscillator strengths are seen to change significantly during the reaction (cf. Tables S3, S20 and S21). Hence, it is difficult to define the states in terms of non-overlapping oscillator strength intervals. This approach has thus been deemed inappropriate for the system considered here. The populations based on energies are determined by the fraction of trajectories in each state at a given time. Moreover, to better compare the evolution of the populations determined here to the one determined using MCTDH, the populations are also transformed to a diabatic basis using auxiliary SHARC scripts. These rely on overlap matrices as well as wavefunction coefficients in the diabatic basis.

When simulating XAS later on, one must be careful to verify whether the first and second excited states do indeed correspond to a hole in (HOMO-1)₀ and (HOMO-2)₀, respectively. At the geometries associated with our investigated time delays, the NTOs for the three valence excitations appear unchanged compared to the NTOs at the initial geometry (see Figs. S3, S46 and S47). This indicates that we can associate the D_n state with a hole in (HOMO- n)₀ throughout.

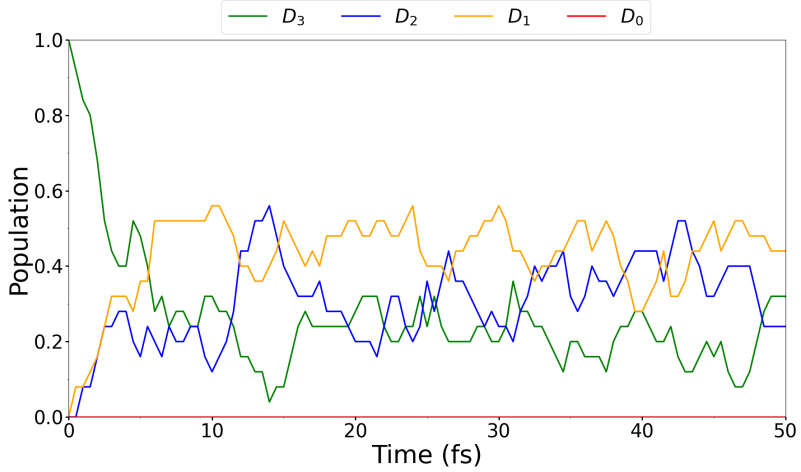
Table II: Excitation energies (eV) and oscillator strengths f_{osc} from D_0 to the excited states D_1 – D_3 calculated at the TDA/BHLYP/cc-pVDZ level of theory at the ground-state optimized structure of the neutral molecule.

Excited state	Excitation energy (eV)	f_{osc}
D_1	1.669	0.000631580
D_2	1.967	0.017129803
D_3	2.100	0.220979269

The TSH simulation gave rise to 3 trajectories jumping to the D_0 state. Plots of the evolution of the populations can be seen in Fig. 6. The diabaticized populations were also determined using an auxiliary SHARC script, and the results are shown in the plots in Fig. 7. The agreement between



(a) Evolution of populations in the full time range.

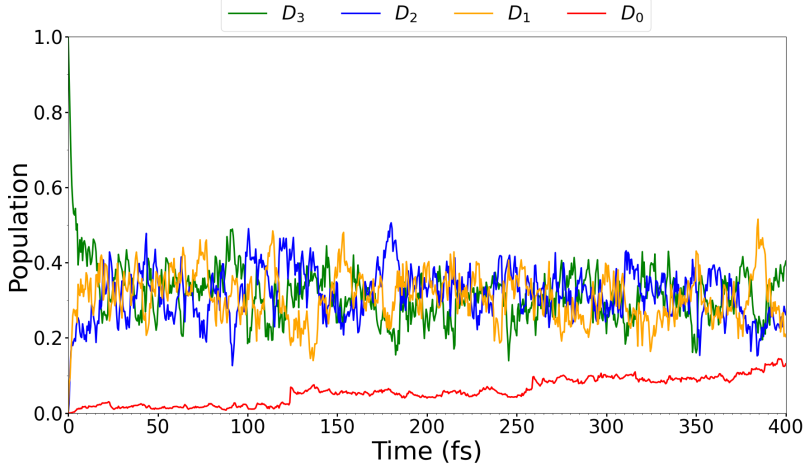


(b) Evolution of populations in the first 50 fs.

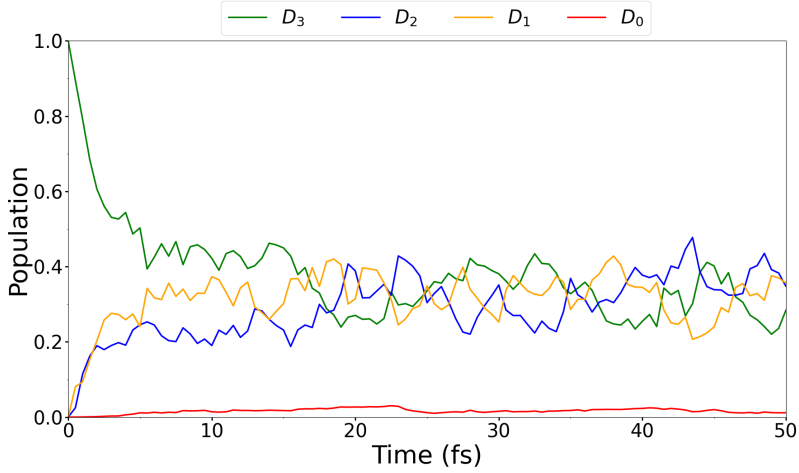
Figure 6: BT-T1⁺: Evolution of classical populations of D_0 , D_1 , D_2 and D_3 in TSH using SHARC dynamics based on energies plotted over the entire simulated time range (6a) and over the first 50 fs (6b). Populations are calculated based on an auxiliary SHARC script.

Figs. 6 and 7 is excellent, although Fig. 7 shows a smoother evolution of the populations compared to Fig. 6. This result indicates that, in this case, the diabatic and adiabatic pictures give rise to the same states, further justifying our choice of denoting the different states as D_n for an empty

(HOMO-n)₀ MO throughout.



(a) Evolution of populations in the full time range.



(b) Evolution of populations in the first 50 fs.

Figure 7: BT-1T⁺: Evolution of the populations of D_0 , D_1 , D_2 and D_3 in TSH using SHARC dynamics based on a transformation to the diabatic basis over the entire simulated time range (7a) and over the first 50 fs (7b). Populations are calculated based on an auxiliary SHARC script.

The TSH simulation shown here exhibits the same rapid decrease in the D_3 population and simultaneous increase in the populations of D_2 and D_1 as also shown by Khalili *et al.*¹⁸ We, however,

obtain a significantly lower yield of D_0 compared to the previous study. This discrepancy could be a result of the different levels of theory used. Furthermore, the wavefunction of the ionized species was determined by Khalili *et al.*¹⁸ based on Koopmans’ theorem,^{67,68} without including additional relaxation. The otherwise good agreement leads us to conclude that the normal modes of interest for the reaction at this level of theory can indeed be determined based on the presented TSH simulation. We also note that the evolution of the populations appears very similar in the two additional TSH simulations presented in the SI, Sections S3.2 and S3.3. In Section S3.2 photoionization is used to generate initial conditions, while in Section S3.3 the dynamics was carried out in the MCH representation for initial conditions generated based on photoexcitation of the cation. This indicates that the results presented are relatively robust with respect to small changes in the initial condition generation and the state representation, in which the dynamics is considered.

B. Determining the normal modes for an MCTDH simulation

When determining which normal modes to include in an MCTDH calculation based on a TSH simulation, many types of analyses can be made;⁶⁹ one can consider the activity of the modes as well as coherence and correlation. The linear vibronic coupling (LVC) parameters can also be investigated. Based on all these types of analyses (see SI Section S3.1), ten normal modes of interest were identified: modes 1, 2, 8, 16, 12, 33, 44, 46, 47 and 48 (labelled based on frequencies of increasing magnitude). These 10 modes were also found to be of importance in the two additional TSH simulations shown in Sections S3.2 and S3.3.

C. Analysis of the generated PES for normal modes of interest

The PESs of the ten chosen normal modes were determined using the VCHAM procedure. Here, the PESs were fitted as harmonic oscillators to best reproduce the adiabatic PESs obtained by quantum chemistry calculations. The fitting parameters for the vibronic coupling Hamiltonian considered^{53,54} can be found in the SI (Section S3.4).

The fitted PESs are shown in Fig. 8. It is observed that, while the fit for normal modes 8, 16, 46, 47 and 48 appear to be in excellent agreement with the calculated points, the fits for the remaining normal modes, however reasonable, show some discrepancy. For normal mode 1, the fit shows a large discrepancy beyond $|Q| = 5$, since the shape is not a parabola as assumed in the harmonic

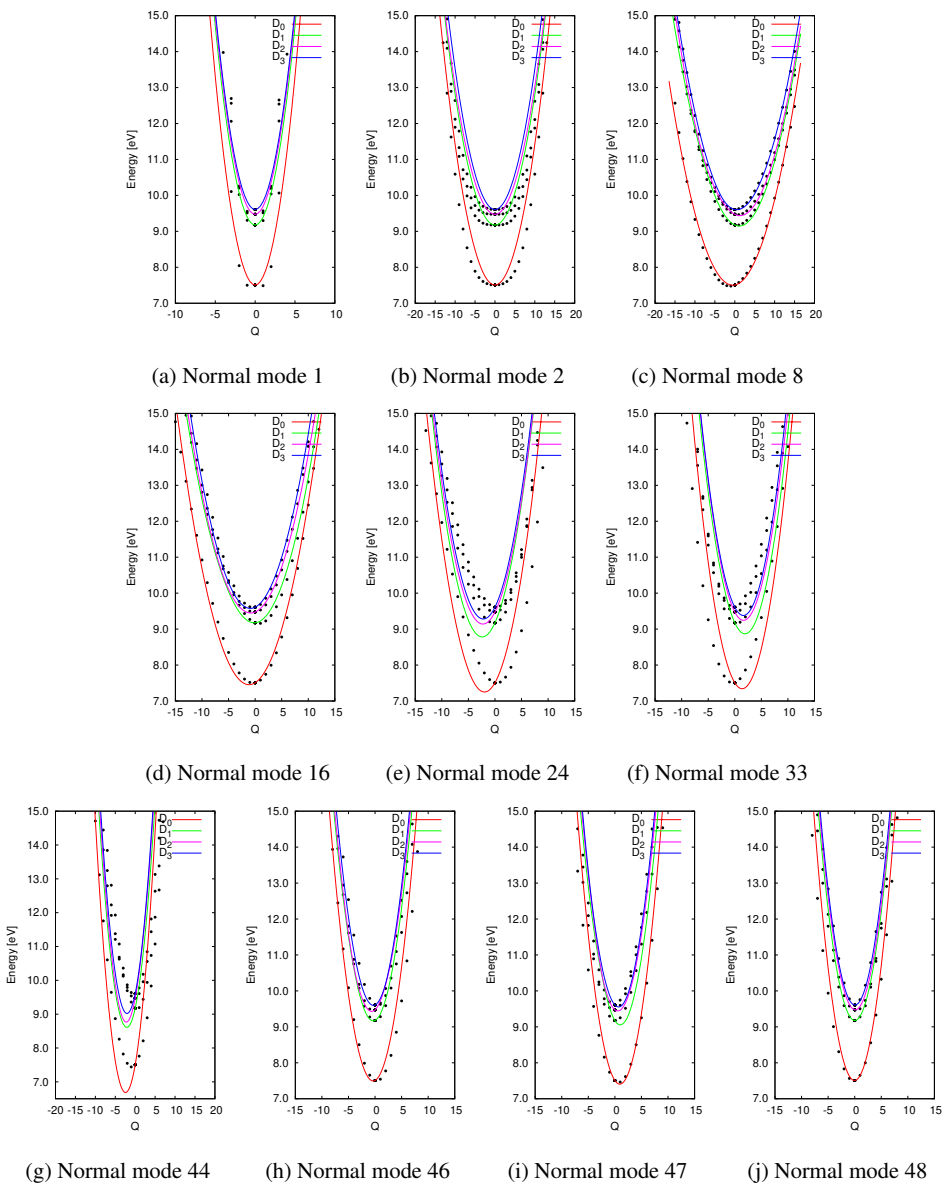


Figure 8: BT-1T⁺: Calculated points as well as fitted PESs along the 10 normal modes considered. Minimum energies do not occur at 0.0 eV as the minimum-energy point is taken as the neutral molecule minima.

oscillator approximation. From the TSH calculation, however, the displacements along normal mode 1 are found to be small ($|Q| < 0.8$), and thus the fit can nonetheless be utilized. The fit of the PES for normal mode 2 is also off between $|Q| = 5$ and $|Q| = 10$, since the predicted PES is narrower than the calculated points would indicate. Again, however, only small displacements were observed in the TSH simulation ($|Q| < 1.0$). If a better agreement at larger Q had been required, one might employ a different model for the fit, instead of the harmonic oscillator. For the last modes, 24, 33 and 44, the general shapes of the PESs are in good agreement with the calculated points, except for small shifts of the minima compared to the quantum chemistry calculations.

When determining which normal modes to include in the MCTDH calculation, we look for two types of modes. Firstly, we are interested in modes that appear to displace the molecule away from the equilibrium (tuning modes). Secondly, modes that potentially give rise to crossing of states (coupling modes) must be considered. Modes 1 and 2 both display a symmetric set of PESs with the minimum energy centered around a zero displacement. While mode 1 does show close-lying PESs for the four states, neither mode shows indication of PESs crossing for the different states until displacements larger than those found in the TSH simulations ($|Q| \geq 7$), and thus these modes are of less interest. Neither of the remaining modes is completely symmetric about their energy minima, although modes 46 and 48 appear almost symmetric. In addition, the minimum of the PESs occur slightly displaced from equilibrium. Thus, these might all be of interest. They all display close-lying states, however only modes 33, 44, 46 and 47 appear to display degeneracies between states at low Q . Investigating the selected modes in terms of their effect on the $S_{BT}-N$, S_T-C and C_2-C_3 bonds, as well as the $C_1-C_2-C_3$ and $C_2-C_3-C_4$ angles and the $C_1-C_2-C_3-S_T$ dihedral angle (see Fig. 1) shows that all modes affect at least one of these geometrical parameters (see Section S3.6). These parameters, also considered by Khalili *et al.*,¹⁸ were all found to be affected by the chosen set of modes. The characters of the modes were further investigated by visualization. It was found that they account for in plane stretches of the molecule as well as in plane movement of the thiophene- and benzothiadiazole-units towards each other (See SI, Section S3.7).

An MCTDH simulation was carried out including all eight modes of interest (8, 16, 24, 33, 44, 46, 47 and 48), where multimode single particle functions were used to combine modes 44 and 48, and modes 46 and 47. These modes can be combined, since they have similar vibrational frequencies. Moreover, their coupling parameters (see Section S3.4), determined by the VCHAM program, were observed to be larger than for other mode combinations. In Fig. 9 the evolution of

the populations over time can be seen for the MCTDH calculation.

D. MCTDH simulation population analysis

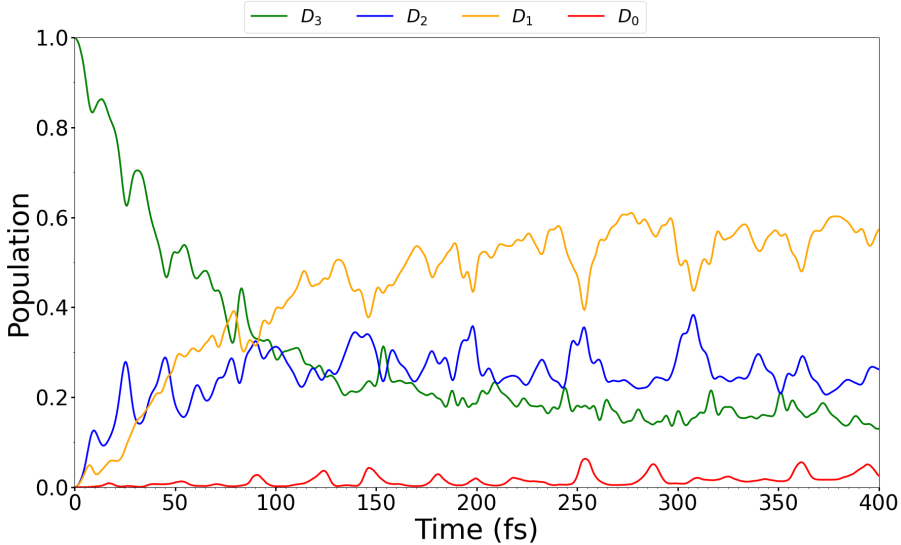


Figure 9: BT-1T⁺: Evolution of the populations of D_0 , D_1 , D_2 and D_3 from an MCTDH simulation with 8 normal modes included.

The MCTDH simulation shows the same general evolution of the populations as observed in the TSH simulation (Fig. 7). We do however note that the population in D_3 decreases much more slowly and that the evolution overall appears smoother. The latter is likely a result of the few simulated trajectories in the TSH calculation. The predicted half-life of the D_3 state in our quantum dynamics simulation is found to be approximately 41.6 fs based on an exponential fit (see Fig. 10). This is significantly longer than the approximately 5 fs obtained from the TSH simulation. However, the overall trends in the evolution of the populations with the initial drop in D_3 population and a rise in D_2 and D_1 is in good agreement with the TSH simulation. That the D_1 population then appears to become dominant is also observed in the TSH simulation. While the population in D_0 was also observed to be low in the TSH simulation done for this study, the D_0 population was found to increase to approximately 90% in 400 fs in the study by Khalili *et al.*¹⁸ This discrepancy must be attributed to differences in the simulation methods. We emphasize

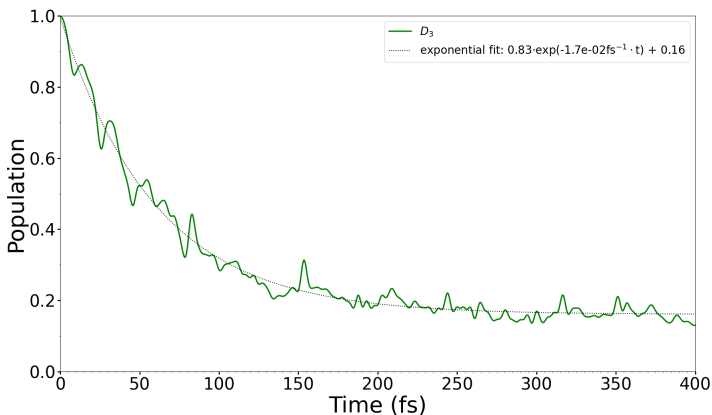


Figure 10: BT-1T⁺: Exponential fit to the population evolution of D_3 for determining the half-life of the state.

here the differences regarding the on-the-fly generation of the PES, which in their study was based on Koopmans' theorem. Furthermore, the choice of quantum chemistry method, and particularly lack of electron correlation in their calculations, might have affected the result. The evolution of the D_1 - D_3 states found by Khalili *et al.*¹⁸ appears however, to be well reproduced by the MCTDH calculation except for the half-life of D_3 . This was found to be 8 fs by Khalili *et al.*¹⁸ (in agreement with our TSH simulation). The longer lifetime of the D_3 state in the MCTDH calculation is attributed to the fact that quantum effects are included in the MCTDH simulation, which is not the case in TSH simulations. Such quantum effects could, e.g., be decoherence, which has been noted to affect excited state lifetimes.⁷⁰ Another reason is the fact that the MCTDH simulation is not full dimensional. Including additional degrees of freedom, and hence restricting the movement of the molecule less, would to some extent decrease the lifetime. To determine the effect of restricting the degrees of freedom, a TSH simulation was performed, where initial conditions were based solely on the normal modes also included in the MCTDH calculation. This did not give rise to any changes in the TSH simulation compared to the results presented here (see Section S3.5). Moreover, as the molecule is relatively rigid (See S1.2), the discrepancy is not mainly attributed more to the lack of decoherence in the TSH simulation, than to the reduced number of DOFs considered in the MCTDH calculation.

VI. XAS

A. Before photoionization

To simulate the XAS before the photoionization process, we calculated the spectrum for the neutral molecule at its equilibrium structure. Experimental XAS spectra have not been reported. The results are shown in Fig. 11. The numerical values of the excitation energies and oscillator strengths are tabulated in Tables S12 (BHHLYP) and S13 (CCSD). The transitions are characterized based on their dominant NTOs in Figs. S30 and S31/S32.

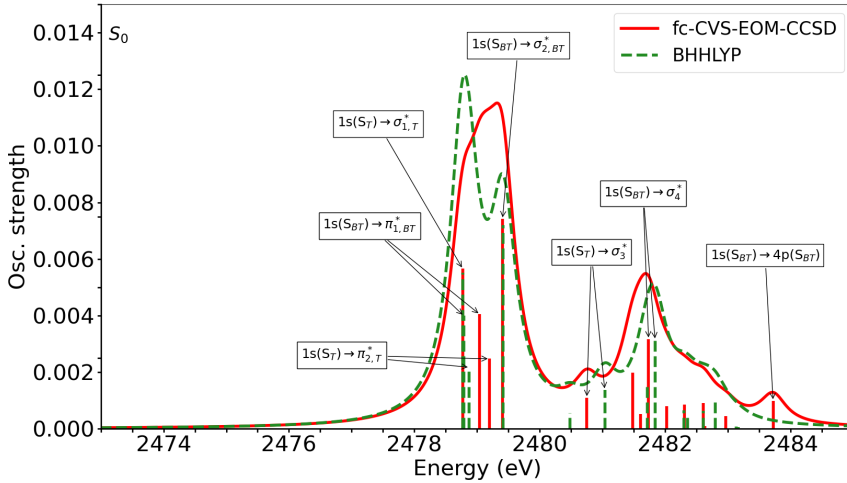


Figure 11: Neutral BT-1T: XAS at the equilibrium geometry of the ground state, calculated at the fc-CVS-EOM-CCSD (red) and TDDFT (green) levels of theory. The calculated transitions were broadened by a Lorentzian function with HWHM=0.25 eV. TDDFT results are shifted by 31.5 eV. Arrows show the main transitions and the labels indicate their character.

Relatively modest differences are observed between the XAS spectral profiles obtained at the fc-CVS-EOM-CCSD and BHHLYP levels of theory. There is, however, a large overall energy shift. Such large energy shifts are commonly observed for TDDFT,⁷¹ whereas fc-CVS-EOM-CCSD generally requires relatively small shifts to align with experiment.^{37,72} Thus, throughout, the TDDFT results have been shifted to align with the fc-CVS-EOM-CCSD results.

According to both electronic structure methods, four electric transitions are responsible for the main band around 2479 eV. The first three transitions almost overlap at the BHHLYP level, whereas the fourth is separated by roughly 0.5 eV. This yields the double peaked shape of the first spectral band in the simulated spectrum. The four transitions are more regularly separated from each other at the fc-CVS-EOM-CCSD level, thus giving rise to one single peak when broadened with the chosen half width at half maximum (HWHM).

The characters of the four transitions are similar for the two methods, according to the NTOs in Figs. S30 and S31/S32. The first transition is assigned as a core excitation from the S_T atom to an antibonding orbital. The electron density of this orbital is predominantly around the thiophene moiety. Furthermore, a noticeable contribution from an in-plane $3p$ orbital on the S_T atom is observed. We label this transition $S_T \rightarrow \sigma_{1,T}^*$. The second transition is $1s(S_{BT}) \rightarrow \pi_{1,BT}^*$, where the $\pi_{1,BT}^*$ orbital is clearly localized on the benzothiadiazole unit. An equivalent $1s(S_T) \rightarrow \pi_{2,T}^*$ transition, with $\pi_{2,T}^*$ mainly on the thiophene unit, is found as the third transition. The fourth transition is the S_{BT} equivalent of the first one, i.e. $1s(S_{BT}) \rightarrow \sigma_{2,BT}^*$, with noticeable contribution of an in-plane $3p$ orbital of S_{BT} . The fc-CVS-EOM-CCSD calculation furthermore predicts an additional low intensity signal at higher energy, which is not captured by BHHLYP within the given number of computed transitions.

The strongest transition of the main spectral band is the one from S_{BT} , but a transition of comparable intensity originating on S_T also contributes greatly to the signal. Hence, the signals from the two S atoms might be very difficult to distinguish, when only considering the ground state XAS.

B. Evaluating the effect of the electronic state

The XAS of the cation has been determined for the four states of interest, D_0 - D_3 , at the two considered levels of theory, see Fig. 12. As the computations are based on UHF and Kohn-Sham calculations, the results show spin contamination. The $\langle S^2 \rangle$ values can be found in Table III. Here, we note that spin contamination in both the BHHLYP and CCSD level calculations is modest. The NTOs of the main peaks can be seen in Section S4.2. It is noted that while the D_0 and D_3 states might be difficult to distinguish, due to the low intensity of the core-to-SOMO transitions, the D_1 and D_2 states are clearly distinguishable. While their core-to-SOMO transitions do fall in the same energy region, there is a difference not only in the intensity of the signals but also in the number

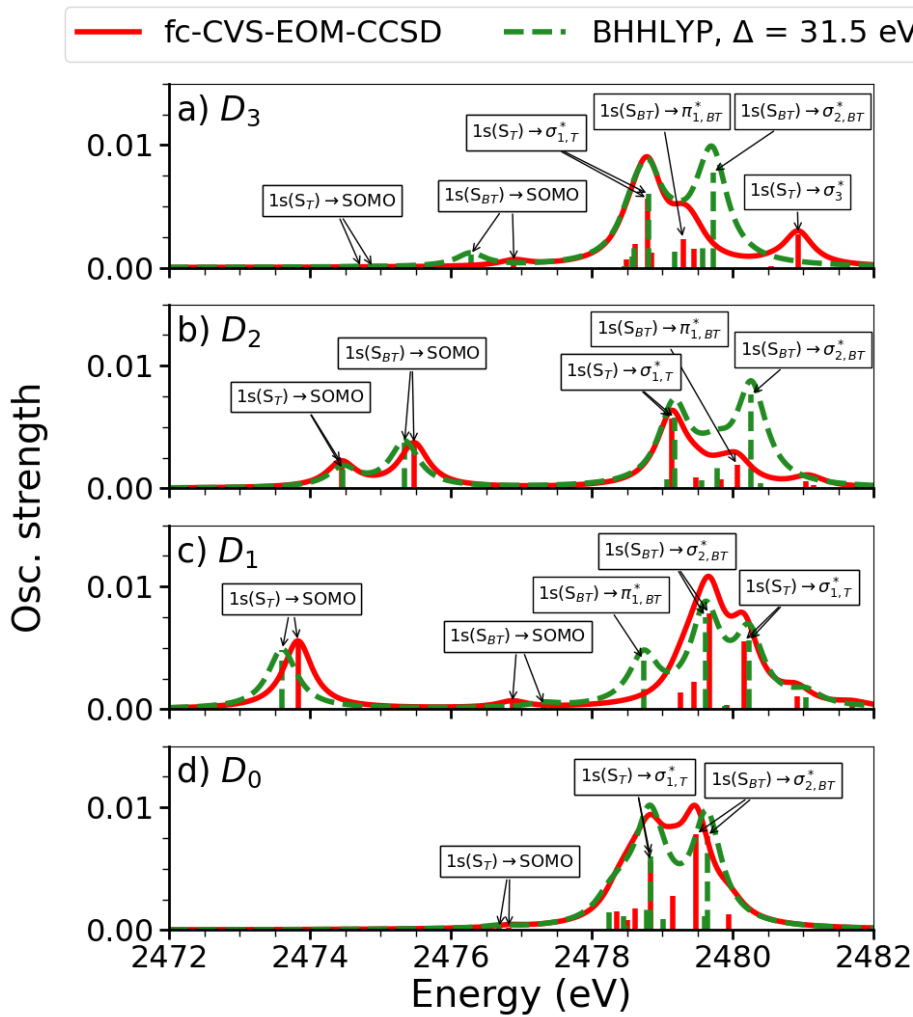


Figure 12: BT-1T⁺: XAS at the ground state equilibrium geometry of the neutral molecule. From top to bottom, spectra are shown for D_3 (a), D_2 (b), D_1 (c) and D_0 (d). In each state the XAS has been calculated at the IMOM-fc-CVS-EOM-CCSD (red) and IMOM-TDDFT (green) levels of theory. HWHM=0.25 eV. Arrows show the main transitions and labels indicate their character.

of signals visible.

In Fig. 12, the effect of the MOs reordering, observed in our approach for generating excited states,

can be seen. We note that the separation between the core-to-SOMO signals vary significantly for the different states. If relaxation of the orbitals is not considered following photoionization, one would expect this separation to remain constant, as the ordering (and relative energies) of the MOs would here be unchanged. Likewise, the separation between the main signal (transitions from core to virtual orbitals) and the core-to-SOMO transitions would in this case be expected to increase from D_1 to D_3 . We, however, observe the opposite trend, which underlines the changes observed in the MOs when they relax to the excited state. Our observations are thus a consequence of the calculation strategy utilizing IMOM to generate the excited states from the neutral ground state by choosing an MO associated with the desired character to be singly occupied. It should be noted that the computations of transitions from core orbitals to virtual orbitals are spin incomplete. This might affect the separation between the core-to-SOMO and main signal. An experiment might provide information on whether the shown trends provide a physical description or if an alternative approach for computing excited states is required. For now however, we content ourselves with the present calculations, noting that they are consistent with our observations of the MOs exchanging positions in the different states (see Fig. 4). While the energy shifts between the core-to-SOMO and core to virtual MOs might not be reliable, we expect the calculation to reflect reliably, which transitions are visible, since, the calculation reflects the character of the SOMOs and fully occupied MOs.

Note however that, in the D_1 -state of the ion, i.e. the hole in the orbital resembling $(\text{HOMO-1})_0$ (and, thus, the HOMO_{D_1} - see Fig. 4), the predicted NTOs differ between the methods. At the BHHLYP level of theory the first bright transition is found to be from S_T to an orbital resembling $(\text{HOMO-1})_0$, as expected. The remaining transitions fall in the same region as the D_0 signal, and involves many of the orbitals also observed for that signal. At the fc-CVS-EOM-CCSD level of theory the dominating NTO pair for the first transition appears to be from S_T to the $(\text{HOMO-2})_0$. Naturally, this orbital should be occupied, and indeed upon inspection of the weights of the transitions contributing to the excitation, the dominating transition is found to be from a core orbital into the MO resembling $(\text{HOMO-1})_0$. Many transitions do, however, contribute significantly to the core excitation and hence, to the NTO pair. The appearance of the NTO pair is therefore attributed to this fact. The computed spectrum is in good agreement with the TDDFT spectrum, which, as mentioned, shows the types of NTO pairs we expect. Moreover, a similar spectrum is obtained at the fc-CVS-EOM-CCSD level of theory by utilizing the orbitals of the cation (D_0) as the initial guess for the IMOM procedure. Here, the expected core to $(\text{HOMO-1})_0$ transition is predicted by

the NTOs for the first core transition (see Section S4.2.2). We therefore conclude that the spectral shape can be predicted by employing IMOM, but that the assignment of NTOs must be done with care. When the calculation methods yield the same results, however, it is considered possible to make character assignments. Furthermore, we find that one can use either the MOs of S_0 as the initial guess for the IMOM procedure or the MOs of D_0 and obtain similar results.

In the ground state of the ion, D_0 , as well as in the D_2 and D_3 states, the NTOs determined for the main transitions are similar in both the BHHLYP and fc-CVS-EOM-CCSD calculations (see Section S4.2). In D_0 , the two main transitions are found to originate on different sulfur atoms. As also observed for the neutral species, their separation is small, and thus only with a very good experimental resolution could these possibly be distinguished. For the D_2 state, we observe the first two bright transitions to be from S_T and S_{BT} respectively, into an orbital resembling the $(\text{HOMO}-2)_0$. Likewise, for D_3 , the first bright transition is found to be from S_T to an orbital resembling $(\text{HOMO}-3)_0$. This signal, however, has very low intensity and is therefore unlikely to be observable in the experiment. The remaining parts of the spectra resemble the D_0 spectrum as also expected.

Table III: Energies of the generated D_n states relative to that of S_0 for each calculation following the IMOM procedure. $\langle S^2 \rangle$ is also reported as a measure of spin contamination. A spin-complete doublet state has $\langle S^2 \rangle = 0.75$. The energies in parenthesis in the last column are the fc-EOM-IP-CCSD ionization energies obtained from neutral BT-1T (see also the SI, Table S5).

State	$\langle S^2 \rangle$		^a Relative energy/eV	
	IMOM-BHHLYP	IMOM-CCSD	IMOM-BHHLYP	IMOM-CCSD
D_3	0.7755	0.757315	9.499	9.776 (9.6183)
D_2	0.7956	0.761953	9.200	9.422 (9.3389)
D_1	0.8357	0.758355	8.846	9.042 (9.0532)
D_0	0.8158	0.789716	7.567	7.844 (7.8053)

^a Computed as the difference between the total energy of the cation and that of the neutral species.

C. Simulation of the XAS at different time delays

The XAS are simulated at three different time delays after photoionization: 0.0 fs, 50 fs and 150 fs. We recall that the NTOs for the three lowest lying valence transitions of the cation were

investigated at the geometries associated with these time delays (see Sections S2.2 and S4.3.1). They showed that, at these time delays, D_n does indeed correspond to a hole in $(\text{HOMO}-n)_0$. Furthermore, to ensure the generation of the correct states in the IMOM procedure, the MOs of the neutral molecule at the geometries associated with the non-zero time delays were determined. For both time delays they were found to retain the ordering seen for the ground state optimized geometry (see Section S4.3, Fig. S44).

The spectra are computed by weighting over the state populations of the MCTDH simulation. Furthermore, they are based on the (overly optimistic) assumption of 100% yield of the initial photoionization. The total spectra (Fig. 13A) are therefore not expected to completely match experiment, as the experimental signal will be a mix of the GS spectrum in Fig. 11 and the shown spectra. The difference signal (Fig. 13B) on the other hand will not be changed except for an overall scaling. Since it is the difference spectrum that is of main interest, this procedure is employed, as the expected yield of the photoionization is not known. The fc-CVS-EOM-CCSD calculations showed poor convergence in the IMOM procedure for displaced geometries. Thus, since we previously found that the XAS are equally well described at the BHHLYP level of theory at a lower computational cost, the tr-XAS is only calculated at this level of theory.

The spectra are evaluated based, not only on the structures determined in the MCTDH simulation, but also based on the ground state optimized structure. This is done in order to evaluate the effect of small structural changes on the XAS. The structures, based on the MCTDH simulation, are average structures, which is only a valid approximation as long as the wavepacket does not show significant density in two different areas. This was not the case for the three time delays considered here (see Section S3.9), but might yet be the case for other time delays. From the difference signal in Fig. 13B it is observed that a decrease in intensity over time occurs in the energy region associated with transitions originating on S_T . Here, a negative difference signal is observed to become more negative over time. An increase in intensity, on the other hand, is observed in the region associated with transitions originating on S_{BT} . Here, a positive difference signal that decrease from 0 fs to 50 fs, but increase slightly from 50 fs to 150 fs is seen. This suggests a decreased electron density around S_T and increased density around S_{BT} , as also noted in section IV. Thus, this study indicates that an electron density transfer from S_T to S_{BT} might indeed be observed in a tr-XAS experiment, confirming the conclusions of Khalili *et al.*¹⁸ In addition, increased intensity is observed in the region where the core-to-SOMO transitions occur, as expected based on an increased population in D_1 and D_2 , which both display bright core-to-SOMO

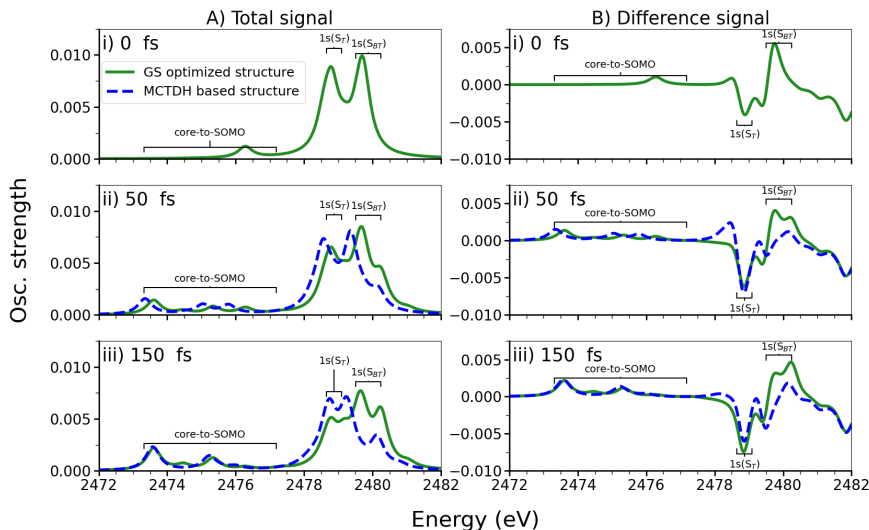


Figure 13: BT-1T⁺: Simulated total tr-XAS, calculated as the sum of the simulated tr-XAS for each state, weighted by their MCTDH-determined populations (left panels) and as difference signals (right panels). The spectra are shown for time delays of 0 fs (top), 50 fs (middle) and 150 fs (bottom). At the two non-zero time delays, the spectra are calculated based on the ground state optimized structure (green) and based on the structures determined by the MCTDH simulation (blue). All spectra were obtained at the BHHLYP level of theory employing the aug-cc-pVTZ basis on sulfur and the cc-pVDZ basis on the remaining atoms. A Lorentzian broadening has been applied with HWHM=0.25 eV. All results are shifted by 31.5 eV. The regions associated with the core-to-SOMO transitions and with transitions originating mainly on S_T and S_{BT} are marked.

transitions. Note also that, when computing the D_2 spectrum at geometries of the non-zero time delays, the intensity of the core-to-SOMO transition originating on S_T is observed to decrease. This observation corroborates the conclusion that a charge transfer occurs (see Section S4.3). The change, however, is not seen to affect the total or difference spectra significantly due to the overall low intensity of the core-to-SOMO transitions. In fact, as can be seen in Figs. 12 and 13, as well as Fig. S43, it appears that while structural changes might affect the spectra to some extent, the main changes, particularly when considering the difference spectra, are caused by changes in the electronic structure. Thus, for systems where only small structural changes can occur, one might

save computational resources by simply computing excited state XAS based on the ground state optimized geometry. It should be emphasized that a dynamics simulation is still required to determine the state populations and hence, the tr-XAS. One might therefore compute the excited state spectra only once per state, rather than at each investigated geometry. This approach however, will not be valid for spectroscopies that are strongly affected by structural changes. Likewise, for very floppy molecules, this approach needs further investigations. Finally, of course, these theoretical findings must be verified experimentally to ensure the validity of the approach also in practice.

VII. SUMMARY AND CONCLUSIONS

A computational study of the tr-XAS of the BT-1T⁺ cation has been presented. It was found that the relevant normal modes for simulating the nuclear dynamics can be identified based on a small set of surface hopping trajectories, as the investigated process to the best of our knowledge does not rely on rare events. A full quantum simulation of the dynamics in reduced space could subsequently be performed based on the determined normal modes. This simulation provided information, not only on the evolution of the molecular structure, but also on the evolution of the populations of relevant doublet states. Our calculation strategy for simulating XAS resulted in the excited state spectra displaying a trend in the separation between core-to-SOMO peaks and the main band that is counter-intuitive, if the orbitals are considered to be unchanged upon photoionization. The observations were, however, consistent with our observations of orbital changes after photoionization.

When simulating the XAS at different time delays, it was found that the relative populations of the involved states affected the difference signals more than small structural changes did. Thus, the total tr-XAS might be constructed from a single geometry, allowing for significant computational savings. A non-adiabatic nuclear dynamics simulation, however, cannot be avoided as the information it provides on the evolution of the state populations is paramount for the computation of the spectra. As the BT-1T⁺ cation investigated is rather rigid, the approach of considering only one geometry, might not be applicable for all molecules, and further investigations of this approach are needed.

Finally, the computed XAS at different time delays revealed increased intensity in energy regions associated with transitions originating on the S_{BT} moiety. At the same time decreased intensities in regions associated with transitions originating on S_T were found. The study thus indicates that

the electron transfer process from S_T to S_{BT} might indeed be probed using tr-XAS, confirming the results of a previous study by other authors at a lower level of theory.

VIII. SUPPLEMENTARY MATERIAL

Additional calculated MOs and NTOs can be found in the Supplementary Information. Here, the initial geometry of the system can also be found. The detailed normal mode analysis is likewise given in the SI, as well as all data tables for the plotted spectra.

Movies of the 8 normal modes considered in the MCTDH simulation are also available.

IX. DATA AVAILABILITY STATEMENT

Further data is available from the corresponding authors upon reasonable request.

ACKNOWLEDGMENTS

The research leading to the presented results has received funding from the Independent Research Fund Denmark, Grants No. 8021-00347B (KBM) and 7014-00258B (SC), and from the Hungarian National Research, Development and Innovation Fund, Grant No. NKFIH PD 134976 (MP). AKSP thanks the DTU Partnership PhD programme for funding. MP acknowledges support from the János Bolyai Scholarship of the Hungarian Academy of Sciences. The authors acknowledge the DTU computational resources,⁷³ on which all calculations were performed.

REFERENCES

- ¹J. Peet, J. Kim, N. Coates, W. L. Ma, D. Moses, A. J. Heeger, and G. C. Bazan, “Efficiency enhancement in low-bandgap polymer solar cells by processing with alkane dithiols,” *Nature Mater* **6**, 497–500 (2007).
- ²E. Bundgaard and F. C. Krebs, “Low band gap polymers for organic photovoltaics,” *Solar Energy Materials and Solar Cells* **91**, 954–985 (2007), low Band Gap Polymer Materials for Organic Solar Cells.
- ³E. Bundgaard, F. Livi, O. Hagemann, J. E. Carlé, M. Helgesen, I. M. Heckler, N. K. Zawacka, D. Angmo, T. T. Larsen-Olsen, G. A. dos Reis Benatto, B. Roth, M. V. Madsen,

- M. R. Andersson, M. Jørgensen, R. R. Søndergaard, and F. C. Krebs, “Matrix organization and merit factor evaluation as a method to address the challenge of finding a polymer material for roll coated polymer solar cells,” *Advanced Energy Materials* **5**, 1402186 (2015), <https://onlinelibrary.wiley.com/doi/pdf/10.1002/aenm.201402186>.
- ⁴G. Li, R. Zhu, and Y. Yang, “Polymer solar cells,” *Nat. Photonics* **6**, 153–161 (2012).
- ⁵A. C. Grimsdale, K. Leok Chan, R. E. Martin, P. G. Jokisz, and A. B. Holmes, “Synthesis of light-emitting conjugated polymers for applications in electroluminescent devices,” *Chemical Reviews* **109**, 897–1091 (2009), <https://doi.org/10.1021/cr000013v>.
- ⁶D. Raychev, O. Guskova, G. Seifert, and J.-U. Sommer, “Conformational and electronic properties of small benzothiadiazole-cored oligomers with aryl flanking units: Thiophene versus furan,” *Computational Materials Science* **126**, 287–298 (2017).
- ⁷A. Gambhir, P. Sandwell, and J. Nelson, “The future costs of opv – a bottom-up model of material and manufacturing costs with uncertainty analysis,” *Solar Energy Materials and Solar Cells* **156**, 49–58 (2016), life cycle, environmental, ecology and impact analysis of solar technology.
- ⁸F. Zhao, J. Zhou, D. He, C. Wang, and Y. Lin, “Low-cost materials for organic solar cells,” *J. Mater. Chem. C* **9**, 15395–15406 (2021).
- ⁹L. Meng, Y. Zhang, X. Wan, C. Li, X. Zhang, Y. Wang, X. Ke, Z. Xiao, L. Ding, R. Xia, H.-L. Yip, Y. Cao, and Y. Chen, “Organic and solution-processed tandem solar cells with 17.3% efficiency,” *Science* **361**, 1094–1098 (2018), <https://www.science.org/doi/pdf/10.1126/science.aat2612>.
- ¹⁰A. Gusain, R. M. Faria, and P. B. Miranda, “Polymer solar cells—interfacial processes related to performance issues,” *Front. Chem.* **7**, 61 (2019).
- ¹¹Q. Liu, Y. Jiang, K. Jin, J. Qin, J. Xu, W. Li, J. Xiong, J. Liu, Z. Xiao, K. Sun, S. Yang, X. Zhang, and L. Ding, “18% efficiency organic solar cells,” *Science Bulletin* **65**, 272–275 (2020).
- ¹²C. Li, J. Zhou, J. Song, J. Xu, H. Zhang, X. Zhang, J. Guo, L. Zhu, D. Wei, G. Han, J. Min, Y. Zhang, Z. Xie, Y. Yi, H. Yan, F. Gao, F. Liu, and Y. Sun, “Non-fullerene acceptors with branched side chains and improved molecular packing to exceed 18% efficiency in organic solar cells,” *Nat. Energy* **6**, 605–613 (2021).
- ¹³Z. Zheng, N. R. Tummala, Y.-T. Fu, V. Coropceanu, and J.-L. Brédas, “Charge-transfer states in organic solar cells: Understanding the impact of polarization, delocalization, and disorder,” *ACS Applied Materials & Interfaces* **9**, 18095–18102 (2017), <https://doi.org/10.1021/acsami.7b02193>.

- ¹⁴C. Dyer-Smith and J. Nelson, "Chapter id-2 - organic solar cells," in *Solar Cells (Second Edition)*, edited by A. McEvoy, L. Castañer, and T. Markvart (Elsevier, 2013) second edition ed., pp. 443–466.
- ¹⁵M. Scarongella, A. Laktionov, U. Rothlisberger, and N. Banerji, "Charge transfer relaxation in donor–acceptor type conjugated materials," *J. Mater. Chem. C* **1**, 2308–2319 (2013).
- ¹⁶A. Iagatti, B. Patrizi, A. Basagni, A. Marcelli, A. Alessi, S. Zanardi, R. Fusco, M. Salvalaggio, L. Bussotti, and P. Foggi, "Photophysical properties and excited state dynamics of 4,7-dithien-2-yl-2,1,3-benzothiadiazole," *Phys. Chem. Chem. Phys.* **19**, 13604–13613 (2017).
- ¹⁷K. Khalili, L. Inhester, C. Arnold, A. S. Gertsen, J. W. Andreasen, and R. Santra, "Simulation of time-resolved x-ray absorption spectroscopy of ultrafast dynamics in particle-hole-excited 4-(2-thienyl)-2,1,3-benzothiadiazole," *Structural Dynamics* **7**, 044101 (2020), <https://doi.org/10.1063/4.0000016>.
- ¹⁸K. Khalili, L. Inhester, C. Arnold, R. Welsch, J. W. Andreasen, and R. Santra, "Hole dynamics in a photovoltaic donor-acceptor couple revealed by simulated time-resolved x-ray absorption spectroscopy," *Structural Dynamics* **6**, 044102 (2019), <https://doi.org/10.1063/1.5097653>.
- ¹⁹K. P. Ghiggino, A. J. Tilley, B. Robotham, and J. M. White, "Excited state dynamics of organic semi-conducting materials," *Faraday Discuss.* **177**, 111–119 (2015).
- ²⁰K. H. Park, W. Kim, J. Yang, and D. Kim, "Excited-state structural relaxation and exciton delocalization dynamics in linear and cyclic π -conjugated oligothiophenes," *Chem. Soc. Rev.* **47**, 4279–4294 (2018).
- ²¹T. J. A. Wolf and M. Gühr, "Photochemical pathways in nucleobases measured with an X-ray FEL," *Philos. Trans. Royal Soc.* **377**, 20170473 (2019), <https://royalsocietypublishing.org/doi/pdf/10.1098/rsta.2017.0473>.
- ²²T. J. A. Wolf, R. H. Myhre, J. P. Cryan, S. Coriani, R. J. Squibb, A. Battistoni, N. Berrah, C. Bostedt, P. Bucksbaum, G. Coslovich, R. Feifel, K. J. Gaffney, J. Grilj, T. J. Martinez, S. Miyabe, S. P. Moeller, M. Mucke, A. Natan, R. Obaid, T. Osipov, O. Plekan, S. Wang, H. Koch, and M. Gühr, "Probing ultrafast $\pi\pi^*/n\pi^*$ internal conversion in organic chromophores via k-edge resonant absorption," *Nat. Commun.* **8** (2017), 10.1038/s41467-017-00069-7.
- ²³C. Bressler and M. Chergui, "Ultrafast x-ray absorption spectroscopy," *Chemical Reviews* **104**, 1781–1812 (2004), <https://doi.org/10.1021/cr0206667>.
- ²⁴N. Hartmann, W. Helml, A. Galler, M. R. M. R. Bionta, J. Grünert, S. L. Molodtsov, K. R. Fergusson, S. Schorb, M. L. Swiggers, S. Carron, C. Bostedt, J.-C. Castagna, J. Bozek, J. M. Glowina,

- D. J. Kane, A. R. Fry, W. E. White, C. P. Hauri, T. Feurer, and R. N. Coffee, “Sub-femtosecond precision measurement of relative x-ray arrival time for free-electron lasers,” *Nature Photon* **8**, 706–709 (2014).
- ²⁵G. Capano, C. J. Milne, M. Chergui, U. Rothlisberger, I. Tavernelli, and T. J. Penfold, “Probing wavepacket dynamics using ultrafast x-ray spectroscopy,” *Journal of Physics B: Atomic, Molecular and Optical Physics* **48**, 214001 (2015).
- ²⁶S. Canton, K. S. Kjær, G. Vankó, T. B. van Driel, S. Adachi, A. Bordage, C. Bressler, P. Chabera, M. Christensen, A. O. Dohn, A. Galler, W. Gawelda, D. Gosztola, K. Haldrup, T. Harlang, Y. Liu, K. B. Møller, Z. Németh, S. Nozawa, M. Pápai, T. Sato, T. Sato, K. Suarez-Alcantara, T. Togashi, K. Tono, J. Uhlig, D. A. Vithanage, K. Wärnmark, M. Yabashi, J. Zhang, V. Sundström, and M. M. Nielsen, “Visualizing the non-equilibrium dynamics of photoinduced intramolecular electron transfer with femtosecond x-ray pulses,” *Nat. Commun.* **6**, 6359 (2015).
- ²⁷W. Helml, I. Grguraš, P. N. Juranić, S. Düsterer, T. Mazza, A. R. Maier, N. Hartmann, M. Ilchen, G. Hartmann, L. Patthey, C. Callegari, J. T. Costello, M. Meyer, R. N. Coffee, A. L. Cavalieri, and R. Kienberger, “Ultrashort free-electron laser x-ray pulses,” *Applied Sciences* **7** (2017), 10.3390/app7090915.
- ²⁸P. M. Kraus, M. Zürch, S. K. Cushing, D. M. Neumark, and S. R. Leone, “The ultrafast x-ray spectroscopic revolution in chemical dynamics,” *Nat. Rev.* **2**, 82–94 (2018).
- ²⁹S. P. Neville, V. Averbukh, M. Ruberti, R. Yun, S. Patchkovskii, M. Chergui, A. Stolow, and M. S. Schuurman, “Excited state x-ray absorption spectroscopy: Probing both electronic and structural dynamics,” *The Journal of Chemical Physics* **145**, 144307 (2016), <https://doi.org/10.1063/1.4964369>.
- ³⁰S. Tsuru, M. L. Vidal, M. Pápai, A. I. Krylov, K. B. Møller, and S. Coriani, “An assessment of different electronic structure approaches for modeling time-resolved x-ray absorption spectroscopy,” *Structural Dynamics* **8**, 024101 (2021), <https://doi.org/10.1063/4.0000070>.
- ³¹D. Cremer, “Density functional theory: coverage of dynamic and non-dynamic electron correlation effects,” *Molecular Physics* **99**, 1899–1940 (2001), <https://doi.org/10.1080/00268970110083564>.
- ³²K. Burke, J. Werschnik, and E. K. U. Gross, “Time-dependent density functional theory: Past, present, and future,” *The Journal of Chemical Physics* **123**, 062206 (2005), <https://doi.org/10.1063/1.1904586>.

- ³³D. L. Wheeler, L. E. Rainwater, A. R. Green, and A. L. Tomlinson, "Modeling electrochromic poly-dioxythiophene-containing materials through tddft," *Phys. Chem. Chem. Phys.* **19**, 20251–20258 (2017).
- ³⁴W. Li, X. Cai, Y. Hu, Y. Ye, M. Luo, and J. Hu, "A tddft study of the low-lying excitation energies of polycyclic cinnolines and their carbocyclic analogues," *Journal of Molecular Structure: THEOCHEM* **732**, 21–32 (2005).
- ³⁵J. P. Perdew and K. Schmidt, "Jacob's ladder of density functional approximations for the exchange-correlation energy," *AIP Conference Proceedings* **577**, 1–20 (2001), <https://aip.scitation.org/doi/pdf/10.1063/1.1390175>.
- ³⁶J. P. Perdew, A. Ruzsinszky, J. Tao, V. N. Staroverov, G. E. Scuseria, and G. I. Csonka, "Prescription for the design and selection of density functional approximations: More constraint satisfaction with fewer fits," *The Journal of Chemical Physics* **123**, 062201 (2005), <https://doi.org/10.1063/1.1904565>.
- ³⁷M. L. Vidal, X. Feng, E. Epifanovsky, A. I. Krylov, and S. Coriani, "New and Efficient Equation-of-Motion Coupled-Cluster Framework for Core-Excited and Core-Ionized States," *J. Chem. Theory Comput.* **15**, 3117–3133 (2019).
- ³⁸R. J. Bartlett and M. Musiał, "Coupled-cluster theory in quantum chemistry," *Rev. Mod. Phys.* **79**, 291–352 (2007).
- ³⁹T. Helgaker, P. Jørgensen, and J. Olsen, *Molecular electronic-structure theory* (John Wiley & Sons, 2014).
- ⁴⁰R. Izsák, "Single-reference coupled cluster methods for computing excitation energies in large molecules: The efficiency and accuracy of approximations," *Wiley Interdiscip. Rev. Comput. Mol. Sci* **10**, e1445 (2020), <https://onlinelibrary.wiley.com/doi/pdf/10.1002/wcms.1445>.
- ⁴¹M. Richter, P. Marquetand, J. González-Vázquez, I. Sola, and L. González, "SHARC: ab initio molecular dynamics with surface hopping in the adiabatic representation including arbitrary couplings," *J. Chem. Theory Comput.* **7**, 1253–1258 (2011).
- ⁴²H.-D. Meyer, U. Manthe, and L. Cederbaum, "The multi-configurational time-dependent hartree approach," *Chemical Physics Letters* **165**, 73–78 (1990).
- ⁴³M. Beck, A. Jäckle, G. Worth, and H.-D. Meyer, "The multiconfiguration time-dependent hartree (mctdh) method: a highly efficient algorithm for propagating wavepackets," *Physics Reports* **324**, 1–105 (2000).

- ⁴⁴F. Neese, “The orca program system,” *WIREs Computational Molecular Science* **2**, 73–78 (2012), <https://wires.onlinelibrary.wiley.com/doi/pdf/10.1002/wcms.81>.
- ⁴⁵F. Neese, “Software update: The orca program system—version 5.0,” *WIREs Computational Molecular Science* **n/a**, e1606 (2022), <https://wires.onlinelibrary.wiley.com/doi/pdf/10.1002/wcms.1606>.
- ⁴⁶T. H. Dunning, “Gaussian basis sets for use in correlated molecular calculations. i. the atoms boron through neon and hydrogen,” *J. Chem. Phys.* **90**, 1007–1023 (1989).
- ⁴⁷D. E. Woon and T. H. Dunning, “Gaussian basis sets for use in correlated molecular calculations. iii. the atoms aluminum through argon,” *J. Chem. Phys.* **98**, 1358–1371 (1993).
- ⁴⁸A. K. Schnack-Petersen, M. Pápai, and K. B. Møller, “Azobenzene photoisomerization dynamics: Revealing the key degrees of freedom and the long timescale of the trans-to-cis process,” *Journal of Photochemistry and Photobiology A: Chemistry* **428**, 113869 (2022).
- ⁴⁹S. Mai, M. Richter, M. Heindl, M. F. S. J. Menger, A. Atkins, M. Ruckebauer, F. Plasser, L. M. Ibele, S. Kropf, M. Oppel, P. Marquetand, and L. González, “SharC2.1: Surface hopping including arbitrary couplings — program package for non-adiabatic dynamics,” sharc-md.org (2019).
- ⁵⁰S. Mai, P. Marquetand, and L. González, “Nonadiabatic dynamics: The sharC approach,” *WIREs Comput. Mol. Sci.* **8**, e1370 (2018).
- ⁵¹F. Neese, “Software update: the orca program system, version 4.0,” *WIREs Computational Molecular Science* **8**, e1327 (2018), <https://wires.onlinelibrary.wiley.com/doi/pdf/10.1002/wcms.1327>.
- ⁵²S. Mai, P. Marquetand, and L. González, “Non-adiabatic and intersystem crossing dynamics in so2. ii. the role of triplet states in the bound state dynamics studied by surface-hopping simulations,” *The Journal of Chemical Physics* **140**, 204302 (2014), <https://doi.org/10.1063/1.4875036>.
- ⁵³H. Köppel, W. Domcke, and L. S. Cederbaum, “Multimode molecular dynamics beyond the born-oppenheimer approximation,” in *Advances in Chemical Physics* (John Wiley & Sons, Ltd, 1984) pp. 59–246, <https://onlinelibrary.wiley.com/doi/pdf/10.1002/9780470142813.ch2>.
- ⁵⁴G. A. Worth, H.-D. Meyer, and L. S. Cederbaum, “Multidimensional dynamics involving a conical intersection: Wavepacket calculations using the MCTDH method,” in *Conical Intersections* (World Scientific, 2004) pp. 583–617, https://www.worldscientific.com/doi/pdf/10.1142/9789812565464_0014.
- ⁵⁵G. A. Worth, M. H. Beck, A. Jäckle, and H.-D. Meyer, “The mctdh package,” (2016).

- ⁵⁶G. Worth, C. Cattarius, and A. Markmann, "Vibronic Coupling Hamiltonian (VCHam) Program," (2004).
- ⁵⁷C. M. Breneman and K. B. Wiberg, "Determining atom-centered monopoles from molecular electrostatic potentials. the need for high sampling density in formamide conformational analysis," *Journal of Computational Chemistry* **11**, 361–373 (1990), <https://onlinelibrary.wiley.com/doi/pdf/10.1002/jcc.540110311>.
- ⁵⁸M. J. Frisch, G. W. Trucks, H. B. Schlegel, G. E. Scuseria, M. A. Robb, J. R. Cheeseman, G. Scalmani, V. Barone, G. A. Petersson, H. Nakatsuji, X. Li, M. Caricato, A. V. Marenich, J. Bloino, B. G. Janesko, R. Gomperts, B. Mennucci, H. P. Hratchian, J. V. Ortiz, A. F. Izmaylov, J. L. Sonnenberg, D. Williams-Young, F. Ding, F. Lipparini, F. Egidi, J. Goings, B. Peng, A. Petrone, T. Henderson, D. Ranasinghe, V. G. Zakrzewski, J. Gao, N. Rega, G. Zheng, W. Liang, M. Hada, M. Ehara, K. Toyota, R. Fukuda, J. Hasegawa, M. Ishida, T. Nakajima, Y. Honda, O. Kitao, H. Nakai, T. Vreven, K. Throssell, J. A. Montgomery, Jr., J. E. Peralta, F. Ogliaro, M. J. Bearpark, J. J. Heyd, E. N. Brothers, K. N. Kudin, V. N. Staroverov, T. A. Keith, R. Kobayashi, J. Normand, K. Raghavachari, A. P. Rendell, J. C. Burant, S. S. Iyengar, J. Tomasi, M. Cossi, J. M. Millam, M. Klene, C. Adamo, R. Cammi, J. W. Ochterski, R. L. Martin, K. Morokuma, O. Farkas, J. B. Foresman, and D. J. Fox, "Gaussian 16 Revision C.01," (2016), gaussian Inc. Wallingford CT.
- ⁵⁹M. Abedi, G. Levi, D. B. Zederkof, N. E. Henriksen, M. Pápai, and K. B. Møller, "Excited-state solvation structure of transition metal complexes from molecular dynamics simulations and assessment of partial atomic charge methods," *Phys. Chem. Chem. Phys.* **21**, 4082–4095 (2019).
- ⁶⁰Y. Shao, Z. Gan, E. Epifanovsky, A. T. Gilbert, M. Wormit, J. Kussmann, A. W. Lange, A. Behn, J. Deng, X. Feng, D. Ghosh, M. Goldey, P. R. Horn, L. D. Jacobson, I. Kaliman, R. Z. Khalullin, T. Kuś, A. Landau, J. Liu, E. I. Proynov, Y. M. Rhee, R. M. Richard, M. A. Rohrdanz, R. P. Steele, E. J. Sundstrom, H. L. W. III, P. M. Zimmerman, D. Zuev, B. Albrecht, E. Alguire, B. Austin, G. J. O. Beran, Y. A. Bernard, E. Berquist, K. Brandhorst, K. B. Bravaya, S. T. Brown, D. Casanova, C.-M. Chang, Y. Chen, S. H. Chien, K. D. Closser, D. L. Crittenden, M. Diedenhofen, R. A. D. Jr., H. Do, A. D. Dutoi, R. G. Edgar, S. Fatehi, L. Fusti-Molnar, A. Ghysels, A. Golubeva-Zadorozhnaya, J. Gomes, M. W. Hanson-Heine, P. H. Harbach, A. W. Hauser, E. G. Hohenstein, Z. C. Holden, T.-C. Jagau, H. Ji, B. Kaduk, K. Khistyayev, J. Kim, J. Kim, R. A. King, P. Klunzinger, D. Kosenkov, T. Kowalczyk, C. M. Krauter, K. U. Lao, A. D.

- Laurent, K. V. Lawler, S. V. Levchenko, C. Y. Lin, F. Liu, E. Livshits, R. C. Lochan, A. Luenser, P. Manohar, S. F. Manzer, S.-P. Mao, N. Mardirossian, A. V. Marenich, S. A. Maurer, N. J. Mayhall, E. Neuscamman, C. M. Oana, R. Olivares-Amaya, D. P. O'Neill, J. A. Parkhill, T. M. Perrine, R. Peverati, A. Prociuk, D. R. Rehn, E. Rosta, N. J. Russ, S. M. Sharada, S. Sharma, D. W. Small, A. Sodt, T. Stein, D. Stück, Y.-C. Su, A. J. Thom, T. Tsuchimochi, V. Vanovschi, L. Vogt, O. Vydrov, T. Wang, M. A. Watson, J. Wenzel, A. White, C. F. Williams, J. Yang, S. Yeganeh, S. R. Yost, Z.-Q. You, I. Y. Zhang, X. Zhang, Y. Zhao, B. R. Brooks, G. K. Chan, D. M. Chipman, C. J. Cramer, W. A. G. III, M. S. Gordon, W. J. Hehre, A. Klamt, H. F. S. III, M. W. Schmidt, C. D. Sherrill, D. G. Truhlar, A. Warshel, X. Xu, A. Aspuru-Guzik, R. Baer, A. T. Bell, N. A. Besley, J.-D. Chai, A. Dreuw, B. D. Dunietz, T. R. Furlani, S. R. Gwaltney, C.-P. Hsu, Y. Jung, J. Kong, D. S. Lambrecht, W. Liang, C. Ochsenfeld, V. A. Rassolov, L. V. Slipchenko, J. E. Subotnik, T. V. Voorhis, J. M. Herbert, A. I. Krylov, P. M. Gill, and M. Head-Gordon, "Advances in molecular quantum chemistry contained in the q-chem 4 program package," *Mol. Phys.* **113**, 184–215 (2015), <https://doi.org/10.1080/00268976.2014.952696>.
- ⁶¹A. T. B. Gilbert, N. A. Besley, and P. M. W. Gill, "Self-consistent field calculations of excited states using the maximum overlap method (mom)," *The Journal of Physical Chemistry A* **112**, 13164–13171 (2008), <https://doi.org/10.1021/jp801738f>.
- ⁶²G. M. J. Barca, A. T. B. Gilbert, and P. M. W. Gill, "Simple models for difficult electronic excitations," *Journal of Chemical Theory and Computation* **14**, 1501–1509 (2018), <https://doi.org/10.1021/acs.jctc.7b00994>.
- ⁶³A. R. Attar, A. Bhattacharjee, C. D. Pemmaraju, K. Schnorr, K. D. Closser, D. Prendergast, and S. R. Leone, "Femtosecond x-ray spectroscopy of an electrocyclic ring-opening reaction," *Science* **356**, 54–59 (2017).
- ⁶⁴A. Bhattacharjee, C. D. Pemmaraju, K. Schnorr, A. R. Attar, and S. R. Leone, "Ultrafast intersystem crossing in acetylacetone via femtosecond X-ray transient absorption at the carbon K-edge," *J. Am. Chem. Soc.* **139**, 16576–16583 (2017).
- ⁶⁵V. Scutelnic, S. Tsuru, M. Pápai, Z. Yang, M. Epshtein, T. Xue, E. Haugen, Y. Kobayashi, A. I. Krylov, K. B. Møller, S. Coriani, and S. R. Leone, "X-ray transient absorption reveals the $1au(n\pi^*)$ state of pyrazine in electronic relaxation," *Nature Communications* **12**, 5003 (2021).
- ⁶⁶G. Schaftenaar and J. Noordik, "Molden: a pre- and post-processing program for molecular and electronic structures," *J. Comput. Aided. Mol. Des.* **14**, 123–134 (2000).

- ⁶⁷R. K. Nesbet, “Electronic correlation in atoms and molecules,” in *Advances in Chemical Physics* (John Wiley & Sons, Ltd, 1965) pp. 321–363, <https://onlinelibrary.wiley.com/doi/pdf/10.1002/9780470143551.ch4>.
- ⁶⁸D. W. Smith and O. W. Day, “Extension of koopmans’ theorem. i. derivation,” *The Journal of Chemical Physics* **62**, 113–114 (1975), <https://aip.scitation.org/doi/pdf/10.1063/1.430253>.
- ⁶⁹S. Mai and L. González, “Identification of important normal modes in nonadiabatic dynamics simulations by coherence, correlation, and frequency analyses,” *The Journal of Chemical Physics* **151**, 244115 (2019), <https://doi.org/10.1063/1.5129335>.
- ⁷⁰E. Heller, J. Joswig, and G. Seifert, “Exploring the effects of quantum decoherence on the excited-state dynamics of molecular systems,” *Theor. Chem. Acc.* **140**, 42 (2021), <https://doi.org/10.1007/s00214-021-02741-0>.
- ⁷¹P. J. Lestrangle, P. D. Nguyen, and X. Li, “Calibration of Energy-Specific TDDFT for Modeling K-edge XAS Spectra of Light Elements,” *J. Chem. Theory Comput.* **11**, 2994–2999 (2015), <https://doi.org/10.1021/acs.jctc.5b00169>.
- ⁷²T. Fransson, I. E. Brumboiu, M. L. Vidal, P. Norman, S. Coriani, and A. Dreuw, “XA-BOOM: An X-ray Absorption Benchmark of Organic Molecules Based on Carbon, Nitrogen, and Oxygen 1s $\rightarrow \pi^*$ Transitions,” *J. Chem. Theory Comput.* **17**, 1618–1637 (2021), <https://doi.org/10.1021/acs.jctc.0c01082>.
- ⁷³DTU Computing Center, “DTU computing center resources,” (2021), <https://doi.org/10.48714/DTU.HPC.0001>.

E.2 Supplementary Information

A theoretical study of the time-resolved X-ray absorption spectrum of the photoionized BT-1T cation.

Supplementary Information.

Anna Kristina Schnack-Petersen,[†] Mátyás Pápai,^{†,‡} Sonia Coriani,^{*,†} and Klaus Braagaard Møller^{*,†}

[†]*Department of Chemistry, Technical University of Denmark, DK-2800 Kongens Lyngby, Denmark*

[‡]*Wigner Research Centre for Physics, P.O. Box 49, H-1525 Budapest, Hungary.*

E-mail: soco@kemi.dtu.dk; kbmo@kemi.dtu.dk

S1 Geometry

S1.1 Optimized structure

Table S1: BT-1T. BHHLYP/cc-pVDZ optimized geometry. Coordinates in Angstrom. Structure optimized on the S_0 PES.

Atom	X	Y	Z
C	0.726222	0.893873	0.075794
C	-0.718468	0.882613	0.054362
C	-1.439133	-0.343481	0.058380
C	-0.715413	-1.490397	0.083788
C	1.467062	-0.344360	0.102315
H	-1.221347	-2.448809	0.087292
H	-2.520729	-0.330222	0.041292
C	2.927810	-0.372735	0.123059
C	3.815553	0.667556	0.087176
C	5.174551	0.254322	0.117554
C	5.314514	-1.094021	0.177909
S	-0.026864	3.156744	0.038729
C	0.710290	-1.486259	0.105082
H	1.207447	-2.448903	0.122298
S	3.789931	-1.891001	0.198281
H	6.226553	-1.671727	0.212238
N	-1.256102	2.088460	0.03207
N	1.227541	2.115306	0.069113
H	3.495580	1.696603	0.040359
H	6.010636	0.941066	0.095221

S1.2 Geometrical change from energy-minimum on S_0 to S_1 at BHHLYP/cc-pVDZ level of theory

Only small changes are observed between the two optimized geometries as can be seen from Table S2, where the change in bond length is $< 4\%$ and the change in angles and dihedral angle is $< 0.5\%$.

Table S2: Change in bond lengths, bond angles and in dihedral angle from energy-minimum on S_0 to S_1 at BHHLYP/cc-pVDZ level of theory.

Bond length	$S_0/\text{\AA}$	$S_1/\text{\AA}$	Abs. change/ \AA
$R_{S_{BT}N_1}$	1.6291	1.6655	0.0364
$R_{S_{BT}N_2}$	1.6311	1.6839	0.0528
$R_{S_TC_3}$	1.7471	1.7650	0.0179
$R_{S_TC_5}$	1.7203	1.7088	0.0115
$R_{C_2C_3}$	2.4935	2.4873	0.0062
Average	-	-	0.025
Bond angle	$S_0/^\circ$	$S_1/^\circ$	Abs. change/ $^\circ$
$\theta_{C_1C_2C_3}$	122.0448	121.4455	0.5993
$\theta_{C_2C_3C_4}$	129.2795	128.7698	0.5097
Average	-	-	0.5545
Dihedral angle	$S_0/^\circ$	$S_1/^\circ$	Abs. change/ $^\circ$
$\phi_{C_1C_2C_3S_T}$	-179.8691	-179.9465	0.0774

S2 Orbitals of interest

S2.1 BHHLYP/cc-pVDZ(all atoms)

The MOs of interest for D_0 were also calculated at the BHHLYP/cc-pVDZ level of theory. They show the same characters of the MOs as seen when using the aug-cc-pVTZ basis on the S atoms and the cc-pVDZ basis on the remaining atoms at either the BHHLYP level of theory or the UHF level of theory (basis for the CC calculations). The MOs can be seen in Fig. S1.

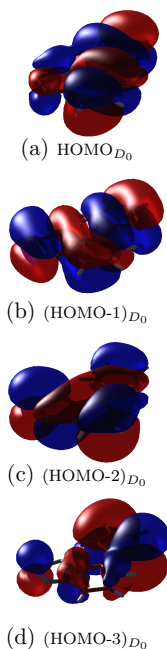


Figure S1: MOs of interest for the cation in D_0 computed at the BHHLYP/cc-pVDZ level of theory.

S2.2 BHHLYP/aug-cc-pVTZ(on S)/cc-pVDZ(remaining atoms)

The HOMO, HOMO-1, HOMO-2 and HOMO-3 have also been computed with the basis used for the XAS calculations. The cation in the ground state, D_0 , was obtained by removing a β -spin electron from the neutral species, leading to a spin contaminated state with $\langle S^2 \rangle = 0.8158$.

The obtained MOs for neutral BT-1T are in good agreement with those presented by Khalili *et al.*,^{1,2} as well as those obtained using the cc-pVDZ basis on all atoms shown in the main text.

The NTOs for the first three valence transitions (computed without TDA) are shown in Fig. S3. These NTOs are in good agreement with those shown in the main text.

The excitation energies and oscillator strengths of the valence transitions at this level of

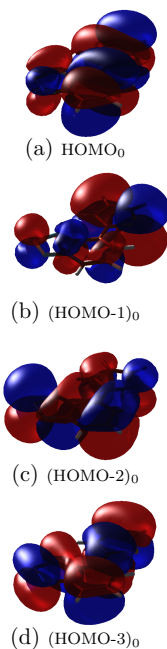


Figure S2: MOs of interest for the neutral molecule calculated at the BHHLYP level of theory with aug-cc-pVTZ basis on S and cc-pVDZ on the remaining atoms at the equilibrium geometry.

theory can be found in table S3. We observe the transitions to be rather close in energy

Table S3: Excitation energies from D_0 to the respective excited states calculated at the BHHLYP level of theory with aug-cc-pVTZ on S and cc-pVDZ on remaining atoms.

Excited state	Excitation energy (eV)	f_{osc}
D_1	1.5123	0.00018
D_2	1.8338	0.08247
D_3	1.8790	0.11920

as also seen in the calculation presented in the main text. The relative energy gaps are furthermore observed to be in reasonably good agreement with the calculated excitation energies using the cc-pVDZ basis on all atoms.

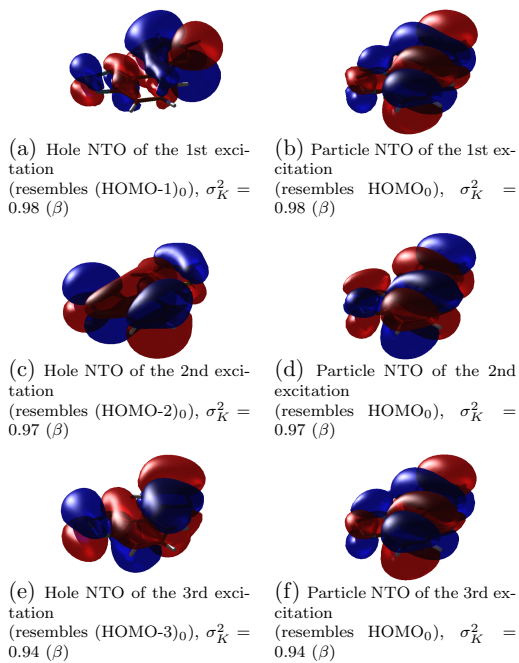


Figure S3: The dominating NTOs for the 3 lowest lying transitions in BT-1T⁺ at the minimum-energy structure of the neutral molecule calculated at the BHHLYP/cc-pVDZ level of theory. The NTOs have been calculated at the BHHLYP level of theory with aug-cc-pVTZ on S and cc-pVDZ on the remaining atoms.

S2.3 EOM-CCSD/aug-cc-pVTZ(S)/cc-pVDZ(remaining atoms)

The MOs determined at the RHF level of theory for neutral BT-1T are shown in Fig. S4. The CC calculations use these RHF orbitals. The RHF MOs are in good agreement with

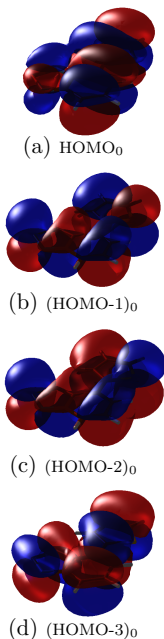


Figure S4: MOs of interest for the neutral molecule calculated at the RHF level of theory with aug-cc-pVTZ basis on S and cc-pVDZ on remaining atoms.

those presented at the BHHLYP level of theory. The CC calculations on the BT-1T⁺ cation, on the other hand, use UHF MOs.

The NTOs for the first three valence transitions of D_0 can be seen in Fig. S5. Observe that in this calculations removal of an electron from the HOMO resulted in a spin contaminated state with $\langle S^2 \rangle = 0.7897$. The NTOs computed at the EOM-CCSD level of theory using the aug-cc-pVTZ basis on S and cc-pVDZ on remaining atoms are again observed to closely resemble those computed at the BHHLYP level of theory.

The excitation energies and oscillator strengths of the valence transitions at this level

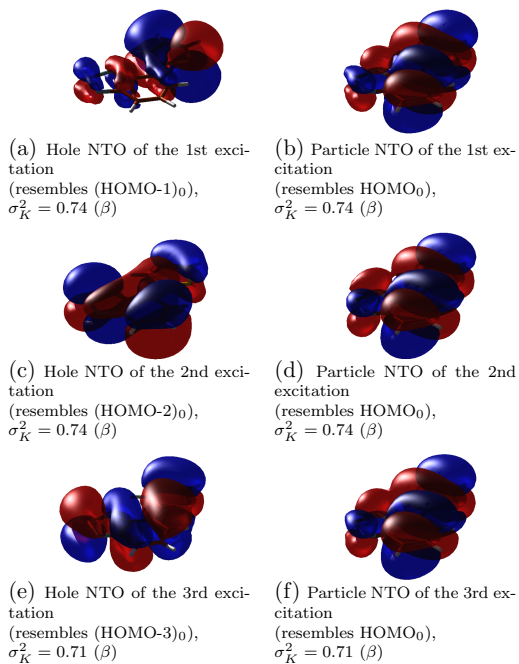


Figure S5: The dominating NTOs for the 3 lowest lying transitions in BT-1T⁺ at the minimum-energy structure of the neutral molecule calculated at the BHHLYP/cc-pVDZ level of theory. The transitions are calculated at the EOM-CCSD level of theory with aug-cc-pVTZ on S and cc-pVDZ on the remaining atoms.

of theory can be found in table S4. We observe the same trends as in the TDDFT-based

Table S4: The three lowest lying excitation energies from D_0 computed at the EOM-CCSD level of theory using the aug-cc-pVTZ basis on S and cc-pVDZ on the remaining atoms.

Excited state	Excitation energy (eV)	f_{osc}
D_1	1.5237	0.000610
D_2	1.9521	0.112195
D_3	2.0205	0.115380

calculations.

The MOs of the cation in its different states are seen in Fig. S6.

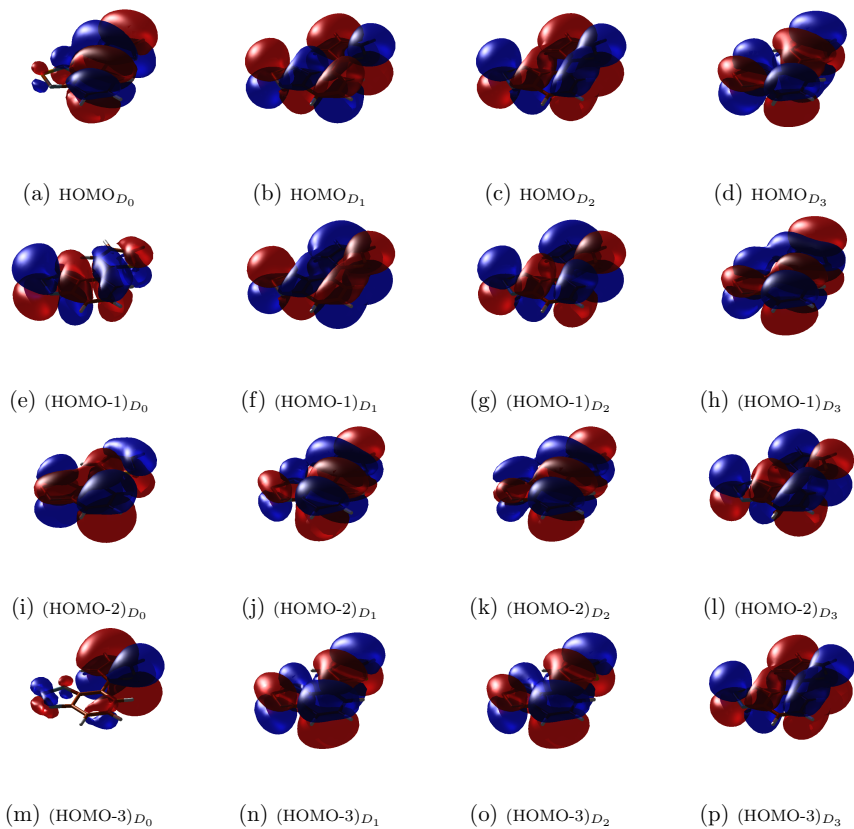


Figure S6: The MOs of interest for D_0 (left) as well as the generated D_1 (left middle), D_2 (right middle) and D_3 (right) excited states calculated at the UHF level of theory (on which the fc-CVS-EOM-CCSD calculations are based) with the aug-cc-pVTZ basis on S and cc-pVDZ on the remaining atoms. The orbitals shown are β -spin orbitals.

S2.3.1 Ionization potentials

Table S5: Ionization energies from S_0 calculated at the fc-(CVS-)EOM-IP-CCSD level of theory using the aug-cc-pVTZ basis on S and cc-pVDZ on the remaining atoms.

Ionization origin	Ionization energy (eV)
HOMO ₀	7.8053
(HOMO-1) ₀	9.0532
(HOMO-2) ₀	9.3389
(HOMO-3) ₀	9.6183
1s(S_T)	2483.7820
1s(S_{BT})	2485.6332

S3 Dynamics

S3.1 SHARC Dynamics Surface Hopping simulation for initial conditions based on a photoexcited cation

The TSH simulation for initial conditions based on photoexcitation of the ion has been carried using the diagonal representation known as SHARC dynamics (see main text). The subsequent normal mode analysis is shown here.

S3.1.1 Activity analysis

When determining which normal modes to include in an MCTDH calculation based on a TSH simulation one could simply consider the activity of each normal mode. This is measured as the standard deviation of Q for each mode based on all trajectories. This measure, however, will include random motion, which can become large. Alternatively, one can consider the average activity, i.e. the standard deviation with respect to an average trajectory, which filters out random motion. In our case, many jumps occur in all trajectories, and thus we consider both the activity for the first 5 fs (before most trajectories jump) and for the full time range.

When we consider simply the activity of the normal modes in either time interval (Figs. S7a and S7b), mode 3 appears to be more active for the first 5 fs, while mode 1 might be

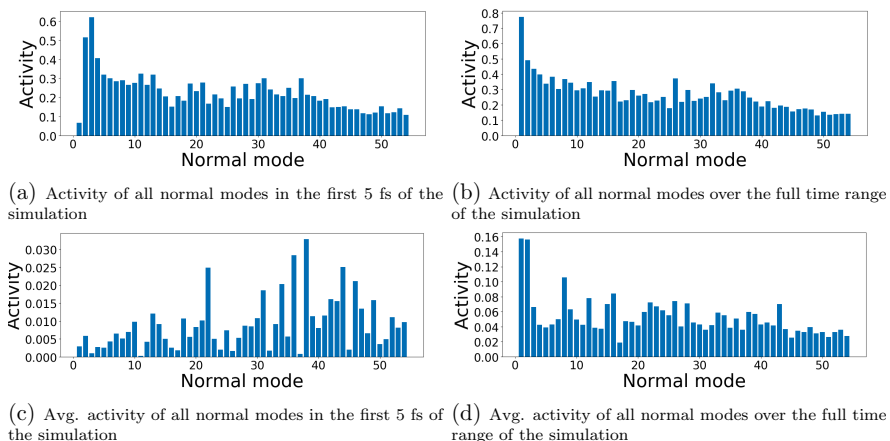


Figure S7: Visualization of activity analysis of the TSH simulation with SHARC dynamics.

more active over the entire time range, however all normal modes show similar activity and thus it is difficult to single out any mode. If we instead consider the average activity, where noise should be filtered out, we note that the overall activity is much lower. Also, similar activities are generally observed for all modes. For the entire time range modes 1 and 2 appear to stand out, as more active and could thus be considered.

S3.1.2 Coherence analysis of TSH results

Mai and González suggested that a coherence analysis was another way of determining the normal modes of importance from a TSH simulation.³ Here, one determines the standard deviation of the average trajectory divided by the standard deviation of all trajectories. This gives an indication of which modes are most active in all trajectories. As noise is filtered out, the importance of each mode in the different trajectories can be considered. Again, we consider the coherence for the first 5 fs and for the full time range.

The result of the analysis is shown in Fig. S8. It is observed that the coherence of all normal modes are rather similar, when considering the full time range. Hence, it is difficult to identify important normal modes based on this. A few normal modes can, however, be

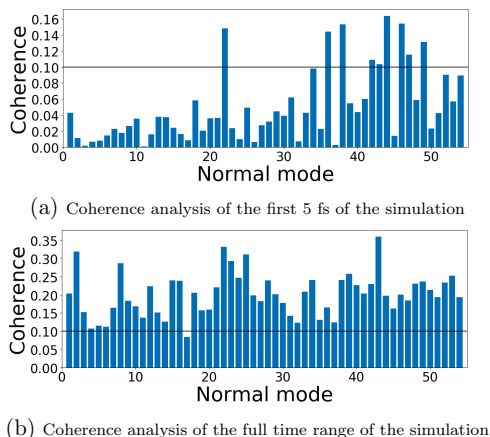


Figure S8: Visualization of coherence analysis of the TSH simulation with SHARC dynamics. The horizontal black line at 0.1 is chosen as in Mai and González.³

singled out for the analysis of the first 5 fs, although the overall coherence is much lower. These modes are modes 22, 36, 38, 44, 46, 47 and 49. Due to the overall similar coherence of the modes, we do not choose to single out modes for further analysis based on the coherence analysis alone. The difficulty in identifying normal modes based on the coherence could be related to the rigidity of the molecule or indeed the limited number of trajectories simulated.

S3.1.3 Correlation analysis of TSH results

Another suggested way of determining relevant normal modes for an MCTDH simulation based on TSH results, is a correlation analysis.³ Here, the correlation between a change in the Q of each normal mode and the energy difference between the active state and the other states have been evaluated.

The results can be found in table S6 and Fig. S9. Here, normal modes 8, 16, 24, 33, 44 and 47 are all found to show a relatively large correlation for for the energy gap to all states, and thus, these might be of interest when performing the MCTDH simulation. It is noted that modes 44 and 47 also appeared to show a large coherence within the first 5 fs of the simulation compared to other modes, and they are therefore doubly interesting to investigate.

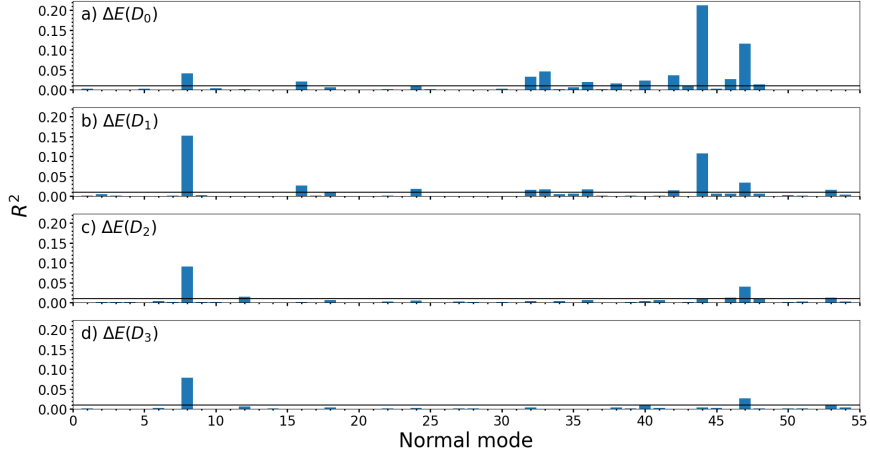


Figure S9: Visualization of the correlation analysis of SHARC dynamics TSH over the entire simulated time range. The correlation is measured as the Pearson correlation coefficient for a linear fit of the energy gap between the active state and the D_0 , D_1 , D_2 or D_3 state and Q for each normal mode. The horizontal black line shows a correlation coefficient of 0.01, which was also used in the study by Mai and González.³

Table S6: Result of correlation analysis of TSH trajectories based on the photoexcited cation over the entire simulated time range. The Pearson correlation coefficient is reported for the correlation of the energy gap of the active state to the D_0 , D_1 , D_2 and D_3 states and Q for each normal mode.

Normal mode	$R^2_{\Delta E(D_0)}$	$R^2_{\Delta E(D_1)}$	$R^2_{\Delta E(D_2)}$	$R^2_{\Delta E(D_3)}$
1	0.0022	0.001	0.0002	0.0009
2	0.0002	0.0049	0.0012	0.0005
3	0.0001	0.0011	0.0011	0.0000
4	0.0000	0.0005	0.0013	0.0000
5	0.0023	0.0001	0.0000	0.0007
6	0.0004	0.0008	0.0043	0.0026
7	0.0009	0.0010	0.0010	0.0003
8	0.0412	0.1519	0.0902	0.0787
9	0.0009	0.0027	0.0013	0.0001
10	0.0044	0.0002	0.0013	0.0005
11	0.0003	0.0004	0.0003	0.0007
12	0.0012	0.0000	0.0146	0.0067
13	0.0000	0.0005	0.0003	0.0005
14	0.0007	0.0008	0.0005	0.0012
15	0.0001	0.0002	0.0000	0.0006
16	0.0208	0.0273	0.0010	0.0001

Table S6 – continued from previous page

Normal mode	$R^2_{\Delta E(D_0)}$	$R^2_{\Delta E(D_1)}$	$R^2_{\Delta E(D_2)}$	$R^2_{\Delta E(D_3)}$
17	0.0006	0.0020	0.0004	0.0000
18	0.0060	0.0097	0.0067	0.0035
19	0.0000	0.0006	0.0005	0.0005
20	0.0001	0.0003	0.0003	0.0005
21	0.0002	0.0000	0.0001	0.0000
22	0.0011	0.0017	0.0023	0.0016
23	0.0004	0.0000	0.0000	0.0001
24	0.0100	0.0184	0.0051	0.0025
25	0.0018	0.0001	0.0004	0.0006
26	0.0002	0.0001	0.0002	0.0000
27	0.0000	0.0000	0.0023	0.0019
28	0.0007	0.0006	0.0012	0.0009
29	0.0004	0.0001	0.0003	0.0000
30	0.0028	0.0001	0.0018	0.0006
31	0.0007	0.0000	0.0003	0.0005
32	0.0326	0.0155	0.0037	0.0044
33	0.0463	0.0169	0.0003	0.0005
34	0.0015	0.0054	0.0042	0.0004
35	0.0066	0.0062	0.0002	0.0008
36	0.0199	0.0174	0.0066	0.0001
37	0.0012	0.0014	0.0000	0.0002
38	0.0166	0.0006	0.0008	0.0033
39	0.0002	0.0010	0.0015	0.0012
40	0.0238	0.0000	0.0036	0.0091
41	0.0001	0.0012	0.0059	0.0029
42	0.0365	0.0149	0.0008	0.0001
43	0.0085	0.0008	0.0017	0.0000
44	0.2121	0.108 0	0.0114	0.0039
45	0.0026	0.0065	0.0000	0.0031
46	0.0270	0.0064	0.0121	0.0000
47	0.1156	0.0345	0.0397	0.0264
48	0.0137	0.0062	0.0094	0.0016
49	0.0000	0.0004	0.0002	0.0002
50	0.0000	0.0026	0.0019	0.0012
51	0.0002	0.0021	0.0029	0.0019
52	0.0001	0.0003	0.0003	0.0000
53	0.0001	0.0154	0.0124	0.0084
54	0.0002	0.0036	0.0023	0.004

S3.1.4 LVC SHARC analysis

It is also possible to calculate the linear vibronic couplings (LVCs) using the initially generated normal mode file (for the neutral molecule), two single point calculations of the cation for each normal mode and auxiliary SHARC scripts.

Based on such an LVC calculation the largest coupling terms between states (λ) were determined (see table S7). Observe that normal mode 1 was not considered by the script due to its very low frequency (6.91 cm^{-1}). We observe that mode 48 appears to couple the initially

Table S7: LVC interstate parameters larger than 0.27 eV for BT-1T⁺.

Normal mode	$\lambda^{(n,m)}/\text{eV}$	state n	state m
46	0.3383928	D_1	D_2
48	0.5572623	D_1	D_2
15	0.2748705	D_1	D_3
22	0.3287164	D_1	D_3
36	0.3719281	D_1	D_3
38	-0.3035377	D_1	D_3
40	-0.3658736	D_1	D_3
46	-0.3705077	D_1	D_3
48	-0.8522828	D_1	D_3
48	-0.5527914	D_2	D_3

excited D_3 state to both D_2 and D_1 . In addition, it gives the strongest coupling between the two states compared to the other modes. Furthermore, mode 46 appears to couple the D_1 state to both the D_2 and the D_3 state. The LVC interstate parameters coupling D_0 to the other states are an order of magnitude smaller than for D_1 - D_3 . The largest ones are however found for modes 20 and 46 (both approximately 0.11 eV) for states D_0 and D_1 , mode 47 (approximately 0.11 eV) for states D_0 and D_1 and mode 48 (approximately -0.08 eV) for states D_0 and D_1 . Normal modes 46 and 48 might therefore also be considered.

S3.2 SHARC Dynamics Surface hopping simulation for initial conditions based on photoionization

A TSH simulation was also carried out for initial conditions based on photoionization of the neutral molecule. Again, SHARC dynamics (the diagonal representation) was employed.

S3.2.1 Population analysis

Here, the evolution of the populations of the TSH simulation starting from initial conditions based on photoionization is shown in Fig. S10. From these initial conditions, none of the

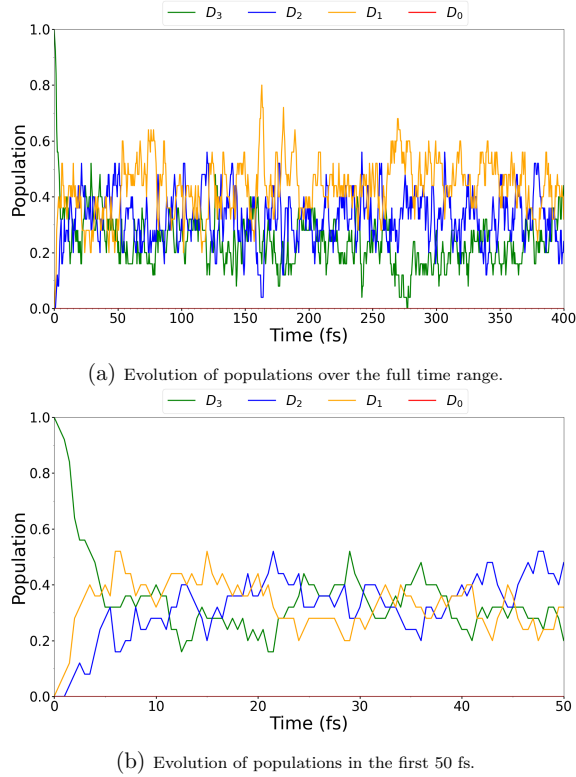


Figure S10: Evolution of classical populations for the ion in TSH starting from initial conditions based on photoionization. The reported populations of states are based on energies.

25 trajectories were found to jump to D_0 within the simulation time. It is observed that the evolution of the populations appear very similar to that found in the main text for the photoexcited cation. The main difference is the yield of population that goes to D_0 , however this small change might be a result of the very limited number of trajectories simulated.

S3.2.2 Activity analysis

As for the TSH simulation for initial states based on photoexcitation, an activity analysis has been carried out and the result can be seen in Fig. S11. As was the case for the population

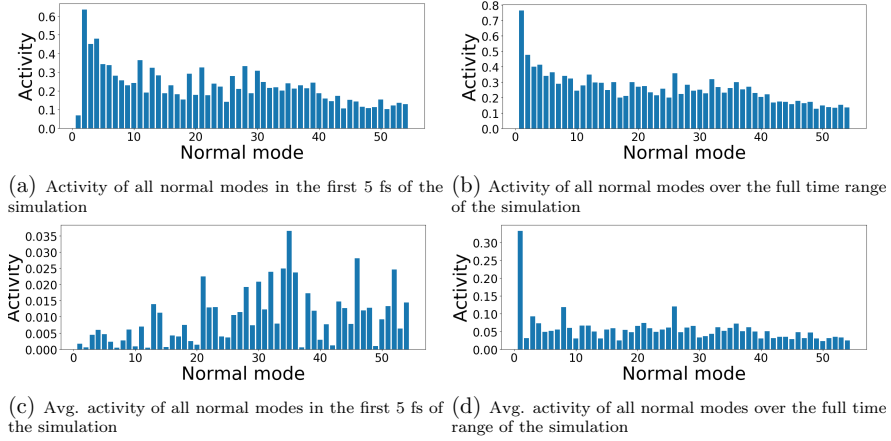


Figure S11: Visualization of activity analysis of the TSH simulation utilizing initial conditions based on photoionization.

analysis, the activities of normal modes appears very similar between the TSH simulations.

When we consider simply the activity of the normal modes in either time interval (Figs. S11a and S11b), we observe mode 2 rather than mode 3 appears to be more active than the other modes for the first 5 fs. Again, mode 1 might be more active over the entire time range. Once more, all normal modes show similar activity, and if the average activity is considered, the overall activity is much lower. For the entire time range, mode 1 appears to stand out, and might thus be considered, as also noted for the other TSH simulation.

S3.2.3 Coherence analysis of TSH results

The result of the coherence analysis for trajectories based on photoionized initial conditions can be found in Fig. S12. Again, the coherence of all normal modes are rather similar for the full time range. The modes that can be singled out for the analysis of the first 5 fs differs

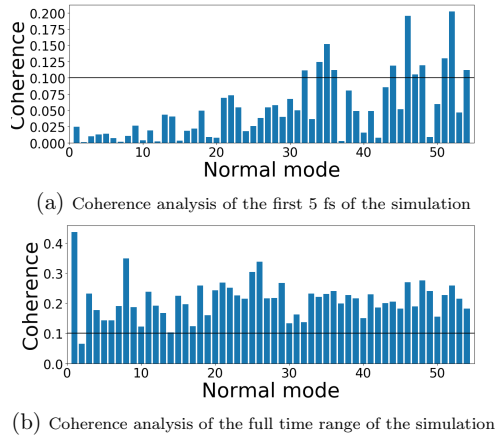


Figure S12: Visualization of coherence analysis of the TSH simulation based on photoionized initial conditions. The horizontal black line at 0.1 is chosen as in Mai and González.³

from those in the other simulation, as it is here modes 34, 35, 44, 46, 48, 51 and 52. Note that modes 44 and 46 were also considered in the simulation based on the excited cation.

S3.2.4 Correlation analysis of TSH results

The results of the correlation analysis for simulation based on photoionized initial conditions can be found in table S8 and Fig. S13. As for the TSH simulation based on excitation of the cation, normal modes 8, 16, 24, 33, 44 and 47 are all found to show some correlation for the energy gap although not for all states. These might therefore be of interest when performing the MCTDH simulation. Furthermore, modes 12 and 32 might be of interest.

Table S8: Result of correlation analysis of TSH trajectories over the entire simulated time range based on photoionized initial conditions. The Pearson correlation coefficient is reported for the correlation between the energy gap of the active state to the D_0 , D_1 , D_2 and D_3 states and Q for each normal mode.

Normal mode	$R^2_{\Delta E(D_0)}$	$R^2_{\Delta E(D_1)}$	$R^2_{\Delta E(D_2)}$	$R^2_{\Delta E(D_3)}$
1	0.0004	0.0035	0.0009	0.0014
2	0.0003	0.0001	0.0012	0.0001
3	0.0011	0.0006	0.0004	0.0012
4	0.0013	0.0004	0.0001	0.0011
5	0.0009	0.0014	0.0016	0.0018
6	0.0005	0.0001	0.0010	0.0019
7	0.0026	0.0035	0.0000	0.0021

Table S8 – continued from previous page

Normal mode	$R^2_{\Delta E(D_0)}$	$R^2_{\Delta E(D_1)}$	$R^2_{\Delta E(D_2)}$	$R^2_{\Delta E(D_3)}$
8	0.0076	0.0318	0.0028	0.0050
9	0.0006	0.0011	0.0016	0.0001
10	0.0014	0.0001	0.0001	0.001
11	0.0033	0.0032	0.0013	0.0091
12	0.0061	0.0048	0.0454	0.0274
13	0.0027	0.0019	0.0000	0.0058
14	0.0014	0.0003	0.0013	0.0013
15	0.0000	0.0001	0.0010	0.0002
16	0.0010	0.0181	0.0273	0.0081
17	0.0000	0.0001	0.0008	0.0001
18	0.0003	0.0018	0.0042	0.0001
19	0.0002	0.0000	0.0001	0.0000
20	0.0000	0.0038	0.0011	0.0068
21	0.0000	0.0000	0.0004	0.0002
22	0.0007	0.0033	0.0167	0.0158
23	0.0019	0.0025	0.0008	0.0025
24	0.0044	0.0158	0.0066	0.0081
25	0.0020	0.0002	0.0002	0.0003
26	0.0004	0.0003	0.0004	0.0004
27	0.0008	0.0021	0.0011	0.0036
28	0.0007	0.0002	0.0003	0.0005
29	0.0029	0.0016	0.0025	0.0012
30	0.0003	0.0004	0.0002	0.0000
31	0.0026	0.0051	0.0060	0.0037
32	0.0129	0.0488	0.0617	0.0387
33	0.0108	0.0688	0.0203	0.0182
34	0.0069	0.0005	0.0005	0.0026
35	0.0077	0.0088	0.0044	0.0074
36	0.0001	0.0223	0.0022	0.0002
37	0.0000	0.0001	0.0065	0.0000
38	0.0049	0.0050	0.0087	0.0021
39	0.0001	0.0059	0.0014	0.0009
40	0.0068	0.0006	0.0116	0.0019
41	0.0058	0.0008	0.0086	0.0011
42	0.0003	0.0534	0.0132	0.0049
43	0.0194	0.0108	0.0006	0.0006
44	0.0009	0.2074	0.0906	0.0246
45	0.0020	0.0101	0.0081	0.0004
46	0.0001	0.0174	0.0003	0.0046

Table S8 – continued from previous page

Normal mode	$R^2_{\Delta E(D_0)}$	$R^2_{\Delta E(D_1)}$	$R^2_{\Delta E(D_2)}$	$R^2_{\Delta E(D_3)}$
47	0.0087	0.0864	0.0007	0.0138
48	0.0025	0.0175	0.0117	0.0002
49	0.0005	0.0003	0.0000	0.0004
50	0.0001	0.0002	0.0007	0.0000
51	0.0000	0.0008	0.0002	0.0000
52	0.0001	0.0000	0.0001	0.0000
53	0.0001	0.0006	0.0	0.0002
54	0.0002	0.0000	0.0003	0.0000

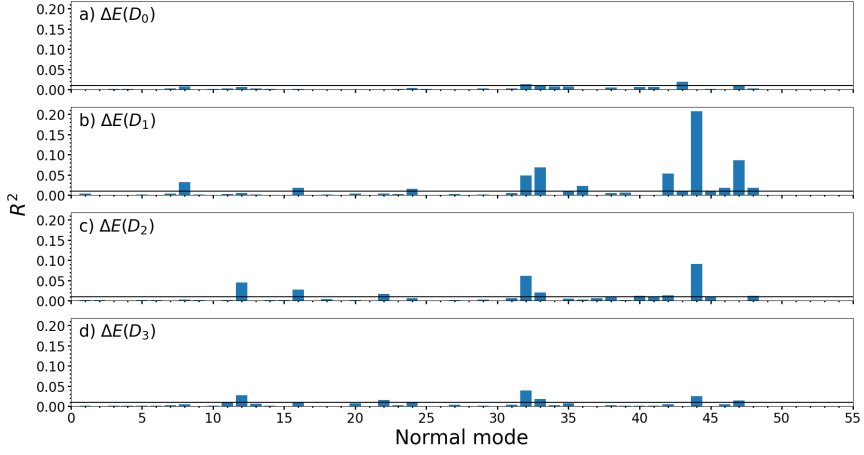


Figure S13: Visualization of the correlation analysis of TSH trajectories based on photoionized initial conditions over the entire simulated time range. The correlation is measured as the Pearson correlation coefficient for a linear fit of the energy gap between the active state and the D_0 , D_1 , D_2 or D_3 state and Q for each normal mode. The horizontal black line shows a correlation coefficient of 0.01, which was also used in the study by Mai and González.³

S3.2.5 LVC SHARC analysis

The largest LVC terms between states were determined (see table S9) for the simulation based on photoionization. Here, mode 54 is observed to couple the initially excited D_3

Table S9: LVC parameters larger than 0.27 eV for BT-1T⁺.

Normal mode	$\lambda^{(n,m)}/\text{eV}$	state n	state m
52	0.3383928	D_1	D_2
54	0.5572623	D_1	D_2
21	0.2748705	D_1	D_3
28	-0.32871641	D_1	D_3
42	0.3719281	D_1	D_3
44	-0.3035377	D_1	D_3
46	-0.3658736	D_1	D_3
52	-0.3705077	D_1	D_3
54	-0.8522828	D_1	D_3
54	-0.5527914	D_2	D_3

state to both D_2 and D_1 and in addition give the strongest coupling between the two states compared to the other modes. Further more mode 52 appears to couple the D_1 state to both the D_2 and the D_3 state. The LVC parameters for the D_0 state to the remaining states are an order of magnitude smaller than for the remaining states. The largest ones are however

found for modes 26 and 52 (both approximately 0.11 eV) for states D_0 and D_1 , mode 53 (approximately 0.11 eV) for states D_0 and D_1 and modes 50 and 54 (approximately 0.08 eV) for states D_0 and D_1 . Normal modes 52 and 54 might therefore also be considered in addition to the other normal modes already discussed above.

S3.3 Regular Surface Hopping with forced jumps for initial conditions based on a photoexcited cation

A TSH simulation was additionally performed utilizing regular surface hopping, i.e., based on the molecular Coulomb Hamiltonian, with the forced jump option enabled for an energy gap of 0.15 eV. Thus, in case of an energy gap of 0.15 eV or less between the current state and the S_0 ground state (GS), the trajectories would be forced to jump to the GS and remain there for the remainder of the simulation. This procedure has been used with success in other studies.⁴⁻⁶ Note however that in this case, the forced jumps cannot occur, as trajectories move between doublet states and does not include the singlet ground state. The simulation considered photoexcited states of the cation for initial conditions.

This simulation was found to yield results in good agreement with the other simulations presented in this study.

S3.3.1 Population analysis

Of the 25 trajectories simulated 5 jumped to the D_0 state within the simulation time. None of these jumps were forced. The evolution of the populations can be seen in Fig. S14.

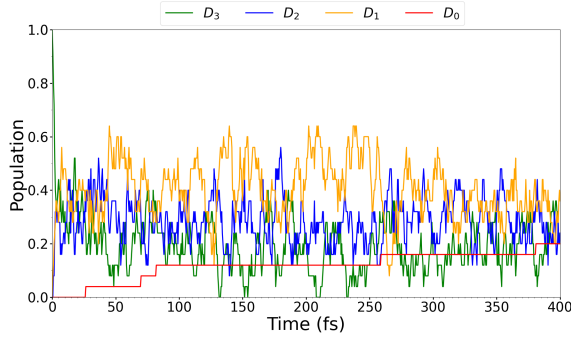


Figure S14: Evolution of populations for the cation in TSH with regular surface hopping based on energies.

S3.3.2 Activity analysis

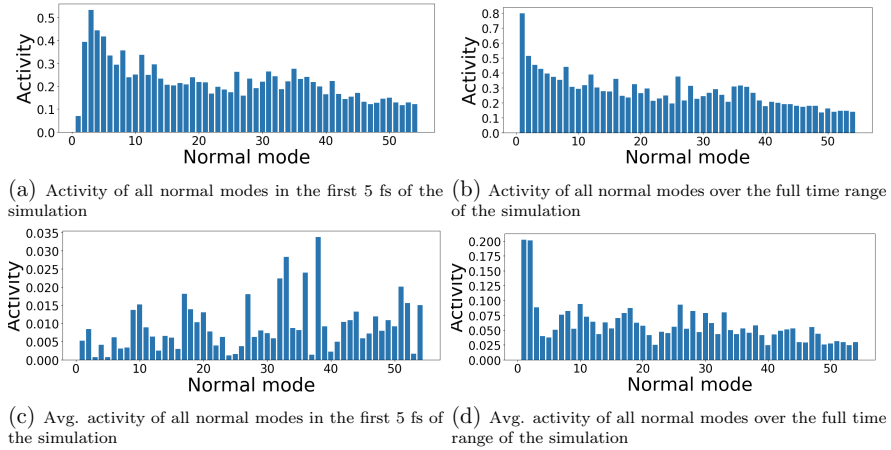


Figure S15: Visualization of activity analysis of the TSH simulation with regular surface hopping.

We observe the same trends as in the simulations without forced jumps using SHARC dynamics.

S3.3.3 Coherence analysis of TSH results

The result of a coherence analysis for the regular surface hopping simulation is shown in Fig. S16. As for the other simulations, it is observed that the coherence of all normal modes are

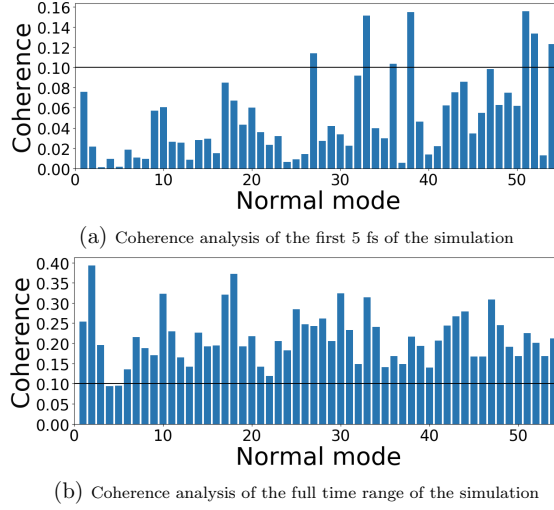


Figure S16: Visualization of coherence analysis of the TSH simulation with regular surface hopping. The horizontal black line at 0.1 is chosen as in Mai and González.³

rather similar when considering the full time range. The same is to some extent true for the first 5 fs, where the overall coherence is lower. Here however a few modes can be observed to be of higher coherence compared to the rest, namely modes 27, 33, 38, 51, 52 and 54.

S3.3.4 Correlation analysis of TSH results

The results of the correlation analysis for the regular surface hopping simulation can be found in table S10 and Fig. S17. As in the other two TSH simulations, normal modes 8, 16, 24, 33, 44 and 47 all appear to show a relatively large correlation for for the energy gap to all states. It is noted that mode 33 also appeared to show a large coherence within the first 5 fs of the simulation compared to other modes, and is therefore doubly interesting.

Table S10: Result of correlation analysis of regular surface hopping TSH trajectories over the entire simulated time range. Pearson correlation coefficients are reported for the correlation of the energy gap between the active state to the D_0 , D_1 , D_2 and D_3 states and Q for each normal mode.

Normal mode	$R^2_{\Delta E(D_0)}$	$R^2_{\Delta E(D_1)}$	$R^2_{\Delta E(D_2)}$	$R^2_{\Delta E(D_3)}$
1	0.0010	0.0100	0.0066	0.0086
2	0.0003	0.0179	0.0144	0.0101
3	0.0000	0.0047	0.0040	0.0039
4	0.0078	0.0005	0.0005	0.0004
5	0.0008	0.0008	0.0008	0.0003

Table S10 – continued from previous page

Normal mode	$R^2_{\Delta E(D_0)}$	$R^2_{\Delta E(D_1)}$	$R^2_{\Delta E(D_2)}$	$R^2_{\Delta E(D_3)}$
6	0.0011	0.0020	0.0037	0.0027
7	0.0037	0.0002	0.0001	0.0000
8	0.0276	0.2216	0.1917	0.1885
9	0.0003	0.0145	0.0112	0.0071
10	0.0010	0.0023	0.0026	0.0008
11	0.0005	0.0020	0.0006	0.0019
12	0.0132	0.0010	0.0159	0.0098
13	0.0000	0.0001	0.0001	0.0000
14	0.0005	0.0008	0.0009	0.0026
15	0.0027	0.0013	0.0012	0.0010
16	0.0323	0.0489	0.0143	0.0105
17	0.0004	0.0000	0.0001	0.0000
18	0.0034	0.0185	0.0167	0.0127
19	0.0017	0.0002	0.0002	0.0001
20	0.0001	0.0023	0.0022	0.0009
21	0.0011	0.0001	0.0003	0.0001
22	0.0001	0.0127	0.0015	0.0012
23	0.0010	0.0004	0.0000	0.0000
24	0.0282	0.0285	0.0145	0.0094
25	0.0001	0.0003	0.0016	0.0006
26	0.0004	0.0000	0.0000	0.0001
27	0.0008	0.0024	0.0036	0.0041
28	0.0001	0.0008	0.0010	0.0005
29	0.0003	0.0017	0.0027	0.0015
30	0.0016	0.0004	0.0002	0.0016
31	0.0002	0.0000	0.0003	0.0000
32	0.0466	0.0253	0.0004	0.0006
33	0.0562	0.0505	0.0170	0.0159
34	0.0001	0.0028	0.0016	0.0008
35	0.0121	0.0057	0.0004	0.0005
36	0.0164	0.0231	0.0144	0.0044
37	0.0021	0.0021	0.0006	0.0006
38	0.0159	0.0008	0.0000	0.0009
39	0.0000	0.0098	0.0103	0.0082
40	0.0307	0.0002	0.0008	0.0030
41	0.0028	0.0050	0.0076	0.0085
42	0.0633	0.0309	0.0180	0.0029
43	0.0016	0.0006	0.0011	0.0001
44	0.2044	0.1719	0.0878	0.0549

Table S10 – continued from previous page

Normal mode	$R^2_{\Delta E(D_0)}$	$R^2_{\Delta E(D_1)}$	$R^2_{\Delta E(D_2)}$	$R^2_{\Delta E(D_3)}$
45	0.0077	0.0064	0.0014	0.0023
46	0.0053	0.0181	0.0230	0.0144
47	0.0790	0.1199	0.1102	0.1049
48	0.0169	0.0162	0.0188	0.0121
49	0.0000	0.0004	0.0002	0.0002
50	0.0000	0.0004	0.0001	0.0000
51	0.0000	0.0009	0.0001	0.0007
52	0.0001	0.0029	0.0022	0.0029
53	0.0003	0.0003	0.0000	0.0001
54	0.0000	0.0001	0.0000	0.0000

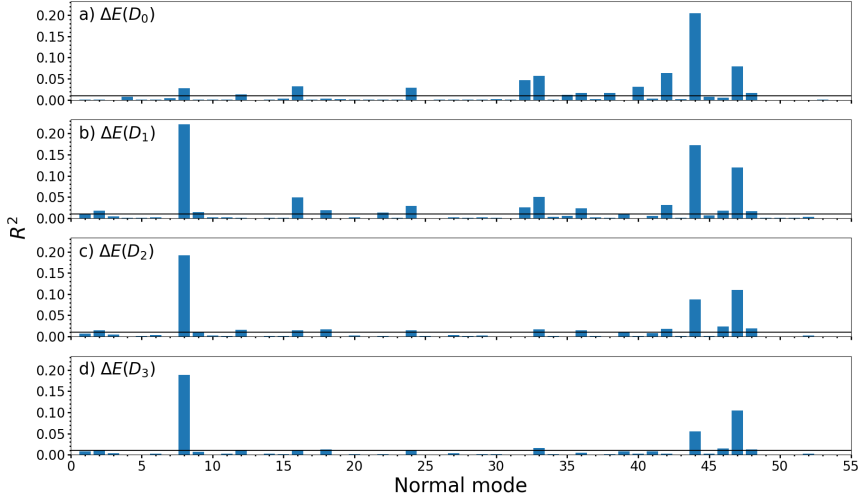


Figure S17: Visualization of the correlation analysis of regular surface hopping TSH trajectories over the entire simulated time range. The correlation is measured as the Pearson correlation coefficient for a linear fit of the energy gap between the active state and the D_0 , D_1 , D_2 or D_3 state and Q for each normal mode. The horizontal black line shows a correlation coefficient of 0.01, which was also used in the study by Mai and González.³

S3.4 Fitting parameters for MCTDH PES

As mentioned in the main text, the PESs for the MCTDH calculation were fitted to a vibronic-coupling Hamiltonian^{7,8} with an harmonic oscillator zero-order term and dimensionless mass-frequency scaled normal coordinates. The Hamiltonian (including the four

electronic states considered) can thus be written as

$$\begin{aligned}
\mathbf{H} = & - \sum_i^f \frac{\omega_i}{2} \frac{\partial^2}{\partial Q_i^2} \mathbf{1} + \sum_i^f \frac{\omega_i}{2} Q_i^2 \mathbf{1} \\
& + \begin{pmatrix} \epsilon_{(D_0)} & 0 & 0 & 0 \\ 0 & \epsilon_{(D_1)} & 0 & 0 \\ 0 & 0 & \epsilon_{(D_2)} & 0 \\ 0 & 0 & 0 & \epsilon_{(D_3)} \end{pmatrix} + \sum_i^f \begin{pmatrix} \kappa_i^{(D_0)} & 0 & 0 & 0 \\ 0 & \kappa_i^{(D_1)} & 0 & 0 \\ 0 & 0 & \kappa_i^{(D_2)} & 0 \\ 0 & 0 & 0 & \kappa_i^{(D_3)} \end{pmatrix} Q_i \\
& + \frac{1}{2} \sum_i^f \begin{pmatrix} \gamma_{i,i}^{(D_0)} & 0 & 0 & 0 \\ 0 & \gamma_{i,i}^{(D_1)} & 0 & 0 \\ 0 & 0 & \gamma_{i,i}^{(D_2)} & 0 \\ 0 & 0 & 0 & \gamma_{i,i}^{(D_3)} \end{pmatrix} Q_i^2 + \frac{1}{2} \sum_{i \neq j}^f \begin{pmatrix} \gamma_{i,j}^{(D_0)} & 0 & 0 & 0 \\ 0 & \gamma_{i,j}^{(D_1)} & 0 & 0 \\ 0 & 0 & \gamma_{i,j}^{(D_2)} & 0 \\ 0 & 0 & 0 & \gamma_{i,j}^{(D_3)} \end{pmatrix} Q_i Q_j \\
& + \sum_i^f \begin{pmatrix} 0 & \lambda_i^{(D_0,D_1)} & \lambda_i^{(D_0,D_2)} & \lambda_i^{(D_0,D_3)} \\ \lambda_i^{(D_1,D_0)} & 0 & \lambda_i^{(D_1,D_2)} & \lambda_i^{(D_1,D_3)} \\ \lambda_i^{(D_2,D_0)} & \lambda_i^{(D_2,D_1)} & 0 & \lambda_i^{(D_2,D_3)} \\ \lambda_i^{(D_3,D_0)} & \lambda_i^{(D_3,D_1)} & \lambda_i^{(D_3,D_2)} & 0 \end{pmatrix} Q_i
\end{aligned} \tag{S1}$$

where f is the number of normal modes, ω_i is the frequency of normal mode i , ϵ_n is the excitation energy for the electronic state n , and $\kappa_i^{(D_n)}$, $\gamma_{i,j}^{(D_n)}$ and $\lambda_i^{(D_n,D_m)}$ are the fitting parameters accounting for linear intra-state coupling, frequency shifts and linear inter-state coupling, respectively. The fitted parameters of the 8 normal modes (8, 16, 24, 33, 44, 46, 47 and 48) considered for MCTDH are:

```

#frequencies

omega_8           = 0.04279 , ev
omega_16          = 0.08304 , ev
omega_24          = 0.11006 , ev
omega_33          = 0.13711 , ev

```

omega_44	=	0.19250 , ev
omega_46	=	0.20387 , ev
omega_47	=	0.20573 , ev
omega_48	=	0.21536 , ev

#energies

E1	=	7.50690 , ev
E2	=	9.17590 , ev
E3	=	9.47390 , ev
E4	=	9.60790 , ev

#on-diagonal linear coupling constants (kappa)

kappa1_8	=	0.02066 , ev
kappa1_16	=	0.09365 , ev
kappa1_24	=	0.26182 , ev
kappa1_33	=	-0.23924 , ev
kappa1_44	=	0.67995 , ev
kappa1_46	=	0.07669 , ev
kappa1_47	=	-0.22080 , ev
kappa1_48	=	0.00696 , ev
kappa2_8	=	-0.05018 , ev
kappa2_16	=	0.01289 , ev
kappa2_24	=	0.32774 , ev
kappa2_33	=	-0.31998 , ev
kappa2_44	=	0.54603 , ev

kappa2_46	=	0.07332 , ev
kappa2_47	=	-0.23898 , ev
kappa2_48	=	-0.00595 , ev
kappa3_8	=	-0.05580 , ev
kappa3_16	=	0.06206 , ev
kappa3_24	=	0.29476 , ev
kappa3_33	=	-0.28300 , ev
kappa3_44	=	0.62693 , ev
kappa3_46	=	0.13962 , ev
kappa3_47	=	-0.12160 , ev
kappa3_48	=	-0.02715 , ev
kappa4_8	=	-0.02209 , ev
kappa4_16	=	0.07334 , ev
kappa4_24	=	0.29989 , ev
kappa4_33	=	-0.28296 , ev
kappa4_44	=	0.57217 , ev
kappa4_46	=	0.06892 , ev
kappa4_47	=	-0.16093 , ev
kappa4_48	=	-0.01266 , ev

#off-diagonal linear coupling constants (lambda)

lambda1_2_8	=	0.01211 , ev
lambda1_2_16	=	-0.01861 , ev
lambda1_2_24	=	0.04906 , ev
lambda1_2_33	=	-0.04662 , ev
lambda1_2_44	=	-0.02302 , ev

lambda1_2_46	=	0.00066 , ev
lambda1_2_47	=	0.00127 , ev
lambda1_2_48	=	0.00009 , ev
lambda1_3_8	=	0.02165 , ev
lambda1_3_16	=	0.00056 , ev
lambda1_3_24	=	-0.00503 , ev
lambda1_3_33	=	-0.02328 , ev
lambda1_3_44	=	-0.01685 , ev
lambda1_3_46	=	-0.04597 , ev
lambda1_3_47	=	0.04097 , ev
lambda1_3_48	=	0.00016 , ev
lambda1_4_8	=	-0.00835 , ev
lambda1_4_16	=	0.00948 , ev
lambda1_4_24	=	0.00244 , ev
lambda1_4_33	=	-0.02142 , ev
lambda1_4_44	=	0.00585 , ev
lambda1_4_46	=	0.00140 , ev
lambda1_4_47	=	0.03196 , ev
lambda1_4_48	=	-0.00014 , ev
lambda2_3_8	=	0.00293 , ev
lambda2_3_16	=	-0.00224 , ev
lambda2_3_24	=	-0.00050 , ev
lambda2_3_33	=	0.02942 , ev
lambda2_3_44	=	0.01714 , ev
lambda2_3_46	=	0.00482 , ev
lambda2_3_47	=	0.00172 , ev
lambda2_3_48	=	-0.00744 , ev

lambda2_4_8	=	0.00566 , ev
lambda2_4_16	=	-0.01808 , ev
lambda2_4_24	=	0.00844 , ev
lambda2_4_33	=	0.01221 , ev
lambda2_4_44	=	0.02129 , ev
lambda2_4_46	=	0.01127 , ev
lambda2_4_47	=	0.00984 , ev
lambda2_4_48	=	0.01414 , ev
lambda3_4_8	=	0.01418 , ev
lambda3_4_16	=	0.00367 , ev
lambda3_4_24	=	0.01469 , ev
lambda3_4_33	=	0.01299 , ev
lambda3_4_44	=	0.01975 , ev
lambda3_4_46	=	0.00753 , ev
lambda3_4_47	=	0.01389 , ev
lambda3_4_48	=	0.01844 , ev

#on-diagonal bilinear coupling constants (gamma)

gamma1_8_8	=	0.00176 , ev
gamma1_8_16	=	0.00001 , ev
gamma1_8_24	=	0.00003 , ev
gamma1_8_33	=	-0.00004 , ev
gamma1_8_44	=	0.00024 , ev
gamma1_8_46	=	0.00006 , ev
gamma1_8_47	=	0.00011 , ev
gamma1_8_48	=	0.00007 , ev

gamma1_16_8	=	0.00001 , ev
gamma1_16_16	=	-0.00032 , ev
gamma1_16_24	=	0.00012 , ev
gamma1_16_33	=	0.00014 , ev
gamma1_16_44	=	0.00019 , ev
gamma1_16_46	=	0.00005 , ev
gamma1_16_47	=	0.00001 , ev
gamma1_16_48	=	0.00010 , ev
gamma1_24_8	=	0.00003 , ev
gamma1_24_16	=	0.00012 , ev
gamma1_24_24	=	0.02645 , ev
gamma1_24_33	=	0.00000 , ev
gamma1_24_44	=	-0.00002 , ev
gamma1_24_46	=	-0.00011 , ev
gamma1_24_47	=	0.00014 , ev
gamma1_24_48	=	-0.00002 , ev
gamma1_33_8	=	-0.00004 , ev
gamma1_33_16	=	0.00014 , ev
gamma1_33_24	=	0.00000 , ev
gamma1_33_33	=	0.03888 , ev
gamma1_33_44	=	-0.00018 , ev
gamma1_33_46	=	0.00004 , ev
gamma1_33_47	=	-0.00003 , ev
gamma1_33_48	=	-0.00005 , ev
gamma1_44_8	=	0.00024 , ev
gamma1_44_16	=	0.00019 , ev
gamma1_44_24	=	-0.00002 , ev

gamma1_44_33	=	-0.00018 , ev
gamma1_44_44	=	0.08898 , ev
gamma1_44_46	=	-0.00004 , ev
gamma1_44_47	=	0.00015 , ev
gamma1_44_48	=	-0.00029 , ev
gamma1_46_8	=	0.00006 , ev
gamma1_46_16	=	0.00005 , ev
gamma1_46_24	=	-0.00011 , ev
gamma1_46_33	=	0.00004 , ev
gamma1_46_44	=	-0.00004 , ev
gamma1_46_46	=	0.02055 , ev
gamma1_46_47	=	0.00022 , ev
gamma1_46_48	=	0.00009 , ev
gamma1_47_8	=	0.00011 , ev
gamma1_47_16	=	0.00001 , ev
gamma1_47_24	=	0.00014 , ev
gamma1_47_33	=	-0.00003 , ev
gamma1_47_44	=	0.00015 , ev
gamma1_47_46	=	0.00022 , ev
gamma1_47_47	=	0.03379 , ev
gamma1_47_48	=	0.00016 , ev
gamma1_48_8	=	0.00007 , ev
gamma1_48_16	=	0.00010 , ev
gamma1_48_24	=	-0.00002 , ev
gamma1_48_33	=	-0.00005 , ev
gamma1_48_44	=	-0.00029 , ev
gamma1_48_46	=	0.00009 , ev

gamma1_48_47	=	0.00016 , ev
gamma1_48_48	=	0.03800 , ev
gamma2_8_8	=	0.00273 , ev
gamma2_8_16	=	0.00001 , ev
gamma2_8_24	=	0.00002 , ev
gamma2_8_33	=	-0.00003 , ev
gamma2_8_44	=	0.00022 , ev
gamma2_8_46	=	0.00004 , ev
gamma2_8_47	=	0.00009 , ev
gamma2_8_48	=	0.00005 , ev
gamma2_16_8	=	0.00001 , ev
gamma2_16_16	=	-0.00511 , ev
gamma2_16_24	=	0.00011 , ev
gamma2_16_33	=	0.00012 , ev
gamma2_16_44	=	0.00017 , ev
gamma2_16_46	=	0.00004 , ev
gamma2_16_47	=	0.00001 , ev
gamma2_16_48	=	0.00008 , ev
gamma2_24_8	=	0.00002 , ev
gamma2_24_16	=	0.00011 , ev
gamma2_24_24	=	0.02321 , ev
gamma2_24_33	=	0.00000 , ev
gamma2_24_44	=	-0.00002 , ev
gamma2_24_46	=	-0.00011 , ev
gamma2_24_47	=	0.00012 , ev
gamma2_24_48	=	-0.00002 , ev
gamma2_33_8	=	-0.00003 , ev

gamma2_33_16	=	0.00012 , ev
gamma2_33_24	=	0.00000 , ev
gamma2_33_33	=	0.03199 , ev
gamma2_33_44	=	-0.00017 , ev
gamma2_33_46	=	0.00002 , ev
gamma2_33_47	=	-0.00003 , ev
gamma2_33_48	=	-0.00003 , ev
gamma2_44_8	=	0.00022 , ev
gamma2_44_16	=	0.00017 , ev
gamma2_44_24	=	-0.00002 , ev
gamma2_44_33	=	-0.00017 , ev
gamma2_44_44	=	0.07752 , ev
gamma2_44_46	=	-0.00006 , ev
gamma2_44_47	=	0.00013 , ev
gamma2_44_48	=	-0.00024 , ev
gamma2_46_8	=	0.00004 , ev
gamma2_46_16	=	0.00004 , ev
gamma2_46_24	=	-0.00011 , ev
gamma2_46_33	=	0.00002 , ev
gamma2_46_44	=	-0.00006 , ev
gamma2_46_46	=	0.01847 , ev
gamma2_46_47	=	0.00020 , ev
gamma2_46_48	=	0.00004 , ev
gamma2_47_8	=	0.00009 , ev
gamma2_47_16	=	0.00001 , ev
gamma2_47_24	=	0.00012 , ev
gamma2_47_33	=	-0.00003 , ev

gamma2_47_44	=	0.00013 , ev
gamma2_47_46	=	0.00020 , ev
gamma2_47_47	=	0.02926 , ev
gamma2_47_48	=	0.00013 , ev
gamma2_48_8	=	0.00005 , ev
gamma2_48_16	=	0.00008 , ev
gamma2_48_24	=	-0.00002 , ev
gamma2_48_33	=	-0.00003 , ev
gamma2_48_44	=	-0.00024 , ev
gamma2_48_46	=	0.00004 , ev
gamma2_48_47	=	0.00013 , ev
gamma2_48_48	=	0.03135 , ev
gamma3_8_8	=	0.00126 , ev
gamma3_8_16	=	0.00001 , ev
gamma3_8_24	=	0.00002 , ev
gamma3_8_33	=	-0.00002 , ev
gamma3_8_44	=	0.00023 , ev
gamma3_8_46	=	0.00004 , ev
gamma3_8_47	=	0.00008 , ev
gamma3_8_48	=	0.00005 , ev
gamma3_16_8	=	0.00001 , ev
gamma3_16_16	=	-0.00769 , ev
gamma3_16_24	=	0.00012 , ev
gamma3_16_33	=	0.00011 , ev
gamma3_16_44	=	0.00019 , ev
gamma3_16_46	=	0.00006 , ev
gamma3_16_47	=	0.00002 , ev

gamma3_16_48	=	0.00009 , ev
gamma3_24_8	=	0.00002 , ev
gamma3_24_16	=	0.00012 , ev
gamma3_24_24	=	0.02297 , ev
gamma3_24_33	=	0.00000 , ev
gamma3_24_44	=	-0.00002 , ev
gamma3_24_46	=	-0.00010 , ev
gamma3_24_47	=	0.00012 , ev
gamma3_24_48	=	-0.00003 , ev
gamma3_33_8	=	-0.00002 , ev
gamma3_33_16	=	0.00011 , ev
gamma3_33_24	=	0.00000 , ev
gamma3_33_33	=	0.03406 , ev
gamma3_33_44	=	-0.00018 , ev
gamma3_33_46	=	0.00002 , ev
gamma3_33_47	=	-0.00003 , ev
gamma3_33_48	=	-0.00004 , ev
gamma3_44_8	=	0.00023 , ev
gamma3_44_16	=	0.00019 , ev
gamma3_44_24	=	-0.00002 , ev
gamma3_44_33	=	-0.00018 , ev
gamma3_44_44	=	0.08097 , ev
gamma3_44_46	=	-0.00012 , ev
gamma3_44_47	=	0.00014 , ev
gamma3_44_48	=	-0.00026 , ev
gamma3_46_8	=	0.00004 , ev
gamma3_46_16	=	0.00006 , ev

gamma3_46_24	=	-0.00010	, ev
gamma3_46_33	=	0.00002	, ev
gamma3_46_44	=	-0.00012	, ev
gamma3_46_46	=	0.01355	, ev
gamma3_46_47	=	0.00018	, ev
gamma3_46_48	=	0.00005	, ev
gamma3_47_8	=	0.00008	, ev
gamma3_47_16	=	0.00002	, ev
gamma3_47_24	=	0.00012	, ev
gamma3_47_33	=	-0.00003	, ev
gamma3_47_44	=	0.00014	, ev
gamma3_47_46	=	0.00018	, ev
gamma3_47_47	=	0.01802	, ev
gamma3_47_48	=	0.00013	, ev
gamma3_48_8	=	0.00005	, ev
gamma3_48_16	=	0.00009	, ev
gamma3_48_24	=	-0.00003	, ev
gamma3_48_33	=	-0.00004	, ev
gamma3_48_44	=	-0.00026	, ev
gamma3_48_46	=	0.00005	, ev
gamma3_48_47	=	0.00013	, ev
gamma3_48_48	=	0.03147	, ev
gamma4_8_8	=	-0.00037	, ev
gamma4_8_16	=	0.00001	, ev
gamma4_8_24	=	0.00002	, ev
gamma4_8_33	=	-0.00002	, ev
gamma4_8_44	=	0.00021	, ev

gamma4_8_46	=	0.00003 , ev
gamma4_8_47	=	0.00008 , ev
gamma4_8_48	=	0.00005 , ev
gamma4_16_8	=	0.00001 , ev
gamma4_16_16	=	-0.00222 , ev
gamma4_16_24	=	0.00011 , ev
gamma4_16_33	=	0.00011 , ev
gamma4_16_44	=	0.00017 , ev
gamma4_16_46	=	0.00004 , ev
gamma4_16_47	=	0.00001 , ev
gamma4_16_48	=	0.00010 , ev
gamma4_24_8	=	0.00002 , ev
gamma4_24_16	=	0.00011 , ev
gamma4_24_24	=	0.02360 , ev
gamma4_24_33	=	0.00001 , ev
gamma4_24_44	=	-0.00002 , ev
gamma4_24_46	=	-0.00011 , ev
gamma4_24_47	=	0.00012 , ev
gamma4_24_48	=	-0.00002 , ev
gamma4_33_8	=	-0.00002 , ev
gamma4_33_16	=	0.00011 , ev
gamma4_33_24	=	0.00001 , ev
gamma4_33_33	=	0.03280 , ev
gamma4_33_44	=	-0.00017 , ev
gamma4_33_46	=	0.00002 , ev
gamma4_33_47	=	-0.00003 , ev
gamma4_33_48	=	-0.00004 , ev

gamma4_44_8	=	0.00021 , ev
gamma4_44_16	=	0.00017 , ev
gamma4_44_24	=	-0.00002 , ev
gamma4_44_33	=	-0.00017 , ev
gamma4_44_44	=	0.08068 , ev
gamma4_44_46	=	-0.00009 , ev
gamma4_44_47	=	0.00014 , ev
gamma4_44_48	=	-0.00026 , ev
gamma4_46_8	=	0.00003 , ev
gamma4_46_16	=	0.00004 , ev
gamma4_46_24	=	-0.00011 , ev
gamma4_46_33	=	0.00002 , ev
gamma4_46_44	=	-0.00009 , ev
gamma4_46_46	=	0.01846 , ev
gamma4_46_47	=	0.00017 , ev
gamma4_46_48	=	0.00004 , ev
gamma4_47_8	=	0.00008 , ev
gamma4_47_16	=	0.00001 , ev
gamma4_47_24	=	0.00012 , ev
gamma4_47_33	=	-0.00003 , ev
gamma4_47_44	=	0.00014 , ev
gamma4_47_46	=	0.00017 , ev
gamma4_47_47	=	0.01953 , ev
gamma4_47_48	=	0.00013 , ev
gamma4_48_8	=	0.00005 , ev
gamma4_48_16	=	0.00010 , ev
gamma4_48_24	=	-0.00002 , ev

gamma4_48_33	=	-0.00004 , ev
gamma4_48_44	=	-0.00026 , ev
gamma4_48_46	=	0.00004 , ev
gamma4_48_47	=	0.00013 , ev
gamma4_48_48	=	0.03045 , ev

S3.5 Surface hopping starting from initial conditions based only on the 8 normal modes included in MCTDH calculation

Another TSH simulation using SHARC Dynamics, but based on initial conditions generated using only the 8 normal modes included in the MCTDH simulation presented in the main text, has been performed based on photoionization. The plot of the evolution of the populations can be seen in Fig. S18. The evolution of the populations are seen to closely resemble

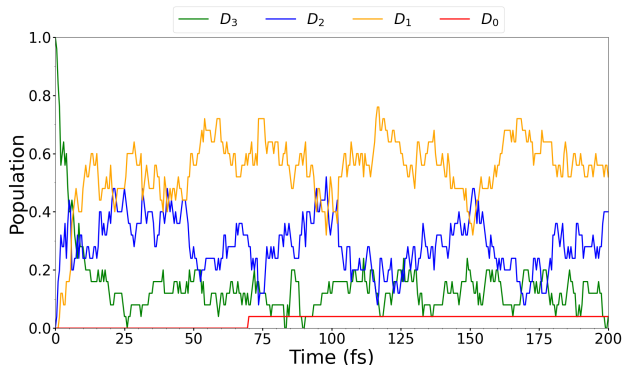


Figure S18: Evolution of the populations of the states for a TSH simulation based on SHARC dynamics and initial conditions generated based on the 8 normal modes found to be of primary interest. The initial conditions were chosen based on photoionization rather than excitation.

those of the other simulations, and thus the shorter lifetime of the initial D_3 state cannot be attributed to the larger number of active normal modes for the initial state generation in the TSH calculation. Instead the discrepancy must be caused by the difference in the simulations, e.g., that TSH does not include any quantum effects.

S3.6 Effect of the 8 normal modes included in MCTDH calculation on geometrical parameters

It is seen from Fig. S19 that modes 16 and 24 affect the dihedral angle, while the two other angles are affected by all modes except 46. Mode 48 does however affect the two angles the most. From Fig. S20 we note that the bond lengths $R_{S_T C}$ are affected by modes 24 and 16.

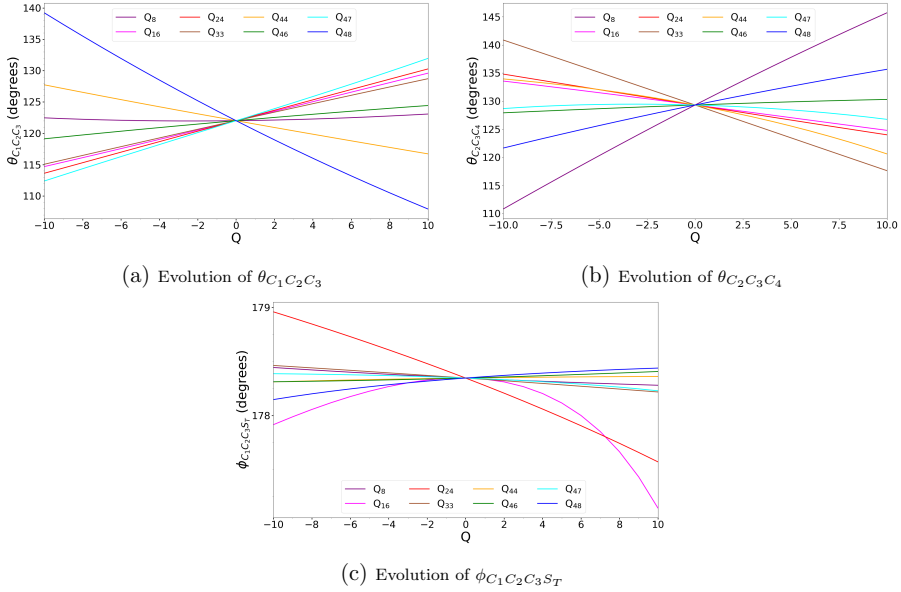


Figure S19: Effect of the 8 chosen normal modes on the angles of interest illustrated as the evolution of the angles for different displacements (Q).

The bond lengths $R_{S_{BT} N}$ are likewise affected by mode 16 and to some extent modes 8, 24 and 46, while the $R_{C_3 C_5}$ bond length is affected mainly by modes 8, 16, 24 and 44. Thus, all the structural parameters investigated are to some degree affected by the chosen set of normal modes.

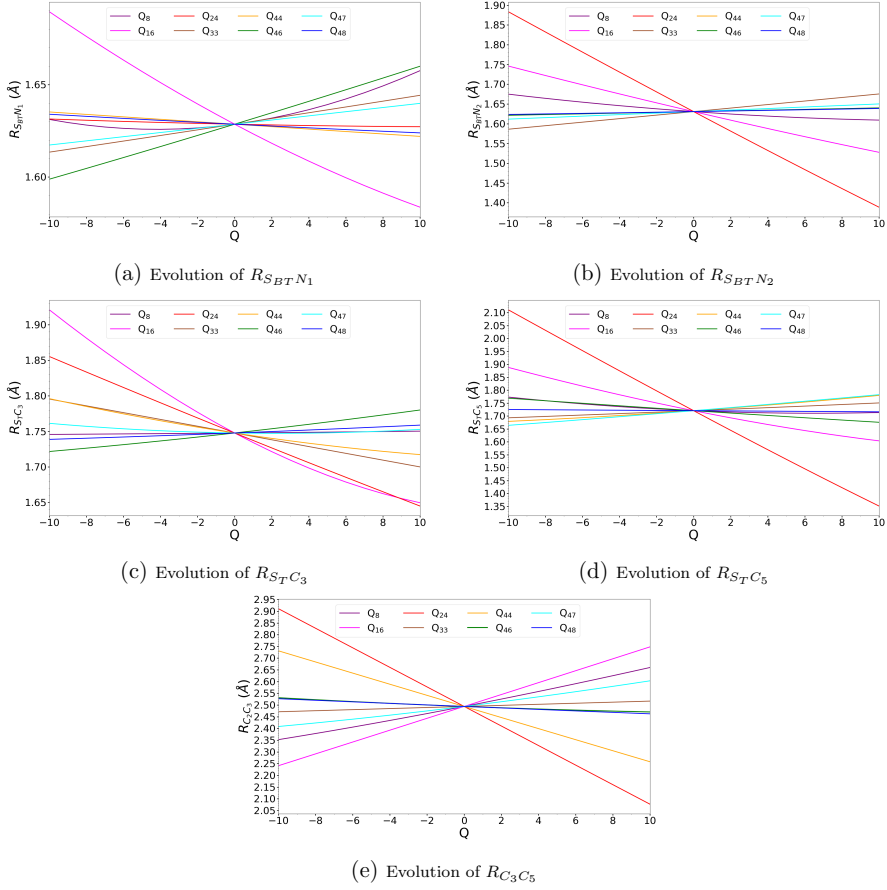


Figure S20: Effect of the 8 chosen normal modes on the bonds of interest illustrated as the evolution of the bond lengths for different displacements (Q).

S3.7 Character of the 8 chosen normal modes

Table S11: Frequencies and characters of the 8 normal modes used in the MCTDH calculation. Se also SI movies.

Normal mode	Frequency/cm ⁻¹	Description
8	345.16	Antisymmetric in plane stretching of the bonds of $\theta_{C_1C_2C_3}$.
16	669.75	Symmetric in plane breathing of the thiophene unit as well as the benzene and thiodiazole making up the benzothiadiazole unit.
24	887.72	In-plane stretching of the S_T -C ₅ and S_{BT} -N ₂ bonds.
33	1105.83	In plane wagging of the CH bonds.
44	1552.62	Symmetric in plane stretching of the thiophene unit
46	1644.29	Antisymmetric in-plane stretch of both the thiophene unit and the benzene ring.
47	1659.28	Antisymmetric in-plane stretch of both the thiophene unit and the benzene ring.
48	1737.00	Symmetric in plane stretch of the benzene ring of the benzothiodiazole unit.

S3.8 MCTDH with 6 normal modes

The 6 normal modes of main interest are determined to be modes 8, 16, 24, 33, 44 and 47, and a simulation including only these has been carried out. Due to fewer normal modes, it was not necessary to utilize mode coupling, and a larger primitive basis (121) could be used. The resulting plot of the evolution of states shows the same trends as the calculation including all 8 modes (see Fig. S21).

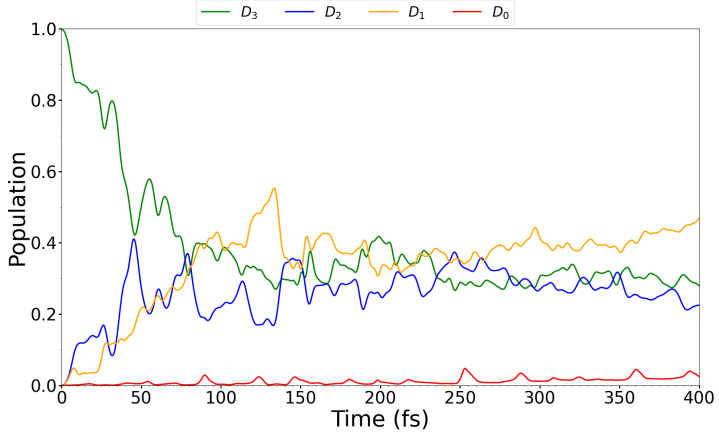


Figure S21: Evolution of populations in the MCTDH simulation with 6 included normal modes.

S3.9 1D density for the active degrees of freedom in the MCTDH simulation

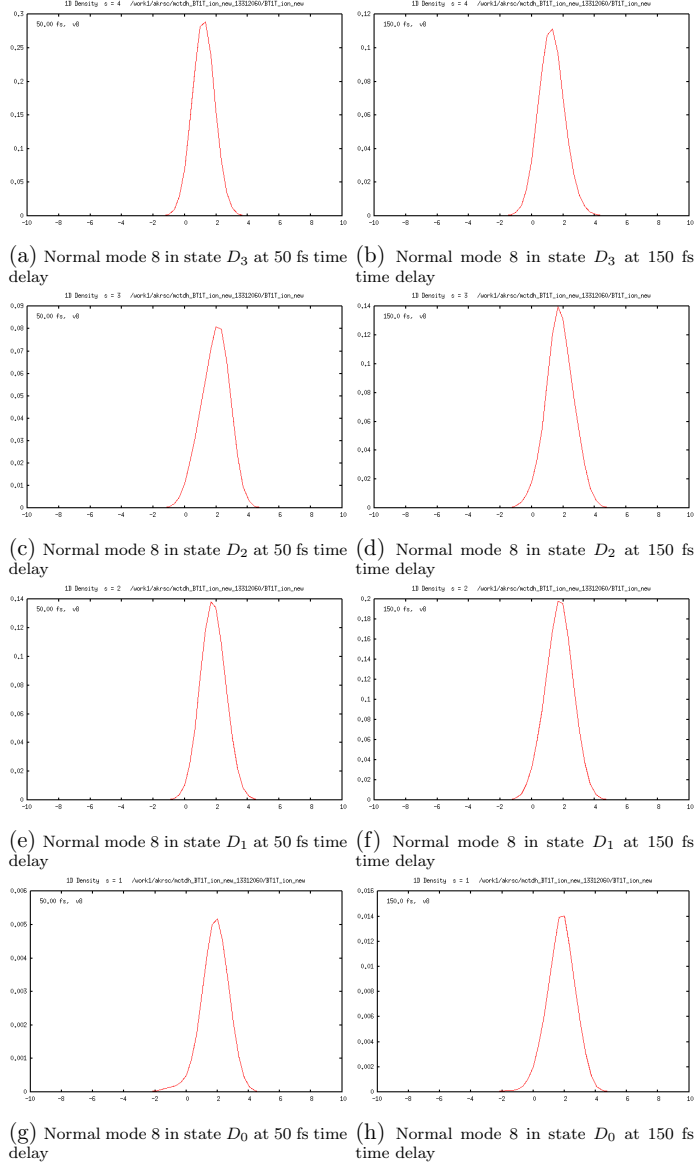


Figure S22: The 1D density of the wavepacket for normal mode 8 in the 4 considered states during the MCTDH simulation for time delays of 50 and 150 fs. The displacement along the normal mode is given on the first axis.

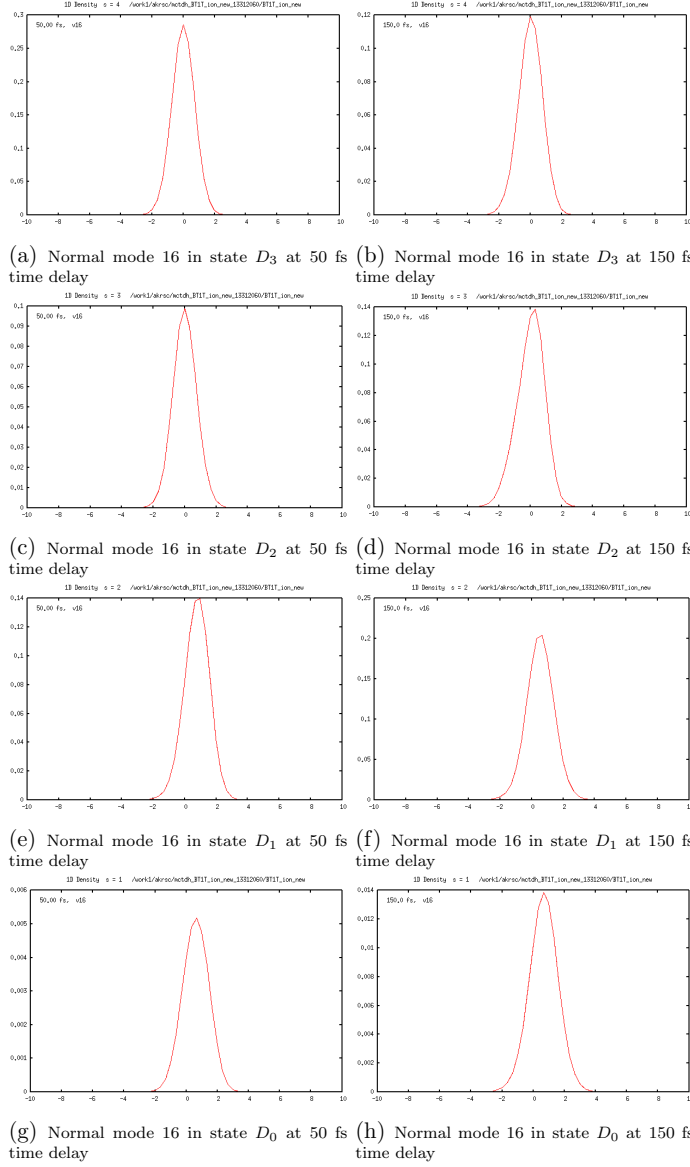


Figure S23: The 1D density of the wavepacket for normal mode 16 in the 4 considered states during the MCTDH simulation for time delays of 50 and 150 fs. The displacement along the normal mode is given on the first axis.

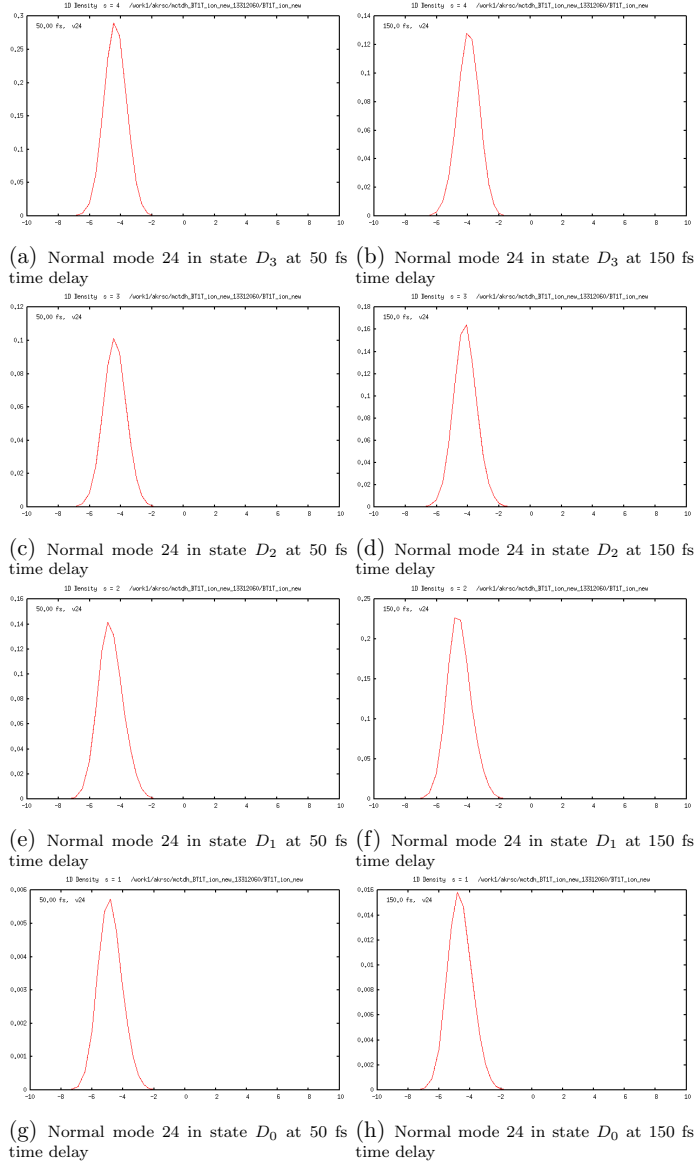


Figure S24: The 1D density of the wavepacket for normal mode 24 in the 4 considered states during the MCTDH simulation for time delays of 50 and 150 fs. The displacement along the normal mode is given on the first axis.

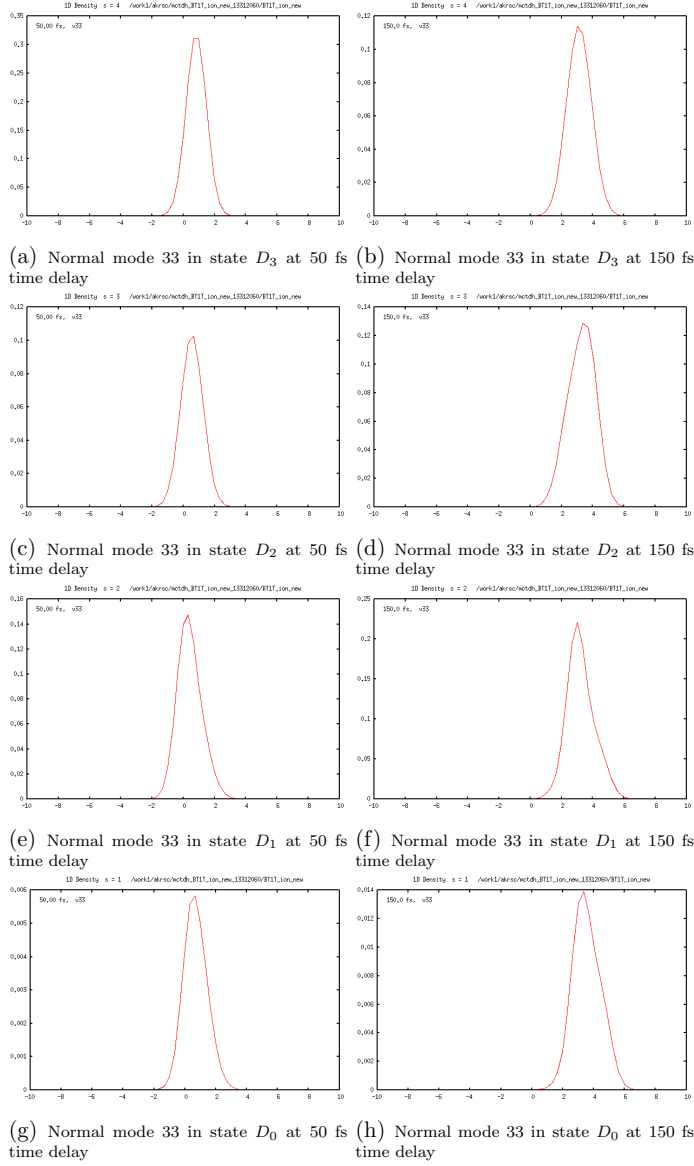


Figure S25: The 1D density of the wavepacket for normal mode 33 in the 4 considered states during the MCTDH simulation for time delays of 50 and 150 fs. The displacement along the normal mode is given on the first axis.

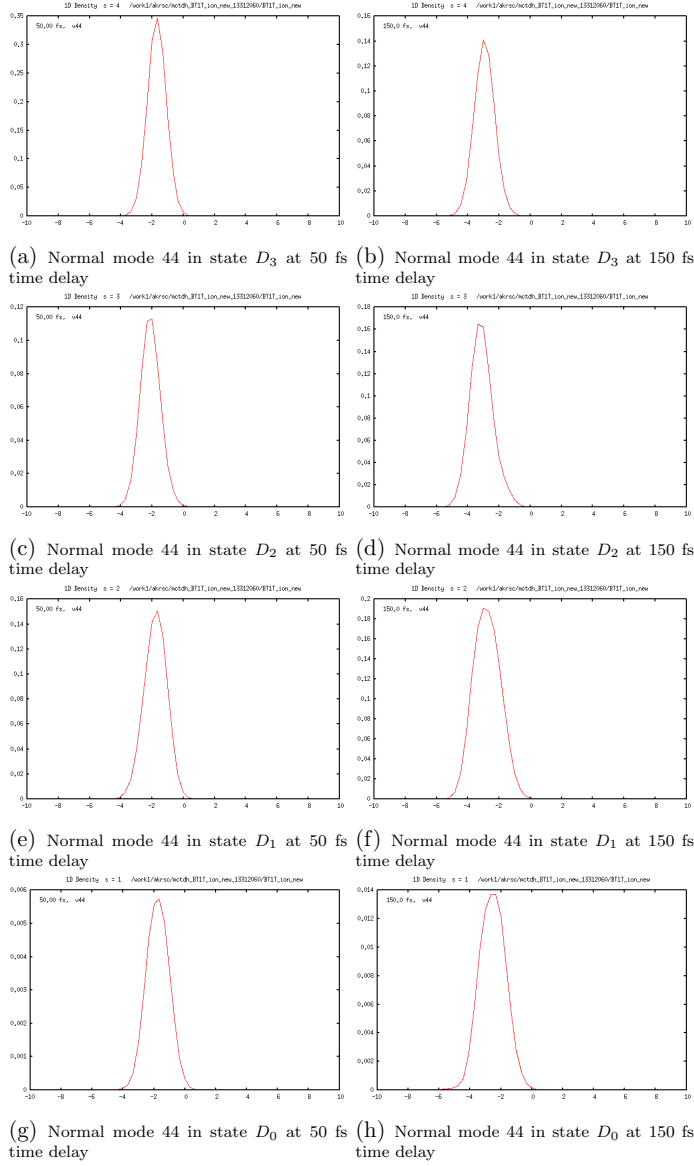


Figure S26: The 1D density of the wavepacket for normal mode 44 in the 4 considered states during the MCTDH simulation for time delays of 50 and 150 fs. The displacement along the normal mode is given on the first axis.

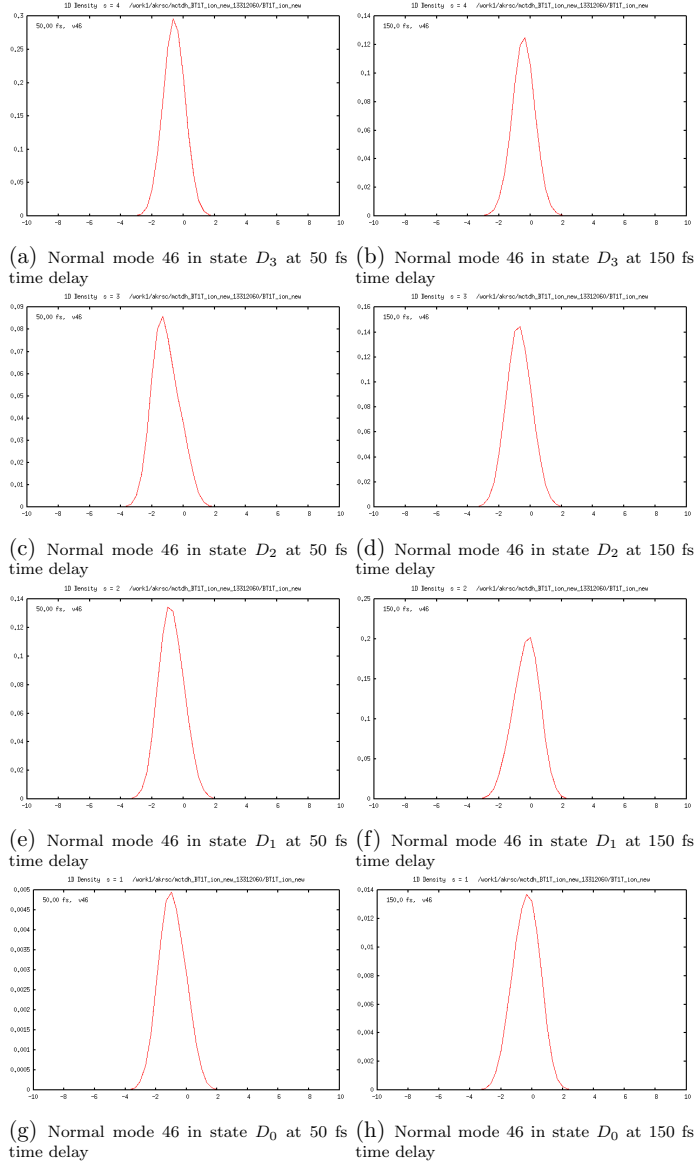


Figure S27: The 1D density of the wavepacket for normal mode 46 in the 4 considered states during the MCTDH simulation for time delays of 50 and 150 fs. The displacement along the normal mode is given on the first axis.

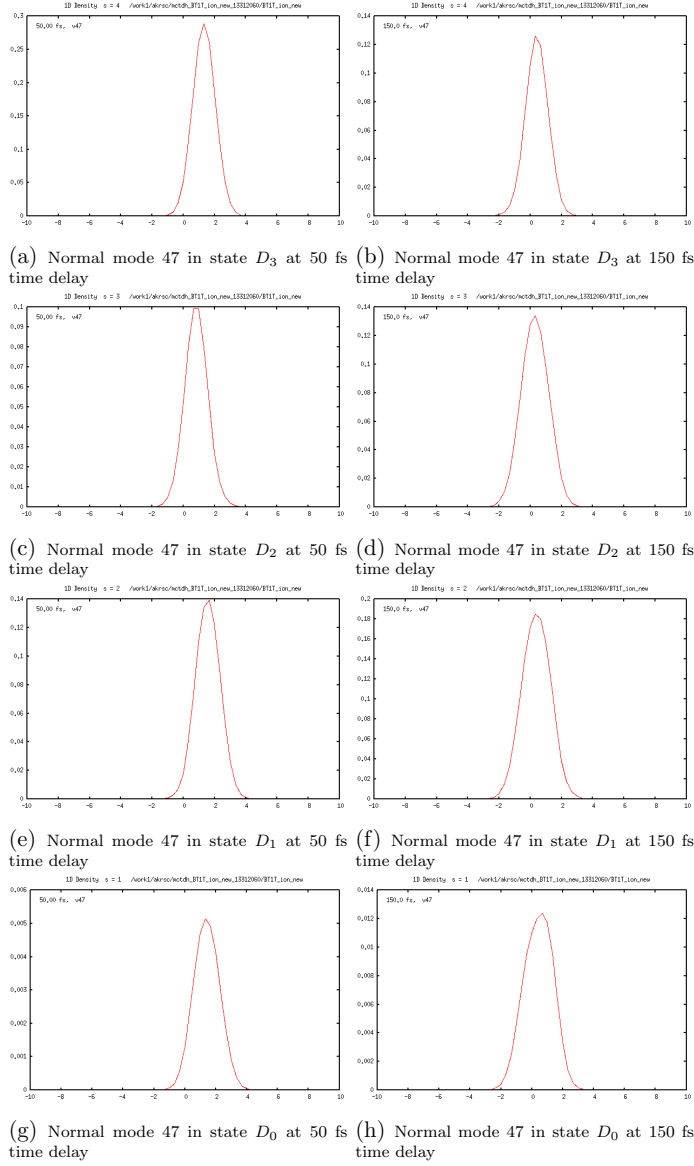


Figure S28: The 1D density of the wavepacket for normal mode 47 in the 4 considered states during the MCTDH simulation for time delays of 50 and 150 fs. The displacement along the normal mode is given on the first axis.

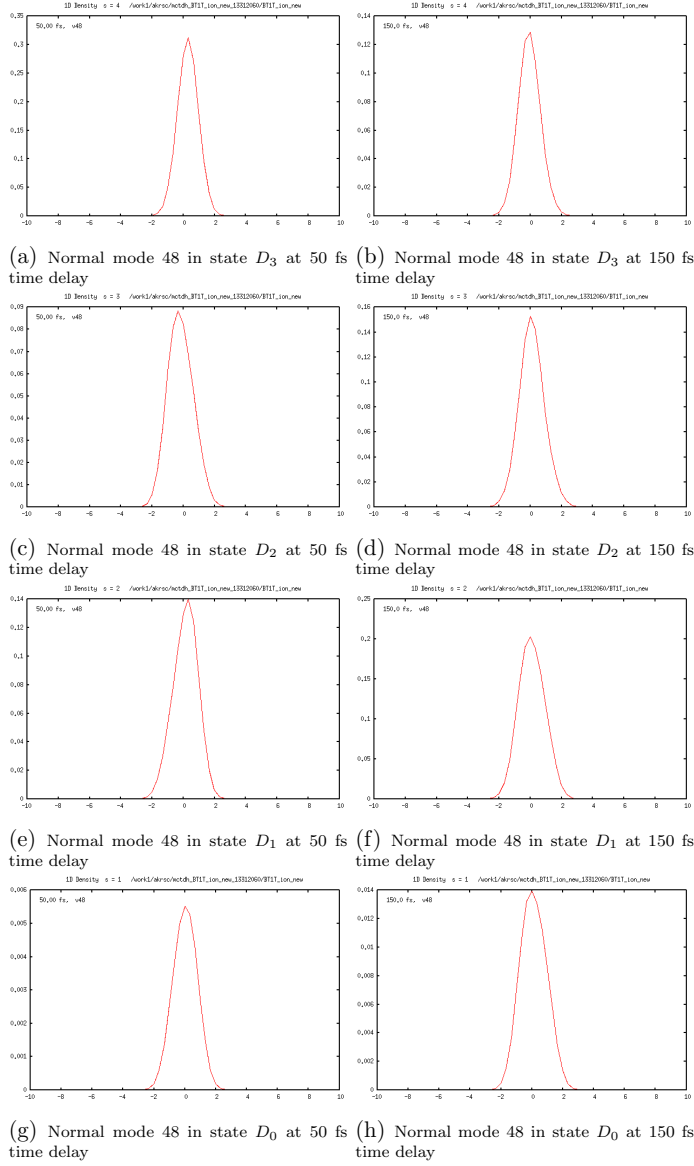


Figure S29: The 1D density of the wavepacket for normal mode 48 in the 4 considered states during the MCTDH simulation for time delays of 50 and 150 fs. The displacement along the normal mode is given on the first axis.

S4 XAS

S4.1 XAS of neutral species

S4.1.1 BHHLYP/aug-cc-pVTZ(S)/cc-pVDZ(remaining atoms)

The sulfur K -edge core excitation energies and oscillator strengths of neutral BT-1T at the BHHLYP level of theory with the aug-cc-pVTZ basis set used on S and the cc-pVDZ basis set used on the remaining atoms can be found in table S12.

Table S12: BT-1T: 15 core excitation energies at the S K -edge and their respective oscillator strengths for the ground state of the neutral molecule. BHHLYP calculations with aug-cc-pVTZ on S and cc-pVDZ on remaining atoms at the ground state optimized geometry. No shifts have been applied to the reported energies.

Energy/eV	f_{osc}
2447.3081	0.0055
2447.3248	0.0040
2447.4139	0.0022
2447.9558	0.0072
2449.0181	0.0006
2449.5727	0.0014
2450.2549	0.0016
2450.3759	0.0031
2450.8342	0.0006
2450.8915	0.0005
2451.1422	0.0006
2451.3381	0.0009
2451.4222	0.0000
2451.6699	0.0001
2451.7010	0.0001

The NTOs of the main peaks of the S_0 spectrum can be seen in Fig. S30.

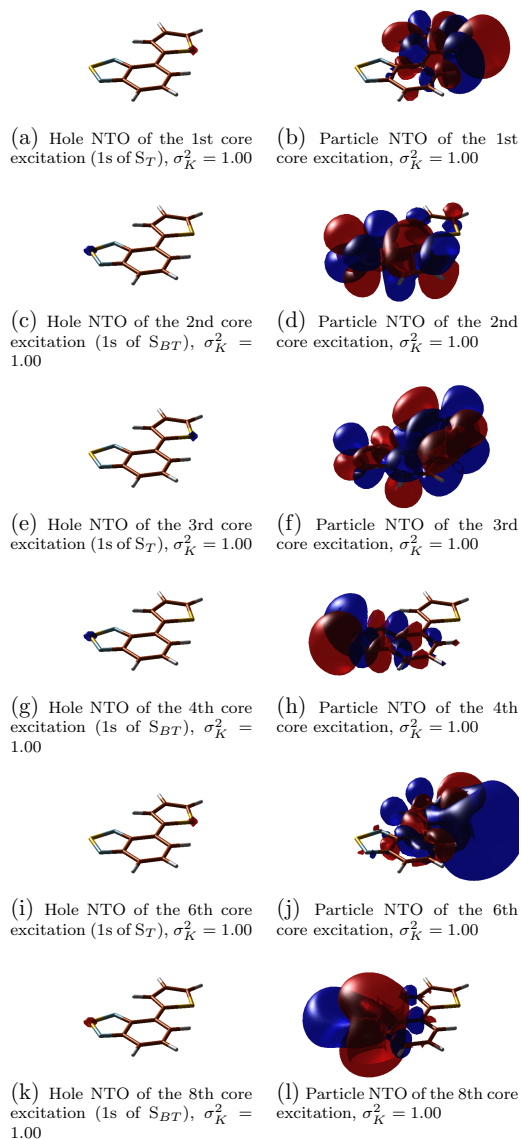


Figure S30: Neutral BT-1T: Dominating orbitals for the 1st-4th, 6th and 8th core transitions from the ground state, calculated at the BHHLYP/aug-cc-pVTZ(S)/cc-pVDZ(remaining atoms) at the ground state optimized geometry.

S4.1.2 fc-CVS-EOM-CCSD/aug-cc-pVTZ(S)/cc-pVDZ(remaining atoms)

The core excitation energies and oscillator strengths for the neutral molecule at the fc-CVS-EOM-CCSD level of theory with aug-cc-pVTZ on S and cc-pVDZ on the remaining atoms can be found in Table S13.

Table S13: Neutral BT-1T: 15 core excitation energies at the S *K*-edge and their respective oscillator strengths of ground state XAS, calculated at the fc-CVS-EOM-CCSD/aug-cc-pVTZ(S)/cc-pVDZ(remaining atoms) at the ground state optimized geometry.

Energy/eV	f_{osc}
2478.7693	0.0057
2479.0386	0.0040
2479.1923	0.0025
2479.4042	0.0074
2480.7483	0.0011
2481.4769	0.0020
2481.6080	0.0005
2481.7322	0.0032
2482.0228	0.0008
2482.3031	0.0009
2482.6052	0.0009
2482.6337	0.0001
2482.9595	0.0005
2483.7182	0.0010
2483.7255	0.0000

The NTOs of the main peaks can be seen in Figs. S31 and S32.

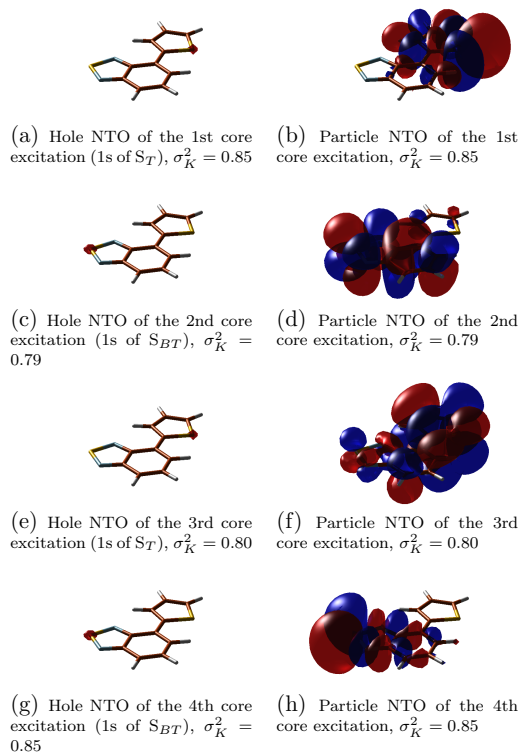


Figure S31: The dominating NTOs for the 1st-4th core transitions of the neutral molecule in the ground state calculated at the fc-CVS-EOM-CCSD level of theory with the aug-cc-pVTZ basis on S and cc-pVDZ on the remaining atoms at the ground state optimized geometry.

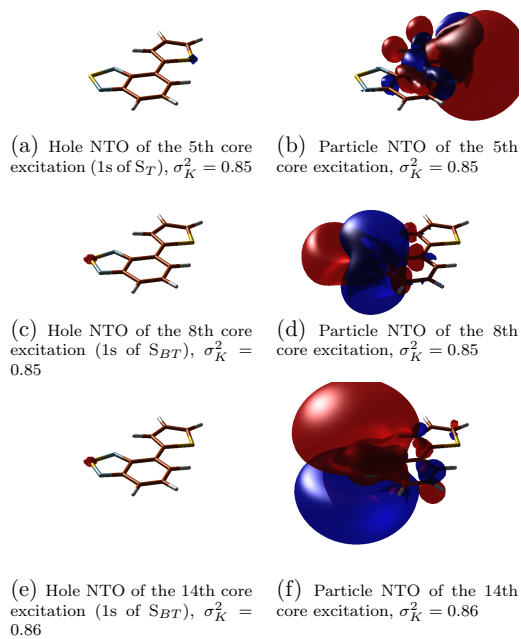


Figure S32: Dominating NTOs for the 5th, 8th, and 14th core transitions in the neutral molecule (in S_0) calculated at the fc-CVS-EOM-CCSD level of theory with the aug-cc-pVTZ basis on S and cc-pVDZ on the remaining atoms at the ground state optimized geometry.

S4.2 XAS of ionized species

S4.2.1 BHHLYP/aug-cc-pVTZ(on S)/cc-pVDZ(remaining atoms)

The core excitation energies and oscillator strengths for the cation at the BHHLYP level of theory with the aug-cc-pVTZ basis set used on S and the cc-pVDZ basis set used on the remaining atoms can be found in table S14.

Table S14: BT-1T⁺: 10 core excitation energies at the S *K*-edge and their respective oscillator strengths for each of the four states of interest calculated at the (IMOM)-BHHLYP level of theory with aug-cc-pVTZ on S and cc-pVDZ on the remaining atoms. No shifts have been applied to the reported energies.

D_0		D_1		D_2		D_3	
Energy/eV	f_{osc}	Energy/eV	f_{osc}	Energy/eV	f_{osc}	Energy/eV	f_{osc}
2445.1816	0.0002	2442.1057	0.0049	2442.9665	0.0016	2443.2263	0.0000
2446.7464	0.0014	2445.8192	0.0003	2443.8409	0.0037	2444.7804	0.0011
2446.9548	0.0011	2447.0174	0.0000	2447.3550	0.0000	2446.9578	0.0001
2446.9720	0.0004	2447.2342	0.0041	2447.5696	0.0008	2447.0688	0.0009
2447.2816	0.0022	2447.7024	0.0000	2447.6759	0.0058	2447.1002	0.0019
2447.3298	0.0060	2448.1123	0.0075	2448.0578	0.0007	2447.3060	0.0060
2447.5112	0.0009	2448.3821	0.0003	2448.2737	0.0018	2447.6719	0.0013
2447.7188	0.0000	2448.7331	0.0056	2448.3439	0.0000	2447.7887	0.0001
2448.0947	0.0012	2449.5416	0.0010	2448.7610	0.0076	2448.0667	0.0017
2448.1376	0.0077	2450.1424	0.0000	2448.8896	0.0004	2448.2212	0.0078

The excited state spectra are generated with IMOM, i.e. a state has been prepared with an electron removed from the (HOMO-*n*)₀ for *n*=0,3 and a ground state-like spectrum has subsequently been determined. This approach was discussed not only for TDDFT, but also for CC methods by Tsuru *et al.*,⁹ and was found to yield good results. Observe, however, that the generated state is not orthogonal to the ground state and that spin contamination occurs. In these calculations, we obtain $\langle S^2 \rangle = 0.8158$ for D_0 (hole in (HOMO)₀), $\langle S^2 \rangle = 0.8357$ for D_1 (hole in (HOMO-1)₀), $\langle S^2 \rangle = 0.7956$ for D_2 (hole in (HOMO-2)₀) and $\langle S^2 \rangle = 0.7755$ for D_3 (hole in (HOMO-3)₀).

The NTOs of the main transitions of the peaks can be found in Figs. S33-S36.

In the D_1 -state of the ion, i.e. the hole in the (HOMO-1)₀ orbital, we observe the first bright transition to be from S_T to an orbital resembling (HOMO-1)₀. The remaining transitions fall in the same region as the D_0 signal, and involves many of the same orbitals. The first of these other NTO pairs actually indicates a transition into an orbital resembling

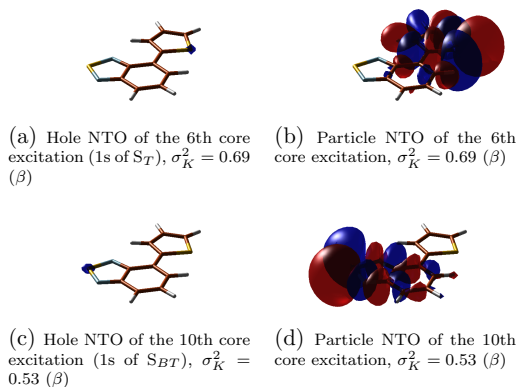


Figure S33: The dominating orbitals for the 6th and 10th core transitions of the ion in D_0 calculated at the BHHLYP level of theory with aug-cc-pVTZ on S and cc-pVDZ on remaining atoms.

the LUMO as shown in Khalili *et al.*²

In the D_2 -state of the ion, i.e. the hole in the $(\text{HOMO-2})_0$ orbital, we observe the first two bright transitions to be from either S_T or S_{BT} into an orbital resembling the $(\text{HOMO-2})_0$. The remaining two NTO pairs observed for the main transitions are again identical to those observed for D_0 .

In the D_3 -state of the ion, i.e. the hole in the $(\text{HOMO-3})_0$ orbital, we observe the first bright transition to be from S_T to an orbital resembling $(\text{HOMO-3})_0$. Note though, that this signal has very low intensity.

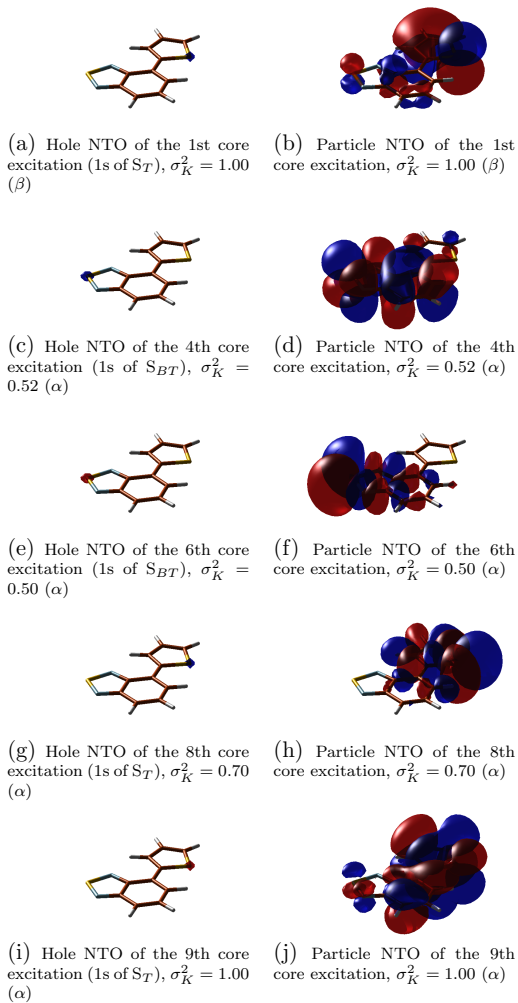


Figure S34: The dominating orbitals for the 1st, 4th, 6th, 8th and 9th core transitions of the ion in D_1 calculated at the IMOM-BHHLYP level of theory with aug-cc-pVTZ on S and cc-pVDZ on remaining atoms.

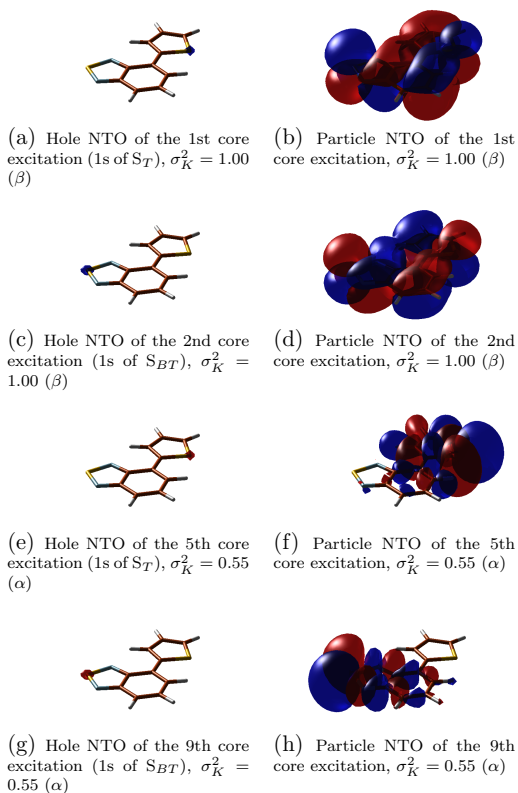


Figure S35: The dominating orbitals for the 1st, 2nd, 5th and 9th core transitions of the ionin D_2 calculated at the IMOM-BHHLYP level of theory with aug-cc-pVTZ on S and cc-pVDZ on remaining atoms.

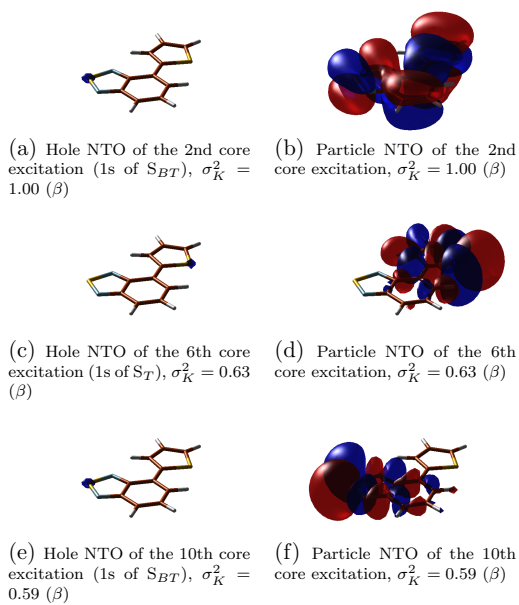


Figure S36: The dominating orbitals for the 2nd, 6th and 10th core transitions of the ion in D_3 calculated at the IMOM-BHHLYP level of theory with aug-cc-pVTZ on S and cc-pVDZ on remaining atoms.

S4.2.2 fc-CVS-EOM-CCSD/aug-cc-pVTZ(on S)/cc-pVDZ(remaining atoms)

The core excitation energies and oscillator strengths for the cation at the fc-CVS-EOM-CCSD level of theory with aug-cc-pVTZ on S and cc-pVDZ on remaining atoms can be found in table S15. All states were generated using IMOM, and are based on a UHF reference

Table S15: BT-1T⁺: 10 core excitation energies at the S *K*-edge and their respective oscillator strengths for each of the four states of interest calculated at the (IMOM-)fc-CVS-EOM-CCSD level of theory with aug-cc-pVTZ on S and cc-pVDZ on remaining atoms. The CC calculation is based on a UHF calculation.

D_0		D_1		D_2		D_3	
Energy/eV	f_{osc}	Energy/eV	f_{osc}	Energy/eV	f_{osc}	Energy/eV	f_{osc}
2476.8241	0.0002	2473.8293	0.0055	2474.448	0.002	2474.8992	0.0000
2478.3614	0.0016	2476.8739	0.0005	2475.4775	0.0036	2476.8969	0.0004
2478.5051	0.0008	2479.2628	0.0014	2478.9053	0.0002	2478.4904	0.0007
2478.6119	0.0018	2479.3550	0.0001	2479.1358	0.0057	2478.6119	0.0019
2478.8319	0.0056	2479.4483	0.0022	2479.48	0.0009	2478.7909	0.0056
2479.1448	0.0028	2479.6680	0.0078	2479.8313	0.0008	2478.8540	0.0012
2479.1642	0.0000	2479.9134	0.0003	2480.0662	0.0019	2479.2956	0.0023
2479.4822	0.0078	2480.1668	0.0056	2480.945	0.0000	2479.4470	0.0015
2479.5291	0.0000	2480.9120	0.0011	2481.038	0.0006	2480.5437	0.0001
2479.9509	0.0013	2481.6946	0.0003	2481.1502	0.0003	2480.9319	0.0027

calculation. Thus, spin-contamination in the CC calculations is found with $\langle S^2 \rangle = 0.7897$ for D_0 (hole in (HOMO)₀), $\langle S^2 \rangle = 0.7584$ for D_1 (hole in (HOMO-1)₀), $\langle S^2 \rangle = 0.7620$ for D_2 (hole in (HOMO-2)₀) and $\langle S^2 \rangle = 0.7573$ for D_3 (hole in (HOMO-3)₀).

The NTOs of the main peaks can be seen in Figs. S37 and S40.

The two main transitions for D_0 show the same NTOs as found in the TDDFT calculations.

Interestingly, the dominating NTO pair for the first core transitions in the ion in the D_1 state appears to be to the (HOMO-2)₀ orbital, which is not consistent with the description of the molecule we expect.

The same types of transitions observable in the TDDFT calculation are found at the CCSD level of theory for D_2 . The first two bright transitions are found to be a result of transitions from S_T and S_{BT} , respectively to an orbital resembling the (HOMO-2)₀.

As also observed at the TDDFT level of theory, the first transition in the D_3 spectrum corresponds to a transition from the 1s on S_{BT} to an orbital resembling (HOMO-3)₀, while

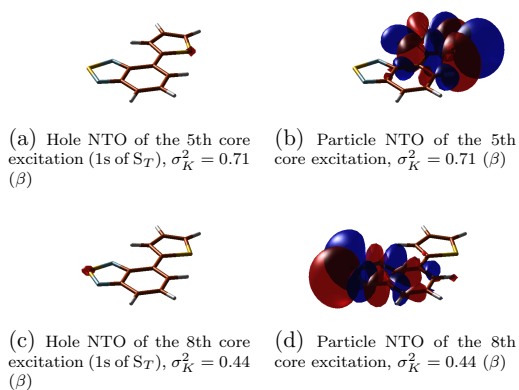


Figure S37: The dominating orbitals for the 5th and 8th core transitions of BT-1T⁺ in the ground state (D_0) calculated at the fc-CVS-EOM-CCSD level of theory with the aug-cc-pVTZ basis in S and cc-pVDZ on remaining atoms at the ground state optimized geometry.

the remaining transitions correspond to transitions also seen in the the D_0 XAS.

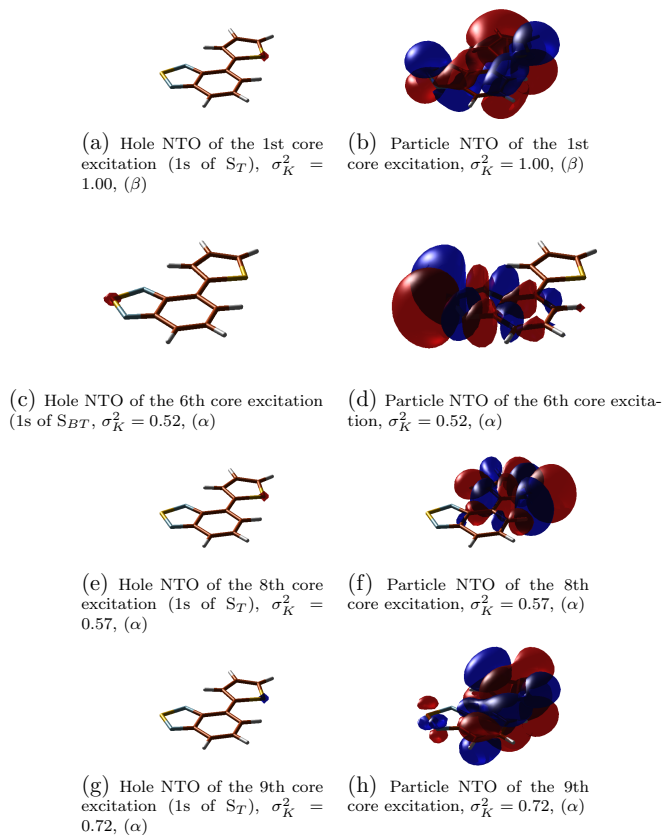


Figure S38: The dominating orbitals for the 1st, 6th, 8th and 9th core transitions of BT-1T⁺ in the D_1 state calculated at the IMOM-fc-CVS-EOM-CCSD level of theory with the aug-cc-pVTZ basis on S and cc-pVDZ on remaining atoms at the excited state optimized geometry.

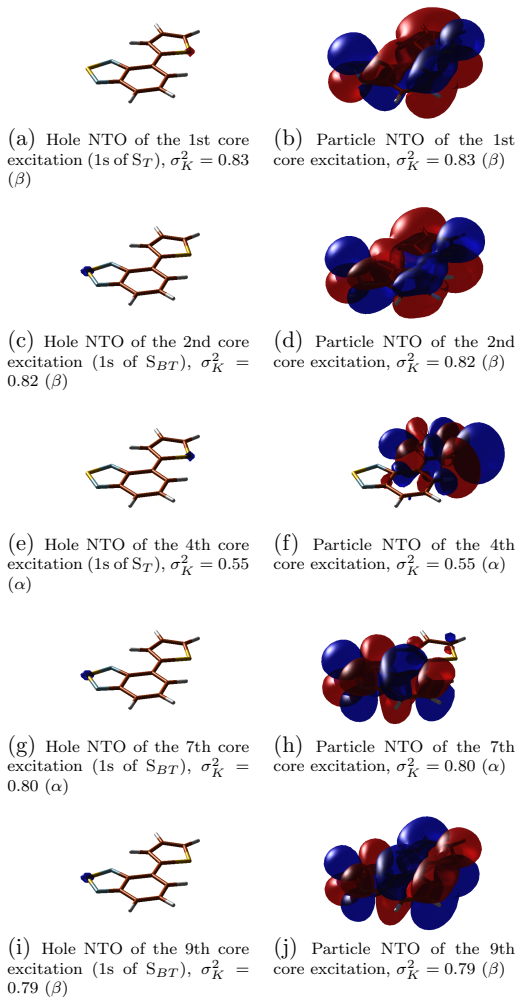


Figure S39: The dominating orbitals for the 1st, 2nd, 4th, 7th and 9th core transitions of BT-1T⁺ in the D_2 state calculated at the IMOM-fc-CVS-EOM-CCSD level of theory with the aug-cc-pVTZ basis in S and cc-pVDZ on remaining atoms at the ground state optimized geometry.

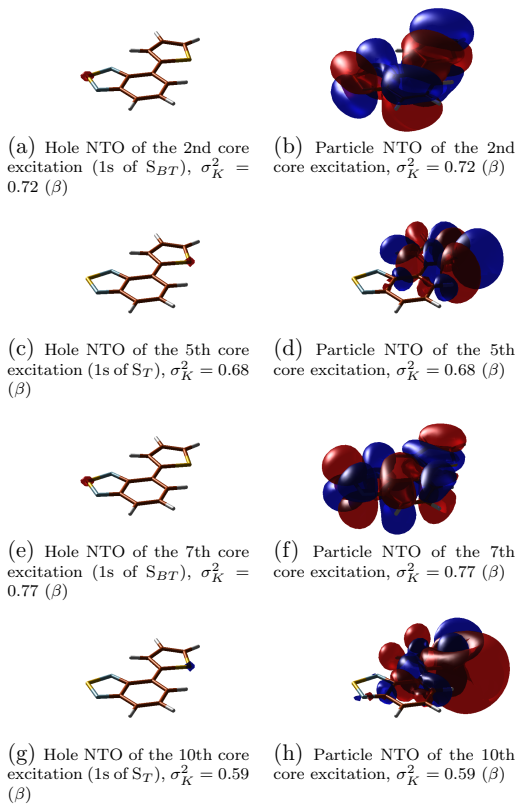


Figure S40: The dominating orbitals for the 2nd, 5th, 7th, and 10th core transitions of BT-1T⁺ in the D_3 state calculated at the IMOM-fc-CVS-EOM-CCSD level of theory with the aug-cc-pVTZ basis in S and cc-pVDZ on remaining atoms at the ground state optimized geometry.

D_1 using IMOM based on the ion rather than the neutral molecule

As the NTO pair for the core-to-SOMO transition in D_1 was unexpected based on which MOs are occupied, a different approach to generate this spectrum has been tested. Here, we use the orbitals of the cation as the initial guess in IMOM. Unfortunately, this cannot be done for all states, as the IMOM procedure in some cases fails to converge, however, for the D_1 state, it is possible. The comparisons between the resulting spectrum and the spectrum obtained using IMOM based on the orbitals of the neutral molecule is shown in Fig. S41. The obtained energies and oscillator strengths can be found in Table S16.

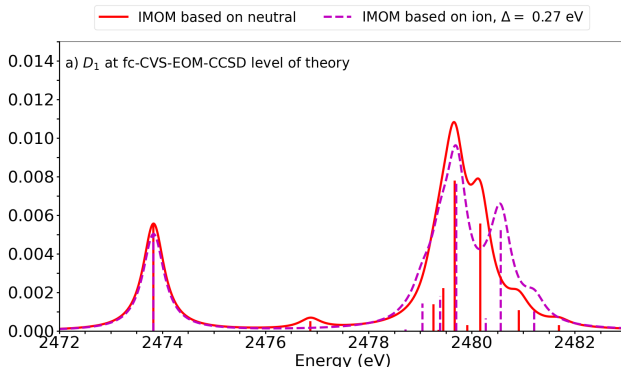


Figure S41: BT-1T⁺: XAS of the D_1 state at the geometry optimized to the ground state of the neutral molecule. The results are shown both when employing IMOM based on the neutral molecule, and when employing IMOM based on the ion. HWHM=0.25 eV.

We observe that the two spectra are very similar except for a small shift. The spectrum calculated with IMOM based on the cation shows a greater resemblance to D_0 at higher energies, and the small second transition is shifted towards higher energy.

The NTOs determined, are found in Fig. S42. We observe that here, the first transition does indeed appear to be into an orbital resembling $(\text{HOMO}-1)_0$, as expected. The remaining three NTO pairs appear identical to those found when employing IMOM based on the orbitals of the neutral molecule. We therefore conclude that, while care should be taken

Table S16: BT-1T⁺: 10 core excitation energies and oscillator strengths for the D_1 state at the geometry optimized to the ground state of the neutral molecule. The results are shown both when employing IMOM based on the neutral molecule, and when employing IMOM based on the ion.

IMOM based on neutral molecule		IMOM based on ion	
Energy/eV	f_{osc}	Energy/eV	f_{osc}
2473.8293	0.0055	2473.5575	0.0050
2476.8739	0.0005	2478.4417	0.0001
2479.2628	0.0014	2478.7767	0.0014
2479.3550	0.0001	2479.1200	0.0018
2479.4483	0.0022	2479.1206	0.0011
2479.6680	0.0078	2479.4324	0.0077
2479.9134	0.0003	2480.0052	0.0007
2480.1668	0.0056	2480.2890	0.0054
2480.9120	0.0011	2480.9437	0.0011
2481.6946	0.0003	2481.4512	0.0000

when assigning NTOs to the different transitions, the overall spectral shape is unchanged.

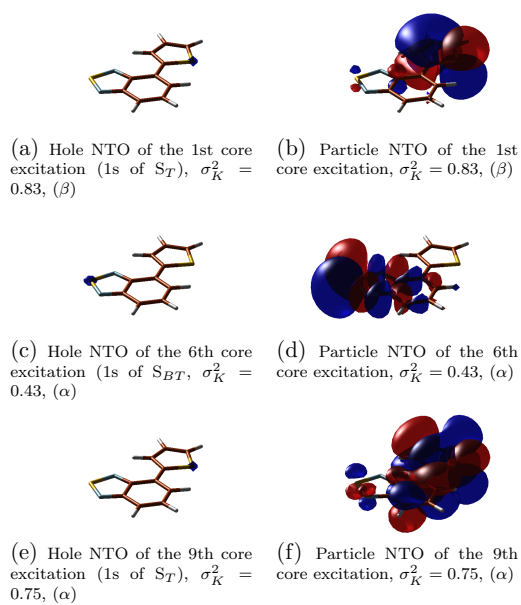


Figure S42: The dominating orbitals for the 1st, 6th and 9th core transitions of BT-1T⁺ in the D_1 state calculated using IMOM based on the ion at the fc-CVS-EOM-CCSD level of theory with the aug-cc-pVTZ basis on S and cc-pVDZ on remaining atoms at the ground state optimized geometry.

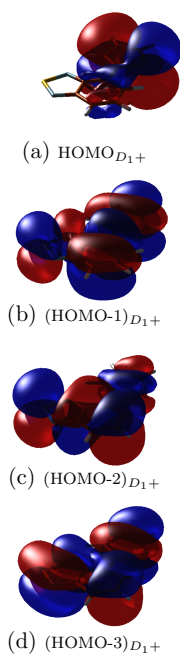


Figure S43: The molecular orbitals of interest for the D_1 state when generated based on the overlap with the MOs of the ion. The MOs are calculated at the UHF level of theory (on which the fc-CVS-EOM-CCSD calculations are based) with aug-cc-pVTZ basis on S and cc-pVDZ on remaining atoms. The orbitals shown are β -spin orbitals.

Core-to-SOMO transitions calculated from ionization potentials

At the EOM-CCSD level of theory it is possible in Q-Chem to determine the transition moment between a core ionized and a valence ionized state. This can be used to determine the intensities of the core-to-SOMO transitions of the photoionized molecule. The excitation energies are here determined as the energy difference between the core ionization and the valence ionization energies. This is based on the assumption that the MOs to retain their relative energies in all states. It is noted that the core-to-SOMO transitions in D_0 and D_3

Table S17: Transition strengths and energies for core-to-SOMO transitions, when determined based on the transition moment between core ionized and valence ionized states. The calculation employed the fc-(CVS-)EOM-CCSD level of theory using the aug-cc-pVTZ basis on S and cc-pVDZ on remaining atoms.

Transition	$\Delta E/\text{eV}$	f_{osc}
$S_T \rightarrow \text{HOMO}_0$	2475.9781	0.000098
$S_{BT} \rightarrow \text{HOMO}_0$	2477.8293	0.000007
$S_T \rightarrow (\text{HOMO}-1)_0$	2474.7320	0.003374
$S_{BT} \rightarrow (\text{HOMO}-1)_0$	2476.5814	0.000283
$S_T \rightarrow (\text{HOMO}-2)_0$	2474.4446	0.000312
$S_{BT} \rightarrow (\text{HOMO}-2)_0$	2476.2954	0.002425
$S_T \rightarrow (\text{HOMO}-3)_0$	2474.1651	0.000005
$S_{BT} \rightarrow (\text{HOMO}-3)_0$	2476.0161	0.000158

are predicted to be dark in good agreement with the IMOM based calculations. Likewise, the D_1 and D_2 core-to-SOMO transitions are found to be bright for S_T and to occur in the same energy region. We also note that the core-to-SOMO transition on S_{BT} in D_2 is found to be the most intense, as also seen using IMOM.

S4.3 XAS at different geometries

The XAS calculated at the BHHLYP level of theory at 0 fs (GS optimized geometry), 50 fs and 150 fs can be seen in Fig. S44 for the four states. The calculated excitation energies and oscillator strengths are reported in tables S18 and S19. It was not possible to converge all fc-CVS-EOM-CCSD calculations (neither using, IMOM, State-Targeted Energy Projection nor Square Gradient Minimization), and such calculations are therefore not shown.

It is observed that the change in geometry does not greatly affect the spectra. Some small overall energetic shifts are seen as well as a few small changes to the relative positions

of the signals. A larger difference is however noted in the D_2 spectra. Based on the geometries generated by the MCTDH simulation only one bright core-to-SOMO peak is observed, whereas the ground state optimized geometry gives rise to two. Note that it is in all three cases the transition from $1s(S_{BT})$ that gives rise to the most intense core-to-SOMO transition, however, the energetic ordering of the two core-to-SOMO transitions change from the GS optimized structure to the structures obtained after a time-delay.

Table S18: BT-1T⁺: 10 core excitation energies at the S K -edge and their respective oscillator strengths for each of the four states of interest calculated at the (IMOM-)BHHLYP level of theory with aug-cc-pVTZ on S and cc-pVDZ on remaining atoms. The geometry is the average structure determined from the MCTDH simulation at a time delay of 50 fs. No shifts have been applied to the reported energies.

D_0		D_1		D_2		D_3	
Energy/eV	f_{osc}	Energy/eV	f_{osc}	Energy/eV	f_{osc}	Energy/eV	f_{osc}
2445.5235	0.0000	2441.8520	0.0054	2443.5440	0.0046	2443.0021	0.0003
2446.2535	0.0013	2446.2483	0.0000	2444.1510	0.0002	2444.2899	0.0015
2446.4209	0.0007	2446.8489	0.0002	2446.5104	0.0002	2446.6185	0.0000
2446.7267	0.0005	2447.0788	0.0038	2446.7010	0.0005	2446.7380	0.0008
2446.9574	0.0062	2447.3830	0.0000	2446.7096	0.0010	2447.0254	0.0069
2446.9731	0.0032	2447.8321	0.0082	2447.1279	0.0063	2447.3607	0.0016
2447.3603	0.0000	2448.2660	0.0001	2447.7775	0.0003	2447.3655	0.0011
2447.6729	0.0001	2448.6614	0.0063	2447.7926	0.0004	2447.4168	0.0001
2447.8151	0.0082	2449.3181	0.0000	2448.2040	0.0004	2447.8343	0.0001
2447.8261	0.0006	2449.3920	0.0001	2448.2514	0.0039	2447.8828	0.0084

Table S19: BT-1T⁺: 10 core excitation energies at the S K -edge and their respective oscillator strengths for each of the four states of interest calculated at the (IMOM-)BHHLYP level of theory with aug-cc-pVTZ on S and cc-pVDZ on remaining atoms. The geometry is the average structure based on the MCTDH simulation at a time delay of 150 fs. No shifts have been applied to the reported energies.

D_0		D_1		D_2		D_3	
Energy/eV	f_{osc}	Energy/eV	f_{osc}	Energy/eV	f_{osc}	Energy/eV	f_{osc}
2445.3921	0.0000	2442.0778	0.0051	2443.7328	0.0044	2443.2276	0.0001
2446.3873	0.0013	2446.2035	0.0001	2444.1163	0.0002	2444.4980	0.0013
2446.4742	0.0008	2446.9410	0.0000	2446.5676	0.0002	2446.5678	0.0010
2446.7847	0.0008	2447.1467	0.0038	2446.7456	0.0013	2446.8236	0.0000
2447.0340	0.0059	2447.2632	0.0000	2446.8493	0.0003	2447.2219	0.0033
2447.0900	0.0027	2447.7171	0.0082	2447.2839	0.0060	2447.2332	0.0045
2447.2853	0.0000	2448.2217	0.0002	2447.7352	0.0006	2447.2550	0.0016
2447.6031	0.0005	2448.6379	0.0062	2447.8150	0.0001	2447.3730	0.0001
2447.7188	0.0001	2449.1883	0.0000	2448.0898	0.0001	2447.8229	0.0001
2447.7440	0.0083	2449.3030	0.0008	2448.1508	0.0003	2447.8431	0.0084

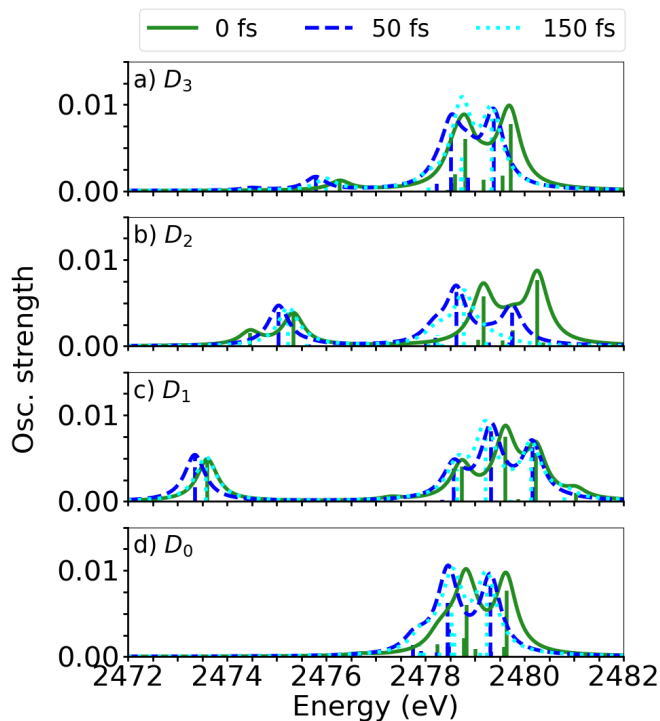


Figure S44: XAS of BT-1T⁺. The spectrum is shown for the D_0 (bottom panel), D_1 (3rd panel), D_2 (2nd panel) and D_3 (top panel). In each state the spectrum has been calculated at the ground state optimized geometry corresponding to a time delay of 0 fs (green), the structure predicted at a 50 fs time delay (blue) as well as the structure predicted at a 150 fs time delay (cyan). All spectra have been determined at the TDDFT (BHHLYP) level of theory. The aug-cc-pVTZ basis was employed on S, while the cc-pVDZ basis was employed on remaining atoms. HWHM=0.25 eV. All results are shifted by 31.5 eV for better comparisons with the other simulated spectra.

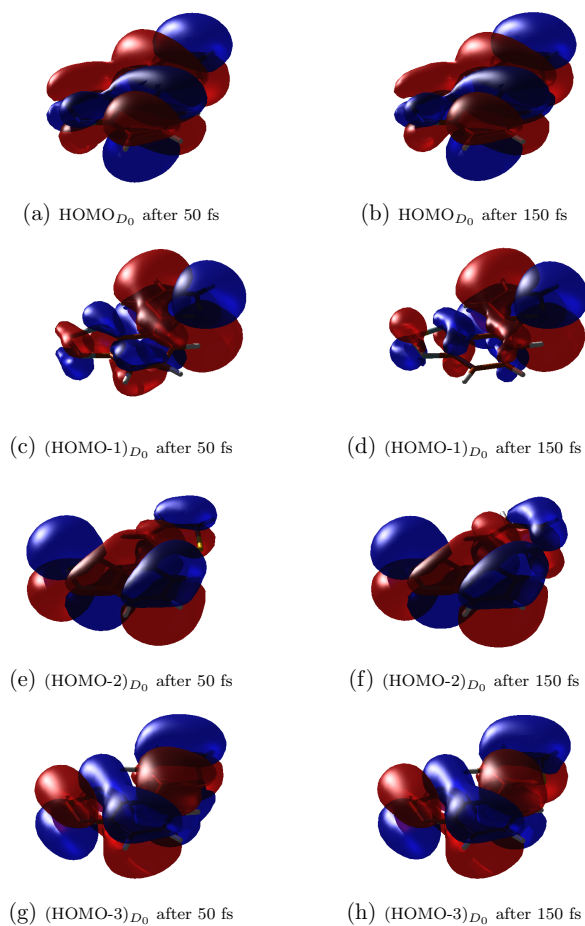


Figure S45: The molecular orbitals of interest for the neutral molecule calculated at D_0 geometry at a time delay of 50 fs (left) and 150 fs (right) at the BHHLYP level of theory with aug-cc-pVTZ basis on S and cc-pVDZ on remaining atoms.

S4.3.1 NTOs for valence excitations at different time delays

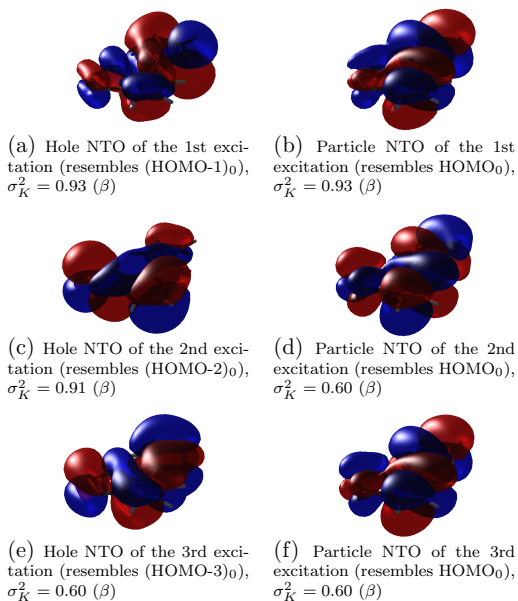


Figure S46: The dominating NTOs for the 3 lowest lying valence transitions in BT-1T⁺ at the 50 fs time delay structure for D_0 . The orbitals have been calculated at the BHHLYP level of theory with aug-cc-pVTZ on S and cc-pVDZ on remaining atoms without use of TDA.

Table S20: The three lowest excitation energies from D_0 calculated at the BHHLYP level of theory with aug-cc-pVTZ on S and cc-pVDZ on remaining atoms for the D_0 structure at 50 fs time delay.

Excited state	Excitation energy (eV)	f_{osc}
D_1	1.6150	0.00500
D_2	1.7756	0.03293
D_3	2.1230	0.00468

While the NTO pairs for the 3 lowest lying valence transitions are observed to remain the same at the two time delays (Figs. S46 and S47), the oscillator strengths of the transitions are seen to change (tables S20 and S21).

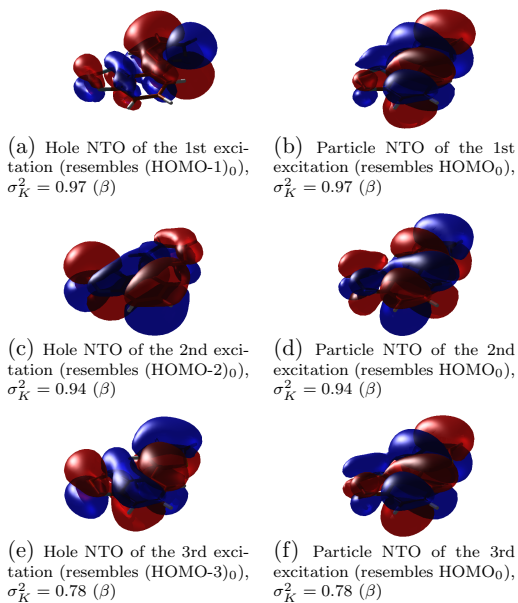


Figure S47: The dominating NTOs for the 3 lowest lying transitions in BT-1T^+ at the 150 fs time delay structure in D_0 . The orbitals have been calculated at the BHHLYP level of theory with aug-cc-pVTZ on S and cc-pVDZ on remaining atoms without use of TDA.

Table S21: The three lowest excitation energies from D_0 calculated at the BHHLYP level of theory with aug-cc-pVTZ on S and cc-pVDZ on remaining atoms for the D_0 structure at 150 fs time delay.

Excited state	Excitation energy (eV)	f_{osc}
D_1	1.4785	0.00057
D_2	1.6928	0.04297
D_3	2.0188	0.04587

S4.3.2 Spin-contamination

Table S22: $\langle S^2 \rangle$ for each BHHLYP level calculation as a measure of spin contamination.

Empty orbital	$\langle S^2 \rangle$	
	50 fs	150 fs
(HOMO-3) ₀	0.8562	0.8322
(HOMO-2) ₀	1.0349	1.0281
(HOMO-1) ₀	0.8803	0.8738
(HOMO) ₀	0.8600	0.8604

References

- (1) Khalili, K.; Inhester, L.; Arnold, C.; Welsch, R.; Andreasen, J. W.; Santra, R. Hole dynamics in a photovoltaic donor-acceptor couple revealed by simulated time-resolved X-ray absorption spectroscopy. *Structural Dynamics* **2019**, *6*, 044102.
- (2) Khalili, K.; Inhester, L.; Arnold, C.; Gertsen, A. S.; Andreasen, J. W.; Santra, R. Simulation of time-resolved x-ray absorption spectroscopy of ultrafast dynamics in particle-hole-excited 4-(2-thienyl)-2,1,3-benzothiadiazole. *Structural Dynamics* **2020**, *7*, 044101.
- (3) Mai, S.; González, L. Identification of important normal modes in nonadiabatic dynamics simulations by coherence, correlation, and frequency analyses. *The Journal of Chemical Physics* **2019**, *151*, 244115.
- (4) Abedi, M.; Pápai, M.; Mikkelsen, K. V.; Henriksen, N. E.; Møller, K. B. Mechanism of Photoinduced Dihydroazulene Ring-Opening Reaction. *J. Phys. Chem. Lett.* **2019**, *10*, 3944–3949.
- (5) Pápai, M.; Li, X.; Nielsen, M. M.; Møller, K. B. Trajectory surface-hopping photoinduced dynamics from Rydberg states of trimethylamine. *Phys. Chem. Chem. Phys.* **2021**, –.
- (6) Schnack-Petersen, A. K.; Pápai, M.; Møller, K. B. Azobenzene photoisomerization dynamics: Revealing the key degrees of freedom and the long timescale of the trans-to-cis process. *Journal of Photochemistry and Photobiology A: Chemistry* **2022**, *428*, 113869.
- (7) Köuppel, H.; Domcke, W.; Cederbaum, L. S. *Advances in Chemical Physics*; John Wiley & Sons, Ltd, 1984; pp 59–246.

- (8) Worth, G. A.; Meyer, H.-D.; Cederbaum, L. S. *Conical Intersections*; World Scientific, 2004; pp 583–617.
- (9) Tsuru, S.; Vidal, M. L.; Pápai, M.; Krylov, A. I.; Møller, K. B.; Coriani, S. An assessment of different electronic structure approaches for modeling time-resolved x-ray absorption spectroscopy. *Structural Dynamics* **2021**, 8, 024101.

APPENDIX F

BT-1T: Molecular Orbitals and XAS Data

F.1 Molecular Orbitals

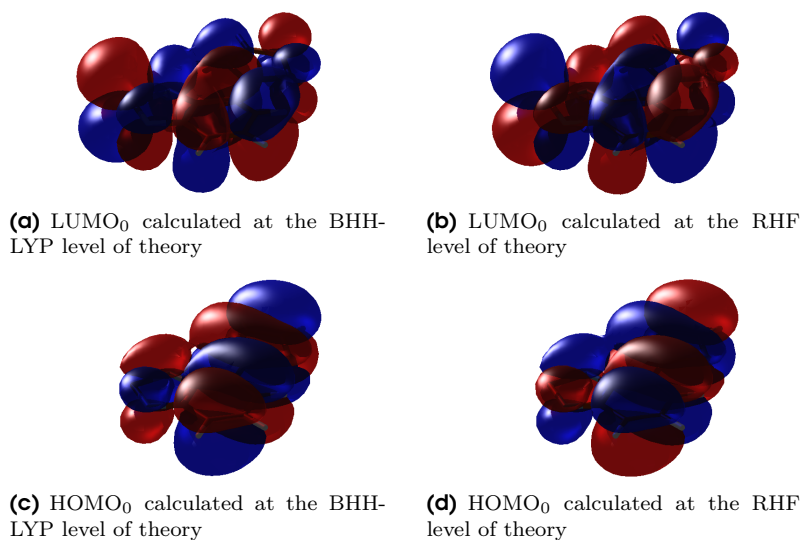


Figure F.1. BT-1T. HOMO and LUMO at the S_0 optimized structure calculated at the BHHLYP/cc-pVDZ level of theory. The MOs are calculated at the BHHLYP (left) and RHF (right) level of theory with the aug-cc-pVTZ basis on S and the cc-pVDZ basis on the remaining atoms. Contour value is ± 0.01 a.u. The HOMOs are from Manuscript 2 (Appendix E).

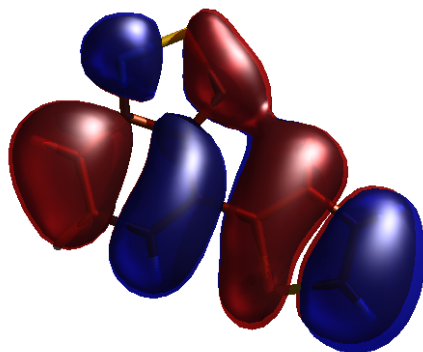


Figure F.2. BT-1T. HOMO_0 at the S_0 optimized structure calculated at the BHHLYP/cc-pVDZ level of theory. The MOs are calculated at the BHHLYP level of theory with the aug-cc-pVTZ basis on S and the cc-pVDZ basis on the remaining atoms. The figure is a different perspective of Fig. F.1c. Contour value is ± 0.01 a.u.

F.2 Natural Transition Orbitals for Valence Excitation at the BHHLYP Level of Theory

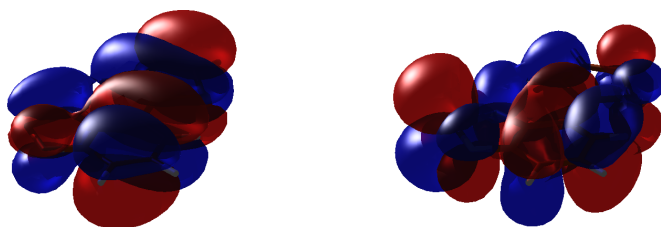


Figure F.3. BT-1T. Main NTOs of the lowest lying valence transition at the S_0 optimized structure calculated at the BHHLYP/cc-pVDZ level of theory. The hole NTO (left) resembles HOMO_0 , while the particle NTO (right) resembles LUMO_0 . The transitions is calculated at the BHHLYP level of theory with the aug-cc-pVTZ basis on S and the cc-pVDZ basis on the remaining atoms. Contour value is ± 0.01 a.u. The NTO weight, σ^2 , is 0.99.

F.3 XAS Data

F.3.1 BHHLYP/aug-cc-pVTZ (S)/cc-pVDZ (remaining atoms)

The core excitation energies and oscillator strengths for the molecule at the BHHLYP level of theory with the aug-cc-pVTZ basis on S and the cc-pVDZ basis on the remaining atoms can be found in tables F.1 and F.2. The excited state calculations employed IMOM. A drawback of the method is the possible spin contamination. This was also observed for these calculations with $\langle S^2 \rangle = 1.0282$ for the S_0 optimized geometry, and $\langle S^2 \rangle = 1.0261$ for the S_1 optimized geometry.

Table F.1. BT-1T. 15 core excitation energies at the S K -edge and their respective oscillator strengths for both S_0 and S_1 calculated at the BHHLYP level of theory at the S_0 optimized geometry. The aug-cc-pVTZ basis was used on S, and the cc-pVDZ basis was used on the remaining atoms. The S_0 results are from Manuscript 2 (Appendix E).

S_0		S_1	
Energy/eV	f_{osc}	Energy/eV	f_{osc}
2447.3081	0.0055	2445.2693	0.0003
2447.3248	0.0040	2445.6750	0.0000
2447.4139	0.0022	2446.4422	0.0025
2447.9558	0.0072	2446.9833	0.0001
2449.0181	0.0006	2447.2625	0.0001
2449.5727	0.0014	2447.3083	0.0057
2450.2549	0.0016	2447.3458	0.0013
2450.3759	0.0031	2447.6582	0.0070
2450.8342	0.0006	2448.4015	0.0012
2450.8915	0.0005	2449.2244	0.0000
2451.1422	0.0006	2449.5116	0.0004
2451.3381	0.0009	2449.6010	0.0002
2451.4222	0.0000	2449.6668	0.0021
2451.6699	0.0001	2449.8335	0.0001
2451.7010	0.0001	2449.9728	0.0027

Table F.2. BT-1T. 15 core excitation energies at the S K -edge and their respective oscillator strengths for both S_0 and S_1 calculated at the BHLYP level of theory at the S_1 optimized geometry. The aug-cc-pVTZ basis was used on S, and the cc-pVDZ basis was used on the remaining atoms.

S_0		S_1	
Energy/eV	f_{osc}	Energy/eV	f_{osc}
2447.1607	0.0040	2445.5876	0.0004
2447.2016	0.0021	2446.0940	0.0000
2447.3141	0.0056	2446.2064	0.0025
2447.6819	0.0076	2446.9705	0.0001
2448.8457	0.0007	2446.9926	0.0001
2449.6624	0.0014	2447.1980	0.0013
2450.0746	0.0038	2447.3186	0.0057
2450.3183	0.0016	2447.3891	0.0073
2450.8797	0.0007	2448.3757	0.0011
2450.9957	0.0005	2449.2682	0.0002
2451.2023	0.0006	2449.3107	0.0000
2451.3764	0.0006	2449.6712	0.0003
2451.4907	0.0000	2449.7059	0.0033
2451.5645	0.0004	2449.7542	0.0021
2451.6481	0.0001	2449.7666	0.0001

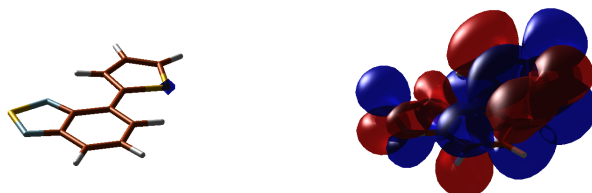
F.3.1.1 Natural Transition Orbitals for S_0 XAS



(a) Hole (left) and particle (right) NTOs of the 1st core excitation. The hole NTO is 1s of S_T . The NTO weight, σ_K^2 , is 1.00.



(b) Hole (left) and particle (right) NTOs of the 2nd core excitation. The hole NTO is 1s of S_{BT} . The NTO weight, σ_K^2 , is 1.00.

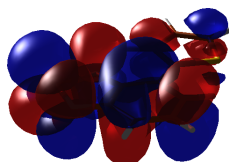
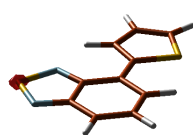


(c) Hole (left) and particle (right) NTOs of the 3rd core excitation. The hole NTO is 1s of S_T . The NTO weight, σ_K^2 , is 1.00.

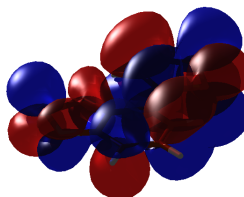
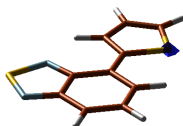


(d) Hole (left) and particle (right) NTOs of the 4th core excitation. The hole NTO is 1s of S_{BT} . The NTO weight, σ_K^2 , is 1.00.

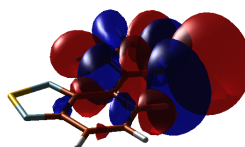
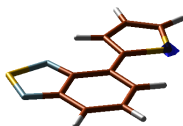
Figure F.4. BT-1T. Main NTOs for the four bright core transitions resulting in the main peak of the S_0 XAS calculated at the BHHLYP level of theory at the S_0 optimized geometry. The aug-cc-pVTZ basis was used on S, and the cc-pVDZ basis was used on the remaining atoms. Contour value is ± 0.01 a.u. The transitions are labelled in Fig. 4.3 based on character. These NTOs are from Manuscript 2 (Appendix E).



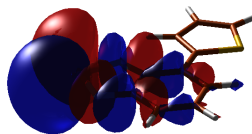
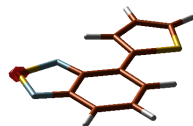
(a) Hole (left) and particle (right) NTOs of the 1st core excitation. The hole NTO is 1s of S_{BT} . The NTO weight, σ_K^2 , is 1.00.



(b) Hole (left) and particle (right) NTOs of the 2nd core excitation. The hole NTO is 1s of S_T . The NTO weight, σ_K^2 , is 1.00.

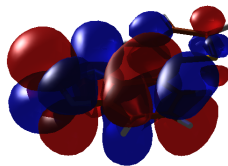
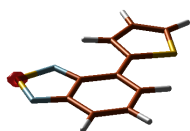


(c) Hole (left) and particle (right) NTOs of the 3rd core excitation. The hole NTO is 1s of S_T . The NTO weight, σ_K^2 , is 1.00.

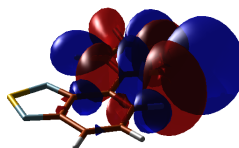
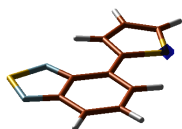


(d) Hole (left) and particle (right) NTOs of the 4th core excitation. The hole NTO is 1s of S_{BT} . The NTO weight, σ_K^2 , is 1.00.

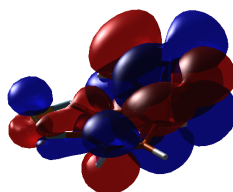
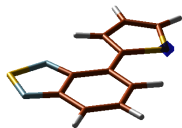
Figure F.5. BT-1T. Main NTOs of the four bright core transitions giving rise to the main peak of the S_0 XAS calculated at the BHHLYP level of theory at the S_1 optimized geometry. The aug-cc-pVTZ basis was used on S, and the cc-pVDZ basis was used on the remaining atoms. Contour value is ± 0.01 a.u. The transitions are labelled in Fig. 6.1 based on character.

F.3.1.2 Natural Transition Orbitals for S_1 XAS

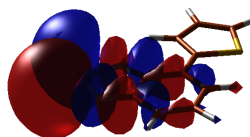
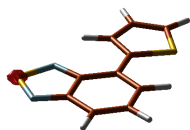
(a) Hole (left) and particle (right) NTOs of the 3rd core excitation. The hole NTO is 1s of S_{BT} . The (α -spin) NTO weight, σ_K^2 , is 1.00.



(b) Hole (left) and particle (right) NTOs of the 6th core excitation. The hole NTO is 1s of S_T . The (β -spin) NTO weight, σ_K^2 , is 0.60.

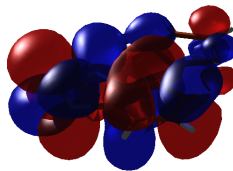
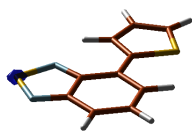


(c) Hole (left) and particle (right) NTOs of the 7th core excitation. The hole NTO is 1s of S_T . The (α -spin) NTO weight, σ_K^2 , is 0.99.

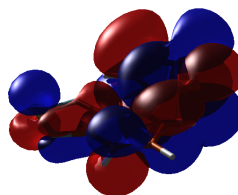
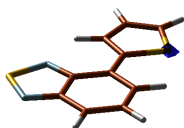


(d) Hole (left) and particle (right) NTOs of the 8th core excitation. The hole NTO is 1s of S_{BT} . The (α -spin) NTO weight, σ_K^2 , is 0.61.

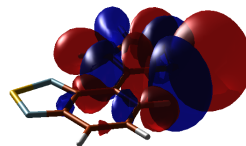
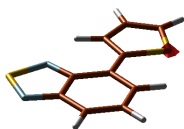
Figure F.6. BT-1T. Main NTOs for the first four bright core transition of the S_1 XAS calculated at the IMOM-BHHLYP level of theory at the S_0 optimized geometry. The aug-cc-pVTZ basis was used on S, and the cc-pVDZ basis was used on the remaining atoms. Contour value is ± 0.01 a.u. The transitions are labelled in Fig. 6.1 based on character.



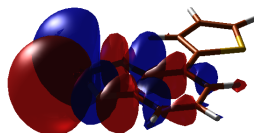
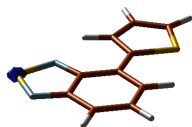
(a) Hole (left) and particle (right) NTOs of the 3rd core excitation. The hole NTO is 1s of S_{BT} . The (α -spin) NTO weight, σ_K^2 , is 0.95.



(b) Hole (left) and particle (right) NTOs of the 6th core excitation. The hole NTO is 1s of S_T . The (α -spin) NTO weight, σ_K^2 , is 1.00.



(c) Hole (left) and particle (right) NTOs of the 7th core excitation. The hole NTO is 1s of S_T . The (β -spin) NTO weight, σ_K^2 , is 0.60.



(d) Hole (left) and particle (right) NTOs of the 8th core excitation. The hole NTO is 1s of S_{BT} . The (α -spin) NTO weight, σ_K^2 , is 0.62.

Figure F.7. BT-1T. Main NTOs for the first four bright core transitions of the S_1 XAS calculated at the IMOM-BHLYP level of theory at the S_1 optimized geometries. The aug-cc-pVTZ basis was used on S, and the cc-pVDZ basis was used on the remaining atoms. Contour value is ± 0.01 a.u. The transitions are labelled in Fig. 6.1 based on character.

F.3.2 fc-CVS-EOM-CCSD/aug-cc-pVTZ (S)/cc-pVDZ (remaining atoms)

The core excitation energies and oscillator strengths for BT-1T at the fc-CVS-EOM-CCSD level of theory with the aug-cc-pVTZ basis on S and the cc-pVDZ basis on the remaining atoms can be found in tables F.3 and F.4. The excited state spectra are generated in two ways. First, by determining the valence excited state and then calculating the transition moments with the core excited states and secondly, by employing IMOM. The former procedure only yields a good description of the transition from the core orbital to the (lowest) singly occupied molecular orbital (SOMO). In the second approach, where IMOM is used, we observe $\langle S^2 \rangle = 1.1888$ for the S_0 geometry and $\langle S^2 \rangle = 1.1793$ for the S_1 geometry.

Table F.3. BT-1T. 15 core excitation energies at the S K -edge and their respective oscillator strengths for both S_0 and S_1 calculated at the fc-CVS-EOM-CCSD level of theory at the S_0 optimized geometry. The aug-cc-pVTZ basis was used on S, and the cc-pVDZ basis was used on the remaining atoms. The S_0 results are from Manuscript 2 (Appendix E).

S_0		S_1 standard CVS-EOM-CCSD		S_1 IMOM	
Energy/eV	f_{osc}	Energy/eV	f_{osc}	Energy/eV	f_{osc}
2478.7693	0.0057	2474.8087	0.0000	2477.4956	0.0003
2479.0386	0.0040	2475.0780	0.0000	2477.6790	0.0000
2479.1923	0.0025	2475.2317	0.0001	2477.9573	0.0025
2479.4042	0.0074	2475.4436	0.0000	2478.5260	0.0002
2480.7483	0.0011	2476.7877	0.0000	2478.7579	0.0057
2481.4769	0.0020	2477.5163	0.0000	2478.7954	0.0006
2481.6080	0.0005	2477.6474	0.0001	2478.9493	0.0013
2481.7322	0.0032	2477.7716	0.0000	2479.1433	0.0066
2482.0228	0.0008	2478.0621	0.0000	2479.9235	0.0012
2482.3031	0.0009	2478.3425	0.0000	2480.5228	0.0000
2482.6052	0.0009	2478.6446	0.0000	2480.8678	0.0018
2482.6337	0.0001	2478.6730	0.0000	2481.0326	0.0004
2482.9595	0.0005	2478.9988	0.0000	2481.3376	0.0023
2483.7182	0.0010	2479.7576	0.0000	2481.6420	0.0000
2483.7255	0.0000	2479.7649	0.0000	2481.6976	0.0013

Table F.4. BT-1T. 15 core excitation energies at the S K -edge and their respective oscillator strengths for both S_0 and S_1 calculated at the fc-CVS-EOM-CCSD level of theory at the S_1 optimized geometry. The aug-cc-pVTZ basis was used on S, and the cc-pVDZ basis was used on the remaining atoms.

S_0		S_1 standard CVS-EOM-CCSD		S_1 IMOM	
Energy/eV	f_{osc}	Energy/eV	f_{osc}	Energy/eV	f_{osc}
2478.7723	0.0057	2475.4302	0.0000	2477.6905	0.0025
2478.8694	0.0040	2475.5273	0.0000	2477.7899	0.0004
2479.0172	0.0025	2475.6751	0.0001	2478.1548	0.0001
2479.1094	0.0078	2475.7674	0.0000	2478.5040	0.0007
2480.8388	0.0011	2477.4968	0.0000	2478.5256	0.0001
2481.3831	0.0038	2478.0410	0.0000	2478.7534	0.0058
2481.4011	0.0005	2478.0591	0.0001	2478.8184	0.0013
2481.5390	0.0021	2478.1969	0.0000	2478.8714	0.0070
2482.0759	0.0009	2478.7338	0.0000	2479.9204	0.0010
2482.3531	0.0008	2479.0110	0.0000	2480.5992	0.0001
2482.6751	0.0010	2479.3331	0.0000	2480.7009	0.0005
2482.7175	0.0000	2479.3754	0.0000	2480.9497	0.0018
2483.0463	0.0005	2479.7043	0.0000	2481.0660	0.0029
2483.7317	0.0000	2480.3896	0.0000	2481.6773	0.0000
2483.8102	0.0009	2480.4681	0.0000	2481.7117	0.0001

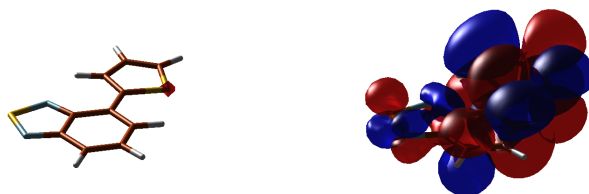
F.3.3 CVS-EOM-CCSD and CVS-EOM-CCSDR(3)/cc-pVDZ

Table F.5. BT-1T. 8 core excitation energies at the S K -edge and their respective oscillator strengths for S_0 calculated at the CVS-EOM-CCSD/cc-pVDZ level of theory. Excitation energies are also reported with the perturbative triples correction, i.e., the CVS-EOM-CCSDR(3)/cc-pVDZ level of theory. The calculations were based on the S_0 optimized geometry.

Energy/eV		f_{osc}
CCSD	CCSDR(3)	CCSD
2485.2667	2483.5301	0.003413
2485.2799	2483.3066	0.002154
2485.3961	2484.2566	0.005263
2486.1038	2485.0517	0.006771
2487.3568	2485.9656	0.002498
2487.6564	2484.9164	0.000308
2488.5034	2487.1908	0.003607
2489.1818	2486.5610	0.000000

F.3.3.1 Natural Transition Orbitals for S_0 XAS

(a) Hole (left) and particle (right) NTOs of the 1st core excitation. The hole NTO is 1s of S_{BT} . The NTO weight, σ_K^2 , is 0.78.



(b) Hole (left) and particle (right) NTOs of the 2nd core excitation. The hole NTO is 1s of S_T . The NTO weight, σ_K^2 , is 0.78.



(c) Hole (left) and particle (right) NTOs of the 3rd core excitation. The hole NTO is 1s of S_T . The NTO weight, σ_K^2 , is 0.84.



(d) Hole (left) and particle (right) NTOs of the 4th core excitation. The hole NTO is 1s of S_{BT} . The NTO weight, σ_K^2 , is 0.85.

Figure F.8. BT-1T: Main NTOs for the first four core transitions in the S_0 XAS calculated at the fc-CVS-EOM-CCSD/cc-pVDZ level of theory at the S_0 optimized geometry. Contour value is ± 0.01 a.u. The transitions are labelled in Fig. 4.5 based on character.

Bibliography

- [1] H. Sahu and H. Ma, “Unraveling Correlations between Molecular Properties and Device Parameters of Organic Solar Cells Using Machine Learning,” *J. Phys. Chem. Lett.*, vol. 10, pp. 7277–7284, 2019.
- [2] C. Milne, T. Penfold, and M. Chergui, “Recent experimental and theoretical developments in time-resolved X-ray spectroscopies,” *Coordin. Chem. Rev.*, vol. 277-278, pp. 44–68, 2014.
- [3] A. Erko, C. Braig, and H. Löchel, “Spectrometers and monochromators for femtosecond soft x-ray sources,” in *Advances in X-Ray/EUV Optics and Components XIV* (A. M. Khounsary, S. Goto, and C. Morawe, eds.), vol. 11108, pp. 39 – 49, SPIE, 2019.
- [4] E. Samoylova, W. Radloff, H.-H. Ritze, and T. Schultz, “Observation of Proton Transfer in 2-Aminopyridine Dimer by Electron and Mass Spectroscopy,” *J. Phys. Chem. A*, vol. 113, pp. 8195–8201, 2009.
- [5] U. Werner, R. Mitrić, and V. Bonačić-Koutecký, “Simulation of time resolved photoelectron spectra with Stieltjes imaging illustrated on ultrafast internal conversion in pyrazine,” *J. Chem. Phys.*, vol. 132, p. 174301, 2010.
- [6] R. Izsák, “Single-reference coupled cluster methods for computing excitation energies in large molecules: The efficiency and accuracy of approximations,” *WIREs Comput. Mol. Sci.*, vol. 10, p. e1445, 2020.
- [7] P. Hohenberg and W. Kohn, “Inhomogeneous Electron Gas,” *Phys. Rev.*, vol. 136, pp. B864–B871, 1964.
- [8] N. Mardirossian and M. Head-Gordon, “Thirty years of density functional theory in computational chemistry: an overview and extensive assessment of 200 density functionals,” *Mol. Phys.*, vol. 115, pp. 2315–2372, 2017.
- [9] J. P. Perdew and K. Schmidt, “Jacob’s ladder of density functional approximations for the exchange-correlation energy,” *AIP Conf. Proc.*, vol. 577, pp. 1–20, 2001.

- [10] J. P. Perdew, A. Ruzsinszky, J. Tao, V. N. Staroverov, G. E. Scuseria, and G. I. Csonka, "Prescription for the design and selection of density functional approximations: More constraint satisfaction with fewer fits," *J. Chem. Phys.*, vol. 123, p. 062201, 2005.
- [11] R. O. Jones, "Density functional theory: Its origins, rise to prominence, and future," *Rev. Mod. Phys.*, vol. 87, pp. 897–923, 2015.
- [12] R. J. Bartlett and M. Musiał, "Coupled-cluster theory in quantum chemistry," *Rev. Mod. Phys.*, vol. 79, pp. 291–352, 2007.
- [13] R. J. Bartlett, "Coupled-cluster theory and its equation-of-motion extensions," *WIREs Comput. Mol. Sci.*, vol. 2, pp. 126–138, 2012.
- [14] F. Coester, "Bound states of a many-particle system," *Nucl. Phys.*, vol. 7, pp. 421–424, 1958.
- [15] F. Coester and H. Kümmel, "Short-range correlations in nuclear wave functions," *Nucl. Phys.*, vol. 17, pp. 477–485, 1960.
- [16] J. Čížek, "On the Correlation Problem in Atomic and Molecular Systems. Calculation of Wavefunction Components in Ursell-Type Expansion Using Quantum-Field Theoretical Methods," *J. Chem. Phys.*, vol. 45, pp. 4256–4266, 1966.
- [17] S. Gozem, A. I. Krylov, and M. Olivucci, "Conical Intersection and Potential Energy Surface Features of a Model Retinal Chromophore: Comparison of EOM-CC and Multireference Methods," *J. Chem. Theory Comput.*, vol. 9, pp. 284–292, 2013.
- [18] N. E. Henriksen and F. Y. Hansen, *Theories of Molecular Reaction Dynamics: The Microscopic Foundation of Chemical Kinetics. Second Edition*. Oxford University Press, 2019.
- [19] A. Rutkowski, "Relativistic perturbation theory. I. A new perturbation approach to the Dirac equation," *J. Phys B Atom M. P.*, vol. 19, p. 149, 1986.
- [20] S. P. A. Sauer, *Molecular Electromagnetism: A Computational Chemistry Approach*. Oxford University Press, 2010.
- [21] P. A. M. Dirac, "The Quantum Theory of the Electron," *Proc. R. Soc. Lond. A*, vol. 117, pp. 610–624, 1928.

- [22] T. Fransson, D. Burdakova, and P. Norman, “K- and L-edge X-ray absorption spectrum calculations of closed-shell carbon, silicon, germanium, and sulfur compounds using damped four-component density functional response theory,” *Phys. Chem. Chem. Phys.*, vol. 18, pp. 13591–13603, 2016.
- [23] P. Atkins, J. de Paula, and R. S. Friedman, *Physical Chemistry: Quanta, Matter and Change, 2nd Edition*. Oxford University Press, 2014.
- [24] P. Atkins and R. S. Friedman, *Molecular Quantum Mechanics, 5th Edition*. Oxford University Press, 2011.
- [25] T. Helgaker, P. Jørgensen, and J. Olsen, *Molecular Electronic-Structure Theory*. John Wiley & Sons, 2014.
- [26] C. D. Sherrill, “Frontiers in electronic structure theory,” *J. Chem. Phys.*, vol. 132, p. 110902, 2010.
- [27] F. Jensen, *Introduction to Computational Chemistry*. Chichester: John Wiley & Sons, 2017.
- [28] O. Sinanoğlu, *Many-Electron Theory of Atoms, Molecules and Their Interactions*, pp. 315–412. John Wiley & Sons, Ltd, 1964.
- [29] D. K. W. Mok, R. Neumann, and N. C. Handy, “Dynamical and Nondynamical Correlation,” *J. Phys. Chem.*, vol. 100, pp. 6225–6230, 1996.
- [30] K. Raghavachari, G. W. Trucks, J. A. Pople, and M. Head-Gordon, “A fifth-order perturbation comparison of electron correlation theories,” *Chem. Phys. Lett.*, vol. 157, pp. 479–483, 1989.
- [31] H. Koch, O. Christiansen, P. Jørgensen, A. M. Sanchez de Merás, and T. Helgaker, “The CC3 model: An iterative coupled cluster approach including connected triples,” *J. Chem. Phys.*, vol. 106, pp. 1808–1818, 1997.
- [32] G. D. Purvis and R. J. Bartlett, “A full coupled-cluster singles and doubles model: The inclusion of disconnected triples,” *J. Chem. Phys.*, vol. 76, pp. 1910–1918, 1982.
- [33] W. Kohn and L. J. Sham, “Self-Consistent Equations Including Exchange and Correlation Effects,” *Phys. Rev.*, vol. 140, pp. A1133–A1138, 1965.
- [34] D. Cremer, “Density functional theory: coverage of dynamic and non-dynamic electron correlation effects,” *Mol. Phys.*, vol. 99, pp. 1899–1940, 2001.

- [35] K. Burke, J. Werschnik, and E. K. U. Gross, "Time-dependent density functional theory: Past, present, and future," *J. Chem. Phys.*, vol. 123, p. 062206, 2005.
- [36] J. Olsen and P. Jørgensen, "Linear and nonlinear response functions for an exact state and for an MCSCF state," *J. Chem. Phys.*, vol. 82, pp. 3235–3264, 1985.
- [37] C. Fuchs, V. Bonačić-Koutecký, and J. Koutecký, "Compact formulation of multiconfigurational response theory. Applications to small alkali metal clusters," *J. Chem. Phys.*, vol. 98, pp. 3121–3140, 1993.
- [38] A. D. McLachlan and M. A. Ball, "Time-dependent Hartree-Fock theory for molecules," *Rev. Mod. Phys.*, vol. 36, pp. 844–855, 1964.
- [39] X. Ren, P. Rinke, C. Joas, and M. Scheffler, "Random-phase approximation and its applications in computational chemistry and materials science," *J. Mater. Sci.*, vol. 47, pp. 7447–7471, 2012.
- [40] A. Heßelmann and A. Görling, "Random-phase approximation correlation methods for molecules and solids," *Mol. Phys.*, vol. 109, pp. 2473–2500, 2011.
- [41] D. Bohm and D. Pines, "A Collective Description of Electron Interactions. I. Magnetic Interactions," *Phys. Rev.*, vol. 82, pp. 625–634, 1951.
- [42] D. J. Rowe, "Equations-of-Motion Method and the Extended Shell Model," *Rev. Mod. Phys.*, vol. 40, pp. 153–166, 1968.
- [43] S. Hirata and M. Head-Gordon, "Time-dependent density functional theory for radicals: An improved description of excited states with substantial double excitation character," *Chem. Phys. Lett.*, vol. 302, pp. 375–382, 1999.
- [44] H. Sekino and R. J. Bartlett, "A linear response, coupled-cluster theory for excitation energy," *Int. J. Quantum Chem.*, vol. 26, pp. 255–265, 1984.
- [45] J. Geertsen, M. Rittby, and R. J. Bartlett, "The equation-of-motion coupled-cluster method: Excitation energies of Be and CO," *Chem. Phys. Lett.*, vol. 164, pp. 57–62, 1989.
- [46] D. Mukherjee and P. Mukherjee, "A response-function approach to the direct calculation of the transition-energy in a multiple-cluster expansion formalism," *Chem. Phys.*, vol. 39, pp. 325–335, 1979.

- [47] M. Caricato, G. W. Trucks, and M. J. Frisch, "On the difference between the transition properties calculated with linear response- and equation of motion-CCSD approaches," *J. Chem. Phys.*, vol. 131, p. 174104, 2009.
- [48] J. F. Stanton and R. J. Bartlett, "The equation of motion coupled-cluster method. A systematic biorthogonal approach to molecular excitation energies, transition probabilities, and excited state properties," *J. Chem. Phys.*, vol. 98, pp. 7029–7039, 1993.
- [49] F. Pawłowski, J. Olsen, and P. Jørgensen, "Molecular response properties from a Hermitian eigenvalue equation for a time-periodic Hamiltonian," *J. Chem. Phys.*, vol. 142, p. 114109, 2015.
- [50] R. Faber and S. Coriani, "Resonant Inelastic X-ray Scattering and Nonresonant X-ray Emission Spectra from Coupled-Cluster (Damped) Response Theory," *J. Chem. Theory Comput.*, vol. 15, pp. 520–528, 2019.
- [51] H. Koch, R. Kobayashi, A. Sanchez de Merás, and P. Jørgensen, "Calculation of size-intensive transition moments from the coupled cluster singles and doubles linear response function," *J. Chem. Phys.*, vol. 100, pp. 4393–4400, 1994.
- [52] A. T. B. Gilbert, N. A. Besley, and P. M. W. Gill, "Self-Consistent Field Calculations of Excited States Using the Maximum Overlap Method (MOM)," *J. Phys. Chem. A*, vol. 112, pp. 13164–13171, 2008.
- [53] G. M. J. Barca, A. T. B. Gilbert, and P. M. W. Gill, "Simple Models for Difficult Electronic Excitations," *J. Chem. Theory Comput.*, vol. 14, pp. 1501–1509, 2018.
- [54] S. D. Folkestad, E. F. Kjøenstad, R. H. Myhre, J. H. Andersen, A. Balbi, S. Coriani, T. Giovannini, L. Goletto, T. S. Haugland, A. Hutcheson, I.-M. Høyvik, T. Moitra, A. C. Paul, M. Scavino, A. S. Skeidsvoll, Å. H. Tveten, and H. Koch, " e^T 1.0: An open source electronic structure program with emphasis on coupled cluster and multilevel methods," *J. Chem. Phys.*, vol. 152, p. 184103, 2020.
- [55] N. H. F. Beebe and J. Linderberg, "Simplifications in the generation and transformation of two-electron integrals in molecular calculations," *Int. J. Quantum Chem.*, vol. 12, pp. 683–705, 1977.
- [56] F. Aquilante, T. B. Pedersen, and R. Lindh, "Low-cost evaluation of the exchange Fock matrix from Cholesky and density fitting representations of the electron repulsion integrals," *J. Chem. Phys.*, vol. 126, p. 194106, 2007.

- [57] T. Helgaker and P. Jørgensen, *Calculation of Geometrical Derivatives in Molecular Electronic Structure Theory*, pp. 353–421. Boston, MA: Springer US, 1992.
- [58] K. Hald, A. Halkier, P. Jørgensen, S. Coriani, C. Hättig, and T. Helgaker, “A Lagrangian, integral-density direct formulation and implementation of the analytic CCSD and CCSD(T) gradients,” *J. Chem. Phys.*, vol. 118, pp. 2985–2998, 2003.
- [59] T. Helgaker and P. Jørgensen, “Analytical Calculation of Geometrical Derivatives in Molecular Electronic Structure Theory,” *Adv. Quant. Chem.*, vol. 19, pp. 183–245, 1988.
- [60] T. Helgaker, S. Coriani, P. Jørgensen, K. Kristensen, J. Olsen, and K. Ruud, “Recent Advances in Wave Function-Based Methods of Molecular Property Calculations,” *Chem. Rev.*, vol. 112, pp. 543–631, 2012.
- [61] A. K. Schnack-Petersen, H. Koch, S. Coriani, and E. F. Kjørstad, “Efficient implementation of molecular CCSD gradients with Cholesky-decomposed electron repulsion integrals,” *J. Chem. Phys.*, vol. 156, p. 244111, 2022.
- [62] I. E. Brumboiu, D. R. Rehn, A. Dreuw, Y. M. Rhee, and P. Norman, “Analytical gradients for core-excited states in the algebraic diagrammatic construction (ADC) framework,” *J. Chem. Phys.*, vol. 155, p. 044106, 2021.
- [63] P. Zimmermann, S. Peredkov, P. M. Abdala, S. DeBeer, M. Tromp, C. Müller, and J. A. van Bokhoven, “Modern X-ray spectroscopy: XAS and XES in the laboratory,” *Coordin. Chem. Rev.*, vol. 423, p. 213466, 2020.
- [64] P. Norman and A. Dreuw, “Simulating X-ray Spectroscopies and Calculating Core-Excited States of Molecules,” *Chem. Rev.*, vol. 118, pp. 7208–7248, 2018.
- [65] Y. Shao, Z. Gan, E. Epifanovsky, A. T. Gilbert, M. Wormit, J. Kussmann, A. W. Lange, A. Behn, J. Deng, X. Feng, D. Ghosh, M. Goldey, P. R. Horn, L. D. Jacobson, I. Kaliman, R. Z. Khaliullin, T. Kuś, A. Landau, J. Liu, E. I. Proynov, Y. M. Rhee, R. M. Richard, M. A. Rohrdanz, R. P. Steele, E. J. Sundstrom, H. L. W. III, P. M. Zimmerman, D. Zuev, B. Albrecht, E. Alguire, B. Austin, G. J. O. Beran, Y. A. Bernard, E. Berquist, K. Brandhorst, K. B. Bravaya, S. T. Brown, D. Casanova, C.-M. Chang, Y. Chen, S. H. Chien, K. D. Closser, D. L. Crittenden, M. Diedenhofen, R. A. D. Jr., H. Do, A. D. Dutoi, R. G. Edgar, S. Fatehi, L. Fusti-Molnar, A. Ghysels, A. Golubeva-Zadorozhnaya, J. Gomes, M. W. Hanson-Heine,

- P. H. Harbach, A. W. Hauser, E. G. Hohenstein, Z. C. Holden, T.-C. Jagau, H. Ji, B. Kaduk, K. Khistyayev, J. Kim, J. Kim, R. A. King, P. Klunzinger, D. Kosenkov, T. Kowalczyk, C. M. Krauter, K. U. Lao, A. D. Laurent, K. V. Lawler, S. V. Levchenko, C. Y. Lin, F. Liu, E. Livshits, R. C. Lochan, A. Luenser, P. Manohar, S. F. Manzer, S.-P. Mao, N. Mardirossian, A. V. Marenich, S. A. Maurer, N. J. Mayhall, E. Neuscamman, C. M. Oana, R. Olivares-Amaya, D. P. O'Neill, J. A. Parkhill, T. M. Perrine, R. Peverati, A. Prociuk, D. R. Rehn, E. Rosta, N. J. Russ, S. M. Sharada, S. Sharma, D. W. Small, A. Sodt, T. Stein, D. Stück, Y.-C. Su, A. J. Thom, T. Tsuchimochi, V. Vanovschi, L. Vogt, O. Vydrov, T. Wang, M. A. Watson, J. Wenzel, A. White, C. F. Williams, J. Yang, S. Yeganeh, S. R. Yost, Z.-Q. You, I. Y. Zhang, X. Zhang, Y. Zhao, B. R. Brooks, G. K. Chan, D. M. Chipman, C. J. Cramer, W. A. G. III, M. S. Gordon, W. J. Hehre, A. Klamt, H. F. S. III, M. W. Schmidt, C. D. Sherrill, D. G. Truhlar, A. Warshel, X. Xu, A. Aspuru-Guzik, R. Baer, A. T. Bell, N. A. Besley, J.-D. Chai, A. Dreuw, B. D. Dunietz, T. R. Furlani, S. R. Gwaltney, C.-P. Hsu, Y. Jung, J. Kong, D. S. Lambrecht, W. Liang, C. Ochsenfeld, V. A. Rassolov, L. V. Slipchenko, J. E. Subotnik, T. V. Voorhis, J. M. Herbert, A. I. Krylov, P. M. Gill, and M. Head-Gordon, "Advances in molecular quantum chemistry contained in the Q-Chem 4 program package," *Mol. Phys.*, vol. 113, pp. 184–215, 2015.
- [66] M. L. Vidal, X. Feng, E. Epifanovsky, A. I. Krylov, and S. Coriani, "New and Efficient Equation-of-Motion Coupled-Cluster Framework for Core-Excited and Core-Ionized States," *J. Chem. Theory Comput.*, vol. 15, pp. 3117–3133, 2019.
- [67] M. L. Vidal, A. I. Krylov, and S. Coriani, "Dyson orbitals within the fc-CVS-EOM-CCSD framework: Theory and application to X-ray photoelectron spectroscopy of ground and excited states," *Phys. Chem. Chem. Phys.*, vol. 22, pp. 2693–2703, 2020.
- [68] F. Neese, "The ORCA program system," *WIREs Comput. Mol. Sci.*, vol. 2, pp. 73–78, 2012.
- [69] E. R. Davidson, "The iterative calculation of a few of the lowest eigenvalues and corresponding eigenvectors of large real-symmetric matrices," *J. Comput. Phys.*, vol. 17, pp. 87–94, 1975.
- [70] L. S. Cederbaum, W. Domcke, and J. Schirmer, "Many-body theory of core holes," *Phys. Rev. A*, vol. 22, pp. 206–222, 1980.

- [71] S. Coriani and H. Koch, “Communication: X-ray absorption spectra and core-ionization potentials within a core-valence separated coupled cluster framework,” *J. Chem. Phys.*, vol. 143, p. 181103, 2015.
- [72] K. D. Nanda and A. I. Krylov, “Cherry-picking resolvents: A general strategy for convergent coupled-cluster damped response calculations of core-level spectra,” *J. Chem. Phys.*, vol. 153, p. 141104, 2020.
- [73] E. S. Sachs, J. Hinze, and N. H. Sabelli, “Frozen core approximation, a pseudopotential method tested on six states of NaH,” *J. Chem. Phys.*, vol. 62, pp. 3393–3398, 1975.
- [74] J. F. Stanton and J. Gauss, “Analytic energy derivatives for ionized states described by the equation-of-motion coupled cluster method,” *J. Chem. Phys.*, vol. 101, pp. 8938–8944, 1994.
- [75] T. Moitra, A. Ponzi, H. Koch, S. Coriani, and P. Decleva, “Accurate Description of Photoionization Dynamical Parameters,” *J. Phys. Chem. Lett.*, vol. 11, pp. 5330–5337, 2020.
- [76] L. J. P. Ament, M. van Veenendaal, T. P. Devereaux, J. P. Hill, and J. van den Brink, “Resonant inelastic x-ray scattering studies of elementary excitations,” *Rev. Mod. Phys.*, vol. 83, pp. 705–767, 2011.
- [77] D. R. Rehn, A. Dreuw, and P. Norman, “Resonant Inelastic X-ray Scattering Amplitudes and Cross Sections in the Algebraic Diagrammatic Construction/Intermediate State Representation (ADC/ISR) Approach,” *J. Chem. Theory Comput.*, vol. 13, pp. 5552–5559, 2017.
- [78] K. D. Nanda, M. L. Vidal, R. Faber, S. Coriani, and A. I. Krylov, “How to stay out of trouble in RIXS calculations within equation-of-motion coupled-cluster damped response theory? Safe hitchhiking in the excitation manifold by means of core–valence separation,” *Phys. Chem. Chem. Phys.*, vol. 22, pp. 2629–2641, 2020.
- [79] P. Norman, D. M. Bishop, H. J. Aa. Jensen, and J. Oddershede, “Near-resonant absorption in the time-dependent self-consistent field and multiconfigurational self-consistent field approximations,” *J. Chem. Phys.*, vol. 115, pp. 10323–10334, 2001.
- [80] P. Norman, D. M. Bishop, H. J. Aa. Jensen, and J. Oddershede, “Nonlinear response theory with relaxation: The first-order hyperpolarizability,” *J. Chem. Phys.*, vol. 123, p. 194103, 2005.

- [81] L. Jensen, J. Autschbach, and G. C. Schatz, "Finite lifetime effects on the polarizability within time-dependent density-functional theory," *J. Chem. Phys.*, vol. 122, p. 224115, 2005.
- [82] S. Coriani, T. Fransson, O. Christiansen, and P. Norman, "Asymmetric-Lanczos-Chain-Driven Implementation of Electronic Resonance Convergent Coupled-Cluster Linear Response Theory," *J. Chem. Theory Comput.*, vol. 8, pp. 1616–1628, 2012.
- [83] S. Coriani, O. Christiansen, T. Fransson, and P. Norman, "Coupled-cluster response theory for near-edge x-ray-absorption fine structure of atoms and molecules," *Phys. Rev. A*, vol. 85, p. 022507, 2012.
- [84] T. Fransson, D. R. Rehn, A. Dreuw, and P. Norman, "Static polarizabilities and C6 dispersion coefficients using the algebraic-diagrammatic construction scheme for the complex polarization propagator," *J. Chem. Phys.*, vol. 146, p. 094301, 2017.
- [85] J. Kauczor, P. Norman, O. Christiansen, and S. Coriani, "Communication: A reduced-space algorithm for the solution of the complex linear response equations used in coupled cluster damped response theory," *J. Chem. Phys.*, vol. 139, p. 211102, 2013.
- [86] J. Kauczor and P. Norman, "Efficient Calculations of Molecular Linear Response Properties for Spectral Regions," *J. Chem. Theory Comput.*, vol. 10, pp. 2449–2455, 2014.
- [87] M. Scheurer, T. Fransson, P. Norman, A. Dreuw, and D. R. Rehn, "Complex excited state polarizabilities in the ADC/ISR framework," *J. Chem. Phys.*, vol. 153, p. 074112, 2020.
- [88] P. Reinholdt, M. S. Nørby, and J. Kongsted, "Modeling of Magnetic Circular Dichroism and UV/Vis Absorption Spectra Using Fluctuating Charges or Polarizable Embedding within a Resonant-Convergent Response Theory Formalism," *J. Chem. Theory Comput.*, vol. 14, pp. 6391–6404, 2018.
- [89] M. S. Nørby, S. Coriani, and J. Kongsted, "Modeling magnetic circular dichroism within the polarizable embedding approach," *Theor. Chem. Acc.*, vol. 137, p. 49, 2018.
- [90] L. Konecny, M. Repisky, K. Ruud, and S. Komorovsky, "Relativistic four-component linear damped response TDDFT for electronic absorption and circular dichroism calculations," *J. Chem. Phys.*, vol. 151, p. 194112, 2019.

- [91] W. Skomorowski and A. I. Krylov, “Feshbach–Fano approach for calculation of Auger decay rates using equation-of-motion coupled-cluster wave functions. I. Theory and implementation,” *J. Chem. Phys.*, vol. 154, p. 084124, 2021.
- [92] W. Skomorowski and A. I. Krylov, “Feshbach–Fano approach for calculation of Auger decay rates using equation-of-motion coupled-cluster wave functions. II. Numerical examples and benchmarks,” *J. Chem. Phys.*, vol. 154, p. 084125, 2021.
- [93] B. N. C. Tenorio, T. A. Voß, S. I. Bokarev, P. Decleva, and S. Coriani, “Multireference Approach to Normal and Resonant Auger Spectra Based on the One-Center Approximation,” *J. Chem. Theory Comput.*, vol. 18, pp. 4387–4407, 2022.
- [94] T. Åberg, “Theory of the Radiative Auger Effect,” *Phys. Rev. A*, vol. 4, pp. 1735–1740, 1971.
- [95] T. Moitra, A. C. Paul, P. Decleva, H. Koch, and S. Coriani, “Multi-electron excitation contributions towards primary and satellite states in the photo-electron spectrum,” *Phys. Chem. Chem. Phys.*, vol. 24, pp. 8329–8343, 2022.
- [96] V. Jain, M. C. Biesinger, and M. R. Linford, “The Gaussian-Lorentzian Sum, Product, and Convolution (Voigt) functions in the context of peak fitting X-ray photoelectron spectroscopy (XPS) narrow scans,” *Appl. Surf. Sci.*, vol. 447, pp. 548–553, 2018.
- [97] J. Pitha and R. N. Jones, “A Comparison of Optimization Methods for Fitting Curves to Infrared Band Envelopes,” *Can. J. Chem.*, vol. 44, pp. 3031–3050, 1966.
- [98] J. P. Malhado, M. J. Bearpark, and J. T. Hynes, “Non-adiabatic dynamics close to conical intersections and the surface hopping perspective,” *Front. Chem.*, vol. 2, pp. 1–21, 2014.
- [99] E. J. Heller, “Time-dependent approach to semiclassical dynamics,” *J. Chem. Phys.*, vol. 62, pp. 1544–1555, 1975.
- [100] M. Beck, A. Jäckle, G. Worth, and H.-D. Meyer, “The multiconfiguration time-dependent Hartree (MCTDH) method: a highly efficient algorithm for propagating wavepackets,” *Phys. Rep.*, vol. 324, pp. 1–105, 2000.

- [101] M. Richter, P. Marquetand, J. González-Vázquez, I. Sola, and L. González, “SHARC: ab initio Molecular Dynamics with Surface Hopping in the Adiabatic Representation Including Arbitrary Couplings,” *J. Chem. Theory Comput.*, vol. 7, pp. 1253–1258, 2011.
- [102] J. C. Tully, “Molecular dynamics with electronic transitions,” *J. Chem. Phys.*, vol. 93, pp. 1061–1071, 1990.
- [103] M. Ben-Nun, J. Quenneville, and T. J. Martínez, “Ab Initio Multiple Spawning: Photochemistry from First Principles Quantum Molecular Dynamics,” *J. Phys. Chem. A*, vol. 104, pp. 5161–5175, 2000.
- [104] H.-D. Meyer, U. Manthe, and L. Cederbaum, “The multi-configurational time-dependent Hartree approach,” *Chem. Phys. Lett.*, vol. 165, pp. 73–78, 1990.
- [105] S. Mai, M. Richter, M. Heindl, M. F. S. J. Menger, A. Atkins, M. Ruckebauer, F. Plasser, L. M. Ibele, S. Kropf, M. Oppel, P. Marquetand, and L. González, “SHARC2.1: Surface Hopping Including Arbitrary Couplings — Program Package for Non-Adiabatic Dynamics.” sharc-md.org, 2019.
- [106] S. Mai, P. Marquetand, and L. González, “Nonadiabatic Dynamics: The SHARC Approach,” *WIREs Comput. Mol. Sci.*, vol. 8, p. e1370, 2018.
- [107] G. A. Worth, M. H. Beck, A. Jäckle, and H.-D. Meyer, “The MCTDH Package-8.4.12,” 2016.
- [108] G. Granucci, M. Persico, and A. Toniolo, “Direct semiclassical simulation of photochemical processes with semiempirical wave functions,” *J. Chem. Phys.*, vol. 114, pp. 10608–10615, 2001.
- [109] S. Mai, P. Marquetand, and L. González, “A general method to describe intersystem crossing dynamics in trajectory surface hopping,” *Int. J. Quantum Chem.*, vol. 115, pp. 1215–1231, 2015.
- [110] E. Wigner, “On the Quantum Correction For Thermodynamic Equilibrium,” *Phys. Rev.*, vol. 40, pp. 749–759, 1932.
- [111] M. Hillery, R. O’Connell, M. Scully, and E. Wigner, “Distribution functions in physics: Fundamentals,” *Phys. Rep.*, vol. 106, pp. 121–167, 1984.
- [112] M. Barbatti and K. Sen, “Effects of different initial condition samplings on photodynamics and spectrum of pyrrole,” *Int. J. Quantum Chem.*, vol. 116, pp. 762–771, 2016.

- [113] M. Barbatti, G. Granucci, M. Persico, M. Ruckebauer, M. Vazdar, M. Eckert-Maksić, and H. Lischka, “The on-the-fly surface-hopping program system Newton-X: Application to ab initio simulation of the nonadiabatic photodynamics of benchmark systems,” *J. Photoch. Photobio. A*, vol. 190, pp. 228–240, 2007.
- [114] M. Barbatti, M. Ruckebauer, F. Plasser, J. Pittner, G. Granucci, M. Persico, and H. Lischka, “Newton-X: a surface-hopping program for nonadiabatic molecular dynamics,” *WIREs Comput. Mol. Sci.*, vol. 4, pp. 26–33, 2014.
- [115] W. Xie, M. Sapunar, N. Došlić, M. Sala, and W. Domcke, “Assessing the performance of trajectory surface hopping methods: Ultrafast internal conversion in pyrazine,” *J. Chem. Phys.*, vol. 150, p. 154119, 2019.
- [116] M. Abedi, M. Pápai, K. V. Mikkelsen, N. E. Henriksen, and K. B. Møller, “Mechanism of Photoinduced Dihydroazulene Ring-Opening Reaction,” *J. Phys. Chem. Lett.*, vol. 10, pp. 3944–3949, 2019.
- [117] M. Pápai, X. Li, M. M. Nielsen, and K. B. Møller, “Trajectory surface-hopping photoinduced dynamics from Rydberg states of trimethylamine,” *J. Phys. Chem. Chem. Phys.*, vol. 23, pp. 10964–10977, 2021.
- [118] A. K. Schnack-Petersen, M. Pápai, and K. B. Møller, “Azobenzene photoisomerization dynamics: Revealing the key degrees of freedom and the long timescale of the trans-to-cis process,” *J. Photoch. Photobio. A*, vol. 428, p. 113869, 2022.
- [119] B. G. Levine, C. Ko, J. Quenneville, and T. J. Martínez, “Conical intersections and double excitations in time-dependent density functional theory,” *Mol. Phys.*, vol. 104, pp. 1039–1051, 2006.
- [120] L. Yue, Y. Liu, and C. Zhu, “Performance of TDDFT with and without spin-flip in trajectory surface hopping dynamics: cis–trans azobenzene photoisomerization,” *J. Phys. Chem. Chem. Phys.*, vol. 20, pp. 24123–24139, 2018.
- [121] G. Granucci, M. Persico, and A. Zocante, “Including quantum decoherence in surface hopping,” *J. Chem. Phys.*, vol. 133, p. 134111, 2010.
- [122] A. Jain, E. Alguire, and J. E. Subotnik, “An Efficient, Augmented Surface Hopping Algorithm That Includes Decoherence for Use in Large-Scale Simulations,” *J. Chem. Theory Comput.*, vol. 12, pp. 5256–5268, 2016.
- [123] B. Auer and S. Hammes-Schiffer, “Localized Hartree product treatment of multiple protons in the nuclear-electronic orbital framework,” *J. Chem. Phys.*, vol. 132, p. 084110, 2010.

- [124] A. Raab, G. A. Worth, H.-D. Meyer, and L. S. Cederbaum, "Molecular dynamics of pyrazine after excitation to the S_2 electronic state using a realistic 24-mode model Hamiltonian," *J. Chem. Phys.*, vol. 110, pp. 936–946, 1999.
- [125] G. Worth, H.-D. Meyer, and L. Cederbaum, "State filtering by a bath: up to 24 mode numerically exact wavepacket propagations," *Chem. Phys. Lett.*, vol. 299, pp. 451–456, 1999.
- [126] S. Mukherjee, M. Pinheiro, B. Demoulin, and M. Barbatti, "Simulations of molecular photodynamics in long timescales," *Philos. T. Roy. Soc. A*, vol. 380, p. 20200382, 2022.
- [127] S. Han, M. Schröder, F. Gatti, H.-D. Meyer, D. Lauvergnat, D. R. Yarkony, and H. Guo, "Representation of Diabatic Potential Energy Matrices for Multiconfiguration Time-Dependent Hartree Treatments of High-Dimensional Nonadiabatic Photodissociation Dynamics," *J. Chem. Theory Comput.*, vol. 18, pp. 4627–4638, 2022.
- [128] G. A. Worth, H.-D. Meyer, and L. S. Cederbaum, *Multidimensional Dynamics Involving a Conical Intersection: Wavepacket Calculations using the MCTDH Method*, pp. 583–617. World Scientific Publishing Co. Pte. Ltd., 2004.
- [129] H. Köuppel, W. Domcke, and L. S. Cederbaum, *Multimode Molecular Dynamics Beyond the Born-Oppenheimer Approximation*, pp. 59–246. John Wiley & Sons, Ltd, 1984.
- [130] A. Lehr, S. Gómez, M. A. Parkes, and G. A. Worth, "The role of vibronic coupling in the electronic spectroscopy of maleimide: a multi-mode and multi-state quantum dynamics study," *Phys. Chem. Chem. Phys.*, vol. 22, pp. 25272–25283, 2020.
- [131] G. A. Worth, M. H. Beck, A. Jäckle, and H.-D. Meyer, "The MCTDH Package-8.5.16," 2022.
- [132] Z. Jin, "Muscarine, imidazole, oxazole and thiazole alkaloids," *Nat. Prod. Rep.*, vol. 33, pp. 1268–1317, 2016.
- [133] P. Lokwani, B. P. Nagori, N. Batra, A. Goyal, S. Gupta, and N. Singh, "Benzoxazole: The molecule of diverse biological activities," *J. Chem. Pharm. Res.*, vol. 3, pp. 302–311, 2011.
- [134] C. W. Lee, O. Y. Kim, and J. Y. Lee, "Organic materials for organic electronic devices," *J. Ind. Eng. Chem.*, vol. 20, pp. 1198–1208, 2014.

- [135] R. Blyth, R. Delaunay, M. Zitnik, J. Krempasky, R. Krempaska, J. Slezak, K. Prince, R. Richter, M. Vondracek, R. Camilloni, L. Avaldi, M. Coreno, G. Stefani, C. Furlani, M. de Simone, S. Stranges, and M.-Y. Adam, "The high resolution Gas Phase Photoemission beamline, Elettra," *J. Electron Spectrosc.*, vol. 101-103, pp. 959–964, 1999.
- [136] A. K. Schnack-Petersen, B. N. C. Tenorio, S. Coriani, P. Decleva, J. Troß, K. Ramasesha, M. Coreno, R. Totani, and A. Röder, "Core spectroscopy of oxazole," *J. Chem. Phys.*, vol. 157, p. 214305, 2022.
- [137] D. P. Chong and C.-H. Hu, "Accurate density functional calculation of core-electron binding energies with a scaled polarized triple-zeta basis set. IV. Application to isomers of C_3H_6O , C_3H_3NO , and C_6H_6 ," *J. Chem. Phys.*, vol. 108, pp. 8950–8956, 1998.
- [138] T. J. Wasowicz, I. Ljubić, A. Kivimäki, and R. Richter, "Core-shell excitation of isoxazole at the C, N, and O K-edges – an experimental NEX-AFS and theoretical TD-DFT study," *Phys. Chem. Chem. Phys.*, vol. 24, pp. 19302–19313, 2022.
- [139] S. Coriani, O. Christiansen, T. Fransson, and P. Norman, "Coupled-cluster response theory for near-edge x-ray-absorption fine structure of atoms and molecules," *Phys. Rev. A*, vol. 85, p. 022507, 2012.
- [140] P. J. Lestranger, P. D. Nguyen, and X. Li, "Calibration of Energy-Specific TDDFT for Modeling K-edge XAS Spectra of Light Elements," *J. Chem. Theory Comput.*, vol. 11, pp. 2994–2999, 2015.
- [141] M. J. Thomason, *Soft X-ray Spectroscopy of Molecular Species in Solution: Studies of Imidazole and Imidazole/Water Systems*. PhD thesis, University of Manchester, 2012.
- [142] E. Bundgaard and F. C. Krebs, "Low band gap polymers for organic photovoltaics," *Sol. Energ. Mat. Sol. C.*, vol. 91, pp. 954–985, 2007.
- [143] G. Li, R. Zhu, and Y. Yang, "Polymer solar cells," *Nat. Photonics*, vol. 6, p. 153–161, 2012.
- [144] D. Raychev, O. Guskova, G. Seifert, and J.-U. Sommer, "Conformational and electronic properties of small benzothiadiazole-cored oligomers with aryl flanking units: Thiophene versus Furan," *Comp. Mater. Sci.*, vol. 126, pp. 287–298, 2017.

- [145] K. Khalili, L. Inhester, C. Arnold, A. S. Gertsen, J. W. Andreasen, and R. Santra, "Simulation of time-resolved x-ray absorption spectroscopy of ultrafast dynamics in particle-hole-excited 4-(2-thienyl)-2,1,3-benzothiadiazole," *Struct. Dynam.*, vol. 7, p. 044101, 2020.
- [146] K. Khalili, L. Inhester, C. Arnold, R. Welsch, J. W. Andreasen, and R. Santra, "Hole dynamics in a photovoltaic donor-acceptor couple revealed by simulated time-resolved X-ray absorption spectroscopy," *Struct. Dynam.*, vol. 6, p. 044102, 2019.
- [147] S. Manikandan, C. B. C. da Silveira, E. V. Beale, C. Cirelli, S. Coriani, A. O. Dohn, K. Haldrup, B. L. Hansen, M. L. Haubro, P. Johnson, V. Kabanova, A. Kahraman, T. I. M. Kapunan, K. Mitterer, K. B. Møller, M. M. Nielsen, A. K. Schnack-Petersen, and J. W. Andreasen, "An experimental and theoretical investigation of BT-1T based on time-resolved X-ray absorption spectroscopy." In preparation.
- [148] K. Aidas, C. Angeli, K. L. Bak, V. Bakken, R. Bast, L. Boman, O. Christiansen, R. Cimiraglia, S. Coriani, P. Dahle, E. K. Dalskov, U. Ekström, T. Enevoldsen, J. J. Eriksen, P. Ettenhuber, B. Fernández, L. Ferrighi, H. Fliegler, L. Frediani, K. Hald, A. Halkier, C. Hättig, H. Heiberg, T. Helgaker, A. C. Hennum, H. Hettema, E. Hjertenæs, S. Høst, I.-M. Høyvik, M. F. Iozzi, B. Jansík, H. J. Aa. Jensen, D. Jonsson, P. Jørgensen, J. Kauczor, S. Kirpekar, T. Kjærgaard, W. Klopper, S. Knecht, R. Kobayashi, H. Koch, J. Kongsted, A. Krapp, K. Kristensen, A. Ligabue, O. B. Lutnæs, J. I. Melo, K. V. Mikkelsen, R. H. Myhre, C. Neiss, C. B. Nielsen, P. Norman, J. Olsen, J. M. H. Olsen, A. Osted, M. J. Packer, F. Pawłowski, T. B. Pedersen, P. F. Provasi, S. Reine, Z. Rinkevicius, T. A. Ruden, K. Ruud, V. V. Rybkin, P. Salek, C. C. M. Samson, A. S. de Merás, T. Saue, S. P. A. Sauer, B. Schimmelpfennig, K. Sneskov, A. H. Steindal, K. O. Sylvester-Hvid, P. R. Taylor, A. M. Teale, E. I. Tellgren, D. P. Tew, A. J. Thorvaldsen, L. Thøgersen, O. Vahtras, M. A. Watson, D. J. D. Wilson, M. Ziolkowski, and H. Ågren, "The Dalton quantum chemistry program system," *WIREs Comput. Mol. Sci.*, vol. 4, pp. 269–284, 2014.
- [149] J. M. H. Olsen, S. Reine, O. Vahtras, E. Kjøllgren, P. Reinholdt, K. O. Hjørth Dundas, X. Li, J. Cukras, M. Ringholm, E. D. Hedegård, R. Di Remigio, N. H. List, R. Faber, B. N. Cabral Tenorio, R. Bast, T. B. Pedersen, Z. Rinkevicius, S. P. A. Sauer, K. V. Mikkelsen, J. Kongsted, S. Coriani, K. Ruud, T. Helgaker, H. J. Aa. Jensen, and P. Norman, "Dalton Project: A Python platform for molecular- and electronic-structure simulations of complex systems," *J. Chem. Phys.*, vol. 152, p. 214115, 2020.

- [150] S. Tsuru, M. L. Vidal, M. Pápai, A. I. Krylov, K. B. Møller, and S. Coriani, “An assessment of different electronic structure approaches for modeling time-resolved x-ray absorption spectroscopy,” *Struct. Dynam.*, vol. 8, p. 024101, 2021.
- [151] E. Wei-Guang Diao, “A New Trans-to-Cis Photoisomerization Mechanism of Azobenzene on the $S_1(n,\pi^*)$ Surface,” *J. Phys. Chem. A*, vol. 108, pp. 950–956, 2004.
- [152] M. Böckmann, N. L. Doltsinis, and D. Marx, “Azobenzene photoswitches in bulk materials,” *Phys. Rev. E*, vol. 78, p. 036101, 2008.
- [153] M. Böckmann, N. L. Doltsinis, and D. Marx, “Nonadiabatic Hybrid Quantum and Molecular Mechanic Simulations of Azobenzene Photoswitching in Bulk Liquid Environment,” *J. Phys. Chem. A*, vol. 114, pp. 745–754, 2010.
- [154] J. A. Gámez, O. Weingart, A. Koslowski, and W. Thiel, “Cooperating Dinitrogen and Phenyl Rotations in trans-Azobenzene Photoisomerization,” *J. Chem. Theory Comput.*, vol. 8, pp. 2352–2358, 2012.
- [155] P. Tavadze, G. Avendaño Franco, P. Ren, X. Wen, Y. Li, and J. P. Lewis, “A Machine-Driven Hunt for Global Reaction Coordinates of Azobenzene Photoisomerization,” *J. Am. Chem. Soc.*, vol. 140, pp. 285–290, 2018.
- [156] F. Aleotti, L. Soprani, A. Nenov, R. Berardi, A. Arcioni, C. Zannoni, and M. Garavelli, “Multidimensional Potential Energy Surfaces Resolved at the RASPT2 Level for Accurate Photoinduced Isomerization Dynamics of Azobenzene,” *J. Chem. Theory Comput.*, vol. 15, pp. 6813–6823, 2019.
- [157] D. Keefer, F. Aleotti, J. R. Rouxel, F. Segatta, B. Gu, A. Nenov, M. Garavelli, and S. Mukamel, “Imaging conical intersection dynamics during azobenzene photoisomerization by ultrafast X-ray diffraction,” *Proc. Natl. Acad. Sci. U.S.A.*, vol. 118, p. e2022037118, 2021.
- [158] H. M. Bandara and S. C. Burdette, “Photoisomerization in different classes of azobenzene,” *Chem. Soc. Rev.*, vol. 41, pp. 1809–1825, 2012.
- [159] L. Ye, C. Xu, F. L. Gu, and C. Zhu, “Functional and Basis Set Dependence for Time-Dependent Density Functional Theory Trajectory Surface Hopping Molecular Dynamics: Cis-Azobenzene Photoisomerization,” *J. Comput. Chem.*, vol. 41, pp. 635–645, 2020.
- [160] M. Pederzoli, J. Pittner, M. Barbatti, and H. Lischka, “Nonadiabatic Molecular Dynamics Study of the cis–trans Photoisomerization of Azobenzene

- Excited to the S1 State,” *J. Phys. Chem. A*, vol. 115, pp. 11136–11143, 2011.
- [161] C. M. Breneman and K. B. Wiberg, “Determining atom-centered monopoles from molecular electrostatic potentials. The need for high sampling density in formamide conformational analysis,” *J. Comput. Chem.*, vol. 11, pp. 361–373, 1990.
- [162] M. J. Frisch, G. W. Trucks, H. B. Schlegel, G. E. Scuseria, M. A. Robb, J. R. Cheeseman, G. Scalmani, V. Barone, G. A. Petersson, H. Nakatsuji, X. Li, M. Caricato, A. V. Marenich, J. Bloino, B. G. Janesko, R. Gomperts, B. Mennucci, H. P. Hratchian, J. V. Ortiz, A. F. Izmaylov, J. L. Sonnenberg, D. Williams-Young, F. Ding, F. Lipparini, F. Egidi, J. Goings, B. Peng, A. Petrone, T. Henderson, D. Ranasinghe, V. G. Zakrzewski, J. Gao, N. Rega, G. Zheng, W. Liang, M. Hada, M. Ehara, K. Toyota, R. Fukuda, J. Hasegawa, M. Ishida, T. Nakajima, Y. Honda, O. Kitao, H. Nakai, T. Vreven, K. Throssell, J. A. Montgomery, Jr., J. E. Peralta, F. Ogliaro, M. J. Bearpark, J. J. Heyd, E. N. Brothers, K. N. Kudin, V. N. Staroverov, T. A. Keith, R. Kobayashi, J. Normand, K. Raghavachari, A. P. Rendell, J. C. Burant, S. S. Iyengar, J. Tomasi, M. Cossi, J. M. Millam, M. Klene, C. Adamo, R. Cammi, J. W. Ochterski, R. L. Martin, K. Morokuma, O. Farkas, J. B. Foresman, and D. J. Fox, “Gaussian 16 Revision C.01,” 2016.

